PLASTIC HINGING BEHAVIOR OF REINFORCED CONCRETE BRIDGE COLUMNS

BY

Zeynep Firat Alemdar

Submitted to the graduate degree program in Civil Engineering and the Graduate Faculty of the University of Kansas in partial fulfillment of the requirements for the degree of Doctor of Philosophy.

_____

Chairperson

Committee Members*:

_____ *

_____ *

_____ *

_____ *

Date Defended: April 26, 2010

The Dissertation Committee for Zeynep Firat Alemdar certifies
that this is the approved version of the following dissertation:

PLASTIC HINGING BEHAVIOR OF REINFORCED CONCRETE BRIDGE

COLUMNS

Committee:

_____
Chairperson

_____

_____

_____

_____

Date approved: _____

ABSTRACT

The location of inelastic deformations in reinforced concrete bridge columns has been examined to simulate the nonlinear response of bridge columns and estimate the ultimate displacement capacity. In bridge columns, these nonlinear deformations generally occur over a finite hinge length. A model of hinging behavior in reinforced concrete bridge columns will help guide proportioning, detailing and drift estimates for performance-based design. Data was collected during the NEESR investigation of the seismic performance of four-span large-scale bridge systems at the University of Nevada Reno that details deformations in column hinging regions during response to strong shaking events. In order to evaluate the plastic hinging regions, a photogrammetric method was used to remotely track deformations of the concrete surface in the joint regions. The surface deformations and rotations of a reinforced concrete bridge column under dynamic loading has been examined and compared with the results obtained from traditional instruments.

This research utilized the experimental data from photogrammetry measurements of bridge column deformations to create a finite element model that realistically represents hinging behavior in a reinforced concrete bridge pier. The three dimensional finite element model of one column was defined with the cap beam on the top of the column and the footing system under the circular column using ABAQUS Finite Element software. The results of the FE model of the bridge column under dynamic loading were obtained and compared with the photogrammetric measurements as well as the data from the traditional instrumentations.

Two plastic hinge length expressions for reinforced concrete bridge columns under static and dynamic loadings have been developed by studying the available test results in the literature. Many of the previous tests were conducted using the static loading and for small-scale components. A few of the tests focused on bridge columns and dynamic loading. Expressions that have been developed to estimate the plastic hinge lengths have either been based on the maximum drift at the top of the column, or the spread of plasticity in the hinging regions. An expression to calculate the maximum drift capacity of a bridge column in double curvature has been derived by considering the deformations due to flexure as influenced by the definition of plastic hinge length (l_p), and the bond-slip effect of the longitudinal reinforcement at the connections. Drift capacity of a bridge column, which corresponds to a 20% reduction in lateral load capacity on the descending branch of the response backbone curve, has been estimated using the new expression and compared with the results that were obtained from the earlier plastic hinge length expressions. The measured drift of the bridge column from the four-span large-scale bridge system test was also compared with the calculated responses from the expressions. The proposed equations provide the best estimate of plastic hinge length for reinforced concrete bridge columns.

ACKNOWLEDGEMENTS

I want to express my sincere gratitude to my advisors, Professors JoAnn Browning and Adolfo Matamoros, for their commitment, guidance, support, and advice throughout my research at the University of Kansas. I would like to thank Dr. Stan Rolfe, Dr. Francis Thomas, and Dr. Daniel Stockli for serving on my dissertation committee.

I would also like to thank for the effort made by the laboratory manager, Patrick Laplace, and a master student, Robbie Nelson, at the University of Nevada Reno. I also want to express gratitude to my colleague, Nick Hunt, for the countless discussions and help about research.

This dissertation is dedicated to my family, especially to my husband, Fatih Alemdar, for his great support and encouragement.

Zeynep Firat Alemdar

TABLE OF CONTENTS

LIST OF TABLES FOR CHAPTERS 1 AND 2

LIST OF FIGURES FOR CHAPTERS 1 AND 2

LIST OF NOTATION

ϕ_p : Plastic curvature

ϕ_m : The maximum curvature

ϕ_y : Curvature at first yield

ϕ_u : The ultimate curvature

l_p : The plastic hinge length

l : The height of a column

Δ_p : The plastic displacement

d : Distance from extreme compression fiber to centroid of tension reinforcement, in. (mm)

w : Uniformly distributed load at a section of maximum moment kip/in., (kN/mm)

V_z : Shear adjacent to a concentrated load or reaction at a section of maximum moment kips, (kN)

M_m : Maximum moment in a length of member kip-in., (kN.mm)

M_e : Elastic-limit resisting moment kip-in., (kN.mm)

M_u : Ultimate resisting moment concurrent with Pu kip-in., (kN.mm)

P_u : Ultimate resisting axial load kips, (kN)

ε_{cue} : Elastic component of ε_{cu}, either calculated or assumed in the range 0.001 to 0.002,

ε_{cu} : Maximum compressive strain in concrete at Mu and Pu, and

ε_{cuo} : Basic maximum compressive strain in concrete

θ_p : The plastic rotation,

k_1 : The influence of the type of reinforcing steel,

k_2 : The influence of column load (when present)

k_3 : The influence of strength of concrete

z : The distance of critical section to point of contraflexure

P : The column load acting in conjunction with bending moment,

P_u : The load capacity as an axially loaded column

c_u : The cube strength of concrete.

d_b : The longitudinal bar diameter

P_e : The design compressive load of the column due to gravity and seismic loading

ϕ : Strength reduction factor

A_g : Gross area of column section, in^2, (mm^2).

A_{ch} : Area of core concrete measured out-to-out of transverse reinforcement

f_{yt} : Yield strength of transverse reinforcement

s : Spacing of transverse reinforcement

b_c : Cross sectional dimension of column core, measured center-to-center of transverse reinforcement

1 INTRODUCTION

1.1 GENERAL

The determination of magnitude and location of inelastic deformations in reinforced concrete bridge columns is a critical step for characterizing the performance of the bridge system in earthquake events. Although it is possible to believe that some ductility will be provided by beam hinges in bridge systems, it is generally the columns of the bridges that must have inelastic rotational capacity. Bridge systems are designed to keep inelastic behavior in the columns and away from the superstructure, which is different than building systems.

If inelastic flexural deformations occur in a reinforced concrete structure due to gravity and lateral loads, these deformations can generally be considered as concentrated over a finite hinge length. The spread of plasticity, or hinge length is an important factor in the analysis of deformation in reinforced concrete bridge structures and includes elastic, plastic and softening stages of response. Little work has been completed to determine hinge lengths in the plastic and softening phases of full-scale reinforced concrete bridge systems. Previous work has relied on determining hinge lengths for small-scale component tests. An evaluation of long-scale system behavior, as described in this study, has the benefit of including the effects of moment redistribution and progression of yielding throughout the entire structure.

1.2 DETERMINATION OF PLASTIC HINGE LENGTH

Plastic hinges occur in the sections that have bending moments that exceed the nominal bending moment associated with yielding of the section. The equivalent plastic hinge length can be calculated based on integration of the curvature distribution for

typical members. To simplify the calculations, an equivalent plastic hinge length l_p can be defined over which the plastic curvature, ϕ_p, is assumed equal to ϕ_m- ϕ_y, where ϕ_m is the maximum curvature and ϕ_y is the yield curvature, as shown in Fig. 1.1(a). The length l_p is determined so that the plastic displacement at the top of the cantilever column, Δ_p, predicted from a displacement design method or from an experiment is the same as that obtained from the actual curvature distribution as shown in Fig. 1.1(a). The lumped plastic rotation, θ_p, along the plastic hinge length is then computed as Eq. 1.1:

$$\theta_p = \phi_p l_p = (\phi_m - \phi_y) \cdot l_p \tag{1.1}$$

The plastic rotation derived using Eq. (1.1) can be used to determine the displacement capacity of a section that experiences inelastic deformations. If the plastic rotation is assumed to be concentrated at midheight of the plastic hinge, the plastic displacement at the top of the cantilever column then becomes Eq. (1.2):

$$\Delta_p = \theta_p (l - 0.5 l_p) = (\phi_m - \phi_y) \cdot l_p \cdot (l - 0.5 l_p) \tag{1.2}$$

where l is the height of the column. The maximum nonlinear drift is then obtained from the plastic displacement at the top of the cantilever. Therefore, a consistent prediction of a plastic hinge length is necessary to examine the theoretical drift capacity of bridge columns.

The hinge length indicates the theoretical length of damage concentration along the column. Although the plastic hinge length should not be considered the required column confinement region, it does indicate the minimum theoretical dimension. The actual confinement region, which was shown as the extent of plasticity in Fig. 1.1 (a), should be longer than the plastic hinge length.

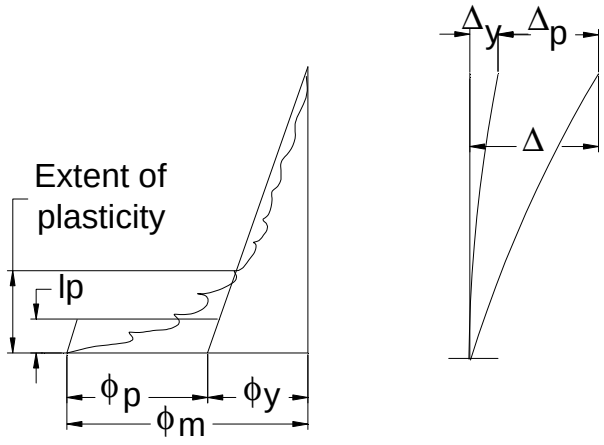

(a) Curvature at maximum response (b) Deflections

Figure 1.1 Curvature and deflection relationships for a reinforced concrete cantilever (Paulay and Priestley 1992).

1.3 LITERATURE REVIEW OF PLASTIC HINGE LENGTH (STATIC TESTS)

The plastic hinge length from static tests has been studied widely by many researchers (Baker 1956, Baker and Amarakone 1964, Mattock 1964, 1967, Corley 1966, Park, Priestley, and Gill 1982, Priestley and Park 1987, Paulay and Priestley 1992, Sheikh and Khoury 1993, Mendis 2001). A detailed review of formulae that are available to calculate the plastic hinge length for reinforced concrete columns are presented in this section. Few studies, however, have been conducted to determine the plastic hinge length in reinforced concrete bridge columns. These studies include Park, Priestley, and Gill 1982, Priestley and Park 1987, Tanaka and Park 1990, Watson and Park 1994, Kovacic 1995, Dodd et al. 2000, Hachem et al. 2003, Bae 2005, and Phan 2007, and are also included in this section. In the dynamic tests, the equation proposed by Priestley et al. (1992) was used to estimate the plastic hinge length before testing the bridge columns, even though this equation was derived using the static test results of columns. Two studies have been done to determine the plastic hinge length with dynamic testing of

reinforced concrete bridge column under dynamic base excitation (Dodd et al. 2000, and Hachem et al. 2003) and these will be discussed later in this chapter.

1.3.1 The Institution of Civil Engineers Committee Report (1962)

The Institute of Civil Engineers committee published a report on the ultimate load design of concrete structures (I.C.E. 1962), which includes the principles of ultimate load theory and its application to design. The report specifies a conservative empirical method of calculating the equivalent plastic hinge length l_p,

$$\frac{l_p}{d} = k_1 k_2 k_3 \left(\frac{z}{d}\right)^{0.25} \tag{1.3}$$

where k_1, k_2, and k_3 represents the influence of the type of reinforcing steel, column load (when present) and strength of concrete in l_p respectively, z is the distance of critical section to point of contraflexure, and d is the effective depth. The coefficients k_1, k_2, and k_3 were determined by examining several series of test results as described next.

From the analysis of test results that are described in this section (Ernst 1957, McCollister et al. 1954, Poologasoundranayagam 1960, and Chan 1955), conservative limiting values for k_1, k_2, and k_3 are given as

$$k_1 = \begin{Bmatrix} 0.7 & mild\ \ steel \\ 0.9 & cold - worked\ steel \end{Bmatrix} \tag{1.4}$$

$$k_2 = 1 + 0.5\frac{P}{P_u} \tag{1.5}$$

$$k_3 = \begin{Bmatrix} 0.6 & c_u = 6,000\,lb/in^2 \ \ (42\,MPa) \\ 0.9 & c_u = 2,000\,lb/in^2 \ \ (14\,MPa) \end{Bmatrix} \tag{1.6}$$

where P is the column load acting in conjunction with bending moment, P_u is the load capacity as an axially loaded column, and c_u is the cube strength of concrete.

Ernst (1957) tested 30 simply-supported beams having 6 in. (150 mm) by 12 in. (305 mm) cross-section, 10 ft. (3050 mm) in length, and a span of 9 ft. (2750 mm) under central point loading. The main parameters were widths of column stubs and tension steel as shown in Fig. 1.2. Column stubs changed in width from 6 to 36 in. (150 mm to 915 mm) at mid-span. The range of tension steel reinforcement ratios was from 1% to 5%. The nominal 28-day cube strength of the concrete was 3000 psi (22 MPa) or 4000 psi (28 MPa). Steel yield strength was approximately 45 ksi (310 MPa).

McCollister et al. (1954) designed 31 beams with 6 in. (150 mm) by 12 in. (305 mm) cross-section and 9 ft. (2750 mm) span. The main variables comprised the concrete strength from 1905 psi (13 MPa) to 6407 psi (44 MPa), tension and compression steel content (from 0.17% to 5.10% and from 0% to 4.08%, respectively), and the effect of column stubs with dimensions of 6 in. (150 mm) by 6 in. (150 mm) cross-section and 12 in. (305 mm) height.

Poologasoundranayagam (1960) tested 38 simply supported beams having 4 in. (100 mm) by 9 in. (230 mm) cross section and spans of 4-6 ft. (1220-1830 mm) under central point loading. The principal factors were strength of concrete from 2,385 psi (16 MPa) to 6,330 psi (44 MPa), percentage of tension reinforcement (0.62% to 5.1%), and quality of steel (mild or cold-worked and post-tensioned high tensile wire).

Chan (1955) conducted three series of tests. The first series consisted of nine short prisms having 6 in. (150 mm) square sections and 11 ½ in. (290 mm) long. They were reinforced with 4 5/8 in. diameter (16 mm) longitudinal bars and used ties. These prisms were pin-ended and loaded under compressive load with an eccentricity of ½ in. (13 mm). Seven cylinders of 6 in. (150 mm) diameter and 12 in. (305 mm) length were tested in the second series. They had the same longitudinal reinforcement with the first

series, but they were loaded in compression with an eccentricity of 1/4 in. (7 mm). The main variable was lateral binding, where spiral reinforcement of ¼ in. (7 mm), 3/16 in. (5 mm), and 1/8 in. (3 mm) diameter bars and pitches from 1 in. (25 mm) to 4 in. (100 mm) were used to confine the specimens. The last series included seven struts with 6 in. (105 mm) by 3-5/8 in. (90 mm) cross section and 52 in. (1320) long. They were symmetrically reinforced with 4 1/2 in. diameter (13 mm) bars, laterally bound with rectangular welded closed links spaced at 3 in. (75 mm). They were tested under axial compression through pins at the ends, and a central lateral point load. It was intended to simulate a plastic hinge formation within the critical region of a column under bending moment and high axial load. The nominal 28-day cube strength of the concrete was 3000 psi (22 MPa) for the first and second series, and 4000 psi (28 MPa) for the last series. Average yield strength of the steel was around 40 ksi (275 MPa).

Chan (1962) evaluated the methods and parameters that were recommended in the ICC report (1962) by studying thirteen column tests, comprising six by Poologasoundranayagam (1960) and seven by Chan (1955), covering a range of P/P_u from 0.06 to 0.78, cube strengths from 2,380 (16 MPa) to 5,160 psi (36 MPa), and symmetrically reinforced steel ratios from 1.23% to 1.92%. Tests were analyzed and compared in order to calculate values of EI_e and θ_p (plastic rotation) as described below.

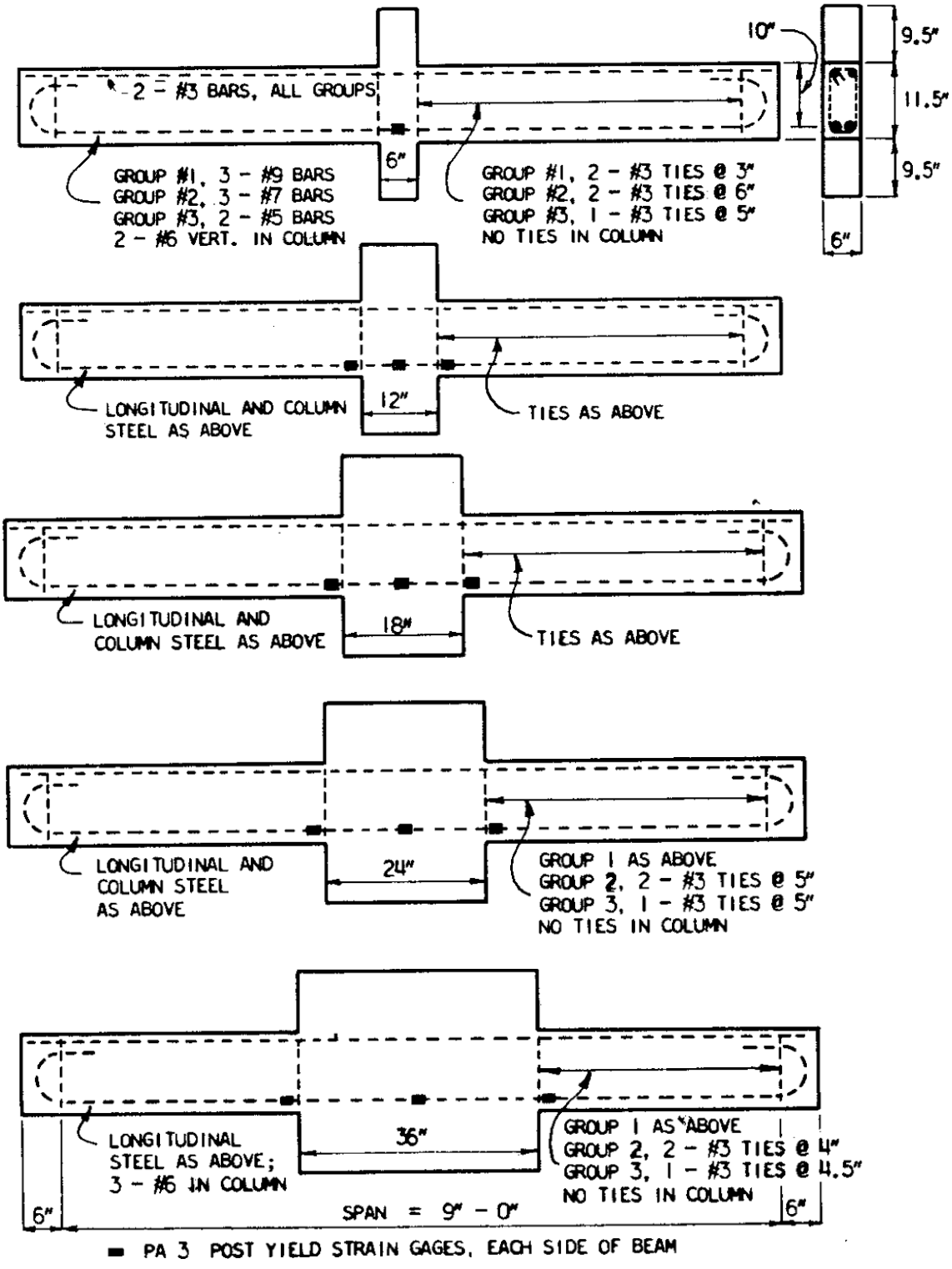

Figure 1.2 Dimensions, steel content, and steel strain locations (Ernst 1957).

The testing procedure was similar to the study of 54 beam tests done by Chan (1954); in addition, values of k_2 were included to consider the effect of the column loading. The histograms of the column test results were expressed as the ratio of experimental to calculated values of EI_e'/ EI_e and θ_p'/ θ_p. They had a similar distribution with the beam test results. Chan observed that the parameters used in Eq. (1.3) were safe and statistically acceptable, however, the number of test results was small and more tests were desired. The author also reported that in a broad range of structural members l_p varies from about 0.4 to 2.4d.

1.3.2 ACI Limits (1968)

The ACI-ASCE Committee 428 on Limit Design (1968) recommended upper and lower plastic hinge limits rather than a single equation. The length along a member from the section of maximum moment, l_p, should be bigger than the lesser of the two values given in Eq. (1.7) and the value given in Eq. (1.8):

$$R_\varepsilon\left(\frac{d}{4}+0.03zR_m\right) \qquad \text{and} \qquad R_\varepsilon d \tag{1.7}$$

but not greater than $R_\varepsilon\left(\frac{d}{2}+0.10zR_m\right)$ (1.8)

in which;

$$R_\varepsilon=\frac{0.004-\varepsilon_{cue}}{\varepsilon_{cuo}-\varepsilon_{cue}}, \tag{1.9}$$

$$z=\frac{4M_m}{4V_z+\sqrt{wM_m}R_m} \tag{1.10}$$

$$R_m=\frac{M_m-M_e}{M_u-M_e} \tag{1.11}$$

where;

d = distance from extreme compression fiber to centroid of tension reinforcement, in. (mm)

w = uniformly distributed load at a section of maximum moment kip/in., (kN/mm)

V_z = shear adjacent to a concentrated load or reaction at a section of maximum moment kips, (kN)

M_m = maximum moment in a length of member kip-in., (kN.mm)

M_e = elastic-limit resisting moment kip-in., (kN.mm)

M_u = ultimate resisting moment concurrent with Pu kip-in., (kN.mm)

P_u = ultimate resisting axial load kips, (kN)

ε_{cue} = elastic component of ε_{cu}, either calculated or assumed in the range 0.001 to 0.002,

ε_{cu} = maximum compressive strain in concrete at Mu and Pu, and

ε_{cuo} = basic maximum compressive strain in concrete (neglecting possible amplifying influences of confinement, loading rate and strain gradients) to which a value in the range 0.003 to 0.004 needs to be assigned.

R_ε restricts the range of total inelastic rotation by providing reduced limits on hinge lengths for the greater assumed values of inelastic strains and curvatures, and increased limits on hinge lengths for the smaller assumed strain values [ACI-ASCE (1968)].

The formulae suggested by ACI 428 committee can be utilized as lower and upper limits for inelastic analysis of normal and high-strength concrete structures. The ACI formulae, however, do not rely on longitudinal and lateral reinforcement ratios.

1.3.3 Park, Priestley, and Gill (1982)

Four full-size reinforced concrete columns with 22 in. (550 mm) square sections and 10.8 ft. (3300 mm) in height were tested by Park et al. (1982). The longitudinal

reinforcement in each column consisted of twelve 0.94-in. (24-mm.) diameter deformed bars having a reinforcement ratio of 1.79%. The yield strength of the longitudinal steel was 55.1 ksi (380 MPa). The transverse steel was plain round bars and the yield strength was 40 ksi (275 MPa). The ranges of the applied axial loads were from $0.2f'_cA_g$ to $0.6f'_cA_g$. Details of column specimens are given in Table 1.1.

The equivalent plastic hinge length, l_p, was calculated by using the Eq. (1.2) for the last load cycle in the test. The plastic displacement, Δ_p, was measured beyond the first yield displacement and plastic curvature, ϕ_u- ϕ_y, was measured beyond the first yield curvature over the 3.9 in. (100 mm) gage length adjacent to the central stub, where ϕ_u is the ultimate curvature and ϕ_y is the yield curvature.

Based on the tests of the four reinforced concrete columns, Park et al. (1982) showed that the calculated equivalent plastic hinge lengths were insensitive to axial load level and had an average value of 0.42*h*, where *h* is the overall section depth. Table 1.1 lists the calculated plastic hinge length results for the tested columns and the ratio of this length to the section depth.

Based on the limited column tests in this study, Park et al. concluded that l_p = 0.4*h* can be used as a simple and safe approximation for plastic hinge lengths in columns. It should be noted that l_p is the equivalent length of plastic hinge to be used in evaluating the ultimate curvature requirements, and should not define the length of the column that needs to be confined along the critical section.

Table 1.1 Details of column specimens and measured test results

Unit	f_c', ksi (Mpa) (1)	Axial Load		Longitudinal Reinf.		Transverse Reinf.				Meas. L_p, in. (mm) (10)	L_p/h (11)
		P, kips (kN) (2)	$P/f_c'A_g$ (3)	f_y, ksi (Mpa) (4)	ρ_l, % (5)	d_b, in. (mm) (6)	f_{yh}, ksi (Mpa) (7)	ρ_s, % (8)	$A_{sh}/A_{sh,ACI}$ (9)		
1	3.35 (23)	408.03 (1815)	0.26	55.1 (380)	1.79	0.39 (10)	43.07 (297)	1.5	0.66	9.53 (242)	0.44
2	6 (41)	602.49 (2680)	0.214	55.1 (380)	1.79	0.47 (12)	45.83 (316)	2.3	0.63	7.44 (189)	0.34
3	3.1 (21)	611.25 (2719)	0.42	55.1 (380)	1.79	0.39 (10)	43.07 (297)	2	0.89	8.62 (219)	0.4
4	3.41 (24)	958.81 (4265)	0.6	55.1 (380)	1.79	0.47 (12)	42.64 (294)	3.5	1.47	10.75 (273)	0.5

1: Compressive cylinder strength of concrete

2: Applied axial load

3: Axial load ratio

4: The yield strength of longitudinal steel

5: The longitudinal reinforcement ratio

6: The diameter of the longitudinal reinforcement

7: The yield strength of transverse steel

8: The volumetric ratio of transverse reinforcement to core concrete

9: The ratio of total effective area of rectangular hoop bars to that required by ACI

10: Measured plastic hinge length

11: The ratio of measured plastic hinge length to the depth of the column

1.3.4 Mander (1983)

Experimental studies conducted by previous investigators at the University of Canterbury (Gill et al. 1979, Potangaroa et al. 1979, Ghee et al. 1981, Davey et al. 1975, Munro et al. 1976 and Heng et al. 1978) have supported the theory that the equivalent plastic hinge length, l_p, may vary from 0.35 to 0.65 of the overall member depth for solid reinforced concrete columns. Based on a comparison of the available results for octagonal specimens (RRU 1983), it was found that the equivalent plastic hinge length is

independent of the axial load level and aspect ratio. A value of l_p = 0.5D was recommended.

After examining the experimental results studied at the University of Canterbury, Mander concluded that contributions to plastic deformation were primarily from two sources: (i) the spread of plasticity along the member length due to the moment gradient and (ii) yield penetration of the longitudinal reinforcement beyond the limits of the plastic hinge. The equivalent length of yield penetration, L_{py}, could be written in terms of the longitudinal bar diameter from the force-deflection analyses:

$$L_{py} = 6.35\sqrt{d_b} \qquad \text{(in.)} \qquad (1.12a)$$

$$L_{py} = 32\sqrt{d_b} \qquad \text{(mm)} \qquad (1.12b)$$

where d_b is the longitudinal bar diameter.

The additional plastic hinge length due to the spread of plasticity along the member length was found to be approximately six percent of the column length, L, after analyzing all the test results. Thus, the equivalent plastic hinge length can be calculated from the equation below.

$$L_p = L_{py} + 0.06L \qquad (1.13)$$

When the predicted and observed results are compared, Eq. (1.13) generally provides a conservative prediction of the equivalent plastic hinge length. Mander also noted that Eq. (1.13) must not be used for estimating the length requiring detailed confinement because plastic curvature would spread over approximately three equivalent plastic hinge lengths.

1.3.5 Priestley and Park (1987)

Instead of obtaining the plastic hinge length using a linear elastic curvature distribution along the column, an alternate approach was developed by Priestley and Park (1987) considering the moment-curvature relationships for different sections along the height of the column. The curvature distribution along the column can be calculated using Eq. (1.14) for any given base moment as shown in Fig. 1.3(a). The predicted displacement at the top of the column is then obtained by integrating the curvature profile.

$$\Delta = \int^{L} \varphi_{(x)} x dx \tag{1.14}$$

Using an incremental analysis based on this procedure results in theoretical difficulties when the moment-curvature relationship has a curve with strength degradation (negative slope). Failure is predicted when the column reaches the maximum load. Sections having moment demands that are less than their capacity are assumed to keep their prior curvatures past the post-peak load behavior.

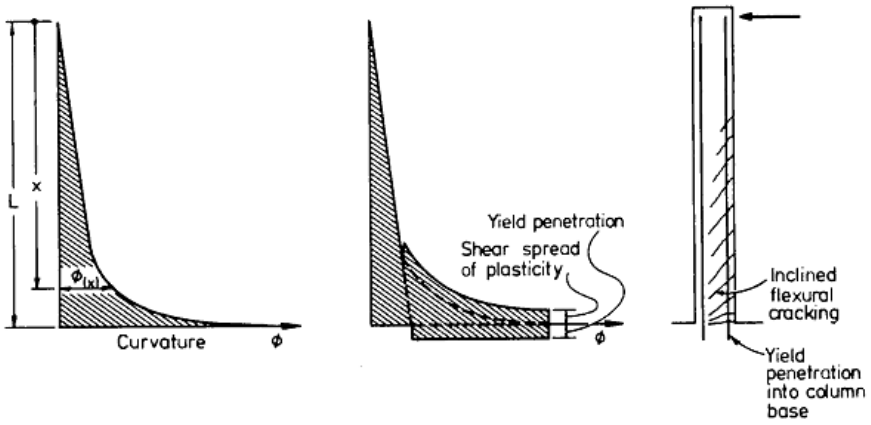

(a) (b)

Figure 1.3 “Exact” curvature distributions for deflection calculations (Priestley and Park 1987)

Priestley and Park (1987) reported that an elasto-plastic approximation should consider a plastic hinge length proportional to the column height L, because the predicted curvature distribution for columns that have identical section dimensions but different heights would be geometrically similar. Although this relationship between the column height and the plastic hinge length was accepted by early models for plastic hinge length (Baker 1964; Corley 1966), it was not supported by previous experimental observations because of two reasons as explained below:

1. The first reason is the slip of longitudinal reinforcement relative to the concrete. Within the plastic hinge region, slip of reinforcement also leads to longitudinal reinforcement strains at sections above the base to be higher than expected. Therefore, the length of yield penetration and resultant slippage will definitely be independent of column height L, and would depend mainly on the diameter of the longitudinal reinforcement.
2. The second reason is the influence of shear on the crack pattern. If flexural cracks are inclined under the influence of shear, the "plane-sections-remain-plane" hypothesis will not be valid, and steel stress and strain will increase above the levels estimated based on the plane-sections hypothesis. This leads to a spread the plasticity, and increases the plastic hinge length. Figure 1.2(b) illustrates the effect of yield penetration and spreading of plasticity due to shear. The lateral deflection of the center of mass of the column is calculated by integrating the modified curvature distribution.

Based on the arguments above, concrete bridge column tests were conducted in two stages. In the first stage, sections including square, rectangular, and circular shapes

were tested under axial load only. The range of longitudinal reinforcement ratios was between 1% and 4%, and the lateral reinforcement ratio was from 0.5% to 1.5% with spiral or circular hoops. The axial load values ranged from $0.2P_o$ to $0.7P_o$, where $P_o=P_e/f_c'A_g$ (P_e is design compressive load of the column due to gravity and seismic loading, f_c' is compressive cylinder strength of concrete, and A_g is gross area of section). In the second stage, the sections included square, diagonal, octagonal, and hollow square shapes were tested under continued axial load and cyclic reversals of bending moment. The test columns were instrumented extensively along the potential plastic hinge regions.

Priestley and Park (1987) proposed a general plastic hinge length formula (Eq. 1.15) based on the new test results.

$$l_p = C_1 L + C_2 d_b + C_3 D \tag{1.15}$$

where L is the distance from the point of contraflexure of the column to the section of maximum moment, d_b is the longitudinal bar diameter, D is section depth (or diameter for circular sections) and C_1, C_2, and C_3 are constants determined from curvature distributions along the column length of the specimen.

Curvature distributions along the length were obtained for all units during the column tests to predict the values of the constants. Best fit values of C_1 = 0.08, C_2 = 6, and C_3 = 0 were found based on the analysis of the test results. Therefore, Eq. 1.15 becomes

$$l_p = 0.08L + 6d_b \qquad \text{(ksi)} \tag{1.16a}$$

$$l_p = 0.08L + 0.88d_b \qquad \text{(MPa)} \tag{1.16b}$$

Priestley and Park (1987) obtained good agreement between the experimentally derived values for l_p and values calculated using Eq. (1.16). The tests that were evaluated included studies outside this program (Gill et al. 1982, Potangaroa et al. 1981, Davey et al. 1975, Munro et al. 1976, Ng et al. 1978, Ghee et al. 1985 and Mander et al. 1984).

The average hinge length that was calculated for all tests was approximately equal to l_p= 0.5D as shown in Table 1.2. The experimental data did not show any relationship between plastic hinge length and axial load ratio, longitudinal reinforcement ratio, or yield stress of longitudinal reinforcement.

Table 1.2.Experimental and predicted plastic hinge lengths

Researchers	Column aspect ratio	Section width, D or h, in. (mm)	Longitudinal bar diameter, db, in. (mm)	Plastic hinge length Lp		
				Experiment	Predicted (Eq. 1.13a)	Experiment/ Predicted
Davey et al.	4	D=19.69 (500)	0.51 (13)	0.54D	0.44D	1.23
	4	D=19.69 (500)	0.51 (13)	0.58D	0.60D	0.97
Munro et al.	5.5	D=19.69 (500)	0.51 (13)	0.45D	0.60D	0.76
Heng et al.	4	D=9.84 (250)	0.51 (13)	0.58D	0.64D	0.91
Gill et al.	2.18	h=21.65 (550)	0.94 (24)	0.44h	0.44h	1
	2.18	h=21.65 (550)	0.94 (24)	0.34h	0.44h	0.77
	2.18	h=21.65 (550)	0.94 (24)	0.40h	0.44h	0.91
	2.18	h=21.65 (550)	0.94 (24)	0.50h	0.44h	1.13
Potangaroa et al.	2	D=23.62 (600)	0.94 (24)	0.35D	0.40D	0.88
	2	D=23.62 (600)	0.94 (24)	0.35D	0.40D	0.88
	2	D=23.62 (600)	0.94 (24)	0.37D	0.40D	0.93
	2	D=23.62 (600)	0.94 (24)	0.42D	0.40D	1.05
Ghee et al.	4	D=15.75 (400)	0.63 (16)	0.54D	0.56D	0.96
	4	D=15.75 (400)	0.63 (16)	0.61D	0.56D	1.09
	4	h=15.75 (400)	0.63 (16)	0.73h	0.56h	1.3
	4	h=15.75 (400)	0.63 (16)	0.55h	0.56h	0.98
Mander et al.	4.27	h=29.53 (750)	0.39 (10)	0.37h	0.42h	0.88
	4.27	h=29.53 (750)	0.39 (10)	0.38h	0.42h	0.9
	4.27	h=29.53 (750)	0.39 (10)	0.40h	0.42h	0.95
	4.27	h=29.53 (750)	0.39 (10)	0.41h	0.42h	0.98
					Average =	0.97

1.3.6 Sakai and Sheikh (1989)

Based on a review of the literature, Sakai and Sheikh (1989) noted that the plastic hinge length increased as the aspect ratio (L/h or L/D, which is equivalent to the shear span-to-depth ratio for cantilever columns) increased. Bilinear curves were developed to give the relationship between the plastic hinge length and the aspect ratio as shown in Figure 1.4. They concluded that the amount of transverse reinforcement, axial load level, and aspect ratio had an influence on the plastic hinge length. The plastic hinge length generally increased with increasing values of each parameter.

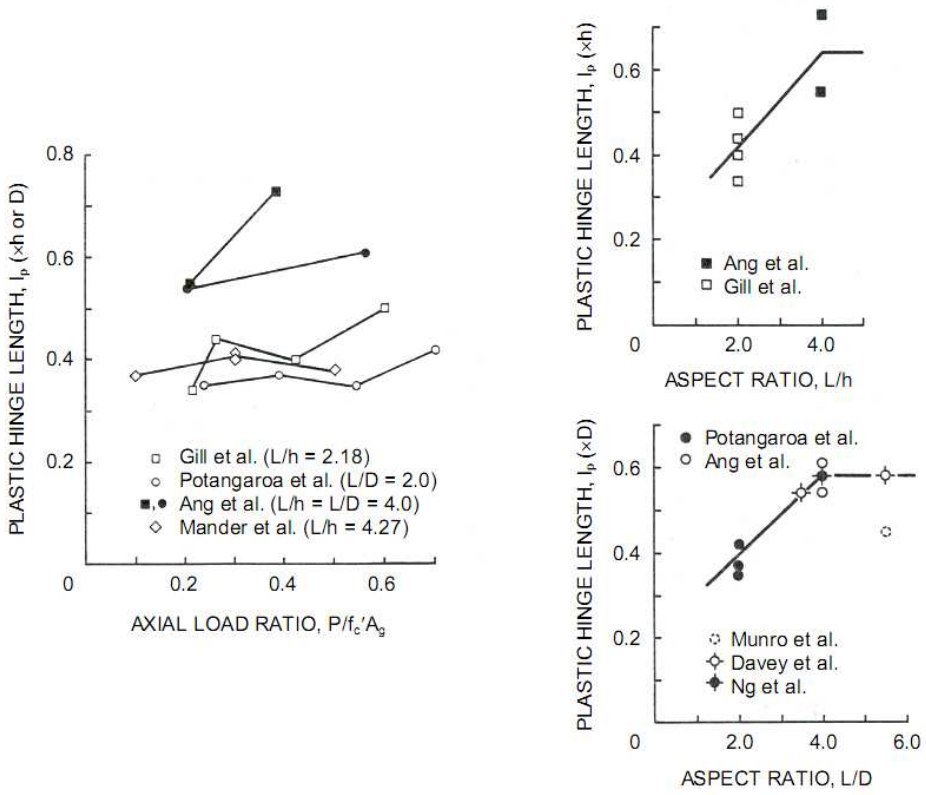

Figure 1.4 Effects of Various Parameters on Plastic Hinge Lengths (Sakai and Sheikh 1989)

1.3.7 Tanaka and Park (1990)

Tanaka and Park (1990) completed two series of column tests. In the first series, four column specimens (Units 1 to 4) had a total height of 5.9 ft. (1800 mm) and 16 in.

(400 mm) square sections. In the second series, four column specimens (Units 5 to 8) had a total height of 5.4 ft. (1650 mm) and 22 in. (550 mm) by 22 in. (550 mm) square sections. The shear span-to-depth ratios were 4 and 3 for the first and second series, respectively. The level of applied axial load ($P/f_c'A_g$), the shear span-to-depth ratio of each column (L/h), the configuration of transverse reinforcement, and anchorage details of that reinforcement were the main variables. Table 1.3 illustrates the mechanical properties of the materials and other details of the column specimens.

The plastic hinge region of the column specimens was designed according to the NZS 3101:1982 code for both confinement and shear. After testing the two series of column units, the equivalent plastic hinge lengths were found to be between 0.40 and 0.75 of the overall depth of the column section. Tanaka and Park (1990) observed that when the axial load level increased, the equivalent plastic hinge length increased.

Table 1.3. Details of column specimens (Tanaka and Park 1990)

Unit	f_c', ksi (Mpa) (1)	$P/f_c'Ag$ (2)	Longitudinal Steel		Transverse Steel				bxh, in. (mm) (9)	L/h (10)	L_p, in. (mm) (11)
			f_y, ksi (MPa) (3)	ρ_l (%) (4)	s_h, in. (mm) (5)	f_{yh}, ksi (MPa) (6)	ρ_s (%) (7)	$A_{sh}/A_{sh,ACI}$ (8)			
1	3.71 (26)	0.2	68.73 (474)	1.57	3.15 (80)	48.29 (333)	2.55	1.06	15.75x15.75	4.00	6.77 (172)
2	3.71 (26)	0.2	68.73 (474)	1.57	3.15 (80)	48.29 (333)	2.55	1.06	15.75x15.75	4.00	8.7 (221)
3	3.71 (26)	0.2	68.73 (474)	1.57	3.15 (80)	48.29 (333)	2.55	1.06	15.75x15.75	4.00	10.6 (269)
4	3.71 (26)	0.2	68.73 (474)	1.57	3.15 (80)	48.29 (333)	2.55	1.06	15.75x15.75	4.00	11.06 (281)
5	4.64 (32)	0.1	74.1 (511)	1.25	4.33 (110)	47.13 (325)	1.70	0.82	21.65x21.65	3.00	8.35 (212)
6	4.64 (32)	0.1	74.1 (511)	1.25	4.33 (110)	47.13 (325)	1.70	0.82	21.65x21.65	3.00	13.66 (347)
7	4.65 (32)	0.3	74.1 (511)	1.25	3.54 (90)	47.13 (325)	2.08	1.00	21.65x21.65	3.00	14.45 (367)
8	4.65 (32)	0.3	74.1 (511)	1.25	3.54 (90)	47.13 (325)	2.08	1.00	21.65x21.65	3.00	18.66 (474)

1: Compressive cylinder strength of concrete

2: Applied axial load ratio

3: The yield strength of longitudinal steel

4: The longitudinal reinforcement ratio

5: Spacing of transverse reinforcement

6: The yield strength of transverse steel

7: The volumetric ratio of transverse reinforcement to core concrete

8: The ratio of total effective area of rectangular hoop bars to that required by ACI

9: Cross sectional dimensions

10: Shear-span-depth ratio

11: Measured plastic hinge length

1.3.8 Paulay and Priestley (1992)

Paulay and Priestley (1992) reported that theoretical values for the equivalent plastic hinge length based on integration of the curvature distribution for typical members should be dependent on *l*, where *l* is the column height. Plastic hinge length values that are needed to calculate a measured lateral displacement, however, were not

consistent with experimentally measured lengths of l_p. As Fig. 1.5 shows, the theoretical curvature distribution ends abruptly at the base of the cantilever (Fig. 1.5b), whereas the actual steel tensile strains should continue for some depth into the footing due to finite bond stress. The elongation of longitudinal bars beyond the theoretical base causes additional rotation and deflection (tensile strain penetration as shown in Fig. 1.5c). The following formula was proposed by revising Eq. (1.16) to consider the effect of flexural reinforcement with different strengths on the length of a plastic hinge formed at the bottom of a cantilever column:

$$l_p = 0.08l + 0.15d_{bl} f_{ye} \geq 0.3d_{bl} f_{ye} \qquad \text{(ksi)} \qquad (1.17a)$$

$$l_p = 0.08l + 0.022d_{bl} f_{ye} \geq 0.3d_{bl} f_{ye} \qquad \text{(MPa)} \qquad (1.17b)$$

where l is the height of the cantilever column, f_{ye} is the yield stress of longitudinal reinforcement, and d_{bl} is the diameter of the longitudinal reinforcement.

Paulay and Priestley (1992) recommended that Eq. (1.17) results in values of l_p close to 0.5d, where d is the section depth, for typical beams and columns. It was observed that the equivalent plastic hinge length and the region of plasticity where special reinforcing detailing is required must be defined separately to ensure dependable inelastic rotation capacity. This difference is shown in Fig. 1.5b by indicating the spread of plasticity over a region outside the equivalent plastic hinge length.

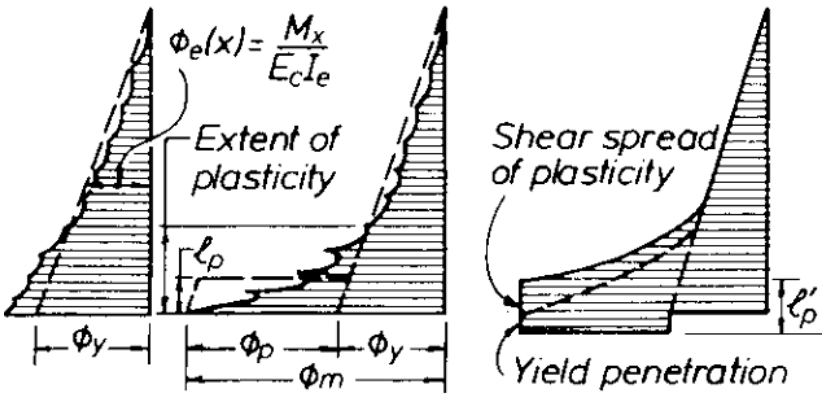

(a) Yield curvatures (b) Curvature at maximum response (c) Equivalent curvatures

Figure 1.5 Theoretical curvature relationships for a prismatic reinforced concrete cantilever column (Paulay and Priestley 1992)

1.3.9 Soesianawati, Park and Priestley (1986), Watson and Park (1994)

Soesianawati et al. (1986) conducted experimental research on four square concrete columns under low axial loads. The column specimens were designed with smaller quantities of confining reinforcement than those recommended by the NZS3101:1982 code (New Zealand Standards). Watson and Park (1994) furthered the experimental research of Soesianawati et al. (1986) by testing five more square columns and two octagonal columns under moderate to high axial compression load levels. Table 1.4 gives the details of the square column specimens, which have 16 in. (400 mm) square cross sections and a height of 64 in. (1600 mm). The shear span-to-depth ratio was 4 for the test specimens.

Units 1 to 4 were subjected to low axial load (P = 0. $1f_c'A_g$ to 0. $3f_c'A_g$). Units 1 and 2 contained 43% and 46% of the New Zealand code recommended quantity of transverse reinforcement. These specimens reached displacement ductility factors of at

least 8 without significant strength degradation, where displacement ductility factor is the ratio of lateral displacement to the displacement at first yield. Unit 3, having 30% of the code required quantity of transverse reinforcement, achieved a displacement ductility factor of 6. Unit 4, designed with 17% of the code recommended quantity of transverse reinforcement, was capable of reaching a displacement ductility factor of 4 and showed hoop anchorage failure and buckling of longitudinal bars.

Units 5 and 6 were tested under high axial load with $P = 0.5f_c'A_g$. These specimens, with 38% and 19% of the confining reinforcement required by the New Zealand code, achieved displacement ductility factors of 6.7 and 5.4, respectively. At the end of the test, buckling of longitudinal bars was observed. The axial load level of $P = 0.7f_c'A_g$ was applied to Units 7, 8 and 9, which contained 48%, 34%, and 93% of the code recommended quantity of confining reinforcement for ductile detailing, respectively. Units 7 and 8 achieved displacement ductility factors of 6.3 and 4.0, respectively. Unit 9 showed remarkably good performance and the test was continued until reaching the displacement ductility factor of 10.

Watson and Park (1994) observed that the length of potential plastic hinge regions increased as the axial load level increased. The other parameters, such as the aspect ratio and the section type of the columns, were found not to have a significant effect. The equivalent plastic-hinge length was calculated using the Eq. (1.16) for column units and found to be 0.56*h, where h= column depth. The NZS 3101-recommended that confined length was insufficient for many columns, particularly for those with large axial compression.

They proposed the following formula (Eq. 1.18) to calculate the length of the confined region for most columns:

$$\frac{l_c}{h} = 1 + 0.4\frac{P}{\phi f_c' A_g} \qquad \text{(ksi)} \qquad (1.18a)$$

$$\frac{l_c}{h} = 1 + 2.8\frac{P}{\phi f_c' A_g} \qquad \text{(MPa)} \qquad (1.18b)$$

where

l_c = length of confined region of column, in. (mm)

h = lateral dimension of rectangular column section, in. (mm)

ϕ = strength reduction factor

f_c' = compressive cylinder strength of concrete, ksi (MPa)

A_g = gross area of column section, $in.^2$, (mm^2).

It is recommended that Eq. (1.18) be used in design. This expression gives l_c equal to h when the axial load is zero, and l_c equal to 3h when the axial load is $0.70A_g f_c'$.

Table 1.4. Details of column specimens (Watson and Park 1994)

Unit	f_c', ksi (MPa) (1)	Axial Load		Longitudinal Reinforcement		Transverse Reinforcement				l_p/h (Eq. 1.13) (10)
		P, kips (kN) (2)	$P/f_c'A_g$ (3)	f_y, ksi (MPa) (4)	ρ_l (%) (5)	d_b, in. (mm) (6)	f_{yh}, ksi (MPa) (7)	ρ_s (%) (8)	$A_{sh}/A_{sh,ACI}$ (9)	
1	6.74 (46)	167 (743)	0.1	64.67 (446)	1.51	0.28 (7)	82 (565)	0.84	0.36	0.56
2	6.38 (44)	475 (2113)	0.3	64.67 (446)	1.51	0.32 (8)	81 (558)	1.2	0.55	0.56
3	6.38 (44)	475 (2113)	0.3	64.67 (446)	1.51	0.28 (7)	82 (565)	0.79	0.36	0.56
4	5.8 (40)	432 (1922)	0.3	64.67 (446)	1.51	0.24 (6)	57 (393)	0.56	0.2	0.56
5	5.95 (41)	737 (3278)	0.5	68.73 (474)	1.51	0.32 (8)	84 (579)	1.15	0.58	0.56
6	5.8 (40)	719 (3198)	0.5	68.73 (474)	1.51	0.24 (6)	87 (600)	0.55	0.29	0.56
7	6.09 (42)	1058 (4706)	0.7	68.73 (474)	1.51	0.47 (12)	69 (476)	2.16	0.9	0.56
8	5.65 (39)	982 (4368)	0.7	68.73 (474)	1.51	0.32 (8)	84 (579)	1.21	0.64	0.56
9	5.8 (40)	1007 (4479)	0.7	68.73 (474)	1.51	0.47 (12)	69 (476)	3.99	1.75	0.56

1: Compressive cylinder strength of concrete

2: Applied axial load

3: Applied axial load ratio

4: The yield strength of longitudinal steel

5: The longitudinal reinforcement ratio

6: The diameter of longitudinal reinforcement

7: The yield strength of transverse steel

8: The volumetric ratio of transverse reinforcement to core concrete

9: The ratio of total effective area of rectangular hoop bars to that required by ACI

10: The ratio of calculated plastic hinge length using Eq. 1.16 to the depth of the column

1.3.10 Sheikh and Khoury (1993), Sheikh, Shah and Khoury (1994)

Sheikh and Khoury (1993) and Sheikh et al. (1994) completed experimental research on six large-scale normal-strength concrete and four high-strength concrete column specimens. The concrete columns were 72.5 in. (1842 mm) high and had 12-in. (305 mm) square cross sections that result in a shear span-to-depth ratio of 6. The

concrete strength, level of axial load, and the percentage of transverse reinforcement were the main test variables. Table 1.5 shows the details of the specimens tested and the applied axial load.

The primary goal of the research was to assess the confinement provisions of the ACI 318 (1989) code. According to this version of the code, the total cross sectional area of rectangular hoop reinforcement for confinement (Ash) should not be less than that given by the following Eq. (1.19a and b):

$$A_{sh} = 0.3sb_c\left(\frac{A_g}{A_{ch}} - 1\right)\frac{f_c^{'}}{f_{yt}} \tag{1.19a}$$

$$A_{sh} = 0.09sb_c\frac{f_c^{'}}{f_{yt}} \tag{1.19b}$$

where

A_g = gross area of column section, in.^{2} (mm^2)

A_{ch} = area of core concrete measured out-to-out of transverse reinforcement, in.^{2} (mm^2)

$f_c^{'}$ = compressive strength of concrete, ksi (MPa)

f_{yt} = yield strength of transverse reinforcement, ksi (MPa)

s = spacing of transverse reinforcement, in. (mm)

b_c = cross sectional dimension of column core, measured center-to-center of transverse reinforcement, in. (mm).

In the ACI 318 code, the length of the column requiring confinement is specified as the greatest of the overall depth (h) of a column at the joint face (where h is the larger sectional dimension for a rectangular column or the diameter of a circular column), one-sixth of the clear height of a column, or 18 in. (457 mm). The spacing of transverse

reinforcement is required to be less than h/4 or $6d_b$, where h is the minimum member dimension and d_b is the diameter of longitudinal reinforcement.

The researchers concluded that a column designed according to the ACI (1989) code requirements has adequate performance in terms of curvature and displacement ductility, but only for certain situations. Depending on the reinforcement detailing and axial load level, the code provisions may give unnecessarily conservative design. It was also observed that the measured plastic hinge lengths were an average value of 1.0*h* in the column tests as shown in Table 1.5, where *h* is the column depth. Most of the column tests were, however, conducted under high axial loads. It also appeared that steel configuration, axial load level, amount of confining steel, and concrete strength did not have an influence on the plastic hinge length.

Table 1.5 Details of specimens (Sheikh and Khoury 1993, 1994)

Spec.	f_c', ksi (MPa) (1)	Longitudinal Steel: No. of bars (2)	Longitudinal Steel: ρ_l (%) (3)	Longitudinal Steel: f_{yl}, ksi (MPa) (4)	ρ_s (%) (5)	f_{yh}, ksi (MPa) (6)	$A_{sh}/A_{sh,ACI}$ (7)	$P/f_c'A_g$ (8)	L_p, in. (mm) (9)	L_p/h (10)
FS-9	4.7 (32)	8	2.44	73.6 (507)	1.68	73.6 (507)	1.46	0.76	13.1 (333)	1.10
ES-13	4.72 (33)	8	2.44	73.6 (507)	1.69	67.3 (464)	1.34	0.76	10.2 (259)	0.85
AS-3	4.81 (33)	8	2.44	73.6 (507)	1.68	73.6 (507)	1.43	0.60	11.5 (292)	0.96
AS-17	4.54 (31)	8	2.44	73.6 (507)	1.68	73.6 (507)	1.52	0.77	12.6 (320)	1.05
AS_18	4.75 (33)	8	2.44	73.6 (507)	3.06	67.3 (464)	2.41	0.77	11.9 (302)	0.99
AS-19	4.68 (32)	8	2.44	73.6 (507)	1.30	73.6 (507) 67 (462)	1.12	0.47	13.9 (353)	1.16
AS-3H	7.86 (54)	8	2.44	73.6 (507)	1.68	73.6 (507)	0.88	0.62	12.7 (323)	1.05
AS-18H	7.93 (55)	8	2.44	73.6 (507)	3.06	67.3 (464)	1.44	0.64	10.7 (272)	0.89
AS-20H	7.78 (54)	8	2.44	73.6 (507)	4.30	67.3 (464)	2.10	0.64	13 (330)	1.08
A-17H	8.57 (59)	8	2.44	73.6 (507)	1.68	73.6 (507)	0.80	0.65	-	-

1: Compressive cylinder strength of concrete

2: Number of bars used in the specimens

3: The longitudinal reinforcement ratio

4: The yield strength of longitudinal steel

5: The volumetric ratio of transverse reinforcement to core concrete

6: The yield strength of transverse steel

7: The total cross sectional area of rectangular hoop reinforcement for confinement according to ACI 318 (1989)

8: Applied axial load ratio

9: The measured plastic hinge length

10: The ratio of measured plastic hinge length to the column depth

*: No. 3 (10) and 6-mm bars were used for the perimeter ties and inner ties, respectively

1.3.11 Kovacic (1995)

As part of a long-term study on the behavior of high-strength concrete structures at the University of Melbourne, Kovacic (1995) conducted an experimental and

theoretical investigation of the full-range behavior of high-strength concrete columns, with the nominal concrete strength as high as 11.6 ksi (80 MPa), and with low axial load ratios ranging between 5% and 20%. Six out of eight column test results (Table 1.3) were within the ACI limits for plastic hinge length given in 1968 (Eq. 1.7 and 1.8), and thus justified using these equations to estimate the hinge lengths for high-strength concrete columns with low axial loads. Kovacic reported that the ACI formulae gave reliable predictions of hinge lengths for high strength concrete columns with low axial loads, but more experiment was required to confirm and extend these observations for columns with high axial loads and for very high concrete strengths.

Table 1.6. Details of beams tested by Kovacic

Label	Span, in. (mm)	Width, in. (mm)	Depth, in. (mm)	Axial force, kips (kN)	Concrete strength f_c', ksi (MPa)	Measured L_p/d	ACI [1]-Lower/d	ACI [2]-Upper/d
D1	50 (1270)	3.15 (80)	5.91 (150)	14.61 (65)	4.82 (33)	0.254	0.37	0.91
D2	50 (1270)	3.15 (80)	5.91 (150)	14.61 (65)	4.74 (33)	0.467	0.37	0.91
D3	50 (1270)	3.15 (80)	5.91 (150)	14.61 (65)	5.61 (39)	0.633	0.37	0.91
D4	50 (1270)	3.15 (80)	5.91 (150)	29.22 (130)	8.43 (58)	0.299	0.37	0.91
D5	50 (1270)	3.15 (80)	5.91 (150)	14.61 (65)	9.33 (64)	0.467	0.37	0.91
D6	50 (1270)	3.15 (80)	5.91 (150)	29.22 (130)	9.4 (65)	0.699	0.37	0.91
D7	50 (1270)	3.15 (80)	5.91 (150)	7.19 (32)	9.11 (63)	0.547	0.37	0.91
D8	50 (1270)	3.15 (80)	5.91 (150)	14.61 (65)	9.46 (65)	0.467	0.37	0.91

1: The ratio of plastic hinge length calculated using ACI lower limit (1968) to the depth of the column

2: The ratio of plastic hinge length calculated using ACI upper limit (1968) to the depth of the column

1.3.12 Bayrak and Sheikh (1997, 1999)

Bayrak and Sheikh (1997) and Bayrak (1999) constructed and tested twenty four square and rectangular concrete column specimens to study the effect of high-strength

concrete columns on plastic hinge length. The concrete strength for standard cylinders ranged between 10,000 and 16,000 psi (72 MPa and 112 MPa). The cross-sections of the columns were 12 in. (305 mm) square, and 12 in. (305 mm) by 10 in. (250 mm) rectangular dimensions with 72.5 in. (1,841 mm) in height. The shear span-to-depth ratios were 6, 7.4 and 5.3.

The plastic hinge lengths of the specimens tested were calculated using the Eq. (1.2) for all the load cycles in which the displacement ductility factor is greater than 4 and then averaged to find the equivalent plastic hinge length for the columns. The experimental plastic hinge lengths were close to the depth of column sections (h) as given in column (9) of Table 1.7. It was suggested that a simpler expression such as L_p = x*h, where x can have a value between 0.9 and 1, is more appropriate to obtain the plastic hinge length for the columns.

In the two studies, as the axial load increased, the deformability of the reinforced concrete columns reduced and strength and stiffness degradation with every load cycle accelerated. Thus, a larger amount of lateral reinforcement was needed to balance this effect. Bayrak and Sheikh (1997) concluded that the axial load level should be considered in the design of confining reinforcement. Based on the test results, the displacement ductility factors decreased with increasing shear span-to-depth ratios (L/h). It was observed that section geometry and shear span-to-depth ratio influenced the member-level ductility parameters (which are the displacement ductility factor, and work damage indicator that was represented by the work done on the column by lateral load), whereas section-level ductility parameters (which are the curvature ductility factor, and energy damage indicator that was defined by energy dissipated in the plastic hinge region) were not affected by these factors.

Table 1.7. Details and test results of column specimens

Unit	f_c' ksi (MPa) (1)	$P/f_c'Ag$ (2)	Longitudinal Steel		Transverse Steel				Section Depth, in. (mm) (9)	Exp. L_p, in. (mm) (10)	L_p/h (11)
			f_y, ksi (MPa) (3)	ρ_l (%) (4)	Spec.,in. (mm) (5)	f_{yh}, ksi (MPa) (6)	ρ_s (%) (7)	$A_{sh}/A_{sh,ACI}$ (8)			
ES-1HT	10.45 (72)	0.5	65.83 (454)	2.58	3.74 (95)	67.14 (463)	3.15	1.13	12.01 (305)	13.82 (351)	1.15
AS-2HT	10.4 (72)	0.36	65.83 (454)	2.58	3.54 (90)	78.59 (542)	2.84	1.19	12.01 (305)	11.73 (298)	0.98
AS-3HT	10.41 (72)	0.5	65.83 (454)	2.58	3.54 (90)	78.59 (542)	2.84	1.19	12.01 (305)	10.87 (276)	0.91
AS-4HT	10.43 (72)	0.5	65.83 (454)	2.58	3.94 (100)	67.14 (463)	5.12	1.83	12.01 (305)	10.71 (272)	0.89
AS-5HT	14.76 (102)	0.45	65.83 (454)	2.58	3.54 (90)	78.59 (542)	4.83	1.08	12.01 (305)	10.31 (262)	0.86
AS-6HT	14.78 (102)	0.46	65.83 (454)	2.58	2.99 (76)	67.14 (463)	6.72	1.62	12.01 (305)	12.64 (321)	1.05
AS-7HT	14.79 (102)	0.45	65.83 (454)	2.58	3.7 (94)	78.59 (542)	2.72	0.8	12.01 (305)	10.55 (268)	0.88
ES-8HT	14.82 (102)	0.47	65.83 (454)	2.58	2.76 (70)	67.14 (463)	4.29	1.08	12.01 (305)	15.16 (385)	1.26
RS-9HT	10.32 (71)	0.34	65.83 (454)	2.74	3.15 (80)	78.59 (542)	3.44	1.72	13.78 (350)	14.09 (358)	1.02
RS-10HT	10.31 (71)	0.5	65.83 (454)	2.74	3.15 (80)	78.59 (542)	3.44	1.72	13.78 (350)	17.48 (444)	1.27
RS-11HT	10.27 (71)	0.51	65.83 (454)	2.74	3.15 (80)	78.59 (542)	5.43	2.29	13.78 (350)	15.59 (396)	1.13
RS-12HT	10.28 (71)	0.34	65.83 (454)	2.74	5.91 (150)	78.59 (542)	1.83	0.92	13.78 (350)	16.42 (417)	1.19
RS-13HT	16.25 (112)	0.35	65.83 (454)	2.74	2.76 (70)	67.43 (465)	3.92	1.09	13.78 (350)	11.65 (296)	0.85
RS-14HT	16.25 (112)	0.46	65.83 (454)	2.74	2.76 (70)	67.43 (465)	3.92	1.09	13.78 (350)	13.82 (351)	1
RS-15HT	8.15 (56)	0.36	65.83 (454)	2.74	3.94 (100)	67.43 (465)	2.75	1.49	13.78 (350)	10.71 (272)	0.78
RS-16HT	8.15 (56)	0.37	65.83 (454)	2.74	5.91 (150)	67.43 (465)	1.83	1	13.78 (350)	14.84 (377)	1.08
RS-17HT	10.74 (74)	0.34	75.55 (521)	2.74	2.95 (75)	197.2 (1360)	1.83	1.39	13.78 (350)	11.65 (296)	0.85
RS-18HT	10.74 (74)	0.5	75.55 (521)	2.74	2.95 (75)	197.2 (1360)	1.83	1.39	13.78 (350)	12.56 (319)	0.91
RS-19HT	10.76 (74)	0.53	75.55 (521)	2.74	2.95 (75)	203.29 (1402)	3.54	2.67	13.78 (350)	13.54 (344)	0.98
RS-20HT	10.76 (74)	0.34	75.55 (521)	2.74	5.51 (140)	203.29 (1402)	1.9	1.43	13.78 (350)	13.74 (349)	1
WRS-21HT	13.24 (91)	0.47	75.55 (521)	2.74	2.76 (70)	67.43 (465)	3.92	1.31	9.84 (250)	11.02 (280)	1.12
WRS-22HT	13.24 (91)	0.31	75.55 (521)	2.74	2.76 (70)	67.43 (465)	3.92	1.31	9.84 (250)	10.98 (279)	1.11
WRS-23HT	10.47 (72)	0.33	75.55 (521)	2.74	3.15 (80)	78.59 (542)	3.44	1.7	9.84 (250)	10.08 (256)	1.03
WRS-24HT	10.47 (72)	0.5	75.55 (521)	2.74	3.15 (80)	78.59 (542)	3.44	1.7	9.84 (250)	9.72 (247)	0.99
									Average		1.01
									Standard Deviation		0.13

Notes to Table 1.7:

1: Compressive cylinder strength of concrete

2: Applied axial load ratio

3: The yield strength of longitudinal steel

4: The longitudinal reinforcement ratio

5: Spacing of transverse reinforcement

6: The yield strength of transverse steel

7: The volumetric ratio of transverse reinforcement to core concrete

8: The total cross sectional area of rectangular hoop reinforcement for confinement according to ACI 318

9: Cross sectional depth

10: The measured plastic hinge length

11: The ratio of measured plastic hinge length to the column depth

*: The maximum average tie strain reached in Specimens RS-17HT, RS-18HT, RS-19HT and RS-20HT is 0.00425. Therefore, maximum attainable strength of 850 MPa is used in the calculations.

1.3.13 Bae (2005)

Based on previous developed work [Bayrak and Sheikh (1997), and Bayrak (1999)], a new experimental program was designed by Bae at the University of Texas at Austin to investigate the influence of certain parameters on plastic hinge length. These parameters were shear span-to-depth ratio (L/h), axial load level (P/P_o), and amount of confining reinforcement (A_{sh}).

In this experimental program, four of the test specimens had column cross-section dimensions of 24 in. (610 mm) by 24 in. (610 mm) and a height of 103.5 in. (2,630 mm), with end stubs having cross-section dimensions of 38 in. (965 mm) by 38 in. (965 mm) and a height of 80 in. (2030 mm). The dimensions of only one specimen called S17-3UT had a 17.25 in. (440 mm) square cross section. Figure 1.6 illustrates a typical specimen. Table 1.8 lists the details of the specimens and the axial load level. The specified nominal 28 day strength of concrete was 4,000 psi (28 MPa) for the first specimen, which was used as a guide to check the performance of the test setup, and 6,000 psi (42 MPa) for the other test specimens.

Table 1.8. Details of test specimens

Specimen	bxh, in. x in. (mm x mm) (1)	f_c', ksi (MPa) (2)	Longitudinal Steel			Transverse Steel			P/P_o (9)
			Bar Size, (SI) (3)	ρ_l (%) (4)	f_{yl}, ksi (MPa) (5)	ρ_s (%) (6)	$f_{yh,}$ ksi (MPa) (7)	$A_{sh}/A_{sh,ACI}$ (8)	
S24-1UT	24 x 24 (610 x 610)	4.3 (30)	No.9 (29)	2.08	84 (579)	1.28	64 (441)	1.04	0.5
S24-2UT	24 x 24 (610 x 610)	6.3 (43)	No.7-1 (22)	1.25	73 (503)	2.04	62 (427)	1.09	0.5
S17-3UT	17.25 x 17.25 (438 x 438)	6.3 (43)	No.5 (16)	1.25	72 (496)	1.76	72 (496)	1.12	0.5
S24-4UT	24 x 24 (610 x 610)	5.3 (37)	No.7-2 (22)	1.25	58 (400)	0.72	66 (455)	0.44	0.2
S24-5UT	24 x 24 (610 x 610)	6 (41)	No.7-2 (22)	1.25	58 (400)	1.3	63 (434)	0.74	0.2

1: Cross sectional dimensions

2: Compressive cylinder strength of concrete

3: Bar sizes for the longitudinal reinforcement according to English and SI units

4: The longitudinal reinforcement ratio

5: The yield strength of longitudinal steel

6: The volumetric ratio of transverse reinforcement to core concrete

7: The yield strength of transverse steel

8: The total cross sectional area of rectangular hoop reinforcement for confinement according to ACI 318

9: The ratio of axial load, where $P_0 = 0.85 f'_c A_c + f_{yl} A_s$

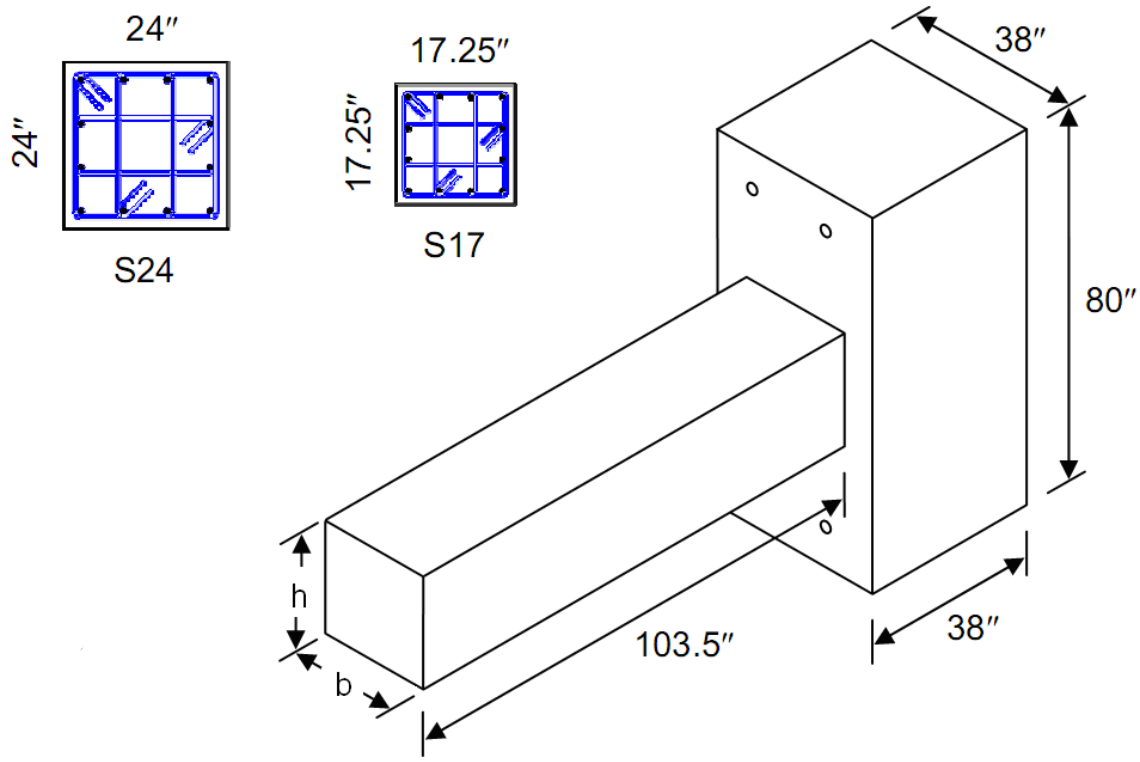

Figure 1.6 Layout of Test Specimens (Bae 2005)

The behaviors that were observed from specimens S24-2UT and S17-3UT were compared in detail to examine the effect of shear span-to-depth ratio (L/h) on the response of concrete columns. Specimens S24-2UT and S17-3UT had 24 in. (610 mm) and 17.25 in. (440 mm) square cross-sections, respectively. These two specimens were designed with similar concrete strength, amount and detail of longitudinal and transverse reinforcement. The only difference between them was the shear span-to-depth ratio for specimens S24-2UT and S17-3UT due to different section sizes. The shear span-to-depth ratios of these specimens were calculated as 5 and 7, respectively. Similar sectional performance was obtained from tests of S24-2UT and S17-3UT. The curvature ductility factors, which are the ratio of ultimate curvature to the curvature at first yield, were

calculated from the backbone curves of specimens S24-2UT and S17-3UT as 8.8 and 9.1, respectively. The member-level deformation capacities of the specimens, however, were quite different. It was observed that as the shear span-to-depth ratio increased from 5 to 7, displacement ductility was significantly decreased from 5.9 to 2.7. The drift capacity then dropped from 2.6% to 1.6%. From all the observations above, it can be summarized that the shear span-to-depth ratio had an important effect on the overall member performance of the test columns.

Bae (2005) introduced an analytical approach to estimate the plastic hinge length of a concrete column. In this approach, first the intensity of concrete compressive strains is measured at critical sections along the length of a column, and then using the compressive strain profile, the yielding region length of longitudinal bars can be estimated. Finally, the plastic hinge length is calculated by subtracting the stub confinement effect (approximately 0.25h where h is the column depth) from the overall length where the compressive bar strains are greater than the yield strain.

A series of theoretical analyses were carried out to study the influence of the shear span-to-depth ratio on the plastic hinge length. A 24 in. (610 mm) square column having different shear span-to-depth ratios (L/h) was designed. The longitudinal reinforcement was constant as $\rho_l = 0.01$. The results of the analyses are shown in Fig. 1.7. The plastic hinge length increased with increasing L/h, and this effect was more pronounced as the axial load increased.

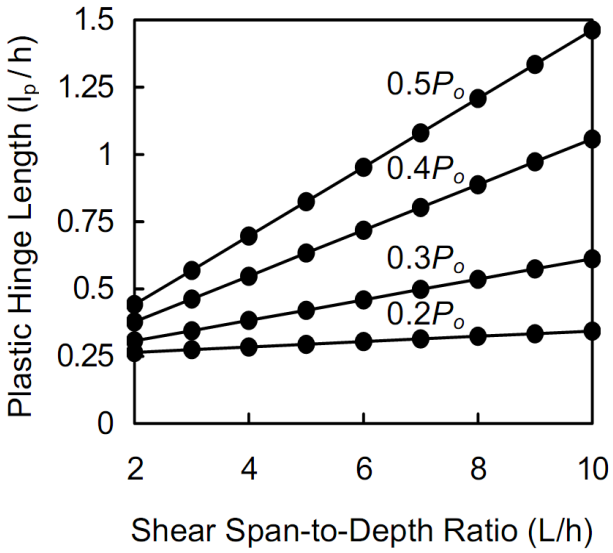

Figure 1.7 Relationship between Plastic Hinge Length and Shear Span-to-Depth Ratio (Bae 2005)

To verify the conclusions observed in the analytical study, specimens S24-4UT and S24-5UT [which were tested under low axial loads ($P = 0.2P_o$)] were examined in greater detail to study the effect of axial load. The behaviors of the specimens S24-4UT and S24-5UT were compared with the behavior of specimen S24-2UT that was tested under a high axial load level of $0.5P_o$. The confinement reinforcement of specimens S24-4UT and S24-5UT were not designed according to the ACI 318-05 code requirements, whereas specimen S24-2UT met the code requirements. The shear span-to-depth ratio (L/h=5) was the same for these specimens. It was observed that the deformation capacity of specimen S24-2UT was less than that of specimens S24-4UT and S24-5UT. The lateral load-displacement responses were normalized to maximum lateral load and yield displacement. The normalized response of S24-4UT, however, showed less ductile response than that of specimen S24-2UT. The member-level ductility parameters

(displacement ductility, and energy absorption) for specimen S24-2UT gave higher values than those of specimen S24-4UT, but less than those of specimen S24-5UT.

To determine the sensitivity of the analysis, a 24 in (610 mm) square column with 120 in. (3,050 mm) length was studied to investigate the effect of axial load on the plastic hinge length. The percentage of longitudinal reinforcement was 1% for each specimen. Concrete strength was 6,000 psi (42 MPa). The yield and ultimate strength of reinforcing bars were 60 ksi (414 MPa) and 90 ksi (620 MPa), respectively. Along the length of columns, the curvature and compressive concrete strain profiles were examined for different axial load levels (from $0.2P_o$ to $0.5P_o$).

Figure 1.8 shows the effect of axial load on curvature and compressive strain of concrete. The curvature profiles are not affected from the various axial load levels whereas the compressive strain profiles indicate the influence of axial load very well.

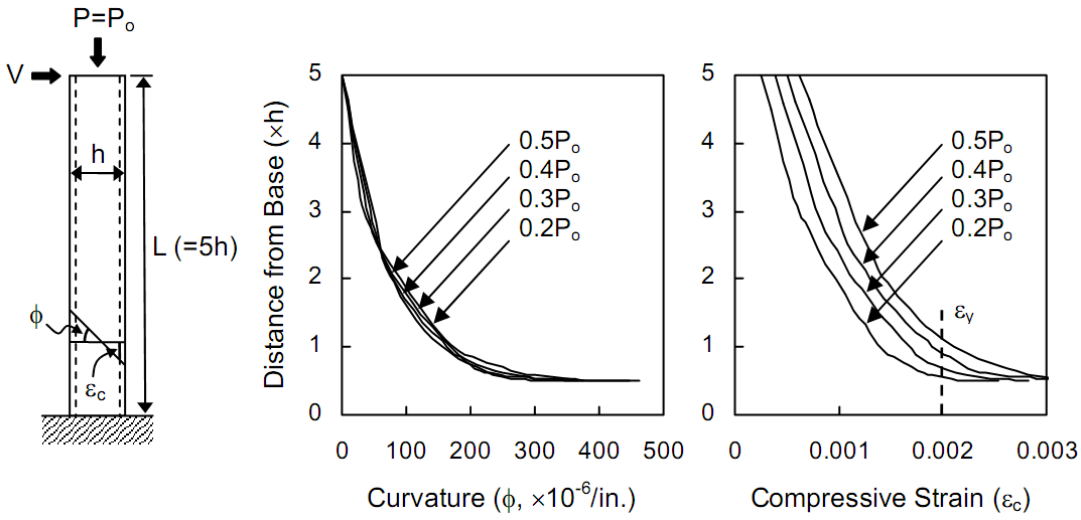

Figure 1.8 Effect of Axial Load on Curvature and Compressive Strain Profiles (Bae 2005)

To estimate the plastic hinge length, the region of reinforcing bars that yield in compression was investigated along the column. Fig. 1.9 shows that the plastic hinge

length is nearly constant for low axial loads ($P \leq 0.2P_o$) where it is approximately equal to h/4. The plastic hinge length increases as axial loads increase ($P>0.2P_o$).

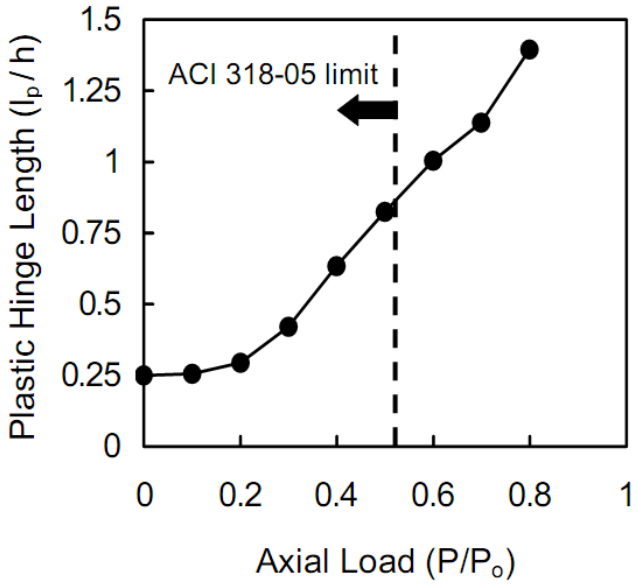

Figure 1.9 Relationship between Plastic Hinge Length and Axial Load (Bae 2005)

The estimated plastic hinge length is approximately equal to 0.8h at the axial load level of $0.52P_o$, which is the maximum axial load allowed by ACI 318-05 ($\varphi P_{n,max} = \varphi \times 0.8P_o = 0.65 \times 0.8P_o = 0.52P_o$ for tie reinforcement). An additional length of 0.25h should be added to the plastic hinge to take into account the stub confinement effect. The required confined length was calculated as 1.05h by adding the largest estimated plastic hinge length and a distance of 0.25h. The length of the region of confinement should be the largest of the overall depth of a column, one-sixth of the clear height of a column, or 18 in. (457 mm) according to Chapter 21 of the ACI 318-05 code. The confinement region length indicated by ACI 318-05 appears to be satisfactory for low axial loads.

To evaluate the effect of longitudinal reinforcement on the plastic hinge lengths, a 24 in. (610 mm) square column with 120 in. (3,050 mm) length was designed. The shear span-to-depth ratio of the column specimens was 5. The curvature and compressive

strain profiles along the length of the column were examined to obtain the plastic hinge lengths. Results showed that as the longitudinal reinforcement ratio (ρ_l) increases, the length of the plastic hinge increases. Figure 1.10 shows the results for different axial load levels.

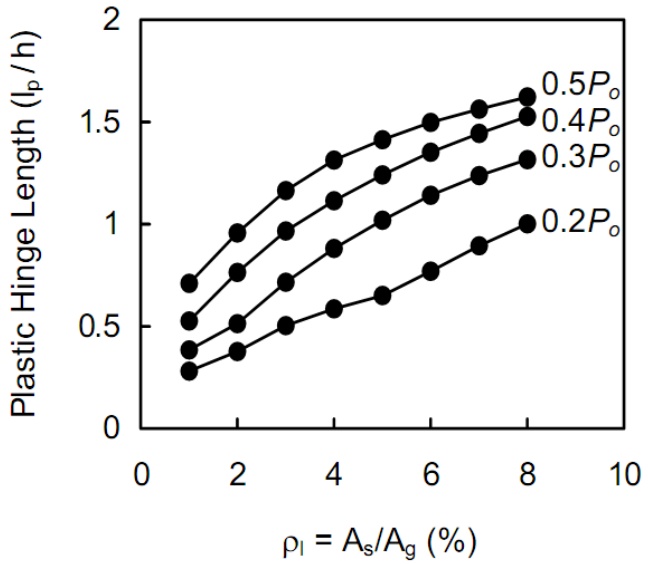

Figure 1.10 Effect of Amount of Longitudinal Reinforcement (Bae 2005)

After all the sensitivity analyses were done, results showed that axial load, shear span-to-depth ratio, and the amount of longitudinal reinforcement significantly influenced the length of plastic hinges. Using linear relationships between the parameters (P/P_o, L/h, and A_s/A_g) and the plastic hinge, a plastic hinge length expression was calibrated based on the analysis results. Equation 1.25 was proposed from the result of a series of least squares analyses that were done on the UW/PEER column database (http://maximus.ce.washington.edu/~peera1/).

$$\frac{l_p}{h} = \left[0.3\left(\frac{P}{P_0}\right) + 3\left(\frac{A_s}{A_g}\right) - 0.1\right]\left(\frac{L}{h}\right) + 0.25 \geq 0.25 \qquad (1.20)$$

The plastic hinge lengths obtained from the analysis of compressive strains along the column height and those from using Eq. 1.20 were compared in Fig. 1.11. It was observed that the plastic hinge lengths estimated by the analytical approach and Eq. 1.20 did not match very well, especially at high axial loads and large shear span-to-depth ratios, because the plastic hinge lengths obtained from the analysis of compressive strains are approximate results. It was important to mention that Bae (2005) proposed to find a simple expression so that conservative estimations for the deformation capacity of concrete columns can be obtained. It can be summarized that moderate plastic hinge length values can be determined using the new formula for a wide range of axial loads, shear span-to-depth ratios, and amount of longitudinal reinforcement.

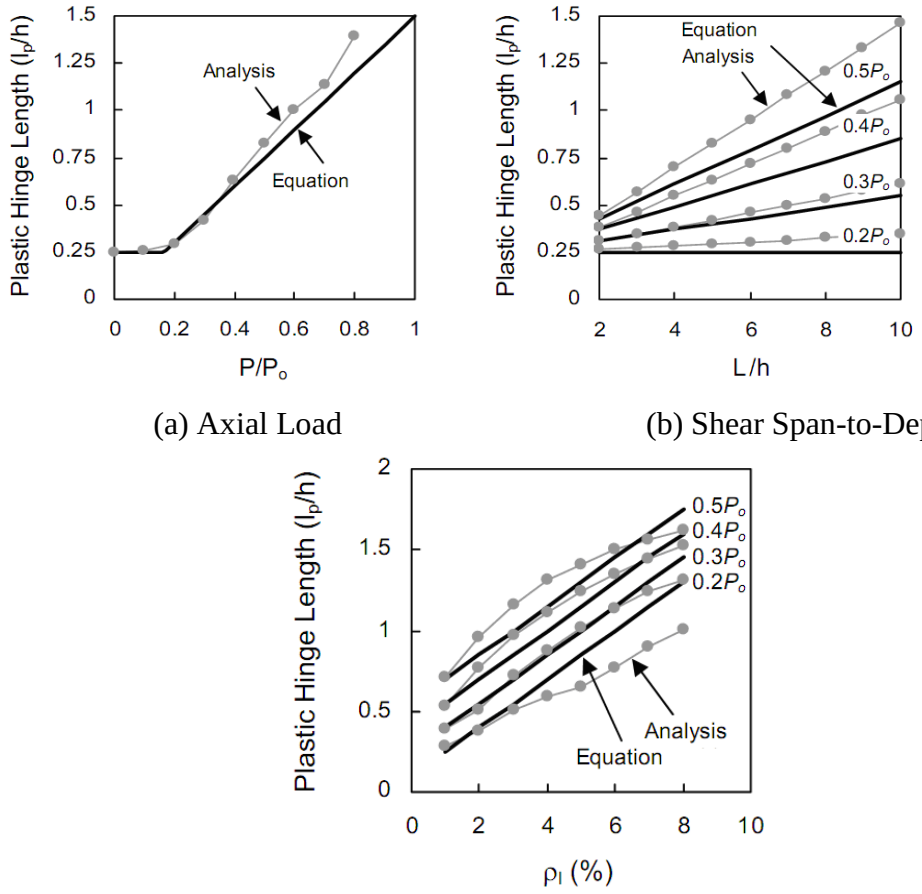

(a) Axial Load (b) Shear Span-to-Depth Ratio

(c) Amount of Longitudinal Reinforcement

Figure 1.11 Comparisons of Plastic Hinge Length (Eq. (1.20) versus Analysis) (Bae 2005)

Table 1.9. Comparisons of measured and proposed plastic hinge lengths

Specimen	Measured L_p	Proposed L_p
S24-1UT	-	-
S24-2UT	0.66h	0.69h
S17-3UT	0.91h	0.86h
S24-4UT	0.49h	0.25h
S24-5UT	0.47h	0.25h

1.3.14 Restrepo, Seible, Stephan, and Schoettler (2006)

To assess the seismic performance of columns using high-strength reinforcing steel, two 35%-scale circular bridge column units were constructed and tested under quasi-static reversed cyclic loading at University of California, San Diego. Unit 1 was built with Grade 60 ASTM A 706 reinforcement whereas Unit 2 was built with high-strength reinforcing steel (94 ksi or 650 MPa) to compare the behavior of columns.

The ultimate displacement capacity for the two tested units was estimated using the equivalent plastic hinge length given by Eq. (1.17) (Paulay and Priestley 1992) and found to be less than the values measured during the tests. The equivalent plastic hinge length given by Eq. (1.17) was subsequently modified using two generic multipliers α and β

$$L_p = \alpha H + \beta f_{ye} d_{bl} \leq 2\beta f_{ye} d_{bl} \tag{1.21}$$

where α is a yield spread coefficient and β is a strain penetration coefficient.

For a cantilever column (Fig. 1.12(a)), the flexural component of lateral deflection at the top of the cantilever δ_{fle} was determined from the integration of the curvature distribution in the column. Fig.1.12(c) shows the moment and curvature distributions along the column height.

$$\delta_{fle} = \int_0^H y\Phi dy = \delta_{elf} + \delta_{pf} \tag{1.22}$$

The resulting deflection can be divided into elastic δ_{elf} (Eq. 1.23a) and plastic δ_{pf} (Eq.1.23b) components that are consistent with the equivalent curvature distribution drawn in Fig. 1.12(d). This calculation is demonstrated in Eq. (1.23):

$$\delta_{elf} = \left(\frac{M}{M_y} \phi_y^{'} \right) \frac{H^2}{3} \tag{1.23a}$$

$$\delta_{pf} = \phi_p \alpha H^2 (1 - \frac{\alpha}{2}) \tag{1.23b}$$

where ϕ_p is the plastic curvature given by Eq. (1.24):

$$\phi_p = \phi - \frac{M}{M_y} \phi_y^{'} \tag{1.24}$$

Combining Eq. (1.22) through (1.24), and finding the solution for α

$$\alpha = 1 - \sqrt{1 - 2 \frac{\delta_{fle} - (\frac{M}{M_y} \phi_y^{'}) \frac{H^2}{3}}{\phi_p H^2}} \tag{1.25}$$

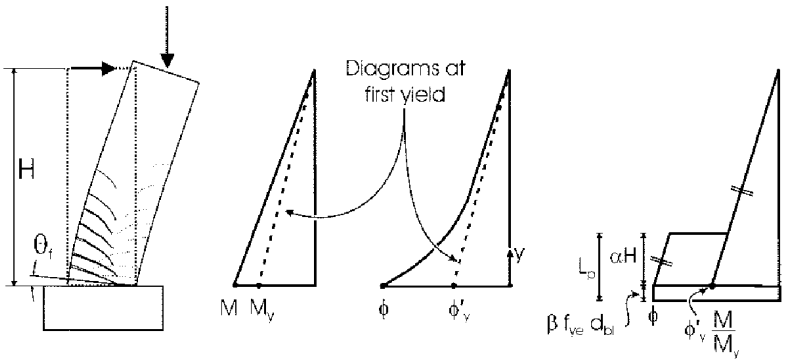

(a) (b) (c) (d)

Figure 1.12 Idealization of curvature distribution in column: (a) column; (b) BMD; (c) curvature diagram; and (d) equivalent curvature diagram (Restrepo et al. 2006)

The strain penetration coefficient β can be obtained from the reading of the first and second displacement transducers that were instrumented immediately above the

column base. The fixed-end rotation shown in Fig. 1.12(a) can be calculated from the first set of displacement transducers if the gauge length is small enough to minimize the effect of local bond slip in the rotation. The second set of displacement transducers is used to estimate the base curvature ϕ shown in Fig. 1.12(d). The plastic hinge length due to strain penetration can be written as

$$\beta f_{ye} d_{bl} = \frac{\theta_f}{\phi} \tag{1.26}$$

Therefore, β is

$$\beta = \frac{\theta_f}{\phi f_{ye} d_{bl}} \tag{1.27}$$

Figure 1.13 and 1.14 illustrate α and β versus the curvature ductility demand gained from both test units, respectively. The values of α = 0.08 and β = 0.15 (if f_{ye} is in MPa, β is equal to 0.022) used in Eq. (1.17) are shown in these figures.

It can be seen that the coefficient α increases as the curvature ductility demand increases because the spread of plasticity takes place gradually until a column reaches its maximum ductility capacity. Figure 1.13 shows that the maximum spread of plasticity is significantly greater than predicted by Paulay and Priestley (1992) for both test results.

Unlike the spread of plasticity coefficient α, the strain penetration coefficient β is absolutely independent from the curvature ductility demand as shown in Fig. 1.14. It is seen that the values of coefficient β obtained for Units 1 and 2 are also greater than the value proposed by Paulay and Priestley (1992). It is expected that equivalent plastic hinge lengths will be greater than those obtained by Eq. (1.17) because both values of coefficients are greater than the values recommended by Paulay and Priestley (1992). Therefore, the theoretical lateral deformation capacity is greatly underestimated for circular columns when using Eq. (1.17).

Restrepo et al. (2006) observed that using higher-strength reinforcement could be promoted in seismic design. In addition, using higher-strength transverse reinforcement restrains the longitudinal reinforcement and prevents buckling. Restrepo et al. observed that the equivalent plastic hinge lengths determined from the test units were greater than the equivalent length predicted by Eq. (1.17) (Paulay and Priestley 1992) by at least 40% as shown in Fig. 1.15.

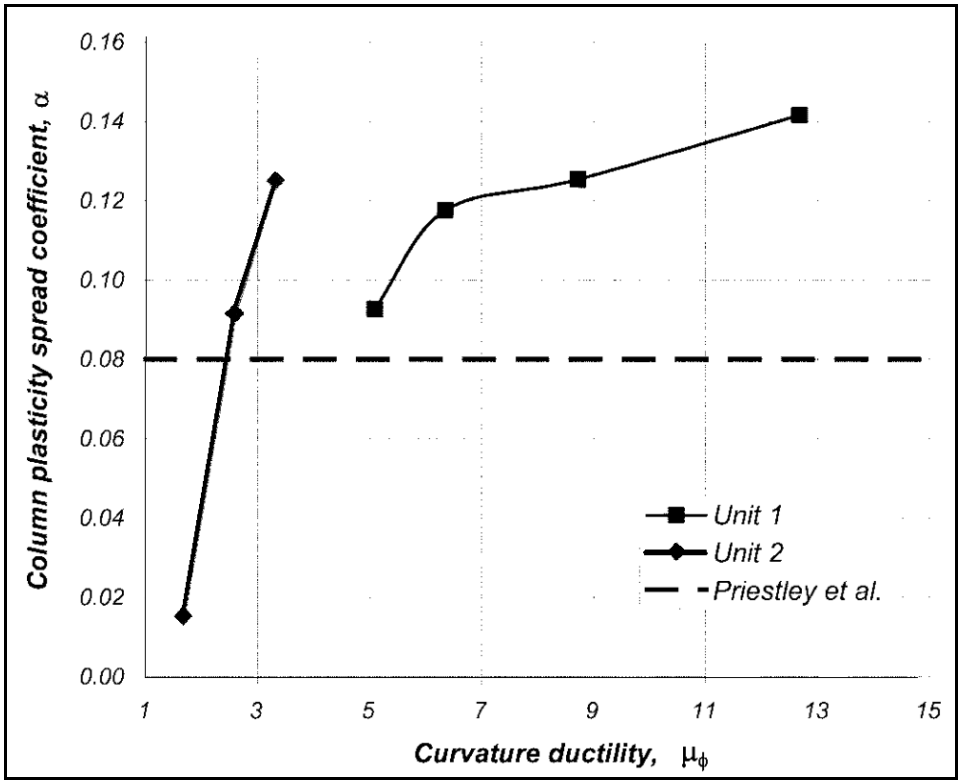

Figure 1.13 Plasticity spread coefficient α ((Restrepo et al. 2006)

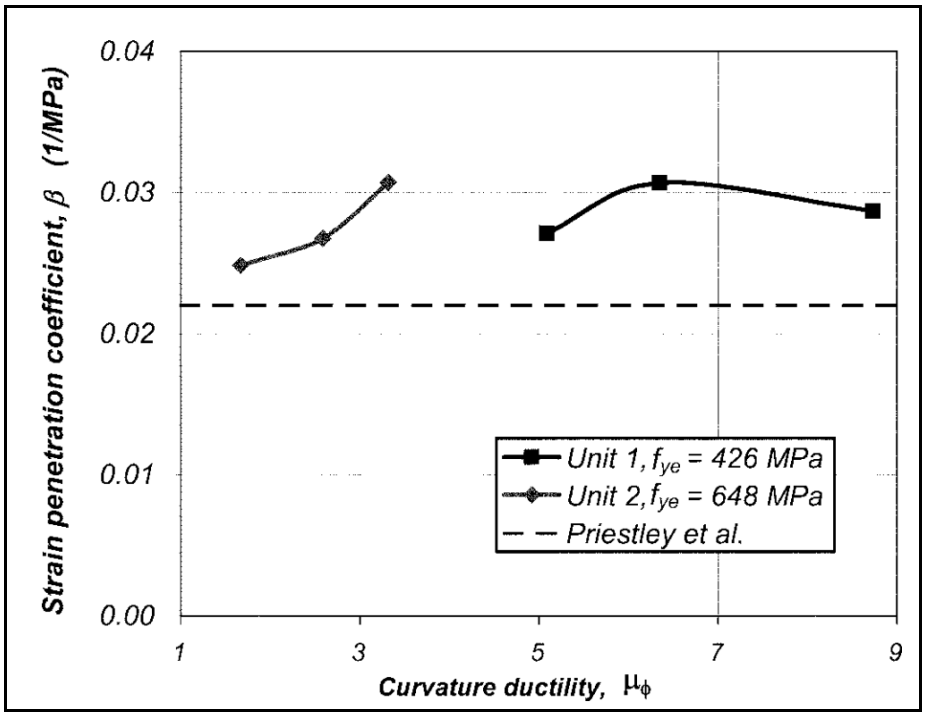

Figure 1.14 Strain penetration coefficient β (Restrepo et al. 2006)

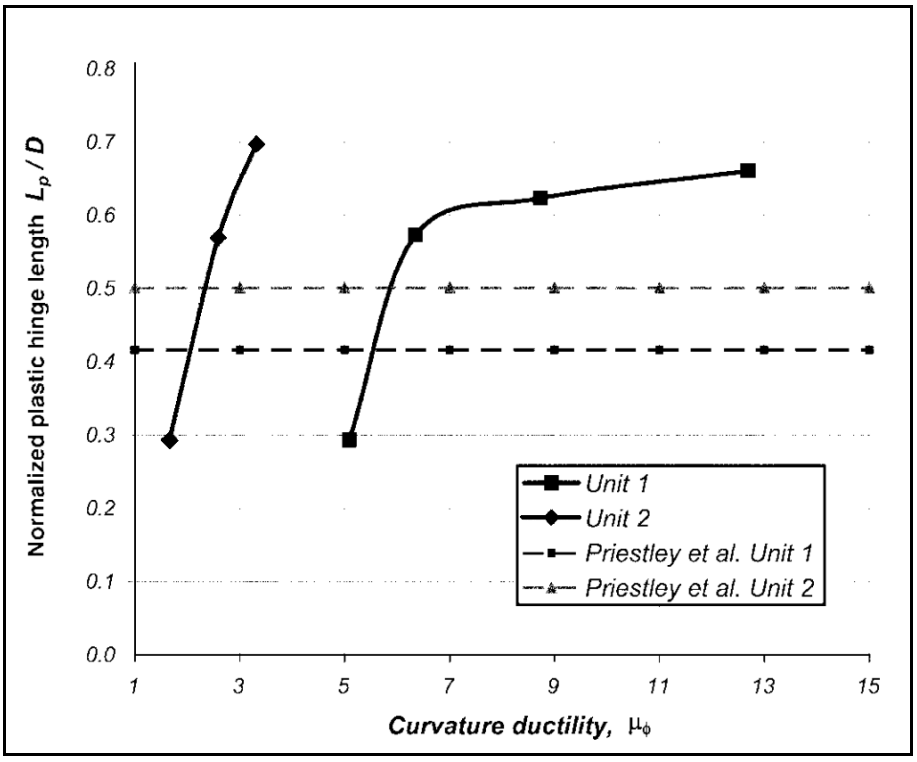

Figure 1.15 Equivalent plastic hinge length as ratio of column diameter (Restrepo et al. 2006)

1.3.15 Phan V., Saiidi M.S., Anderson J., and Ghasemi H. (2007)

Phan et al. (2007) designed two one-third scale reinforced concrete bridge columns (labeled NF-1 and NF-2) that were tested on a shake table at the University of Nevada, Reno Large Scale Structures Laboratory to investigate near-fault ground motion effects on bridge columns. NF1 and NF2 had the same cross-sectional properties and column height. The only difference was that NF1 was designed according to 2004 Caltrans Seismic Design Criteria (SDC) version 1.3, whereas NF2 was designed based on the AASHTO 2002 Standard Specifications for Highway Bridges (AASHTO 2002). NF1 column specimen was nearly identical to 9F1 that was tested in the same laboratory during a previous study (Laplace 2005). The only difference between NF-1 and 9F1 was that NF-1 was subjected to near-fault impulsive ground motion whereas 9F1 was tested under an earthquake record that did not include forward directivity effects (El Centro 1940).

Paulay and Priestley's equation (Eq. 1.17) was used to estimate the theoretical plastic hinge length (l_p) for each specimen. The theoretical values are generally conservative for conventional reinforced concrete columns. For all three specimens, the theoretical l_p was calculated as 11.26 in. (286 mm). Table 1.10 lists the measured l_p for all the test specimens to examine whether current methods for calculating l_p may underestimate the actual value in structures subjected to near-fault ground motions (Hamilton et al. 2001). The measured l_p were 51-95% longer than those determined using Eq. (1.17). The l_p for specimen NF-2 was very similar to that of specimen 9F1, and l_p for NF-1 was also comparable. Phan et al. concluded that there did not appear to be enough evidence to make alterations of l_p based on these tests.

Table 1.10 Measured plastic hinge lengths

Specimen	Column diameter d, in. (mm)	Concrete strength $f_c^{'}$, ksi (MPa)	Steel strength f_y, ksi (MPa)	Span/depth L/d	Plastic hinge length l_p, in. (mm)	Ratio to diameter l_p/d
NF-1	16 (406)	6 (41)	68.01 (469)	4.5	22 (559)	1.38
NF-2	16 (406)	6.15 (42)	68.01 (469)	4.5	17.05 (433)	1.07
9F1	16 (406)	6 (41)	68.01 (469)	4.5	17.01 (432)	1.06

1.3.16 Berry, Lehman, and Lowes (2008)

Berry et al. (2008) used the data from the tests of large-scale circular bridge columns to evaluate the models for performance-based earthquake engineering requirements for bridge columns, including a new expression for plastic hinge length. Thirty-seven spiral-reinforced column tests out of 168 possible tests in the UW-PEER Structural Performance Database (Berry 2004) were constructed with modern design details after 1980. Each of these columns had the following design details, which were used to define modern designed bridge columns:

- Axial load ratio: $P/f_c^{'}A_g \leq 0.3$, where P is the column axial load, $f_c^{'}$ is the concrete compressive strength, and A_g is the gross section area of the column;
- Spiral pitch $\leq 6d_b$, where d_b is the diameter of the longitudinal reinforcement;
- Effective confinement ratio $\rho_{eff} \geq 0.05$, where

$$\rho_{eff} = \frac{\rho_s f_{ys}}{f_c^{'}} \tag{1.28}$$

where ρ_s is the spiral reinforcement ratio which is the ratio of spiral reinforcement volume to the volume of core concrete, and f_{ys} is the yield strength of the spiral;

- Depth of cover concrete over transverse reinforcement ≤ 0.1D, where D is the diameter of the column; and
- Longitudinal reinforcement ratio ≤ 4%.

Berry et al. (2008) evaluated the plastic hinge length expression provided by Paulay and Priestley (1992) which has been adopted by California Department of Transportation. A new expression was proposed by the authors:

$$l_p = \lambda_1 D + \lambda_2 L + \lambda_3 \frac{f_y d_b}{\sqrt{f_c'}} \tag{1.29}$$

The last term in Eq. 1.29 was added to include the effect of strain penetration on the spread of plasticity. The new expression was calibrated using the test data and the parameters (λ_1, λ_2, and λ_3) were determined using available optimization algorithms. Two plastic hinge length expressions were defined as an optimal and a recommended expression. The optimal expression was determined from the minimum value of the errors, which were the errors associated with simulation of the column force-displacement response history, and the errors due to the ratio of measured-to-calculated displacements at the beginning of spalling and bar buckling. The optimal expression is written as:

$$l_p = 0.0375L + 0.01\frac{f_y d_b}{\sqrt{f_c'}} \quad \text{(psi)} \tag{1.30a}$$

$$l_p = 0.0375L + 0.12\frac{f_y d_b}{\sqrt{f_c'}} \quad \text{(MPa)} \tag{1.30b}$$

A simplified recommended expression that represents a slight increase in error (from 8.05 to 8.09) is given for design purposes:

$$l_p = 0.05L + 0.008\frac{f_y d_b}{\sqrt{f_c'}} \qquad \text{(psi)} \qquad (1.31a)$$

$$l_p = 0.05L + 0.1\frac{f_y d_b}{\sqrt{f_c'}} \qquad \text{(MPa)} \qquad (1.31b)$$

The force-displacement response predicted using Eq. (1.31a and b) for columns with different axial load and aspect ratios shows good comparison with the envelope to the measured cyclic response, as shown for selected tests in Fig. 1.16.

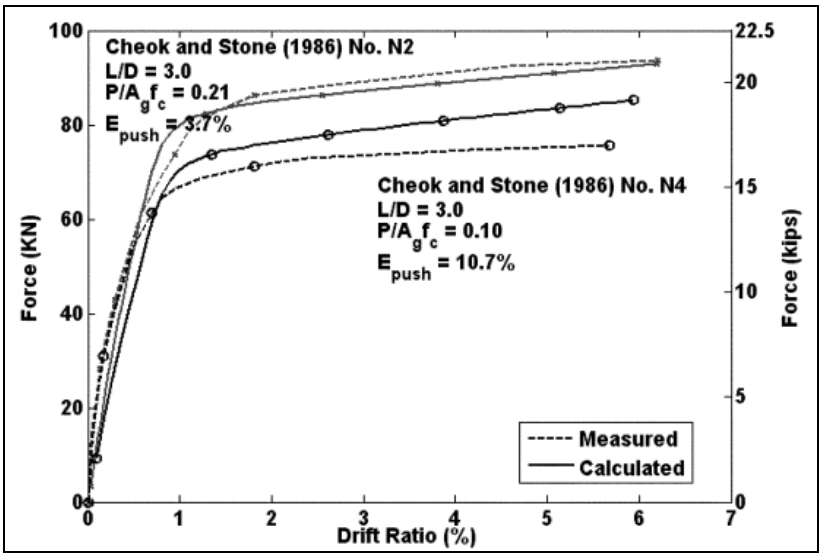

(a) Columns with different axial load ratios

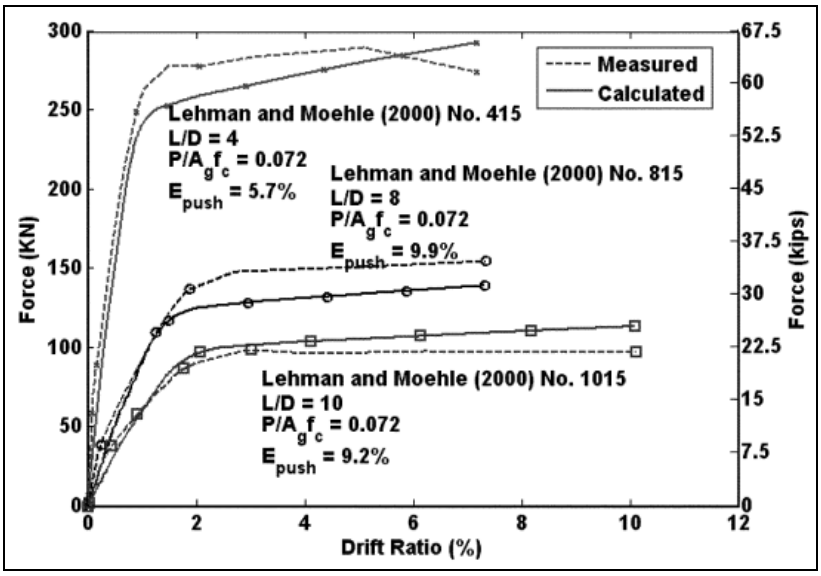

(b) Columns with different aspect ratios

Fig. 1.16 Simulated and observed force-drift ratio for columns with different design parameters (Berry et al. 2008)

1.4 LITERATURE REVIEW OF PLASTIC HINGE LENGTH (DYNAMIC TESTS)

1.4.1 Dodd et al. (2000)

Fourteen one-sixth scale single-stem reinforced concrete cantilever columns with various aspect ratios and axial-load ratios were tested on a shaking table to investigate the applicability of current design provisions and theoretical models that are based on test data from quasi-statically tested specimens, to more realistic dynamic base excitation conditions that columns experience during earthquakes.

The main parameters of interest were the aspect ratio of the columns, the axial load ratio, the base flexibility, the base input motions, and the effect of initial low-level shaking on the response of columns to subsequent higher-level shakes. Table 1.11 lists details of all 14 columns. All of the columns were 200 mm in diameter and contained 18

uniformly distributed longitudinal bars having a 0.24 in. (6 mm) diameter with an average yield stress of 65 ksi (450 MPa). The longitudinal steel ratio was 1.62%. The compressive strengths at the time of testing were given in Table 1.11. Columns with aspect ratios of 4, 7, and 10 were tested to provide data on a range of flexurally dominated columns. Axial-load ratios of 0.05 and 0.4 were chosen to check the behavior of columns above and below the balance point on the axial load moment interaction diagram.

A record based on the 1940 El Centro N-S component earthquake was used as a base motion for all columns except 1a, 2a, and 3a, which were subjected to a uniform sinusoidal base motion.

The effective plastic hinge length on a bridge column was considered to be the equivalent length over which all plasticity takes place with a constant plastic curvature. The plastic hinge length was calculated using the equation proposed by Priestley et al. (1992) and the reduction factor defined by Zahn et al. (1986). The reduction factor was to be 0.5+1.67P/(fc'Ag) for P/(fc'Ag) less than 0.3 to modify Priestley's equation. It was observed from the experimental values that axial load has an effect on the plastic hinge length and the equation overestimates the plastic hinge length for the columns. It was also determined from the comparisons of calculated and measured plastic hinge length values that Zahn's recommendation is mostly conservative and agrees well with the measured values for all the columns having different aspect ratios.

Table 1.11 Details of the column properties

Column No.	f_c', ksi (MPa) (1)	$P/f_c'A_g$ (3)	Longitudinal Steel		Transverse Steel		D, in. (mm) (8)	L/D (9)	Calc. L_p, in. (mm) (10)	Meas.L_p, in. (mm) (11)
			f_y, ksi (MPa) (4)	ρ_l (%) (5)	f_{yh}, ksi (MPa) (6)	ρ_s (%) (7)				
1a	5.9 (41)	0.04	65 (448)	1.62	37.7 (260)	0.88	7.9 (201)	4	4.84 (123)	3.54 (90)
1b	4.64 (32)	0.051	65 (448)	1.62	37.7 (260)	0.88	7.9 (201)	4	4.84 (123)	3.35 (85)
2a	5 (34)	0.048	65 (448)	1.62	37.7 (260)	1.06	7.9 (201)	7	6.73 (171)	4.92 (125)
2b	4.39 (30)	0.054	65 (448)	1.62	37.7 (260)	1.06	7.9 (201)	7	6.73 (171)	5.31 (135)
3a	5.42 (37)	0.044	65 (448)	1.62	36.25 (250)	0.66	7.9 (201)	10	8.62 (219)	7.68 (195)
3b	4.22 (29)	0.056	65 (448)	1.62	36.25 (250)	0.66	7.9 (201)	10	8.62 (219)	5.91 (150)
4	5.71 (39)	0.391	65 (448)	1.62	37.7 (260)	0.94	7.9 (201)	4	4.84 (123)	4.72 (120)
5	5.39 (37)	0.388	65 (448)	1.62	37.7 (260)	1.02	7.9 (201)	7	6.73 (171)	11.02 (280)
6	5.6 (39)	0.387	65 (448)	1.62	36.25 (250)	0.79	7.9 (201)	10	8.62 (219)	10.83 (275)
7	5.99 (41)	0.04	65 (448)	1.62	36.25 (250)	0.46	7.9 (201)	4	4.84 (123)	3.35 (85)
8	5.81 (40)	0.392	65 (448)	1.62	37.7 (260)	0.94	7.9 (201)	4	4.84 (123)	7.48 (190)
9	5.86 (40)	0.041	65 (448)	1.62	36.25 (250)	0.46	7.9 (201)	7	6.73 (171)	5.31 (135)
10	5.35 (37)	0.044	65 (448)	1.62	37.7 (260)	0.88	7.9 (201)	4	4.84 (123)	3.74 (95)
11	6.24 (43)	0.358	65 (448)	1.62	37.7 (260)	0.94	7.9 (201)	4	4.84 (123)	7.68 (195)

1: Compressive cylinder strength of concrete

2: Applied axial load

3: Applied axial load ratio

4: The yield strength of longitudinal steel

5: The longitudinal reinforcement ratio

6: The yield strength of transverse steel

7: The volumetric ratio of transverse reinforcement to core concrete

8: Diameter of the columns

9: Aspect ratio

10: Calculated plastic hinge length using Eq. 1.17

11: The measured plastic hinge length

1.4.2 Hachem et al. (2003)

The dynamic testing of four circular reinforced concrete bridge columns on the earthquake simulator of the Earthquake Engineering Research Center at the University of California Berkeley was conducted to study the behavior of ductile bridge columns subjected to cyclic loading.

The specimens had a circular section with a diameter of 16 in. (405 mm) and the aspect ratio was 6. The axial load in the columns was taken to be 0.1Agfc' assuming a typical Caltrans concrete design strength of 3.25 ksi (22.4 MPa). Since the actual concrete compressive strength was 5.7 ksi (39.3 MPa) on average, the real axial load ratio was about $0.06f'_cA_g$. The yield strength of longitudinal reinforcement was 60 ksi (414 MPa). The longitudinal reinforcement consisted of 12 No. 4 deformed grade 60 (A706) reinforcing bars. The longitudinal and volumetric spiral reinforcement ratios were 1.2% and 0.54%, respectively.

The specimens were divided into two groups. In each group, one specimen was tested under one component of the ground motion, while the other specimen was subjected to two components of the motion. The first pair was subjected to a modified version of the Olive View record of the 1994 Northridge earthquake, which was a near-fault ground motion containing a high velocity pulse. The second pair was tested under the 1985 Chile earthquake recorded at the Llolleo station, which was 40 miles (64 km) away from the epicenter of the event.

The plastic hinge length before testing the circular bridge columns under bidirectional earthquake loading was estimated using the equation proposed by Priestley et al. (1992). The equation resulted in a plastic hinge length of 13.3 in. (338 mm). After testing the columns, it was also observed that plastic hinge length ranged from 12 in.

(305 mm) to 14 in. (356 mm) which was about 0.75D, where D is the diameter of the columns. The estimated plastic hinge length was within the observed range.

1.5 SUMMARY

Reinforced concrete bridge systems are generally designed to form plastic hinges in columns rather than the beams in the superstructure. Special detailing must be provided in reinforced concrete bridge columns along and beyond concentrated yielded regions (designated as the plastic hinge zones) to provide satisfactory behavior during response to strong ground motions. In addition, simple models to estimate drift in reinforced concrete bridge columns can be developed using a definition of lumped plasticity in the defined plastic hinge zone. Therefore, models that accurately locate the development and progression of hinging in reinforced concrete bridge systems support the improvement of calculations for local (damage in hinging regions and beyond) and global (maximum drift response) performance parameters.

Many researchers have studied the plastic hinge length in column elements depending on various parameters, such as axial load, yield penetration, shear spreading of plasticity, shear span-to-depth ratio, and the amount of longitudinal reinforcement. Various expressions were proposed by several researchers to estimate the plastic hinge length in these elements. The following are the observations investigated by the previous researchers:

- **Axial Load**. Extensive research has been conducted to examine the influence the level of axial load on plastic hinge length (ICC Committee Report (1962), Park et al. (1982), Priestley and Park (1987), Sakai and Sheikh (1989), Tanaka and Park (1990), Sheikh (1993, and 1994), Watson and Park (1994), Kovacic (1995), Bayrak and Sheikh (1997, and 1999), Dodd et al. (2000), and

Bae (2005)). The observations, however, are in disagreement. As mentioned in the studies of Park et al. (1982) and Priestley and Park (1987), the plastic hinge length was comparatively insensitive to axial load level. Park et al. (1982) concluded that l_p = 0.4h can be used as a simple and safe approximation for plastic hinge lengths in columns. On the contrary, Tanaka and Park (1990), Watson and Park (1994), Bayrak and Sheikh (1997, and 1999), Dodd et al. (2000), and Bae (2005) reported that the plastic hinge length increased with increasing axial load level. Only Watson and Park (1994) and Bae (2005) proposed expressions to consider the effect of axial load. Also, Kovacic (1995) justified the ACI (1968) limits for plastic hinge length for high strength concrete columns with low axial loads. The expressions are repeated here for clarity:

$l_p = 0.4*h$ (Park et al. 1982)

$$\frac{l_c}{h} = 1 + 0.4\frac{P}{\phi f_c^{'} A_g} \quad \text{(Watson and Park 1994)} \quad (1.18a)$$

$$\frac{l_p}{h} = \left[0.3\left(\frac{P}{P_0}\right) + 3\left(\frac{A_s}{A_g}\right) - 0.1\right]\left(\frac{L}{h}\right) + 0.25 \geq 0.25 \quad \text{(Bae 2005)} \quad (1.20)$$

- **Yield Penetration and Shear Spreading**. Mander (1983), Priestley and Park (1987), Paulay and Priestley (1992), and Restrepo (2006) investigated the effects of yield penetration and shear spreading of plasticity. They proposed their formulae with respect to the longitudinal reinforcement diameter (d_b) and the column height (L or H) based on the experimental results. Paulay and Priestley (1992), and Restrepo (2006) also considered the effect of yield stress of the longitudinal reinforcement in their expressions:

$$l_p = 0.08L + 6d_b \qquad \text{(Priestley and Park 1987)} \qquad (1.16)$$

$$l_p = 0.08l + 0.15d_{bl} f_{ye} \geq 0.3d_{bl} f_{ye} \qquad \text{(Paulay and Priestley 1992)} \qquad (1.17a)$$

$$\left.\begin{aligned} L_p &= \alpha H + \beta f_{ye} d_{bl} \leq 2\beta f_{ye} d_{bl} \\ \alpha &= 1 - \sqrt{1 - 2\frac{\delta_{fle} - (\frac{M}{M_y}\phi_y')\frac{H^2}{3}}{\phi_p H^2}} \\ \beta &= \frac{\theta_f}{\phi f_{ye} d_{bl}} \end{aligned}\right\} \qquad \text{(Restrepo 2006)} \qquad (1.21)$$

$$\left.\begin{aligned} L_p &= L_{py} + 0.06L \\ L_{py} &= 6.35\sqrt{d_b} \end{aligned}\right\} \qquad \text{(Mander 1983)} \qquad (1.13)$$

$$l_p = 0.05L + 0.008\frac{f_y d_b}{\sqrt{f_c'}} \qquad \text{(Berry et al. 2008)} \qquad (1.31a)$$

- **Shear Span-to-Depth Ratio.** Shear span-to-depth ratio was one of the main variables for Sakai and Sheikh (1989), Tanaka and Park (1990), Bayrak and Sheikh (1997, and 1999) and Bae (2005). All of the observations given by the researchers above were consistent that plastic hinge length increased with increasing shear span-to-depth ratio. Bae (2005) first attempted to study the relationship between the plastic hinge length and the shear span-to-depth ratio and proposed a new expression:

$$\frac{l_p}{h} = \left[0.3\left(\frac{P}{P_0}\right) + 3\left(\frac{A_s}{A_g}\right) - 0.1\right]\left(\frac{L}{h}\right) + 0.25 \geq 0.25 \qquad \text{(Bae 2005)} \qquad (1.20)$$

- **Member Dimensions.** Early expressions for plastic hinge length used the relationship between the column height, the cross sectional depth, and/or the diameter of longitudinal reinforcement with the plastic hinge length. The column height (L) and the depth (d or h) represented the flexural response of

the columns, whereas the diameter of longitudinal reinforcement corresponded to the slip behavior of the reinforcement. They were not dimensionless parameters. In later expressions, however, dimensionless parameters such as axial load ratio, and shear-span-to-depth ratio were accepted. But, in more recent expressions (Berry et al. (2008)), the member height (L) and the yield penetration were considered one again to best represent member behavior.

- **Dynamic Tests**. The studies conducted by Dodd et al. (2000), and Hachem et al. (2003) utilized the equation proposed by Priestley et al. (1992) to estimate the plastic hinge length before testing the circular columns under earthquake loading . This equation was developed using the static test results of 20 bridge columns having a shear-span-to-depth ratio between 2 and 5.5. According to dynamic test results, it was concluded that the estimated plastic hinge length values based on static tests overestimated the measured plastic hinge length for some columns, but were within a reasonable range of the measured dynamic test results for other columns. This deserves further study, and will be investigated in this research.

The expressions that have been developed in the literature are based on component tests and analyses of their data. The question that remains is how these estimations of plastic hinge length, damage locations, and estimates of column drift may change in large scale system tests. This question is the focus of the current study.

1.6 OBJECTIVE AND SCOPE

The objective of the current research is to study the plastic hinge length, the effect of the spread of plasticity on estimates of drift, and the progression of damage in reinforced concrete bridge systems during response to earthquake motions. The scope of research to accomplish these objectives includes the followings:

- A model is built to estimate the plastic hinge length in reinforced concrete bridge systems based on experimental results of a large-scale four-span bridge test. Detailed data along the hinging regions of a reinforced concrete bridge column are collected during the test to calibrate the model.
- Based on an analysis of available test results, a new expression for L_p/d is proposed.
- Parametric analysis is performed to evaluate the effect of axial load, the amount of the longitudinal reinforcement, shear span-to-depth ratio of the column, and the slip of reinforcement on the response of the model.
- Based on this analysis, a new expression is proposed for plastic hinge length.
- Finally, an analytical approach for the spread of plasticity and simple drift calculations are also developed.

2 PHOTOGRAMMETRIC MEASUREMENTS OF CONCRETE COLUMN DEFORMATIONS

2.1 INTRODUCTION

The research presented in this document is part of a George E. Brown, Jr. Network for Earthquake Engineering Simulation (NEES) payload study to investigate the seismic performance of four-span large scale bridges using conventional and innovative materials. The focus of the work is to accurately record and analyze deformations in plastic hinging locations in concrete bridge structures through an investigation of actual hinging behavior in large-scale tests of bridge systems subjected to multiple excitations. In order to evaluate the plastic hinging regions, a photogrammetric method was used to remotely track deformations of the concrete surface in the joint regions. Photogrammetry is a non-invasive technique of remote visualization of the target components and a computer rendering of the motion (Jauregui et al. 2006). This computer reconstruction is based on the tracked motion of the target components. The method of application in this study holds several advantages over traditional sensors, including experimental components that are simple to construct and more economical for typical laboratory environments.

Two test specimens were evaluated at the NEES Equipment Site at the University of Nevada (UNR) in the study. The first was a proof-of-concept test of a bridge column in which deformations were recorded in one target area. In the second test, the photogrammetry method was used to track deformations in the hinging regions of one bridge column in a large-scale four-span bridge test. Both tests employed strong ground motion to excite the structure, with the first test in one direction and the second with bi-directional loading.

Analysis of deformations in the hinging regions was completed by considering movement of discrete points on the column surface. This chapter details the specimen dimensions and material properties as well as the experimental setup to complete the proof-of-concept test and large-scale bridge test using photogrammetry methods. Challenges in determining surface deformations are examined, including the resolution of unclear images and the consistent and predictable definition of points on the surface. Results for displacement calculations on a gridded surface and cross-section rotation calculations are discussed.

2.2 PROOF-OF-CONCEPT TEST

On December 14, 2005, a proof-of-concept test for photogrammetry measurements of concrete elements under earthquake loadings was completed at the UNR earthquake laboratory. The purpose of this proof-of-concept test was to investigate the ability of the method to accurately trace the dynamic movement and rotation of the column as a function of time.

A circular reinforced concrete column (SVTN) was tested under different earthquake loadings on one of the three biaxial shaking tables in the UNR lab. The concrete compressive strength was 4.03 ksi (28 MPa) and the yield strength of the steel in the column was 71 ksi (490 MPa). The diameter of the column was 12 in. (305 mm), and the total height was 98.5 in (2500 mm). The circular column had 3% longitudinal reinforcement and 1.82% transverse reinforcement ratios. Figure 2.1 shows the cross-section of the tested column.

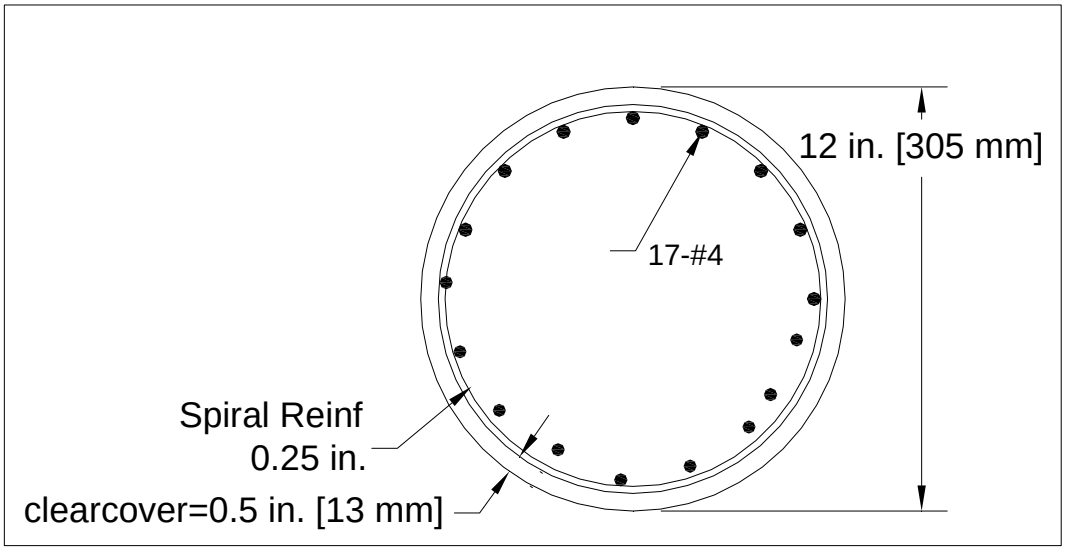

Fig. 2.1 Cross-section of the column

In order to keep track of the displacements on the column surface during the test, a grid system was applied to the column surface (Fig. 2.2). Figure 2.2 also shows the traditional linear vertical displacement transducers (LVDT) instrument that was used during the test. The grid was applied to the surface using a cardboard stencil at the University of Kansas and black and white paint. First a uniform black background was applied, and then the stencil was used to apply the white grid marks. The grid consisted of vertical and horizontal lines spaced irregularly around the face of the circular column. The irregular spacing of the grid marks allows for a detailed analysis of the column circular surface. The grid system was applied above the column plastic hinging region to avoid the congestion of LVDT instrumentation. Displacement and rotation calculations are reported for the location marked A in Fig. 2.2.

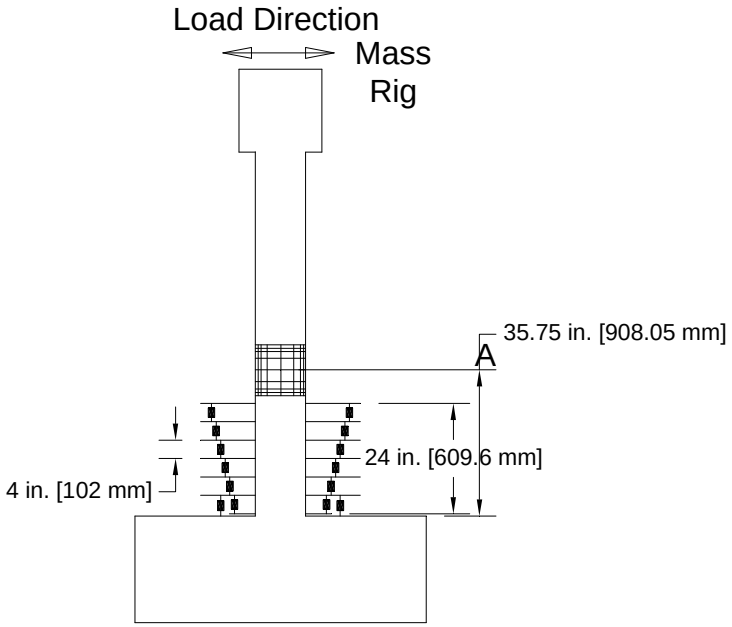

Fig. 2.2 Grid Setup

The experimental set-up was completed with a camera tower, cameras and recording system. The specific equipment and materials used in this test are listed below:

- A system of two cameras: model name DXB-9212EF and 0.5-in. (13 mm) Starlight 600 TVL super high resolution black-white recording properties. The angles from left and right cameras to the column were 60° (Fig. 2.3).
- Video-lens zooms: 60-300mm (2.36 in. – 11.81 in.) F4-5.6 capturing capability.
- VCR systems: JVC HR-S2902U brand and high resolution stereo video cassette recorder.
- Monitor: a black and white monitor to show the field of view of the camera.
- An aluminum tower: an aluminum frame made with 2-in. (51 mm) thickness extruded aluminum material. The tower has 2 levels to place

cameras. Only the first level of the tower used in the proof-of-concept test. Because the height of the first level was 94.5 in. (2400 mm), metal and masonry units were placed under the legs of the tower to enable the cameras to photograph at the level of the grid (Fig. 2.4).

- Connections: small aluminum connections which are 30°, 45° and 60°-angle pieces.

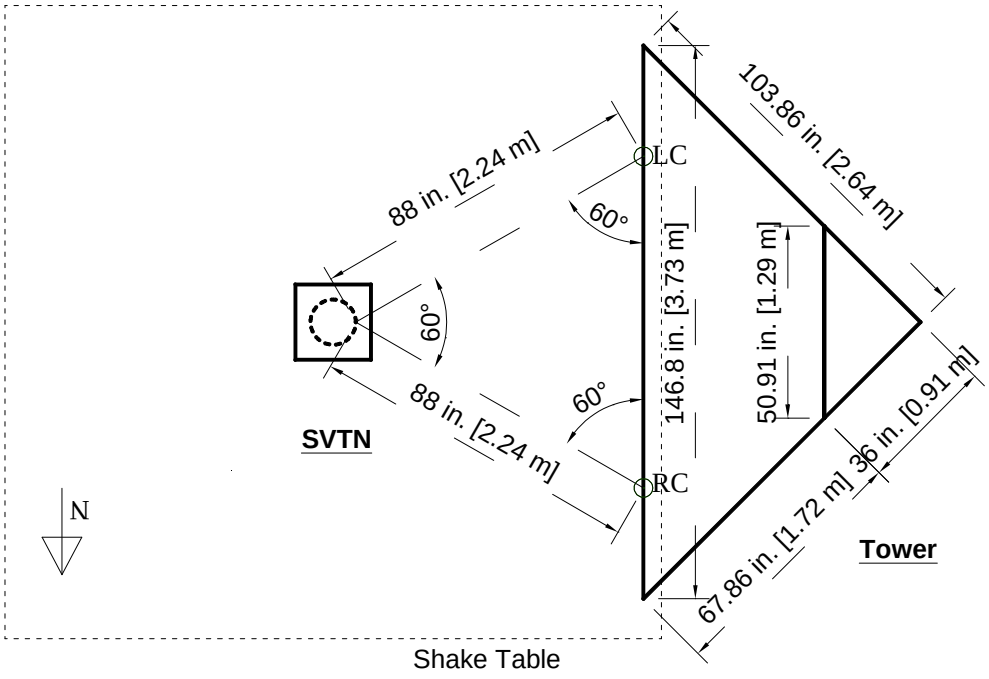

LC – Location of Left Camera

RC – Location of Right Camera

Fig. 2.3 Location of the column and the tower position

Fig. 2.4 The aluminum tower setup

The earthquake motion applied during the tests was recorded at the Rinaldi receiving station during the 1994 Northridge earthquake (6.7 Richter magnitude). The maximum acceleration of the record is 0.838g. The Rinaldi record was scaled to obtain earthquake motions with peak ground accelerations from 0.15g to 1.66g. The acceleration history for the original record is shown in Fig. 2.5.

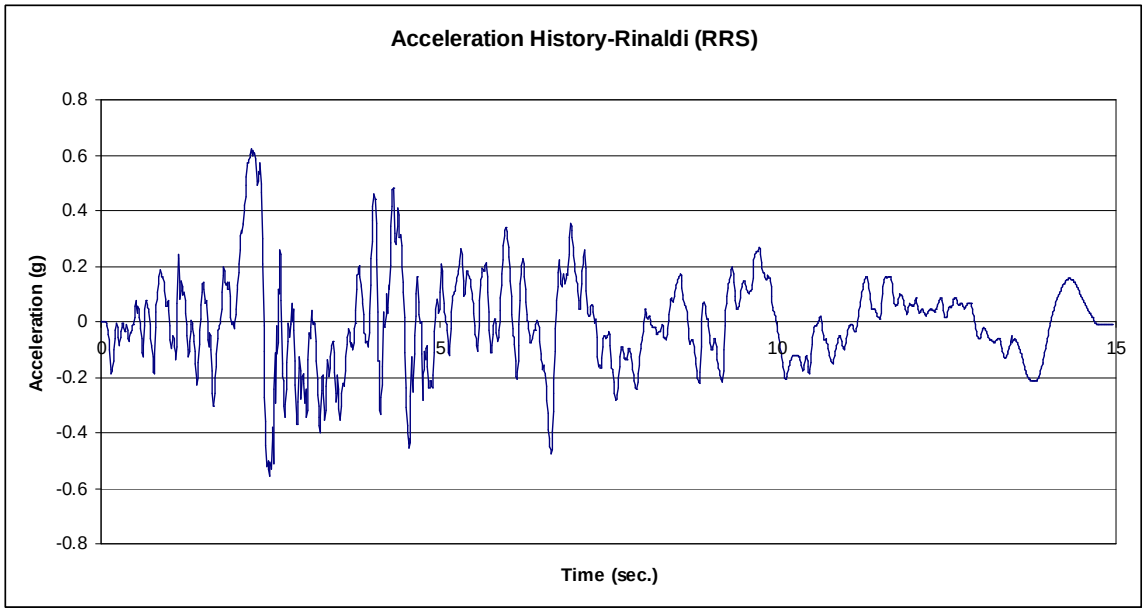

Fig. 2.5 Acceleration history of the Rinaldi earthquake record

Due to setup limitations in the lab, the distance between the cameras and the column was 88 in. At this distance, the field of view was too narrow to include two vertical lines in the photographs at all times. Therefore, the proof-of-concept test focused on vertical rotation of the column and did not consider the cross-sectional rotation of the column.

Calculated displacements and rotations using the LVDT data and photogrammetry measurements are compared at Point A on the painted grid (Fig. 2.2). Figure 2.6 shows the comparison for calculated displacements. Because of a limitation of the number of frames that may be considered in a single analysis, the photogrammetry results are shown in two pieces (Run1L and Run2L). The results from two runs are superimposed and demonstrate good continuity for calculated displacements.

The LVDT displacement values are obtained by first considering the relative displacement between the displacement transducer recordings at the top of the column and the absolute displacement of the shaking table. Displacements at Point A are

estimated by linearly interpolating between the relative displacement at the top of the column and zero displacement at the base to the height of Point A. Displacements values using the photogrammetry data are determined as the relative motion of Point A. As shown in Fig. 2.6, the displacement results in terms of periodicity and amplitude of motion are well-represented by the photogrammetry analysis. The permanent deformation noted at the end of the test is also captured in the photogrammetry analysis.

Rotations of the horizontal line are compared in Fig. 2.7. Rotations of the horizontal line Cross section rotations using the LVDT data are first estimated at each LVDT location by dividing the relative vertical displacement between two opposing LVDTs by the column width. As expected, the change in cross section rotation over the column height of the hinging region decreased with increasing column height. To estimate the rotation at Point A, it was assumed that the change in rotation between the two highest LVDT locations remained constant to Point A.

Rotations of the cross-section based on photogrammetry measurements were estimated assuming no shear distortions occurred in the grid region. Using this assumption, a cross-section rotation may be estimated by considering the vertical rotation between two points. An average rotation over the height of the column between the base and Point A was then calculated as the transverse displacement of Point A divided by the height to that point. In the comparison of vertical rotation calculations (Fig. 2.7), the periodicity of the rotational response is again well-represented, but amplitudes are as much as 13% less than the LVDT values. This difference is likely because of the rough estimation that is provided by extrapolated rotations from LVDT data and average rotations provided by the photogrammetry measurements.

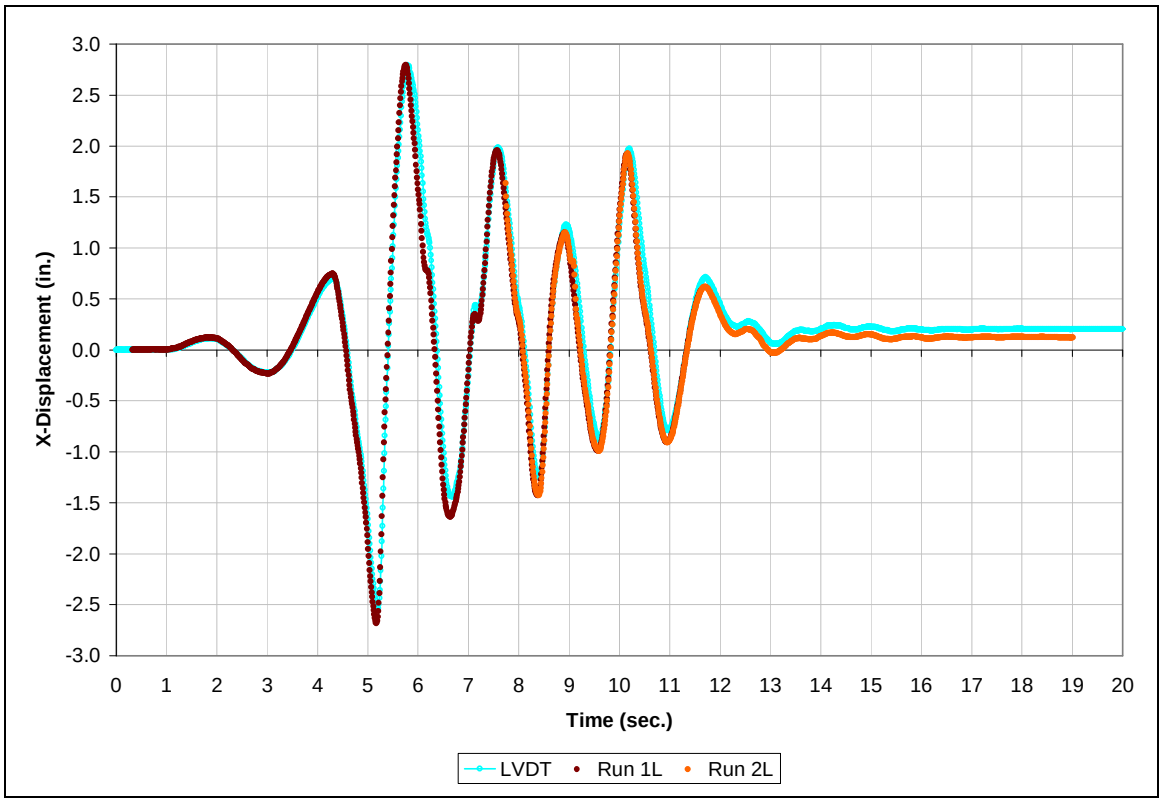

Fig. 2.6 Displacement @ Grid Level A vs. Time (Rinaldi 0.95g) (1 in. = 254 mm)

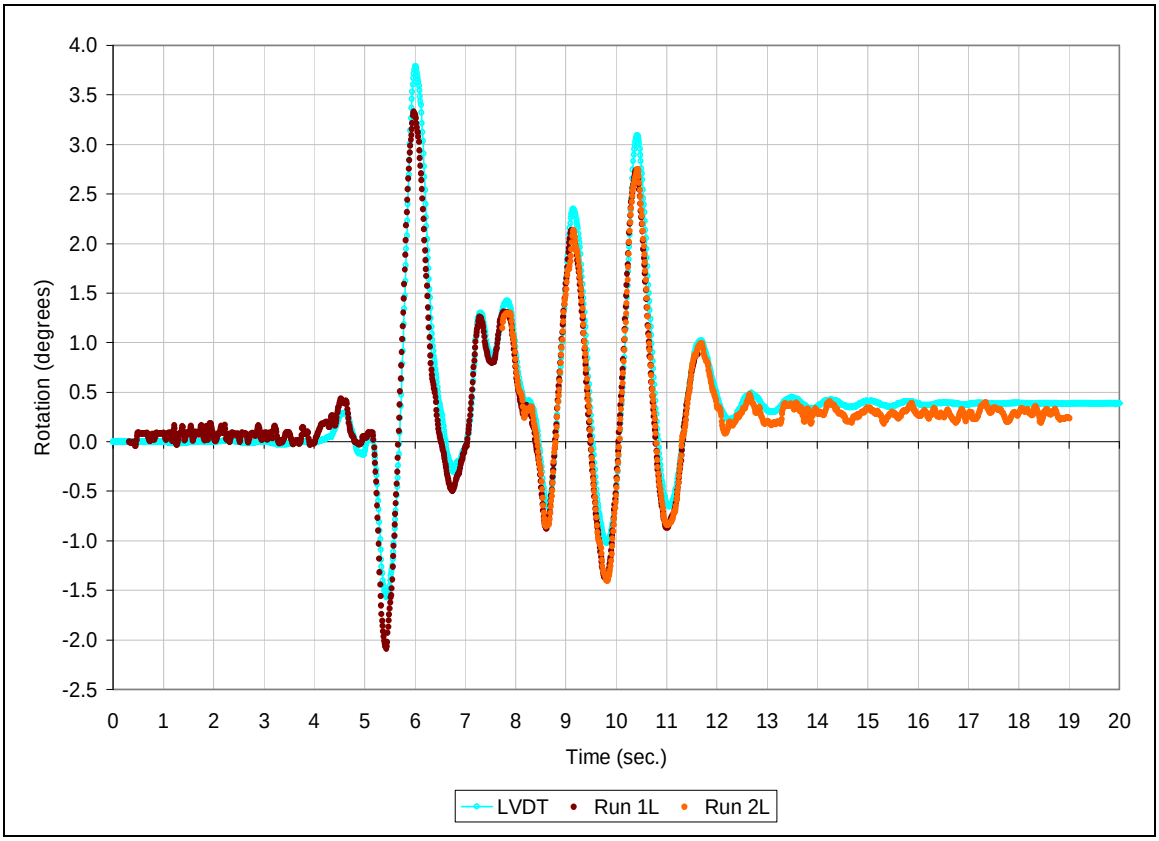

Fig. 2.7 Rotation @ Grid Level A vs. Time (Rinaldi 0.95g)

2.3 LARGE SCALE FOUR-SPAN RC BRIDGE TEST

A four-span large scale reinforced concrete bridge was tested on February 12-15, 2007 at the UNR laboratory. Representatives from NEES, CALTRANS, UNR, KU, other participating universities, and local media congregated in the test area. Photogrammetry measurements were taken in two hinging regions, which required the use of four cameras and two grid configurations. The significance of this test was that it was a large-scale bridge with columns having double curvature response and resisting massive earthquake forces. Also, biaxial earthquake loading was employed. Challenges that are addressed in the photogrammetry analysis included irregular image quality and inconsistent definition of points on the concrete surface.

2.3.1 Description of Specimen

The test specimen consisted of a four-span reinforced concrete bridge with end abutments as shown in (Fig. 2.8). The bridge was quarter-scale with two interior spans that were 29 ft. (8.84 m) in length, and two exterior spans of 24.5 ft. (7.47 m) for a total length of approximately 110 ft. (33.5 m). The clear heights of the bents were 5, 6 and 7 ft. (1.52, 1.83, and 2.13 m), with the tallest bent in the middle (Bent 2). The superstructure consisted of a solid slab that was post-tensioned in both the longitudinal and transverse directions. The bridge also included abutment seats at both ends that were driven in the longitudinal direction by dynamic hydraulic actuators. The depth of the cap beams was 15 in. (0.38 m). The total length of the cap beams (perpendicular to the longitudinal axis of the bridge) was 98 in. (2.49 m). The concrete compressive strength used in the bridge (excluding the slab) was 6.7 ksi (46 MPa) and reinforcement was ASTM A706 Grade 60. The bents were numbered Bent 1, Bent 2, and Bent 3 starting from left (South) to right (North). The east column of Bent 3 was selected to be the target

structure for applying the painted grids. Figures 2.9, 2.10 and 2.11 show the elevation and side views of Bents 1, 2 and 3, respectively.

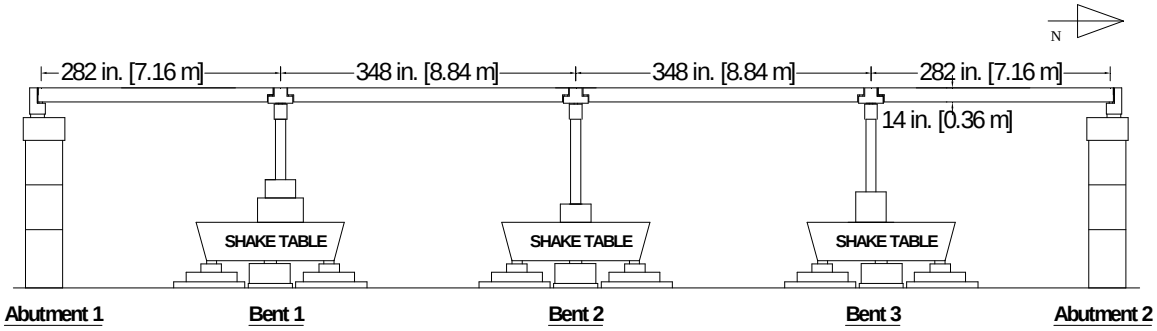

Fig. 2.8 Elevation view of the four-span bridge

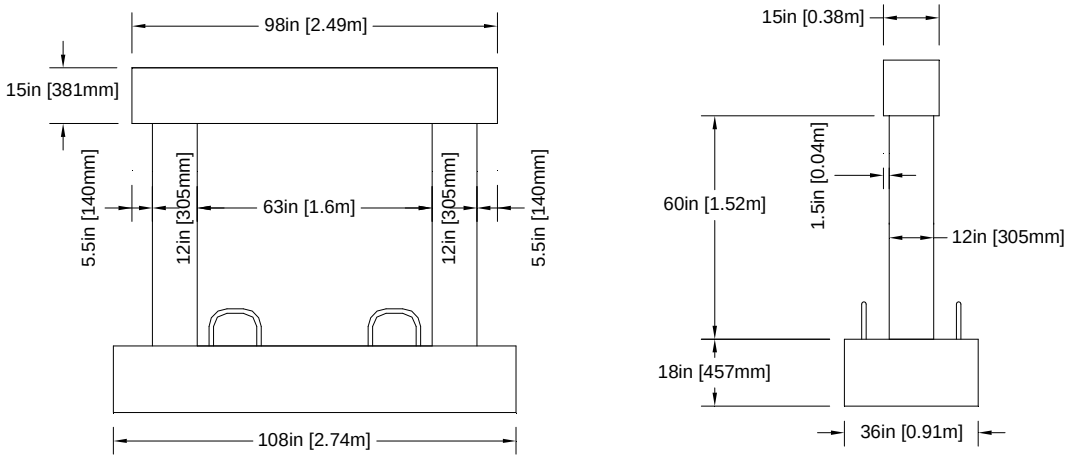

Fig. 2.9 Elevation and side view of the Bent1

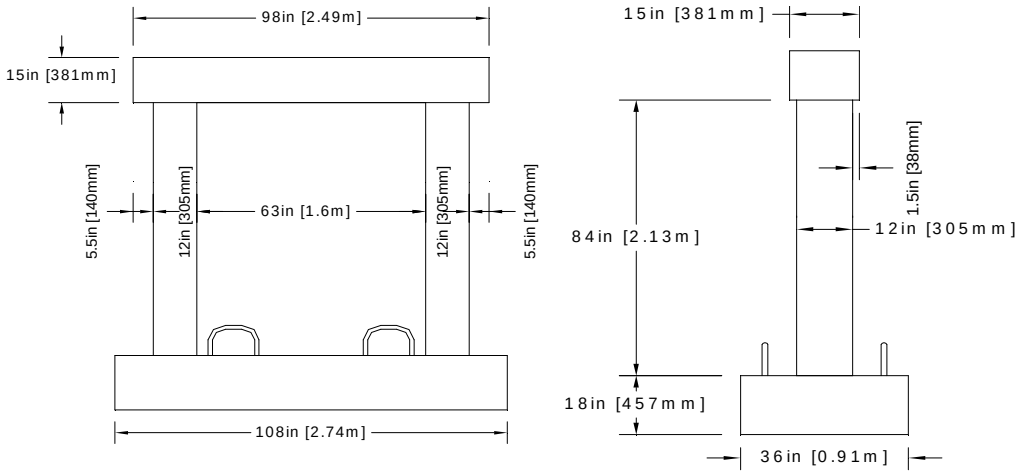

Fig. 2.10 Elevation and side view of the Bent2

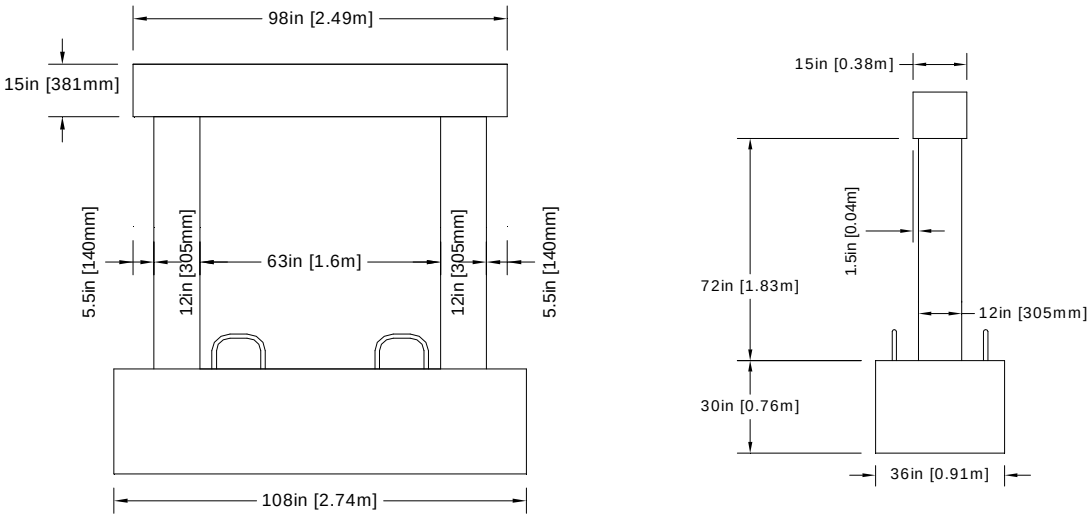

Fig. 2.11 Elevation and side view of the Bent 3

2.3.2 Experimental Setup

The top and bottom hinging regions of the east column of Bent 3 were the focus for collecting photogrammetry data in the large-scale four-span reinforced concrete bridge test. Two grid systems were applied (Fig. 2.12). The bottom grid consisted of vertical and horizontal lines spaced irregularly around the face of the circular column (Fig. 2.13). As shown in Fig. 2.4, the same grid system was applied in the proof-of-

concept test. The top grid used a different configuration consisting of lines and squares (Fig. 2.3b) that resembled the spacing of the lines in the bottom grid. The top grid was applied to track the displacements of the isolated points (squares), similar to applications in earlier photogrammetry methods that were completed at the University of Kansas laboratory (Reetz, 2005).

To apply the grid systems, the column was first spray-painted black for a solid dark background. The lines and squares were lightly traced with a pencil, and then a single stencil was used to fill in the lines and squares using a white paint.

The same aluminum tower as described in the proof-of-concept test Section (2.2) was used to support the cameras, including the second level of the tower for the tests. Two cameras were mounted on each level (at 94.5 in. (2400 mm) and 159 in. (4039 mm) height) (Fig. 2.14). In the first level of the tower, due to changes in the height level of the hinge region, the height of the cameras was increased to directly view the bottom grid region. This was accomplished by placing small aluminum columns to mount the cameras on the tower (Fig. 2.14). Metal weight pieces were placed at each side of the base of the tower to provide balance on the strong floor (Fig. 2.15). There were four VCR systems and two monitors (two channels for each monitor) used in the test.

Fig. 2.12 Grid systems on the Bent3 east column surface

(a) (b)

Fig. 2.13 Close view of (a) bottom and (b) top grid systems

Fig. 2.14 The aluminum tower and four cameras

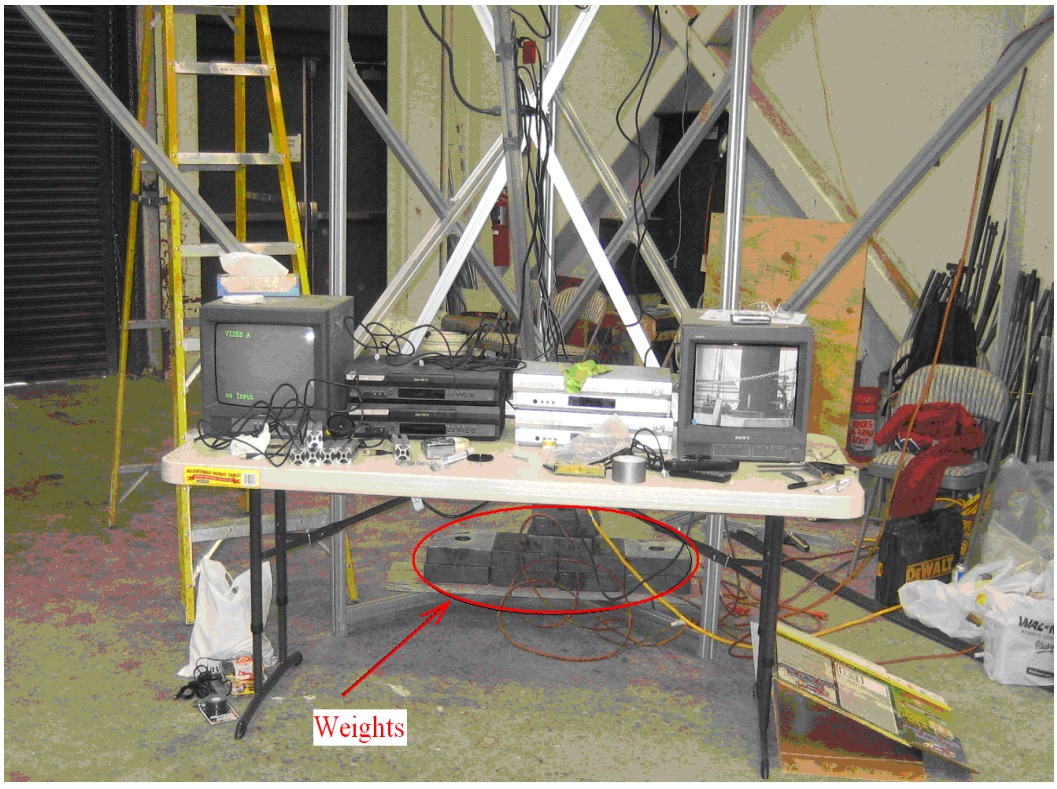

Fig. 2.15 Metal weight pieces placed on each side of the tower

The distance between the east column of Bent 3 and the tower was 288 in. (7315 mm). The angle from the left camera to the column was 73.58°, and from the right camera to the column was 44.97° on the horizontal plane (Fig. 2.16). The tower was located on the north-east side of the UNR laboratory.

Figure 2.17 shows the numbers of all points defined by the grid systems. The points on the bottom and top grid systems were defined at the intersections of the thick vertical and horizontal lines. The locations of a series of linear vertical displacement transducers (LVDTs) and one displacement transducer (DT7) monitored by the research team at UNR are also shown in Fig.2.17.

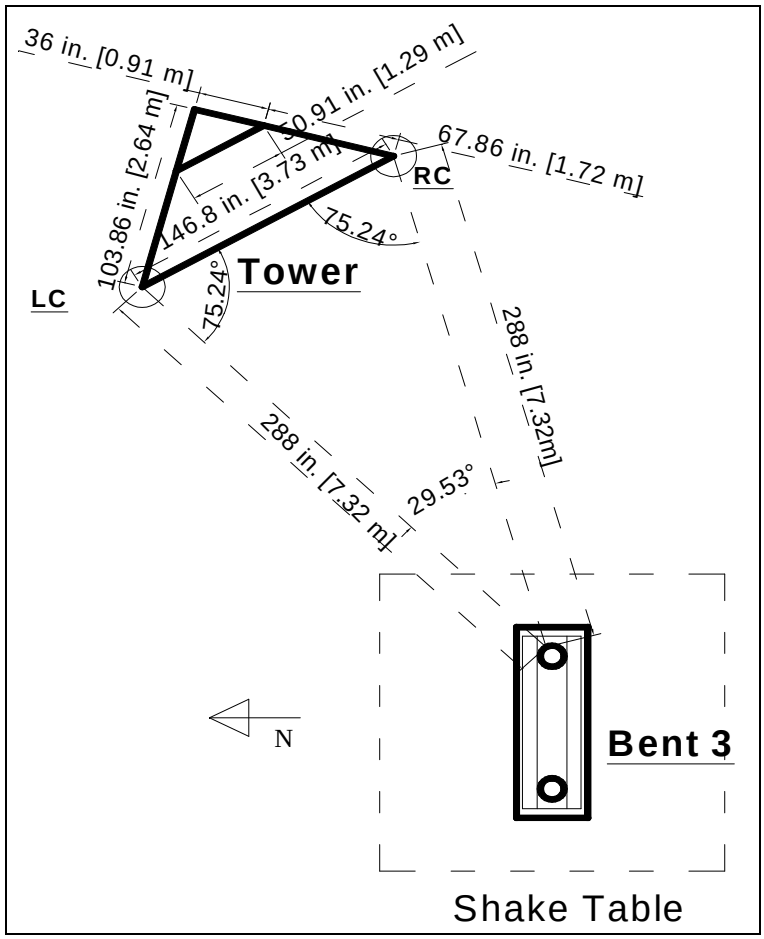

LC – Location of Left Camera

RC – Location of Right Camera

Fig. 2.16 Location of the Bent 3 east column and the aluminum tower

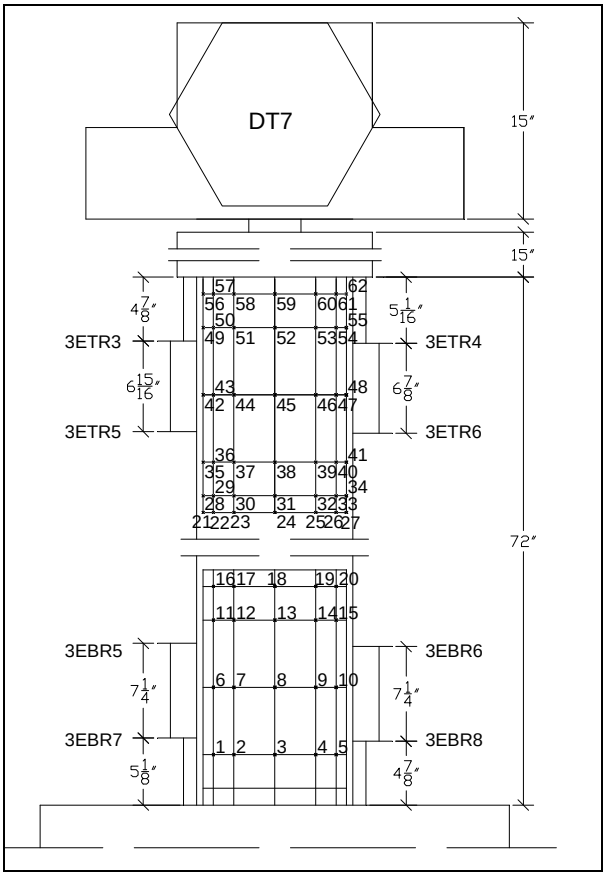

Fig. 2.17 Grid system and LVDT locations on column in the Bent 3 east column

2.3.3 Earthquake Loading

The earthquake motion used in the tests consisted of biaxial and uniaxial applications of scaled motions measured at the Century City Country Club during the 1994 Northridge, California earthquake. This motion was applied 13 times with six different scaled intensities having increased amplitude so that the progression of damage could be tracked from pre-yield to failure as shown in Table 2.1. A white noise excitation was applied before each change in ground motion intensity to test for system identification.

The first damage to the bridge system occurred in the columns of Bent 3 (the bent with medium height) and then the columns of Bent 1 (the bent with the shortest height).

The earthquake intensity was not increased after the 1.20g motion (Test 6) because the reinforcement in the left column of Bent 1 started to buckle. Almost all of the longitudinal bars in the columns of Bent 1 had buckled by Test 6. The same motion was repeated one more time before the test was completed.

Other damage that was noted during the test included small amounts of cracking in the bent caps, and some spalling of the cover concrete of the abutment seats and the superstructure. The cracks at the bent caps began after the first test (Test 1A) and progressed until the tests were done. The spalling of the concrete cover of the abutment seats occurred after Test 6.

Table 2.1 Earthquake motion levels applied during the test

Test No.	Test Date	Motion Level	Test Type	Motion PGA (g)	
				Trans.	Long.
WN01	2/12/2007		White Noise (Trans.)		
WN02			White Noise (Long.)		
1A		1	W/Restrainer1	-	0.09
1B		1	W/Restrainer2	-	0.09
1C		1	Longitudinal	-	0.09
1D		1	Biaxial	0.075	0.09
WN11	2/13/2007		White Noise (Trans.)		
WN12			White Noise (Long.)		
2		2	Biaxial	0.15	0.18
WN21			White Noise (Trans.)		
WN22			White Noise (Long.)		
3		3	Biaxial		
WN31			White Noise (Trans.)		
WN32			White Noise (Long.)		
4A		4	W/Restrainer1	-	0.6
4B		4	W/Restrainer2	-	0.6
4C		4	Longitudinal	-	0.6
4D		4	Biaxial	0.5	0.6
WN41	2/14/2007		White Noise (Trans.)		
WN42			White Noise (Long.)		
5		5	Biaxial	0.75	0.9
WN51	2/15/2007		White Noise (Trans.)		
WN52			White Noise (Long.)		
6		6	Biaxial	1	1.2
WN61			White Noise (Trans.)		
WN62			White Noise (Long.)		
6		6	Biaxial	1	1.2

2.3.4 Results

Due to shaking effects on the strong floor during the test, there is a chance for movement of the base of the aluminum tower. In order to eliminate the extra movement

from the tower shakings, a fixed point on the wall was identified and tracked during the strong excitations (Fig. 2.18).

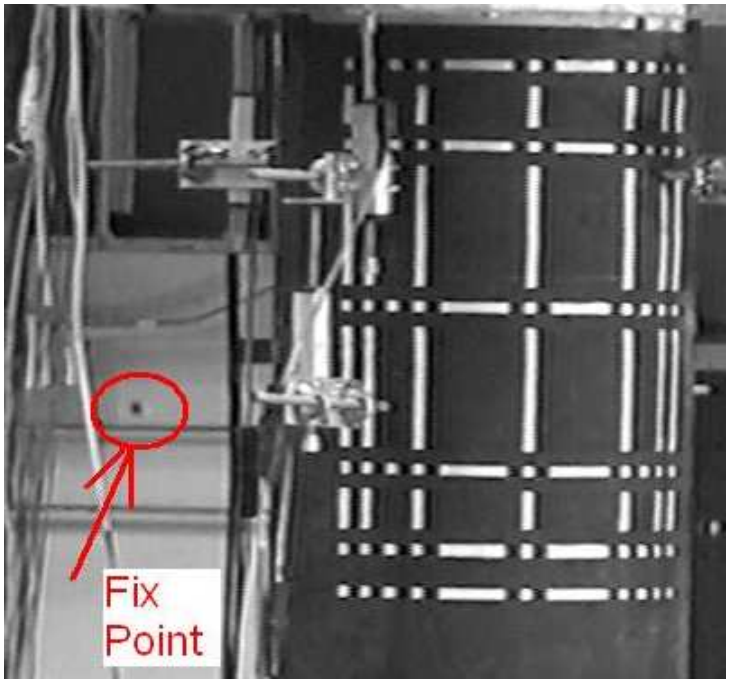

Fig. 2.18 Fix point on the wall at the back of the column

The lateral displacement of the fixed point on the wall (Fig. 2.19) was determined and subtracted from the lateral displacements of the grid points to obtain the displacements of the column caused by the shake table motions. The calculated tower displacements as indicated by the movement of the fix point are very close to zero in value (within one or two pixels of value) and did not significantly affect the results. The vertical displacement of the fixed point was also calculated (Fig. 2.20), but it does not need to be subtracted from the vertical displacement of the grid point because cross-sectional rotation calculations are based on relative vertical movement between two points on the column.

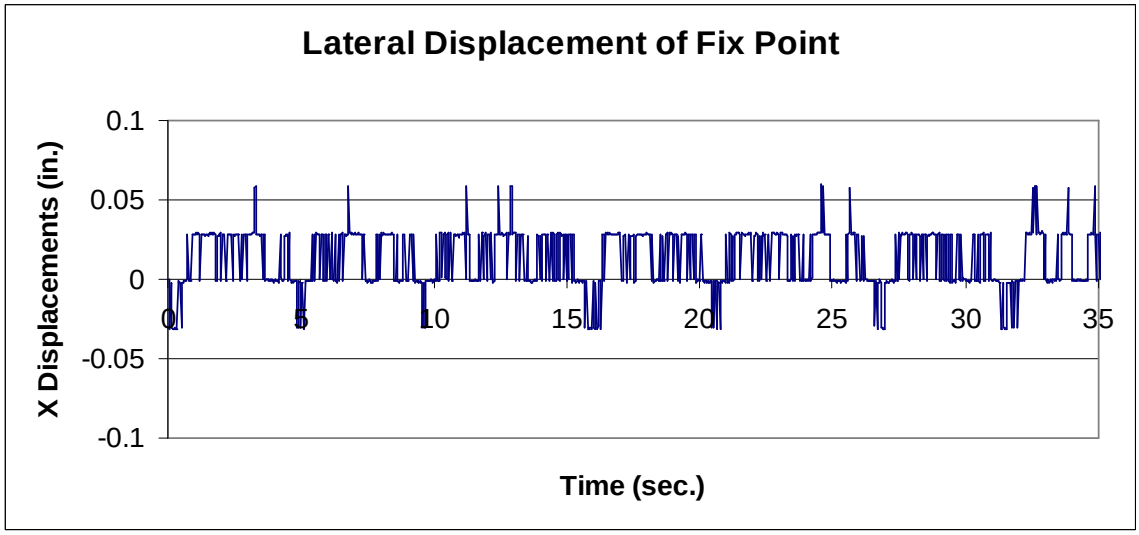

Fig. 2.19 Lateral displacement of fixed point on the wall at Test 4D (1 in. = 254 mm)

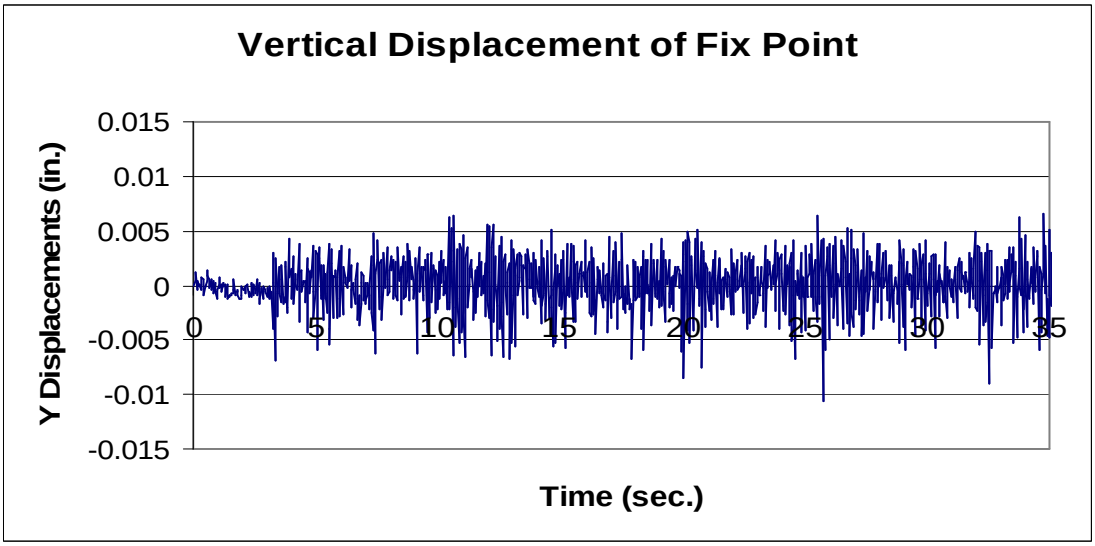

Fig. 2.20 Vertical displacement of fixed point on the wall at Test 4D (1 in. = 254 mm)

2.3.4.1 Definition of Points on Surface

Deformations were evaluated considering displacements and cross-sectional rotation of various locations on the column. For each deformation that was calculated, it was necessary to have a consistent and predictable definition of points on the column surface. Challenges in the photogrammetry analysis included some instances of poor images and the reliability of the selected method to define the points, as described below.

There are some differences in the data provided by LVDT instrumentation and that recorded for photogrammetry application. The rotation calculations obtained using photogrammetry analysis represents the cross-sectional rotations based on the movement of the column, which includes not only flexural but also rigid body rotation. Rotations calculated using the LVDT data from the test includes only flexural contributions. The LVDT instrumentation was set to record movement in the transverse and longitudinal planes, and photogrammetry measuruments were recorded at an angle between the LVDT instrumentation. This difference in orientation is accounted for in the analysis and results presented in this section.

- **Unclear Images**

Interactive Data Language (IDL) was used to analyze the video images that were recorded during the test. Each video was first divided into over one thousand images for individual analysis. The displacement of a unique point in an image was defined as the relative horizontal movement of that point between successive images. However, at times it was difficult to keep track of a *unique* point because of the quality of the images.

The image (640 x 480) was written as 480 lines that are 640 pixels wide. The odd-numbered lines are written first, followed by the even-numbered lines so that the image is really two images offset by $1/60^{th}$ of a second. The first "partial image" (half of the total image) is comprised of the odd lines, and the second "partial image" is comprised of the even lines. Due to the shaking effect from the strong floor during the tests and the incompatibility in recording frequency between the cameras and the earthquake motions, many images were compromised. Some of the images appeared as double lines for each horizontal and vertical line, and some were simply blurry images. Table 2.2 shows the number of corrupted images that were recorded during each test

motion and the total percentage of corrupted images recorded by each camera. The "Image Group" number in the table signifies a grouping of images that could be analyzed at one time. Therefore, "Image Group 1" contains images from the earliest time in a test. Each image represents $1/30^{th}$ of a second during the test. The total number of images reviewed in a single analysis ranged from 339 to 998. The percentage of corrupted images ranges from 0-62%. For recordings at the top of the column, the percentage of corrupted images exceeded 4% when at least one component of shaking exceeded 0.5g with a maximum of 30% corrupted images (Test 4D Top Right Camera). Recording quality was much more sensitive at the base of the column, with as much as 24% corrupted images during Test 2 (Bottom Left Camera), which had a peak ground acceleration of only 0.15g. The images recorded early (Image Group 1) in each shake table test ranged from 8-62% corrupted, the recordings from Test 5 Bottom Left Camera having 62% corrupted images.

Table 2.2 Corrupted images during the tests

Camera (Fig. 2.16)	**Top Left**			**Top Right**			**Bottom Left**			**Bottom Right**		
Test	**2**			**2**			**2**			**2**		
Image Groups	**1**	**2**		**1**	**2**		**1**	**2**	**3**	**1**	**2**	**3**
No. of corrupted images	27	0		28	0		80	0	0	72	0	0
No. of total images	899	299		899	349		339	339	339	339	339	339
Corruption Percentage	3	0		3	0		24	0	0	21	0	0
Test	**4D**			**4D**			**4D**			**4D**		
Image Groups	**1**	**2**	**3**	**1**	**2**	**3**	**1**	**2**	**3**	**1**	**2**	**3**
No. of corrupted images	100	0	0	102	10	0	171	40	0	193	10	0
No. of total images	339	339	339	339	339	339	339	339	339	339	339	339
Corruption Percentage	29	0	0	30	3	0	50	12	0	57	3	0
Test	**5**			**5**			**5**			**5**		
Image Groups	**1**			**1**			**1**	**2**	**3**	**1**	**2**	**3**
No. of corrupted images	220			136			210	55	0	180	15	0
No. of total images	899			899			339	339	339	339	339	339
Corruption Percentage	24			15			62	16	0	53	4	0
Test	**6**			**6**			**6**			**6**		
Image Groups	**1**	**2**		**1**	**2**		**1**	**2**		**1**	**2**	
No. of corrupted images	210	0		200	0		221	0		264	0	
No. of total images	999	339		999	339		999	339		999	339	
Corruption Percentage	21	0		20	0		22	0		26	0	

One option to improve calculations of displacements and rotations using the corrupted images is to consider only the even-numbered or odd-numbered lines, separately. If the even and odd lines are separated, the double image effect that is produced by a shift between the two halves of the image being written can be avoided by considering only one "half image" at a time. Figures 2.21 and 2.22 show the results of the analysis of even lines, odd lines and the combination of the two for the entire test 4D and a 5 second interval for each analysis, respectively. It is difficult to distinguish the results in Fig. 2.21. As shown in Fig. 2.22, the even- and odd-line analyses are very similar in smoothness, but the combined image shows irregularities in the movement of the point.

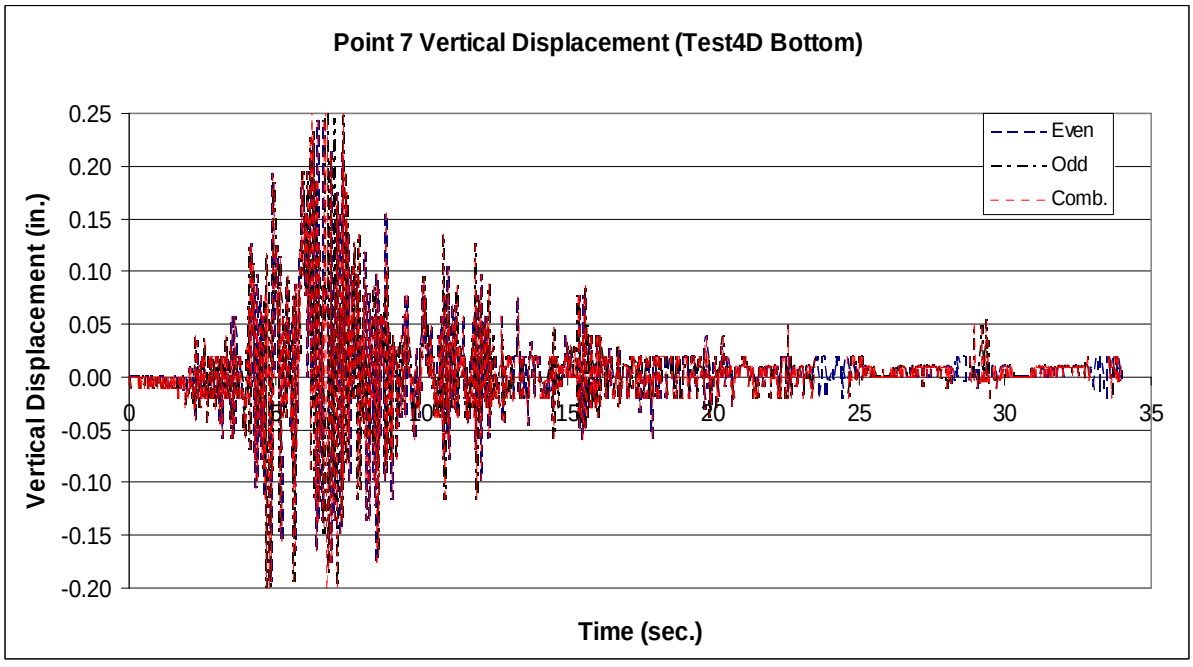

Fig. 2.21 Point 7 vertical displacement at the bottom grid system (1 in. = 254 mm)

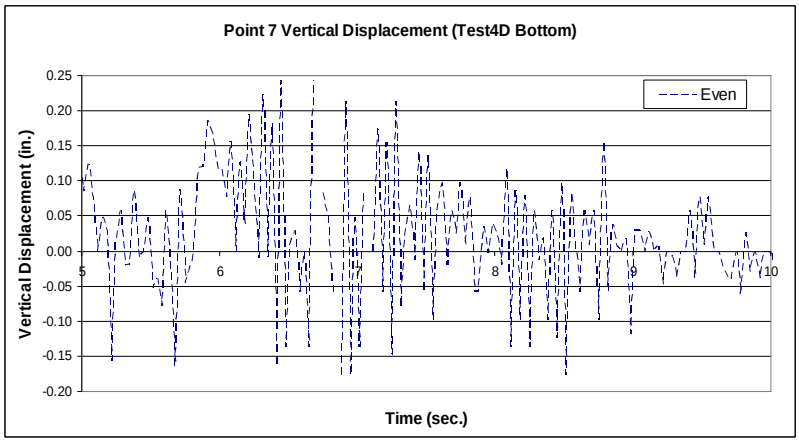

a) Even Line

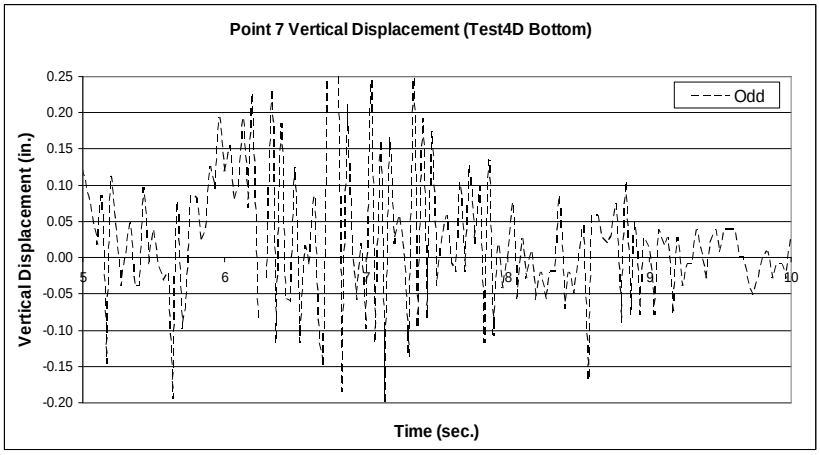

b) Odd Line

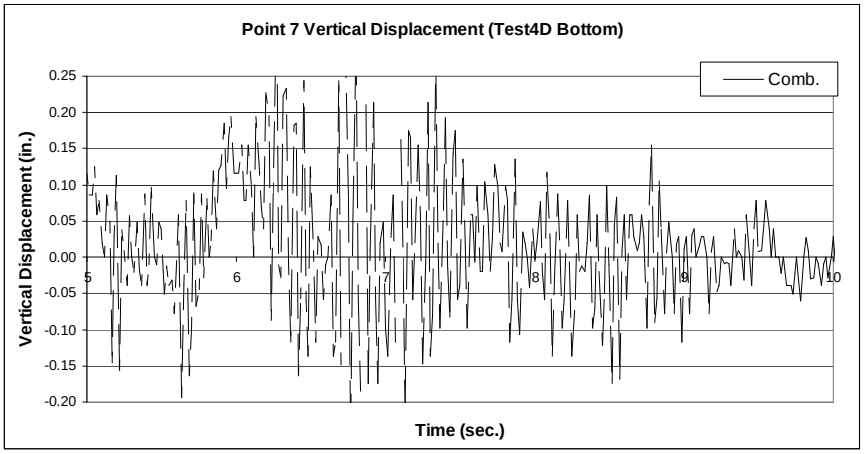

c) Combination

Fig. 2.22 Five second interval to compare even- odd- and combination-line analyses (1 in. = 254 mm)

The vertical displacement results of Point 7 in the even and odd line analyses are compared with the LVDT 3EBR7 reading (the closest UNR measurement to the point on the bottom grid system as shown in Fig. 2.17) in Figs. 2.23-2.24. Figure 2.25 shows only the LVDT 3EBR7 recorded displacements for clarity. Because of the larger disparity noted in the figures between peak displacement values recorded in the odd-line analysis (Fig. 2.24) and LVDT recordings, the even line approach (Fig. 2.23) is selected to provide better photogrammetry results.

Rotation of horizontal line is calculated as the relative vertical displacements of the horizontal line that Points 7 and 8 align and divided by the horizontal distance between the points. For the photogrammetry analysis, the horizontal distance between the points changes within each image. Figure 2.26 shows the rotation of horizontal line calculated using Points 7 and 8 at 12 inches (305 mm) from the bottom fixity in the transverse direction. The appearance of "noise" with nearly constant magnitude is a result of single pixel differences in calculated displacements (pixelization).

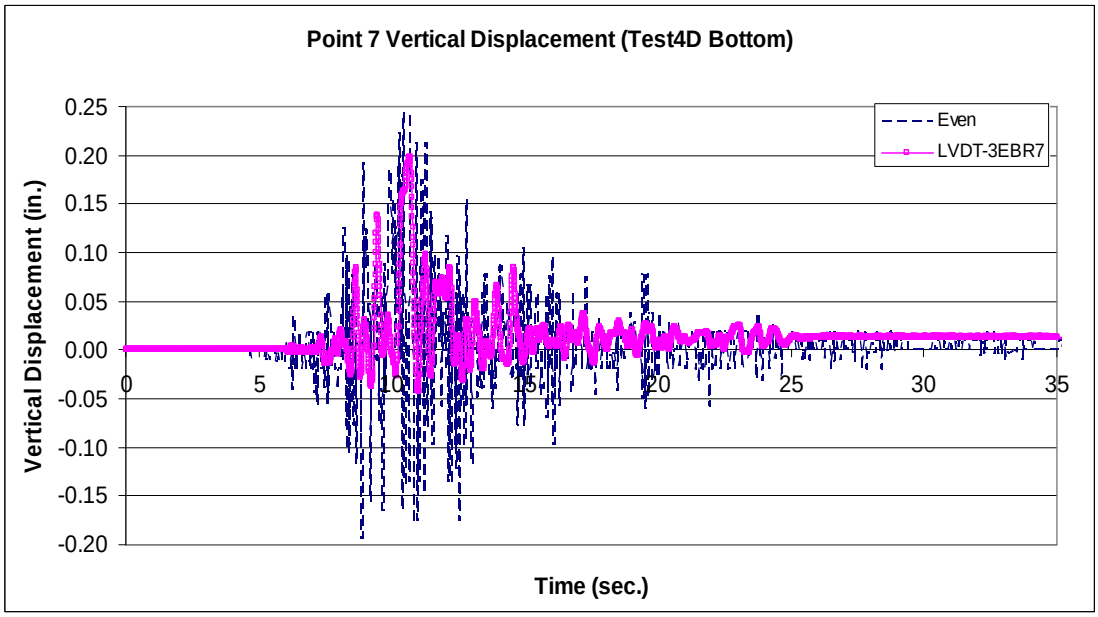

Fig. 2.23 Comparison of Point 7 vertical displacement for even lines with LVDT 3EBR7 data (1 in. = 254 mm)

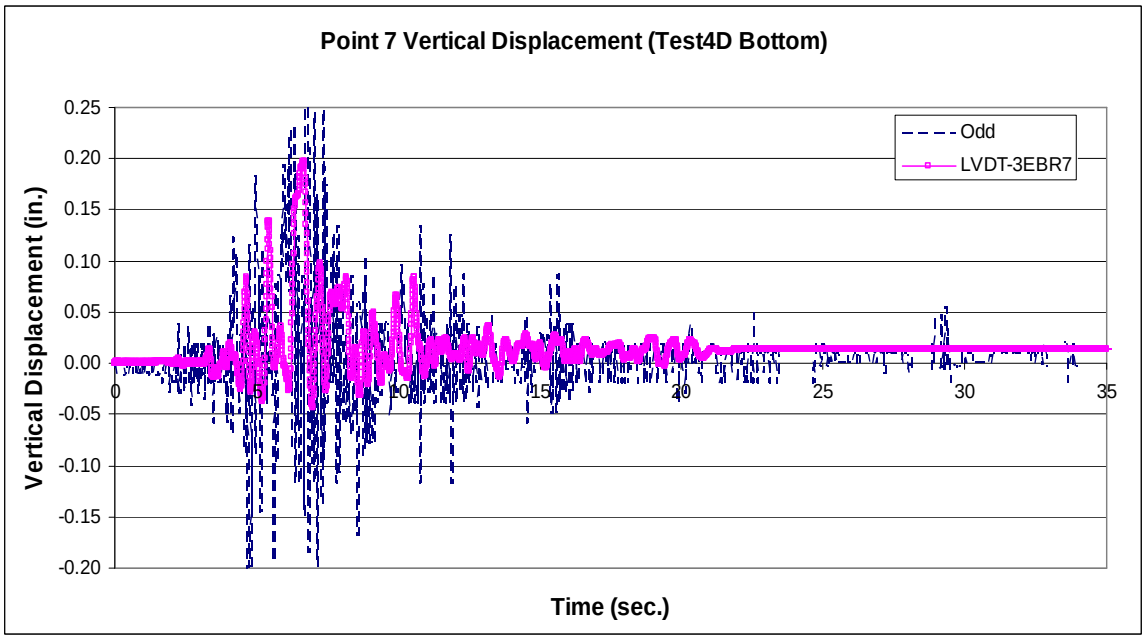

Fig. 2.24 Comparison of Point 7 vertical displacement for odd lines with LVDT 3EBR7 data (1 in. = 254 mm)

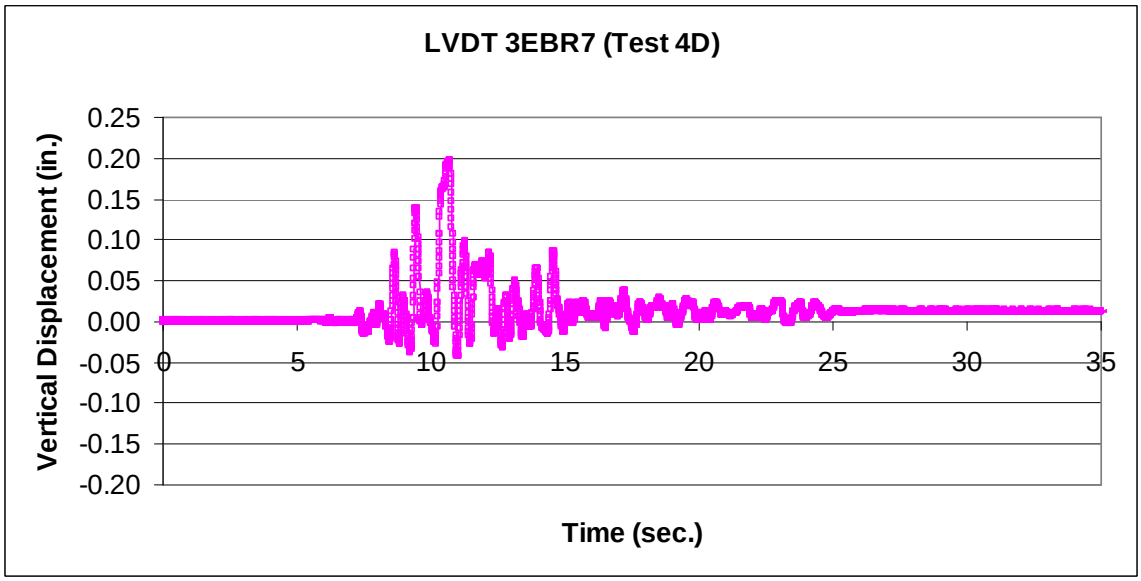

Fig. 2.25 LVDT 3EBR7 vertical displacement history (1 in. = 254 mm)

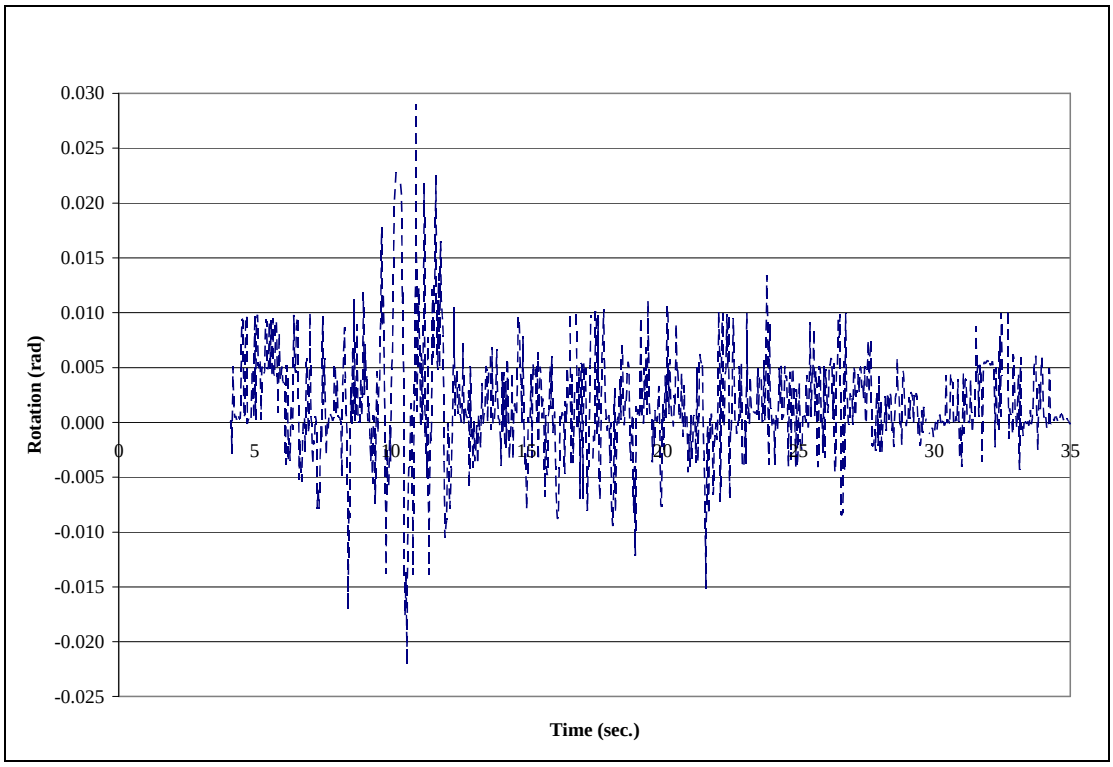

Fig. 2.26 Rotation of horizontal line calculated from Points 7 and 8 at the bottom grid in the transverse direction

- **Intersecting Lines to Define Points**

There are several options for defining each unique point on the grid, all of which were considered and the best overall representation selected as described in this section. Points on the grid are defined by the intersection of the thick vertical and horizontal lines. The vertical and horizontal lines are 0.25 in. (6 mm) thick; therefore, there are several ways to define a line within that thickness. One option is to seek a definition of the mid-point of each 0.25-in. (6 mm) thickness and define a "middle line" as the connection of those points (Fig. 2.27). Another option is to define the edges of the lines. For this option, the "edge lines" may be defined by points of a particular light intensity value, or a change in relative intensity between the black to white paint transition.

Finally, the length of the line that is used to define each Point on the grid also will influence results. Each of these options is discussed below.

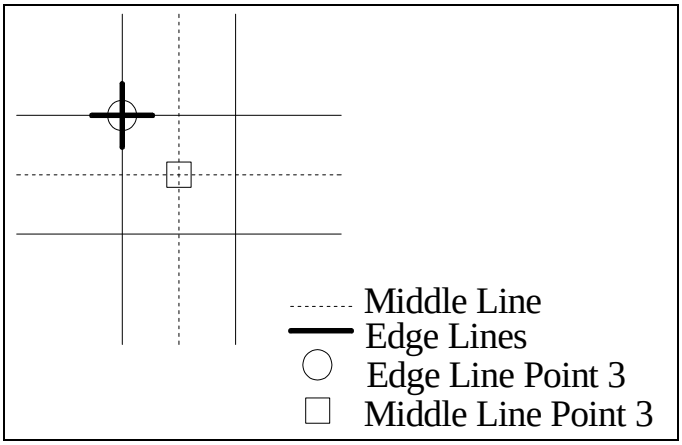

Fig. 2.27 Close up of lines used to define Point 3 (Fig. 2.17)

1. *Middle Lines:* In IDL program, the intensity of each pixel was determined for each image in the analysis. To define the middle lines, a threshold value of light intensity (Robert threshold) was used to define the left and right boundaries for vertical lines and top and bottom boundaries for horizontal lines in the images. The definitions of the boundaries of the lines were completed for a cropped image area. The intensity of each pixel of a given line was then determined between the defined boundaries for the vertical and horizontal lines. In theory, the maximum pixel intensity would define a unique line through the middle portion of each 0.25-in. (6 mm) line. The locations of the maximum pixel value along the thickness of the lines near Point 8 are shown in Fig. 2.28. To get refined results for the maximum intensity pixel locations, the area around the maximum intensity pixel locations were searched in detail. Because the location of the maximum pixel intensity varied over the length of each line, the middle points did not

align to form a smooth middle line. Therefore, the displacements and the cross-sectional rotation results obtained using this method were not very accurate.

The vertical displacements of Point 7 and 9 are compared with LVDT 3EBR7 and 3EBR8 readings in Figs. 2.29 and 2.30. As shown in the figures, the peak values represent LVDT measurement fairly well, but there is a lot of high frequency noise in the plots. The resulting calculated rotation at about 12 in. (305 mm) from the footing of Bent3 is shown in Fig. 2.31. As expected, the detailed calculation of the rotation varies widely.

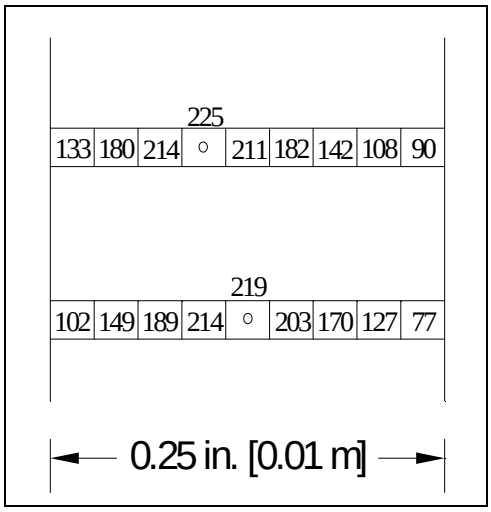

Fig. 2.28 Pixel intensities of two different levels in an image

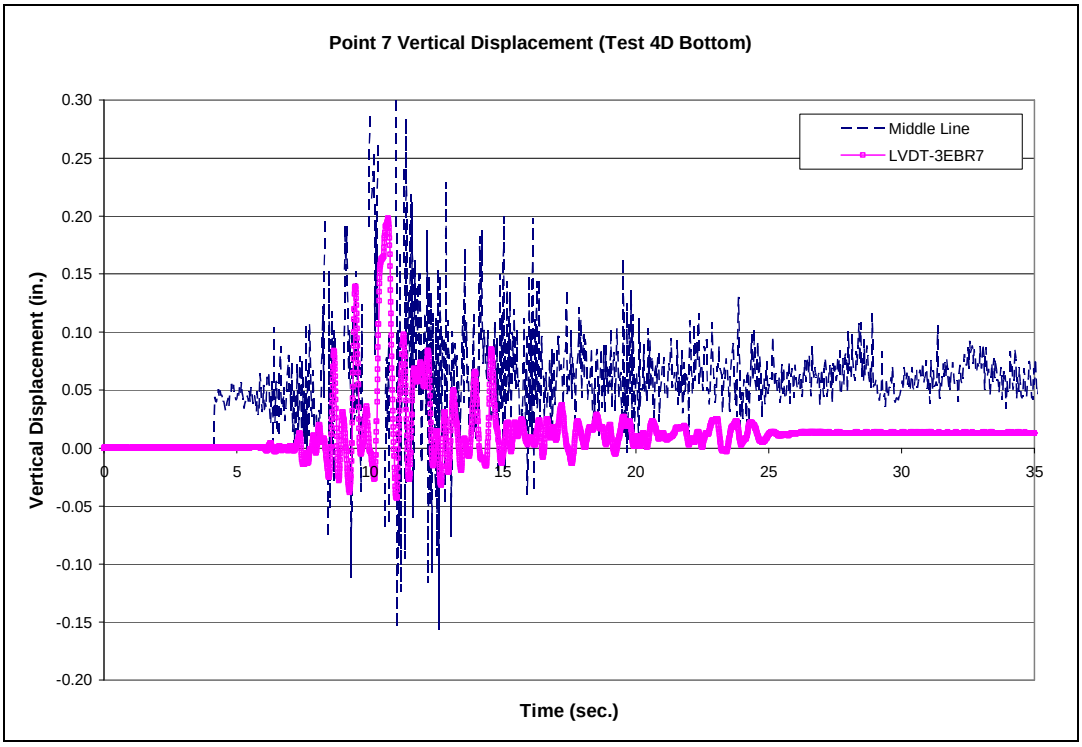

Fig. 2.29 Comparison of Point 7 vertical displacement with LVDT 3EBR7 data (1 in. = 254 mm)

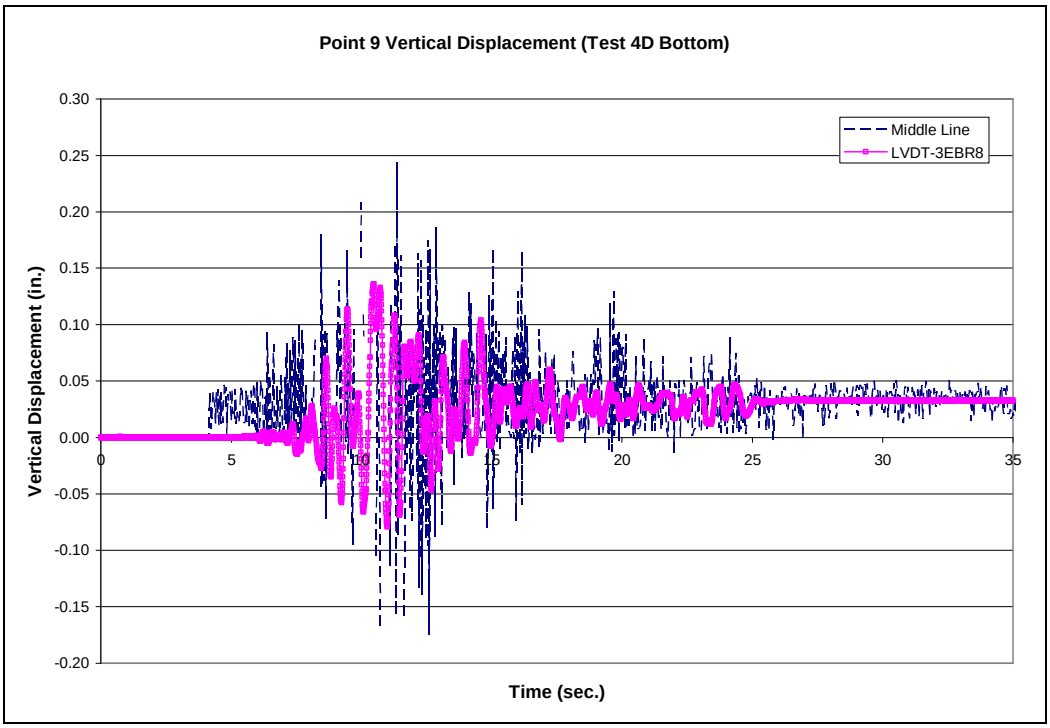

Fig. 2.30 Comparison of Point 9 vertical displacement with LVDT 3EBR8 data (1 in. = 254 mm)

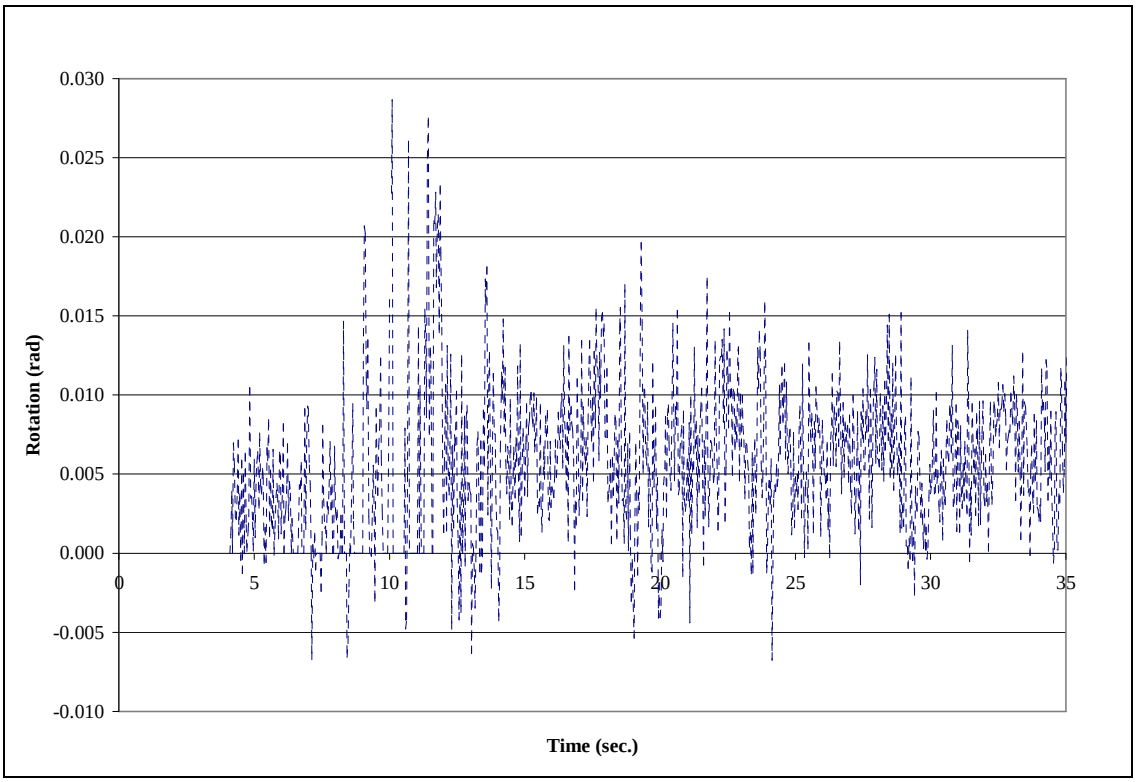

Fig. 2.31 Rotation of horizontal line using Points 7 and 9

To enhance the middle-line calculations, an average cross-sectional rotation over the height defined between two vertically connected points was calculated. For example, the vertical and horizontal displacements of Points 7, 8, 12 and 13 were first determined using the average vertical displacements of Points 7 and 12 and Points 8 and 13 were then calculated. An average rotation between these points was determined and is shown in Fig. 2.32. The average rotation obtained from IDL results at about 10 in. (254 mm) from the bottom hinging level was not improved using this method, with the magnitude of maximum rotation greatly magnified using the average values.

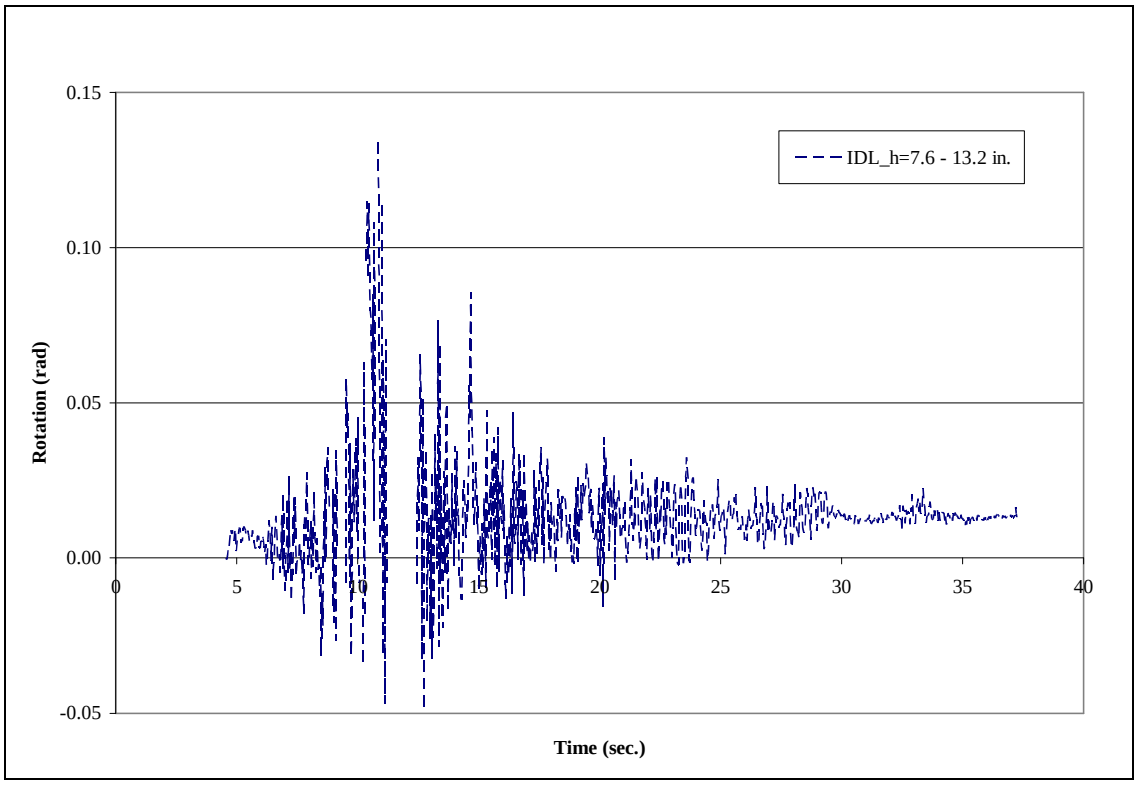

Fig. 2.32 Average rotation of four Points on the column surface

2. *Edge Lines*: Because of the thickness of the horizontal and vertical lines that define the grid system, the exact unique location of each Point (generally located at the intersection of the thick horizontal and vertical grid lines) may be defined in several ways. The "middle-line" method, as discussed previously, did not yield reliable results. Another method is to consider the edges of the thick grid lines to define two new lines (edge-lines) for each grid line. Therefore, at the intersection of the thick grid lines that generally defines a Point, there are actually four intersections of the edge lines to consider as possible unique locations of that Point (see Fig. 2.33, for example, Point 12 and Point 13 a, b, c, and d). In IDL programming language, the equations of the edge lines were obtained by defining the

boundaries of the thick grid lines using the constant Robert threshold value, as described in the previous section. Possible corner locations of the selected points (locations a, b, c, or d in Fig. 2.33) were calculated from the intersections of the four edge lines. Cross-sectional rotations were then computed using the same corners of paired Points (for example, a, b, c and d matching corners of Points 12 and 13).

Figures 2.34 through 2.37 show the rotation of horizontal line results calculated between the corners of the Points. Also, these four corner rotations were averaged to obtain the middle point (Point 12 and 13) rotation response. Figure 2.38 shows the middle point rotation result for Test 4D. The middle Point was selected to calculate the rotations for photogrammetry results because the corner rotation results give high values and more high frequency noise than the middle point rotation result.

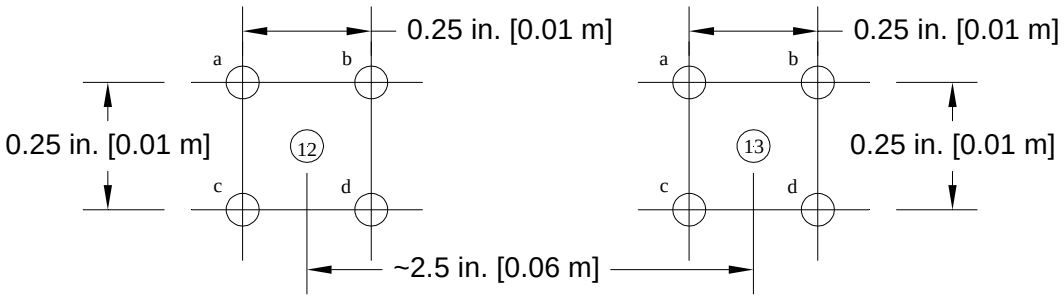

Fig. 2.33 Four corners surrounding general location of Point 12 and 13

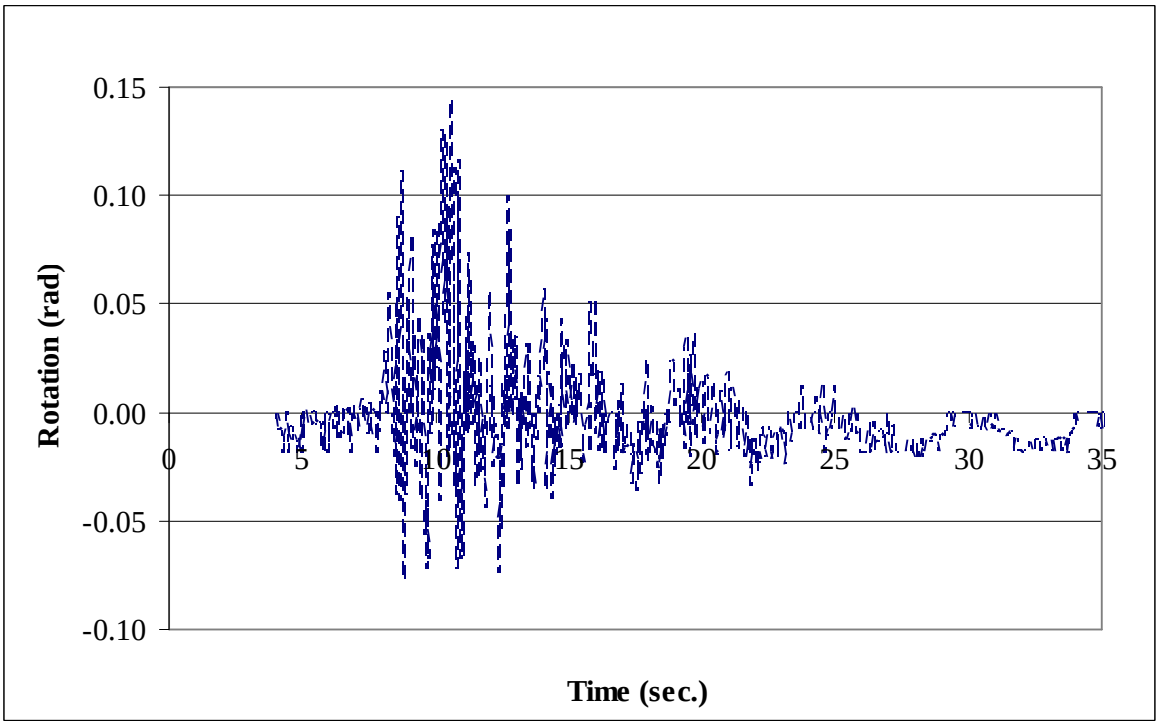

Fig. 2.34 Corner (a) rotation of Point 12 and 13

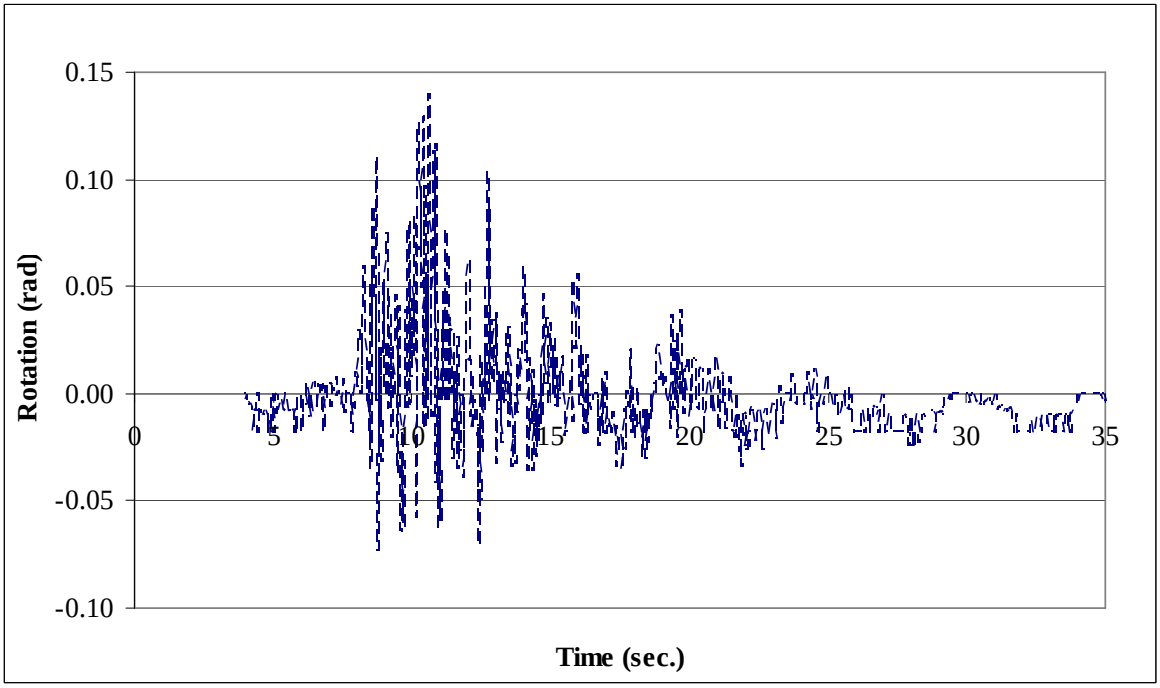

Fig. 2.35 Corner (b) rotation of Point 12 and 13

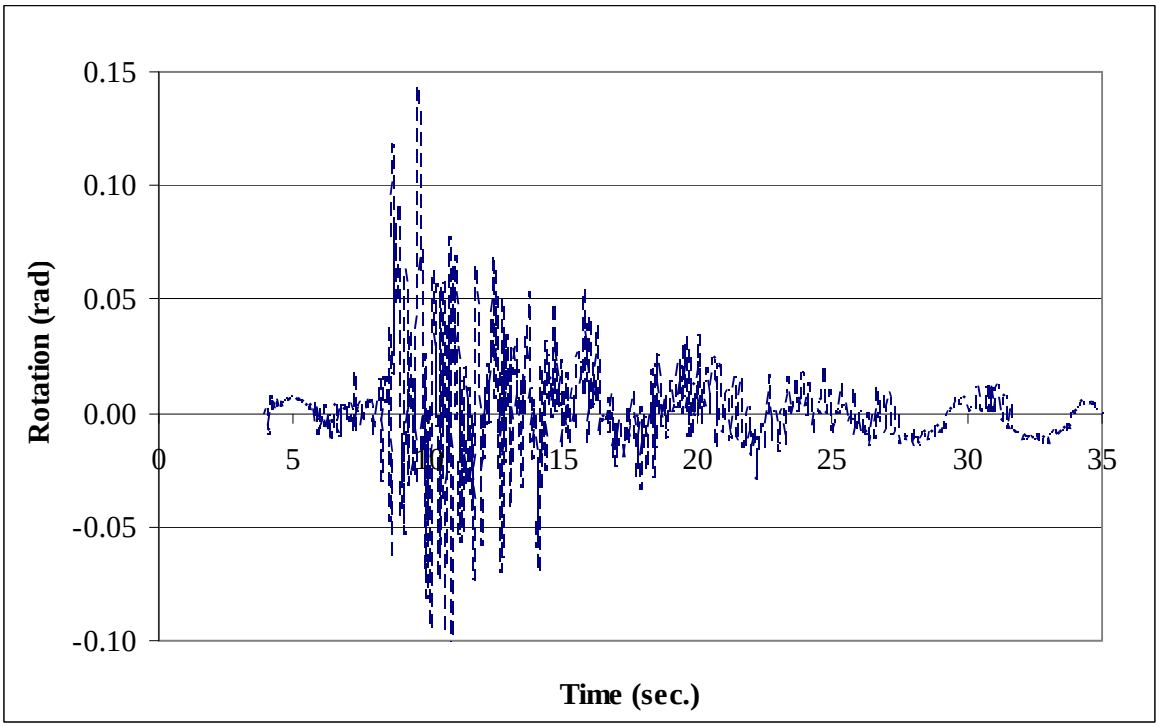

Fig. 2.36 Corner (c) rotation of Point 12 and 13

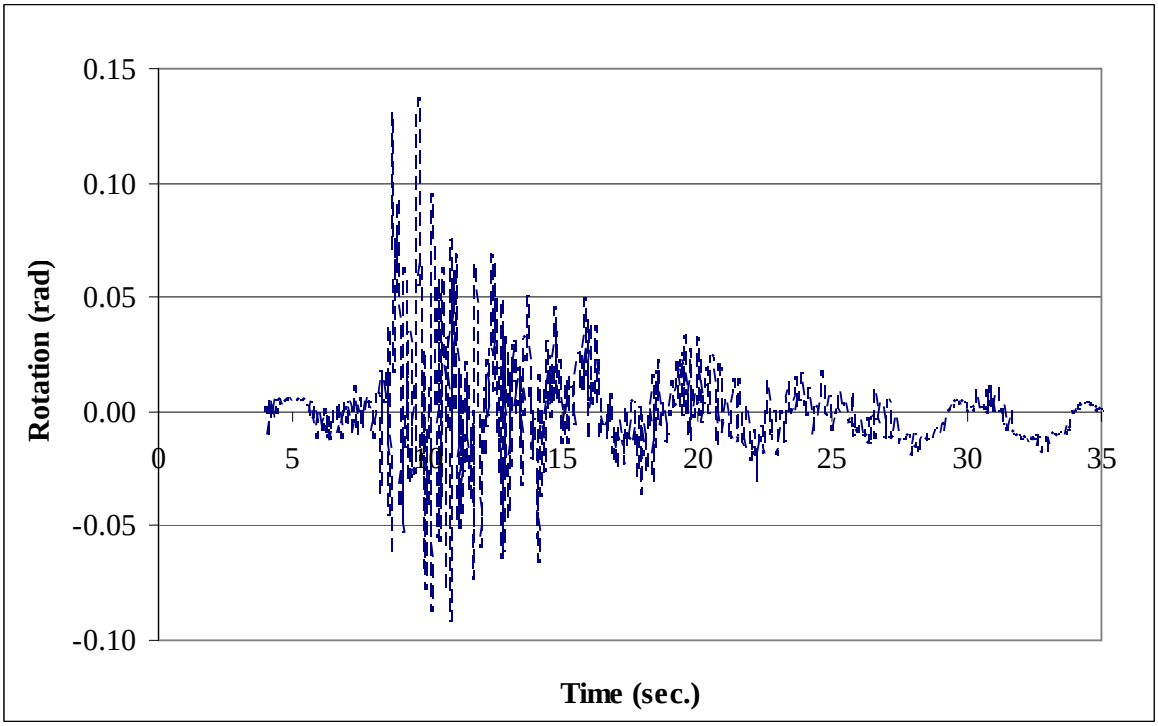

Fig. 2.37 Corner (d) rotation of Point 12 and 13

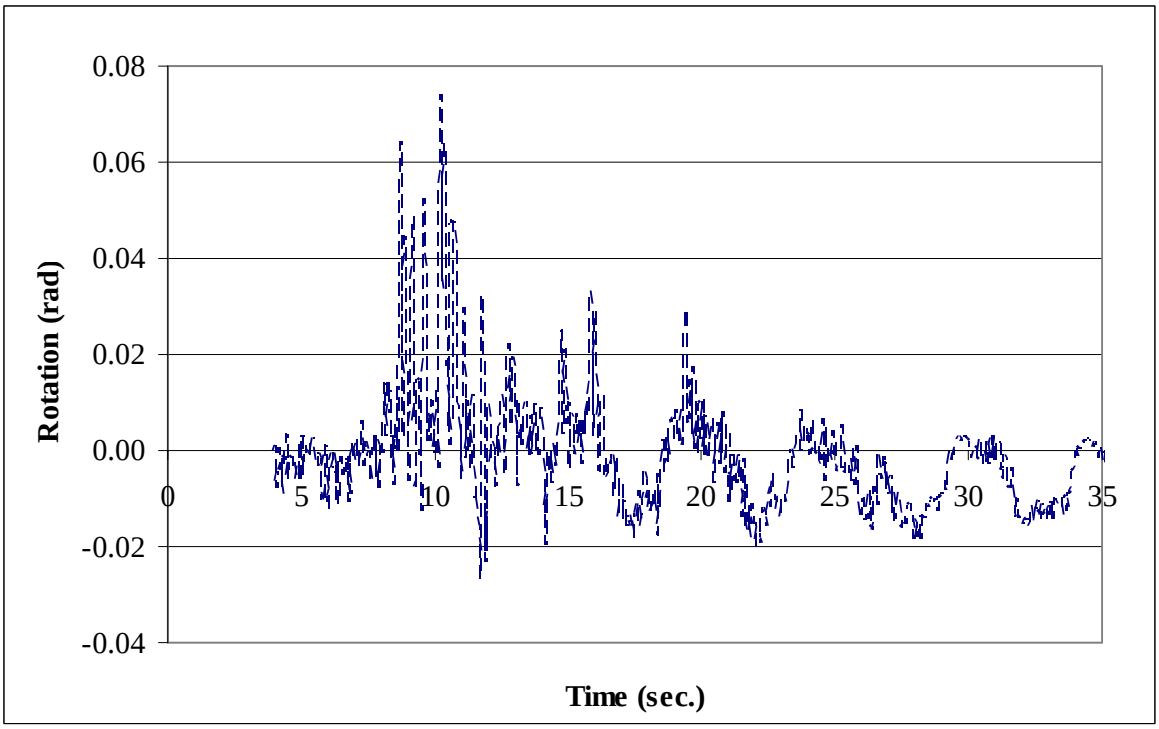

Fig. 2.38 Average rotation of Point 12 and 13

3. *Selecting Points to Define Lines- Constant Robert Threshold vs. Intensity Difference:* Two different approaches were used to define the boundaries of the edge lines. In the first approach, a constant Robert threshold value that adequately defined the transition from black to white paint was determined from the first image in each image group. A line length was assigned and the equations of the four edge lines were calculated. Various degrees of polynomials were considered to define the edge lines, but simple first degree (linear) representation proved to be the best fit. The edge line lengths were set between values of 0.5 in. (13 mm) and 1.0 in. (25 mm) depending on the relative distance between the grid lines. Even-numbered lines were used in the analysis, as described previously (Section 2.3.4.1 Unclear Images).

The vertical displacements of Point 7 and 9 were tracked during Test 4D and compared with LVDT 3EBR7 and 3EBR8 readings (Figs. 2.39-40). The vertical displacement results for Point 7 and 9 follow the general periodicity and have similar peak values as the LVDT measurements. The rotation of horizontal line obtained using the constant Robert threshold approach is shown in Fig. 2.41. As shown in Fig. 2.41, due to pixelization there is some constant noise at the end of the test.

In the second approach, the intensity differences in consecutive pixels were obtained using the IDL program, and the maximum difference was used to define the boundaries for the four edge lines. All other parameters remained constant.

Figures 2.42-2.43 show the vertical displacements of Point 7 and 9 as compared with LVDT measurements. Rotation of horizontal line was computed using the relative vertical displacements of the two points normalized to the horizontal distance between the points in Fig. 2.44. As shown in Figs. 2.39 through 2.44, using the constant Robert threshold method produces more reliable results. The intensity-difference approach results in approximately twice the magnitude of the rotation than the constant Robert threshold method, and much more high frequency noise in displacements and the rotations.

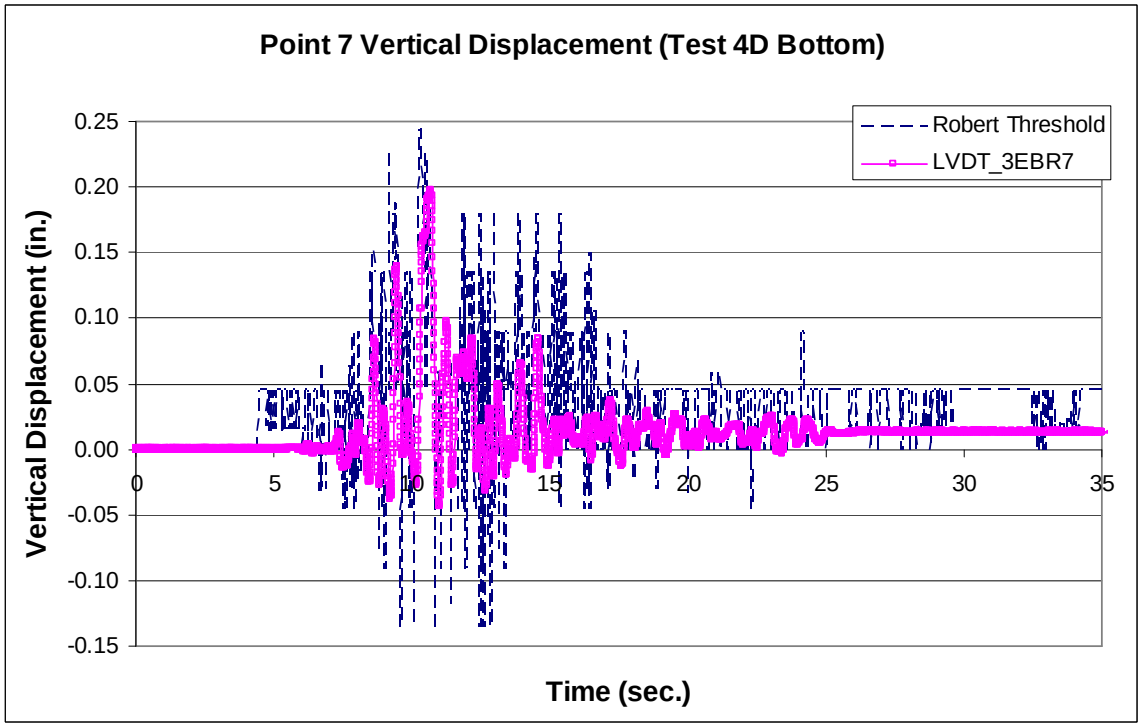

Fig. 2.39 Point 7 vertical displacement vs. LVDT 3EBR7 data (1 in. = 254 mm)

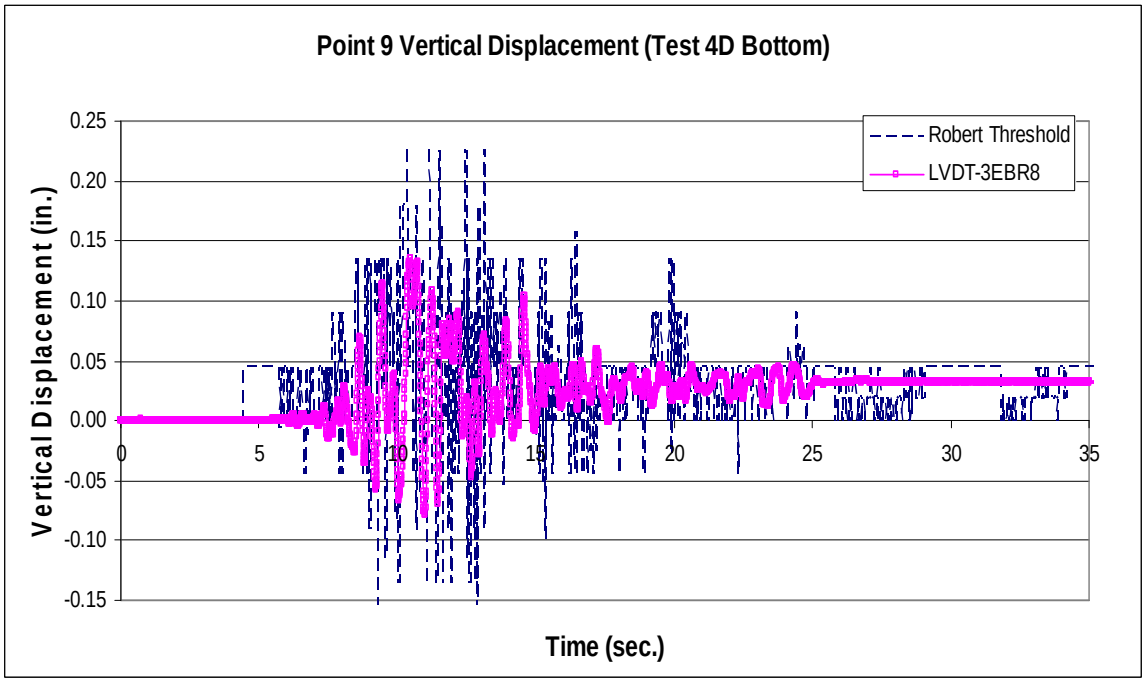

Fig. 2.40 Point 9 vertical displacement vs. LVDT 3EBR8 data (1 in. = 254 mm)

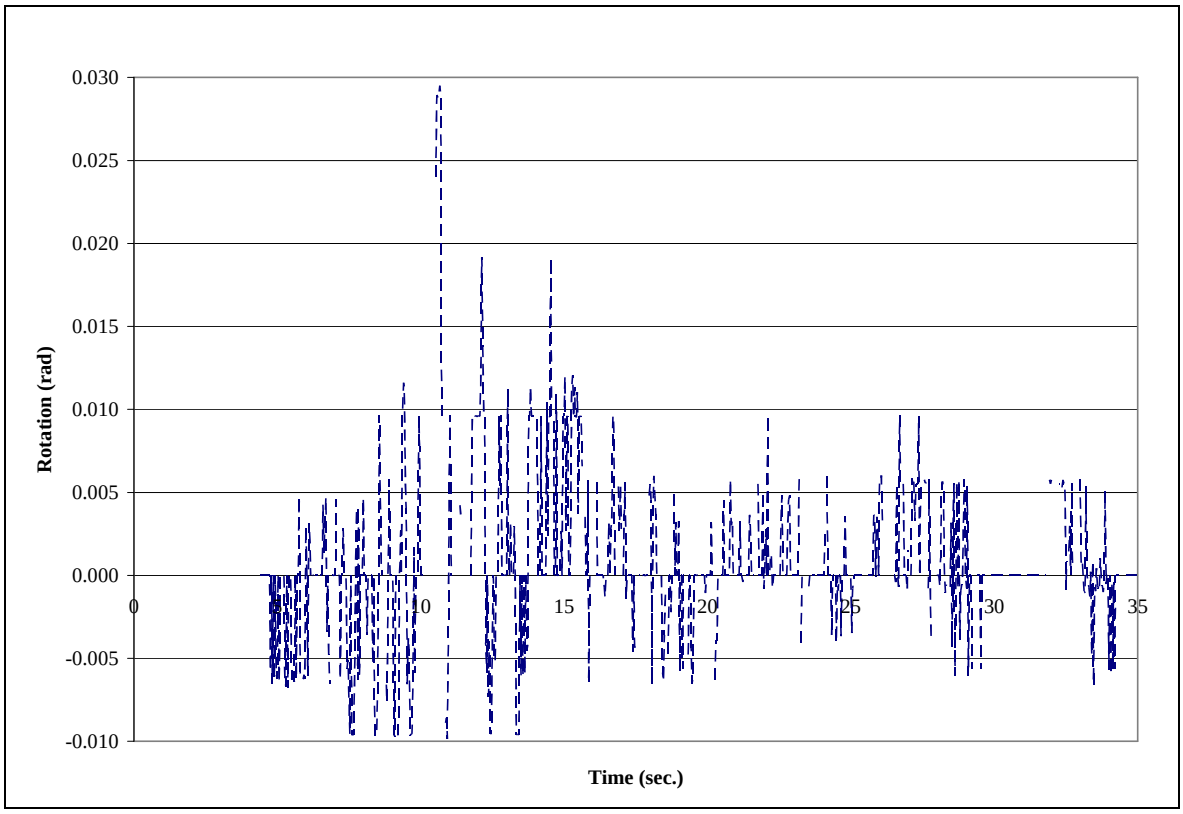

Fig. 2.41 Rotation of horizontal line obtained using the constant Robert threshold

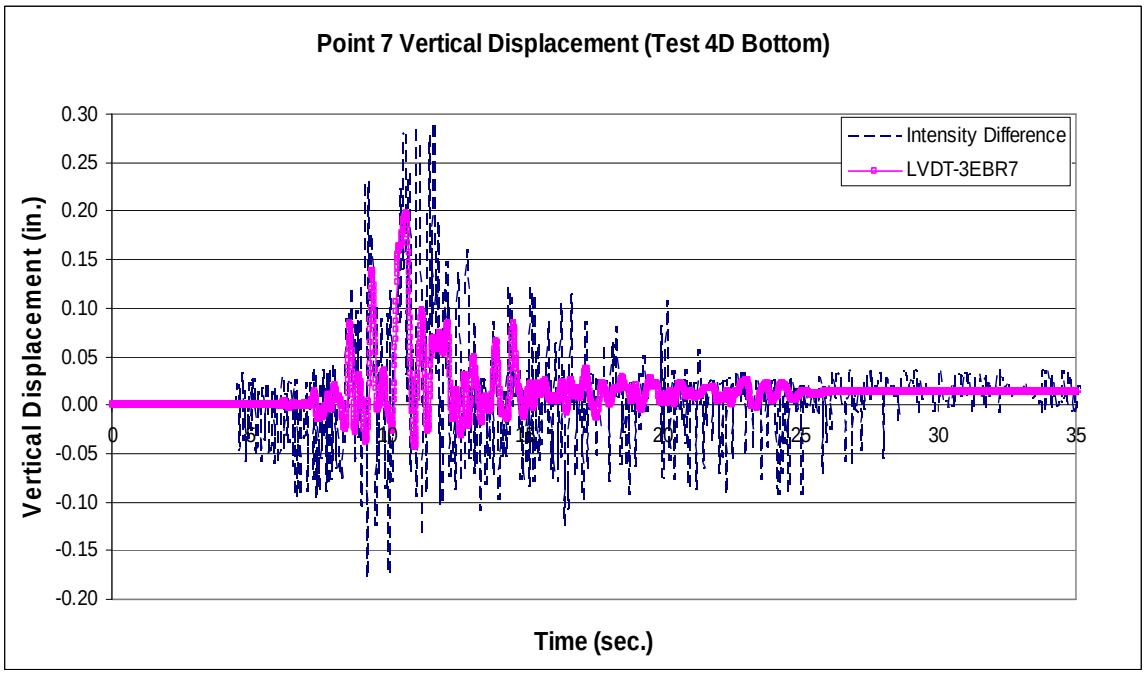

Fig. 2.42 Point 7 vertical displacement compared with LVDT 3EBR7 data (1 in. = 254 mm)

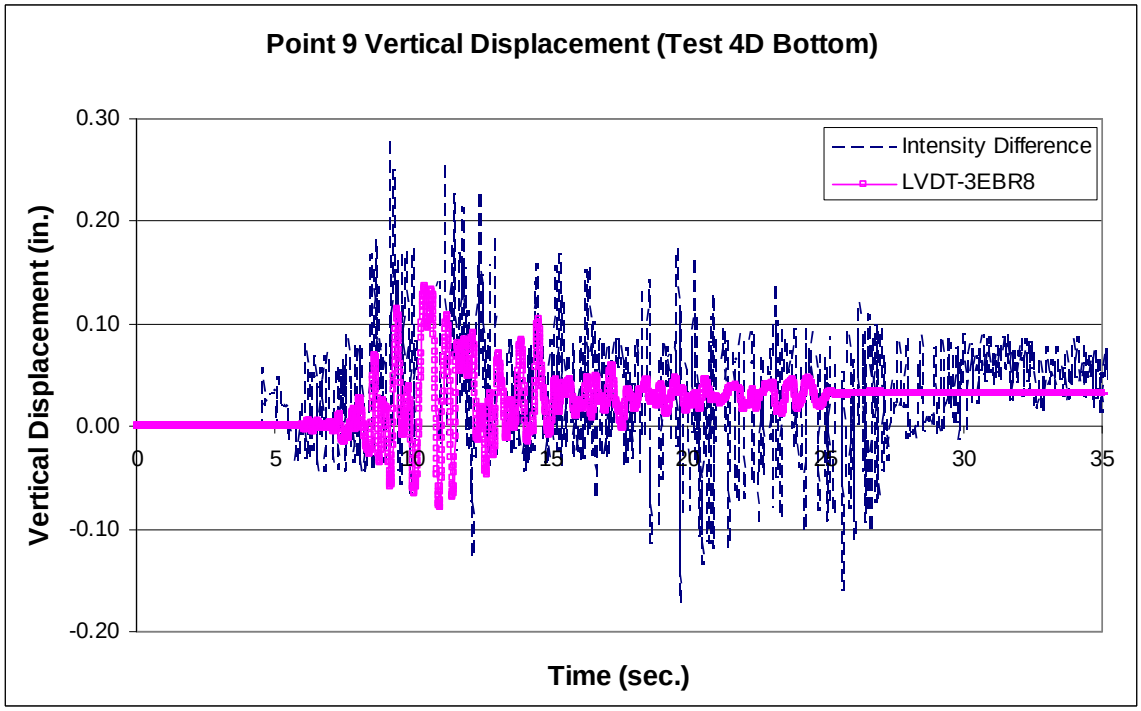

Fig. 2.43 Point 9 vertical displacement compared with LVDT 3EBR8 data (1 in. = 254 mm)

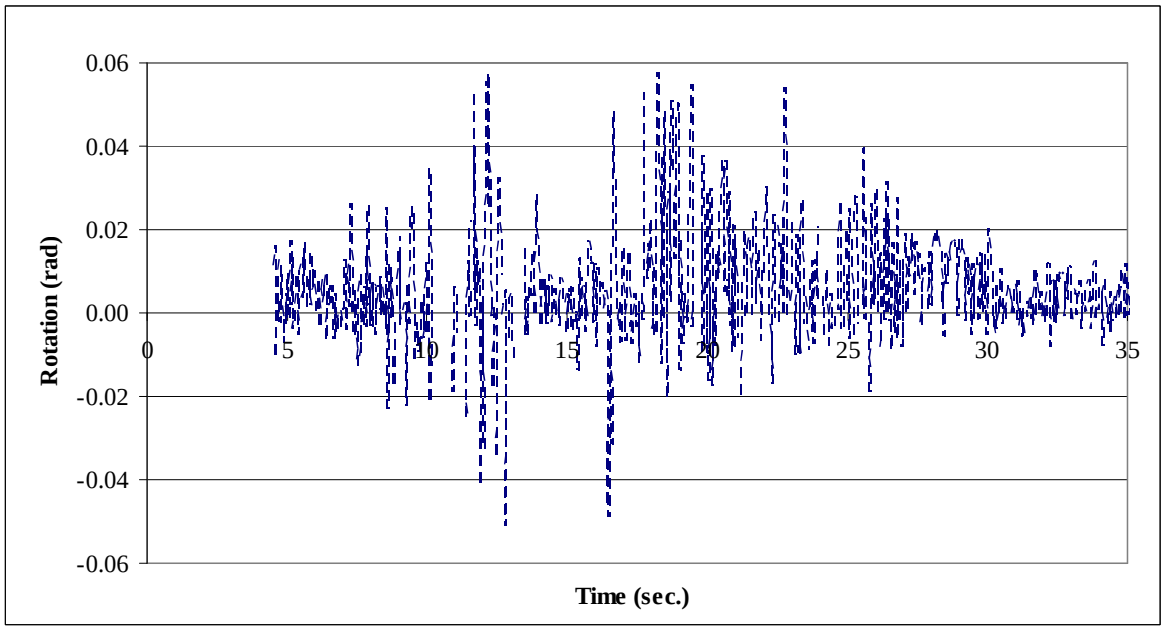

Fig. 2.44 Rotation of horizontal line at h=7.7 in. (196 mm) from the bottom fixity

4. *Long Lines vs. Short Lines:* When using the constant Robert threshold method, the length of the edge line controls the number of points used to define that line, and therefore, the equation of the line. Longer (1.5 in. (38 mm) to 3.0 in. (76 mm)) edge-line lengths were investigated to determine the influence on the definition of a unique Point. Even-numbered lines were used in the analysis.

The vertical displacements of Point 7 and 9 were determined and compared with LVDT 3EBR7 and 3EBR8 readings (Figs. 2.45-2.46). The resulting cross-sectional rotation is shown in Fig. 2.47 and compared with the calculated rotation from LVDT data at approximately 12 in. from the footing of Bent3. The short line and long line analyses can be compared by examining cross-sectional rotation calculated from each analysis (Figs. 2.41 and 2.47, respectively). There is approximately 0.011 radians of constant noise shown in the long-line results (Fig. 2.47), whereas the short-line results (Fig. 2.41) show approximately half the magnitude and less frequency of noise. The short-line definition was selected for all ensuing calculations.

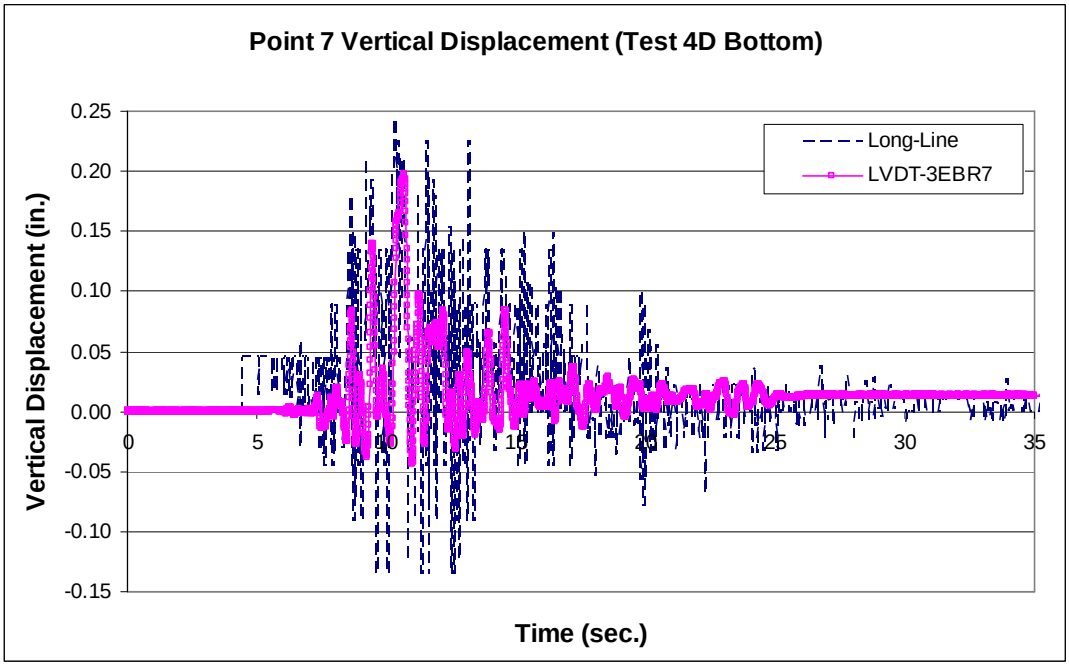

Fig. 2.45 Comparison of Point 7 vertical displacement with LVDT 3EBR7 data (1 in. = 254 mm)

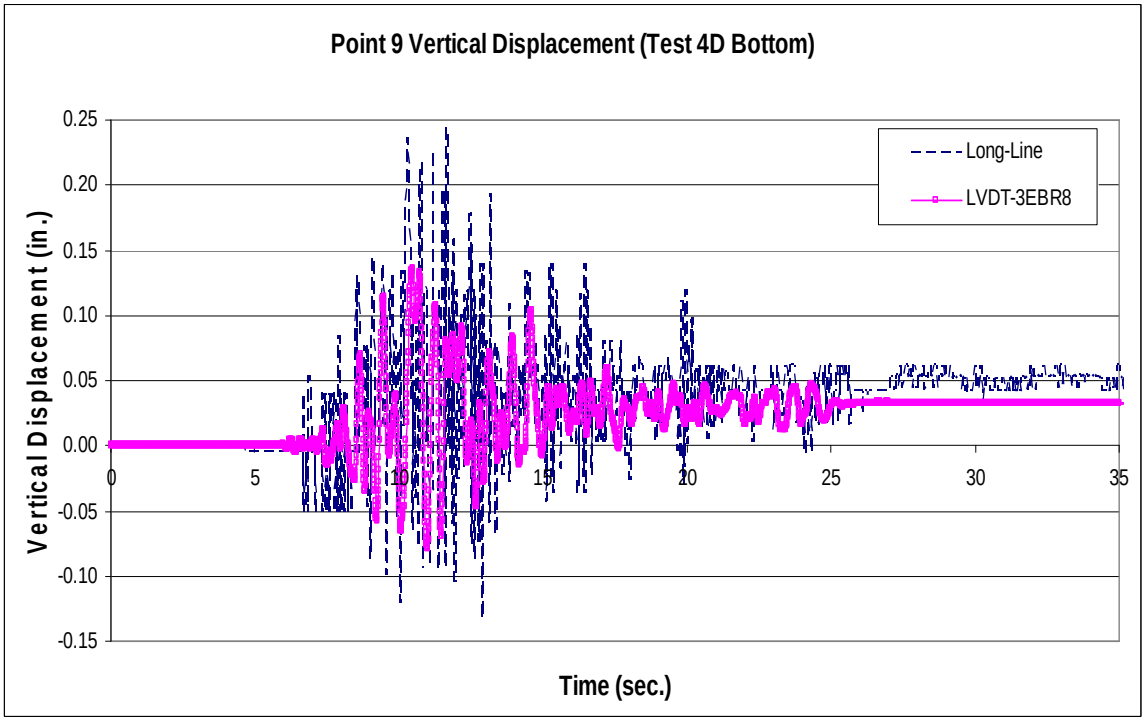

Fig. 2.46 Comparison of Point 9 vertical displacement with LVDT 3EBR8 data (1 in. = 254 mm)

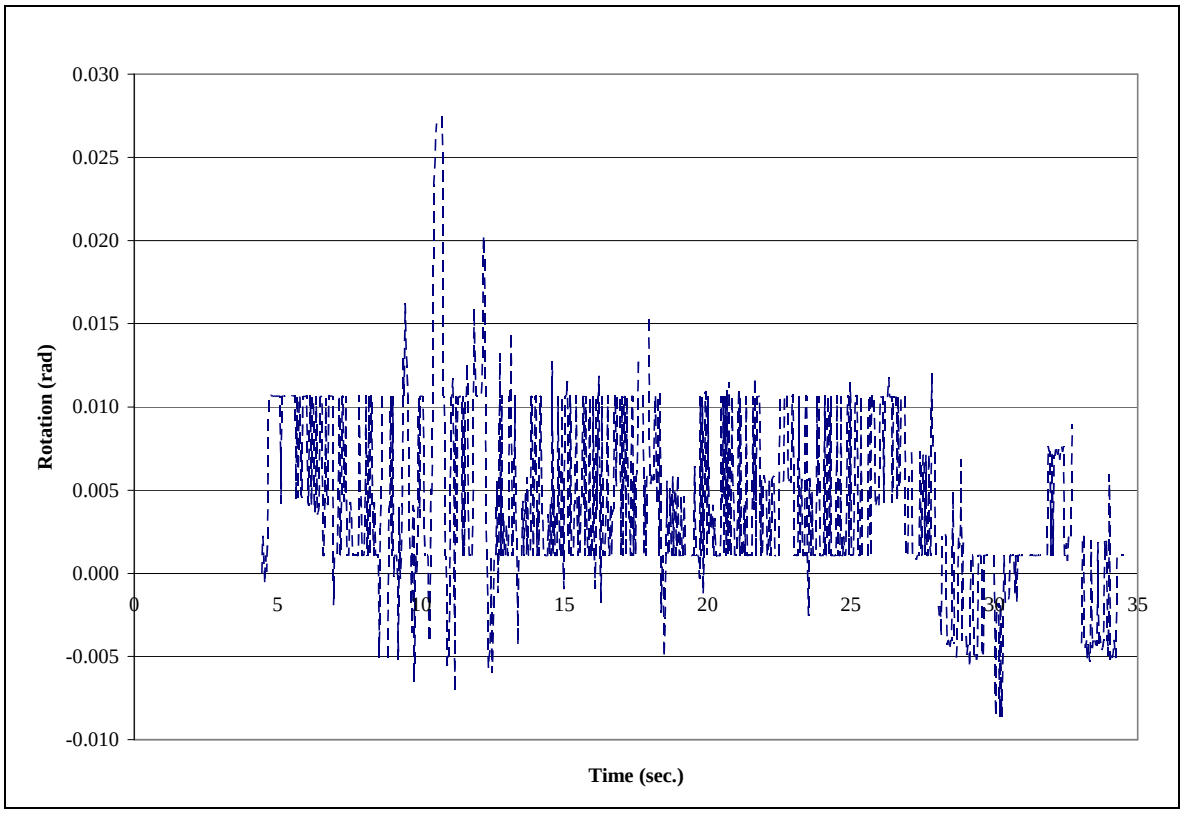

Fig. 2.47 Rotation of horizontal line calculated using long-line

- **Evaluation of Grid System**

As described in Section 2.3.2, two separate grid systems were used to evaluate the displacements for photogrammetry analysis. In the displacement calculations of the top grid system, Unique points in the targets (squares) were defined by seeking the maximum pixel intensity over the thickness of the square, similar to Middle Lines analysis described in Section 2.3.4.1 Intersecting Lines. However, the value of pixel intensity did not change significantly over the thickness of the square, and the definition of the Point location was found to vary from frame to frame. An example of the calculated displacement of Point 46 defined using the maximum intensity in the square is shown in Fig. 2.48 and compared with LVDT data. By contrast, results obtained using the Edge Lines to

calculate corner points and the Average Point location is shown in Fig. 2.49 and compared with LVDT data. As shown in both figures, the vertical displacement of the middle point follows the LVDT 3ETR4 data when the Edge Lines method is used and gives much closer results than the vertical displacement using the maximum intensity approach.

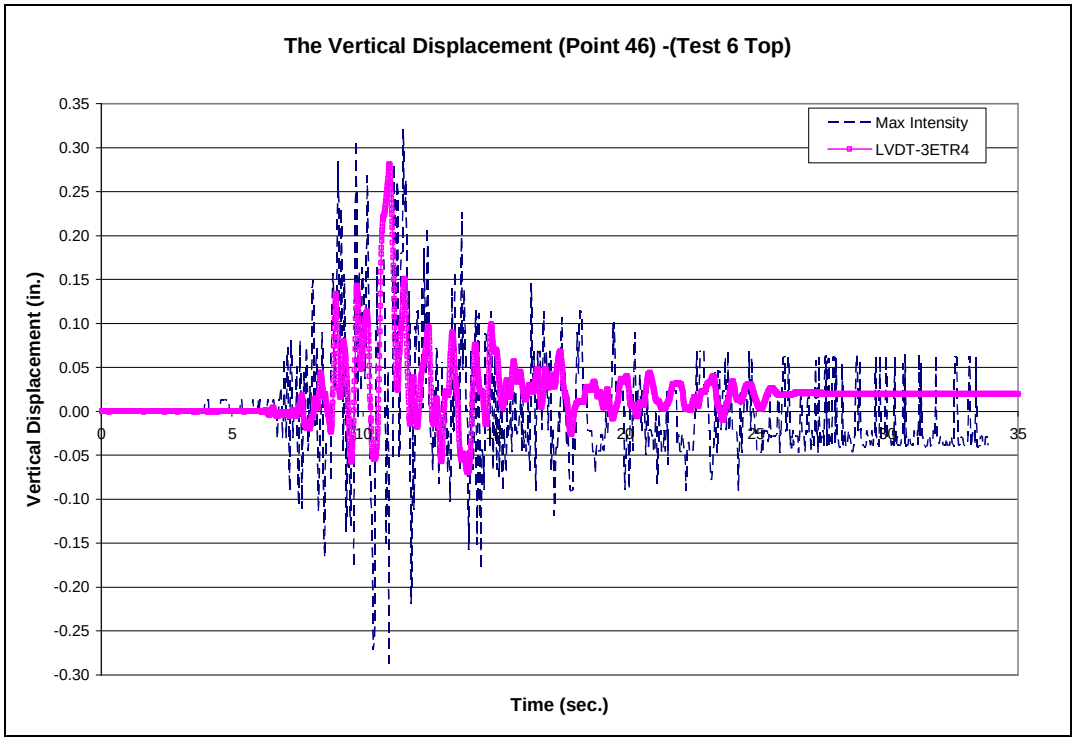

Fig. 2.48 Comparison of Point 46 vertical displacement with LVDT 3ETR4 data using the maximum intensity approach (1 in. = 254 mm)

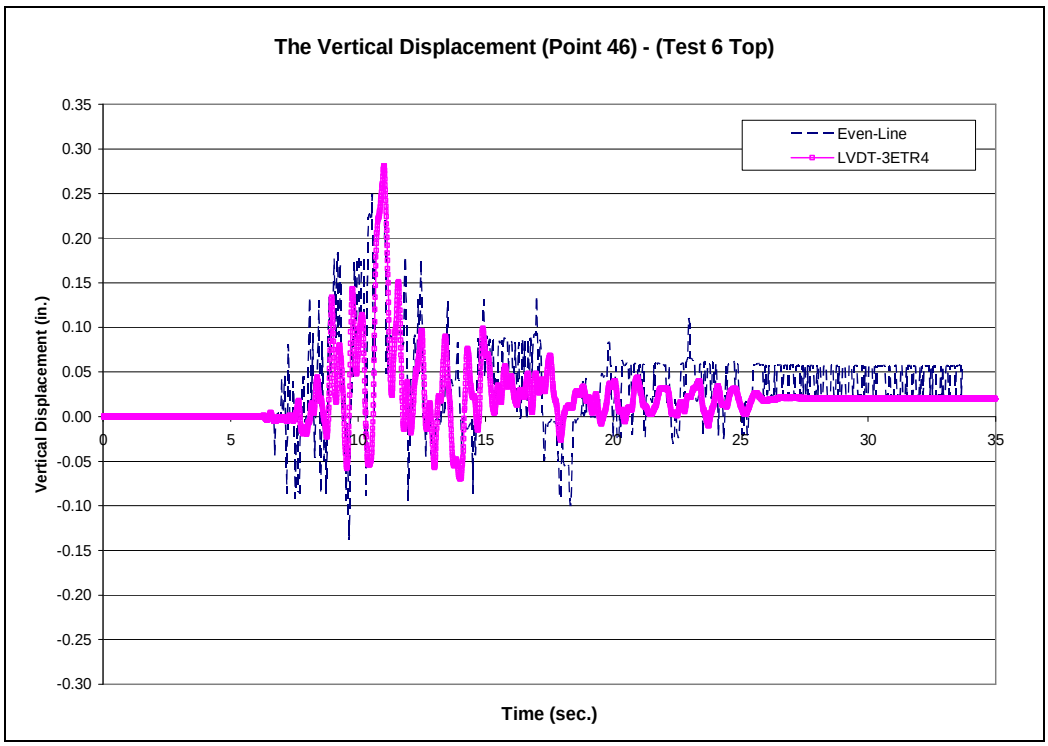

Fig. 2.49 Comparison of Point 46 vertical displacement with LVDT 3ETR4 data using the Edge Lines method (1 in. = 254 mm)

- **Rotation of Vertical Lines vs. Rotation of Horizontal Lines on Column Surface**

As described in Section 2.2 Proof-of-Concept Test, a rotation of vertical line for the column can be calculated using transverse movements of points that are aligned vertically, and this rotation represents the average cross-sectional rotation between those two points if shear deformations can be neglected. To see the difference between calculated rotations of vertical lines and rotations of horizontal lines, movements of points on the bottom and top grid systems were determined (Fig. 2.17). The rotation of vertical line was calculated using the relative lateral displacements of two vertically-aligned points on the grid surface divided by the vertical distance between the points. Rotations of horizontal lines are calculated as described previously.

The lateral displacements of Point 3 and 8 on the bottom grid were tracked during Test 4D motion to calculate rotations of vertical line (Fig. 2.50). Points 7 and 9 shown in Fig. 2.17 were selected and the vertical movements of the Points were determined to calculate the rotation of horizontal line during Test 4D. The rotation of horizontal line results is shown in Fig. 2.51. Also, the rotation of vertical line and the rotation of horizontal line are compared in Fig. 2.52.

In order to compare the rotation of vertical line and rotation of horizontal line at the top grid, Point 38 and 52 were selected and tracked during Test 4D. Figure 2.53 shows the rotation of vertical line results calculated between Point 38 and 52. Point 44 and 46 were selected to determine the rotation of horizontal line shown in Fig. 2.54. The comparison between the rotation of vertical line and rotation of horizontal line results are shown in Fig. 2.55. As an average measurement, the rotation of vertical line provides a smoother trace than the rotation of horizontal line calculations from the photogrammetry data. Comparisons for the three different tests at each cross-sectional rotation location are found in Appendix A.

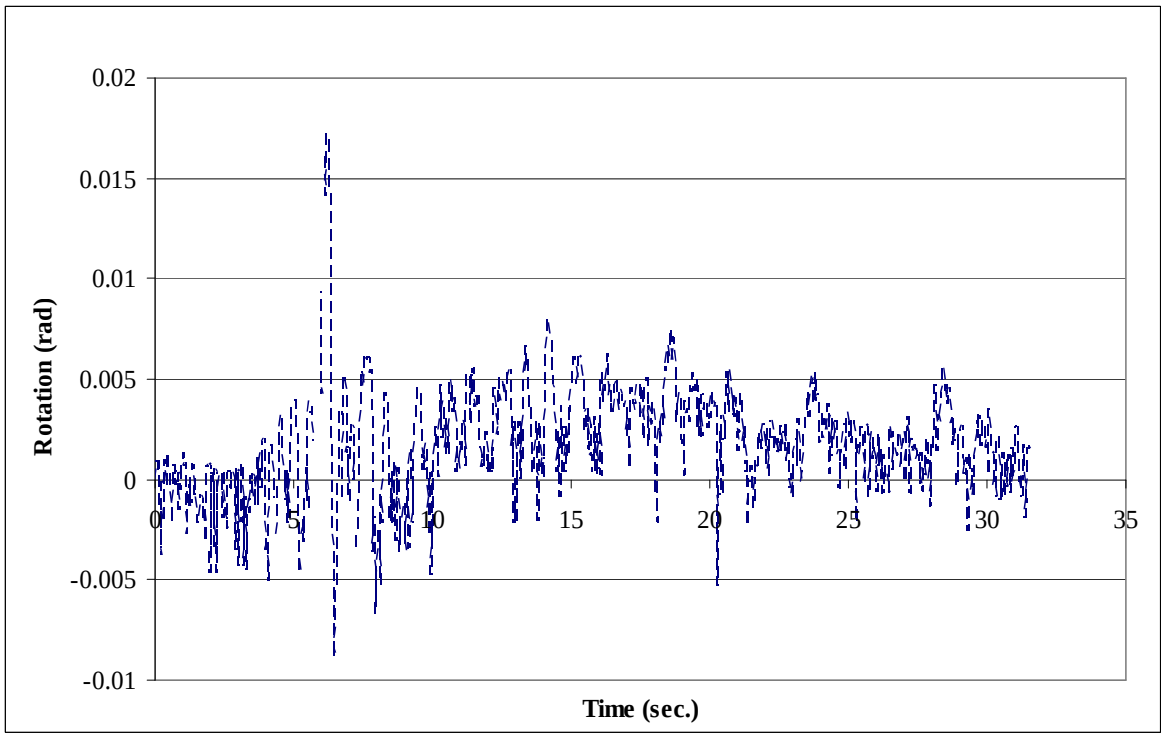

Fig. 2.50 Rotation of vertical line calculated using Point 3 and 8

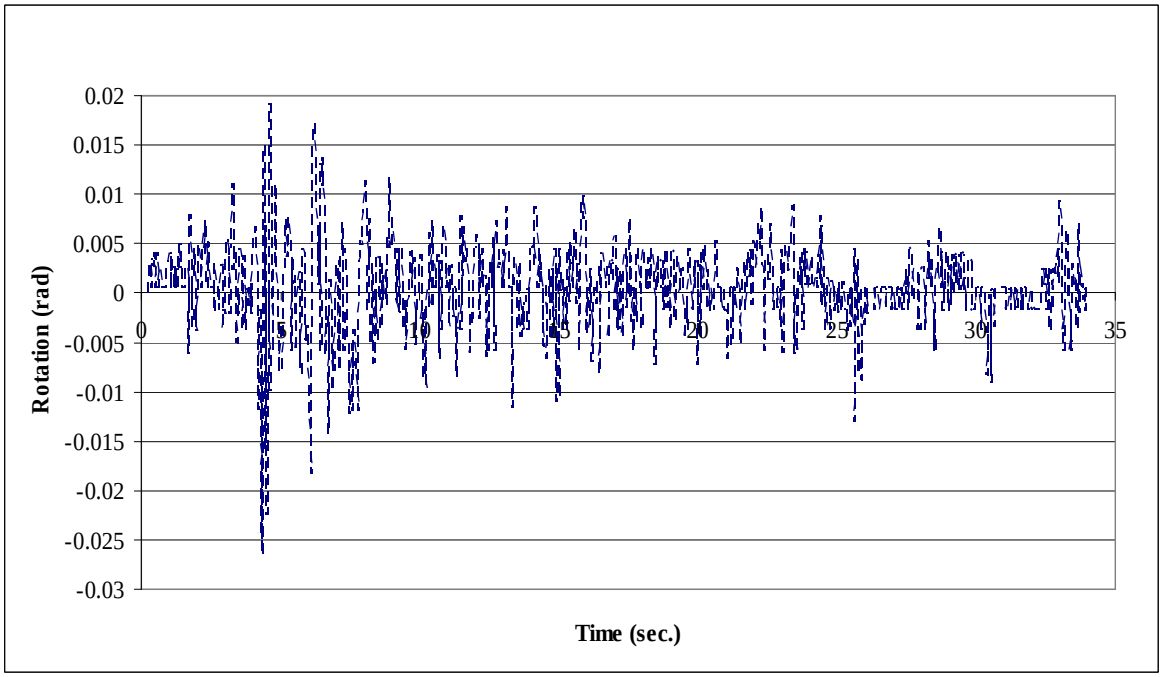

Fig. 2.51 Rotation of horizontal line using Point 7 and 9

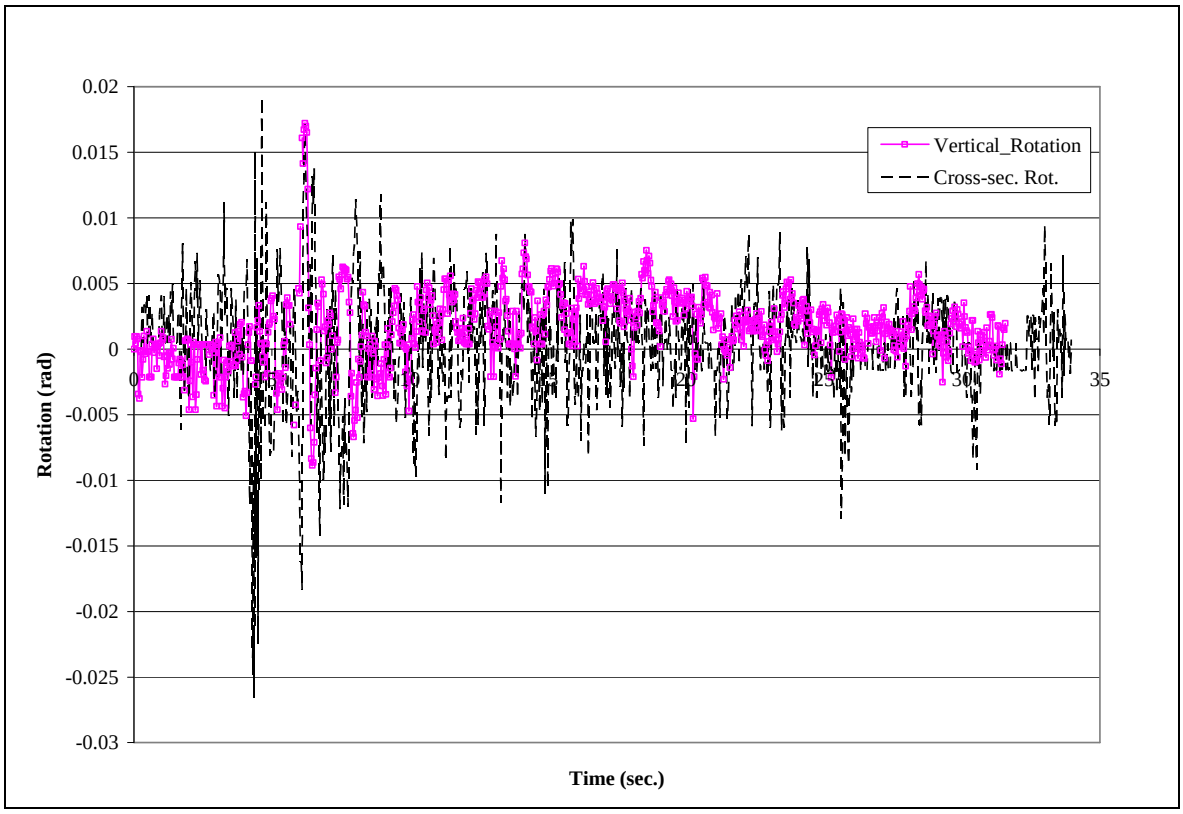

Fig. 2.52 Comparison of rotations (local vs. average) in Test 4D

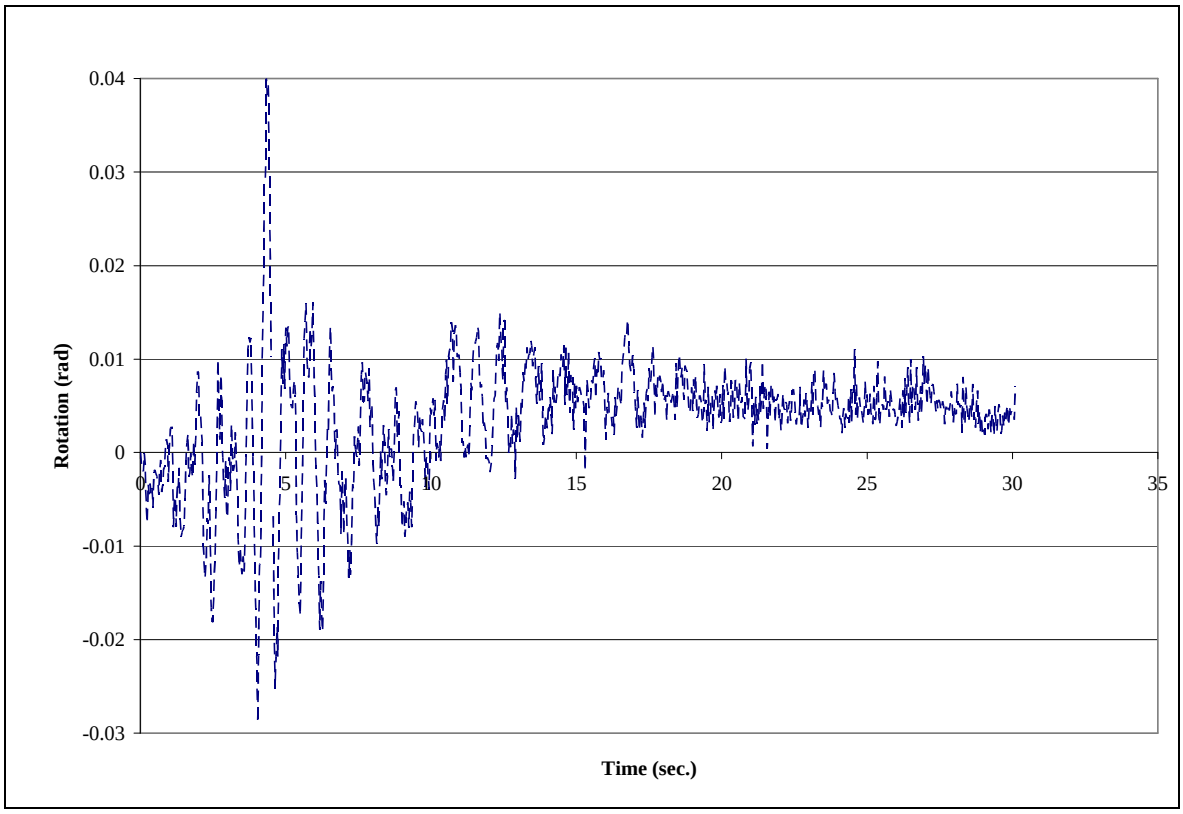

Fig. 2.53 Rotation of vertical line calculated using Point 38 and 52

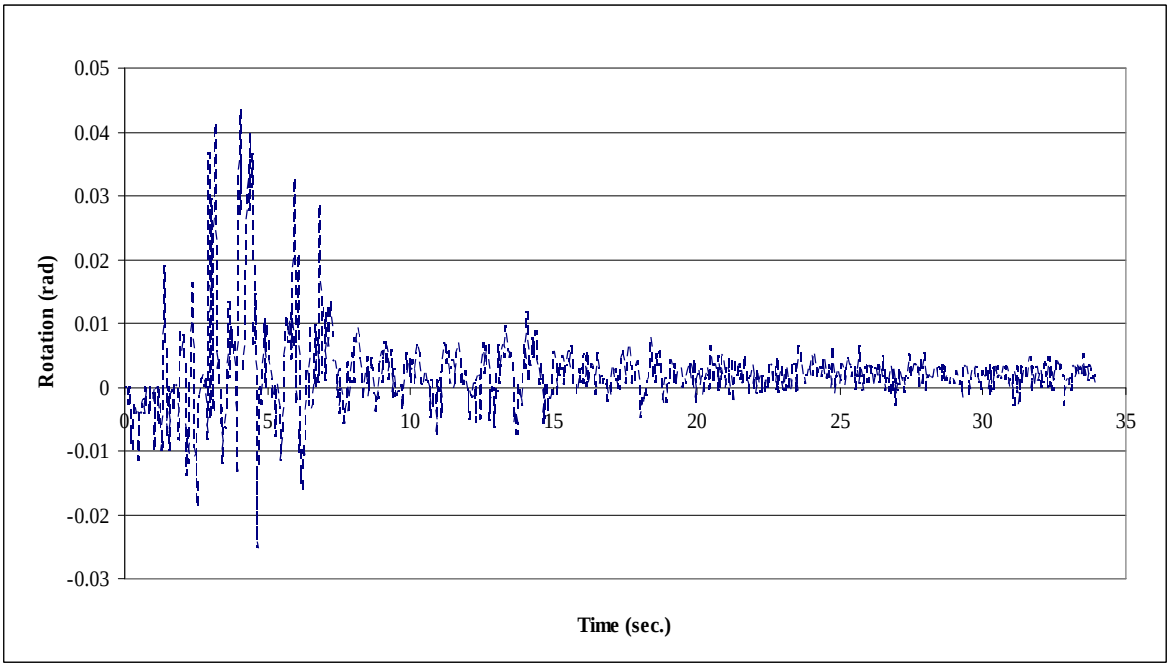

Fig. 2.54 Rotation of horizontal line using Point 44 and 46

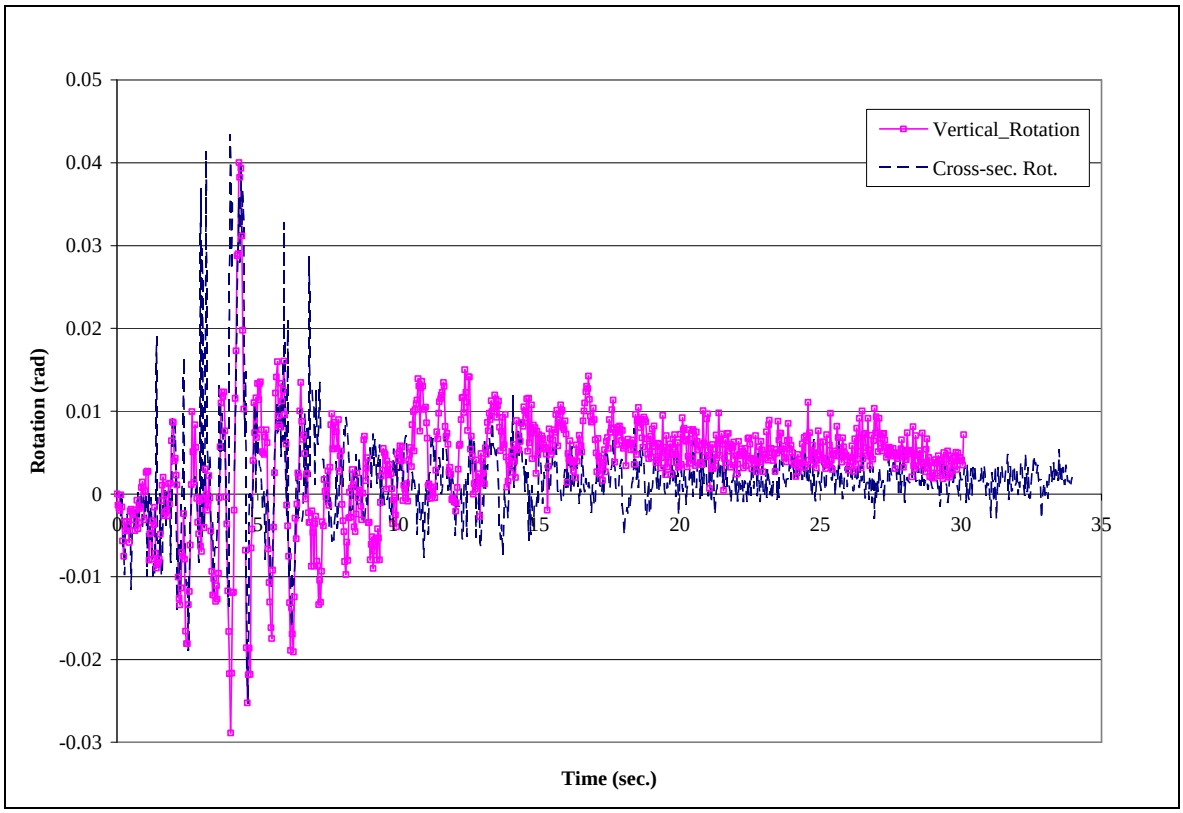

Fig. 2.55 Comparison of rotations (local vs. average) in Test 4D

2.3.4.2 Displacements

The grid that is used to provide photogrammetry data is advantageous when considering the deformation to the column surface over a continuum, which may be correlated with detailed Finite Element results. By contrast, LVDT instrumentation will provide only discrete displacement data in a single direction. In addition, if significant damage occurs to the concrete surface, LVDTs measurements may become dysfunctional, but the painted grid surface may be reconstructed in an image and photogrammetry data preserved. This section describes the displacement calculations in the gridded surfaces for multiple earthquake excitations. Displacement histories for all gridded Points and earthquake motions are shown in Appendix B.

- **Top of the Column**

Point 59 in the top grid system (Fig. 2.17), which was the closest point to the top of the column, was selected to track the peak displacement along the direction that the left cameras have 15.25° counter clockwise from the longitudinal direction of the bridge. The displacements at grid Point 59 captured during Test 2, Test 4D, and Test 6 are compared with the combined components of DT7, which recorded the transverse displacement of the Bent 3 at the middle of the bridge deck, and DS5 and DS1 measurements, which measured the gap size history and the displacement of the north abutment in the longitudinal direction of the bridge, during the same motions in Figs. 2.56, 2.57, and 2.58, respectively. There is approximately 23.3 in. (592 mm) between the transverse beam and Point 59. Because the column is in double curvature during the test, the lateral displacements at these two heights are assumed to be similar.

Considering Figs. 2.56-2.58, the overall periodicity of the two measurements correlate very well, with differences in magnitude primarily attributed to the height flexibilities differentials of the transverse beam and column hinging region. In addition, the photogrammetry measurements capture movement in the column, which may differ at discrete time from movement of the cap beam that is captured by LVDT instrumentations. Some variations in periodicity between the photogrammetry displacement results and the readings of the displacement transducers are noted (for example, between the time periods of 12 and 13.5 seconds in Fig. 2.56), and in these cases the photogrammetry results have been visually confirmed with the associated images. As shown in all figures, the lateral displacements are reliable and correlate with the LVDT instrumentation data.

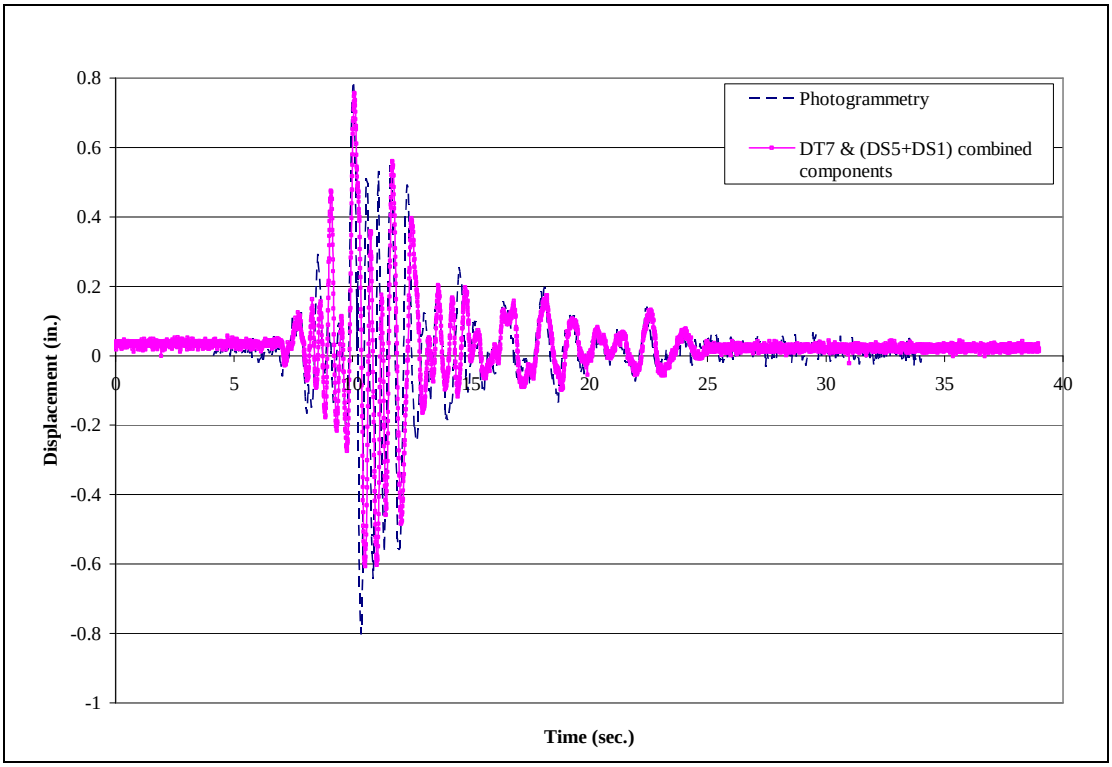

Fig. 2.56 Comparison of Drift at Point 59 for Test 2 (1 in. = 254 mm)

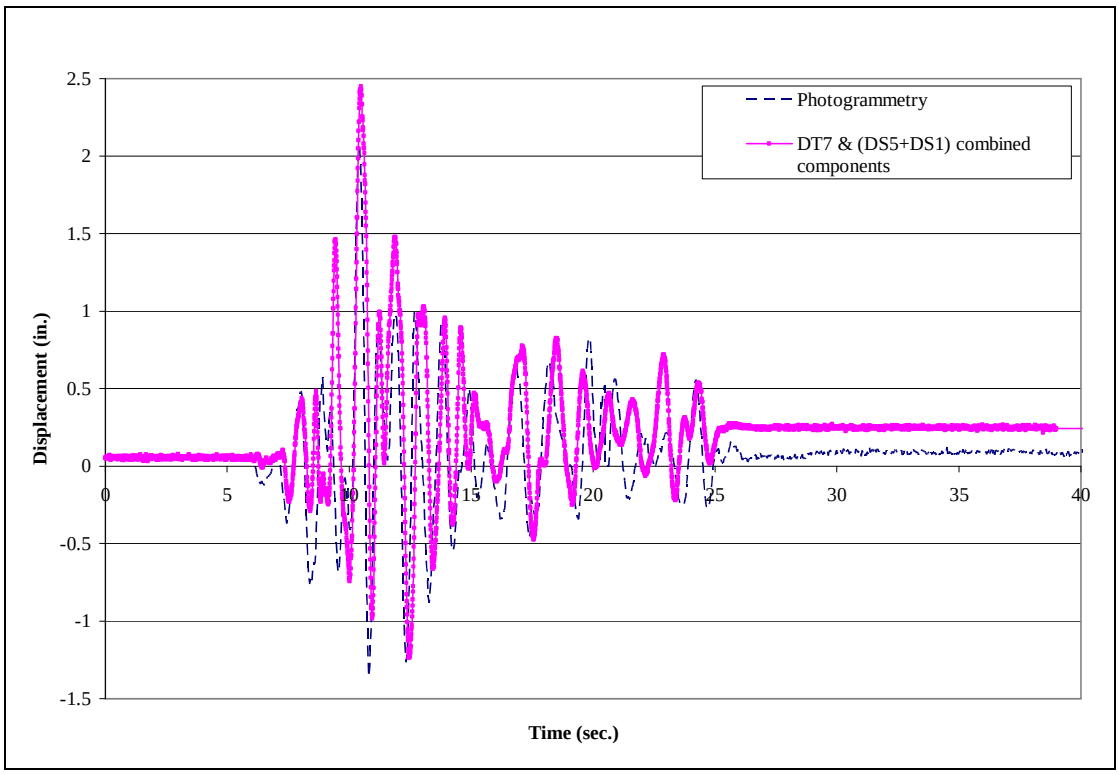

Fig. 2.57 Comparison of Drift at Point 59 for Test 4D (1 in. = 254 mm)

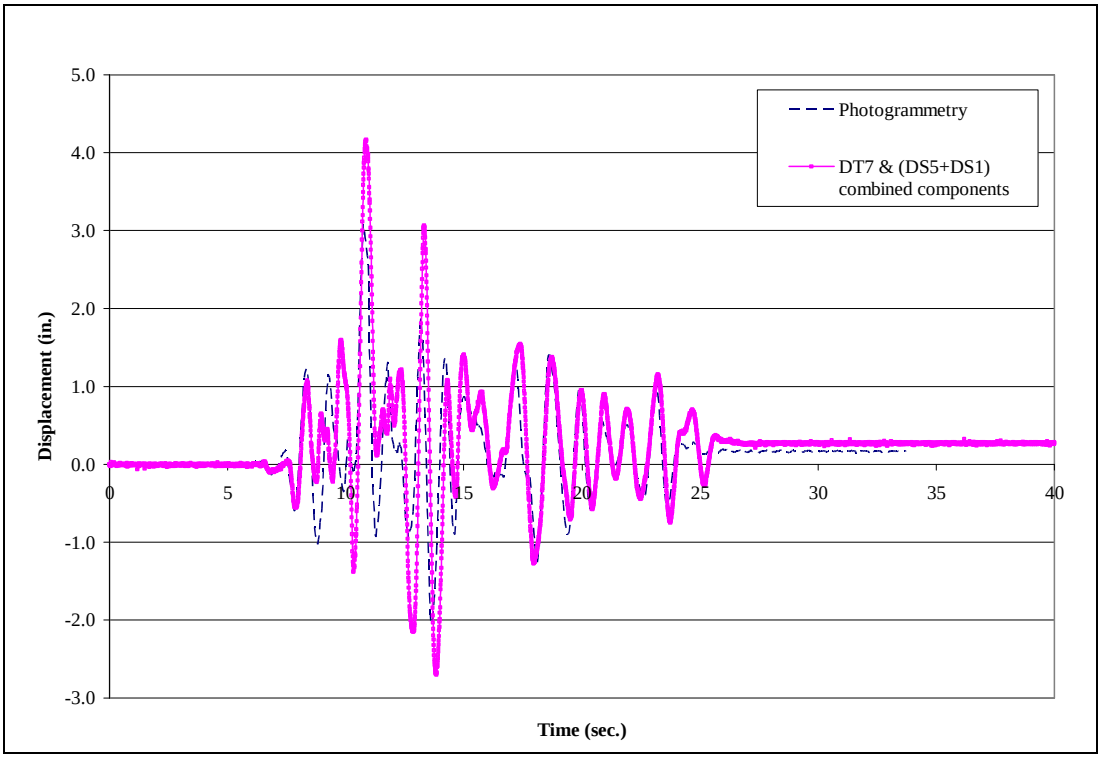

Fig. 2.58 Comparison of Drift at Point 59 for Test 6 (1 in. = 254 mm)

The maximum calculated displacements using photogrammetric measurements for the three different earthquake motions are compared with the UNR maximum movement recorded by the combined components of DT7, DS5 and DS1. The maximum displacements calculated in the photogrammetry analyses were normalized by the maximum combined displacement of DT7, DS5 and DS1 transducers. Figure 2.59 shows the ratios for the three different motions plotted in terms of peak ground acceleration (PGA) for Test2, Test 4D, and Test 6. As shown in Fig. 2.59, the ratio decreases with increasing motion intensity. The ratio ranges from 1.04 in Test 2 to 0.74 in Test 6. In the higher intensity test, much damage was noticed at the cap beam and more relative movement between the top of the column and the DT7 location is probable. In addition, it is important to note that the quality of images decreases with increasing earthquake intensity and incompatibilities in recording frequency between the cameras and the earthquake motions occurred more frequently.

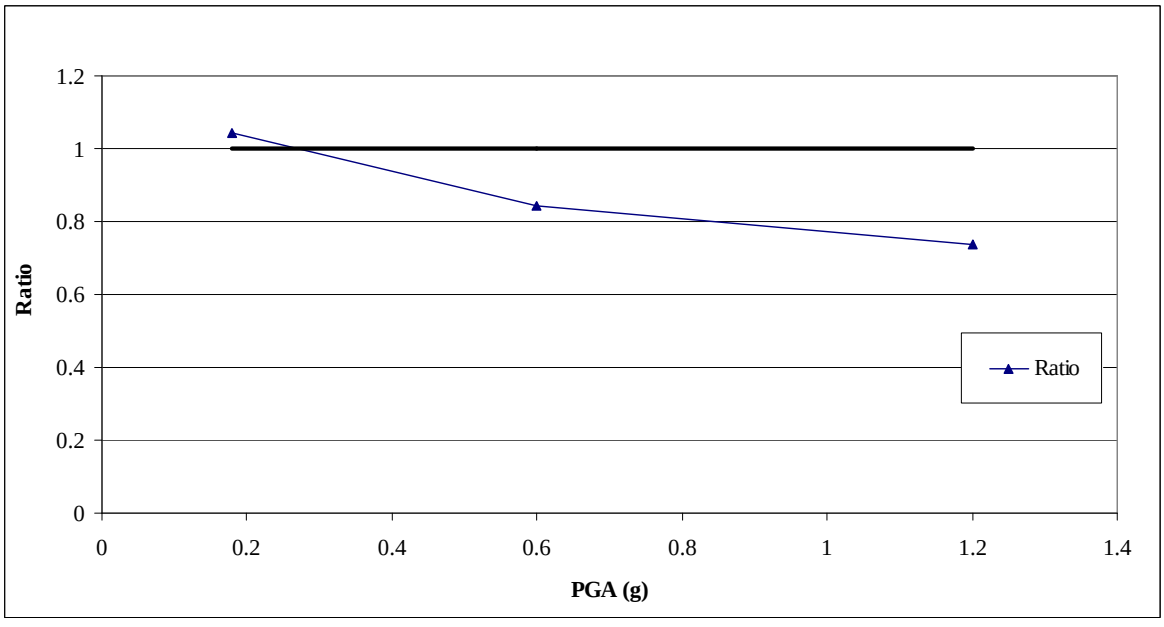

Fig. 2.59 Maximum lateral movement ratios between photogrammetry and LVDT results

- **Hinging Regions**

The displacement calculations are repeated at each of the grid points along the hinging surface. Three vertical lines, as defined by the grids shown in Fig. 2.17, are monitored through each test. On the middle line, the selected Points are 3, 8, 13, and 18 at the bottom grid and 38, 45, 52, and 59 at the top grid system. For the left line, Points 2, 7, 12, and 17 are chosen at the bottom and Points 37, 44, 51 and 58 are selected at the top. For the right line, Points 4, 9, 14, and 19 and 39, 46, 53, and 60 are calculated at the bottom and top, respectively.

Plots illustrating the calculated deformed shapes in the hinging region for Test 2 are shown in Figs. 2.60, 2.61, and 2.62. The overall deformed shape of the column for Test 2 at the maximum column drift is shown in Fig. 2.60. The deformations in the hinging regions are compared in Figs. 2.61 and 2.62 with the associated column images at the time of maximum column drift. The deformations (Figs. 2.61-2.62) correlate well with the associated images. For Test 2, little nonlinear deformation is noted.

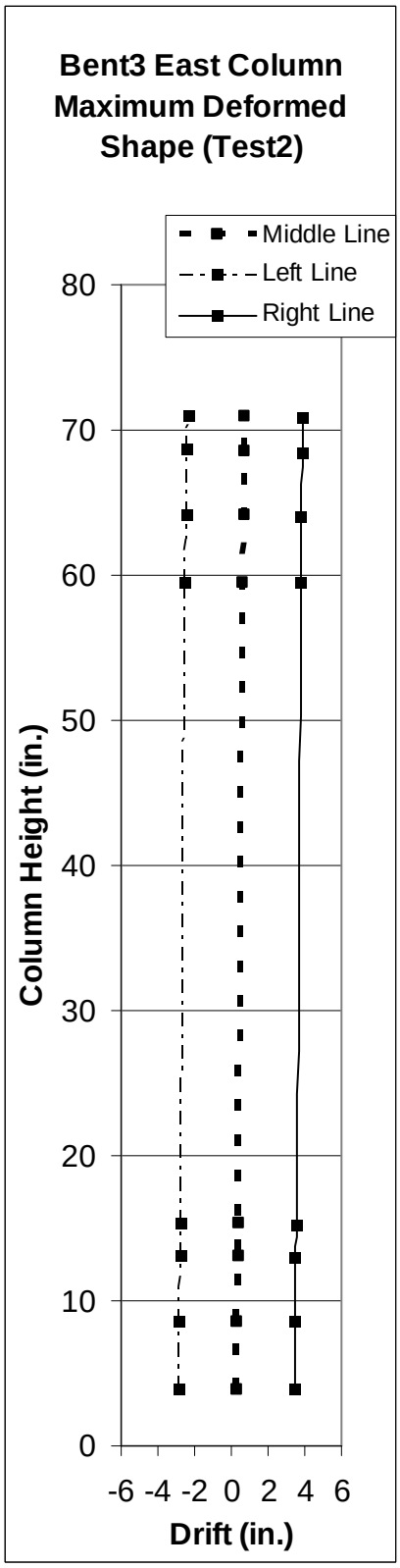

Fig. 2.60 Overall deformed shape along the column height at maximum column drift

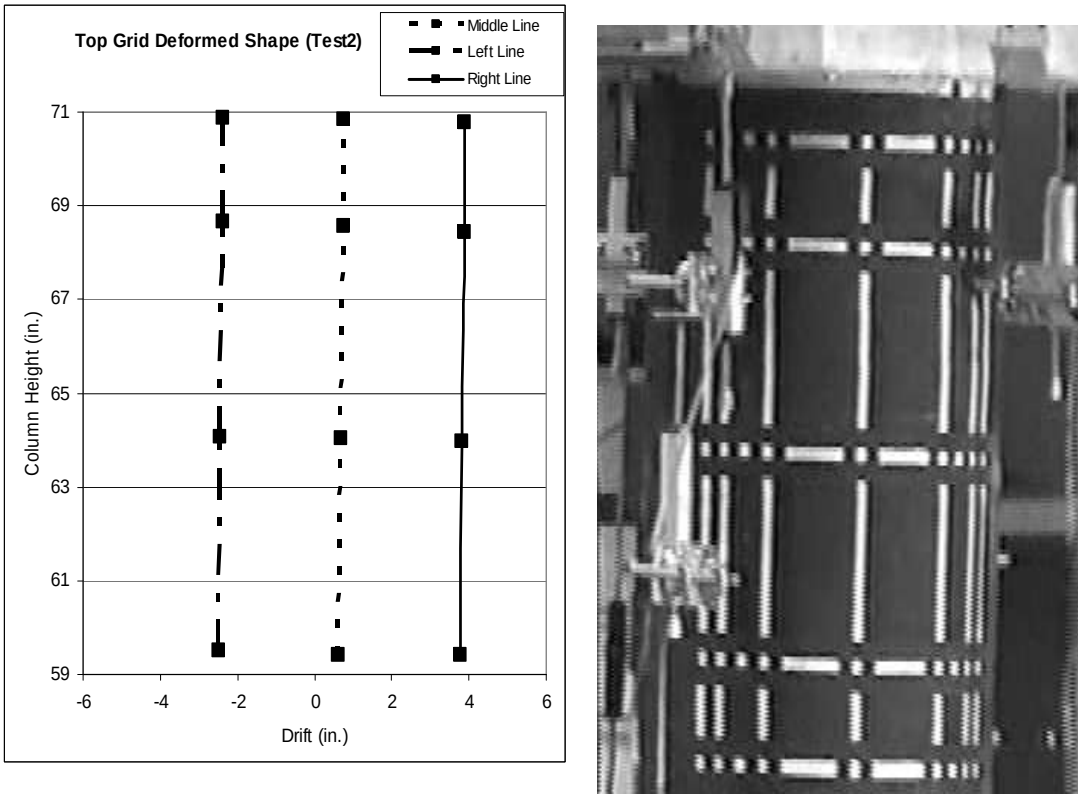

Fig. 2.61 Top grid deformed shape with picture comparison at maximum column drift

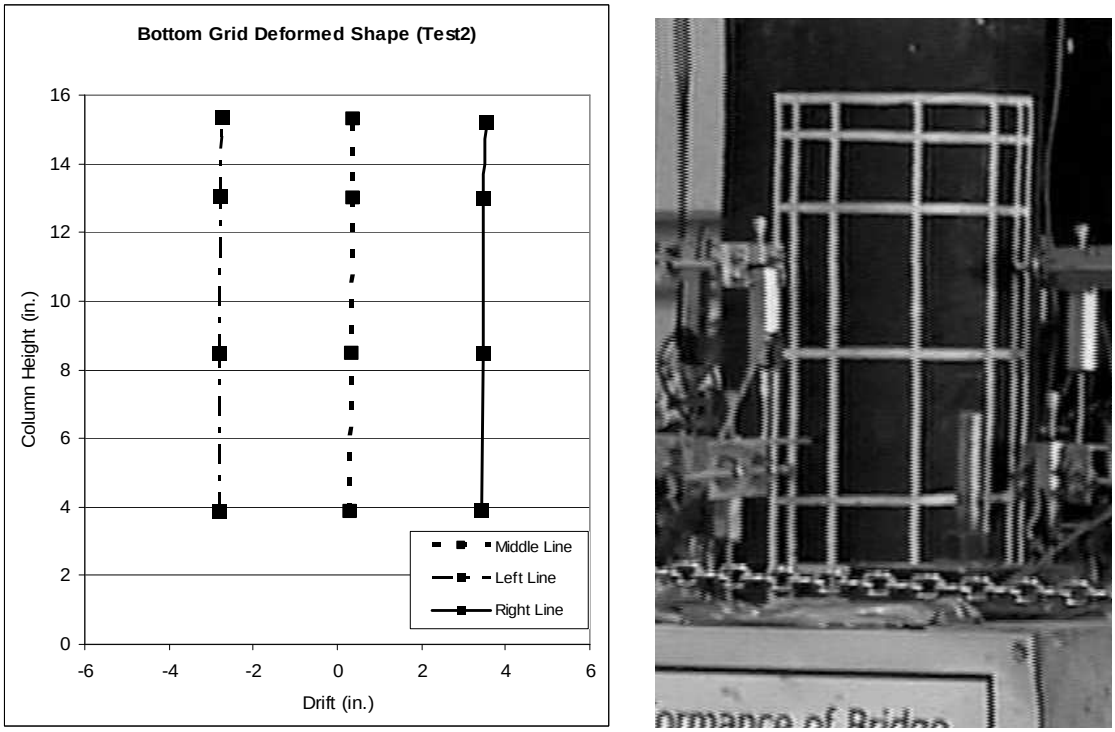

Fig. 2.62 Bottom grid deformed shape with picture comparison at maximum column drift

The same calculations are repeated for Test 4D (Table 2.1). Figure 2.63 shows the overall deformed shape of the column at the maximum column drift. Reverse curvature is noted in the top and bottom hinging regions in Fig. 2.63. The deformations in the hinging regions are compared in Figs. 2.64 and 2.65 with the associated column images at the time of maximum column drift. For Test 4D, nonlinear deformation is noted very clearly in the top hinging region.

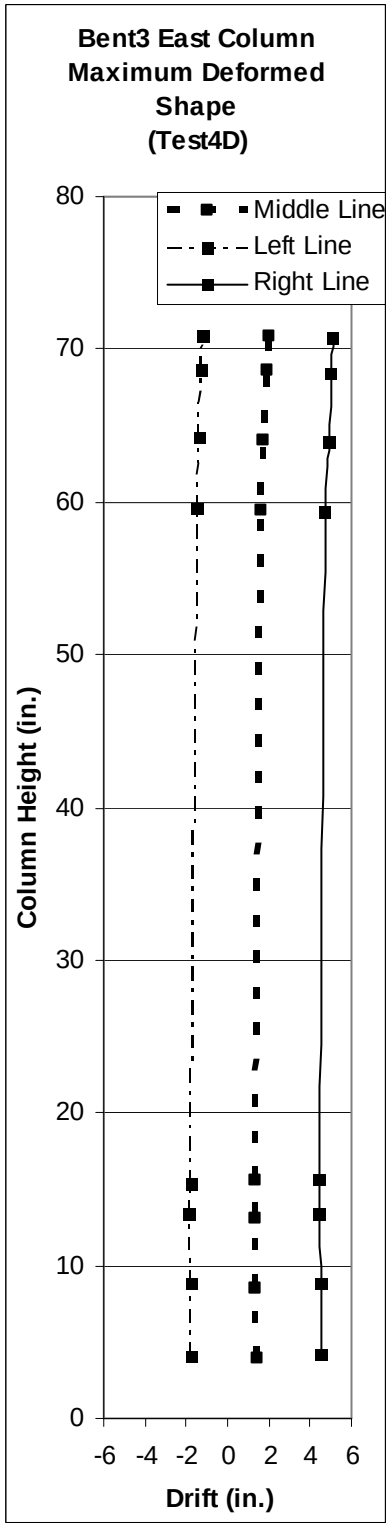

Fig. 2.63 The overall deformed shape along the column height at maximum column drift

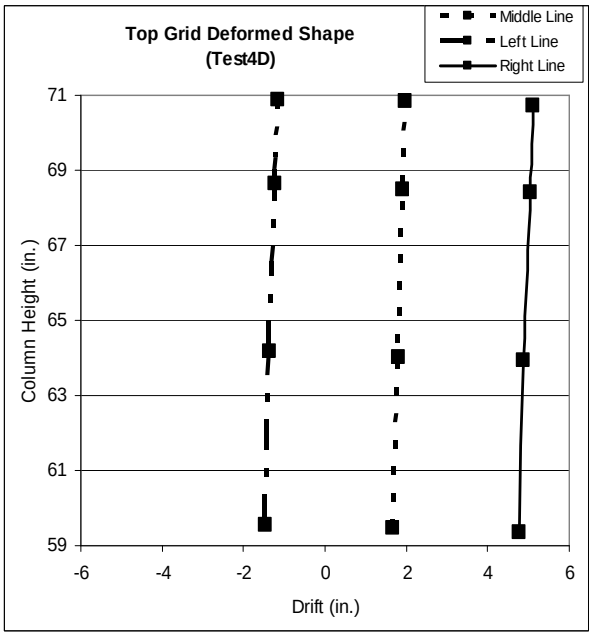

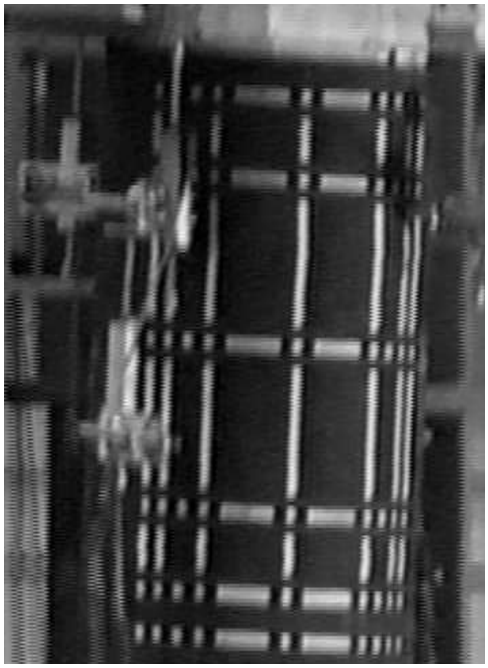

Fig. 2.64 Top grid deformed shape with picture comparison at maximum column drift

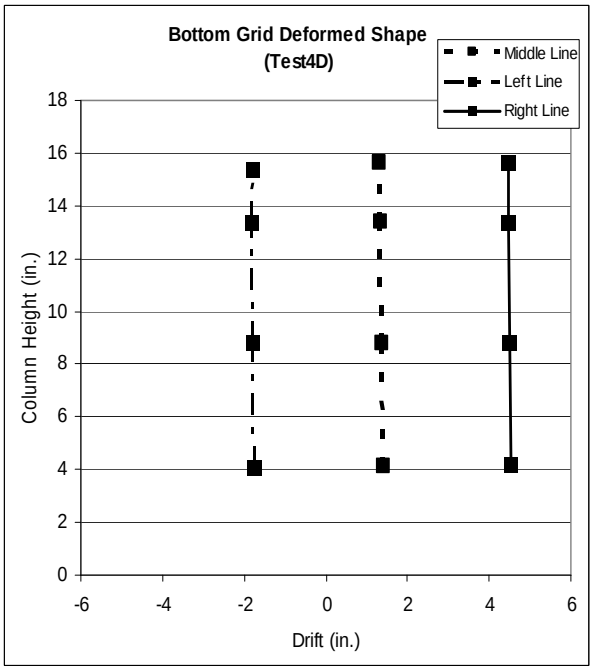

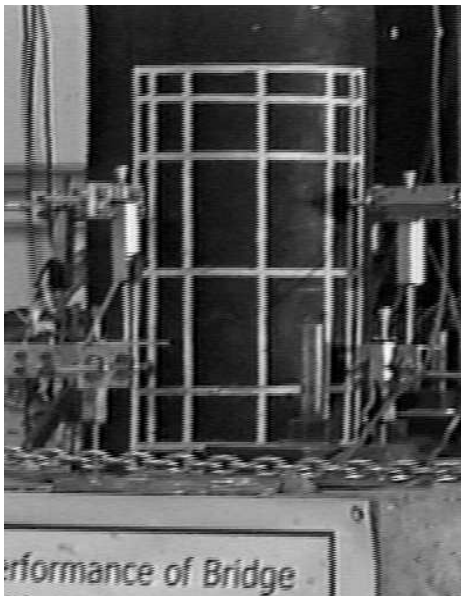

Fig. 2.65 Bottom grid deformed shape with picture comparison at maximum column drift

The overall deformed shape of the column at the maximum column drift is shown for Test 6 in Fig. 2.66. Reverse curvature is profoundly noted for Test 6, similar to the deformed shape for Test 4D. The deformations in the hinging regions are compared in Figs. 2.67 and 2.68 with the associated column images at the time of maximum column drift. The deformations represent the images very well.

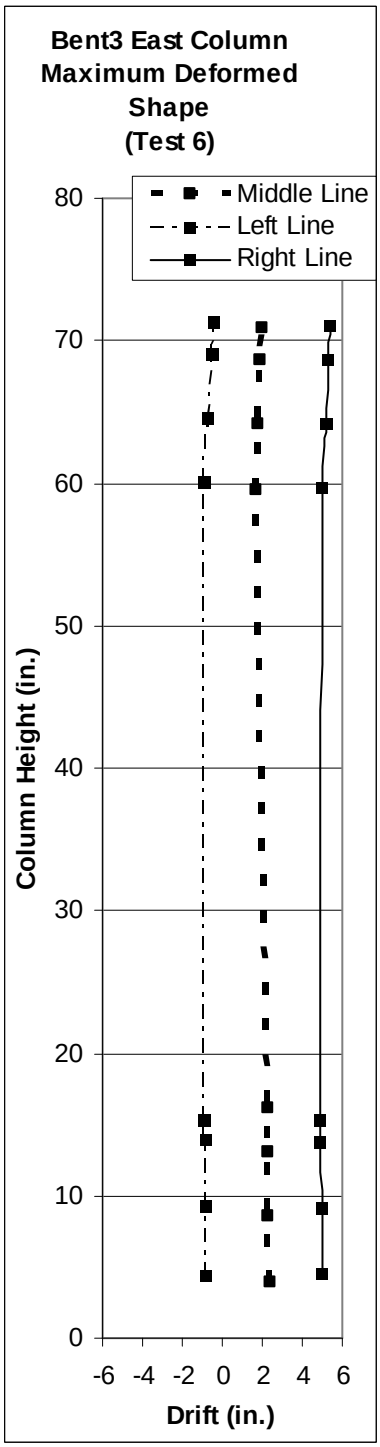

Fig. 2.66 The overall deformed shape along the column height at maximum column drift

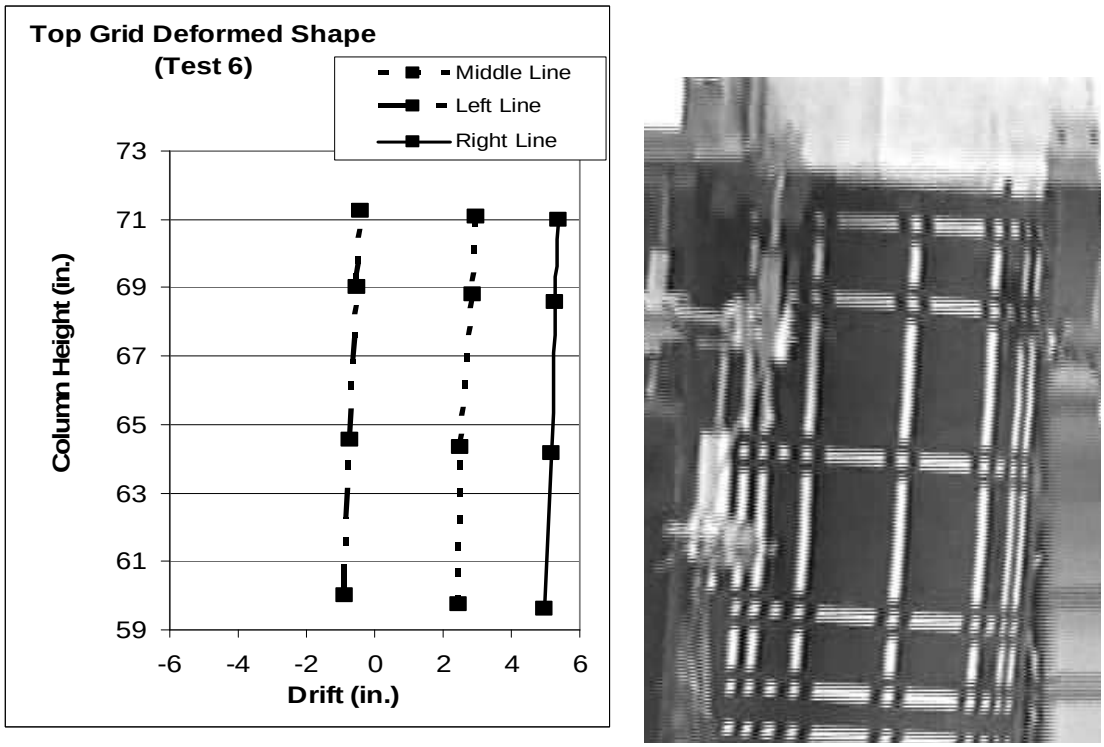

Fig. 2.67 Top grid deformed shape with picture comparison at maximum column drift

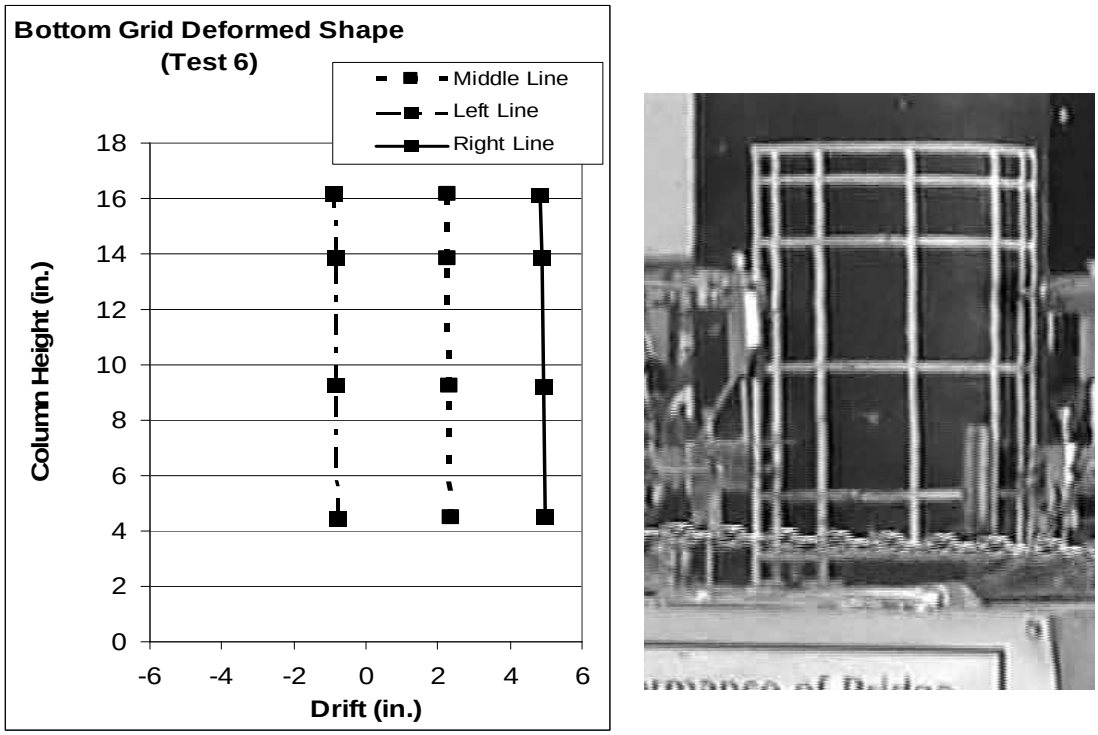

Fig. 2.68 Bottom grid deformed shape with picture comparison at maximum column drift

2.3.4.3 Rotations

As described previously, several methods were evaluated to define the unique points to calculate the displacements and rotation results from photogrammetry data. First, using only the even-numbered lines from each frame was used to capture a more consistent image (without double lines) for analysis. Then, a definition of vertical and horizontal grid lines was determined. In the first definition, the mid-point of each 0.25-in. (6 mm)-thick vertical and horizontal grid line was sought and a "middle line" was defined as the connection of these points. In the second definition, the edge lines were analyzed to obtain the four corner points at each intersecting thick grid line, and also the average middle point between the corner points. In addition, the length used to define the edge lines was examined in detail. After all these trials, using the even-numbered lines from each image, with the average middle of the corner points, with 0.5 in. (13 mm)– 1.5 in. (38 mm) in length provided the most consistent results. Using this approach defined by the edge-lines of the thick grid lines to calculate the rotations of horizontal line at a given height of the column, there is a large amount of pixelization noted (Fig. 2.51) and it is difficult to follow the periodicity of the earthquake shakings. By contrast, rotations of vertical lines provided smoother traces than the rotations of horizontal lines in the photogrammetry data (Fig. 2.52). It is important to note that the rotations of vertical lines are average rotations over a given column height defined by the monitored Points. This section will describe the best final rotation results.

The rotations of vertical lines calculated using Points 3 and 8 and Points 8 and 13 on the bottom grid are shown in Figs. 2.69 and 2.70 for Test 2. There is a small amount of constant noise (pixelization) in the figures because the amplitude of motion in Test 2 is small. Figures 2.71 and 2.72 show the rotations of vertical lines at the top grid level

(Points 38 and 45 and Points 45 and 52) during Test 2. (The general periodicity of motion can be decerned among the constant noise at low amplitudes of motion.)

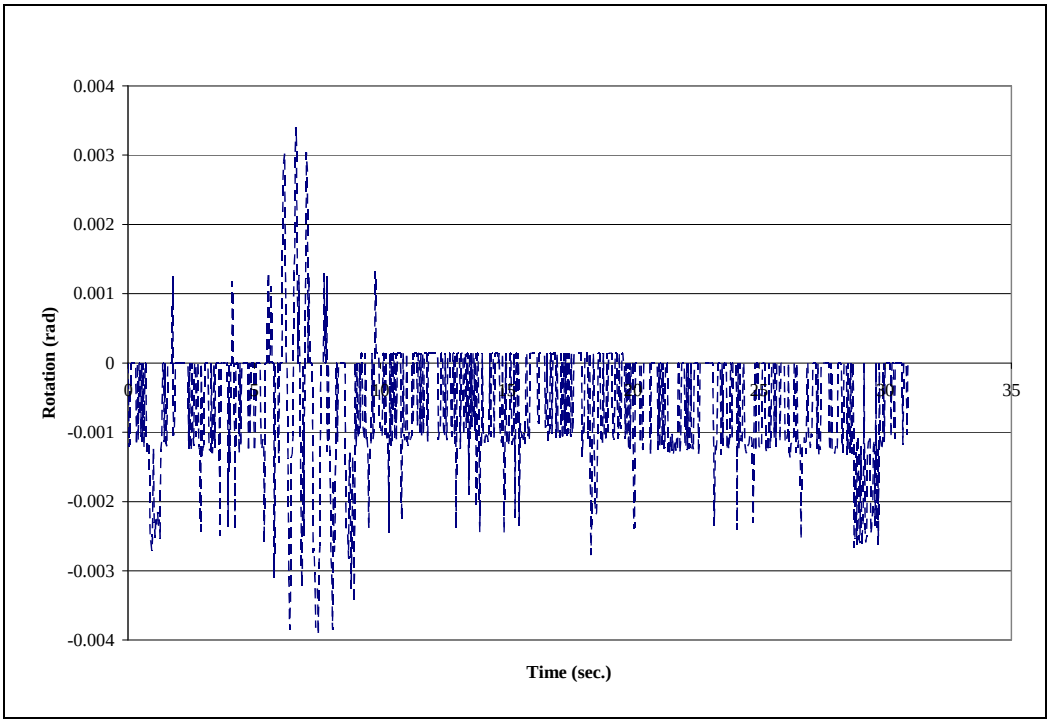

Fig. 2.69 Rotation of vertical line calculated using Point 3 and 8 for Test 2

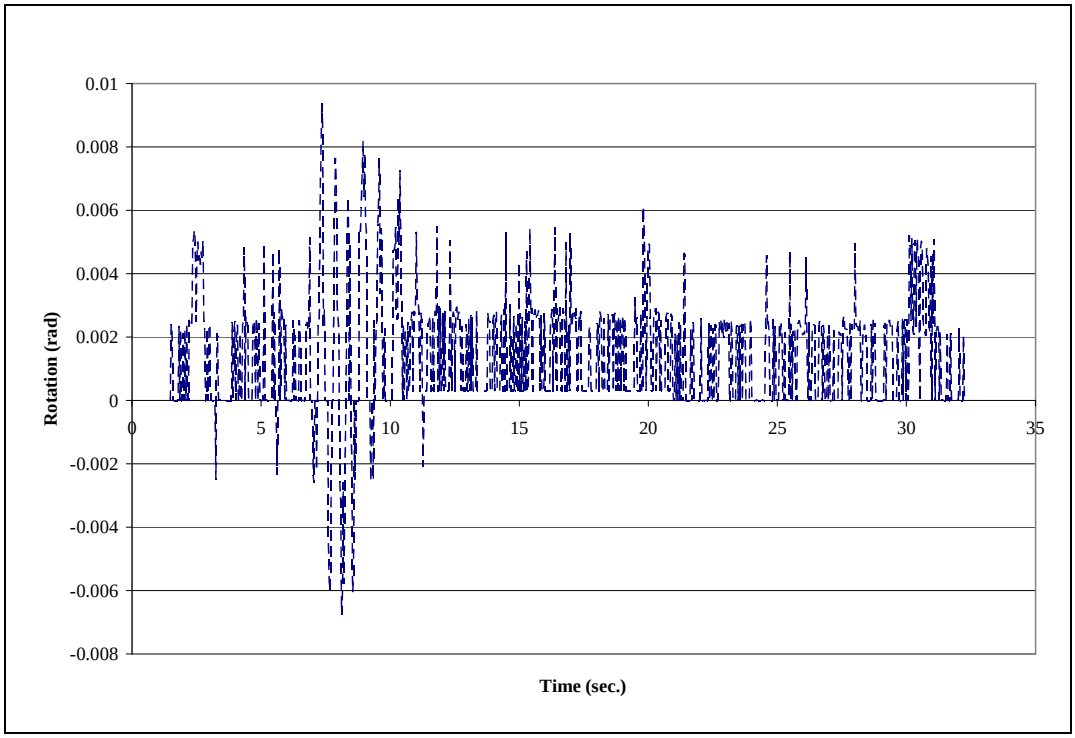

Fig. 2.70 Rotation of vertical line calculated using Point 8 and 13 for Test 2

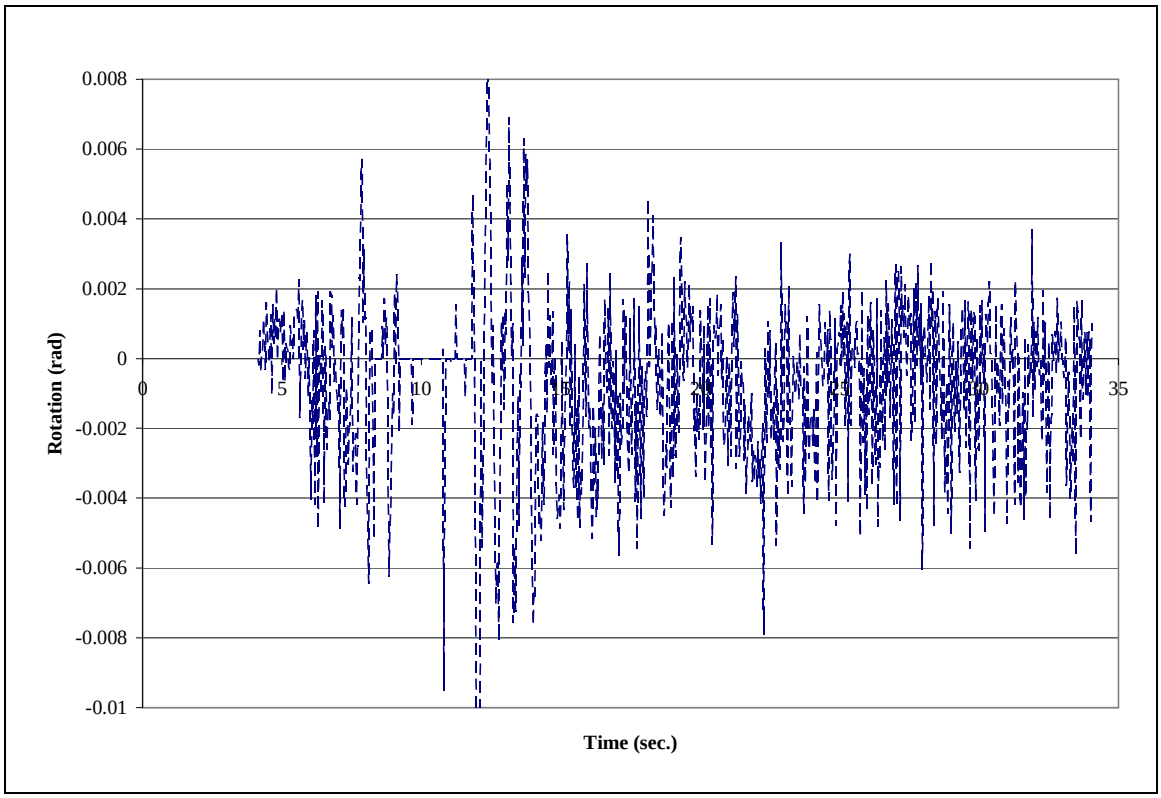

Fig. 2.71 - Rotation of vertical line calculated using Point 38 and 45 for Test 2

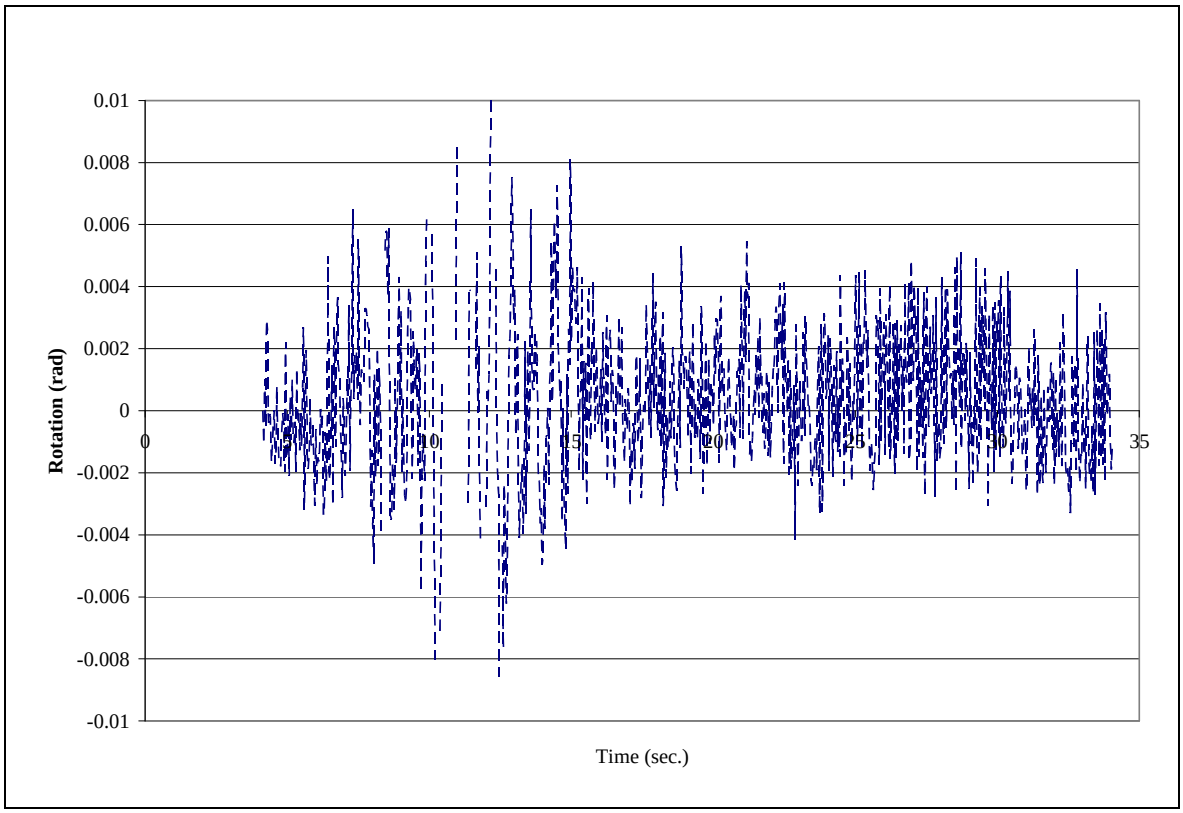

Fig. 2.72 - Rotation of vertical line calculated using Point 45 and 52 for Test 2

The rotations of vertical line calculated from Points 3 and 8 and Point 8 and 13 for Test 4D are shown in Figures 2.73 and 2.74. Figures 2.75 and 2.76 show the rotations of vertical line at the top grid level for Test 4D.

Figures 2.77 and 2.78 show the results for the bottom hinging region for Test 6, and Figures 2.79 and 2.80 show for the top hinging region. Both figures provide similar peak values and periodicity.

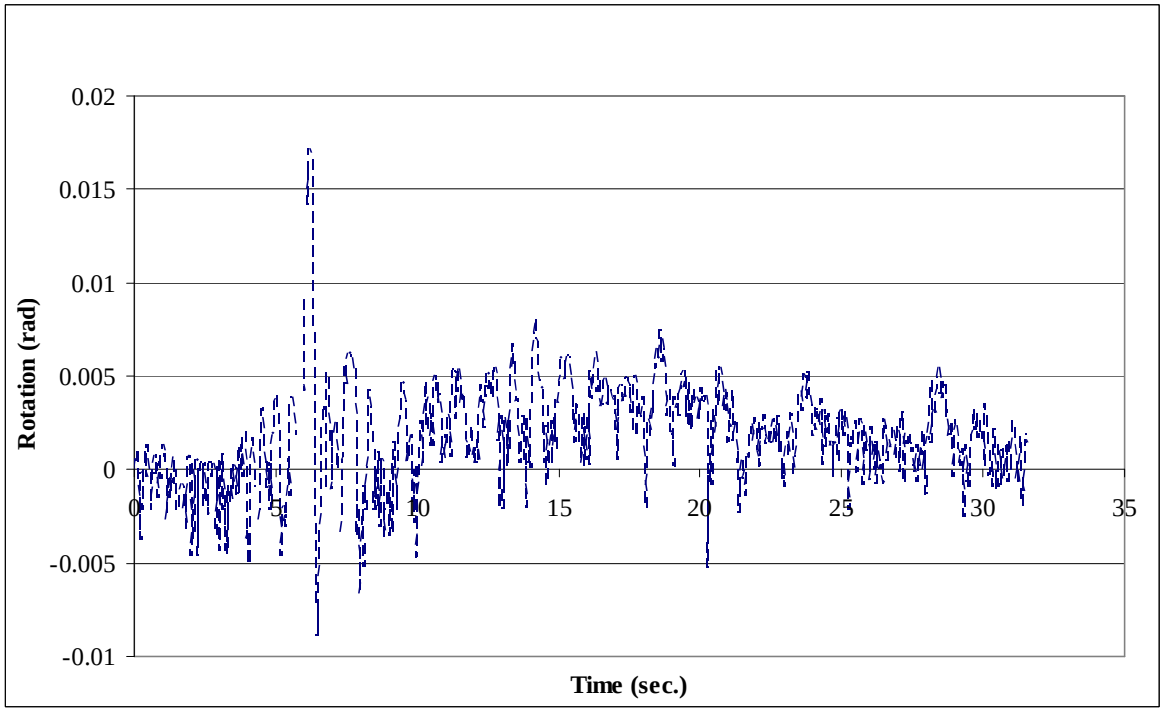

Fig. 2.73 - Rotation of vertical line calculated using Point 3 and 8 for Test 4D

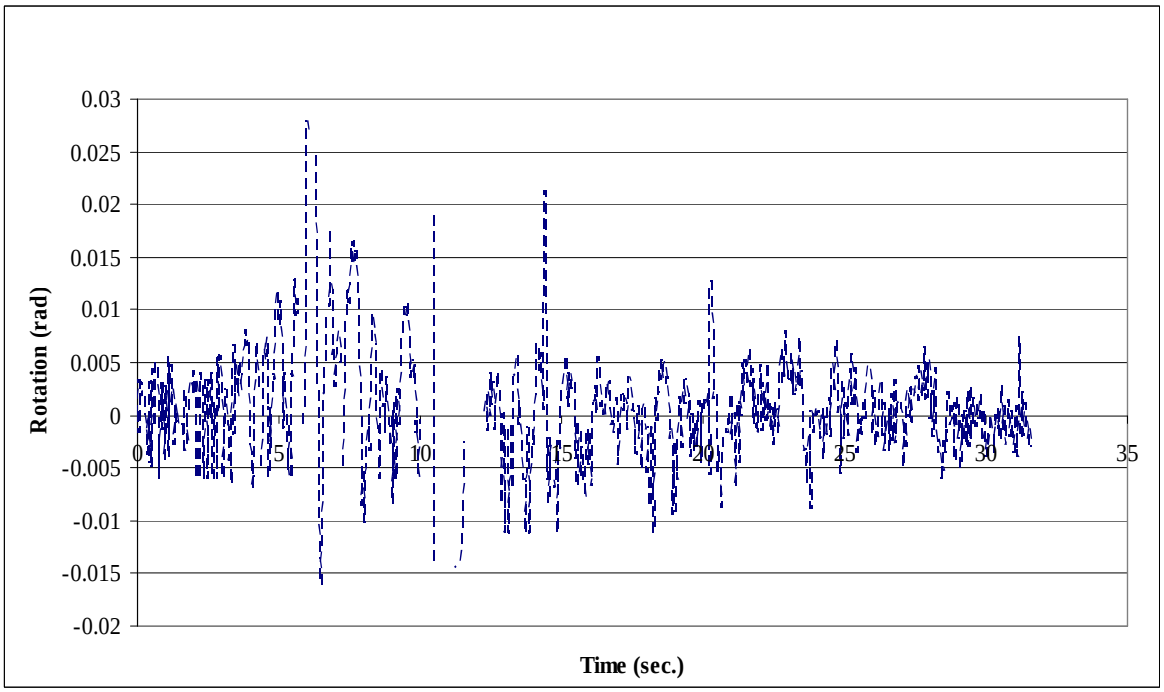

Fig. 2.74 Rotation of vertical line calculated using Point 8 and 13 for Test 4D

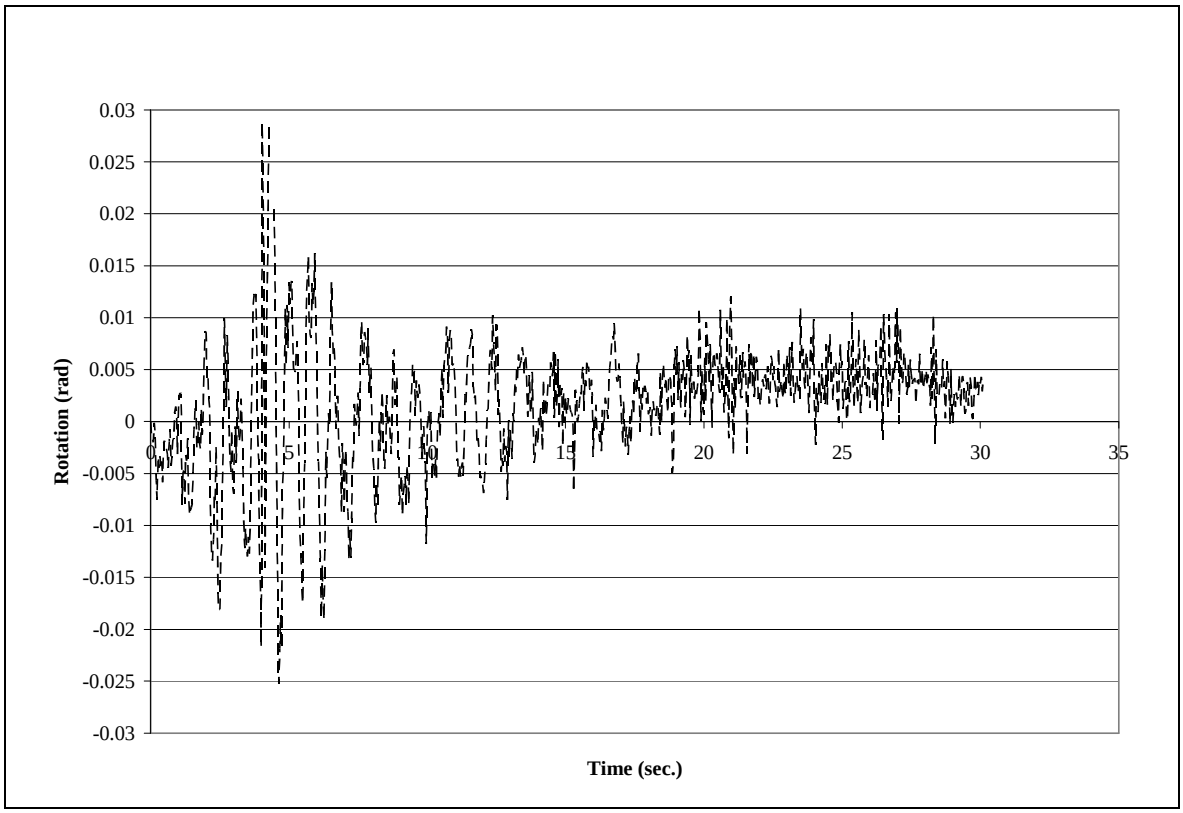

Fig. 2.75 Rotation of vertical line calculated using Point 38 and 45 for Test4D

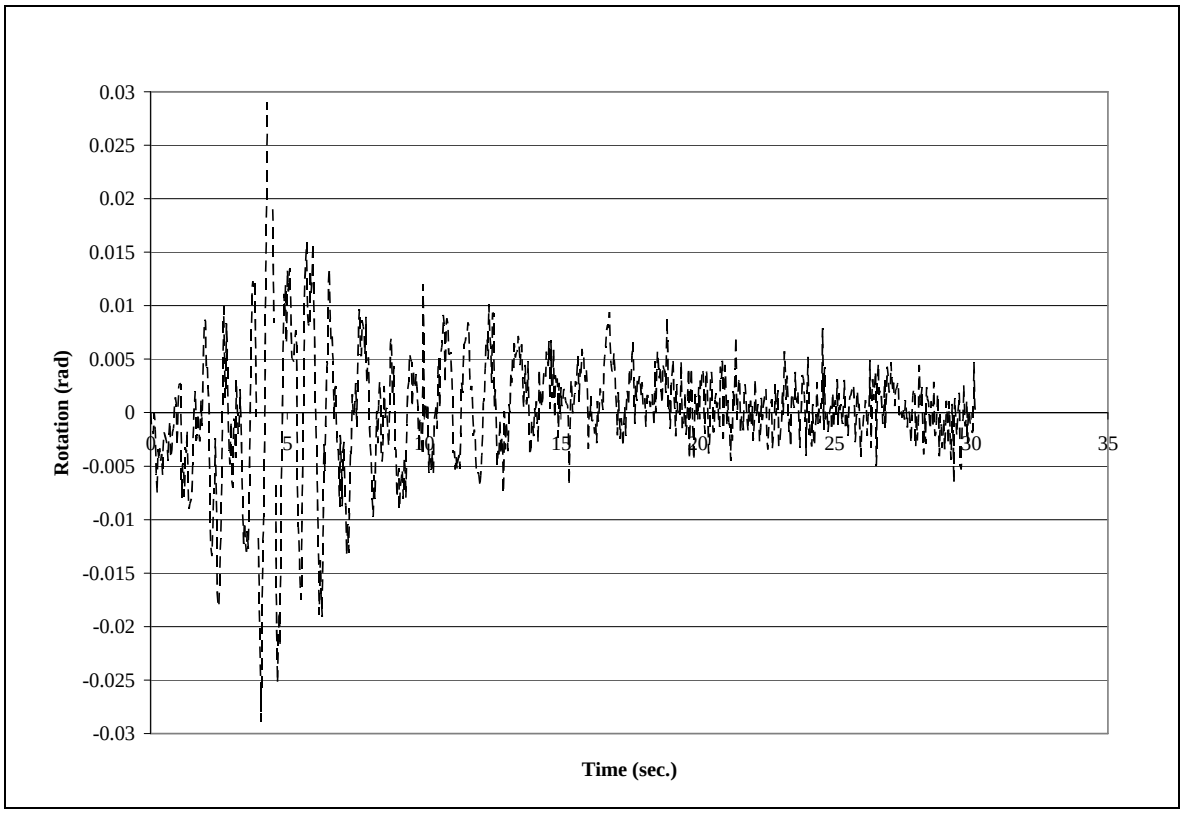

Fig. 2.76 Rotation of vertical line calculated using Point 45 and 52 for Test4D

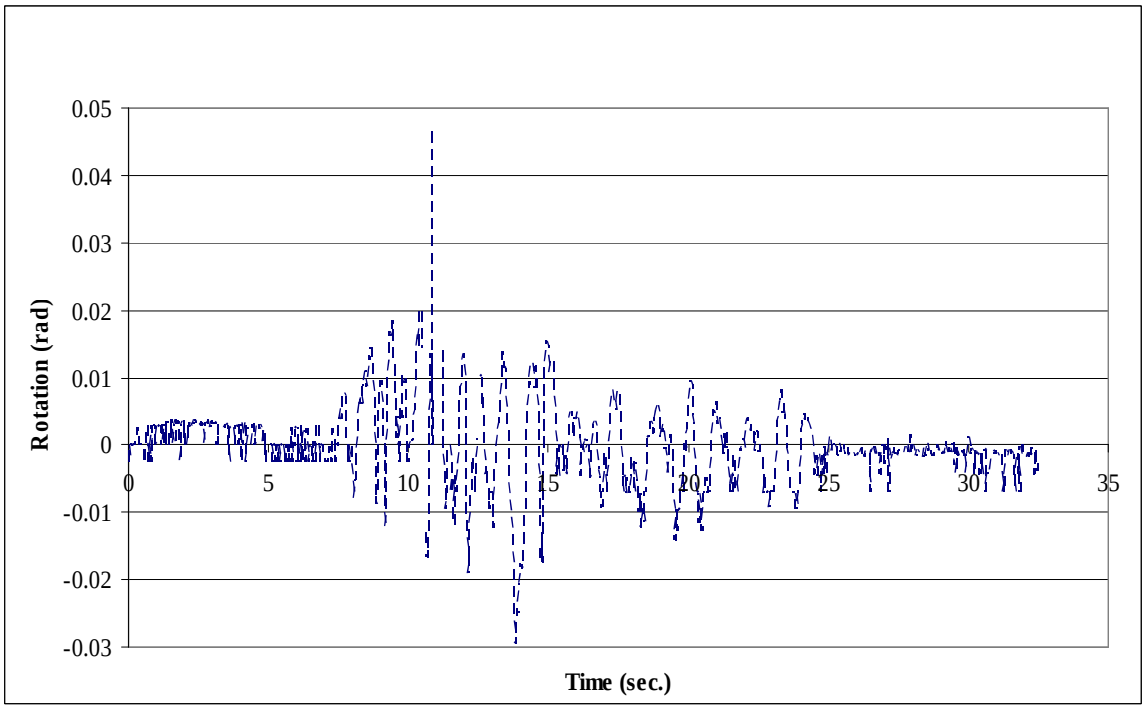

Fig. 2.77 Rotation of vertical line calculated using Point 3 and 8 for Test 6

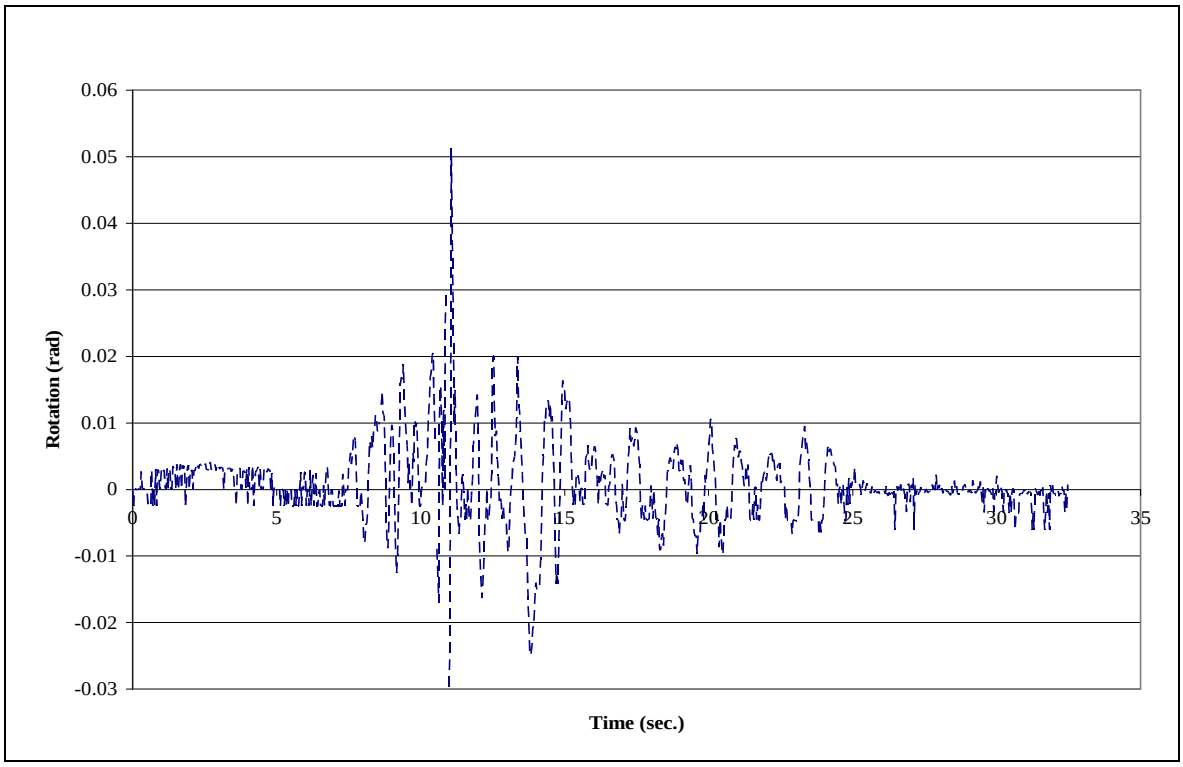

Fig. 2.78 Rotation of vertical line calculated using Point 8 and 13 for Test 6

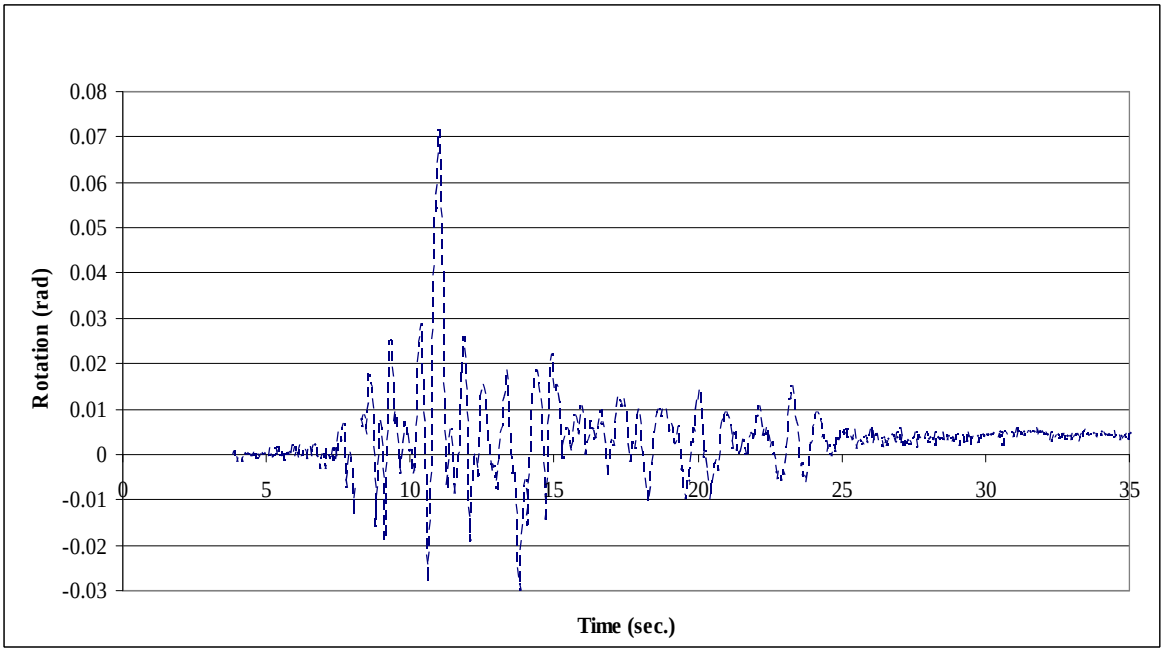

Fig. 2.79 Rotation of vertical line calculated using Point 38 and 45 for Test 6

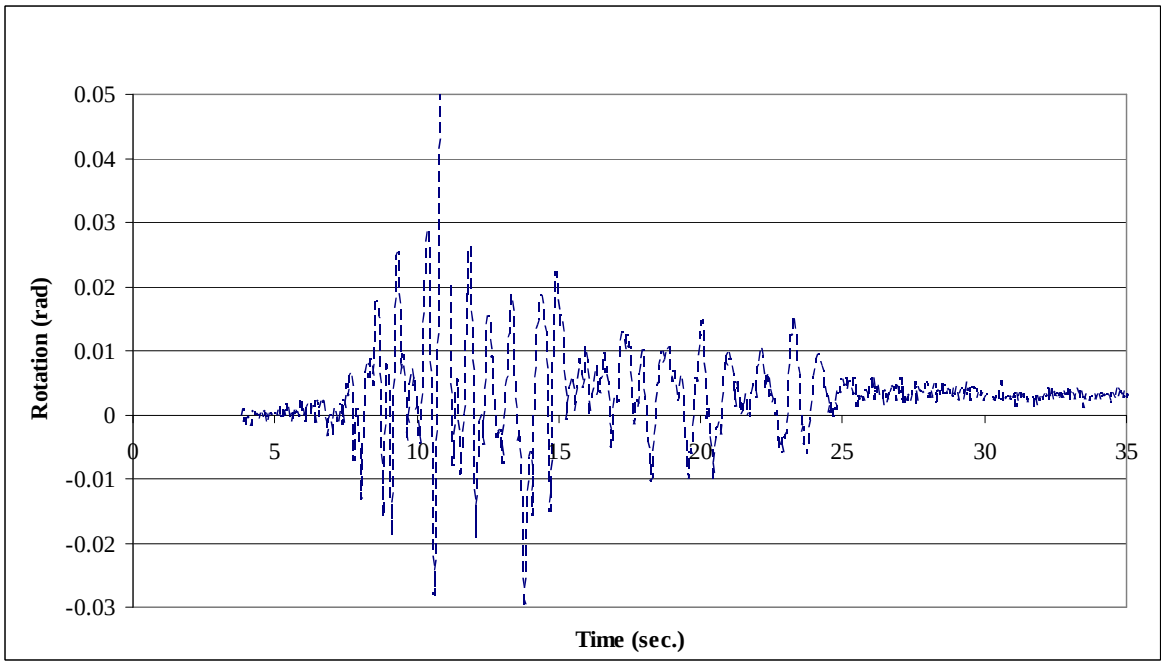

Fig. 2.80 Rotation of vertical line calculated using Point 45 and 52 for Test 6

To determine the relative success of the photogrammetry methods to capture rotations, the maximum rotations of vertical line calculated using photogrammetry measurements for the three different earthquake motions are normalized with the maximum cross-sectional rotations obtained from LVDT data. Figure 2.81 shows the ratios for the three different motions at the two hinging regions with each region having two different point levels plotted in terms of peak ground acceleration (PGA) for Test2, Test 4D, and Test 6. As shown in the figure, the ratios vary greatly, with the ratio ranges in the bottom hinging region between 0.91 in Test 6 and 1.31 in Test 2, and in the top hinging region ranges between 1.11 in Test 6 and 4.75 in Test 2. The results for the top and bottom hinging regions well represent the LVDT data in Test 6. The results in the top hinging region are greatly amplified from the LVDT results for Tests 2 and 4D. Even with these large differences between the calculated vertical rotation and LVDT data calculation, it is interesting to note that the maximum rotations represented by vertical

rotations using the photogrammetry data closely match the maximum values calculated from cross-sectional rotations (Fig. 2.55).

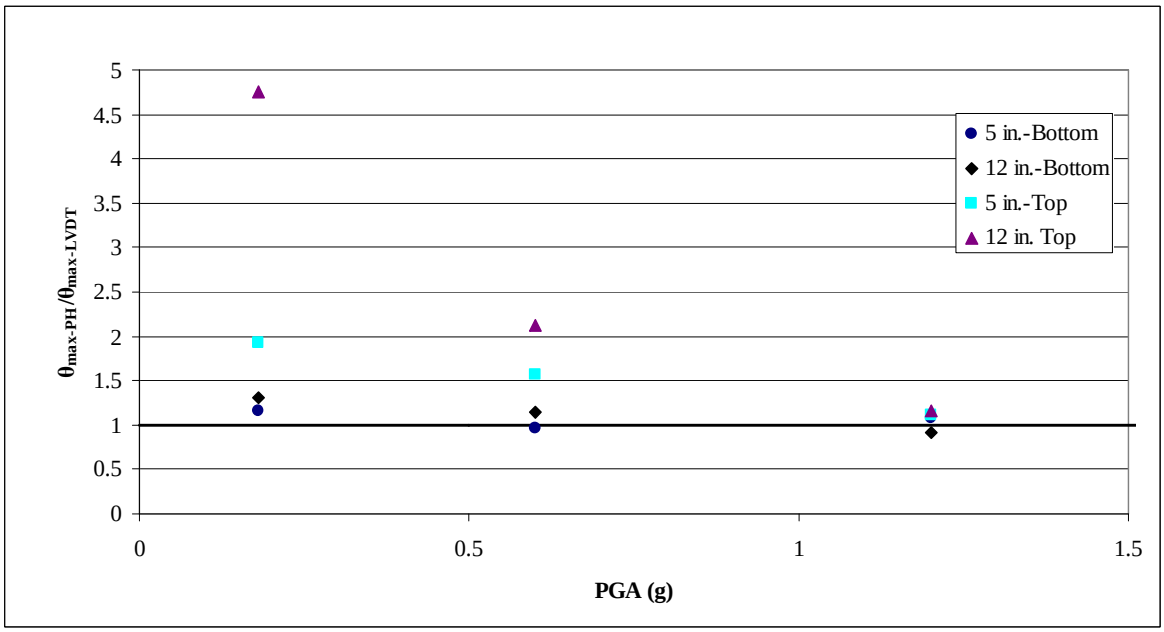

Fig. 2.81 Maximum rotation ratios between photogrammetry compared LVDT results

2.4 CONCLUSION

For each deformation calculation, it is necessary to have a consistent and predictable definition of points on the column surface. The quality of images captured during the test and the similar pixel intensities across the grid line thickness presented challenges for calculating consistent displacement and rotation results. The following conclusions are made regarding the analysis of the deformations in the hinging region during response to strong ground shaking:

- The best image quality is obtained by using the even-numbered lines from each frame in time.

- The edges of the 0.25-in. (6 mm) thick grid lines are best defined using a constant Robert threshold value.
- The best definition of a unique point on the column surface is obtained by using the edge-lines of the 0.25-in. (6 mm) thick grid lines to define four corner points at the intersection of each horizontal and vertical grid line, and then averaging these points to define a "middle point". The edge-lines are best defined using lengths of 0.5-1.5 in. (13 mm – 38 mm).
- The periodicity and amplitude of the displacements calculated at the top of the column correlate very well with the combined components of DT7, DS5 and DS1 transducer measurements.
- Overall, displacement calculations at each grid point follow the periodicity of motion captured by the displacement transducers very well.
- The rotations of vertical line calculated using photogrammetry data, as an average rotation between two consecutive grid points, represent the cross-sectional rotations calculated using the LVDT data in periodicity very well. The traces are smoother than the detailed rotation calculation of horizontal lines for photogrammetry data. The maximum amplitude of rotation is similar between rotation of vertical line and rotation of horizontal line calculated using the photogrammetry data.

Suggested changes in future experimental setups to increase the quality of the images for photogrammetry analysis include:

- The edge of the vertical and horizontal grid lines should be much sharper, with distinct change in intensity from the "black" to "white" regions in the grid.

- A circular component should be added to the grid region to aid in determining the rotation of the column. Any changes in the curvature to the circle would provide additional information on the rotational motion of the column.
- Cameras that operate using progressive scan rather than interlaced images when recording the events should be used.

3 MANUSCRIPT 1: PHOTOGRAMMETRIC MEASUREMENTS OF RC BRIDGE COLUMN DEFORMATIONS

Zeynep Firat Alemdar[a,*], JoAnn Browning[b] and Jeffrey Olafsen[c]

[a] 1147 Learned Hall, Department of Civil, Env, and Arch. Engineering, University of Kansas, Kansas, USA

[b] 2150 Learned Hall, Department of Civil, Env, and Arch. Engineering, University of Kansas, Kansas, USA

[c] Department of Physics, Baylor University, Texas, USA

[*] Corresponding author Tel: +1 785 864 3760 Fax: +1 785 864 5631 E-mail addresses: zeynep@ku.edu (Z. F. Alemdar).

ABSTRACT:

The determination of the location of nonlinear response in structural systems is an important step to predict the performance of the system under different loading conditions. In bridge columns, these nonlinear deformations generally occur over a finite hinge length. A model of hinging behavior in reinforced concrete bridge columns will help guide proportioning, detailing and drift estimates for performance-based design. Data was collected during the NEESR investigation of the seismic performance of four-span large-scale bridge systems at the University of Nevada Reno that details deformations in column hinging regions during response to strong shaking events. A photogrammetry method was applied using a reference grid on the top and bottom column surfaces to accurately record and analyze deformations in the plastic hinging regions. The method of application in this study holds several advantages over traditional sensors including that it is a remote visualization technique, inexpensive and simple to

analyze the results. The surface deformations and rotations of a reinforced concrete bridge column under dynamic loading has been examined and compared with the results obtained from traditional instruments.

KEYWORDS: Reinforced concrete bridge column, photogrammetry, hinging region, earthquake loading, frequency domain error.

1. Introduction

This research aims to record and analyze deformations in plastic hinging locations in concrete bridge structures through an investigation of actual hinging behavior in large-scale tests of bridge systems subjected to multiple excitations. In order to evaluate the behavior of plastic hinging regions, a photogrammetric method was used to remotely track deformations of the concrete surface in the hinging regions. Photogrammetry is a non-invasive technique of remote visualization of the target components and a computer rendering of the motion [1]. The tracked motion of the target components, which were discrete points on the column surface along the joint regions, was reduced using a computer program to obtain the lateral displacements of the points and to calculate the vertical and cross-sectional rotation between these points. Photogrammetry measurements were recorded at the bottom and top hinging regions of the column. The analysis of simple and inexpensive photogrammetric data was the main focus of this study.

2. Experimental program

Previous research of reinforced concrete column hinging behavior has focused on small scale component tests under static loadings. Most of these tests were of cantilever columns in single curvature response [2-15]. Only two studies have included dynamic tests of reinforced concrete bridge columns to determine the deformations in hinging regions [16-17]. The four-span reinforced concrete bridge that was tested at the University of Nevada Reno (UNR) laboratory on February 12-15, 2007 was significant because it was a large-scale bridge system with columns in double curvature response. In addition, massive earthquake motions were applied in the longitudinal and transverse directions of the bridge.

Traditional instrumentation that have been widely used to collect deformation data from static and dynamic tests include LVDTs (linear variable differential transformers), displacement transducers, accelerometers, and strain gages. These instruments are attached to the concrete surface and require electrical connection to a data acquisition system. As damage occurs to concrete elements, the cover concrete can spall, gages can fail, and data may be lost. A newer method used to collect deformation data is by photogrammetry with an advanced non-contact measurement system such as Krypton system. These systems consist of a suite of cameras, a set of infrared LEDs (light-emitting diodes), and control software. For data acquisition during testing, the Krypton cameras are mounted on a reference frame away from the specimen and LEDs are attached to the specimen surface. The three-dimensional motions of infrared LEDs (light-emitting diode) are tracked during testing. Several studies have been completed using the Krypton LED-based 3D displacement measuring system [18-21]. Reducing and organizing the large amount of data that is collected from this system, hovewer, is

difficult. Other limitations of using such advanced systems include the possibility of lost LEDs during testing due to specimen damage, and the prohibitive cost of the system for many structural engineering laboratories.

The four-span large scale reinforced concrete bridge test provided a platform to compare traditional instrumentation measurements with those obtained using a simple photogrammetry method. The photogrammetry method required only the application of a reference grid on the concrete surface and a system of cameras to record the motion of the bridge system. The photogrammetry data showed that the accuracy of the measurements was approximately 0.04 in. (1 mm). The application of the photogrammetry method held several advantages over traditional sensors. The cameras were more economical than those used in other advanced non-contact measuring systems and could be used in any laboratory. The photographic data did not rely on any physical connection to the specimen. In addition, any concrete marking that were lost from excessive deformations could be reconstructed to a certain extent based on surrounding elements in the frames.

2.1 Specimen details

The test specimen consisted of the four-span reinforced concrete bridge with end abutments as shown in Fig. 1. The bridge was quarter-scale with two 29-ft (8.84 m) interior spans, and two 24.5-ft (7.47 m) exterior spans for a total length of approximately 110 ft (33.5 m). The clear heights of the bents were 5, 6 and 7 ft (1.52, 1.83, and 2.13 m), with the tallest bent in the middle (Bent 2). The superstructure consisted of a solid slab that was post-tensioned in both the longitudinal and transverse directions. The bridge

also included abutment seats at both ends that were driven in the longitudinal direction by dynamic hydraulic actuators. The depth of the cap beams was 15 in. (0.38 m). The total length of the cap beams (perpendicular to the longitudinal axis of the bridge) was 98 in. (2.49 m). The concrete compressive strength used in the bridge (excluding the slab) was 6.7 ksi (46.2 MPa) and reinforcement was ASTM A706 Grade 60. The bents were numbered Bent 1, Bent 2, and Bent 3 starting from left (South) to right (North).

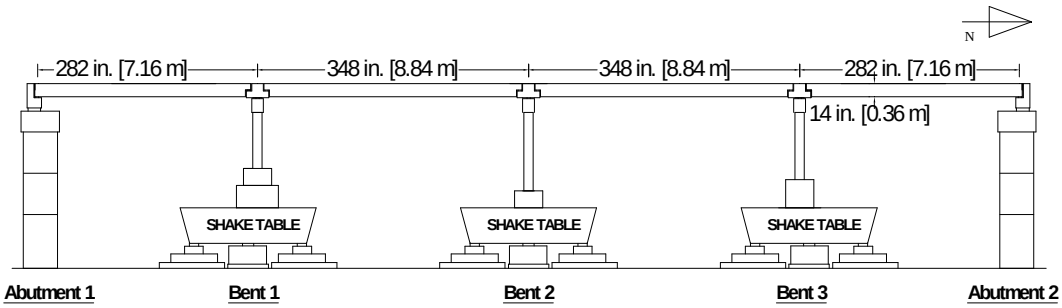

Fig. 1 Elevation view of the four-span bridge

2.2 Photogrammetric application setup

Photogrammetry data was collected at the top and bottom hinging regions of the east column of Bent 3 during the tests. Two grid systems were applied to the surface of the column as shown in Fig. 2. The bottom grid consisted of vertical and horizontal lines spaced irregularly around the face of the circular column. Deformation data was collected at various points of the intersecting lines. The top grid system used a combination of lines and squares, having the same spacing as the lines in the bottom grid. This top grid pattern was applied to simulate “targets” on the column surface.

To apply the grid systems, the column was first spray-painted black for a solid dark background. The lines and squares were lightly traced with a pencil, and then a single stencil was used to fill in the lines and squares using white paint.

(a)

(

b)

Fig. 2 Close view of (a) bottom and (b) top grid systems

A series of linear vertical displacement transducers (LVDTs) were used to record deformations in the transverse and longitudinal direction of the bridge, as shown in Fig. 2. One displacement transducer (DT7) was located at the middle of the t-beam on the top of the cap beam (Fig. 3). The LVDT and DT7 data were collected by the research team at UNR.

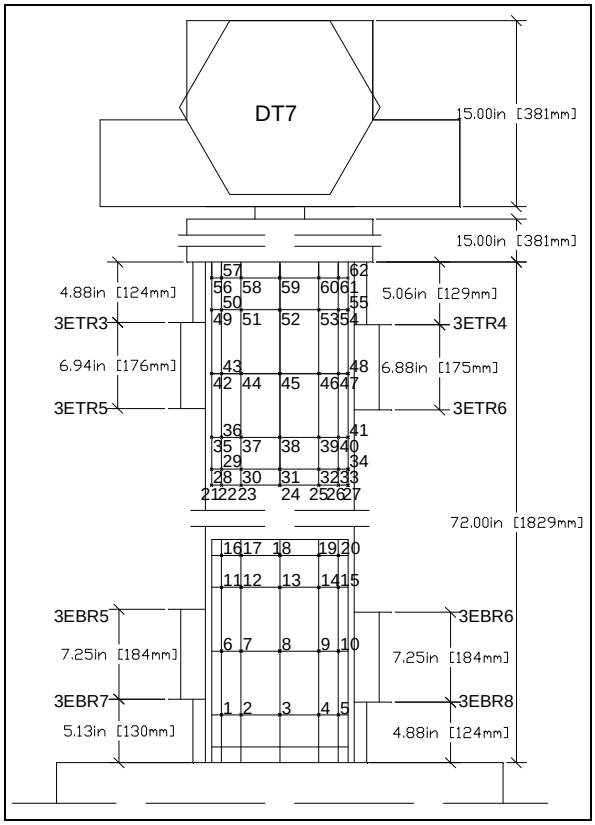

Fig. 3 Grid system and LVDT locations on column in the Bent 3 east column

An aluminum tower was built to hold the cameras that would record the column deformations caused by the earthquake events (Fig. 4). The tower had two levels to allow recordings at the top and bottom plastic hinging regions. A system of two cameras (DXB-9212EF model Starlight 600 TVL super high resolution) with black-white recording properties was mounted on each level [at 94.5 in. (2400 mm) and 159 in. (4039 mm) height]. Video-lens zooms had 60-300 mm F4-5.6 capturing capability.

Fig. 4 The aluminum tower and four cameras

2.3 Earthquake loading

The motions that were used for the shaking table tests were based on the 1994 Northridge earthquake as measured at the ground station at the Century City Country Club North. The Century City station is owned by the California Strong Motion Instrumentation Program, and is located at 34.063 latitude, -118.418 longitude. Both the 90 degree and 360 degree lateral components were used in the tests. The same motion was used for each test, but the peak ground acceleration (PGA) of the motion was amplified as additional tests were completed. Over the course of the tests, the PGA of the original motion was scaled from 0.075g to 1.0g in transverse direction (90 degree component) and from 0.09g to 1.2g in longitudinal direction (360 degree component) as

shown in Table 1. The earthquake motion was applied for uniaxial and biaxial tests of the structural system. The motion was applied 13 times with six different scaled intensities so that the progression of damage would be evaluated from pre-yield to failure during the shaking tests.

Table 1 Earthquake motion levels applied during the tests

Test No.	Test Date	Motion Level	Test Type	Motion PGA (g)	
				Trans.	Long.
1A	2/12/2007	1	Longitudinal	-	0.09
1B		1	Longitudinal	-	0.09
1C		1	Longitudinal	-	0.09
1D		1	Biaxial	0.075	0.09
2	2/13/2007	2	Biaxial	0.15	0.18
3		3	Biaxial		
4A		4	Longitudinal	-	0.6
4B		4	Longitudinal	-	0.6
4C		4	Longitudinal	-	0.6
4D		4	Biaxial	0.5	0.6
5	2/14/2007	5	Biaxial	0.75	0.9
6	2/15/2007	6	Biaxial	1	1.2
6		6	Biaxial	1	1.2

3. Definition of unique points on column surface

The primary focus of this investigation was to determine displacements and rotations of points on the column surface during the earthquake loading. This was only possible by having a consistent and predictable definition of points, which was complicated by several degraded images and ambiguous locations of precise points on the painted surface. In addition, there were some inherent differences in the data obtained with LVDT instrumentation and that recorded for the photogrammetry application. One of these differences was that the rotation calculations obtained using photogrammetry

analysis represented the rotations of horizontal lines based on the movement of the column, which included flexural and rigid body components. Rotations calculated using the LVDT measurements from the test included only flexural contributions. Another difference was that the LVDT instrumentation was set to record movement in the transverse and longitudinal planes, whereas the photogrammetry measurements were recorded at a horizontal angle between the orthogonal directions, as selected with the setup of the aluminum tower and the cameras (Fig. 4). These differences are discussed and accounted for in the analysis and results.

A measure of the 'best' definition of unique points and deformations was made using a FDE (frequency domain error) index as developed by Dragovich and Lepage [22]. The FDE index is used to compare time-domain response waveforms such as those described in this study. The FDE method uses the Fourier spectra of the response signals, which are non-periodic and comprised of multiple frequencies, to calculate the index. Fast Fourier Transform was used to determine the composition of frequencies of the photogrammetry responses. The starting and ending frequencies were selected to be between 0.5 Hz and the Nyquist frequency, which is $f_n = 1/(2\Delta_t)$ with Δ_t as the time interval of the series. The FDE index accounts for both the amplitude and phase differences between the response signals and gives a number between 0 and 1 as a measure of the goodness-of-fit, where zero indicates a perfect correlation. The amplitude error is a measure of the difference between the values of the response signals, and the phase angle is the angle that the resultant vector of the signals makes with respect to the real axis in the real-complex plane. From the study by Dragovich and Lepage, an FDE value equal to 0.75 represented a poor correlation, and an FDE value of 0.25 represented a very good correlation. These correlations, however, were based on analytical responses

of reinforced concrete frames, and comparisons of two experimental measurements would be expected to have more noise than analytical responses.

3.1. Challenges with unclear images

Interactive Data Language (IDL) was used to analyze the video images that were recorded during the test. Each video was first divided into over one thousand images for individual analysis. The displacement of a unique point in an image was defined as the relative horizontal movement of that point between successive images. At times, however, it was difficult to keep track of a unique point because of the quality of the images.

Each image (640 x 480) was written as 480 lines that were 640 pixels wide, and represented $1/30^{th}$ of a second during the test. The images were interlaced: the odd-numbered lines are written first, followed by the even-numbered lines so that the image was really two images offset by $1/60^{th}$ of a second. The first "partial image" (half of the total image) was comprised of the odd lines, and the second "partial image" was comprised of the even lines. Due to shaking of the strong floor during the tests and the incompatibility in recording frequency between the cameras and the earthquake motions, several images were degraded in quality (corrupted). As a result, some of the horizontal and vertical lines appeared as double lines, and some images were simply blurry. In future tests, cameras that operate with progressive scan rather than interlaced images should be employed to avoid these problems.

The even-numbered and odd-numbered lines of the images were considered separately to improve the calculations of displacements and rotations with the corrupted images. When the image was divided into separate images of even and odd lines, the

double image effect that was produced by a shift between the two halves of the image being written was eliminated. The vertical displacement results of Point 7 (located in Fig. 3) from the even and odd line analyses were reduced from the Test 4D motion (Table 1).

A comparison of the calculated response obtained from the photogrammetry analysis and the measured response from traditional instruments was completed. The calculated photogrammetric response was sensitive to how unique points on the column surface were defined. The quality of the images during the shaking events affected the final representation of the column deformations. The vertical displacement results of Point 7 are compared with the LVDT 3EBR7 readings in Figs. 4 and 5 for even and odd line analyses, respectively. FDE indexes were calculated for the vertical displacements of Point 7 in the even and odd analysis as compared to LVDT 3EBR7 results. Table 2 shows that the amplitude error is very good at only 0.16 for the even line analysis, whereas it is 0.19 for the odd line analysis. The phase errors (periodicity errors) are very similar at around 0.50. Overall, the total FDE index is slightly smaller for the even line analysis than the odd lines, and is indicative of which set of lines (even/odd) captured first.

Table 2 FDE index results for Point 7

	FDE Results		
Comparisons	Amplitude	Phase	Total
Fig. 7-Even line analysis vs. LVDT	0.16	0.51	0.67
Fig. 8-Odd line analysis vs. LVDT	0.19	0.49	0.68
Fig. 11-Vertical vs. horizontal line rotation	0.12	0.58	0.70
Fig. 12-Photo vs. Displacement	0.10	0.45	0.55

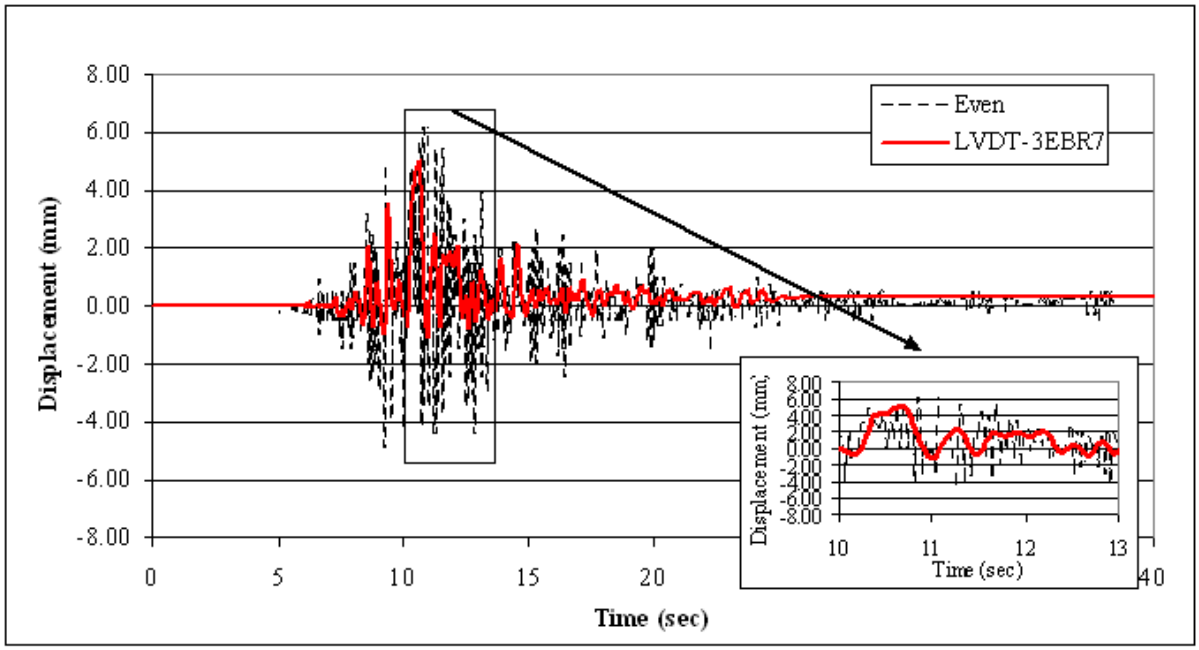

Fig. 5 Comparison of Point 7 vertical displacement for even lines with LVDT 3EBR7 data

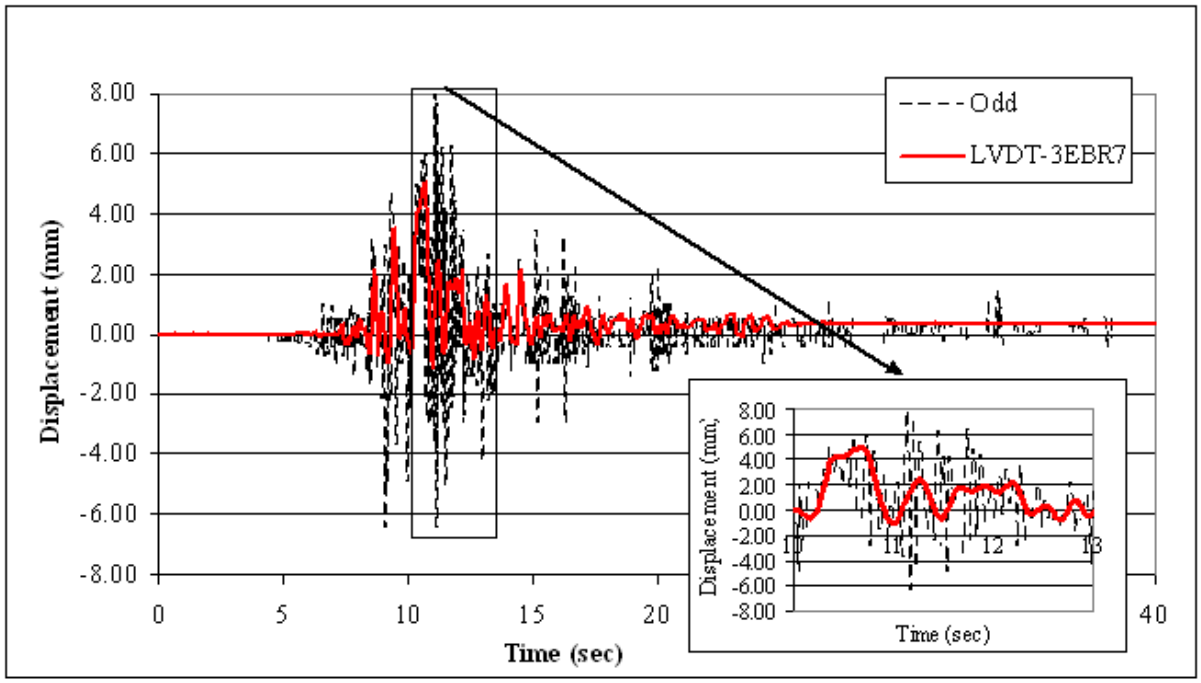

Fig. 6 Comparison of Point 7 vertical displacement for odd lines with LVDT 3EBR7 data

3.2. Intersecting of vertical and horizontal grid lines

The definition of each unique point on the grid surface was a critical step to obtain the displacements of the points and rotations of sections of the column. The intersection of the thick vertical and horizontal lines (0.25 in. thick) was used to define the points, however, there were several ways to consider creating a line within that thickness. One option was to find the mid-point of each 0.25-in. thickness and define a "middle line" with the connection of those points (Fig. 6). The pixel that had the maximum intensity value in the intersections of the horizontal and vertical lines was defined as the mid-point within the thickness.

The edges of the thick grid lines were considered as a second option to define two new lines (edge-lines) for each horizontal and vertical grid line. Using this option, there were four intersections of the edge lines to consider as possible unique locations of that Point, as seen in Fig. 7. In this method, the "edge lines" may be determined by points of a particular light intensity value, a Robert Threshold, or as a considerable difference in relative intensity between the black to white paint transition. The length of the line also had an effect on the results. Longer [1.5 in. (38 mm) to 3.0 in. (76 mm)] and shorter [0.5 in. (13 mm) to 1.5 in. (38 mm)] edge-line lengths were investigated to determine the influence on the definition of a unique Point.

The best representation of a unique Point was obtained from the average of four corner point coordinates. First, the four corner points at the intersection of each horizontal and vertical grid line were defined using the edge-lines of the 0.25-in.-thick grid lines. These edge lines were defined using a constant Robert threshold value of 50 with a short edge line length that ranged from 0.5-1.5 in. The coordinates of the four corner points were then averaged to define a "middle point".

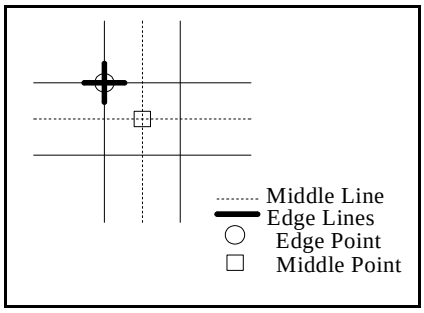

Fig. 7 Close up of lines used to define Point 3 (Fig. 3)

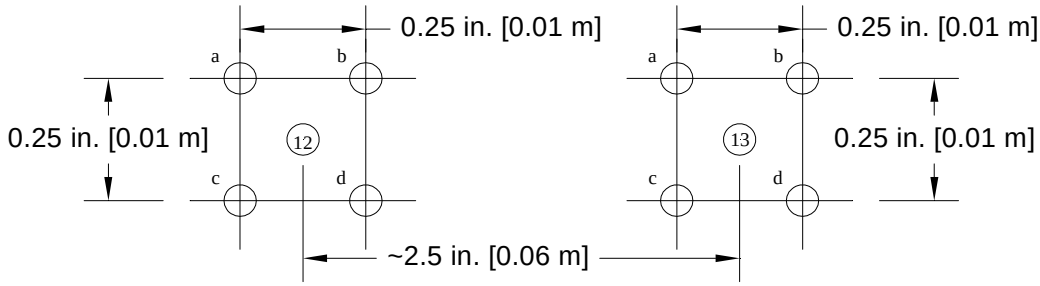

Fig. 8 Four corners surrounding general location of Point 12 and 13

3.3. Comparison of rotation of vertical line and rotation of horizontal line

It is of interest to compare the rotations of lines defined by the relative movement of two points that are aligned vertically (representing an average cross sectional rotation over the height bounded by the two points) and two points that are aligned horizontally (representing the cross sectional rotation at the height of the two points). The rotation of a horizontal line on the column bottom surface was calculated using the even-numbered lines from the photogrammetry measurements. The rotation of a horizontal line was approximated as the relative vertical displacement between two points divided by the horizontal distance between these points. The change in horizontal distance between the

points within each image was accounted for in the analysis. The rotation of a vertical line on the column was approximated using the relative transverse displacements of two points as reduced from photogrammetry data that were aligned vertically on the grid surface divided by the length between those lines. This rotation represents the average cross-sectional rotation between those two points if shear deformations can be neglected. Figure 8 shows the rotation of a vertical line that was calculated using the lateral displacements of Points 3 and 8 on the bottom grid as were tracked during the Test 4D motion. Figure 9 shows the rotation of a horizontal line located at the top of the region encompassed by the vertical line (calculated using the vertical displacements of Points 7 and 9).

The comparison between the rotations of the vertical line shown in Fig. 8 and the horizontal line shown in Fig. 9 is shown in Fig. 10. Although the top and bottom hinging regions had numerous cracks and some spalling of the concrete on the column surface, to the extent that a few lateral reinforcing bars and yielding of the longitudinal bars were revealed, the photogrammetry method was able to capture the rotations well. As an average measurement, the rotation of the vertical line provides a smoother trace than the rotation of the horizontal line that was calculated with the photogrammetry data. The correlation between the rotation of vertical and horizontal line was examined using the FDE index (Table 2), and the amplitude error was found to be 0.12, which represents a very good correlation. The phase error, however, was 0.58 and the total FDE index was 0.70, which overall was a fair correlation.

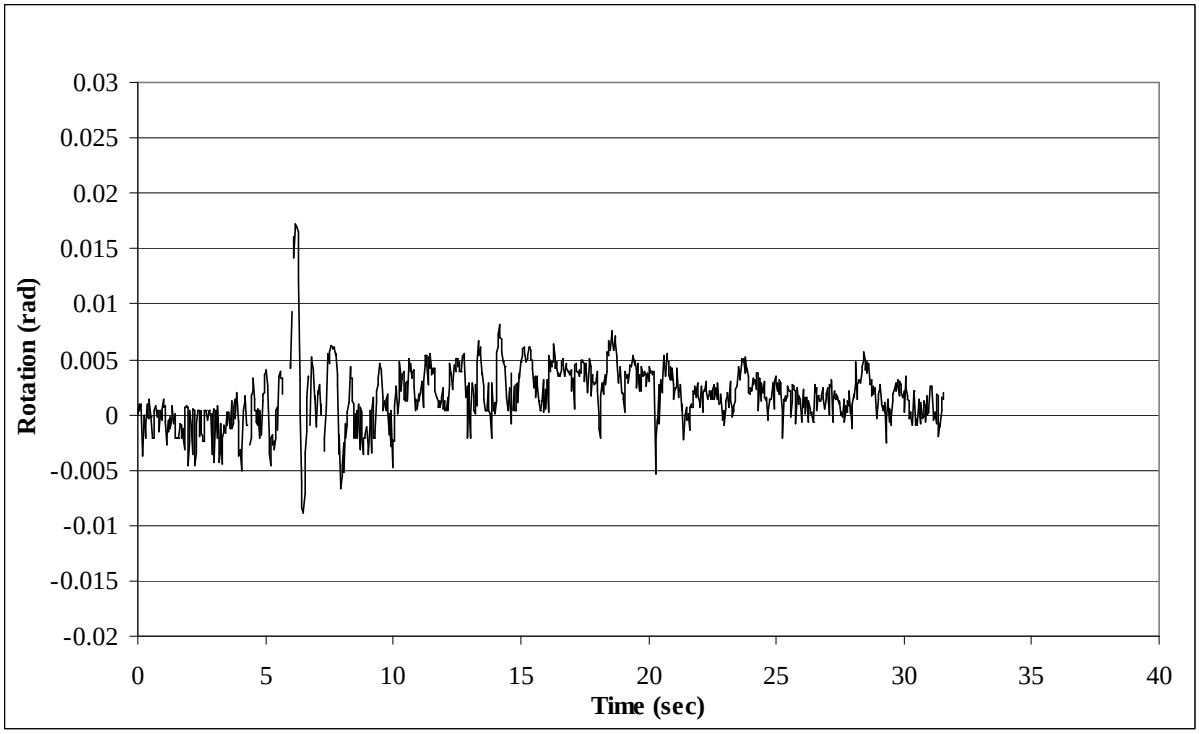

Fig. 9 Rotation of a vertical line calculated using Point 3 and 8

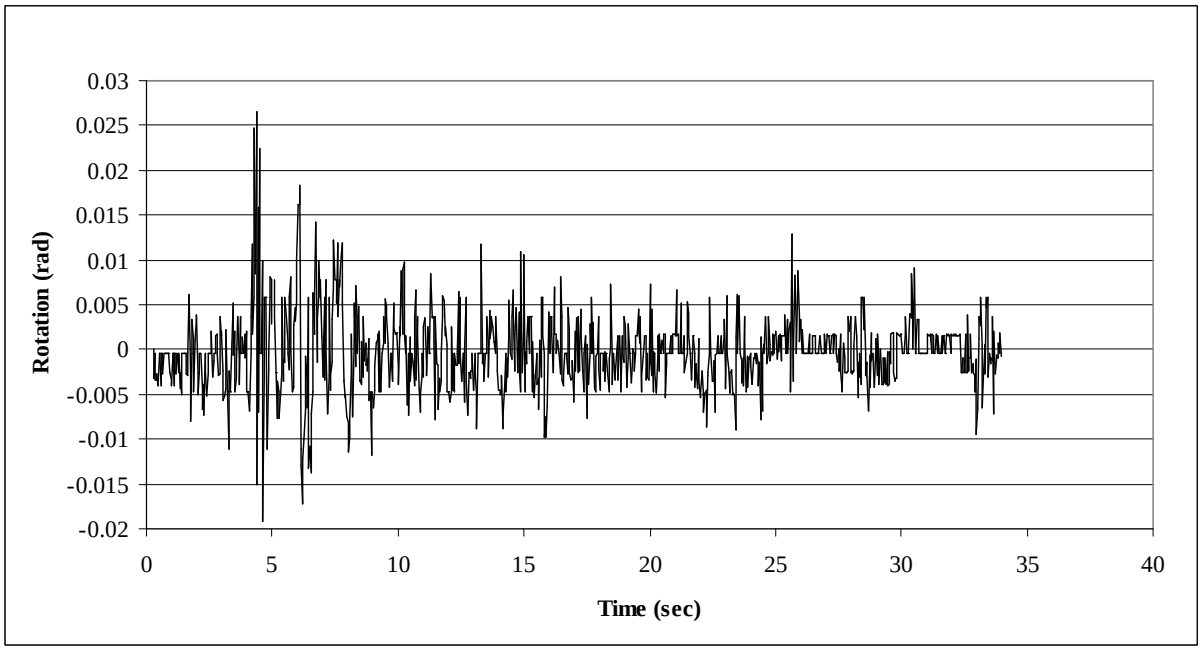

Fig. 10 Rotation of a horizontal line using Points 7 and 9

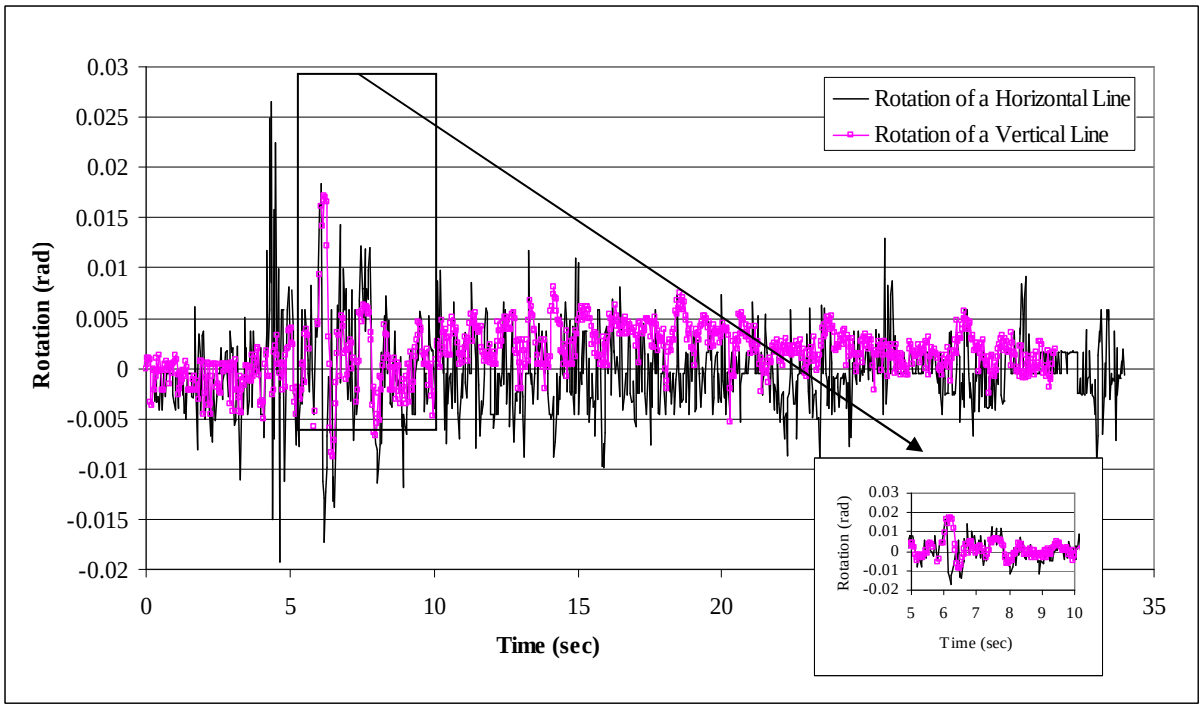

Fig. 11 Comparison of rotations (local vs. average) in Test 4D

3.4. Determining the deformed shape of the column hinges

The grid system used to collect photogrammetry data is advantageous when determining plastic hinge lengths as compared to traditional measurements garnered from strain gages and LVDTs. With photogrammetry, the deformation of the column surface can be determined over a continuum, whereas LVDT instrumentation provides displacement data for discrete points. In addition, if significant damage occurs to the concrete surface LVDT measurements may become dysfunctional, but the painted grid surface may be reconstructed in an image and photogrammetry data preserved during the tests.

The transverse and vertical displacements of each grid point along the top and bottom hinging surfaces were calculated for each test (Table 1). Point 59 in the top grid

system (Fig. 3), which was the closest point to the top of the column, was selected to track the transverse displacement along the direction of the focal plane of the cameras on the left side of the aluminum tower. The projection of the camera view from the tower had an angle of 15.25° with the longitudinal direction of the bridge (Fig. 4). The transverse displacements of grid Point 59 captured during Test 4D was compared with the combined components of the displacement transducers mounted on the bridge deck and the north abutment as shown in Fig. 11 and described next. First, the measurements recorded by DT7 (transverse displacement of Bent 3 at mid-height of the bridge deck) were used to obtain the transverse component along the focal plane of the cameras. Then, DS5 and DS1 measurements were combined together to find the longitudinal component of the displacement (DS5 recorded the gap size between the north abutment and the bridge deck while DS1 measured the movements of the north abutment in the longitudinal direction of the bridge). Although there was approximately 23.3 in. (592 mm) between the transverse beam and Point 59, the column deformed in double curvature and the lateral displacements at these two heights were assumed to be similar. As seen in Fig. 11, the overall periodicity of the two measurements correlates very well, with differences in magnitude primarily attributed to small flexibilities of the transverse beam creating differential movement between the top beam and Point 59 in the column hinging region.

The FDE index analysis was used to compare the results of transverse displacements at Point 59 and the movement recorded by the displacement transducers. The amplitude error was found to be 0.10, which represented a very good correlation between the photogrammetry and displacement transducers results (Table 2). This is significant as the maximum displacement of bridge columns is an important parameter

used to qualify expected damage during earthquake events. The phase angle error was calculated to be 0.45, which was a good correlation result.

The deformed shapes of the hinging regions were defined over a continuum by considering the movements of a suite of Points in the regions [23]. The displacement calculations were repeated at each of the grid points along the hinging surface. Three vertical lines, as defined by the grids shown in Fig. 3, were monitored in Test 4D. On the middle line, the selected Points were 3, 8, 13, and 18 for the bottom grid and 38, 45, 52, and 59 for the top grid system. For the left line, Points 2, 7, 12, and 17 were chosen at the bottom and Points 37, 44, 51 and 58 were selected at the top. For the right line, displacements of Top Points 4, 9, 14, and 19 and Bottom Points 39, 46, 53, and 60 were monitored. The deformations in the top and bottom hinging regions during Test 4D, as represented by dotted lines connecting the displaced points, are compared in Figs. 12 and 13 with the associated column images at the time of maximum column drift. Reverse curvature is correctly represented in the top and bottom hinging regions. Slight nonlinear deformation is also visible in the top hinging region. The deformations captured by the photogrammetry data represent the images very well as seen in Figs. 12 and 13.

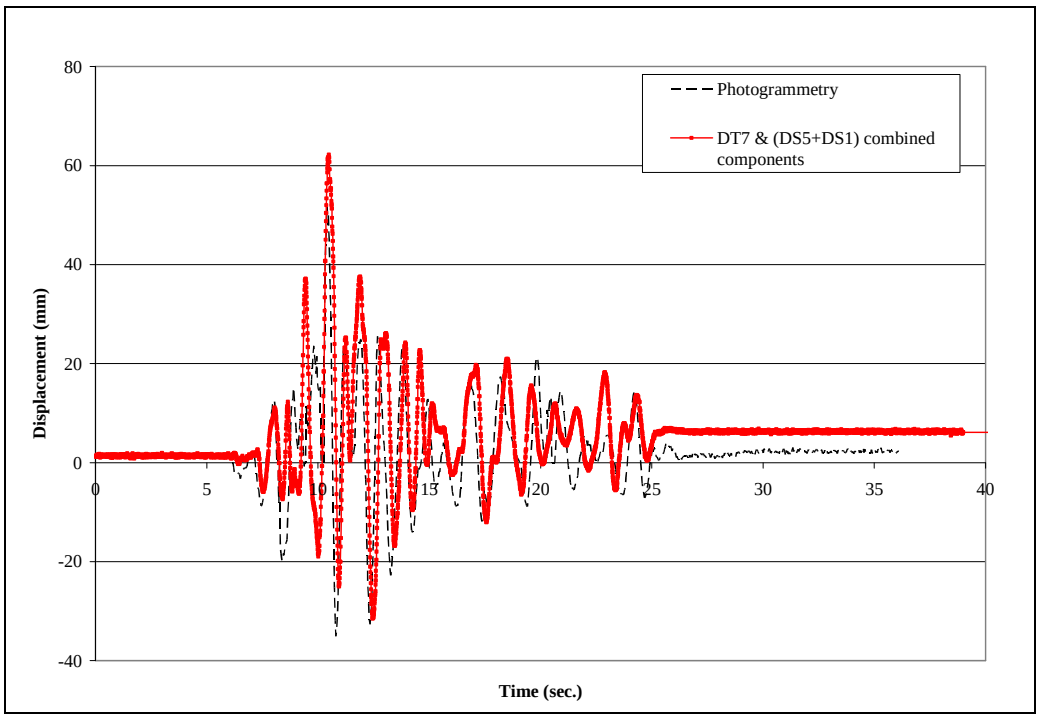

Fig. 12 Comparison of Drift at Point 59 for Test 4D

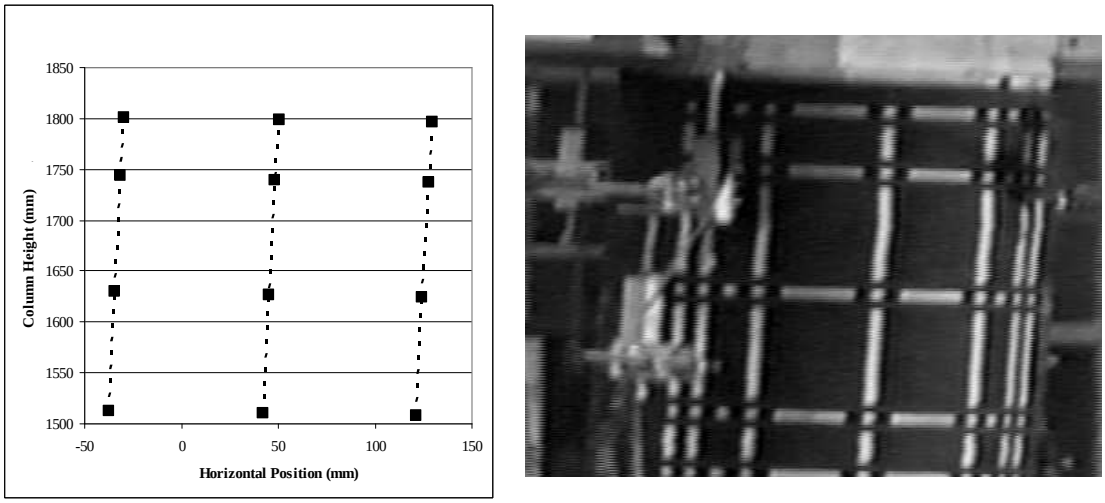

Fig. 13 Top grid deformed shape with picture comparison at maximum column drift during Test 4D

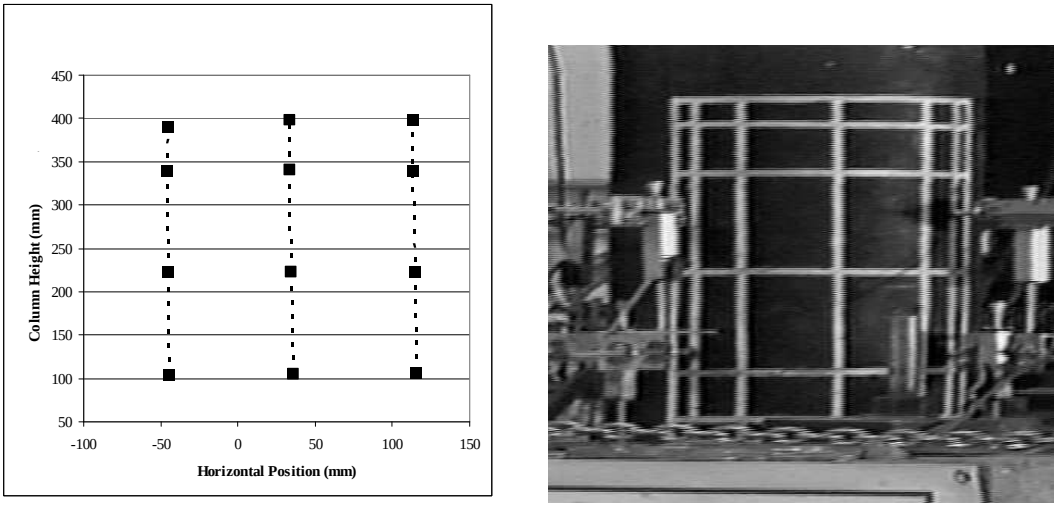

Fig. 14 Bottom grid deformed shape with picture comparison at maximum column drift during Test 4D

4. Conclusions

A simple photogrammetry analysis method was applied to evaluate the deformations of a bridge column surface in plastic hinging locations during the response to strong ground motion. The definition of points on the column surface was completed by using the edge-lines of the 0.25-in. (6 mm) thick grid lines to define four corner points at the intersection of each horizontal and vertical grid line, and then averaging these points to define a "middle point". The edge-lines were best defined using a constant Robert threshold value and short line lengths of 0.5-1.5 in. (13 mm – 38 mm). The even-numbered lines from each frame (partial image) were selected to improve the quality of the images recorded during the tests. The following conclusions are made regarding the analysis of the deformations in the hinging region during response to strong ground shaking:

- The FDE indexes obtained for the vertical displacements of Point 7 in the even and odd analysis gave very good correlations between the calculated amplitude using photogrammetry data and the measured responses from the LVDT 3EBR7 recordings. The phase error results had fair FDE values (approximately 0.50), and fair overall values (0.67 and 0.68).
- The rotation of a vertical line calculated using photogrammetry data, as an average representation of cross-sectional rotation, provided a better representation of the column rotation than the rotation defined by a horizontal line. The correlation between the amplitudes of the rotations of horizontal and vertical lines gave very good results as found in the FDE index calculations. The overall correlation was fair because of differences in phase angles.
- The amplitude of the displacements calculated at the top of the column correlate very well with the results from the combinations of DT7, DS5 and DS1 transducer measurements at the superstructure of the bridge as represented in the FDE index calculation. The overall correlation was good.
- The deformed shape of the top and bottom hinging regions was constructed using the displacement of the points on the column surface. The deformed shapes show a good match with the images at the maximum drift of Test 4D by correctly representing double curvature of the column and the general deformed shape of the hinging region.

Acknowledgements

This project gratefully acknowledges the support of NSF grant #0532084, Joy Pauschke Program Director. The assistance and support of Prof. Saiid Saiidi, Graduate Research Assistant Roby Nelson, the entire staff of the research facilities at the University of Nevada Reno, and Graduate Student Nick Hunt at University of Kansas are also gratefully acknowledged. Prof. Olafsen was supported in part by a Big XII Faculty Fellowship. Additional support from KU Transportation Research Institute is gratefully acknowledged.

References

[1] Jauregui D., Ruinian J., K. White. Review of close-range photogrammetry applications in bridge engineering. Washington D. C. Transportation Research Board, 2006.

[2] Baker A.L.L. Ultimate load theory applied to the design of reinforced and prestressed concrete frames. Concrete Publications Ltd., London. 1956.

[3] Baker A.L.L., Amarakone A.M.N. Inelastic hyperstatic frame analysis. Proc. International Symposium on the Flexural Mechanics of Reinforced Concrete, ACI SP-12 Miami, pp. 85-142. 1964.

[4] Mattock A.H. Rotational capacity of hinging regions in reinforced concrete beams. Proc. International Symposium on the Flexural Mechanics of Reinforced Concrete, ACI SP-12 Miami, pp. 143-181. 1964.

[5] Corley W. G. Rotational capacity of reinforced concrete beams. J Struct Division ASCE 1966; V. 92, No. ST5, pp. 121-146.

[6] Park R., Priestley M. J. N., Gill W. D. Ductility of square-confined concrete columns. J Struct ASCE 1982; 108 No. ST4. 929-950.

[7] Priestley M. J. N., Park R. Strength and ductility of concrete bridge columns under seismic loading. ACI Struct J 1987 V.84 Issue 1. pp. 61-76.

[8] Tanaka H., Park R. Effect of lateral confining reinforcement on the ductile behavior of reinforced concrete columns. Research Report 90-2. Department of Civil Engineering, University of Canterbury, Christchurch, New Zealand. 458 pp. 1990.

[9] Paulay T., Priestley M. J. N. Seismic design of reinforced concrete and masonry structures. John Wiley & Sons, Inc. 1992.

[10] Sheikh S.A., Khoury S.S. Confined concrete columns with stubs. ACI Struct J 1993 V. 90 No. 4 pp. 414-431.

[11] Watson S., Park R. Simulated seismic load tests on reinforced concrete columns. J Struct Engineering, ASCE 1994; V. 120, No. 6, June, pp. 1825-1849.

[12] Kovacic D. Design of high-strength concrete columns. M.Eng. thesis. the University of Melbourne; 1995.

[13] Mendis P. Plastic hinge lengths of normal and high-strength concrete in flexure. Advances in Structural Engineering 2001 V. 4 No. 4 pp. 189-195.

[14] Bae S. Seismic performance of full-scale reinforced concrete columns. Ph.D. dissertation, Austin (TX): the University of Texas; 2005.

[15] Phan V., Saiidi M.S., Anderson J., Ghasemi H. Near-fault ground motion effects on reinforced concrete bridge columns. Journal of Structural Eng. 2007; V.133, Issue 7, pp. 982-989.

[16] Dodd L.L. The dynamic behavior of reinforced concrete bridge piers subjected to New Zealand seismicity. Ph.D. thesis, the University of Canterbury Christchurch New Zealand; 1992.

[17] Hachem M. M., Mahin S.A., Moehle J.P. Performance of circular reinforced concrete bridge columns under bidirectional earthquake loading. Report No. PEER 2003/06, Pac. Earthq. Eng. Research Center, University of California at Berkeley, Feb. 2003, 490 pp.

[18] Brueggen B., Waugh J., Aaleti S., Johnson B., French C., Sritharan S. et al. Tests of structural walls to determine deformation contributions of interest for performance-based design. Proc. of 2007 ASCE Structures Congress, Long Beach, CA, 2007.

[19] Matamoros A. B., Matchulat L., Woods C. Axial load failure of shear critical columns subjected to high levels of axial load. Proc. 14th World Conference on Earthquake Engineering. 2008.

[20] Matchulat Lisa. Mitigation of collapse risk in vulnerable concrete buildings, M.E., University of Kansas; 2009.

[21] Leon R.T., Kim D.K., Hajjar, J.F. Limit state response of composite columns and beam-columns. Part 1: Formulation of design provisions for the 2005 AISC Specification, AISC Engineering Journal, Vol. 44, No. 4, pp. 341-358. 2007.

[22] Dragovich JJ., Lepage A. FDE index for goodness-of-fit between measured and calculated response signals. Earthquake Engineering and Structural Dynamics 2009;38:1751-1758.

[23] Firat Alemdar Z. Evaluation of plastic hinge regions in reinforced concrete bridge systems. Ph.D. dissertation, Lawrence (KS): the University of Kansas; 2010.

4 MANUSCRIPT 2: MODELING SURFACE DEFORMATIONS AND HINGING REGIONS IN REINFORCED CONCRETE BRIDGE COLUMNS

Zeynep Firat Alemdar[a,*], Adolfo Matamoros[b] and JoAnn Browning[c]

[a] 1147 Learned Hall, Department of Civil, Env, and Arch. Engineering, University of Kansas, Kansas, USA

[b] 2150 Learned Hall, Department of Civil, Env, and Arch. Engineering, University of Kansas, Kansas, USA

[c] 2150 Learned Hall, Department of Civil, Env, and Arch. Engineering, University of Kansas, Kansas, USA

[*] Corresponding author Tel: +1 785 864 3760 Fax: +1 785 864 5631 E-mail addresses: zeynep@ku.edu (Z. F. Alemdar).

1. Introduction

The determination of hinging regions and damage locations in reinforced concrete bridge columns is a critical step to evaluate the performance of a bridge system under earthquake events. Bridge systems are designed to keep inelastic behavior in the columns and away from the superstructure, which is different than building systems. In bridge systems, the columns of the bridges must generally provide the inelastic rotational capacity for the structure.

The length of the spread of plastic behavior in columns, or plastic hinge length, has been studied extensively by many researchers [1-10]. This study investigates the plastic hinge length in reinforced concrete bridge columns, focusing on a bridge system

under dynamic loads. A consistent prediction of a plastic hinge length is necessary to examine the theoretical drift capacity of bridge columns. The hinge length also indicates the theoretical length of damage concentration along the column. Previous work has relied on determining expressions to estimate hinge lengths from small-scale component tests. An evaluation of large-scale system behavior has the benefit of including the effects of moment redistribution and progression of yielding throughout the entire structure. As moments are redistributed, the order of hinges in the bridge system and the magnitude of plastic deformations in each column can change.

Modeling the magnitude of surface deformations in hinging regions is crucial to detail the spread of plasticity in the hinging regions during the response of earthquake loading. In the reported study, a photogrammetry method was used to remotely track deformations of a concrete bridge column surface in a distributed region rather than at a specific location. The bridge column was tested as part of a large-scale bridge test at the University of Nevada Reno (UNR) [11]. The photogrammetry method holds several advantages over traditional sensors, including that the experimental components are simple to construct, are more economical for typical laboratory environments, and are likely to fail less at large deformation than traditional strain measurement devices. In addition, extensive surface deformations and rotations in the hinging regions can be collected with this method.

This research uses experimental data from photogrammetry measurements of bridge column deformations tested at UNR to create a finite element model that realistically represents deformations in a reinforced concrete bridge pier. Experimental data was obtained from the application of the photogrammetry method. Cameras were used to record the movements during earthquake shakings of two grid systems applied to

the column. The displacements were reduced using the pictures recorded by the cameras. The bridge column was analyzed using Finite element (FE) analysis with the ABAQUS [12] software. Analyses of the bridge column under monotonic and earthquake-induced deformations were completed, and the load deflection curve under monotonic loading was compared with a similar curve produced using the Modified Compression Field Theory. The FE model results under earthquake-induced deflections were compared with the photogrammetry measurements.

2. Description of four-span large scale reinforced concrete bridge test

A large-scale reinforced concrete bridge system was tested on February 12-15, 2007 at the UNR laboratory under biaxial earthquake loadings. The test specimen consisted of a four-span reinforced concrete bridge with end abutments as shown in Fig. 1. The bridge was quarter-scale with two interior and two exterior spans that were 29 ft (8840 mm) and 24.5 ft (7470 mm) in length, respectively. The total length of the bridge system was approximately 110 ft (33528 mm). The clear heights of the bents were 5, 6 and 7 ft (1524, 1830, and 2130 mm), with the tallest bent in the middle (Bent 2). The concrete compressive strength used in the bridge (excluding the post-tensioned slab) was 6.7 ksi (46.2 MPa) and the yield strength of the reinforcement was Grade 60 ASTM A706 (414 MPa) deformed bar. The columns had double curvature response and resisted high intensity earthquake motions during testing. The superstructure consisted of a post-tensioned solid slab both in the longitudinal and transverse directions. The bridge also had abutment seats at both ends that were driven in the longitudinal direction by dynamic hydraulic actuators to simulate the gap closure and impact at the abutments.

The top and bottom hinging regions of the east column of Bent 3 were the main targets to collect photogrammetric data in the large-scale four-span reinforced concrete bridge test. The column that was selected for application of the photogrammetry method was 72 in. (1829 mm) long and 12 in. (305 mm) in diameter, with a 0.5 in. (13 mm) concrete cover. The column consisted of 16 No.3 (16-10M) longitudinal reinforcement equally spaced along the radial direction. The cap beam is 15 in. (381 mm) by 15 in. with a 23- in. (584 m) width. The total length of the cap beams along the transverse direction of the bridge was 98 in. (2490 m).

Two different grid systems were applied to track the displacements of the columns (Fig. 2). To construct these grid systems, the bridge column was first spray-painted black to obtain a solid dark background and the lines and squares were lightly traced with a pencil, and then they were filled in using a single stencil and white paint. The bottom grid had vertical and horizontal lines spaced irregularly around the face of the circular column while the top grid used a different configuration that was composed of lines and squares so as to be similar to the spacing of the lines in the bottom grid. The intersections of the thick vertical and horizontal lines in both regions were numbered and used to obtain the best definition of Points along the column surface after the analysis of the photogrammetry data as shown in Fig. 3 [13].

The biaxial and uniaxial scaled motions measured at the Century City Country Club during the 1994 Northridge, California earthquake were applied during the bridge tests. This earthquake motion was used 13 times with increasing amplitude in order to monitor the progression of damage from pre-yield to failure. A white noise excitation was also applied before each ground motion intensity change to test for system

identification. The un-scaled lateral and longitudinal components of Northridge earthquake motion were given in Figs. 4 and 5.

An aluminum tower was built to place cameras to record the earthquake events during the shaking tests. The tower had two levels to monitor of the two plastic hinging regions. DXB-9212EF model Starlight 600 TVL super high resolution cameras with black-white recording properties were placed on each level of the tower and video-lens zooms having 60-300mm F4-5.6 capturing capability were used with the cameras to clearly see the grid surfaces as shown in Fig. 6. Two monitors (two channels for each monitor) were set up to show the field of view of the cameras during the tests. The distance between the east column of Bent 3 and the tower was 288 in (7315 mm). The angles from the left and right cameras to the column were 73.58° and 44.97° on the horizontal plane as shown in Fig. 7, respectively. Therefore, the displacements from photogrammetric measurements were obtained along the direction of the focal plane and compared with the combined displacements of transverse and longitudinal displacement transducers on the superstructure of the bridge.

3. Finite element model of the bridge column

A three dimensional finite element model of the east column of Bent 3 was defined with the cap beam on the top of the column and the footing system under the circular column using ABAQUS Finite Element software. A concrete damaged plasticity model was utilized in the FE analysis to define the uniaxial compressive and tensile concrete material properties of the bridge column, while elastic concrete material properties were assumed for the cap beam and footing of the system. The properties of

the concrete in the core and cover were defined using a plasticity based material model. The stress-strain curve in compression was defined using the Mander unified stress-strain model under monotonic loading at slow strain rates [14] as shown in Fig. 8. The maximum strain was selected to be 0.1, similar to the research done by Scott et al. (1982), Spacone et al. (1996), and Yassin (1994) who used the maximum concrete strain in compression as 0.06. The response of concrete subjected to the moderately rapid load rates, as associated with earthquake ground motions, was also considered. The dynamic magnification factors that were used in the analysis followed the recommendations of Mander (1984), who used regression analyses of the experimental results of Watstein (1953) on plain concrete specimens of different strengths. The relationships for the dynamic strength of concrete (D_f) are as follows.

$$(f'_{co})_{dyn} = D_f f'_{co} \quad (1)$$

where:

$(f'_{co})_{dyn}$ = the compressive strength of concrete under rapid loading

f'_{co} = the quasi-static compressive strength of concrete in MPa (1 Mpa=145 psi).

$$D_f = \frac{1+\left[\frac{\varepsilon_c}{0.035(f'_{co})^2}\right]^{1/6}}{1+\left[\frac{0.00001}{0.035(f'_{co})^2}\right]^{1/6}} \quad (2)$$

where ε_c= rate of strain in s^{-1}.

Dynamic strain rates were also considered for the proposed model of the reinforced concrete bridge column. Previous work in numerical modeling [19] and experimental dynamic testing of full-scaled models [20] investigated the strain rate associated with earthquake loading of reinforced concrete structures. This research and the investigations of others [21] identified the maximum strain rate in reinforced

concrete structures subjected to severe earthquake ground motion to be between 0.001 strain per second and 0.25 strain per second. An appropriate maximum strain-rate for the case of crushing of plain concrete is estimated assuming that crushing occurs once some inelastic deformation has occurred in the bridge. A maximum strain rate for consideration of the concrete crushing strength was assumed to be 0.05 strain per second according to these investigations.

Stiffness relationships in the FE model were complex. The relationships for the dynamic stiffness factor (D_E) that were used in the model were very similar to the dynamic strength equations, as shown below:

$$(E_c)_{dyn} = D_E E_c \tag{3}$$

$$D_E = \frac{1+\left[\dfrac{\varepsilon_c}{0.035(f'_{co})^3}\right]^{1/6}}{1+\left[\dfrac{0.00001}{0.035(f'_{co})^3}\right]^{1/6}} \tag{4}$$

where $(E_c)_{dyn}$ = Elasticity modulus of concrete under dynamic loading

ε_c = Compressive strain of concrete (in./in.).

The stress-strain curve for concrete in uniaxial tension was studied using the equations proposed by Bhide (1987), Vecchio and Collins (1982), and Collins and Mitchell (1987). These three different tension models are compared in Fig. 9. The Bhide (1987) tension model was chosen for this study because it provided the best convergence. The model also takes into account the ability of the concrete to have a tension stiffening effect. To model this behavior, the modulus of rupture was taken to be $4.0*\sqrt{(f'_c)}$. The angle of cracking was assumed to be 35° to obtain smooth decreases in the tensile stresses after cracking.

A uniaxial bilinear steel model with isotropic kinematic hardening properties was used to simulate the behavior of the longitudinal steel. Isotropic parameters were implemented using the classical stress-strain relationship for ductile steel according to ASTM A706 Grade 60 Steel. In order to adjust the steel strength for loading in the range of strain rates developed under earthquake shakings, dynamic magnification factors were calculated. The data for A615 steel [21] showed that the dynamic yield strength was approximately 10 percent larger than the static yield strength. According to investigations done by Manjoine (1944), the maximum increase in ultimate strength of mild structural steel was approximately 4%. Several studies [21, 25, and 26] indicated that increased strain rate had relatively little effect on the elastic modulus of steel. The dynamic factor of 10 percent for the yield strength was used in the material model and compared as shown in Fig. 10.

Kinematic hardening properties were defined including cyclic strain softening as defined by Ma et al. (1976). A reinforcing steel element was modeled with the cyclic material properties that had been proposed by Ma et al. (1976) and subjected to reversed cyclic loading. The stress-strain curve of an element along the steel member was obtained from the FE analysis and compared with the experimental data conducted by Ma et al. (1976) as shown in Fig. 11. The FE model represented the results reported by Ma et al. (1976) very well.

Mesh sensitivity analysis was studied under monotonic loading for the FE model of the bridge column. The axial load on the column consisted of an imposed weight of 47.2 kips applied as a uniform pressure at the surface of the cap beam in the FE model. The two-directional shaking table displacement measurements that were recorded by the research team at UNR were applied at the bottom surface of the footing as transverse and

longitudinal direction displacement histories. The circular column, cap beam and the footing were modeled using 3D continuum 8-node brick elements, whereas longitudinal reinforcement and transverse steel hoops were defined using 1D 2-node linear truss elements. The longitudinal steel had a cross-sectional area of 0.11 in.^{2} (71 mm^2) and transverse hoops had 0.029 in.^{2} (18.7 mm^2) cross-sectional area evenly distributed every 1.25 in. (32 mm) along the column. The brick elements had twenty integration points distributed throughout its physical volume. A reduced integration scheme was utilized to reduce the computation time for the analysis.

The FE mesh of the solid elements was generated considering the location of the longitudinal reinforcement. Truss elements were linked to the edge of the solid elements using an embedded constraint option. To determine the mesh sensitivity in the FE model, three different models having mesh sizes of 3 in. (76 mm), 1 in. (25 mm) and 0.5 in. (13 mm) along the top and bottom hinging regions of the column and 4 in. (102 mm) outside the regions were studied. A coarser mesh was used for the cap beam and the footing because they were modeled with elastic material properties. The FE model was analyzed under increasing lateral loads. Figure 12 shows that the 1 in. (25 mm) mesh model gave a better force-displacement distribution when compared to similar curves generated using the Modified Compression Field Theory [28] and the result of a moment-curvature program (Curve). The analysis of the 0.5 in. (13 mm) mesh model along the hinging regions took 2 times longer than using 1 in. (25 mm) mesh without any benefit in model performance. The 1 in. mesh size was chosen for future analyses.

The success of the model is measured by how accurately the response of the structure is represented. To accomplish this measurement, a quantitative procedure is used to compare measured and calculated response values. This measure was made using

a FDE (frequency domain error) index as developed by Dragovich and Lepage [29]. The FDE index is used to compare time-domain response waveforms such as earthquake responses obtained in this study. The FDE method uses the Fourier spectra of the response signals, which are non-periodic and comprised of multiple frequencies, to calculate the index. Fast Fourier Transform was used to determine the composition of frequencies of the photogrammetry responses. The starting and ending frequencies were selected to be between 0.5 Hz and the Nyquist frequency, which is $f_n = 1/(2\Delta_t)$ with Δ_t as the time interval of the series. The FDE index accounts for both the amplitude and phase differences between the response signals and gives a number between 0 and 1 as a measure of the goodness-of-fit, where zero indicates a perfect correlation. The amplitude error is a measure of the difference between the values of the response signals, and the phase angle is the angle that the resultant vector of the signals make with respect to the real axis in the real-complex plane. From the study by Dragovich and Lepage, an FDE value equal to 0.75 represented a poor correlation, and an FDE value of 0.25 represented a very good correlation.

The results of the FE model of the bridge column under dynamic loading were obtained and compared with the photogrammetric measurements. The FE model of the Bent 3 east column was analyzed under the earthquake loading, which were selected to have biaxial components of 0.5 g maximum ground acceleration in transverse direction and 0.6 g maximum ground acceleration in the longitudinal direction (Test 4D). The displacements at grid Point 59, as shown in Fig. 3, were reduced from the photogrammetric data during Test 4D. These displacements are compared with the combined components of the displacement transducers mounted on the bridge deck and the north abutment, which recorded the transverse displacement of Bent 3 at the middle

of the bridge deck (DT7), and measured the gap size history and the displacement of the north abutment in the longitudinal direction of the bridge (DS5 and DS1) during the same motions. Figure 13 shows the comparison of the displacement history. The FDE index analysis was completed to compare the results obtained from the photogrammetry method with the measured displacement transducers. The amplitude error was found to be 0.10, which represented a very good correlation between the photogrammetry and displacement transducers results (Table 1). The phase angle error was calculated to be 0.45, which was a good correlation result. Although they were separated by 23 in. (584 mm), the displacements at these two points were similar because of the double curvature along the column.

The displacement history at the top and bottom hinging regions from the FE model were also compared with the photogrammetric data. In the bottom hinging region, the displacement history at Point 2 as shown marked on the grid surface in Fig.3 is plotted in Fig. 14. Point 51 (Fig. 3) was selected to compare the displacement at the top hinging region. The periodicities of the two measurements of the motion are very similar as seen in Figures 14 and 15. The amplitude and phase errors of the lateral displacements (Table 1) had very good correlations, ranging from 7.3% to 9.4% in amplitude error and from 14 % to 25% in phase error. The FE model provides very good results.

The effect of yield strength of the longitudinal reinforcement was considered because limited information about the stress-strain relationships was available to use in the analysis. The lateral response at the top and bottom points shown in Fig. 3 (Point 2 and 51) was insensitive to the yield strength as shown in Fig. 14 and 15. The vertical displacement response and cross-sectional rotation were sensitive to yield strength, and so responses were calculated using yield strength values of 64, 70, 75, and 80 ksi (441,

483, 517, and 552 MPa). Figures 16-19 show the comparisons of vertical displacements at the location of LVDT 3ETR4, which was instrumented 5 in. (127 mm) below the cap beam as shown in Fig. 3, for each yield strength. Figures 20-27 show the comparisons of the measured cross-sectional rotations at the locations of LVDTs (LVDT 3ETR3 and 3ETR4 and LVDT 3ETR5 and 3ETR6) that were located at 5 in. (127 mm) and 12 in. (305 mm) below the cap beam with the calculated FE analysis results. The correlations between the vertical displacement obtained from the FE model and the LVDT measurements were examined using the FDE index for each yield strength value as given in Table 2. As yield strength was increased from 64 ksi to 80 ksi, the total FDE index decreased from 31% to 18% for vertical displacement calculations. It is evident that the yield strength of 80 ksi provides a very good comparison as shown in Fig. 28. Figures 29 and 30 show that the FDE index results for the cross-sectional rotations at 5 in. (127 mm) and 12 in. (305 mm) are very similar to each other for all yield strength values analysis and represent very good correlations.

The effect of the flexural stiffness of the cap beam was examined to simulate the rotation of the cap beam during response to ground motions. The flexural stiffness of the cap beam was calculated and modeled in the program by defining a linear-elastic rotational spring at the center of the right face of the cap beam. The stiffness was computed as 10^9 lb-in. (113*10^6 N-m). It was varied from 10^8 lb-in. (113*10^5 N-m) to the real value in the model to determine the effect of the flexural stiffness of the cap beam on the response of the bridge column. Yield strengths of the reinforcement of 68 and 75 ksi (469 MPa and 517 MPa) were used in the model to find the best definition of the cap beam stiffness. Figures 31-33 show the comparisons of the vertical displacements from the analyses with the yield strength defined to be 68 ksi (469 MPa).

The stiffness values were taken to be 10^8 lb-in. (113*10^5 N-m), 1.5*10^8 lb-in. (17*10^6 N-m), and 5*10^8 lb-in. (56.5*10^6 N-m.). The vertical displacement comparisons are shown in Figs. 34 and 35 for the yield strength of 75 ksi (517 MPa). An FDE index analysis was used to determine the best correlation between the analyses. Figures 36 and 37 show that as the stiffness of the cap beam increases, the FDE decreases. The stiffness of 5*10^8 lb-in. (56.5*10^6 N-m) gives the best comparison when the yield strength of the steel is equal to 75 ksi (517 MPa) as shown in Table 3. In Table 3, as the stiffness of the cap beam was increased from 1*10^8 lb-in. (113*10^5 N-m) to 5*10^8 lb-in. (56.5*10^6 N-m), the amplitude error decreased from 41% to approximately 10%, for either f_y=68 ksi (469 MPa) or f_y=75 ksi (517 MPa). The phase error with constant cap beam stiffness increased, however, from 20% to 33% with f_y=68 ksi (469 MPa), and from 20% to only 29% with f_y=75 ksi (517 MPa).

When reinforced concrete structures are subjected to cyclic loading, they experience progressive damage and a reduction in stiffness. At very high deformations, it is inevitable to expect significant damage and stiffness degradation in the bridge column, therefore, stiffness degradation and stiffness recovery variables were used in the concrete plastic damage model. The stiffness degradation parameters d_c and d_t defined in the concrete plasticity model in ABAQUS are numerical values which depend on inelastic compressive strain or tensile crack displacement. When the post-peak compressive stress or tensile crack displacement increases, the material sustains non-recoverable damage, and the stiffness of the material reduces after a load reversal occurs. In this study, the compression stiffness degradation parameters for core and cover concrete were defined as exponential functions dependent on the plastic component of the compressive strain. Equations 5 and 6 were utilized for core and cover concrete respectively:

$$d_c = 1 - e^{-30\varepsilon_{pl}} \quad (5)$$

$$d_c = 1 - e^{-160\varepsilon_{pl}} \quad (6)$$

where ε_{pl} is the plastic component of the compressive strain. The compression stiffness degradation model for the core and cover concrete are shown in Figs. 38 and 39. The compression stiffness recovery variable (w_c) was taken between 0.5 and 1.0, which implies that as cracks close during load reversal the compression stiffness will be completely recovered.

The tension stiffness degradation parameter was defined by a linear function in which a 50 percent reduction of the elastic stiffness was assumed to occur when the critical crack bandwidth value was reached, and 98 percent of the elastic stiffness when the critical crack bandwidth was doubled. Figure 40 shows the tension stiffness degradation model. The tension stiffness recovery variable (w_t) was taken to be between 0 and 1.0 in the FE analyses.

Several combinations of different compression and tension stiffness recovery variables as given in Table 4 were defined in the model to obtain the best parameters. The comparisons of vertical displacements are shown in Figs. 41-44. The FDE indexes were also calculated to determine the best combinations of the parameters (Table 4). As seen in Fig. 45, the best combination of recovery variables are w_c =0.8 and w_t =1.0. These stiffness recovery variables were chosen for future analysis.

The effect of the bond-slip at the column interfaces was considered in the FE analysis because when a column is subjected to axial load and flexure, the longitudinal reinforcement displaces in tension and in compression as a result of the strain in the embedded bar. The effects of the slip were modeled using linear-elastic springs at the beam-column interface. Given the large development length afforded by the foundation

and cap beam this was considered to be an adequate assumption. The properties of the springs were computed as follows. The slip displacement is calculated by integrating the axial strains over the anchored bar length. The slip of the longitudinal reinforcement results in additional member end rotation that is not related to flexural deformations. Experimental results from four double curvature columns indicated that the bar slip deformations may be as large as the flexural deformations [30]. The value of the slip deformations did not vary much with increasing lateral displacement or damage in the tests. Numerous experimental studies have been completed to define the anchorage behavior of the reinforcing bars. Several analytical bond-slip models have been developed using these experimental results. Using a bilinear strain distribution as shown in Fig. 46, the slip in the model was ultimately determined from Eq. 7 and 8.

$$slip = \int_0^{l_d} \varepsilon dx = \frac{\varepsilon_s l_d}{2} \qquad \varepsilon_s \le \varepsilon_y \tag{7}$$

$$slip = \int_0^{l_d} \varepsilon dx + \int_{l_d}^{l_d'} \varepsilon dx = \frac{\varepsilon_s l_d}{2} + \frac{l'_d}{2}\left(\varepsilon_s + \varepsilon_y\right) \qquad \varepsilon_s > \varepsilon_y \tag{8}$$

The development lengths over the elastic and inelastic regions of the reinforcement (l_d and l'_d) were calculated from the equilibrium of forces in the reinforcement as given in Eq. 9. A uniform bond stress of u_b, which was equal to $6\sqrt{f'_c}$, was assumed in the elastic range (Fig. 46).

$$l_d = \frac{f_y d_b}{4u_b} \tag{9}$$

In the inelastic portion of the slip, the slope of the force-slip relationship (Fig. 47) was assumed to be 1% of the slope of the elastic range. The total slip was calculated to be 0.08 in. (2 mm) in the FE model having the yield strength of the longitudinal reinforcement of 64 ksi (441 MPa).

The vertical displacement at the location of LVDT 3ETR4 was obtained from the FE analysis and compared with the measured displacement at the face of the column, as shown in Fig. 48. The vertical displacement result give higher values than those found in Fig. 3 when the yield strength was equal to 64 ksi (441 MPa) and no bond-slip behavior was defined in the FE model. The rotations, however, followed the measured LVDT data very well as shown in Fig. 49 and 50. An FDE index analysis was used to determine the effect of the added bond-slip deformation in the FE model (Fig. 51). Table 5 shows that as the bond-slip effect was introduced in the FE model, the total FDE error increased from 30% to 43%. At best it can be concluded that bond-slip deformations are not an important component to the response of the bridge column.

The deformed shapes of the hinging regions were defined over a continuum by considering the movements of selected Points in the regions [13]. Three grid lines in the column hinging regions were selected to define the lateral displacements. These lines were called Middle, Left, and Right lines because of their locations on the grid (Fig. 2). Four Points on each grid line were selected to obtain the lateral displacements using the Photogrammetric data. The lateral displacements were connected using a line to simulate the deformed shape of the column. The lateral displacements of the same points on the column surface shown in Fig. 3 were also determined from the FE model at the time of the maximum drift during response to the Test 4D motion. Yield strengths of 64 and 80 ksi (441 and 552 MPa) were considered to obtain results with the FE model. Figure 52 shows the comparisons of the deformed shapes reduced from the photogrammetry data and the FE model when the yield strength of the steel is equal to 64 ksi (441 MPa). For the 80 ksi (552 MPa) yield strength, the deformed shapes are compared in Fig. 53. the deformed shape obtained from the FE model with the yield strength of 80 ksi (552 MPa)

follows the deformed shape reduced from the photogrammetry better than the results with the yield strength of 64 ksi (441 MPa).

4. Conclusions

The best FE model of the reinforced concrete bridge column subjected to earthquake motion was produced using the following properties:

- The static increasing lateral load analysis results showed that using a 1 in. (25 mm) mesh along the top and bottom hinging regions of the bridge column provided a similar force-displacement curve as that obtained using the Modified Compression Field Theory.
- According to the analyses results using different yield strengths for the steel, using the yield strength of 80 ksi (552 MPa) gave the best FDE index value.
- The flexural stiffness of the cap beam should be defined to be 5*10^8 lb-in. (56.5*10^6 N-m).
- The compression and tension stiffness recovery variables used in the FE model were determined to be w_c =0.8 and w_t =1.0.
- The error calculated from the vertical displacement response including the bond-slip effect of the longitudinal reinforcement was higher than the error associated with the response having no bond-slip effect.

Using these modeling parameters, the FE model adequately represented the drift response of the bridge column and plastic deformation behavior in response to strong ground motion. The comparisons of the calculated and measured lateral displacement

responses of points in the hinging regions gave very good results, as calculated with the FDE index analysis. Finally, the deformed shape of the bridge column generated using the FE model results followed the deformed shape of the column reduced from the Photogrammetric data.

Table 1 FDE results for lateral displacement comparisons

(FE vs. Photogrammetry measurements)

	Amplitude error (%)	Phase error (%)	Total error (%)
Comparison of Point 59	10	45	55
Comparison of Point 2	7.3	14	22
Comparison of Point 51	9.4	25	34

Table 2 FDE results for different yield strength analyses

(FE vs. LVDT measurements)

	Yield strength of the steel (ksi)	Amplitude error (%)	Phase error (%)	Total error (%)
Vertical Displacement	64	8.9	22	31
	70	7.3	17	24
	75	6.6	14	21
	80	6.4	12	18
Rotation @ 5 in. below the cap beam	64	20	6.6	27
	70	20	6.6	27
	75	19	7.1	26
	80	17	9.7	27
Rotation @ 12 in. below the cap beam	64	7.3	5.4	13
	70	7.3	5.4	13
	75	6.8	5.8	13
	80	6.9	5.9	13

Table 3 FDE results for analyses with different stiffness of the cap beam analysis

(FE vs. LVDT vertical displacement measurements)

	Flexural stiffness of cap beam lb-in. (N-m)	Amplitude error (%)	Phase error (%)	Total error (%)
fy = 68 ksi (469 MPa)	1*10^8 lb-in. (113*10^5 N-m)	41	20	61
	1.5*10^8 lb-in. (17*10^6 N-m)	24	23	47
	5*10^8 lb-in. (56.5*10^6 N-m)	11	33	44
fy = 75 ksi (517 MPa)	1*10^8 lb-in. (113*10^5 N-m)	41	20	61
	5*10^8 lb-in. (56.5*10^6 N-m)	9.4	29	38

Table 4 FDE results for different degradation parameters

(FE vs. vertical deformations 5 in. below tha cap beam as measured with LVDTs)

Stiffness degredation variables	Amplitude error (%)	Phase error (%)	Total error (%)
w_c=0.5, w_t=0	11	26	37
w_c=0.8, w_t=0	11	28	39
w_c=1, w_t=0.8	11	29	40
w_c=0.8, w_t=1	8.9	22	31

Table 5 FDE results for bond-slip model

(FE vs. LVDT vertical displacement measurements)

Bond-Slip Model	Amplitude error (%)	Phase error (%)	Total error (%)
with Slip	13	31	43
without Slip	8.9	22	30

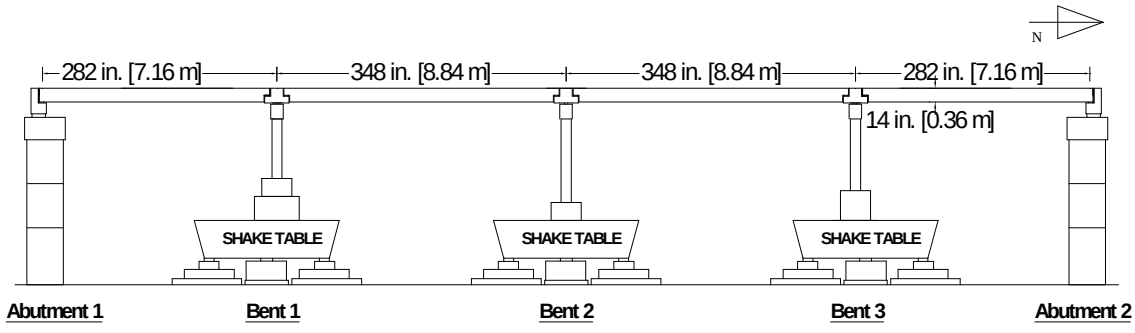

Fig. 1 Elevation view of the four-span bridge

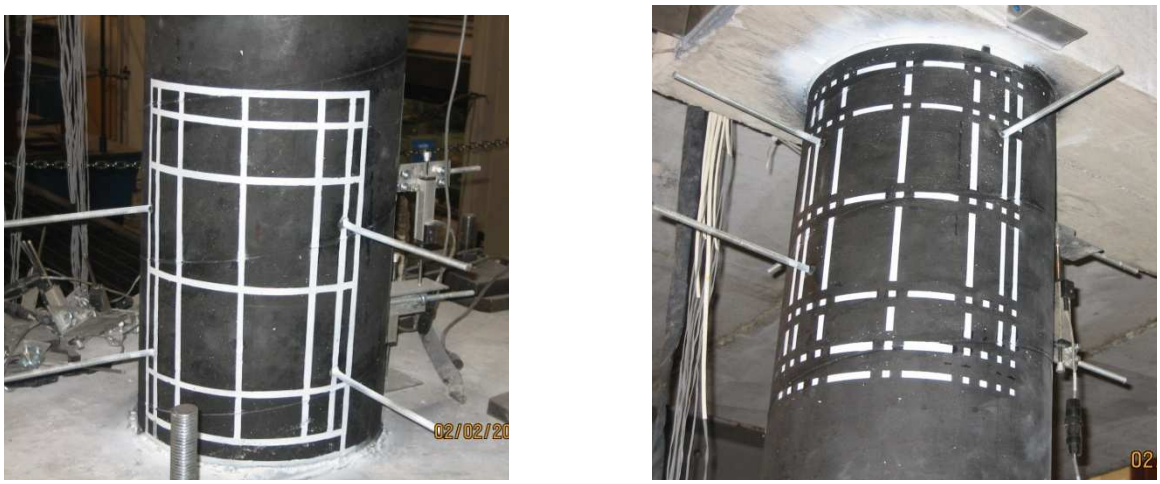

(a) (b)

Fig. 2 Close view of (a) bottom and (b) top grid systems

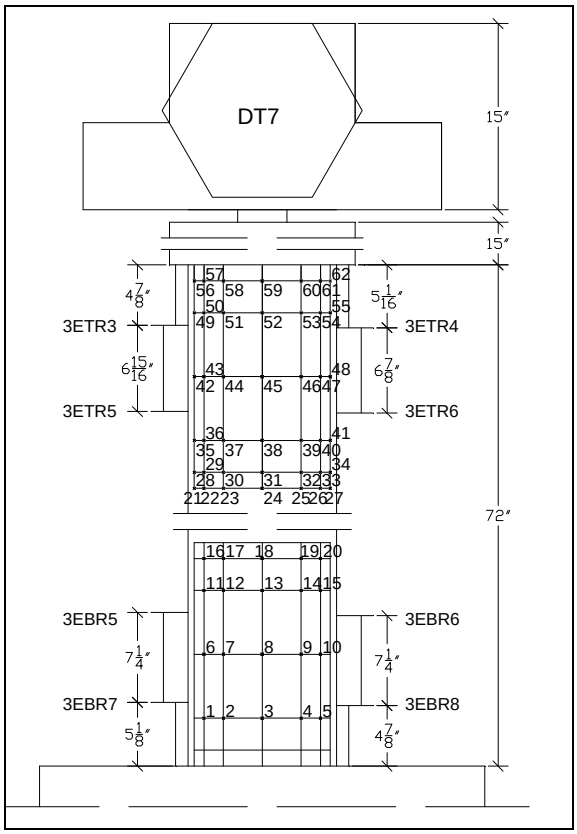

Fig. 3 Grid system and LVDT locations on column in the Bent 3 east column

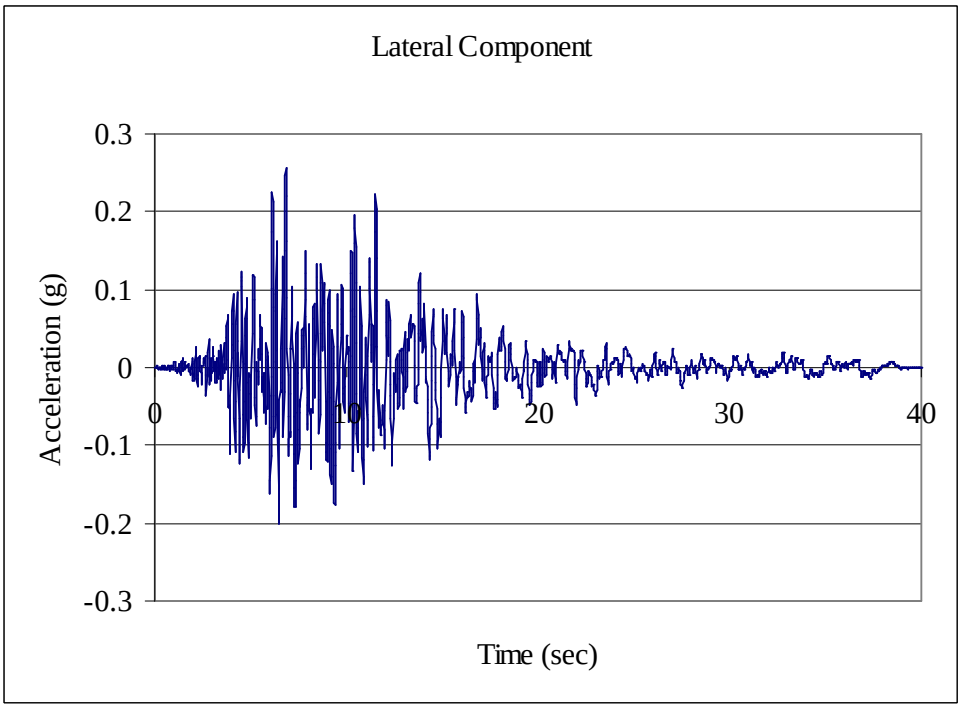

Fig. 4 Lateral component of Northridge earthquake record

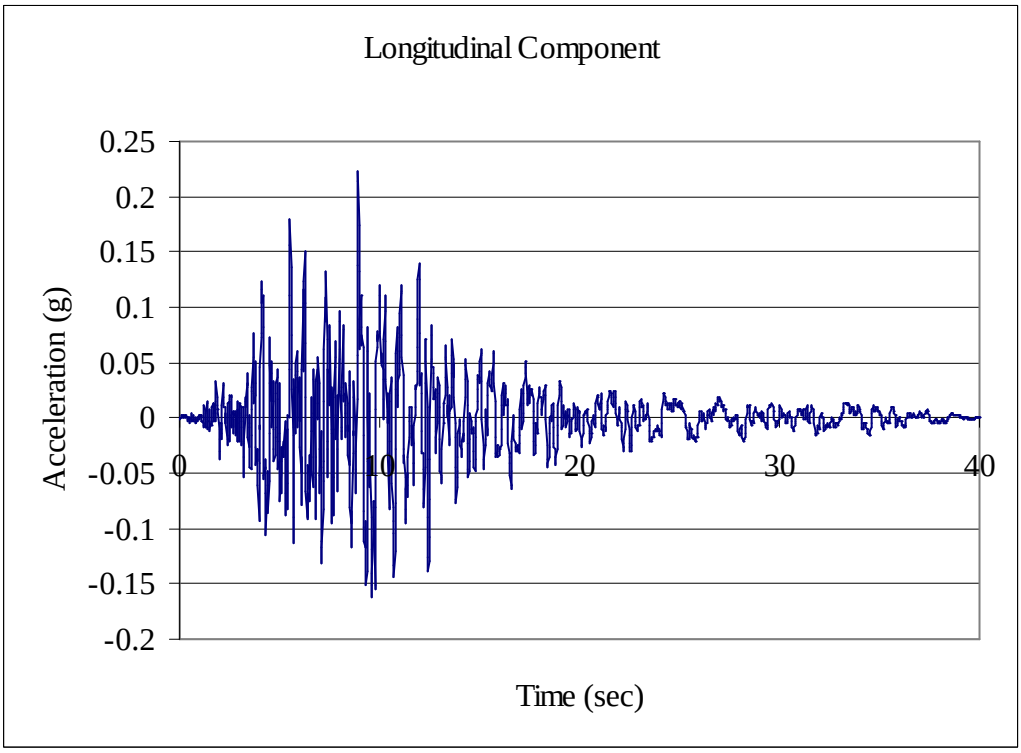

Fig. 5 Longitudinal component of Northridge earthquake record

Fig. 6 The aluminum tower and four cameras

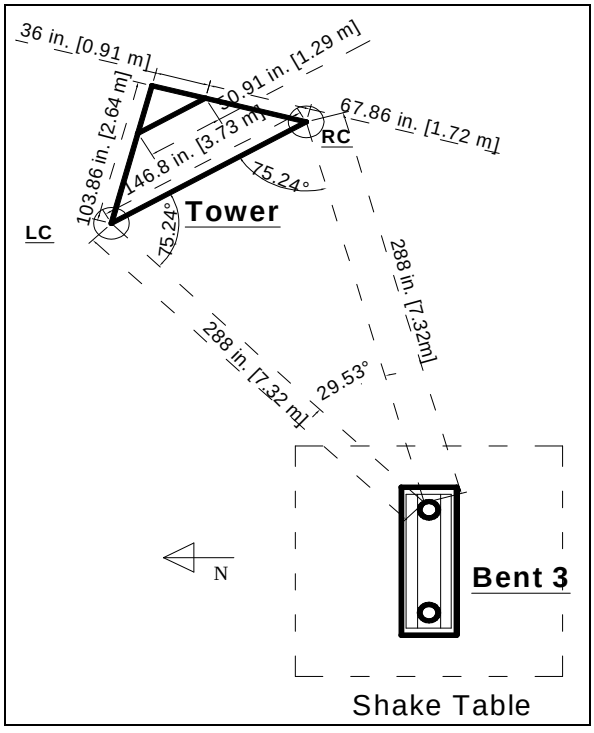

LC – Location of Left Camera

RC – Location of Right Camera

Fig. 7 Location of the Bent 3 east column and the aluminum tower

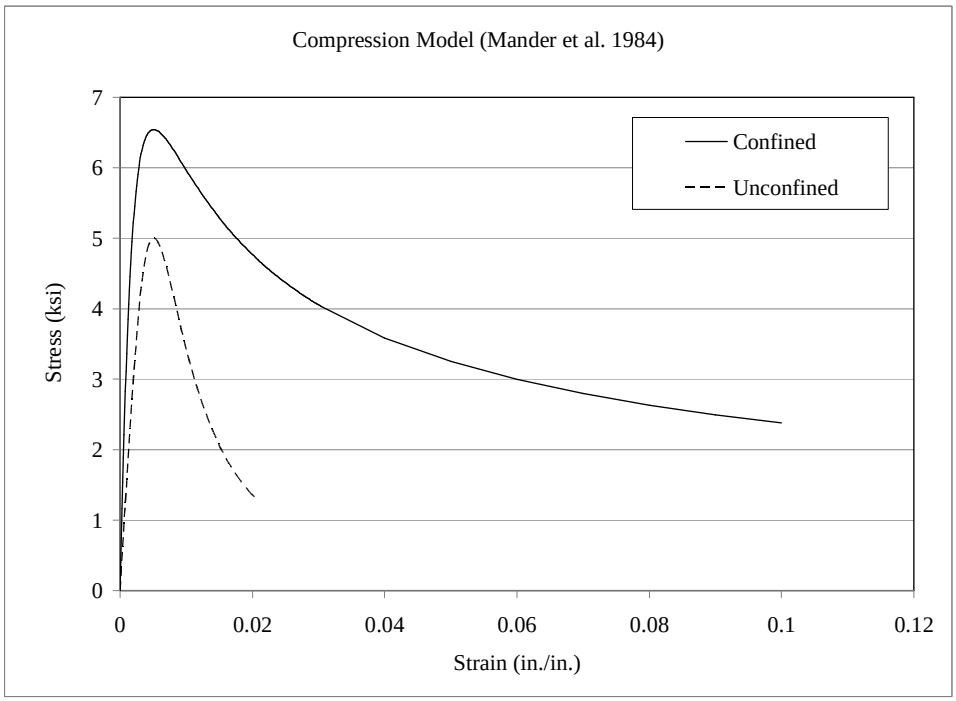

Fig. 8 Concrete compression model

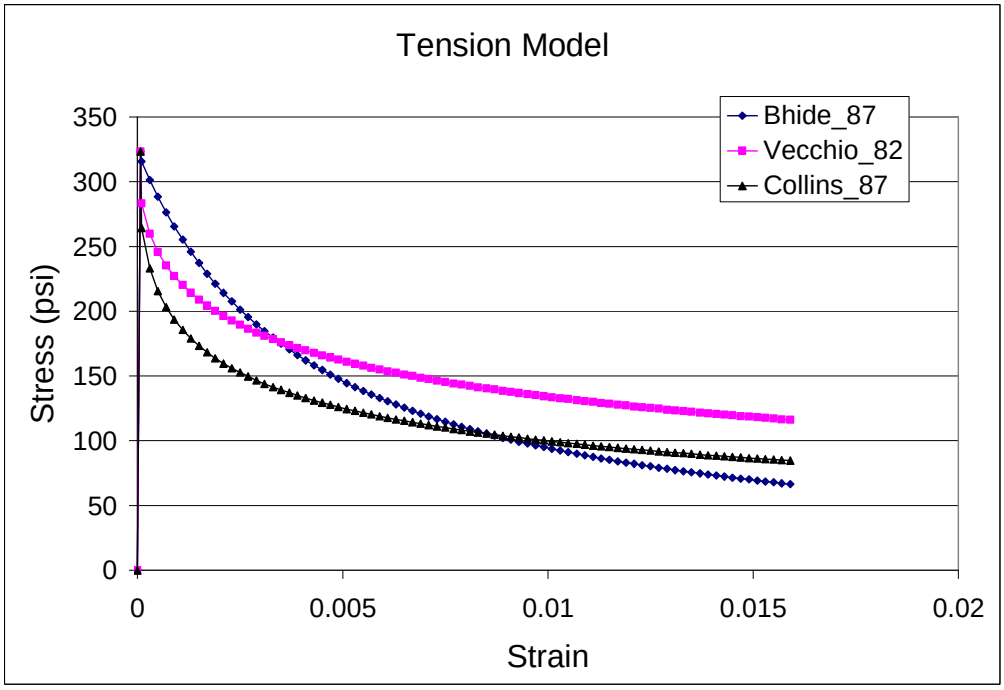

Fig. 9 Concrete tension model

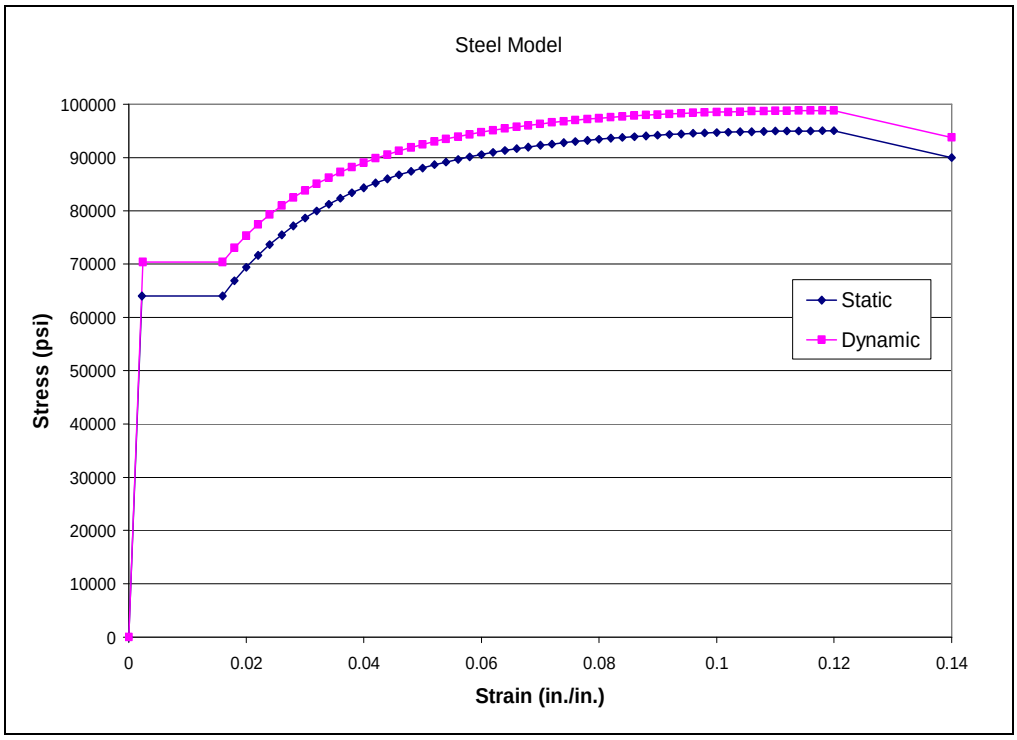

Fig. 10 Stress-strain relationship for longitudinal reinforcement under monotonic tension loading

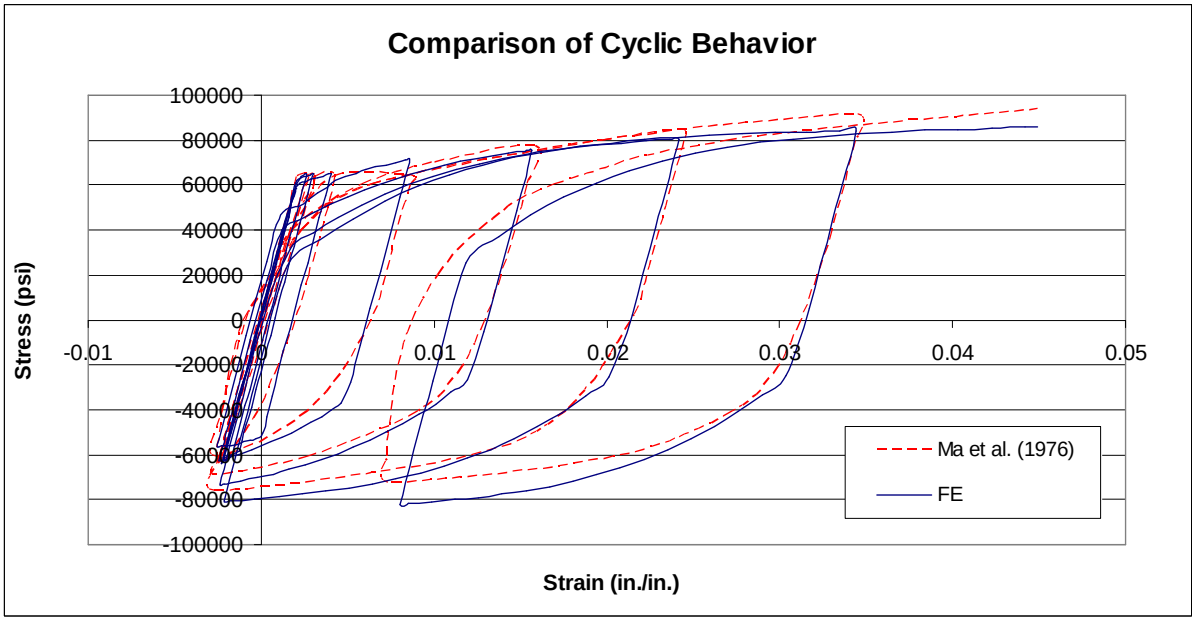

Fig. 11 Comparison between computed and measured stress-strain response of reinforcing steel subjected to reversed cyclic loading (Experimental data from Ma et al. (1976))

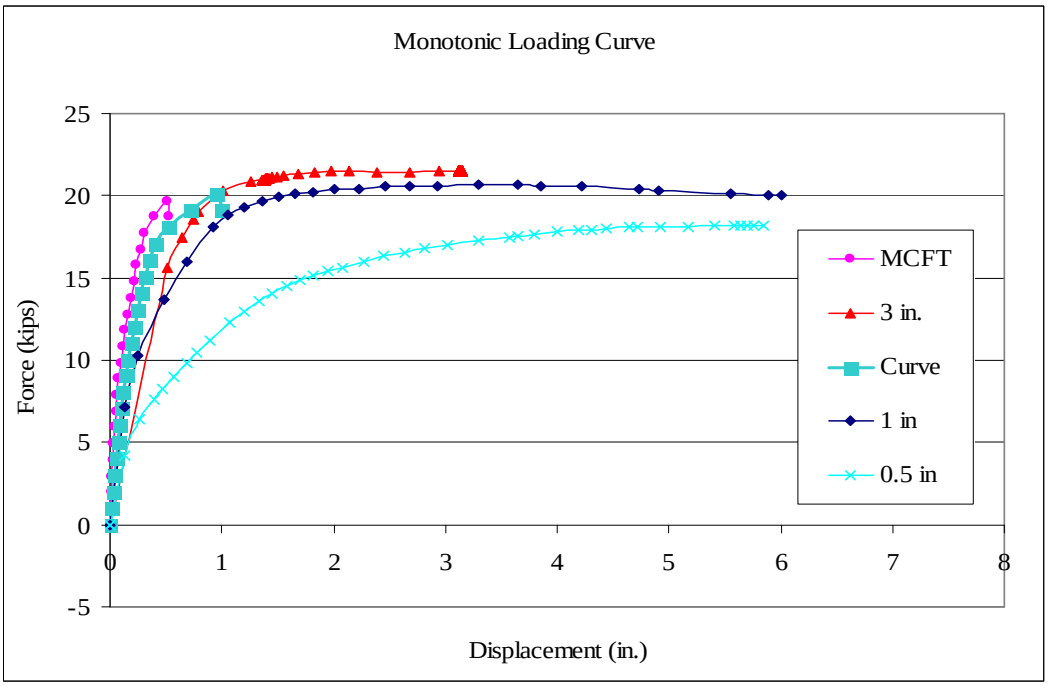

Fig. 12 Load-deflection curves for monotonic loading analysis of FE model of the bridge column with various mesh densities

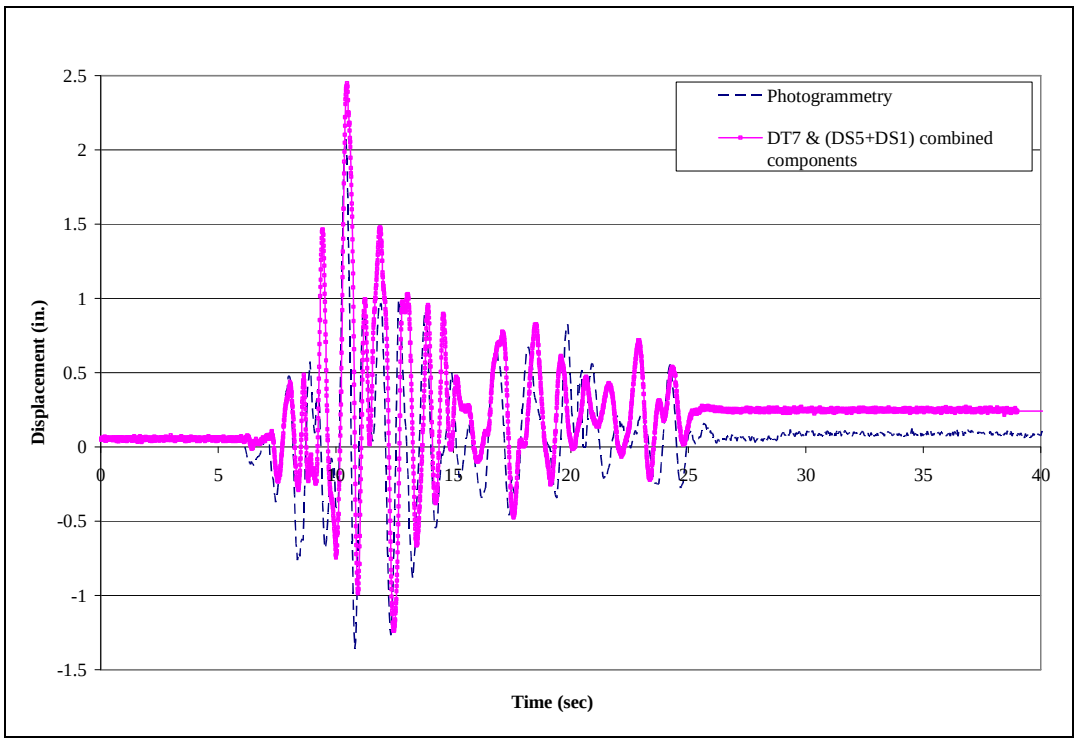

Fig. 13 Comparison between inferred lateral displacements from Photogrammetry analysis at Point 59 and measured data with displacement transducers

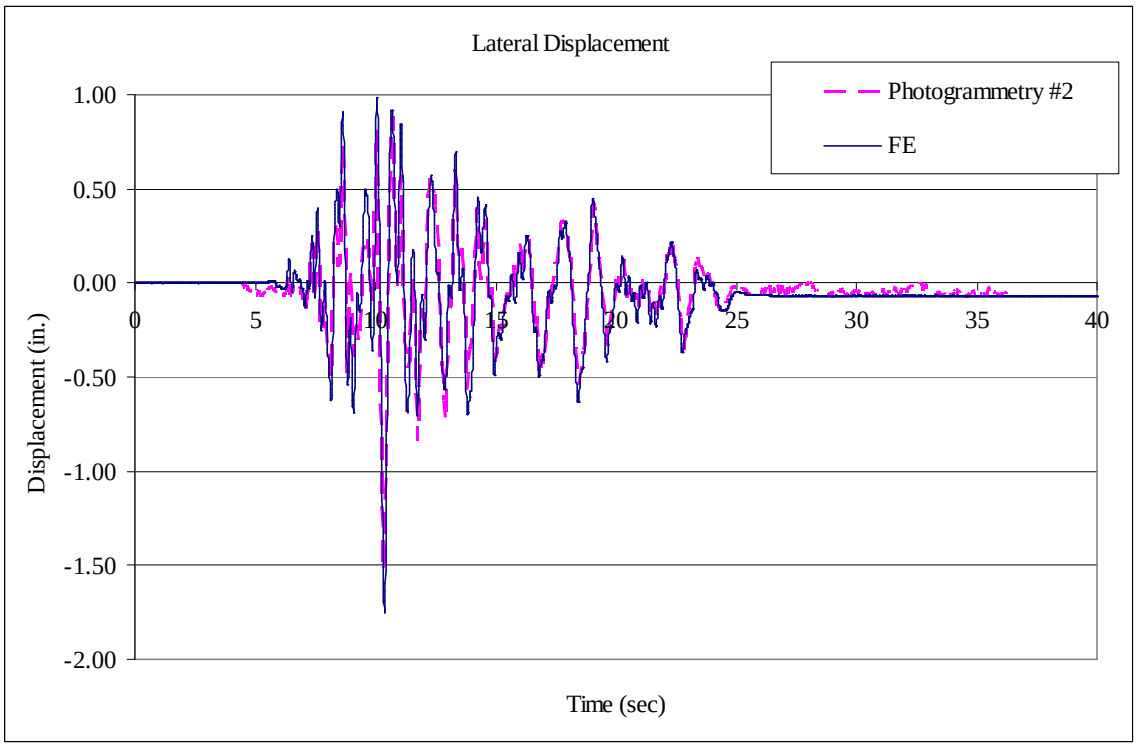

Fig. 14 Lateral displacement comparison between Point 2 of photogrammetry grid and FE analysis at the bottom hinging region

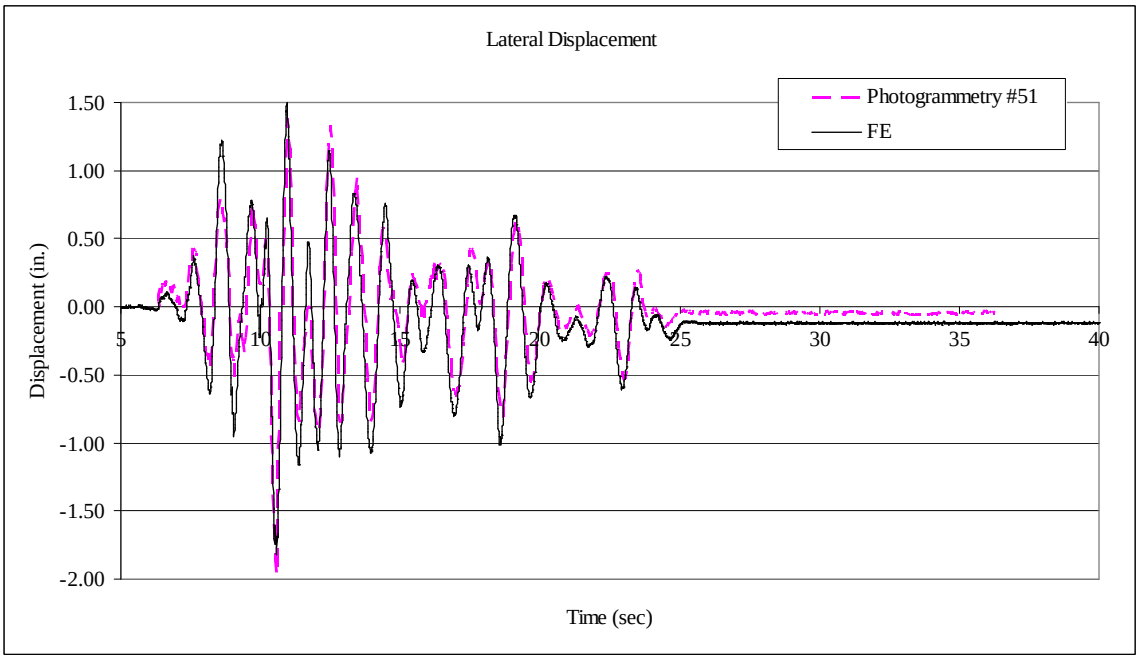

Fig. 15 Lateral displacement comparison between Point 51 of photogrammetry grid and FE analysis at the top hinging region

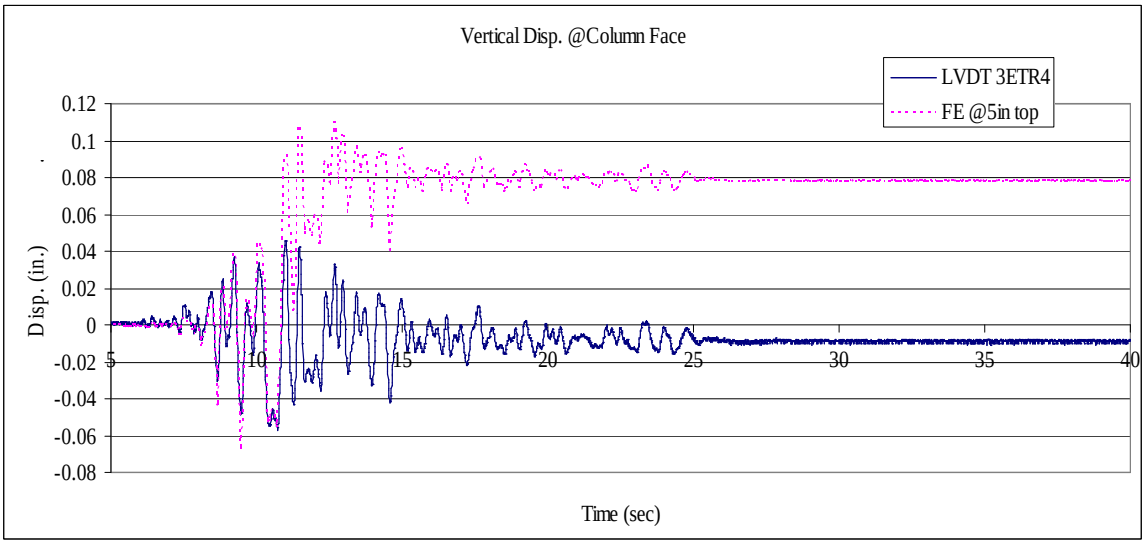

Fig. 16 Vertical displacement comparison between FE analysis result and LVDT measurements at the location of LVDT 3ETR4 (f_y=64 ksi)*

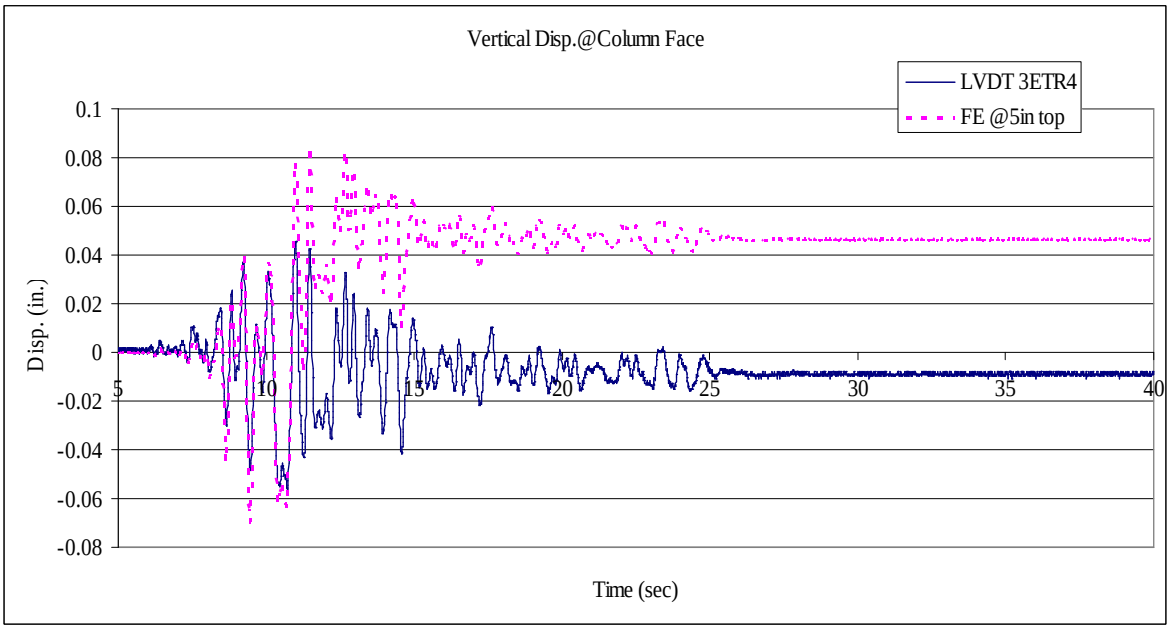

Fig. 17 Vertical displacement comparison between FE analysis result and LVDT measurements at the location of LVDT 3ETR4 (f_y=70 ksi) *

* Infinitely stiff cap beam, w_c =0.8 and w_t =1.0.

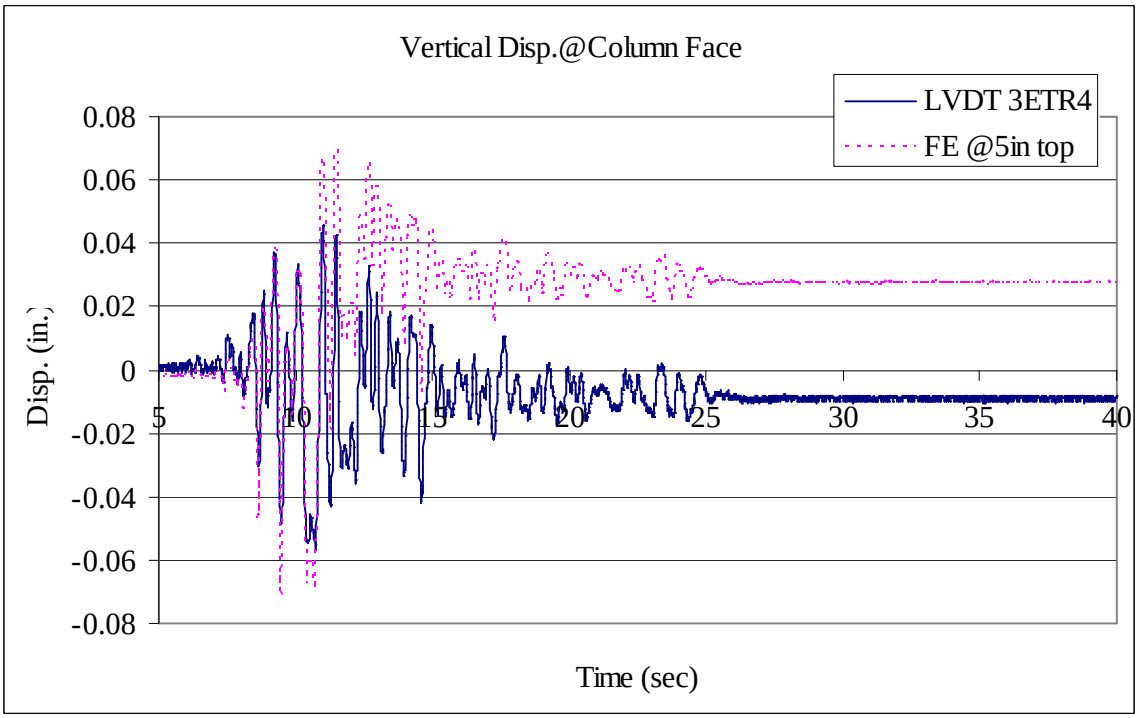

Fig. 18 Vertical displacement comparison between FE analysis result and LVDT measurements at the location of LVDT 3ETR4 (f_y=75 ksi) *

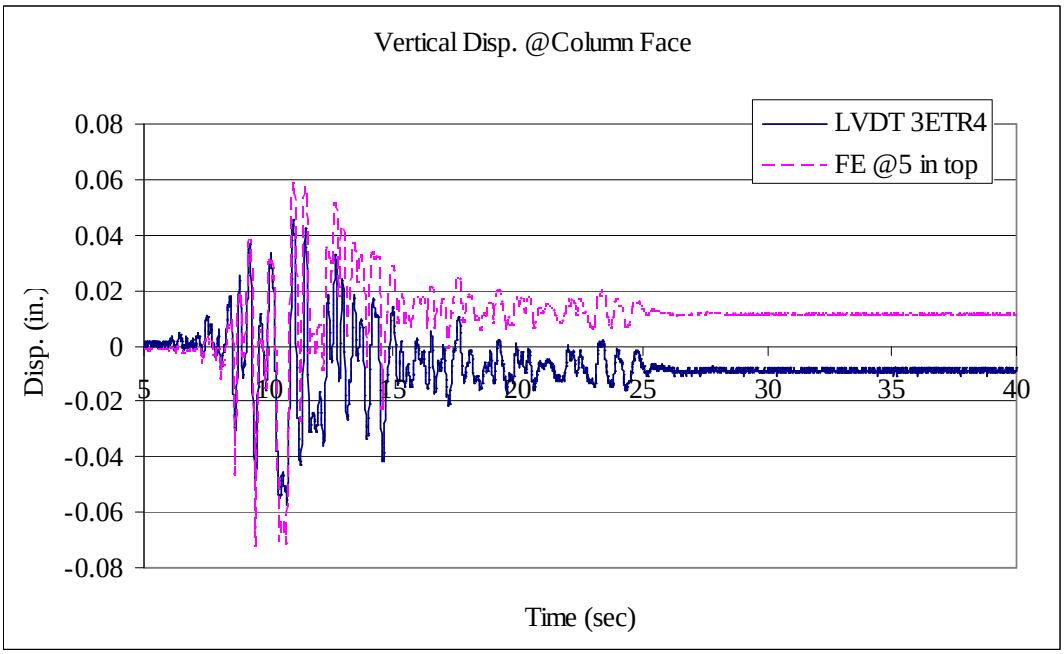

Fig. 19 Vertical displacement comparison between FE analysis result and LVDT measurements at the location of LVDT 3ETR4 (f_y=80 ksi) *

* Infinitely stiff cap beam, w_c =0.8 and w_t =1.0.

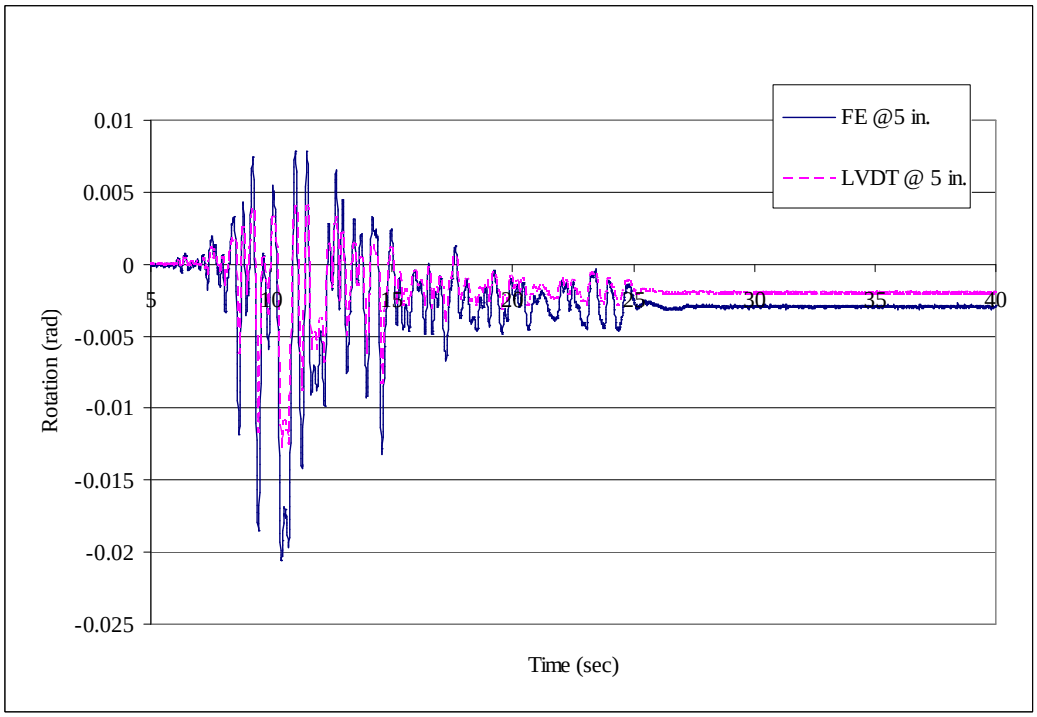

Fig. 20 The cross-sectional rotation comparison between FE analysis result and LVDT measurements at the location of LVDT 3ETR3 and 3ETR4 (f_y=64 ksi)*

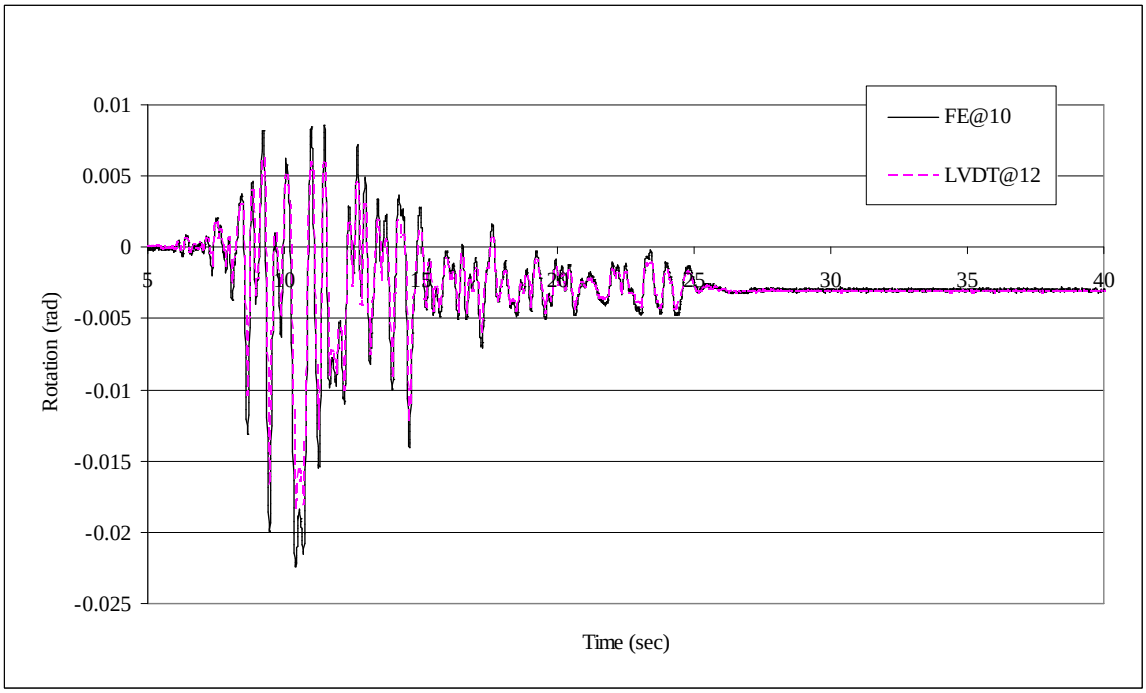

Fig. 21 The cross-sectional rotation comparison between FE analysis result and LVDT measurements at the location of LVDT 3ETR5 and 3ETR6 (f_y=64 ksi) *

* Infinitely stiff cap beam, w_c =0.8 and w_t =1.0.

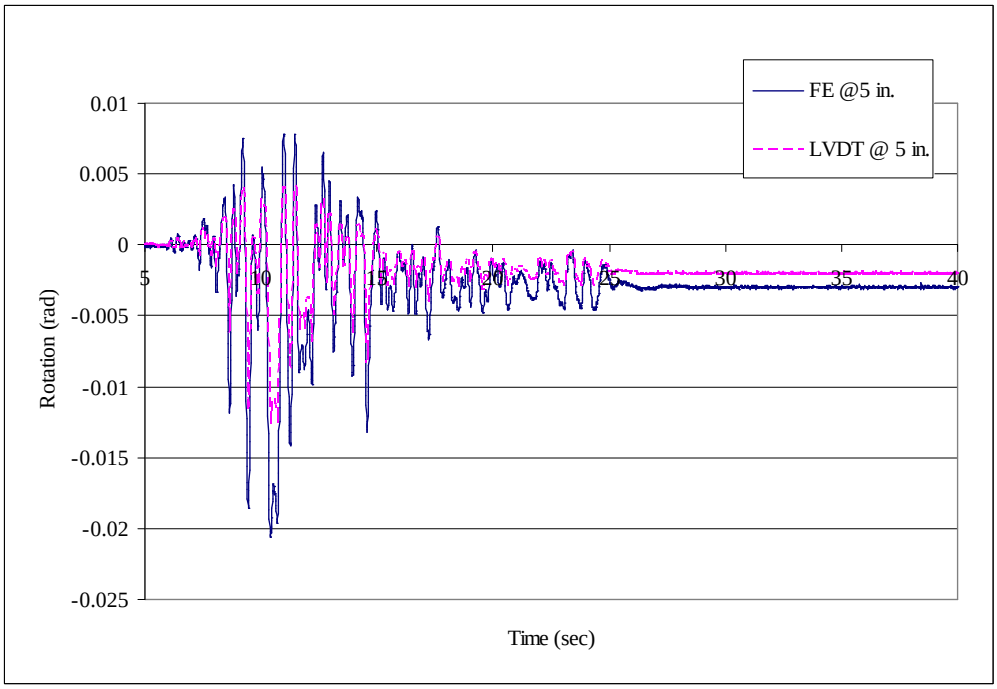

Fig. 22 The cross-sectional rotation comparison between FE analysis result and LVDT measurements at the location of LVDT 3ETR3 and 3ETR4 (f_y=70 ksi) *

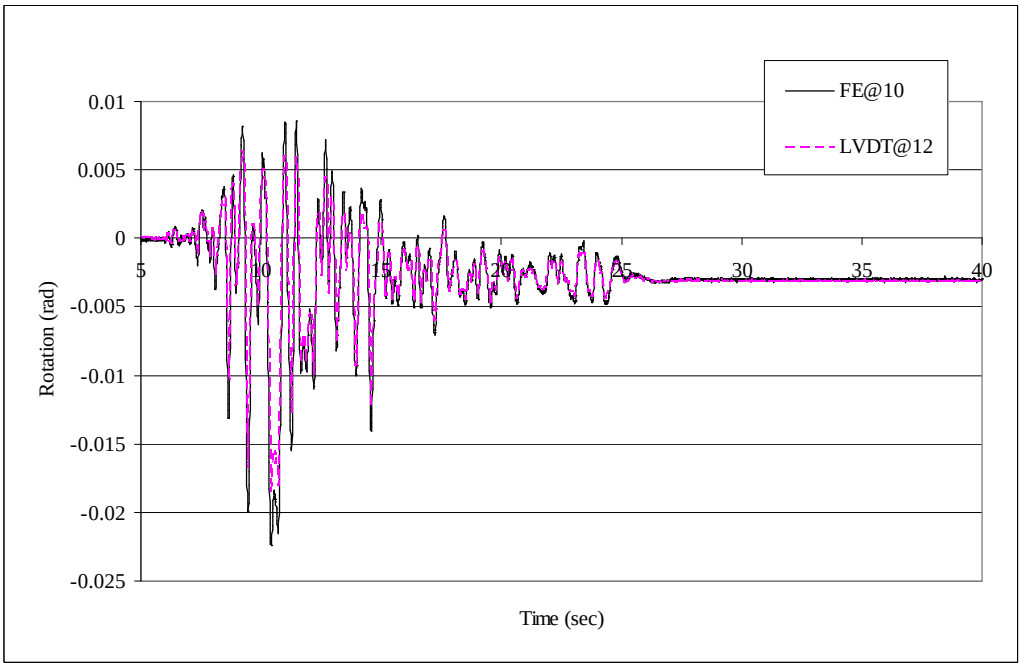

Fig. 23 The cross-sectional rotation comparison between FE analysis result and LVDT measurements at the location of LVDT 3ETR5 and 3ETR6 (f_y=70 ksi) *

* Infinitely stiff cap beam, w_c =0.8 and w_t =1.0.

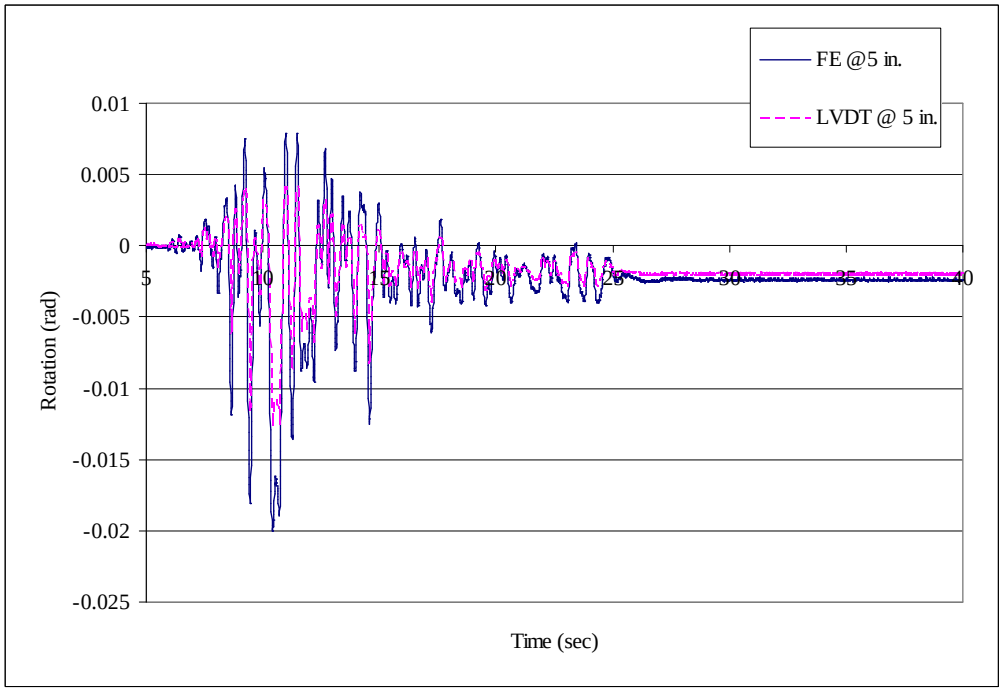

Fig. 24 The cross-sectional rotation comparison between FE analysis result and LVDT measurements at the location of LVDT 3ETR3 and 3ETR4 (f_y=75 ksi) *

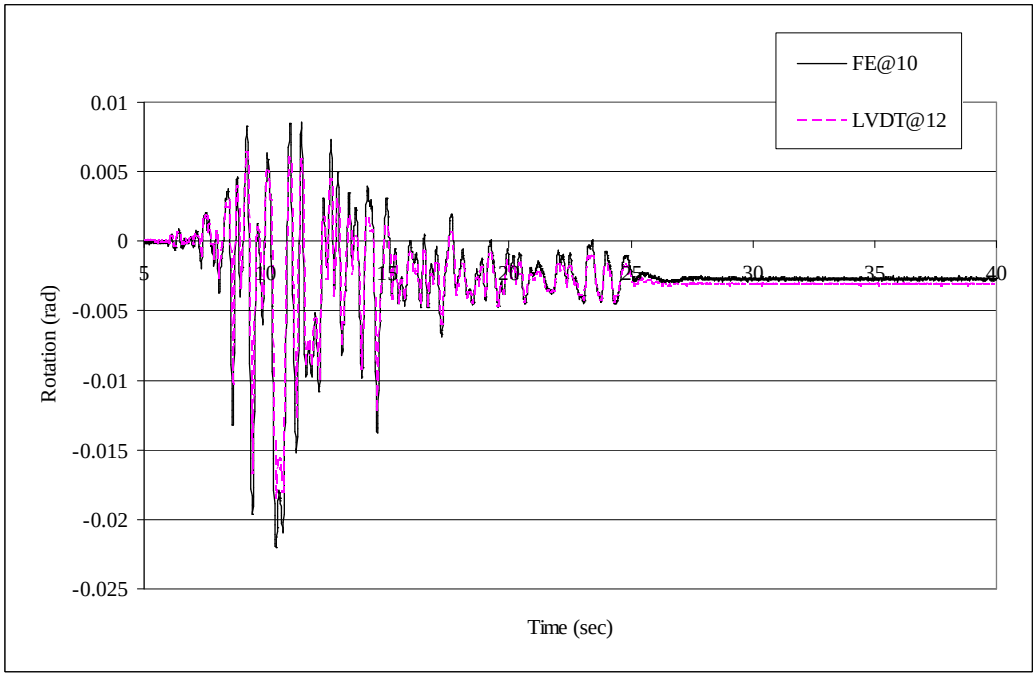

Fig. 25 The cross-sectional rotation comparison between FE analysis result and LVDT measurements at the location of LVDT 3ETR5 and 3ETR6 (f_y=75 ksi) *

* Infinitely stiff cap beam, w_c =0.8 and w_t =1.0.

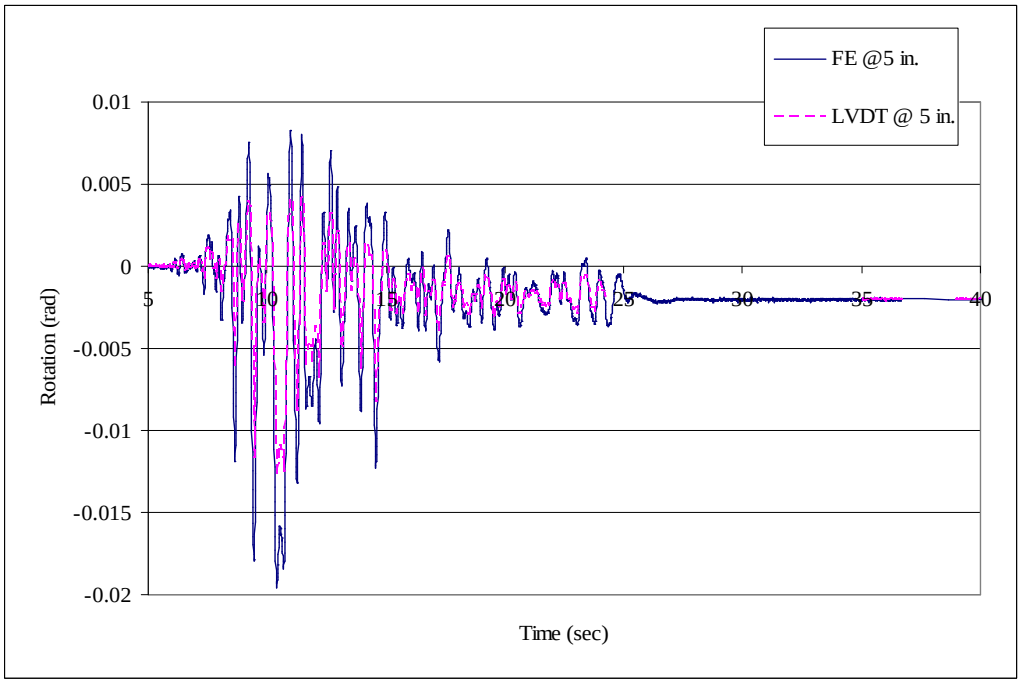

Fig. 26 The cross-sectional rotation comparison between FE analysis result and LVDT measurements at the location of LVDT 3ETR3 and 3ETR4 (f_y=80 ksi) *

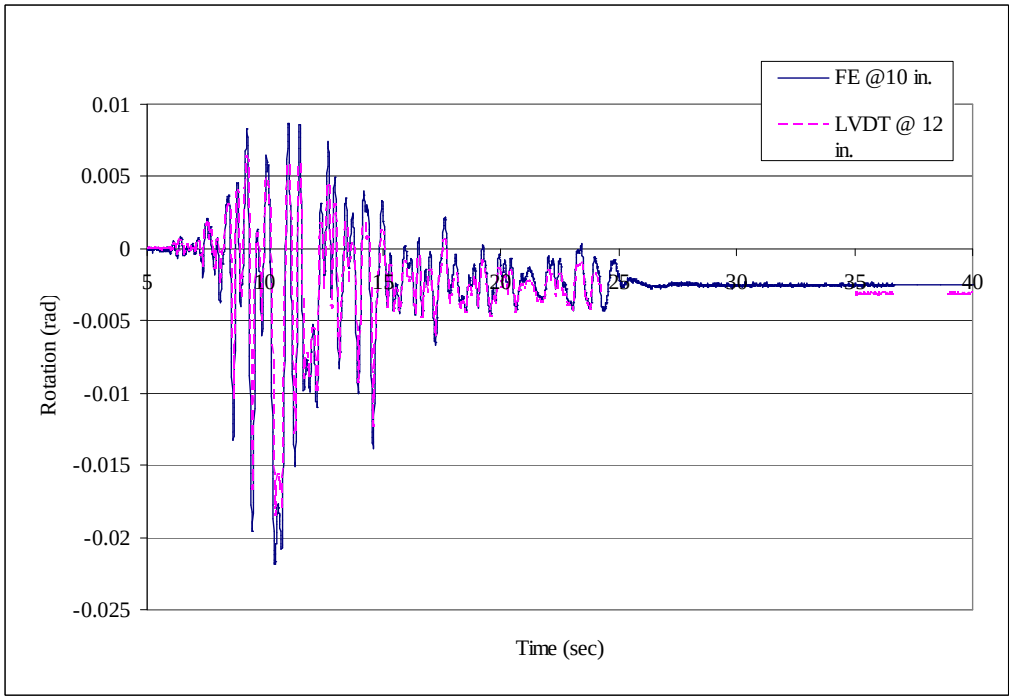

Fig. 27 The cross-sectional rotation comparison between FE analysis result and LVDT measurements at the location of LVDT 3ETR5 and 3ETR6 (f_y=80 ksi) *

* Infinitely stiff cap beam, w_c =0.8 and w_t =1.0.

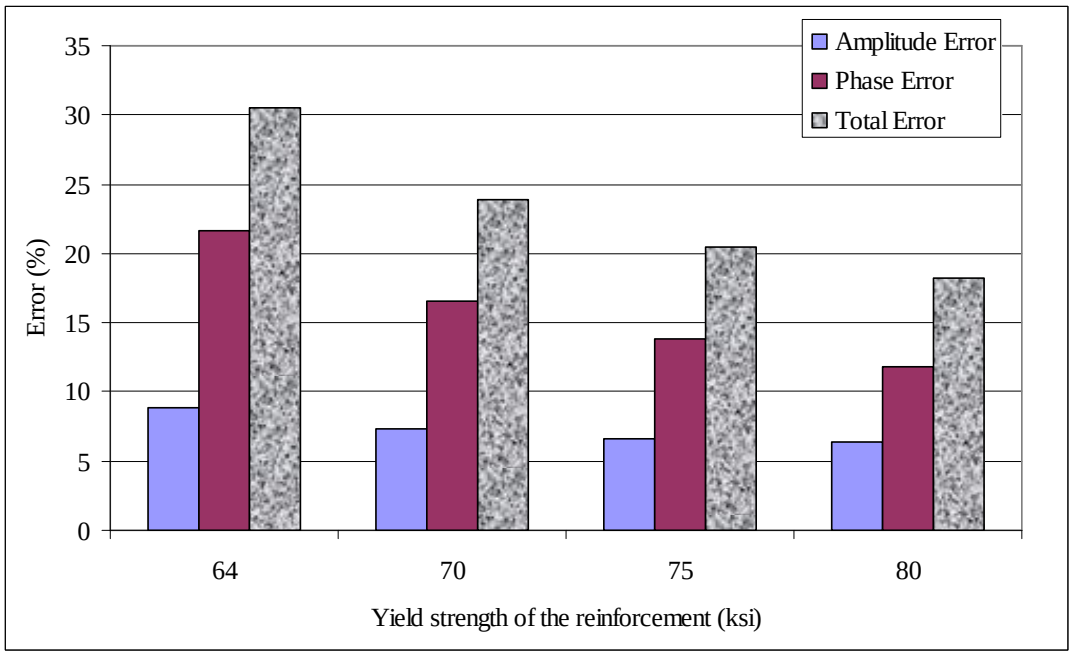

Fig. 28 The comparison of FDE index errors for different yield strength of steel (FE vs. LVDT vertical displacement measurements)

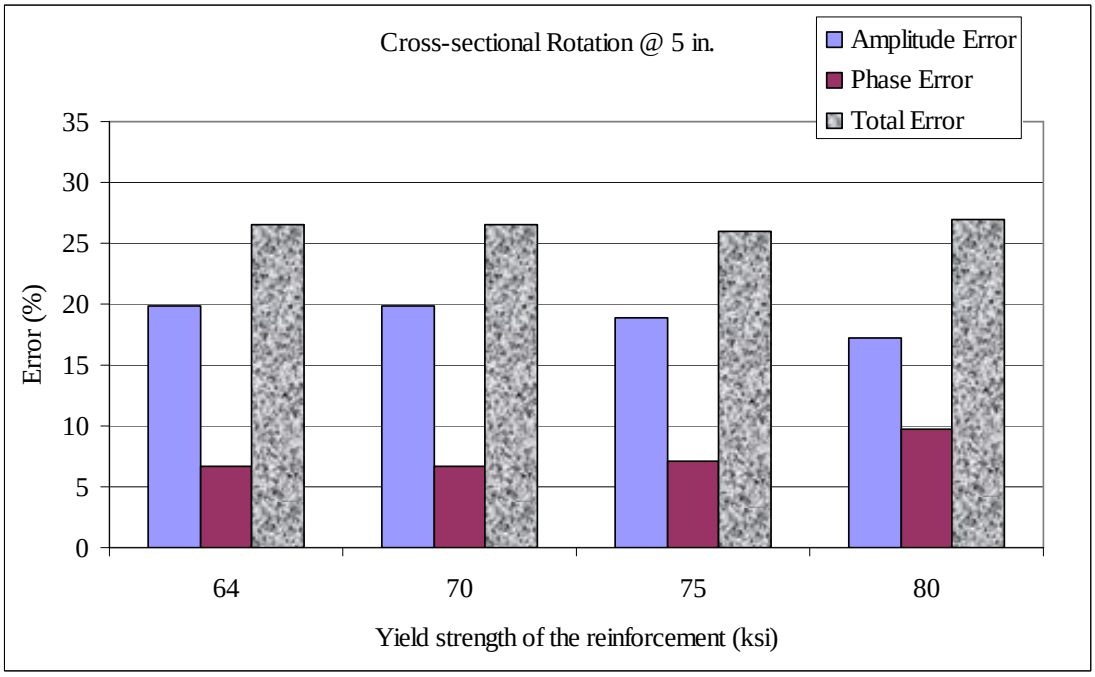

Fig. 29 The comparison of FDE index errors for cross-sectional rotation at 5 in. below cap beam using different yield strength of steel (FE vs. LVDT vertical displacement measurements)

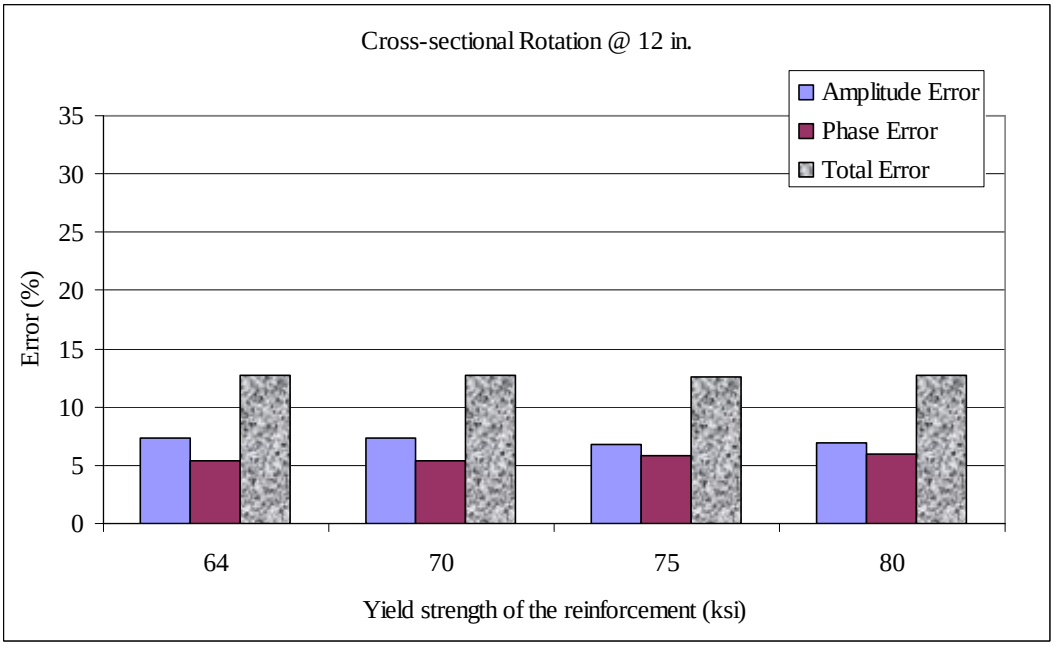

Fig. 30 The comparison of FDE index errors for cross-sectional rotation at 12 in. below cap beam using different yield strength of steel (FE vs. LVDT vertical displacement measurements)

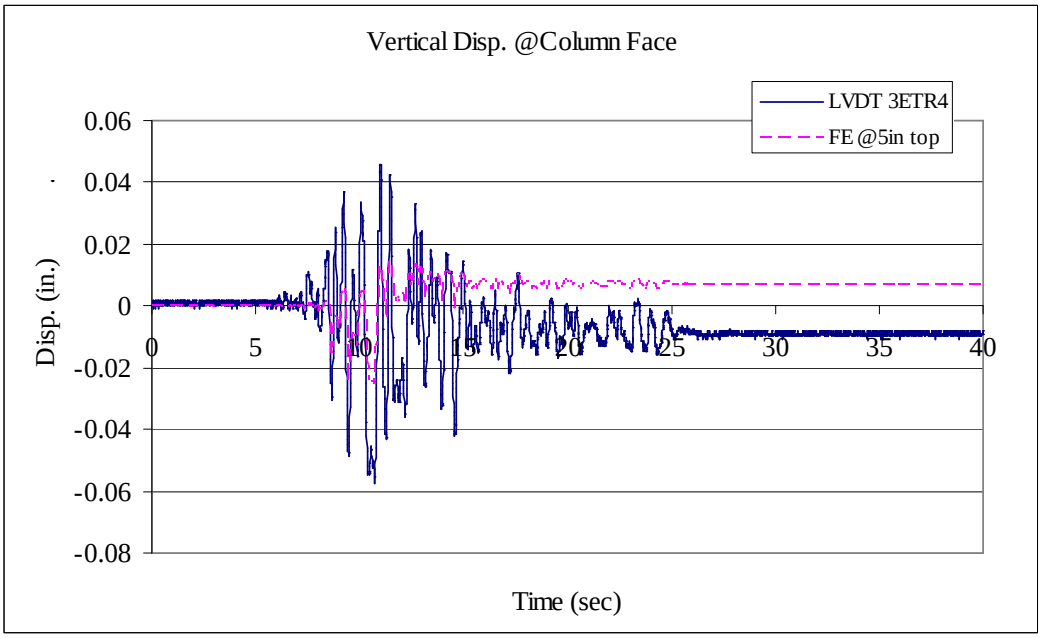

Fig. 31 Vertical displacement comparison between FE analysis result and LVDT measurements at the location of LVDT 3ETR4 for K=1*10^8 lb-in. (f_y=68 ksi)*

* Linear-elastic rotational spring, w_c =0.8 and w_t =1.0.

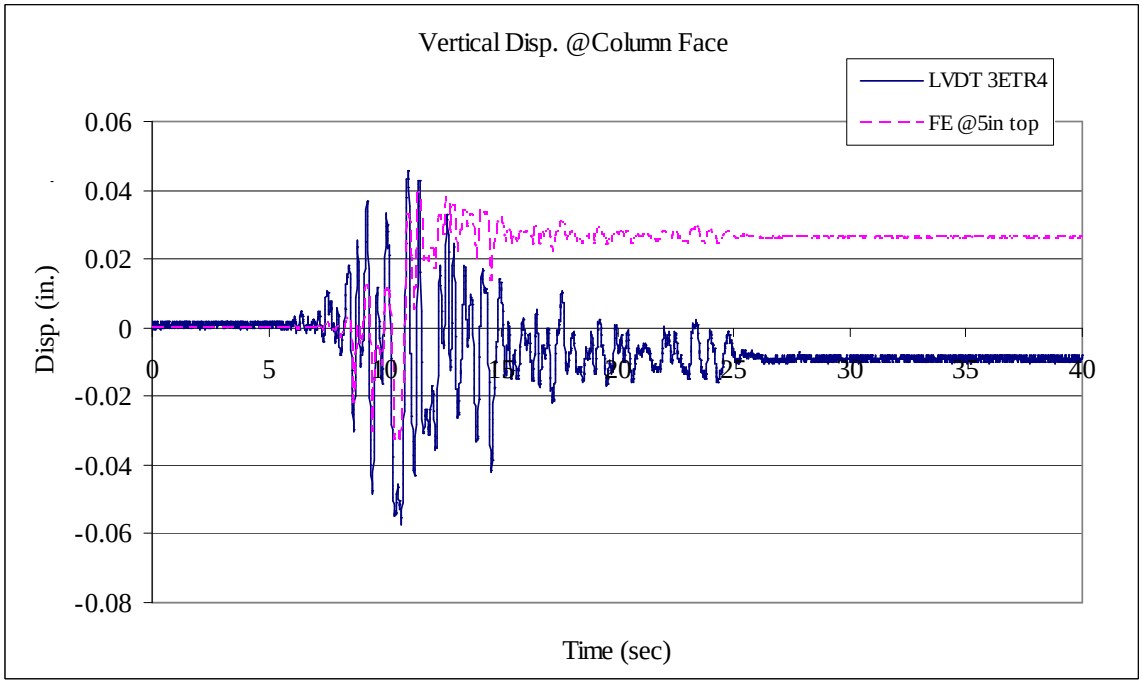

Fig. 32 Vertical displacement comparison between FE analysis result and LVDT measurements for K=1.5*10^8 lb-in. (f_y=68 ksi) *

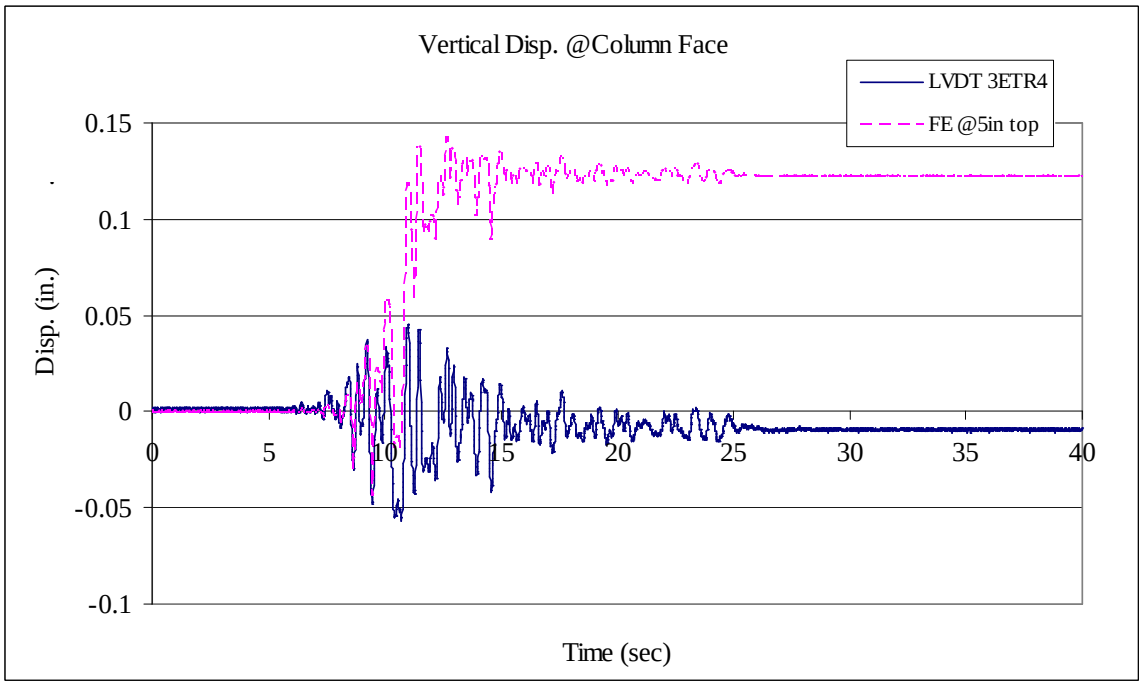

Fig. 33 Vertical displacement comparison between FE analysis result and LVDT measurements for K=5*10^8 lb-in. (f_y=68 ksi) *

* Linear-elastic rotational spring with 10^8 lb-in. capacity, w_c =0.8 and w_t =1.0.

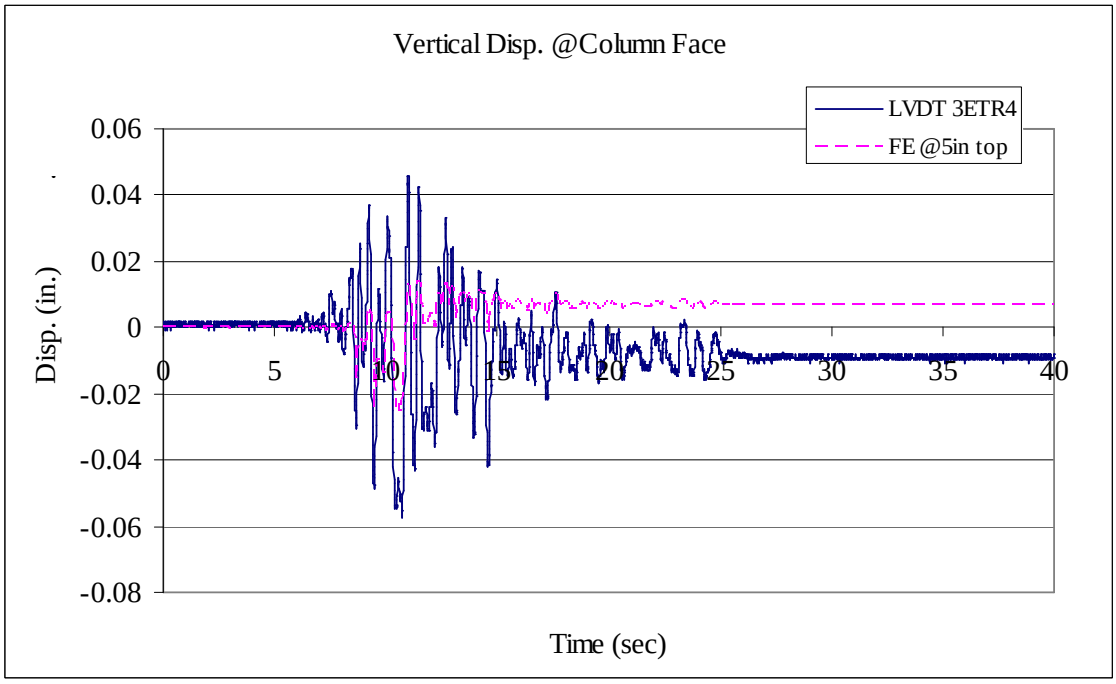

Fig. 34 Vertical displacement comparison between FE analysis result and LVDT measurements for K=1*10^8 lb-in. (f_y=75 ksi) *

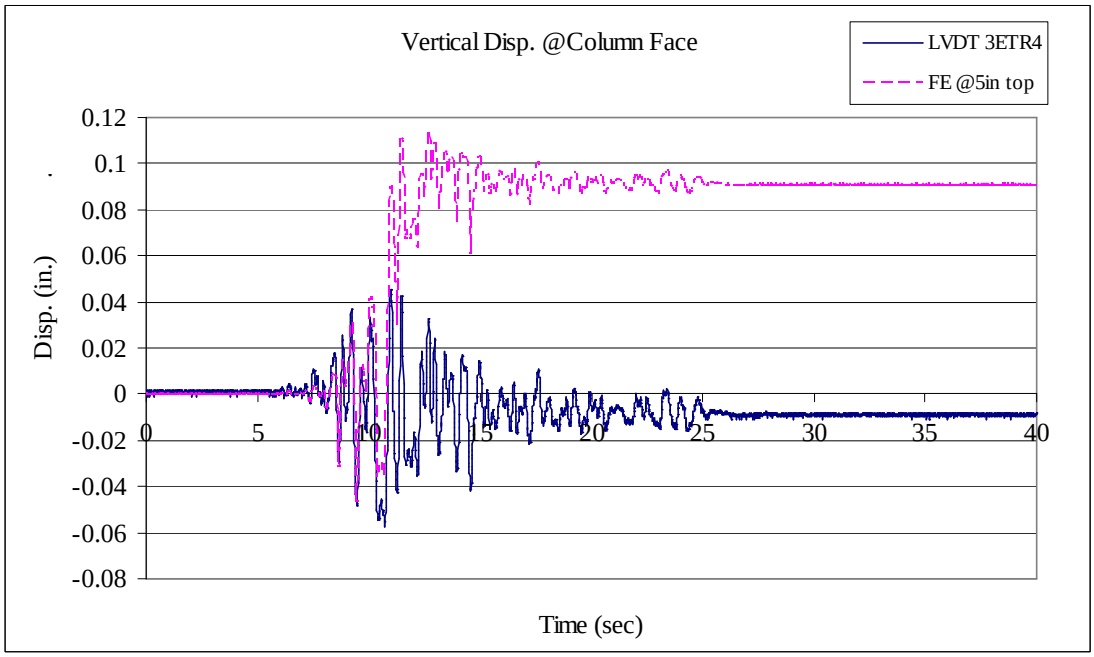

Fig. 35 Vertical displacement comparison between FE analysis result and LVDT measurements for K=5*10^8 lb-in. (f_y=75 ksi) *

* Linear-elastic rotational spring, w_c =0.8 and w_t =1.0.

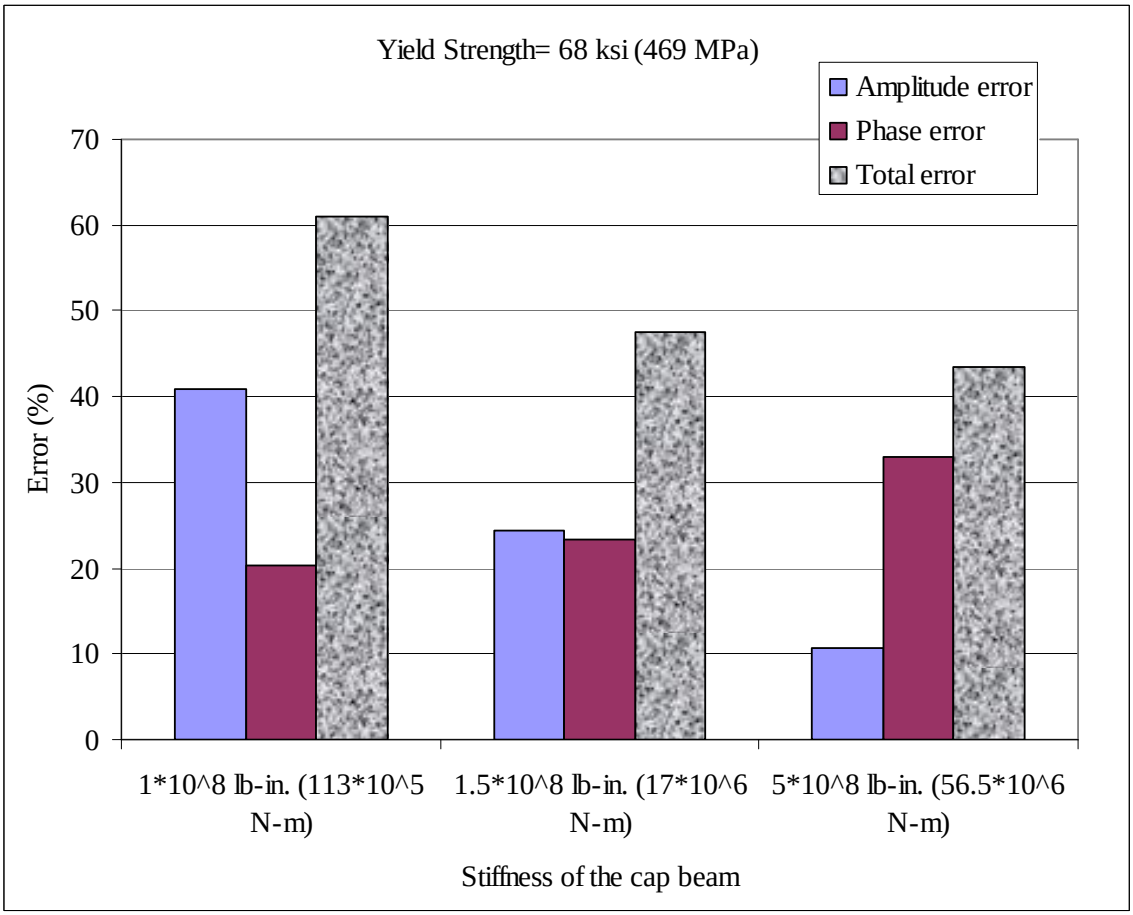

Fig. 36 The comparison of FDE index errors for different stiffness of the cap beam (FE vs. LVDT vertical displacement measurements) (f_y=68 ksi) *

* Linear-elastic rotational spring, w_c =0.8 and w_t =1.0.

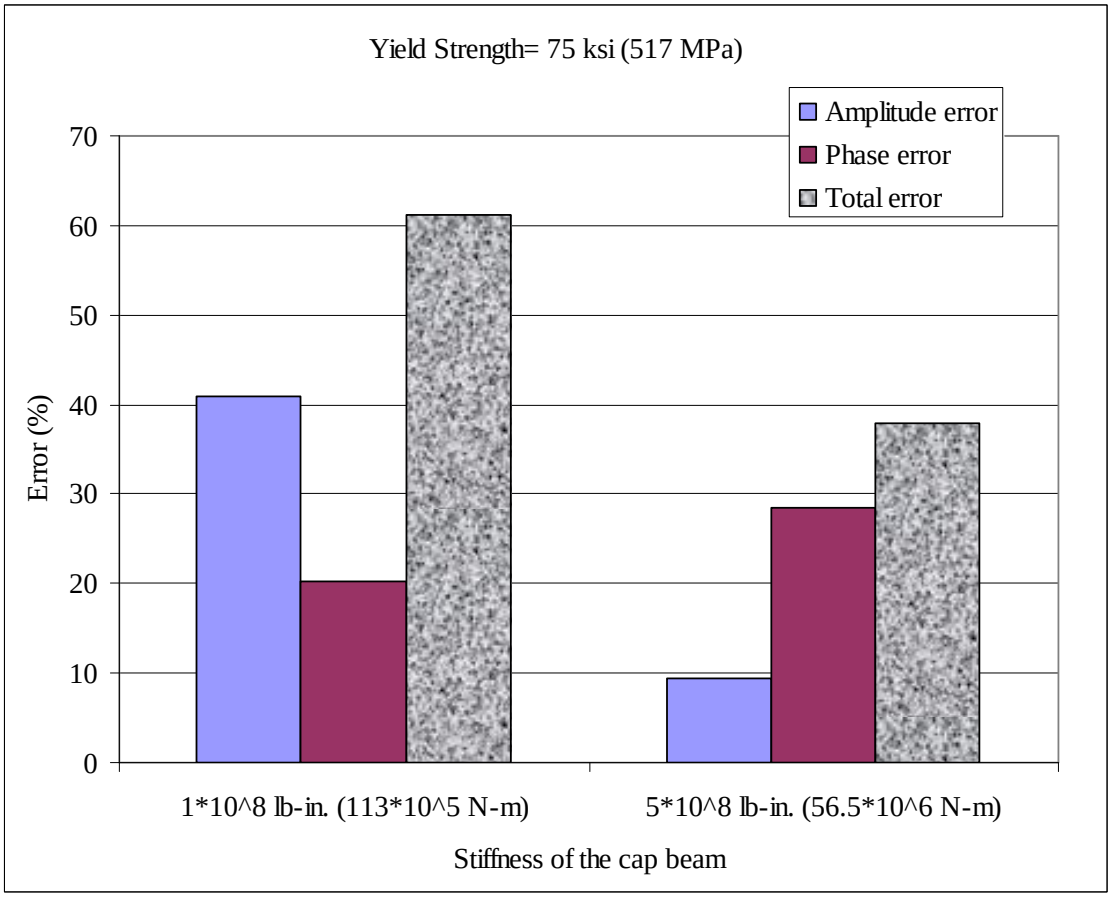

Fig. 37 The comparison of FDE index errors for different stiffness of the cap beam (FE vs. LVDT vertical displacement measurements) (f_y=75 ksi) *

* Linear-elastic rotational spring, w_c =0.8 and w_t =1.0.

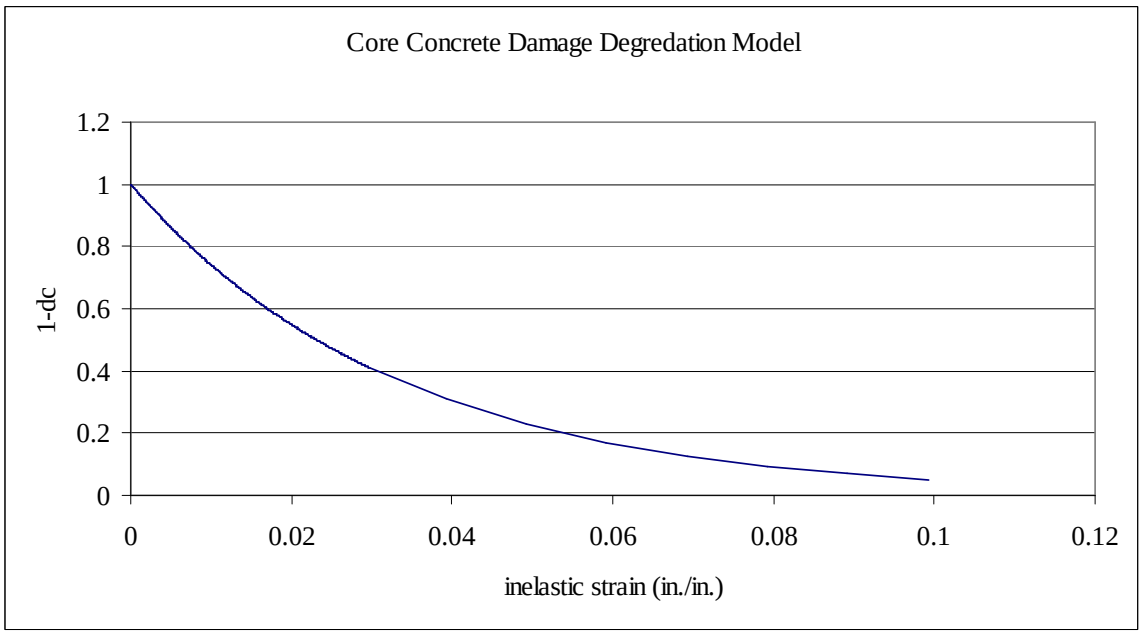

Fig. 38 The compression stiffness degradation model for core concrete of the bridge column

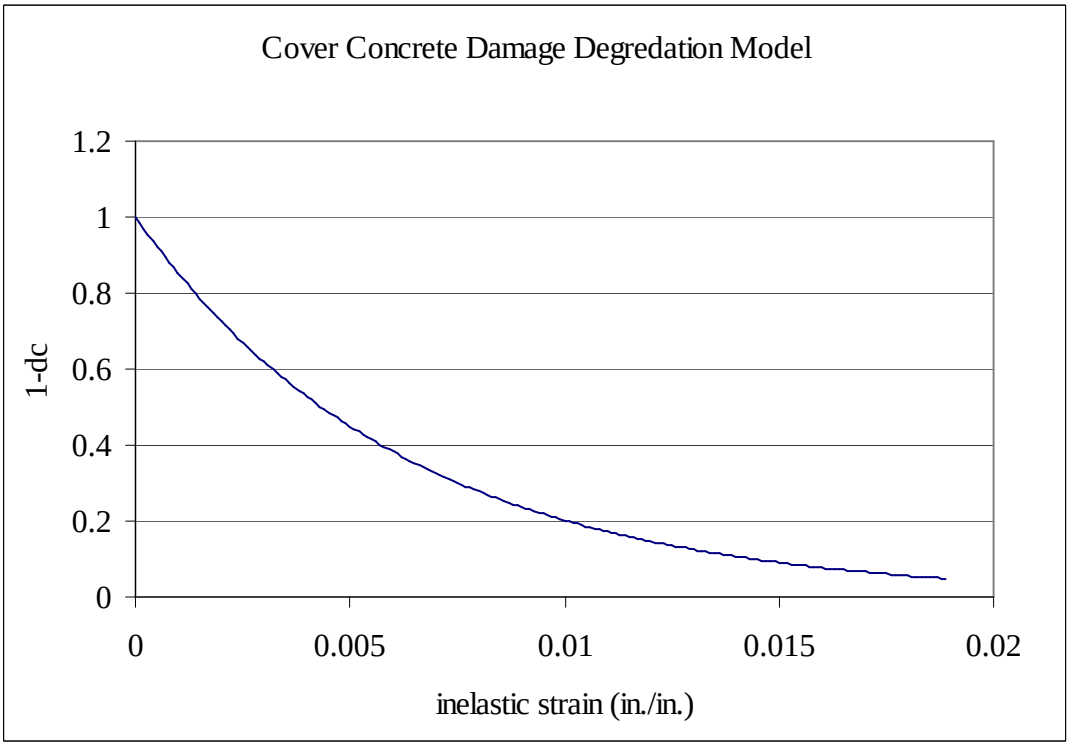

Fig. 39 The compression stiffness degradation model for cover concrete of the bridge column

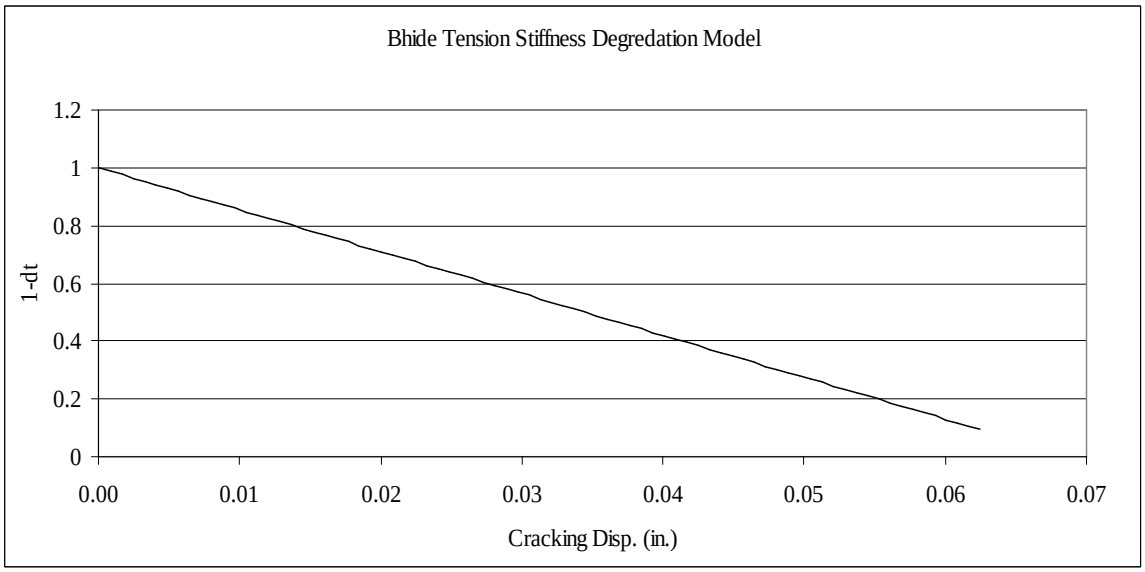

Fig. 40 The tension stiffness degradation model for core and cover concrete of the bridge column

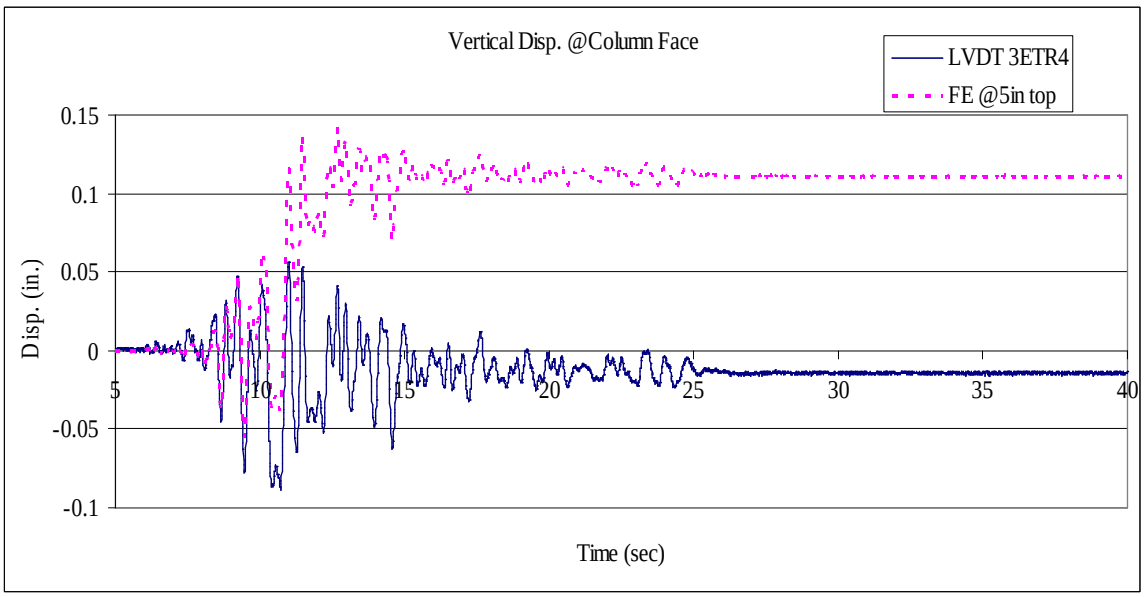

Fig. 41 Vertical displacement comparison between FE analysis result and LVDT measurements for w_c=0.5, w_t= 0*

* Infinitely stiff cap beam.

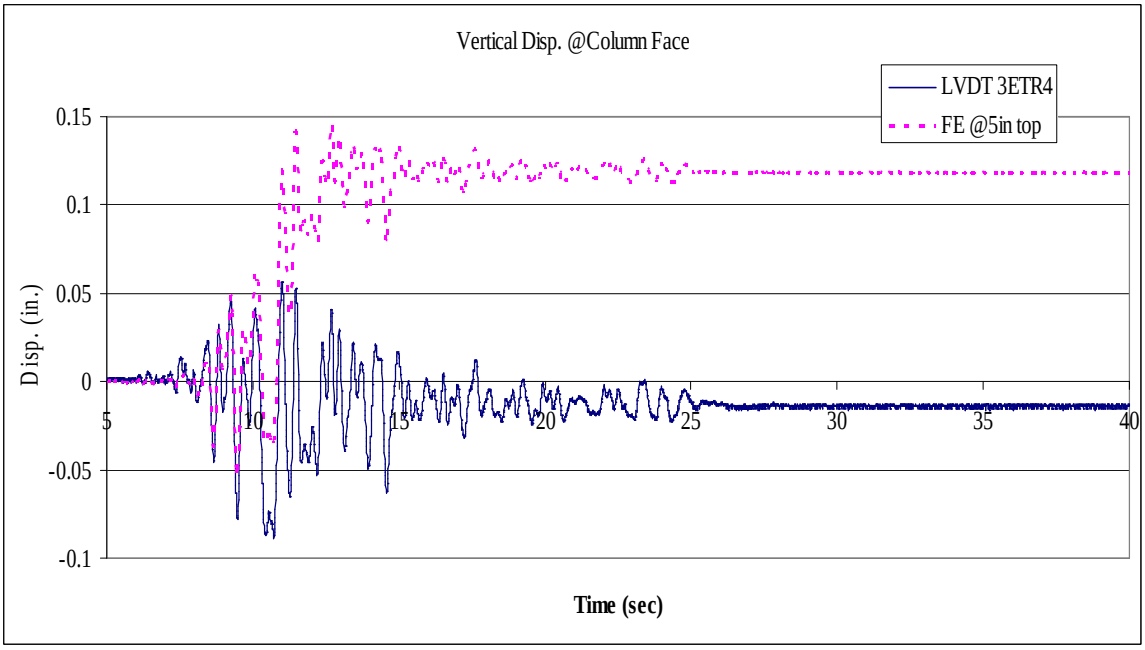

Fig. 42 Vertical displacement comparison between FE analysis result and LVDT measurements for w_c=0.8, w_t= 0 *

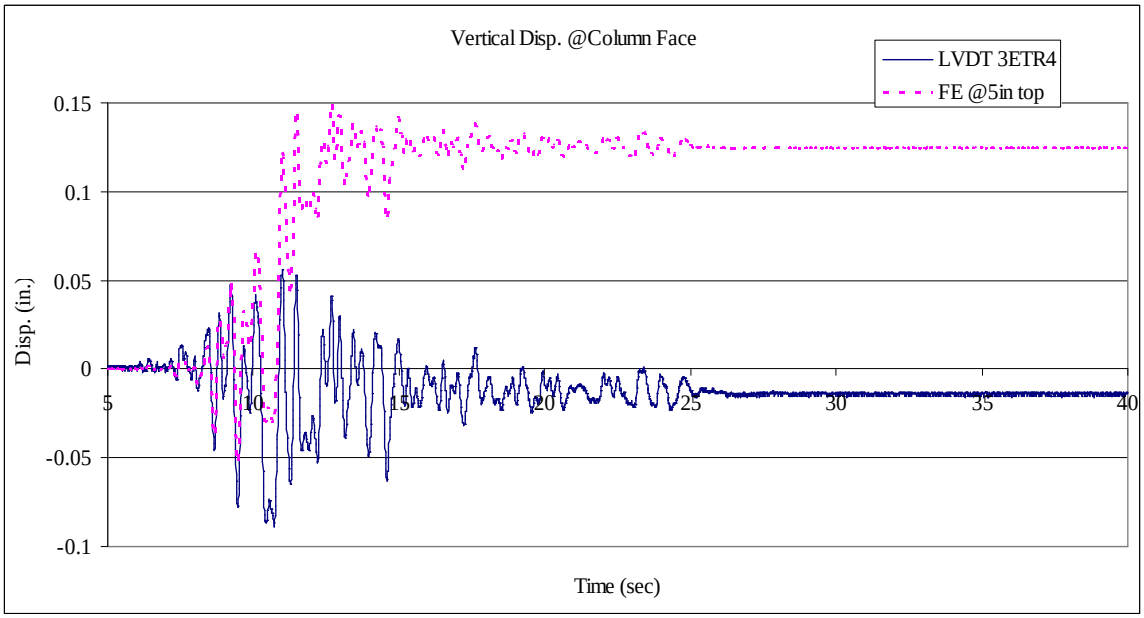

Fig. 43 Vertical displacement comparison between FE analysis result and LVDT measurements for w_c=1, w_t= 0.8*

* Infinitely stiff cap beam.

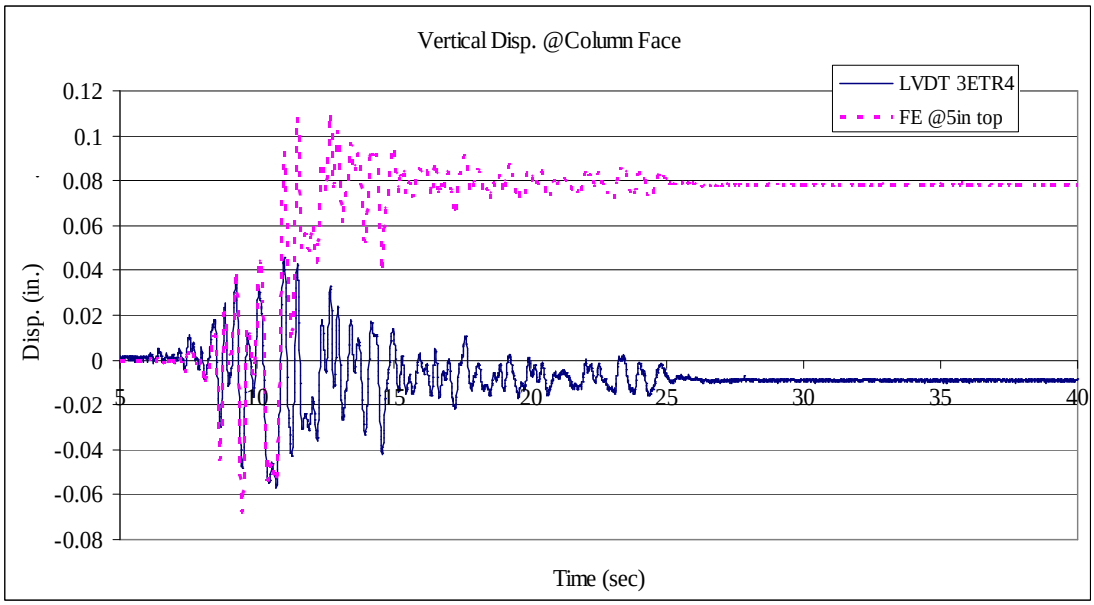

Fig. 44 Vertical displacement comparison between FE analysis result and LVDT measurements for w_c=0.8, w_t= 1*

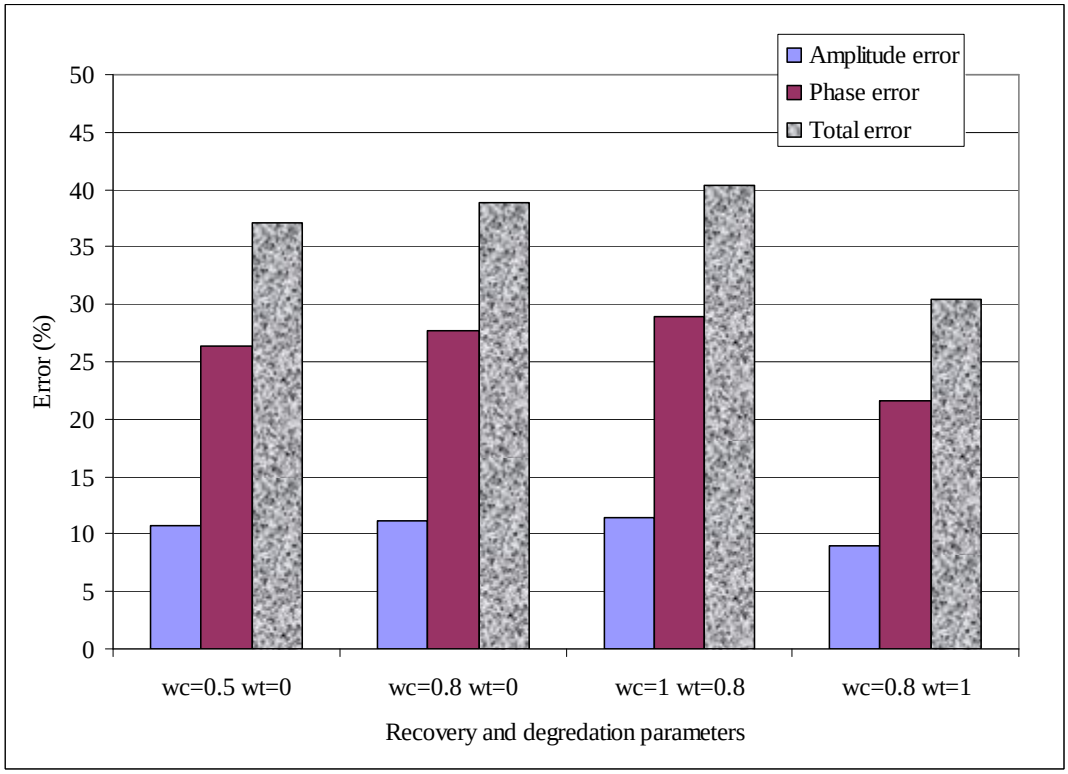

Fig. 45 The comparison of FDE index errors for different recovery and degradation parameters (FE vs. LVDT vertical displacement measurements) *

* Infinitely stiff cap beam.

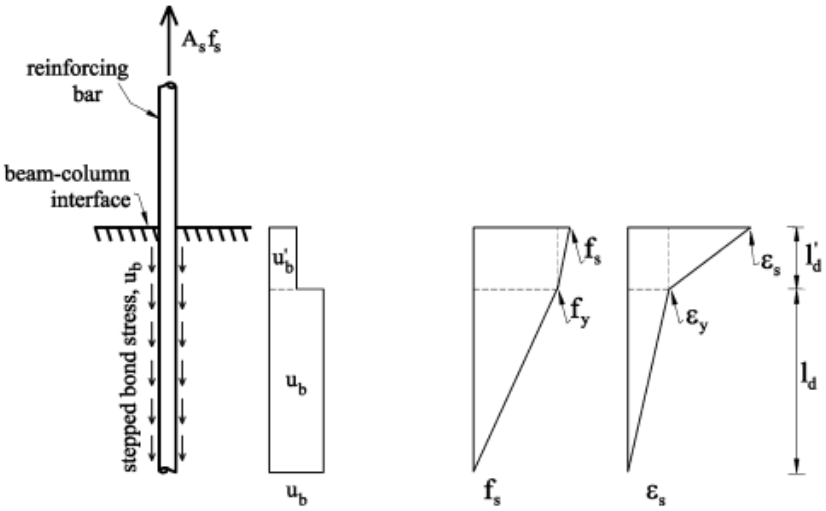

Fig. 46 Column deformations due to bar slip

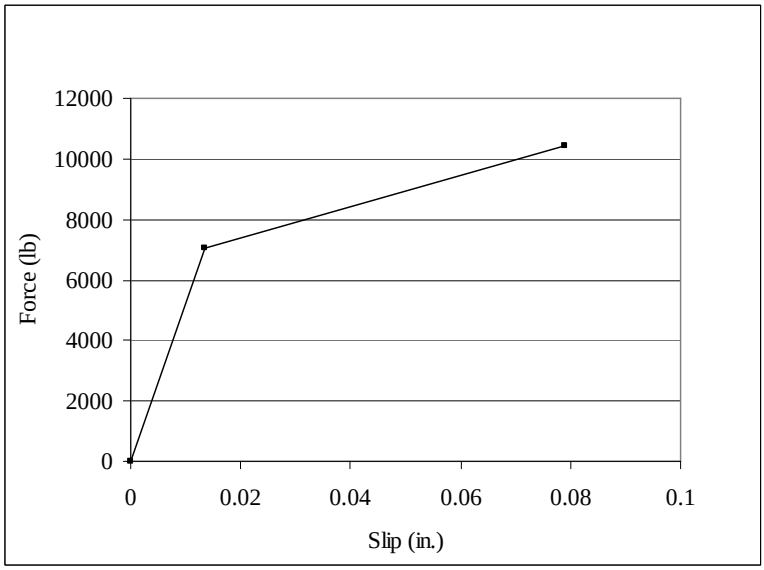

Fig. 47 Assumed slip behavior in the FE model

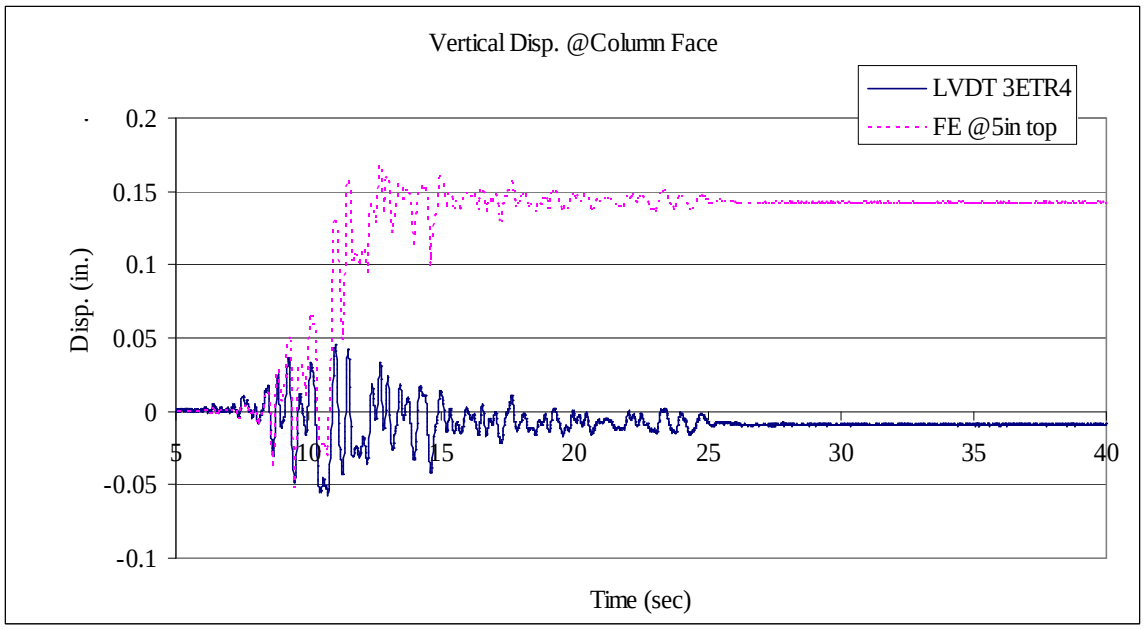

Fig. 48 Vertical displacement comparison between FE analysis result and LVDT measurements at the location of LVDT 3ETR4*

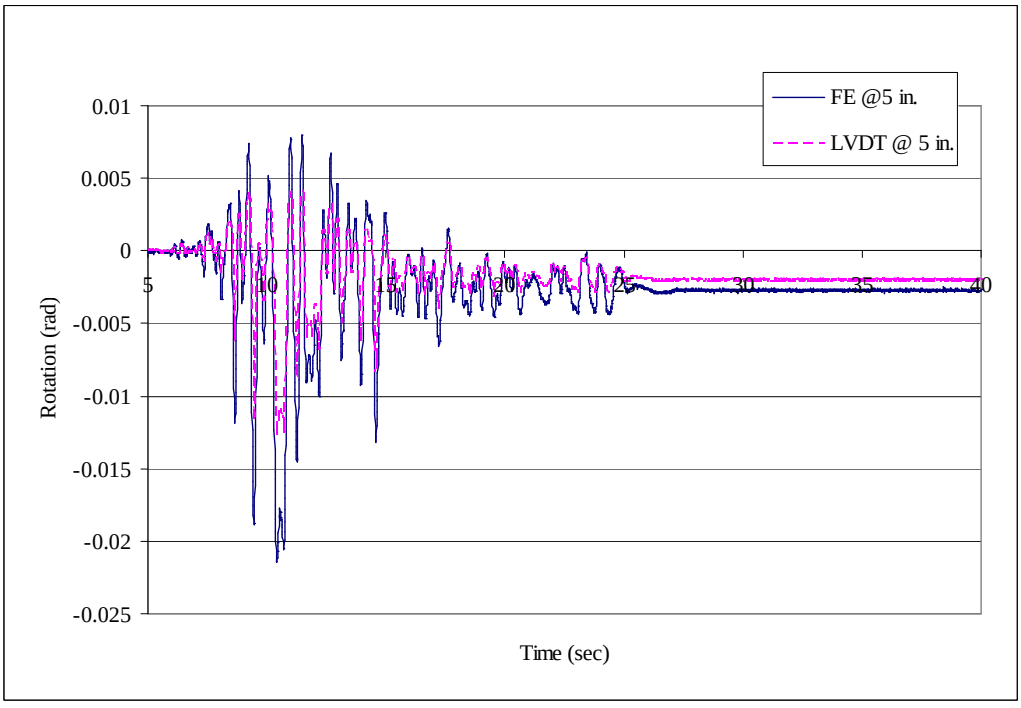

Fig. 49 The cross-sectional rotation comparison at the location of LVDT 3ETR3 and 3ETR4*

* Infinitely stiff cap beam, bond-slip effect included at the interfaces, w_c=0.8, w_t= 1.

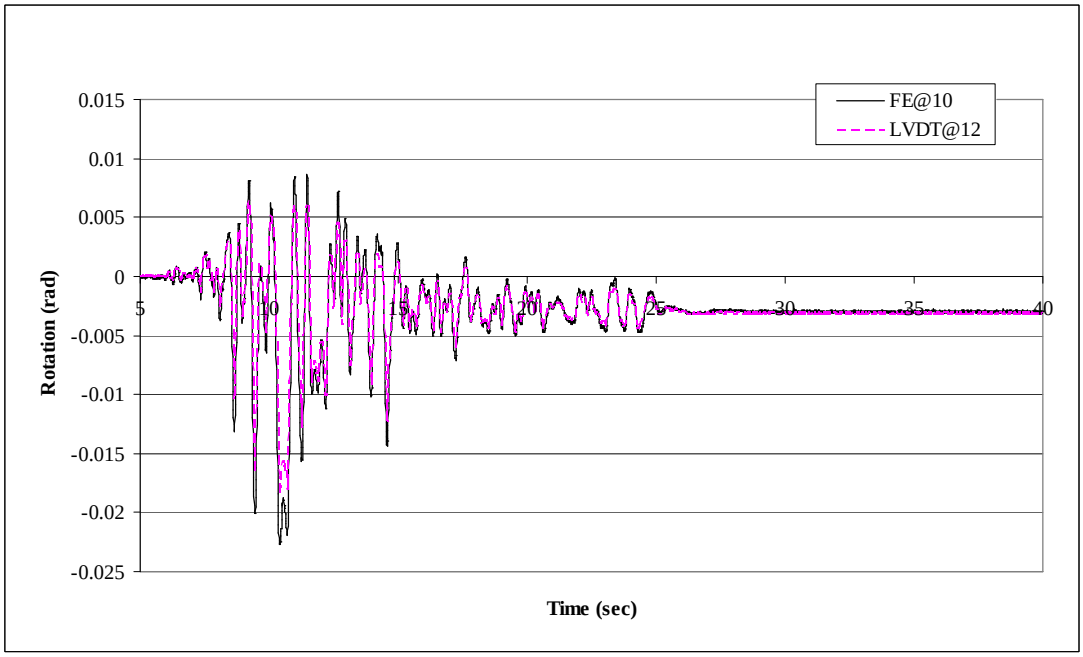

Fig. 50 The cross-sectional rotation comparison at the location of LVDT 3ETR5 and 3ETR6*

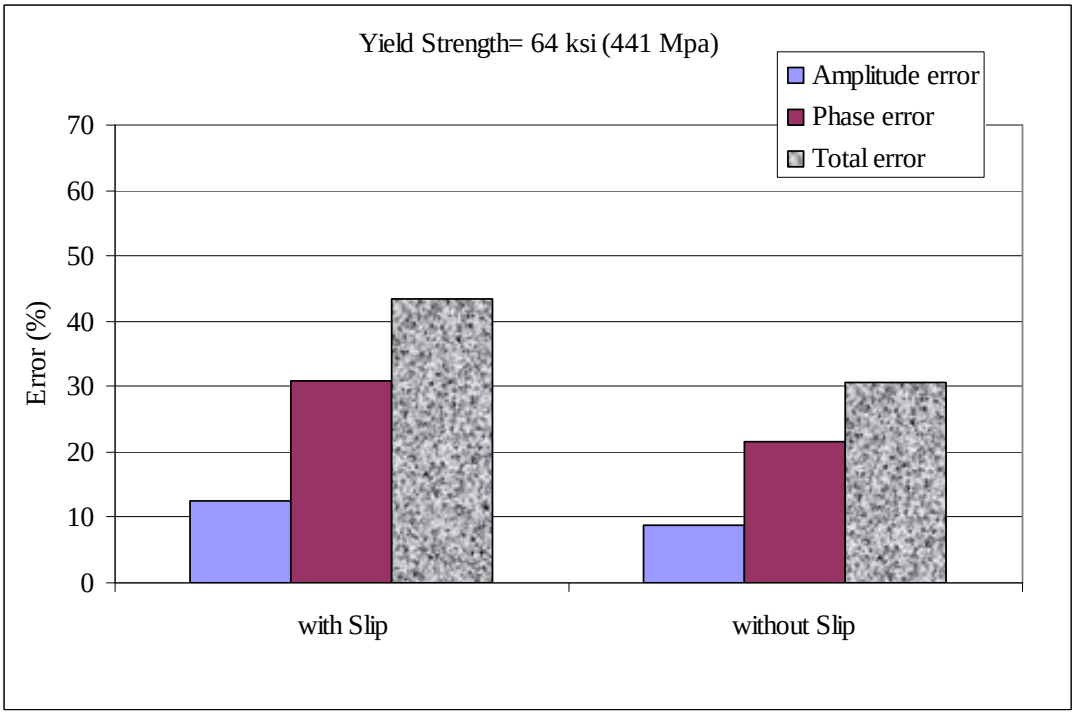

Fig. 51 The comparison of FDE index errors for bond-slip models (FE vs. LVDT vertical displacement measurements)*

* Infinitely stiff cap beam, bond-slip effect included at the interfaces, w_c=0.8, w_t= 1.

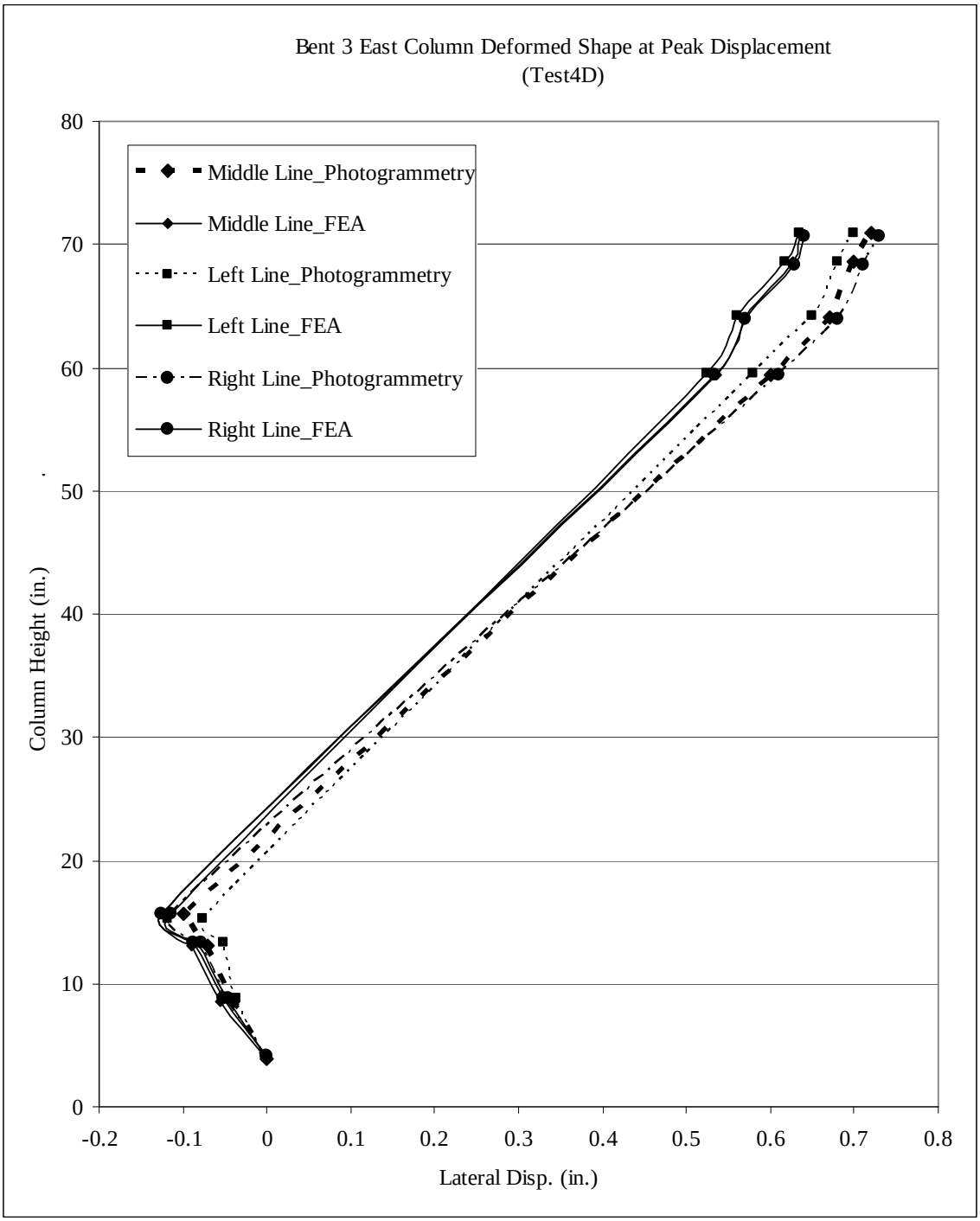

Fig. 52 Deformed shape of the bridge column at the maximum drift during Test 4D (f_y=64 ksi)*

* Infinitely stiff cap beam, bond-slip effect included at the interfaces, w_c=0.8, w_t= 1.

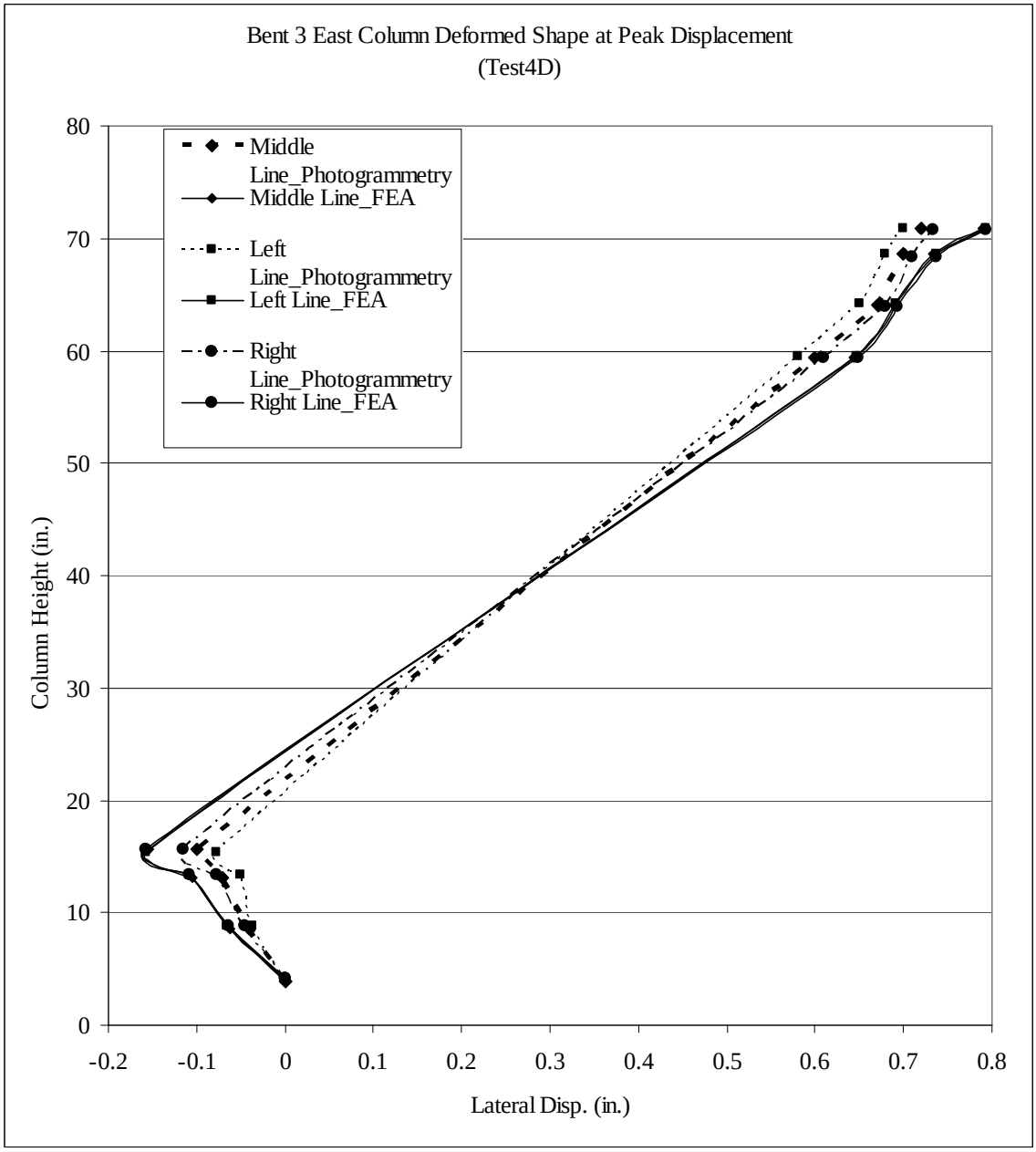

Fig. 53 Deformed shape of the bridge column at the maximum drift during Test 4D (f_y=80 ksi) *

* Infinitely stiff cap beam, bond-slip effect included at the interfaces, w_c=0.8, w_t= 1.

REFERENCES

1. Baker A.L.L. Ultimate load theory applied to the design of reinforced and prestressed concrete frames. Concrete Publications Ltd., London. 1956.
2. Baker A.L.L., Amarakone A.M.N. Inelastic hyperstatic frame analysis. Proc. International Symposium on the Flexural Mechanics of Reinforced Concrete, ACI SP-12 Miami, pp. 85-142. 1964.
3. Mattock A.H. Rotational capacity of hinging regions in reinforced concrete beams. Proc. International Symposium on the Flexural Mechanics of Reinforced Concrete, ACI SP-12 Miami, pp. 143-181. 1964.
4. Mattock, A.H. Discussion of rotational capacity of hinging regions in reinforced concrete beams. by Corley, W.G., Journal of the Structural Division, ASCE, V. 93, No. ST2, Apr., pp. 519-522. 1967.
5. Corley W. G. Rotational capacity of reinforced concrete beams. J Struct Division ASCE 1966; V. 92, No. ST5, pp. 121-146.
6. Park R., Priestley M. J. N., Gill W. D. Ductility of square-confined concrete columns. J Struct ASCE 1982; 108 No. ST4. 929-950.
7. Priestley M. J. N., Park R. Strength and ductility of concrete bridge columns under seismic loading. ACI Struct J 1987 V.84 Issue 1. pp. 61-76.
8. Paulay T., Priestley M. J. N. Seismic design of reinforced concrete and masonry structures. John Wiley & Sons, Inc. 1992.
9. Sheikh S.A., Khoury S.S. Confined concrete columns with stubs. ACI Struct J 1993 V. 90 No. 4 pp. 414-431.

10. Mendis P. Plastic hinge lengths of normal and high-strength concrete in flexure. Advances in Structural Engineering 2001 V. 4 No. 4 pp. 189-195.
11. Firat Alemdar Z., Browning J., Olafsen J. 2010. “Photogrammetric Measurements of RC Bridge Column Deformations”, Engineering Structures, submitted.
12. ABAQUS, Version 6.8-2, Simulia, 2009, http://www.simulia.com.
13. Firat Alemdar Z., Browning J., Olafsen J., and Nick Hunt. 2008. “Monitoring RC Bridge Column Hinging With Photogrammetry”, 14th World Conference on Earthquake Engineering, Bejing, China.
14. Mander J. B., Priestley M. J. N., and Park R. Seismic Design of Bridge Piers. Department of Civil Engineering Research Report 84-2, University of Canterbury, 483 pp. 1984.
15. Scott, B.D., Park, R., and Priestley, M.J.N. Stress-strain behavior of concrete confined by overlapping hoops at low and high strain rates. ACI Struct J 1982 V. 79 No. 1 pp. 13-27.
16. Spacone, E., Filippou, F., and Taucer, F. F. Fibre beam-column model for nonlinear analysis of r/c frames: part 1. formulation. Earthquake Eng. And Structural Dynamics, V. 25, 711-725, 1996.
17. Yassin, M. Nonlinear analysis of prestressed concrete structures under monotonic and cyclic loads. Ph.D. Thesis, University of California, Berkeley 1994.
18. Watstein, D. Effect of straining rate on the compressive strength and elastic properties of concrete. Am. Conc. Inst. J., 24(8), 729-744. 1953.
19. Wakabayashi, M. Design of Earthquake-Resistant Buildings. New York:McGraw-Hill, 1986.

20. Hosoya, H. et al. Strain rate in the members of reinforced concrete frame structure during an earthquake and its effects. Journal of Structural and Construction Engineering (Transactions of AIJ) 499 (1997): 77-83.
21. Mahin, S.A., V.V. Bertero, M.B. Atalya and D. Rea. Rate of loading effects on uncracked and repaired reinforced concrete members. Report UCB/EERC-72/09. Berkeley: EERC, University of California, 1972.
22. Bhide, S. B., and Collins, M. P. Reinforced concrete elements in shear and tension. Publication No. 87-02, Department of Civil Engineering, University of Toronto, Jan. 1987, 308 pp.
23. Vecchio, F. J., and Collins, M. P. Response of reinforced concrete to in-plane shear and normal stresses. Publ. No. 82-03, Dept. of Civil Engineering, Univ. of Toronto. 1982.
24. Collins, M. P., and Mitchell, D. Prestressed concrete basics. Canadian Prestressed Concrete Institute, Ottawa. 1987.
25. ACI Committee 439. Effect of steel strength and of reinforcement ratio on the mode of failure and strain energy capacity of reinforced concrete beams. ACI Journal 66 (3) (1969): 165-173.
26. CEB-FIP. CEB-FIP Model Code 1990: Design Code. London: T Telford, 1993.
27. Ma, S-Y.M., V.V. Bertero and E.P. Popov. Experimental and analytical studies of the hysteretic behavior of reinforced concrete rectangular and t-beams. Report No. EERC-76-2. Berkeley: EERC, University of California, 1976.
28. Response-2000. Reinforced concrete sectional analysis using the modified compression field theory. Version 1.0.5, last accessed 2010, http://www.ecf.utoronto.ca/~bentz/r2k.htm.

29. Dragovich JJ., Lepage A. FDE index for goodness-of-fit between measured and calculated response signals. Earthquake Engineering and Structural Dynamics 2009;38:1751-1758.
30. Sezen, H. Seismic Behavior and Modeling of Reinforced Concrete Building Columns. Ph.D. Thesis. University of California, Berkeley. 2002.

5 MANUSCRIPT 3: PLASTIC HINGE LENGTH EXPRESSION FOR RC BRIDGE COLUMNS

Zeynep Firat Alemdar[a,*], JoAnn Browning[b] and Adolfo Matamoros[c]

[a] 1147 Learned Hall, Department of Civil, Env, and Arch. Engineering, University of Kansas, Kansas, USA

[b] 2150 Learned Hall, Department of Civil, Env, and Arch. Engineering, University of Kansas, Kansas, USA

[c] 2150 Learned Hall, Department of Civil, Env, and Arch. Engineering, University of Kansas, Kansas, USA

[*] Corresponding author Tel: +1 785 864 3760 Fax: +1 785 864 5631 E-mail addresses: zeynep@ku.edu (Z. F. Alemdar).

1. Introduction

The determination of magnitude and location of inelastic deformations in reinforced concrete bridge columns is a critical step for characterizing the performance of the bridge system in earthquake events. Although it is possible to believe that some ductility will be provided by beam hinges in bridge systems, it is generally the columns of the bridges that must have inelastic rotational capacity. Bridge systems are designed to keep inelastic behavior in the columns and away from the superstructure, which is different than building systems. Plastic hinging regions indicate the area of concentrated damage for bridge columns that experience inelastic deformations. Therefore, a consistent prediction of a plastic hinge length is also necessary to evaluate the length of the column that needs to be confined along the critical section. Simple expressions for

plastic hinging regions also enable the development of estimates of column drift capacity and drift demand.

The plastic hinge length in reinforced concrete columns has been studied widely by many researchers [2-16]. Previous experimental research has generally been conducted using static loading and for small-scale components such as beams and columns. The real load distribution due to earthquake excitations of a structure would be different from static loading, and elements would behave differently. In addition, an evaluation of large-scale system behavior will include the effects of moment redistribution and progression of yielding throughout the entire structure.

Only a few of the previous studies have focused on determining the plastic hinge length in reinforced concrete bridge columns, and instead have focused on building-type columns. The location and the progression of plastic hinge length in reinforced concrete bridge columns would differ from reinforced concrete buildings. In addition, many of the parameters such as axial load ratio, diameter of the longitudinal reinforcement and the cross-sectional dimensions of the columns in the previous tests are not appropriate for reinforced concrete bridge columns [12-16, 24].

Expressions that have been developed to estimate the length of plastic hinges have either been based on the maximum drift at the top of the column, or the spread of plastic behavior in the hinging regions. Plastic hinge lengths have been calculated for 51 of the reported tests from the measured maximum top displacement using the lumped-plasticity model [7, 10, 17, 20, 21, 26-29]. Only 21 test data included the measured plastic hinge length from using the spread of plasticity approach [15, 16, 19, 22, 23, and 25]. The lumped-plasticity model has generally been used to simulate the nonlinear response of bridge columns and estimate the ultimate displacement capacity, which is an

important requirement of performance-based earthquake engineering (PBEE). In addition, Mander (1983) stated that the plastic hinge length must not be used for estimating the length requiring detailed confinement because plastic curvature would spread over approximately three equivalent plastic hinge lengths. Therefore, the evaluation of the spread of plasticity in the hinging regions might be useful to predict the required detailing in the confinement region. It has also observed that the equivalent plastic hinge length and the region of plasticity where special reinforcing detailing is required must be defined separately to ensure dependable inelastic rotation capacity [11].

This research defines a new plastic hinge length expression that is appropriate for static and dynamic loading cases for reinforced concrete bridge columns. Previous plastic hinge length expressions were evaluated using the static test measurements. In the new expression, however, both static and dynamic test results have been considered to obtain the best fit for every loading condition. The new expression has been obtained by doing a multivariable linear regression analysis using the previous test results in the literature.

The drift capacity of a bridge column, which corresponds to a 20% reduction in lateral load capacity on the descending branch of the response backbone curve, is estimated using the new expression and compared with the results that were obtained from the earlier plastic hinge length expressions. An expression to calculate the maximum drift capacity of a bridge column in double curvature is derived by considering the deformations due to flexure as influenced by the definition of plastic hinge length (l_p), and the bond-slip effect of the longitudinal reinforcement at the connections. A four-span large-scale bridge system was tested under biaxial earthquake loadings at the University of Nevada Reno, as shown in Fig. 1, to obtain the transverse and longitudinal

displacements at the cap beam on the bridge columns of Bent 3 and compared with the calculated response from the expression [30].

2. Analytical Investigation: Expressions Derived Using Static Test Results

Previous plastic hinge length models were developed using experimental results from static tests. A suite of 115 column tests that represent typical elements in reinforced concrete buildings and bridges that encompass a wide range of parameters were used. Axial load level, compressive strength of concrete, yield strength of longitudinal reinforcement, diameter of longitudinal reinforcement, and section dimensions are some of the main variables in the static tests. The minimum and maximum ranges of the main variables used in the literature are given in Table 1.

In the studies performed before 1983, the cross-section dimensions of a column were the main parameters used to determine the plastic hinge length of a column. With the results of Mander's tests at the University of Canterbury [8], the strain penetration effect of the longitudinal reinforcement was found to be an important factor within the plastic hinge region, and the diameter of the longitudinal reinforcement was incorporated into new expressions. After the effect of axial load on plastic hinge length calculation was discovered, Soesianawati et al. (1986) and Watson et al. (1994) added the axial load ratio into their expressions. Later expressions incorporate dimensionless parameters such as longitudinal reinforcement ratio, and shear span to depth ratio into expressions [15]. Table 2 shows various plastic hinge length expressions that have been developed to predict the plastic hinge length of reinforced concrete columns.

A small suite of 10 dynamic test results with relevance to determining plastic hinge length expressions have been collected. Hachem et al. (2003) and Dodd et al.

(2000) used the equation proposed by Priestley et al. (1992) and estimated the plastic hinge length before testing circular bridge columns under uniaxial and bidirectional earthquake loading. The main parameters in the tests were aspect ratio of the columns (4 to 10) to characterize the flexurally dominated columns, axial load level ($0.04A_g f'_c$ – $0.4 A_g f'_c$), and longitudinal reinforcement ratio (1.2%-1.62%). The plastic hinge length was measured according to the spread of plasticity model in the study of Hachem et al. (2003). Dodd et al. (2000) calculated the plastic hinge lengths from the maximum drift of the columns. After testing the columns, it was also observed that the estimated plastic hinge lengths were within the range of measured values as shown in Table 3. The average measured plastic hinge length value from the testing of four identical columns [19] was about 13 in. (330 mm) as given in PEER 2003/06 report. It was clear from the experimental values that the equation proposed by Priestley et al. (1992) overestimated the plastic hinge length for all of the columns as shown in Table 3.

Two new expressions to calculate the plastic hinge length in reinforced concrete bridge columns have been derived using the measured plastic hinge length values from yield curvature and the plastic hinge length values that were calibrated to calculate the correct maximum top displacement during the static and dynamic tests. The experimental data was limited to contain the data which characterize modern bridge column design criteria as described next, and included 72 out of the 115 tests from the literature. Fifty one plastic hinge length data included the plastic hinge length values calculated from the measured top displacement as given in Table 4. The remaining 21 test data measured the plastic hinge length as defined where the curvature is bigger than the yield curvature of the columns that were tested, as shown in Table 5. The test data was limited to represent modern bridge columns, which meet the following design criteria:

- An axial load ratio P/f'_cA_g less than or equal to 0.3, where P is the column axial load, f'_c is the concrete compressive strength, A_g is the gross section area of the column,
- A longitudinal reinforcement ratio less than or equal to 3%,
- A compressive strength of the concrete less than or equal to 10 ksi to represent modern bridge columns.

Each parameter of the equations in Table 1.2 was considered in the analysis to determine their affect on estimates of plastic hinge lengths. In order to obtain the best fit expressions for the plastic hinge length over the cross-sectional dimension, multivariable linear regression analysis was used. A number of different combinations of parameters were examined including the length of the columns, axial load ratio, diameter of the longitudinal reinforcement, yield strength of the reinforcement, compressive strength of the concrete, shear span to depth ratio, and the diameter of the longitudinal reinforcement normalized with yield strength of the reinforcement and the compressive strength of the concrete. The determining factor for selecting the best-fit equation was the minimum coefficient of variation (COV) of measured L_p/d (ratio of plastic hinge length to section dimension) to that of calculated L_p/d. After analyses of the various combinations, the column height and the diameter of the longitudinal reinforcement normalized with yield strength of the reinforcement and the compressive strength of the concrete (representing bending along the column height and the bond-slip deformation effect) were found to be the parameters that produced the best-fit expressions. The best-fit expression derived using 51 test data based on calibrated value of lp to calculate the maximum drift capacity is given in Eq. 1.

$$\frac{L_p}{d} = \frac{1}{5} + \frac{3 f_y d_b}{500\sqrt{f_c'}} + \frac{L}{1000} \qquad \text{(psi and in.)} \qquad (1a)$$

$$\frac{L_p}{d} = \frac{1}{4} + \frac{3 f_y d_b}{10000\sqrt{f_c'}} + \frac{L}{25000} \qquad \text{(MPa and mm)} \qquad (1b)$$

The best-fit expression based on measured spread of plasticity (21 test data set) is given in Eq. 2.

$$\frac{L_p}{d} = \frac{3}{10} + \frac{f_y d_b}{1000\sqrt{f_c'}} + \frac{L}{2500} \quad \text{(psi and in.)} \qquad (2a)$$

$$\frac{L_p}{d} = \frac{3}{10} + \frac{3 f_y d_b}{100000\sqrt{f_c'}} + \frac{L}{5000} \qquad \text{(MPa and mm)} \qquad (2b)$$

The new expressions were compared with previous plastic hinge length models. In order to compare the different expressions, the measured plastic hinge length was divided by the calculated plastic hinge length obtained from the expressions available. The best fit lines were drawn using the ratios of measured to calculated plastic hinge lengths based on each equation available in the literature. Figure 2 shows the comparisons of the ratio of measured to calculated plastic hinge lengths with varied parameter ($f_y d_b/\sqrt{f'_c}$) in Eq. 1 for all data. The ratio of measured to calculated plastic hinge length results were closest to unity for the new expression. The ratio of measured to calculated plastic hinge length values determined by the equations of Park (1982) and Paulay (1992) were the next best for representing the data at low axial loads. The comparison of the ratio of measured to calculated plastic hinge length result with varied bridge column height is shown in Fig. 3 for Eq. 1. The ratio of measured to calculated plastic hinge length results from the new expression (Eq. 1) were the closest to unity with respect to the column height. The ratio of measured to calculated plastic hinge length values determined by the equations of Mander (1983), Park (1987), and Paulay

(1992) intersected unity well, which was very similar to the results found in Fig. 1 except Paulay (1992) overestimated the plastic hinge length with respect to column height.

The calculated COV values for the ratio of measured to calculated plastic hinge length are between 0.37 and 0.57 for each expression. The new expression had the lowest COV value equal to 0.37. The COV of Park et al. (1982) equation was 0.39, which is the second best COV value after the new expression. Bae's equation gave the highest COV (0.57) for all data with low axial load. The COV values were 0.41, 0.42, 0.45, and 0.45 for Paulay (1992), Park (1987), Mander (1983), and Berry (2008) respectively.

Figure 4 shows the comparisons of the ratio of measured to calculated plastic hinge lengths with varied value of the first parameter in Equation 2 and the best fit lines drawn using the ratios for each available expression based on the 21 test data set. The ratio of measured to calculated plastic hinge length results were closest to unity for the new expression with respect to $f_y d_b/\sqrt{f'_c}$. The ratio of measured to calculated plastic hinge length values determined by the equations of Mander (1983) and Park (1987) were the next best results after the new expression values. The comparison of the ratio of measured to calculated plastic hinge lengths with varied bridge column height is shown in Fig. 5 for the 21 test data set. The ratio of measured to calculated plastic hinge length results from the new expression (Eq. 2) were the closest to unity with respect to the column height. The ratio of measured to calculated plastic hinge length values determined by the equations of Mander (1983) and Park (1987) followed a similar trend as the new expression.

The calculated COV values for each expression using the analysis of 21 test data based on the measured spread of plasticity are between 0.27 and 0.46. The new expression had a COV value equal to 0.30, and the COV of the Mander (1983) equation

was 0.27. The Bae (2005) and Berry (2008) equations gave the highest COV (0.46) for low axial load level. The COV values were 0.32, 0.40, and 0.44 for Park (1987), Park (1982), and Paulay (1992) respectively.

The COV of Eq. 1 was also determined using the 21 test data of plastic hinge length derived considering the length of the column with curvature values greater than the yield curvature ($\varphi > \varphi_y$) to determine how reliable Eq. 1 is to estimate the actual spread of plasticity. The ratios of plastic hinge length values from the new expression (Eq. 1) to the measured plastic hinge length results were calculated. The COV was found to be 0.34, which is an average COV compared to that of the other expressions. This analysis shows that the behavior of columns when considering the maximum drift capacity and spread of plasticity ($\varphi > \varphi_y$) is different.

It is of interest to consider the effect of the axial load level when using each expression. All the expressions except Berry (2008), which was derived only for bridge columns with $P/A_g f'_c$ less than or equal to 0.3, were developed for a wide range of axial loads. In the literature, some of the plastic hinge length expressions work well for high axial load ratios, whereas they fail to give satisfactory results for low axial load ratios. Figure 6 shows the effectiveness of the plastic hinge length calculations for a wide range of axial load ratios. Although only Bae's equation includes an axial load parameter, some of the other equations show considerable changes of measured to calculated ratios of L_p/d with increasing levels of axial load. It is important to note that the COV values varied between 0.16 and 0.30 for high axial load ratios. The COV values were 0.16, 0.17, 0.17, 0.18, 0.27, 0.28, 0.28, and 0.30 for Park (1987), Mander (1983), Berry (2008), Priestley (1992), Bae (2005), Park et al. (1982), and the proposed equations (1.1 and 1.2) respectively. It appears that most equations have a much better correlation for the plastic

hinge length with high axial load, and the behavior of columns is quite different under high axial load than low axial load. The proposed expression had a good COV value equal to 0.30, which compared very well to the COV at low axial load ratio of (0.37). Therefore, the use of Eq. 1 and Eq. 2 provide satisfactory predictions both for high and low axial load levels. At high axial load ratios, the proposed expression can be normalized by 1.4 to provide a good estimate for the plastic hinge length.

3. Analytical Investigation: Correlation With Measured Maximum Drift

The new expression was used to calculate the maximum drift of the bridge column tested at UNR as described previously. A drift expression was derived using a lumped-plasticity model with a fixed plastic hinge length (l_p) for a double curvature column. Flexural deformations and slip of the longitudinal reinforcement at the cap beam and footing interface were considered in the maximum drift expression, and given in Equation 1.3. The first and last terms in Eq. 3 represent the flexural displacement in the elastic and plastic range, and the second term represents the slip contribution to the top displacement.

$$\frac{l_p}{d} = \frac{\phi_y l^2}{6} + \frac{d_b f_y^{\ 2}}{48 E_s \sqrt{f_{'c}}} * \frac{L}{d - d^{'}} + \varphi_p l_p (L - l_p) \qquad (3)$$

The bridge column was tested using the biaxial applications of scaled motions recorded at the Century City Country Club during the 1994 Northridge, California earthquake [31]. The maximum drift was measured to be 5.3 in. in the transverse direction of the bridge after all the motions were applied. The maximum drift values of the bridge column were calculated using the plastic hinge length expressions (Table 2) and compared with the measured data in Table 5. The Park (1982) plastic hinge length

equation gave the closest value (5.94 in.) to the measured test data. The proposed expression (Eq. 1) also estimated the measured data very well and provided the second best estimate of 6.5 in. after the Park (1982) equation. The maximum drift value was also determined using Equation 2 and found to be 7.1 in., which is the third best correlation to the real test data.

4. Conclusions

A review of literature shows that an expression for plastic hinge length can be developed based on values used to produce best estimates of maximum drift capacity or can be developed to represent the spread of plasticity along the height of the column. This study produced equations that characterize the behavior of these two groups of data better than any existing equation of l_p, and shows that the behavior is different between these two methods. The following conclusions are made:

1. Estimates of plastic hinge length used to calculate the maximum drift capacity are shorter in value than estimates of plastic hinge length based on spread of plastic curvature over height of column.
2. The spread of plasticity at low axial loads is different than at high axial loads. Most existing equations are better fit at high axial loads. The proposed equations have nearly constant fit across axial loads, but best fit at low axial loads, which represent bridge columns.
3. The maximum drift of the one column tested under dynamic loads was best represented using the simple plastic hinge length estimate proposed by Park (1982). More parametric study is needed to understand the spread of plasticity.

Table 1 Static test data properties

Parameters	P/P_u (1)	L, in. (mm) (2)	d_b, in. (mm) (3)	ρ_l (%) (4)	$f'_{c,}$ ksi (kN/mm^2) (5)	$f_{y,}$ ksi (kN/mm2) (6)
Minimum	0.003	25 (635)	0.24 (6.1)	0.7	3.1 (0.021)	43.5 (0.3)
Maximum	0.77	360 (9144)	1.75 (44.45)	5.65	16.25 (0.11)	75.55 (0.52)

1: Axial load ratio

2: The length of column

3: The diameter of the longitudinal reinforcement

4: Longitudinal reinforcement ratio

5: The compressive strength of concrete

6: The yield strength of longitudinal steel

Table 2 Expressions available in the literature

Authors	Expressions
Park et al. (1982), ksi (MPa)	$0.4*d$ (1)
Park (1987), ksi (MPa)	$0.08*L$ (2)$+6d_b$ (3) $(0.08*L+0.88*d_b)$
Priestley (1992), ksi (MPa)	$0.08*L+.15d_{bl}f_{ye}$ (4)$>0.3d_{bl}f_{ye}$ $(0.08*L+.022d_{bl}f_{ye}>0.3dblfye)$
Mander (1983), ksi (MPa)	$6.35*\sqrt{(d_b)}+0.06*L$ $(32*\sqrt{(d_b)}+0.06*L)$
Bae (2005)	{(0.3*(P/P_0 (5))+3*(As (6)/Ag)-0.1)*(L/h)+.25}*h
Berry (2008), psi (MPa)	optimal: 0.0375*L+0.01*fy (7)d_b/sqrt(fc')(8) $(0.0375*L+0.12*f_yd_b/sqrt(f'_c))$ simplified: $0.05*L+.008fyd_b/sqrt(f_c')$ $(0.05*L+0.1f_yd_b/sqrt(f'_c))$

1: The section depth

2: The length of column

3: The diameter of the longitudinal reinforcement

4: The yield strength of longitudinal steel

5: Axial load capacity of the section

6: Area of the longitudinal reinforcement

7: The yield strength of longitudinal steel

8: Compressive strength of the concrete

Table 3 Calculated and measured plastic hinge length results.

	L/d[1]	Calculated Lp, in. (mm)	Measured Lp, in. (mm)
Hachem (2003)	6	13.30 (338)	13 (330)
Dodd (2000)	4	4.84 (123)	3.54 (90)
	4	4.84 (123)	3.35 (85)
	7	6.73 (171)	4.92 (125)
	7	6.73 (171)	5.31 (135)
	10	8.62 (219)	7.68 (195)
	10	8.62 (219)	5.91 (150)
	4	4.84 (123)	3.35 (85)
	7	6.73 (171)	5.31 (135)
	4	4.84 (123)	3.74 (95)

1: Aspect ratio

Table 4 Column properties and calculated plastic hinge length values

	d or h, in. (mm) (1)	Measured Lp, in. (mm) (2)	Lp/d (3)	P/f'cAg (4)	L/d (5)	L, in. (mm) (6)	db, in. (mm) (7)	fy, ksi (MPa) (8)	f'c, ksi (MPa) (9)	ρl (%) (10)
Park (1982)	22 (559)	9.68 (246)	0.44	0.26	2.18	48 (1219)	0.94 (24)	55.1 (380)	3.35 (23)	1.79
	22 (559)	7.48 (190)	0.34	0.21	2.18	48 (1219)	0.94 (24)	55.1 (380)	6 (41)	1.79
Priestley (1987)	19.69 (500)	10.63 (270)	0.54	0.11	4.00	70 (1778)	0.51 (13)	54.08 (373)	4.81 (33)	2.70
	19.69 (500)	11.42 (290)	0.58	0.11	4.00	108 (2743)	0.51 (13)	53.8 (371)	5.04 (35)	2.70
	19.69 (500)	8.86 (225)	0.45	0.00	5.50	108 (2743)	0.51 (13)	44.22 (305)	5.8 (40)	2.57
	23.62 (600)	8.27 (210)	0.35	0.15	2.00	47 (1194)	0.94 (24)	43.94 (303)	4.35 (30)	2.43
	15.75 (400)	8.51 (216)	0.54	0.20	4.00	63 (1600)	0.63 (16)	44.67 (308)	3.77 (26)	2.43
	15.75 (400)	8.66 (220)	0.55	0.21	4.00	63 (1600)	0.63 (16)	61.93 (427)	3.63 (25)	1.51
	29.53 (750)	10.93 (278)	0.37	0.10	4.27	126 (3200)	0.39 (10)	48.58 (335)	5.8 (40)	2.84
	29.53 (750)	11.81 (300)	0.40	0.30	4.27	126 (3200)	0.39 (10)	48.58 (335)	4.21 (29)	2.84
	29.53 (750)	12.31 (313)	0.42	0.30	4.27	126 (3200)	0.39 (10)	48.58 (335)	4.64 (32)	2.84
Tanaka (1990)	15.75 (400)	6.77 (172)	0.43	0.20	4.00	63 (1600)	0.79 (20)	68.73 (474)	3.71 (26)	1.57
	15.75 (400)	8.7 (221)	0.55	0.20	4.00	63 (1600)	0.79 (20)	74.1 (511)	4.64 (32)	1.57
	15.75 (400)	10.6 (269)	0.67	0.20	4.00	63 (1600)	0.79 (20)	74.1 (511)	4.64 (32)	1.57
	15.75 (400)	11.06 (281)	0.70	0.20	4.00	63 (1600)	0.79 (20)	74.1 (511)	4.65 (32)	1.57
	21.65 (550)	8.35 (212)	0.39	0.10	3.00	65 (1651)	0.79 (20)	74.1 (511)	4.65 (32)	1.25
	21.65 (550)	13.66 (347)	0.63	0.10	3.00	65 (1651)	0.5 (13)	68 (469)	6 (41)	1.25
	21.65 (550)	14.45 (367)	0.67	0.30	3.00	65 (1651)	0.5 (13)	68 (469)	6.15 (42)	1.25
	21.65 (550)	18.66 (474)	0.86	0.30	3.00	65 (1651)	0.5 (13)	68 (469)	6 (41)	1.25
Kovacic (1995)	6.46 (164)	1.5 (38)	0.25	0.16	8.46	50 (1270)	0.47 (12)	58 (400)	4.82 (33)	5.65
	6.46 (164)	2.76 (70)	0.47	0.17	8.46	50 (1270)	0.47 (12)	58 (400)	4.74 (33)	5.65
	6.46 (164)	3.74 (95)	0.63	0.14	8.46	50 (1270)	0.47 (12)	58 (400)	5.61 (39)	5.65
	6.46 (164)	1.77 (45)	0.30	0.19	8.46	50 (1270)	0.47 (12)	58 (400)	8.43 (58)	5.65

Table 4 Column properties and calculated plastic hinge length values (continued)

	d or h, in. (mm) (1)	Measured Lp, in. (mm) (2)	Lp/d (3)	P/f'cAg (4)	L/d (5)	L, in. (mm) (6)	db, in. (mm) (7)	fy, ksi (MPa) (8)	f'c, ksi (MPa) (9)	ρl (%) (10)
Kovacic (1995)	6.46 (164)	2.76 (70)	0.47	0.08	8.46	50 (1270)	0.47 (12)	58 (400)	9.33 (64)	5.65
	6.46 (164)	4.13 (105)	0.70	0.17	8.46	50 (1270)	0.47 (12)	58 (400)	9.4 (65)	5.65
	5.73 (146)	3.23 (82)	0.55	0.04	8.46	50 (1270)	0.47 (12)	58 (400)	9.11 (63)	4.71
	5.73 (146)	2.76 (70)	0.47	0.08	8.46	50 (1270)	0.47 (12)	58 (400)	9.46 (65)	4.71
Lehman and Moehle (2000)	24 (610)	14 (356)	0.58	0.07	4.00	96 (2438)	0.63 (16)	60 (414)	4.2 (29)	1.50
	24 (610)	22 (559)	0.92	0.07	8.00	192 (4877)	0.63 (16)	60 (414)	4.2 (29)	1.50
	24 (610)	25 (635)	1.04	0.07	10.00	240 (6096)	0.63 (16)	60 (414)	4.2 (29)	1.50
	24 (610)	14 (356)	0.58	0.07	4.00	96 (2438)	0.63 (16)	60 (414)	4.2 (29)	0.75
	24 (610)	14 (356)	0.58	0.07	4.00	96 (2438)	0.63 (16)	60 (414)	4.2 (29)	3.00
Calderone (2000)	24 (610)	13.5 (343)	0.56	0.09	3.00	72 (1829)	0.75 (19)	60 (414)	4 (28)	2.70
	24 (610)	24.5 (622)	1.02	0.09	8.00	192 (4877)	0.75 (19)	60 (414)	4 (28)	2.70
	24 (610)	29 (737)	1.21	0.09	10.00	240 (6096)	0.75 (19)	60 (414)	4 (28)	2.70
Dodd (2000)	7.9 (201)	3.54 (90)	0.45	0.04	4.00	31.6 (803)	0.24 (6)	65 (448)	5.9 (41)	1.62
	7. 9 (201)	3.35 (85)	0.42	0.05	4.00	31.6 (803)	0.24 (6)	65 (448)	4.64 (32)	1.62
	7.9 (201)	4.92 (125)	0.62	0.05	7.00	55.3 (1405)	0.24 (6)	65 (448)	5 (34)	1.62
	7. 9 (201)	5.31 (135)	0.67	0.05	7.00	55.3 (1405)	0.24 (6)	65 (448)	4.39 (30)	1.62
	7.9 (201)	7.68 (195)	0.97	0.04	10.00	79 (2007)	0.24 (6)	65 (448)	5.42 (37)	1.62
	7. 9 (201)	5.91 (150)	0.75	0.06	10.00	79 (2007)	0.24 (6)	65 (448)	4.22 (29)	1.62
	7.9 (201)	3.35 (85)	0.42	0.04	4.00	31.6 (803)	0.24 (6)	65 (448)	5.99 (41)	1.62
	7. 9 (201)	5.31 (135)	0.67	0.04	7.00	55.3 (1405)	0.24 (6)	65 (448)	5.86 (40)	1.62
	7.9 (201)	3.74 (95)	0.47	0.04	4.00	31.6 (803)	0.24 (6)	65 (448)	5.35 (37)	1.62
Moyer and Kowalsky (2002)	18 (457)	8.97 (228)	0.50	0.04	4.67	84 (2134)	0.75 (19)	60 (414)	4.74 (33)	2.00
	18 (457)	8.97 (228)	0.50	0.04	4.67	84 (2134)	0.75 (19)	60 (414)	4.96 (34)	2.00

Table 4 Column properties and calculated plastic hinge length values (continued)

	d or h, in. (mm) (1)	Measured Lp, in. (mm) (2)	Lp/d (3)	P/f'cAg (4)	L/d (5)	L, in. (mm) (6)	db, in. (mm) (7)	fy, ksi (MPa) (8)	f'c, ksi (MPa) (9)	ρl (%) (10)
Moyer and Kowalsky (2002)	18 (457)	8.97 (228)	0.50	0.04	4.67	84 (2134)	0.75 (19)	60 (414)	4.6 (32)	2.00
	18 (457)	8.97 (228)	0.50	0.04	4.67	84 (2134)	0.75 (19)	60 (414)	4.92 (34)	2.00
Phan (2007)	15.95 (405)	22.01 (559)	1.38	0.08	4.50	72 (1829)	0.75 (19)	73.6 (507)	4.7 (32)	2.00
	15.93 (405)	17.05 (433)	1.07	0.08	4.50	72 (1829)	0.75 (19)	73.6 (507)	4.72 (33)	2.20
	16.05 (408)	17.01 (432)	1.06	0.08	4.50	72 (1829)	0.75 (19)	73.6 (507)	4.81 (33)	2.00

1: Section dimension of the column tested.

2: Measured plastic hinge length displacement during testing.

3: The ratio of plastic hinge length to the section dimension

4: Applied axial load ratio

5: Aspect ratio

6: The length of the columns

7: The diameter of longitudinal reinforcement

8: Yield strength of the longitudinal reinforcement

9: Compressive strength of the concrete

10: The ratio of longitudinal reinforcement

11: The average plastic hinge length result was used from the experimental data ranging from 12 in. to 14 in. as given in PEER report.

Table 5 Column properties and measured plastic hinge length values

	d or h, in. (mm) (1)	Measured Lp, in. (mm) (2)	Lp/d (3)	P/f'cAg (4)	L/d (5)	L, in. (mm) (6)	db, in. (mm) (7)	fy, ksi (MPa) (8)	f'c, ksi (MPa) (9)	ρl (%) (10)
Cheok and Stone (1986)	9.8 (249)	11.6 (295)	1.18	0.20	3.00	29.5 (749)	1.75 (44)	57 (393)	3.35 (23)	1.45
	9.8 (249)	10.2 (259)	1.05	0.10	6.00	59 (1499)	1.75 (44)	57 (393)	3.68 (25)	0.70
	9.8 (249)	7.5 (191)	0.76	0.10	3.00	29.5 (749)	1.75 (44)	57 (393)	3.55 (24)	1.45
	9.8 (249)	9.6 (244)	0.98	0.20	3.00	29.5 (749)	1.75 (44)	57 (393)	3.53 (24)	1.45
	9.8 (249)	10.6 (269)	1.08	0.10	6.00	59 (1499)	1.75 (44)	57 (393)	3.37 (23)	0.70

Table 5 Column properties and measured plastic hinge length values (continued)

	d or h, in. (mm) (1)	Measured Lp, in. (mm) (2)	Lp/d (3)	P/f'cAg (4)	L/d (5)	L, in. (mm) (6)	db, in. (mm) (7)	fy, ksi (MPa) (8)	f'c, ksi (MPa) (9)	ρl (%) (10)
Wong et al. (1990)	15.75 (400)	9.84 (250)	1.42	0.19	2.00	31.5 (800)	0.63 (16)	61.35 (423)	5.51 (38)	3.20
Kunnath (1997)	12 (305)	7.09 (180)	0.59	0.09	4.50	54 (1372)	0.38 (10)	65 (448)	4.21 (29)	2.00
	12 (305)	7.12 (181)	0.59	0.09	4.50	54 (1372)	0.38 (10)	65 (448)	4.21 (29)	2.00
	12 (305)	5.91 (150)	0.49	0.09	4.50	54 (1372)	0.38 (10)	65 (448)	4.76 (33)	2.00
	12 (305)	5.90 (150)	0.49	0.09	4.50	54 (1372)	0.38 (10)	65 (448)	4.76 (33)	2.00
	12 (305)	7.87 (200)	0.66	0.09	4.50	54 (1372)	0.38 (10)	65 (448)	4.71 (32)	2.00
	12 (305)	7.68 (195)	0.64	0.10	4.50	54 (1372)	0.38 (10)	65 (448)	3.92 (27)	2.00
	12 (305)	8.66 (220)	0.72	0.10	4.50	54 (1372)	0.38 (10)	65 (448)	3.92 (27)	2.00
	12 (305)	7.87 (200)	0.66	0.10	4.50	54 (1372)	0.38 (10)	65 (448)	3.92 (27)	2.00
Bae (2005)	24 (610)	11.76 (299)	0.49	0.20	4.31	103.5 (2629)	0.63 (16)	64.67 (446)	6.38 (44)	1.25
	24 (610)	11.28 (287)	0.47	0.20	4.31	103.5 (2629)	0.63 (16)	64.67 (446)	6.38 (44)	1.25
Watson (1994)	15.75 (400)	4.09 (104)	0.26	0.10	4.00	63 (1600)	0.63 (16)	64.67 (446)	5.8 (40)	1.51
	15.75 (400)	5.2 (132)	0.33	0.30	4.00	63 (1600)	0.63 (16)	68.73 (474)	5.95 (41)	1.51
	15.75 (400)	6.46 (164)	0.41	0.30	4.00	63 (1600)	0.63 (16)	68.73 (474)	5.8 (40)	1.51
	15.75 (400)	4.09 (104)	0.26	0.30	4.00	63 (1600)	0.63 (16)	68.73 (474)	6.09 (42)	1.51
Hachem (2003) (11)	16 (406)	13 (330)	0.81	0.06	6.00	96 (2438)	0.5 (13)	60 (414)	5.7 (39)	1.20

Table 6 Maximum drift estimates

Authors	l_p (in.)	Δ_{max} (in.) (transverse dir.)	Δ (% difference)
Test data	-	5.3	-
Park (1982)	4.8	5.9	12.0
Mander (1983)	8.2	9.4	77.0
Park (1987)	8.0	9.2	73.0
Priestley (1992)	9.4	10.4	97.0
Bae (2005)	3.0	4.0	-25.0
Berry (2008)	5.9	7.1	35.0
Eq. 1	5.4	6.5	23.0
Eq. 2	5.9	7.1	23.0

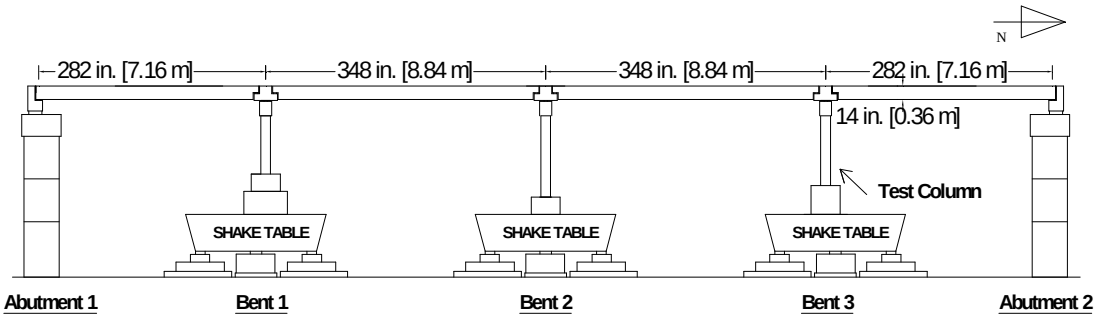

Fig. 1 Elevation view of the four-span bridge

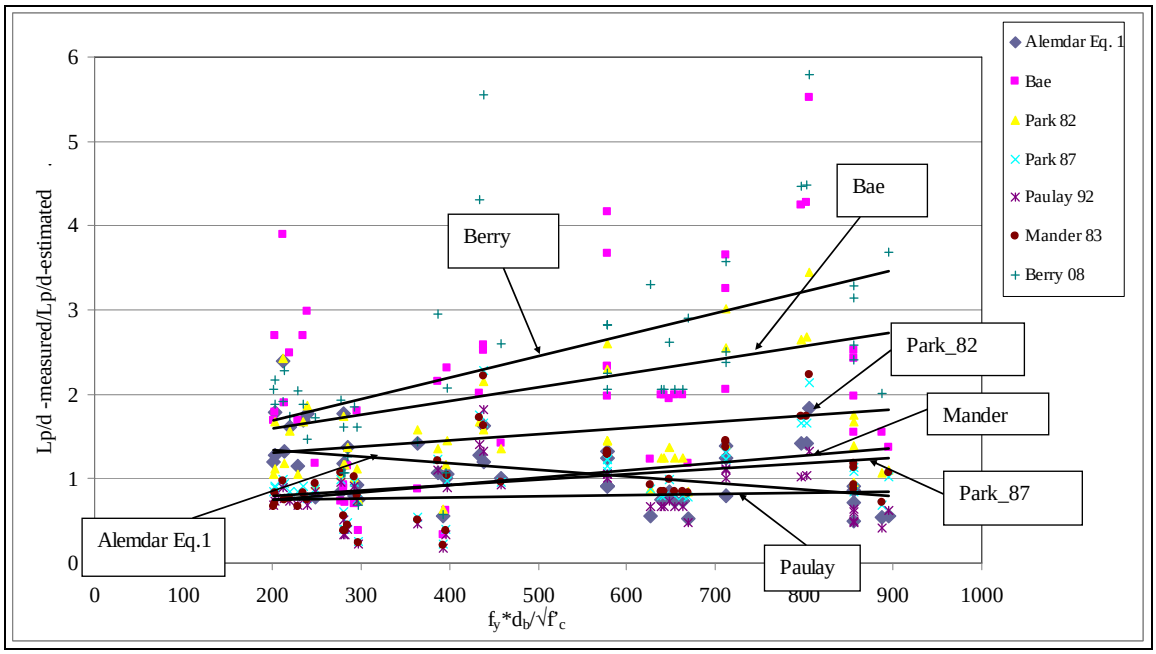

Figure 2 Comparisons of the plastic hinge length expressions results with Equation 1

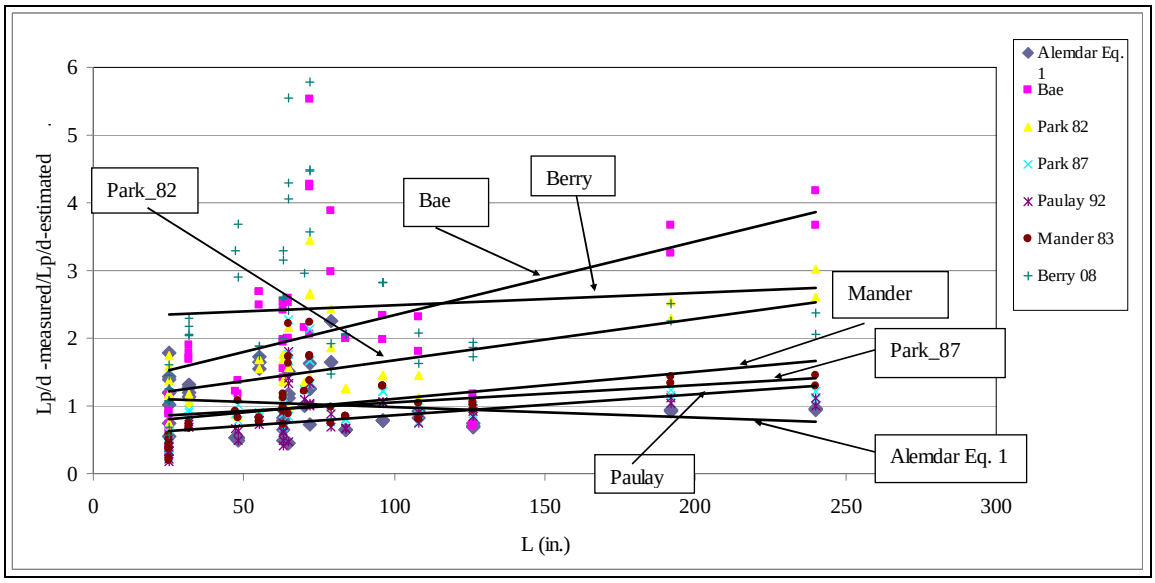

Figure 3 Comparisons of the plastic hinge length expressions results with Equation 1

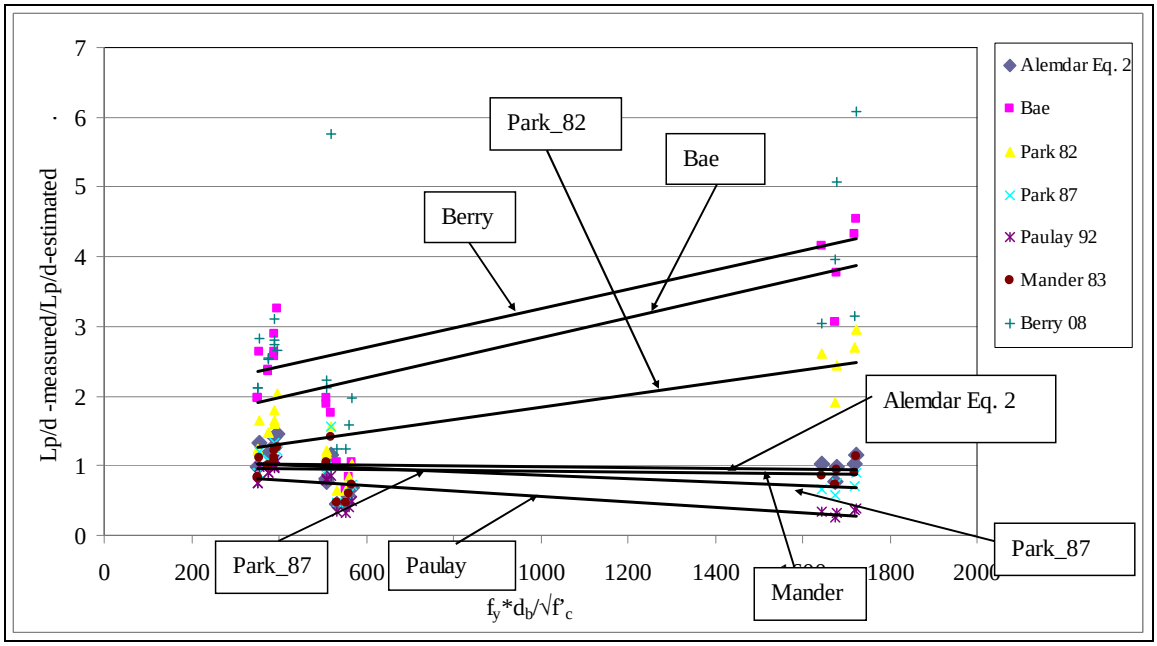

Figure 4 Comparisons of the plastic hinge length expressions results with Eq. 2

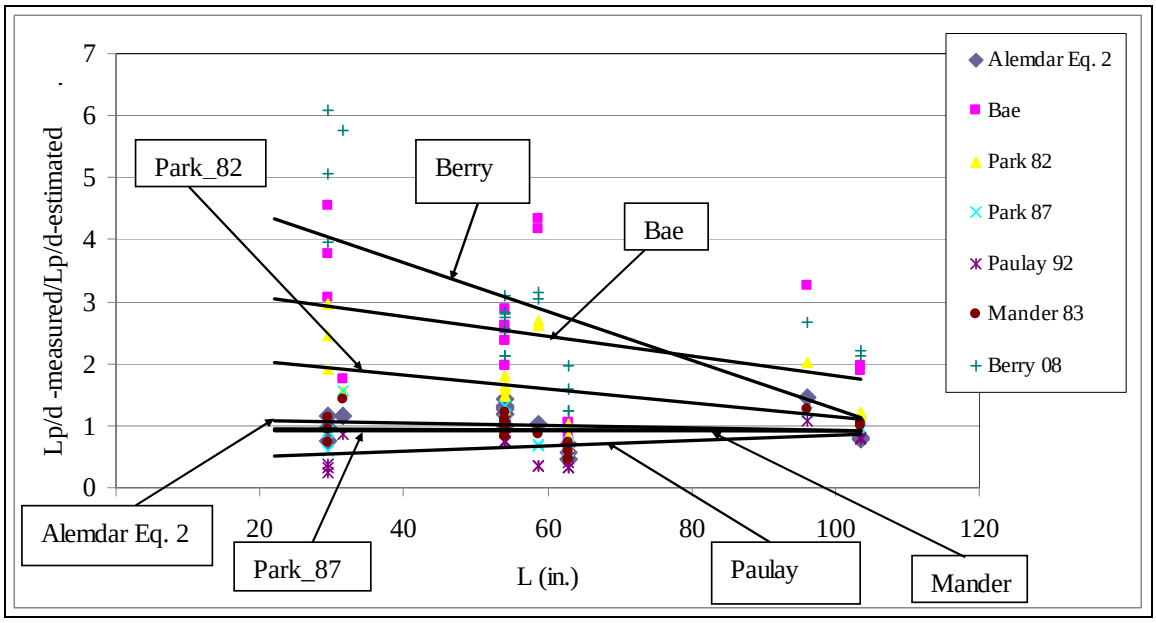

Figure 5 Comparisons of the plastic hinge length expressions results with Eq. 2

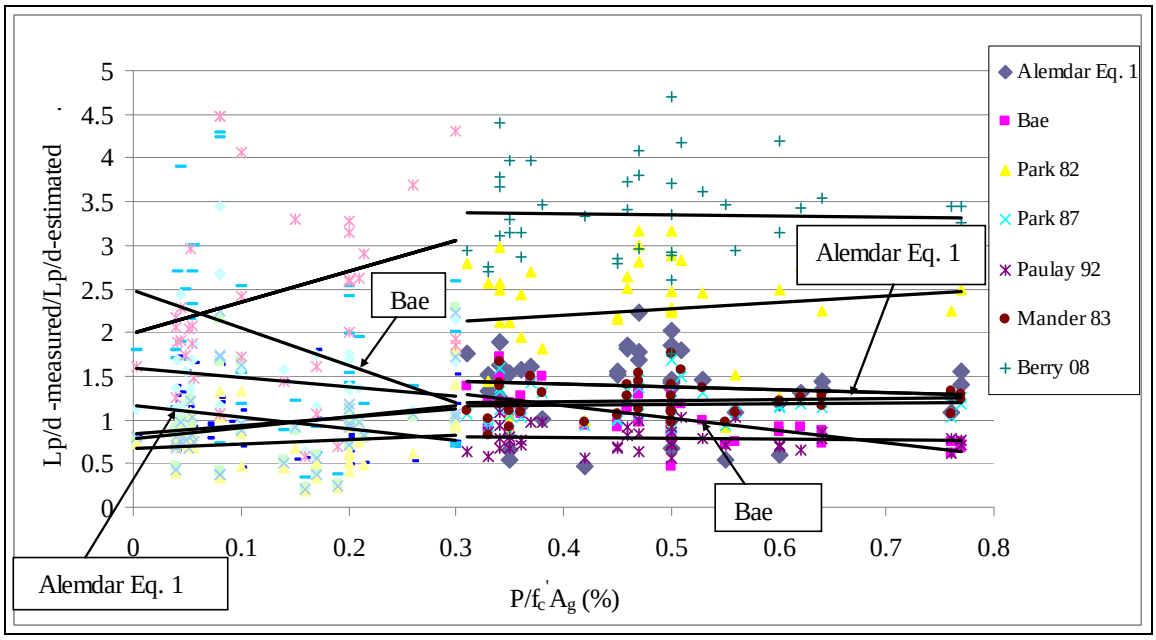

Figure 6 Comparisons of the normalized plastic hinge length results with axial load level.

REFERENCES

1. ABAQUS, Version 6.8-2, *Simulia*, 2009, http://www.simulia.com.
2. Baker, A.L.L. (1956), "Ultimate Load Theory Applied to the Design of Reinforced and Prestressed Concrete Frames," Concrete Publications Ltd., London.
3. Baker, A.L.L. and Amarakone, A.M.N. (1964), "Inelastic Hyperstatic Frame Analysis," Proceedings International Symposium on the Flexural Mechanics of Reinforced Concrete, ACI SP-12, Miami, pp. 85-142.
4. Mattock, A.H. (1964), "Rotational Capacity of Hinging Regions in Reinforced Concrete Beams," Proceedings International Symposium on the Flexural Mechanics of Reinforced Concrete, ACI SP-12, Miami, pp. 143-181.
5. Mattock, A.H. (1967), Discussion of "Rotational Capacity of Hinging Regions in Reinforced Concrete Beams," by Corley, W.G., Journal of the Structural Division, ASCE, V. 93, No. ST2, Apr., pp. 519-522.
6. Corley, W.G. (1966), "Rotational Capacity of Reinforced Concrete Beams," Journal of the Structural Division, ASCE, V. 92, No. ST5, Oct., pp. 121-146.
7. Park R., Priestley M. J. N., and Gill W. D. (1982), "Ductility of Square-Confined Concrete Columns", Struct. J., ASCE, 108, No. ST4, 929-950.
8. Mander J. B. (1983), "Seismic Design of Bridge Piers", PhD Thesis, University of Canterbury, Christ Church, New Zealand.
9. Soesianawati, M.T., Park, R. and Priestley, M.J.N. (1986), "Limited Ductility Design of Reinforced Concrete Columns," Research Report 86-10, Department of

Civil Engineering, University of Canterbury, Christchurch, New Zealand, Mar., 208 pp.

10. Priestley, M. J. N., and Park R. (1987), “Strength and Ductility of Concrete Bridge Columns Under Seismic Loading”, ACI Structural Journal, V.84, Issue 1, pp. 61-76.
11. Paulay T., and Priestley M. J. N. (1992), “Seismic Design of Reinforced Concrete and Masonry Structures”, John Wiley & Sons, Inc.
12. Sheikh, S.A. and Khoury, S.S. (1993), “Confined Concrete Columns with Stubs,” ACI Structural Journal, V. 90, No. 4, July-Aug., pp. 414-431.
13. Sheikh, S.A., Shah, D.V. and Khoury, S.S. (1994), “Confinement of High-Strength Concrete Columns,” ACI Structural Journal, V. 91, No. 1, Jan.-Feb., pp. 100-111.
14. Bayrak, O. and Sheikh, S.A. (1997), “High-Strength Concrete Columns under Simulated Earthquake Loading,” ACI Structural Journal, V. 94, No. 6, Nov.-Dec., pp. 708-722.
15. Bae, S. (2005), “Seismic Performance of Full-Scale Reinforced Concrete Columns”, PhD Dissertation, the University of Texas at Austin, Austin, TX, 311 pp.
16. Watson, S. and Park, R. (1994), “Simulated Seismic Load Tests on Reinforced Concrete Columns,” Journal of Structural Engineering, ASCE, V. 120, No. 6, June, pp. 1825-1849.
17. Phan V., Saiidi M.S., Anderson J., and Ghasemi H. (2007), “Near-Fault Ground Motion Effects on Reinforced Concrete Bridge Columns”, Journal of Structural Eng., V.133, Issue 7, pp. 982-989.

18. Berry, M., Lehman D. E., and Lowes L. N. (2008), “Lumped-Plasticity Models for Performance Simulation of Bridge Columns”, ACI Structural Journal, V. 105, No. 3, May-June, pp. 270-279.
19. Hachem M. M., Mahin, S.A., and Moehle J.P. “Performance of Circular Reinforced Concrete Bridge Columns under Bidirectional Earthquake Loading.” Report No. PEER 2003/06, Pacific Earthquake Engineering Research Center, University of California at Berkeley, Feb. 2003, 490 pp.
20. Dodd L.L., “The Dynamic Behavior of Reinforced Concrete Bridge Piers Subjected to New Zealand Seismicity”, PhD. Thesis, the University of Canterbury Christchurch New Zealand, Feb. 1992, 448 pages.
21. Dodd, L. L., and Cooke, N., “Capacity of Circular Bridge Columns Subjected to Base Excitation,” ACI Structural Journal, Vol. 97, No.2, March-April 2000, pp.297-308.
22. Kunnath, Sashi, K.; El-Bahy, Ashraf; Taylor, Andrew; and Stone, William, Cumulative Seismic Damage of Reinforced Concrete Bridge Piers, Technical Report NCEER-97-0006, National Center for Earthquake Engineering Research, September 1997, 147 pp.
23. Cheok, G.S.; and Stone, William C., Behavior of 1/6-Scale Model Bridge Columns Subjected to Cycle Inelastic Loading, NBSIR 86-3494, Center for Building Technology, National Engineering Laboratory, National Institute of Standards and Technology, Gaithersburg.
24. Stone, William C.; and Cheok, Geraldine S., Inelastic Behavior of Full-Scale Bridge Columns Subjected to Cyclic Loading, NIST BSS 166, Building Science

Series, Center for Building Technology, National Engineering Laboratory, National Institute of Standard, 1989.

25. Wong, Y.L.; Paulay, T.; and Priestley, M.J.N., Squat Circular Bridge Piers Under Multi-Directional Seismic Attack, Report 90-4, Department of Civil Engineering, University of Canterbury, Christchurch, New Zealand, October 1990, 264 pp.
26. Tanaka, H. and Park, R. (1990), “Effect of Lateral Confining Reinforcement on the Ductile Behavior of Reinforced Concrete Columns,” Research Report 90-2, Department of Civil Engineering, University of Canterbury, Christchurch, New Zealand, June, 458 pp.
27. Moyer, M.J. and Kowalsky, M.J., "Influence of tension strain on buckling of reinforcement in RC bridge columns." ACI Structural Journal, 2002.
28. Calderone, A.J., Lehman, D.E.; Moehle, J.P.; "Behavior of Reinforced Concrete Bridge Columns Having Varying Aspect Ratios and Varying Lengths of Confinement," Pacific Earthquake Engineering Research Center, PEER 2000/08, 2000.
29. Lehman, D.E.; Moehle, J.P.; "Seismic Performance of Well-Confined Concrete Bridge Columns," Pacific Earthquake Engineering Research Center, PEER 1998/01, Dec. 2000.
30. Firat Alemdar, Z.; Browning J.; Olafsen J.; "Photogrammetric Measurements of RC Bridge Column Deformations,” Engineering Structures, 2010 (submitted).
31. Firat Alemdar, Z.; “Plastic hinging behavior of reinforced concrete bridge columns” Ph.D. dissertation, Lawrence (KS): the University of Kansas; 2010.
32. Kovacic D. (1995), “Design of High-Strength Concrete Columns”, M.Eng. Thesis, the University of Melbourne.

6 CONCLUSIONS

This study focused on the plastic hinging behavior of reinforced concrete bridge columns. A review of the literature revealed that most of the tests that have explored this behavior have developed calibrated expressions to estimate regions of lumped plasticity, which are then used to estimate maximum drift. There are a fewer number of tests that have actually measured the spread of plasticity. In addition, the number of tested elements that are representative of bridge columns (having lower axial load, lower reinforcement ratios, and reasonable concrete compressive strengths) is limited. This study sought to better define the plastic hinging behavior of reinforced concrete bridge columns by taking detailed measurements of the column deformations in a large-scale 4-span bridge test at the University of Nevada Reno, modeling the column using finite elements, and developing separate expressions to calculate the maximum drift and the spread of plasticity.

Three manuscripts were developed in the course of this research study. The conclusions from each manuscript are repeated below.

From Manuscript 1: Photogrammetric Measurements of Reinforced Concrete Bridge Column Deformations

- Application of a simple photogrammetry method was used to evaluate the deformations of a bridge column that was part of a bridge system tested at UNR.
- According to the FDE index calculations, the lateral deformations of the bridge column reduced from the photogrammetric data gave very good correlations with

the FE model of the column as well as the traditional instrumentation measurements.

- The rotation of a vertical line on the grid surface provided a good representation of the column rotation.
- The deformed shape of the bridge column was constructed using the lateral displacements of the points on the bottom and top grid surfaces and matched well with the images at the time of maximum drift of Test 4D.

From Manuscript 2: Modeling surface Deformations and Hinging Regions in Reinforced Concrete Bridge Columns

- Using a 1 in. (25 mm) mesh along the hinging regions of the bridge column provided a similar force-displacement curve with the Modified Compression Field Theory.
- According to the FDE index analysis, using the yield strength of 80 ksi (552 MPa) gave the best correlations between the FE model and the traditional instrumentations.
- The flexural stiffness of the cap beam can be modeled by defining a rotational spring with 5*10^8 lb-in. (56.5*10^6 N-m) capacity.
- The tension and compression recovery variables were utilized to consider the reduction in stiffness of the concrete.
- The best FE model of the bridge column under dynamic loading was defined using a stress-strain relationship for the longitudinal steel and concrete with the dynamic magnification factors and including the tension stiffening effect.

- The bond-slip effect was defined in the FE model to consider the slip of the longitudinal steel at the column interfaces.
- The FE model of the bridge column followed a similar deformed shape obtained from the photogrammetry data.

From Manuscript 3: Plastic Hinge Length Expression for Reinforced Concrete Bridge Columns

- Two different plastic hinge length expressions were developed using the plastic hinge length test data available in the literature. Equation 1 was produced based on the plastic hinge length values that were calibrated to calculate the correct maximum drift at the column. Equation 2 was developed using the measured plastic hinge length values based on the spread of plastic curvature along the height of the column.
- The proposed equations gave the best fit at low axial loads.
- The maximum drift capacity of the bridge column was estimated using the proposed equations. The results show that the proposed equations give very good estimates of the maximum drift capacity for the bridge column under dynamic loading.
- The plastic hinge length calculated using Eq. 1 gives shorter in value than that of Eq. 2. More parametric analysis is required to evaluate the effect of the spread of plasticity.

The study of plastic hinging regions for reinforced concrete bridge columns shows that best estimates of the plastic hinge length depends on the goal of the analysis:

either for estimating the maximum drift capacity, or the spread of plasticity ($\varphi > \varphi_y$). In either case, it was found that plastic deformations can be measured with a simple photogrammetry method during dynamic tests. The plastic behavior of the column was also adequately represented using finite element modeling. Separate equations were developed to represent the plastic hinge length for a lumped plasticity model (to estimate the maximum drift) and for the spread of plasticity. The developed expressions provide better estimates of plastic hinge lengths for lumped plasticity models at low axial loads than any other expression that was considered. The proposed expression for a lumped plasticity model was used effectively to estimate the maximum drift capacity. More parametric analysis is needed, however, to understand the behavior of the spread of plasticity.

REFERENCES FOR CHAPTERS 1 AND 2

ACI-ASCE Committee 428 (1968). "Progress Report on Code Clauses for Limit Design," ACI Journal, 65, No.9, pp. 713-715.

ACI Committee 318 (1989). "Building Code Requirements for Reinforced Concrete and Commentary (ACI 318-89/ACI 318R-89)," American Concrete Institute, Detroit, Michigan, 351 pp.

ACI Committee 318 (2005). "Building Code Requirements for Reinforced Concrete and Commentary (ACI 318-05/ACI 318R-05)," American Concrete Institute, Detroit, Michigan, 423 pp.

Ang Beng Ghee, Priestley M. J. N., and Park R. (1981). "Ductility of Reinforced Concrete Bridge Piers under Seismic Loading," Department of Civil Engineering Research Report 81-3, University of Canterbury.

Bae, S. (2005). "Seismic Performance of Full-Scale Reinforced Concrete Columns," PhD Dissertation, the University of Texas at Austin, Austin, TX, 311 pp.

Bae, S. and Bayrak O. "Plastic Hinge Length of Reinforced Concrete Columns," ACI Structural Journal, V. 105, N. 3, May-June 2008, pp. 290-300.

Baker, A.L.L. (1956). “Ultimate Load Theory Applied to the Design of Reinforced and Prestressed Concrete Frames,” Concrete Publications Ltd., London.

Baker, A.L.L. and Amarakone, A.M.N. (1964). “Inelastic Hyperstatic Frame Analysis,” Proceedings International Symposium on the Flexural Mechanics of Reinforced Concrete, ACI SP-12, Miami, pp. 85-142.

Bayrak, O. and Sheikh, S.A. (1997). “High-Strength Concrete Columns under Simulated Earthquake Loading,” ACI Structural Journal, V. 94, No. 6, Nov.-Dec., pp. 708-722.

Bayrak, O. (1999). “Seismic Performance of Rectilinearly Confined High Strength Concrete Columns,” Ph.D. dissertation, University of Toronto, Ontario, Canada, 339 pp.

Berry, M., Parish, M., and Eberhard, M. (2004). “PEER Structural Performance Database User’s Manual,” PEER Research Report, University of California-Berkeley, Berkeley, CA, 2004, http://nisee.berkeley.edu/spd.

Berry, M., Lehman D. E., and Lowes L. N. (2008). “Lumped-Plasticity Models for Performance Simulation of Bridge Columns,” ACI Structural Journal, V. 105, No. 3, May-June, pp. 270-279.

Chan W. W.L. (1954). “An Investigation of the Characteristics of Plastic Hinges in Reinforced Concrete,” PhD. Thesis, the University of London.

Chan W. W. L. (1955). “The Ultimate Strength and Deformation of Plastic Hinges in Reinforced Concrete Frameworks,” Magazine of Concrete Research, Vol. 7, No. 21, pp. 121-132.

Chan W. W. L. (1962). “Rotation of Reinforced Concrete Plastic Hinges at Ultimate Load,” Magazine of Concrete Research, V. 14, Issue 41, pp. 63-72.

Corley, W.G. (1966). “Rotational Capacity of Reinforced Concrete Beams,” Journal of the Structural Division, ASCE, V. 92, No. ST5, Oct., pp. 121-146.

Davey B. E., and Park R. (1975). “Reinforced Concrete Bridge Piers Under Seismic Loading,” Department of Civil Engineering Research Report 75-3, University of Canterbury.

Dodd L.L. (1992). “The Dynamic Behavior of Reinforced Concrete Bridge Piers Subjected to New Zealand Seismicity,” PhD. Thesis, the University of Canterbury Christchurch New Zealand, 448 pages.

Dodd, L. L., and Cooke, N. (2000). “Capacity of Circular Bridge Columns Subjected to Base Excitation,” ACI Structural Journal, Vol. 97, No.2, pp.297-308.

Ernst G. C. (1957). “Plastic Hinging at the Intersection of Beams and Columns,” Journal of American Concrete Institute, Vol. 28, No.12, pp.1119-1144.

Gill W. D., Park R., and Priestley M. J. N. (1979). “Ductility of Rectangular Reinforced Concrete Columns with Axial Load,” Department of Civil Engineering Research Report 79-1, University of Canterbury.

Hachem M. M., Mahin, S.A., and Moehle J.P. (2003). “Performance of Circular Reinforced Concrete Bridge Columns under Bidirectional Earthquake Loading,” Report No. PEER 2003/06, Pacific Earthquake Engineering Research Center, University of California at Berkeley, 490 pp.

I.C.E. Research Committee (1962). “Ultimate Load Design of Concrete Structures,” Proceedings of I.C.E. (London), Vol. 21, pp. 399-442.

Kovacic D. (1995). “Design of High-Strength Concrete Columns,” M.Eng. Thesis, the University of Melbourne.

Mander J. B. (1983). “Seismic Design of Bridge Piers,” PhD Thesis, University of Canterbury, Christ Church, New Zealand.

Mander J. B., Priestley M. J. N., and Park R. (1984). “Seismic Design of Bridge Piers,” Department of Civil Engineering Research Report 84-2, University of Canterbury, 483 pp.

Mattock, A.H. (1964). “Rotational Capacity of Hinging Regions in Reinforced Concrete Beams,” Proceedings International Symposium on the Flexural Mechanics of Reinforced Concrete, ACI SP-12, Miami, pp. 143-181.

Mattock, A.H. (1967). “Discussion of “Rotational Capacity of Hinging Regions in Reinforced Concrete Beams,” by Corley, W.G., Journal of the Structural Division, ASCE, V. 93, No. ST2, Apr., pp. 519-522.

McCollister H. M., Siess C. P., and Newmark N. M. (1954). “Load Deformation Characteristic of Simulated Beam-Column Connections in Reinforced Concrete,” University of Illinois, Civil Engineering Studies, Structural Research Series.

Mendis, P. (2001). “Plastic Hinge Lengths of Normal and High-Strength Concrete in Flexure,” Advances in Structural Engineering, V. 4, No. 4, Oct., pp. 189-195.

Munro I. R. M., Priestley M. J. N., and Park R. (1976). “Seismic Behavior of Reinforced Concrete Bridge Piers,” Department of Civil Engineering Research Report 76-7, University of Canterbury.

Ng Kit Heng, Priestley M. J. N., and Park R. (1978). “Seismic Behavior of Circular Reinforced Concrete Bridge Piers,” Department of Civil Engineering Research Report 78-14, University of Canterbury.

Park R., Priestley M. J. N., and Gill W. D. (1982). “Ductility of Square-Confined Concrete Columns,” Struct. J., ASCE, 108, No. ST4, 929-950.

Paulay T., and Priestley M. J. N. (1992). “Seismic Design of Reinforced Concrete and Masonry Structures,” John Wiley & Sons, Inc.

Phan V., Saiidi M.S., Anderson J., and Ghasemi H. (2007). “Near-Fault Ground Motion Effects on Reinforced Concrete Bridge Columns,” Journal of Structural Eng., V.133, Issue 7, pp. 982-989.

Poologasoundranayagam K. (1960). “An analytical and experimental investigation of the formation and behavior of plastic hinges in prestressed and reinforced concrete frames,” Ph.D. Thesis, pp. 187.

Potangaroa R. T., Priestley M. J. N., and Park R. (1979). “Ductility of Spirally-Confined Reinforced Concrete Columns under Seismic Loading,” Department of Civil Engineering Research Report 79-8, University of Canterbury.

Priestley M. J. N., Park R., and Potangaroa R. T. (1981). “Ductility of Spirally-Confined Reinforced Concrete Columns,” Proceedings, ASCE, V.107, ST1, pp.181-202.

Priestley, M. J. N., and Park R. (1987). “Strength and Ductility of Concrete Bridge Columns under Seismic Loading,” ACI Structural Journal, V.84, Issue 1, pp. 61-76.

Restrepo J. I., Seible F., Stephan B., and Schoettler J. M. (2006). “Seismic Testing of Bridge Columns Incorporating High-Performance Materials,” ACI Structural Journal, V.103, Issue 4, pp. 496-504.

RRU Project 4805 (1983). “Ductility of Reinforced Concrete Bridge Piers Under Seismic Loading,” Road Research Unit Newsletter, RRU NL 75, National Roads Board, Wellington, New Zealand, pp.27-28.

Sakai, K. and Sheikh, S.A. (1989). “What Do We Know about Confinement in Reinforced Concrete Columns? (A Critical Review of Previous Work and Code Provisions),” ACI Structural Journal, V. 86, No. 2, Mar.-Apr., pp. 192-207.

Sheikh, S.A. and Khoury, S.S. (1993). “Confined Concrete Columns with Stubs,” ACI Structural Journal, V. 90, No. 4, July-Aug., pp. 414-431.

Sheikh, S.A., Shah, D.V. and Khoury, S.S. (1994). “Confinement of High-Strength Concrete Columns,” ACI Structural Journal, V. 91, No. 1, Jan.-Feb., pp. 100-111.

Soesianawati, M.T., Park, R. and Priestley, M.J.N. (1986). “Limited Ductility Design of Reinforced Concrete Columns,” Research Report 86-10, Department of Civil Engineering, University of Canterbury, Christchurch, New Zealand, Mar., 208 pp.

Standards Association of New Zealand (1982). “New Zealand Standard Code of Practice for the Design of Concrete Structures,” NZS 3101, Wellington, New Zealand.

Watson, S. and Park, R. (1994). “Simulated Seismic Load Tests on Reinforced Concrete Columns,” Journal of Structural Engineering, ASCE, V. 120, No. 6, June, pp. 1825-1849.

Tanaka, H. and Park, R. (1990). “Effect of Lateral Confining Reinforcement on the Ductile Behavior of Reinforced Concrete Columns,” Research Report 90-2, Department of Civil Engineering, University of Canterbury, Christchurch, New Zealand, June, 458 pp.

APPENDIX A

Appendix A contains the comparisons of rotations at each LVDT location for the three different tests as described in Chapter 2.

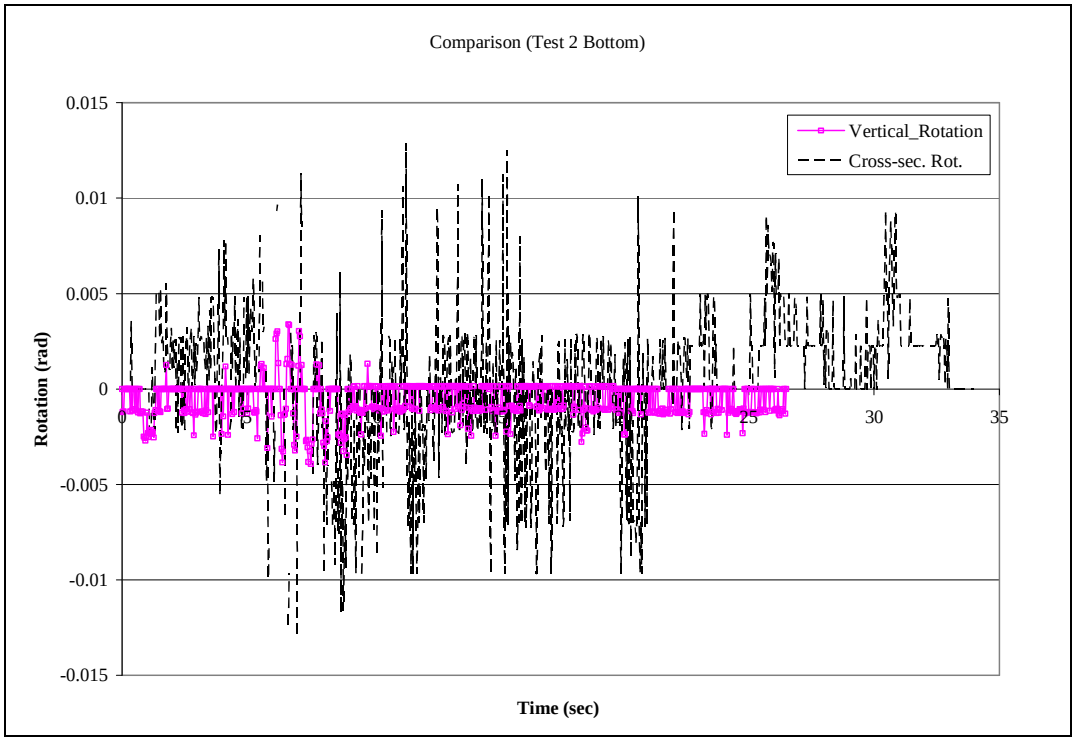

Fig. A-1: Comparison of rotations (local vs. average) at Point 3-8

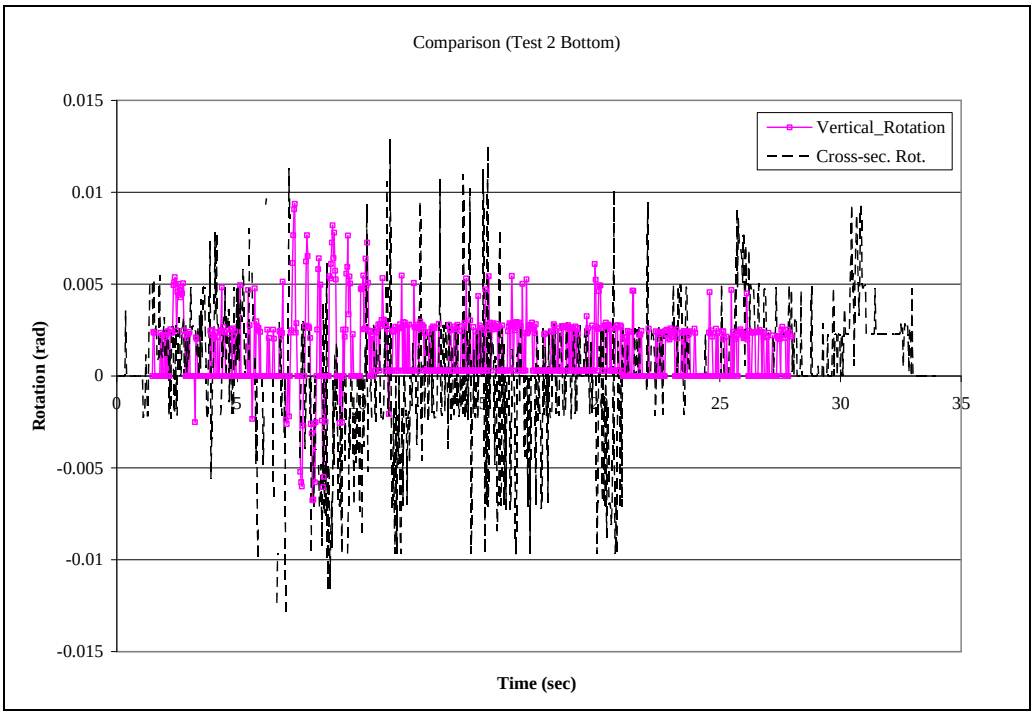

Fig. A-2: Comparison of rotations (local vs. average) at Point 8-13

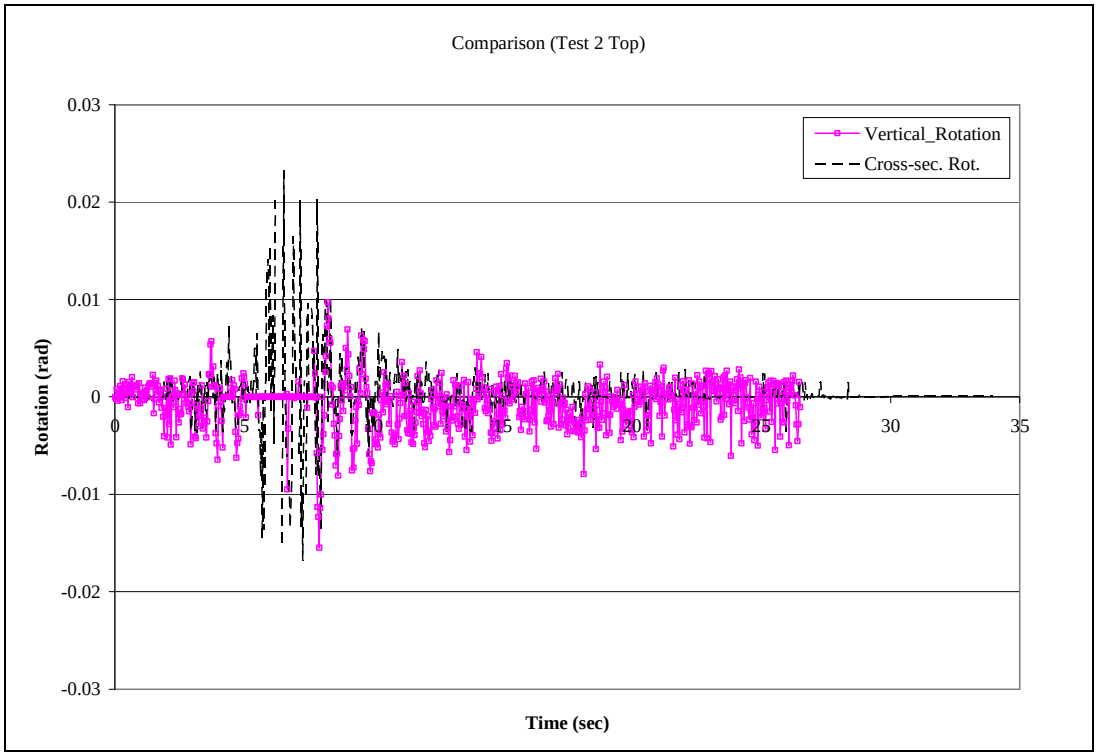

Fig. A-3: Comparison of rotations (local vs. average) at Point 38-45

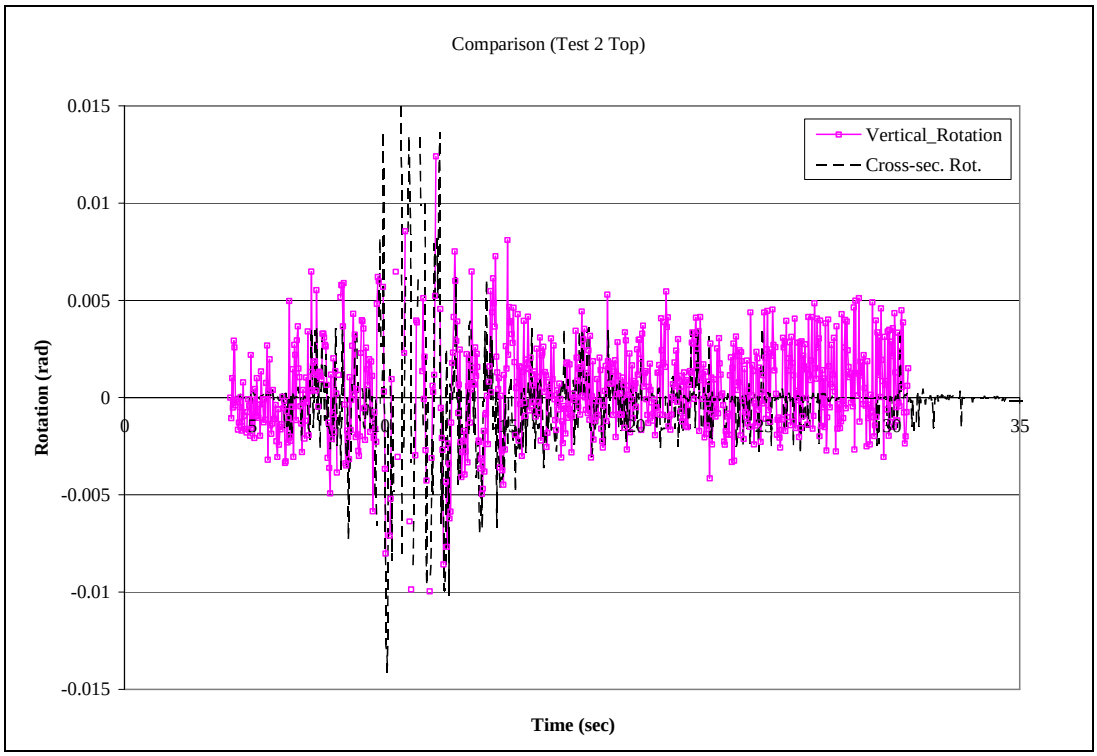

Fig. A-4: Comparison of rotations (local vs. average) at Point 45-52

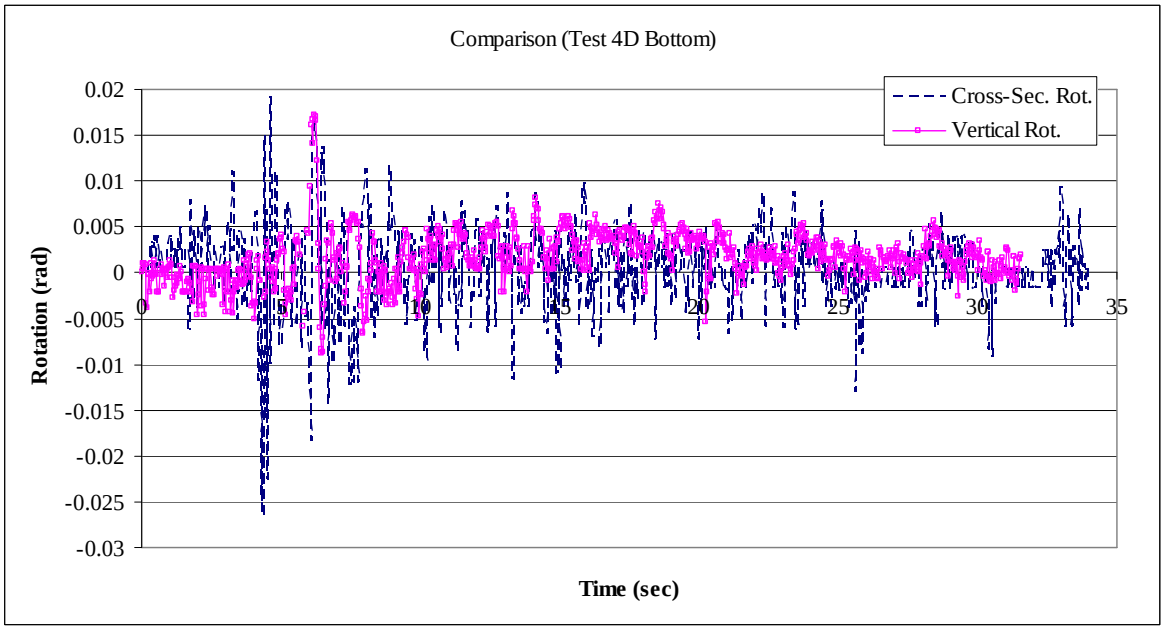

Fig. A-5: Comparison of rotations (local vs. average) at Point 3-8

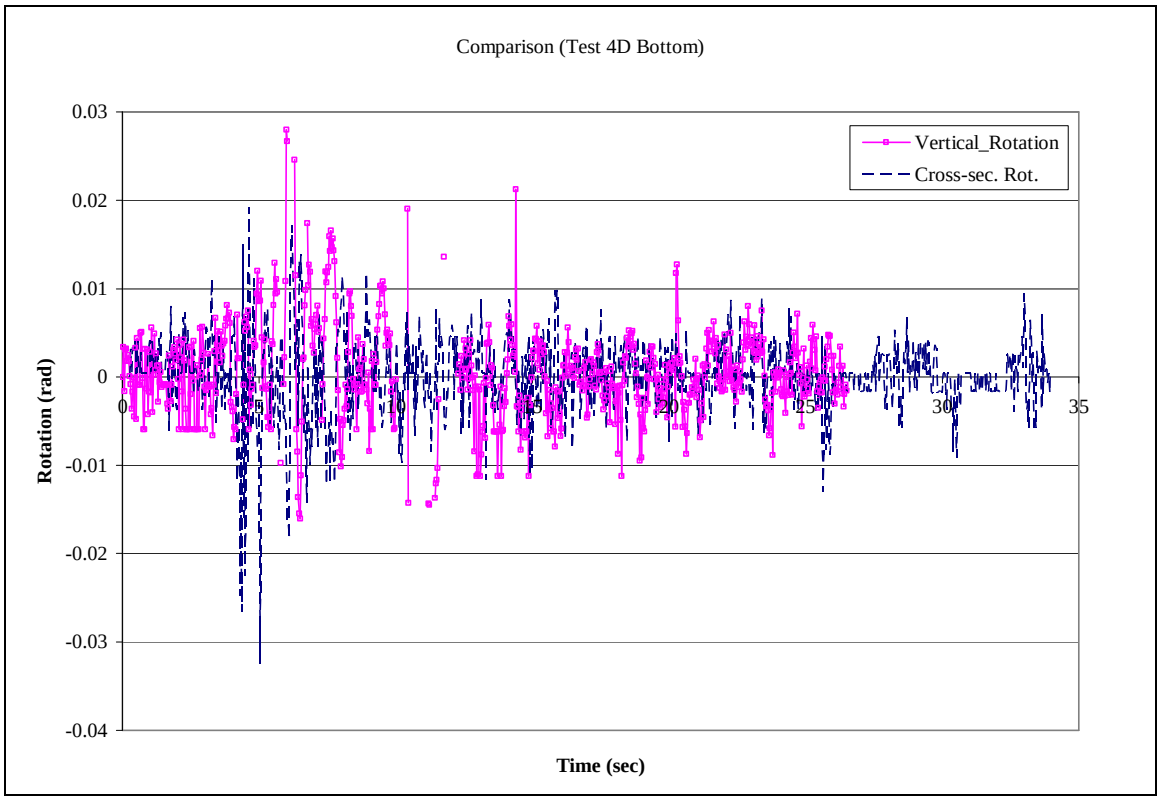

Fig. A-6: Comparison of rotations (local vs. average) at Point 8-13

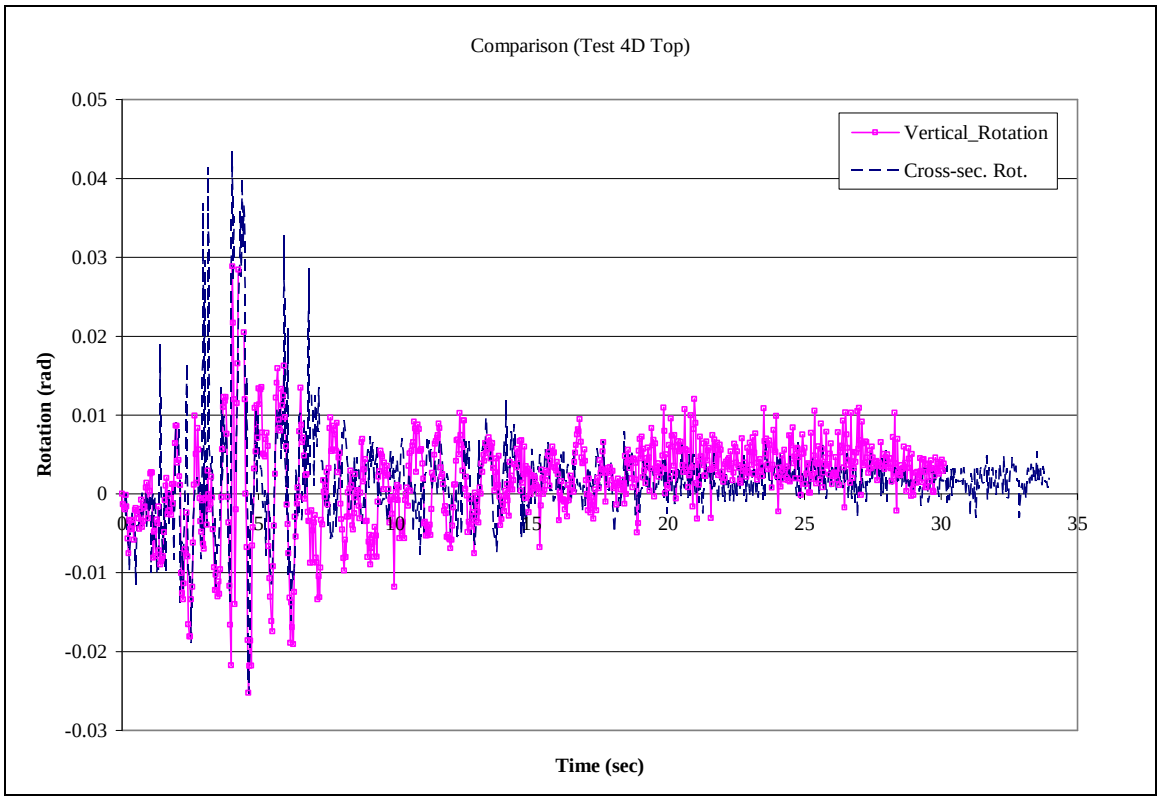

Fig. A-7: Comparison of rotations (local vs. average) at Point 38-45

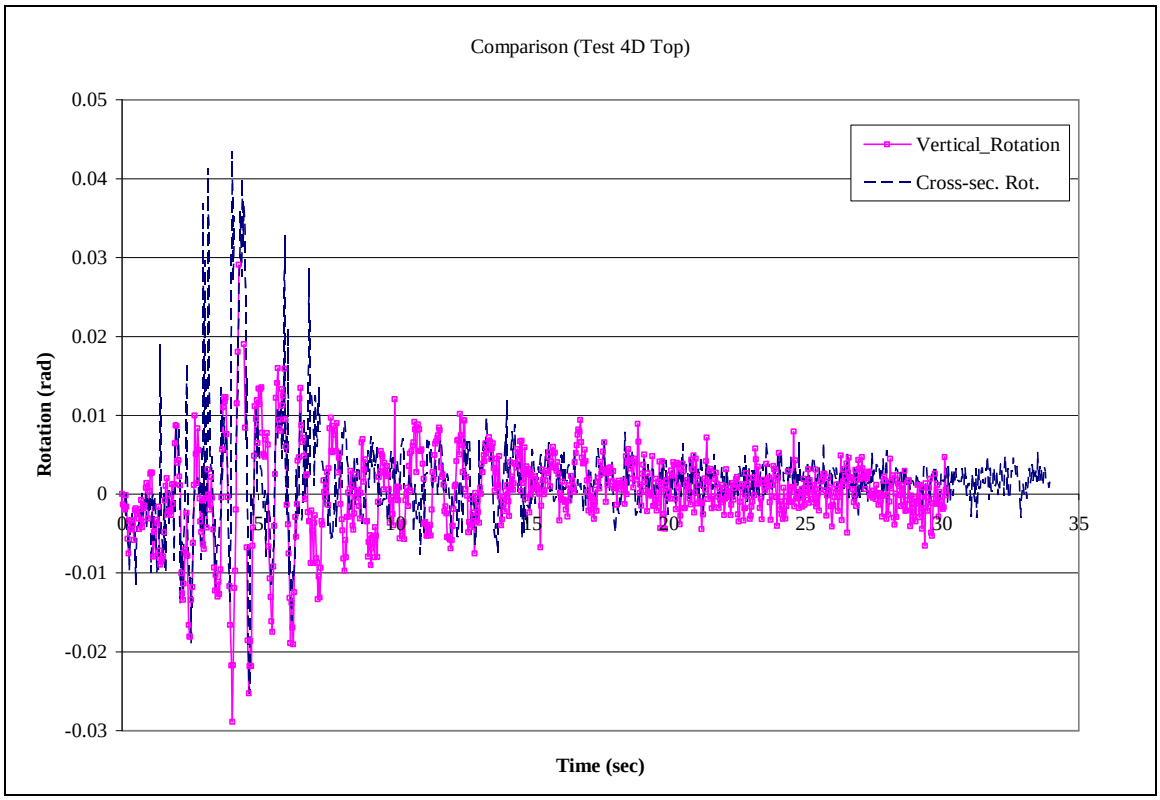

Fig. A-8: Comparison of rotations (local vs. average) at Point 45-52

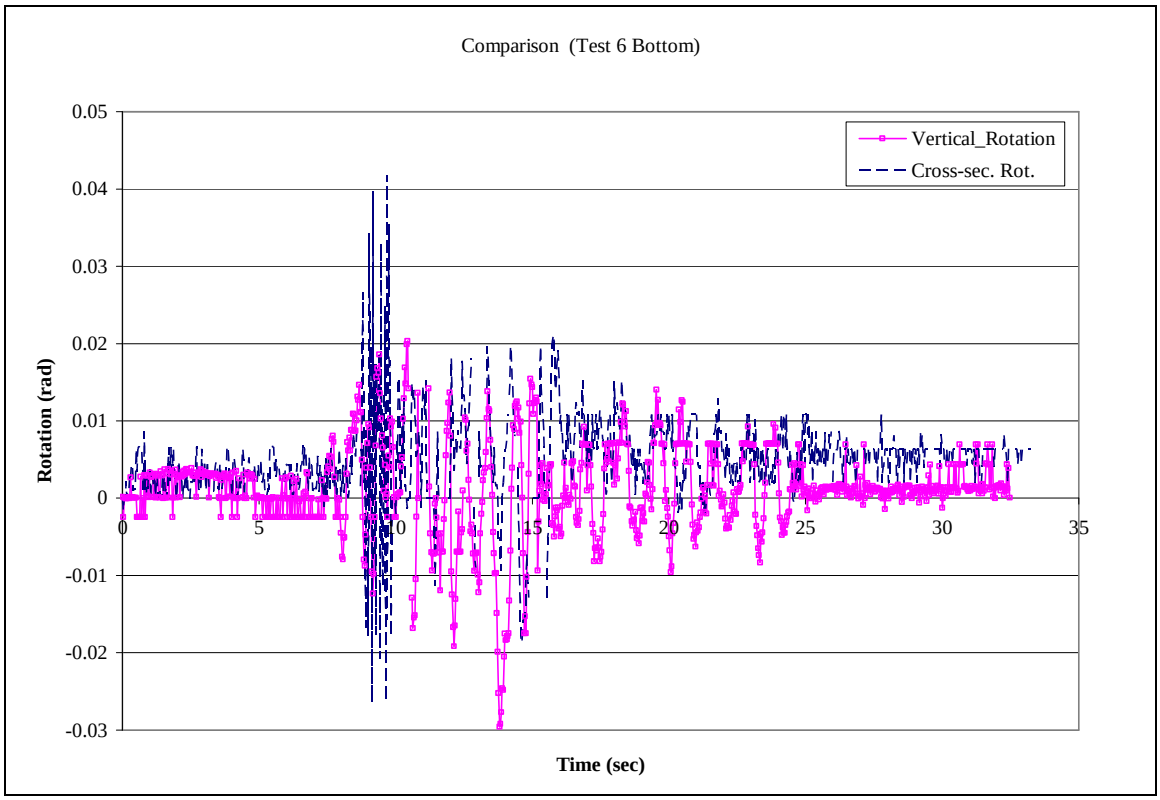

Fig. A-9: Comparison of rotations (local vs. average) at Point 3-8

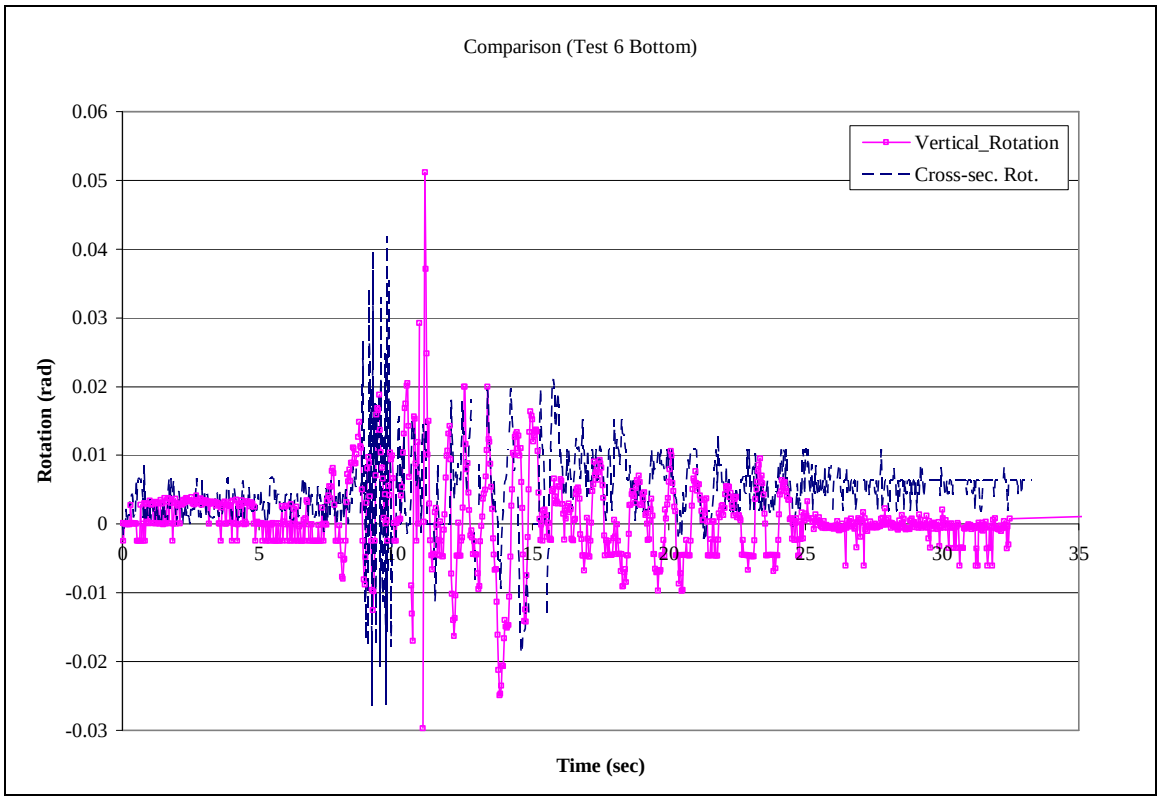

Fig. A-10: Comparison of rotations (local vs. average) at Point 8-13

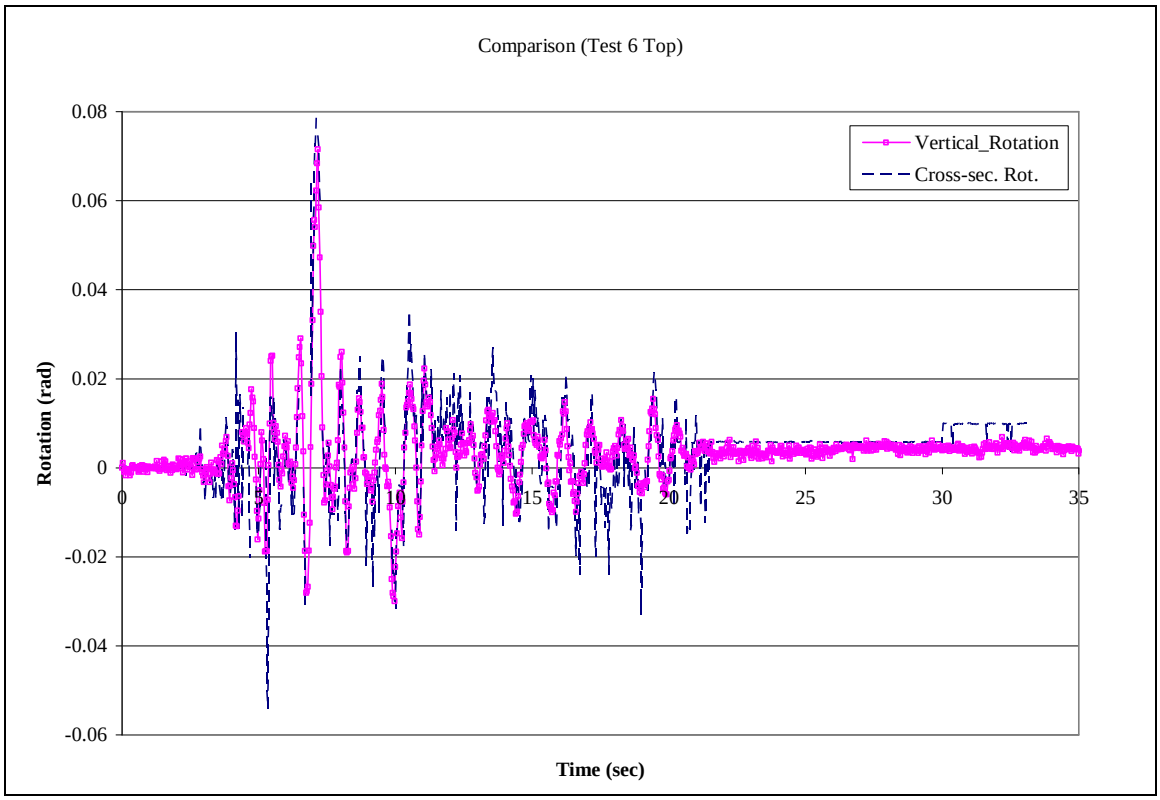

Fig. A-11: Comparison of rotations (local vs. average) at Point 38-45

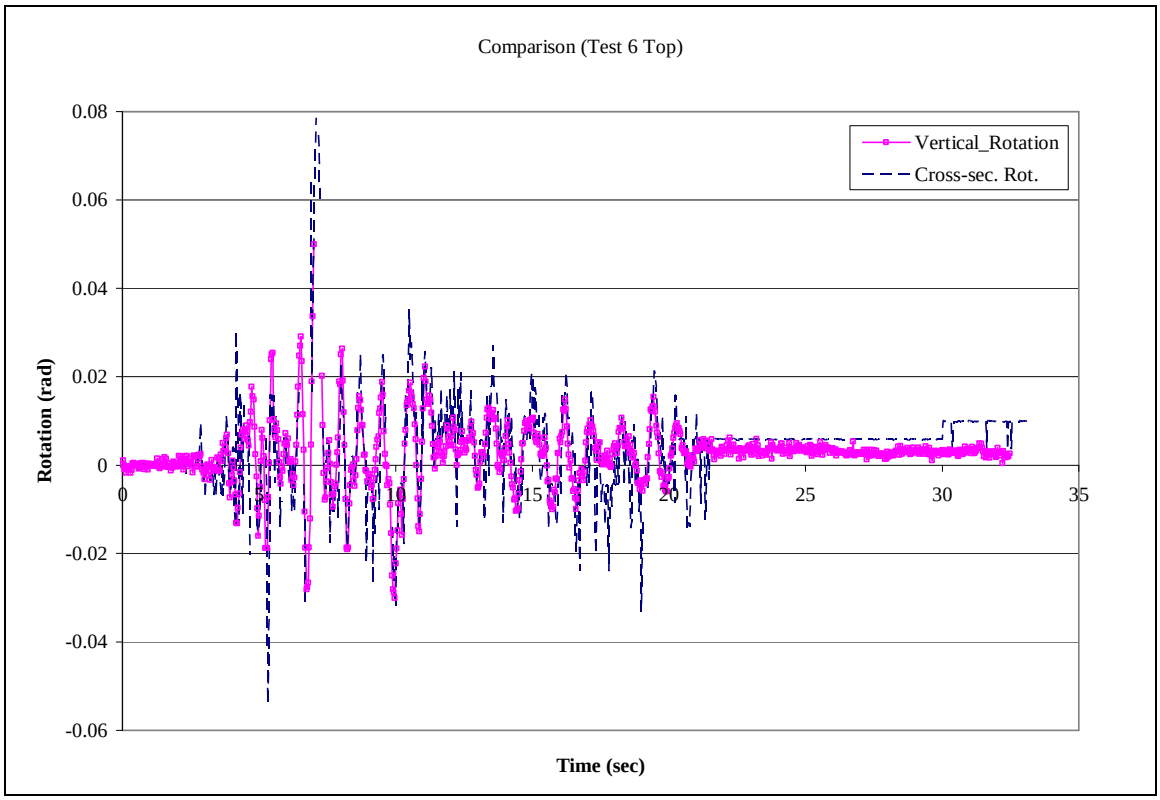

Fig. A-12: Comparison of rotations (local vs. average) at Point 45-52

APPENDIX B

Appendix B presents the comparisons of lateral displacements at each point on the grid surface for the three different tests described in Chapter 2.

Note: Comparisons are done with the combined movements of DT7, DS5 and DS1 instrumentation. Note that there is difference of amplitude between the results because of a difference in height at the points of measurements.

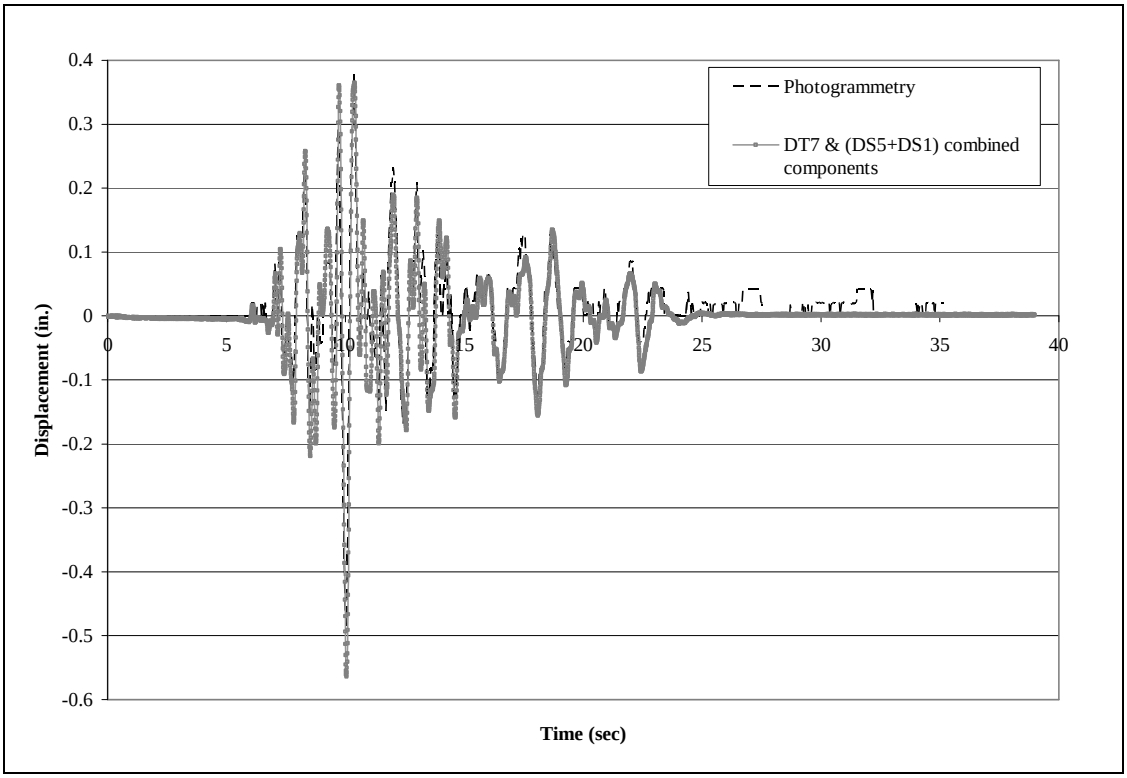

Fig. B-1: Lateral movement of Point 2 for Test 2 (1 in. = 254 mm)

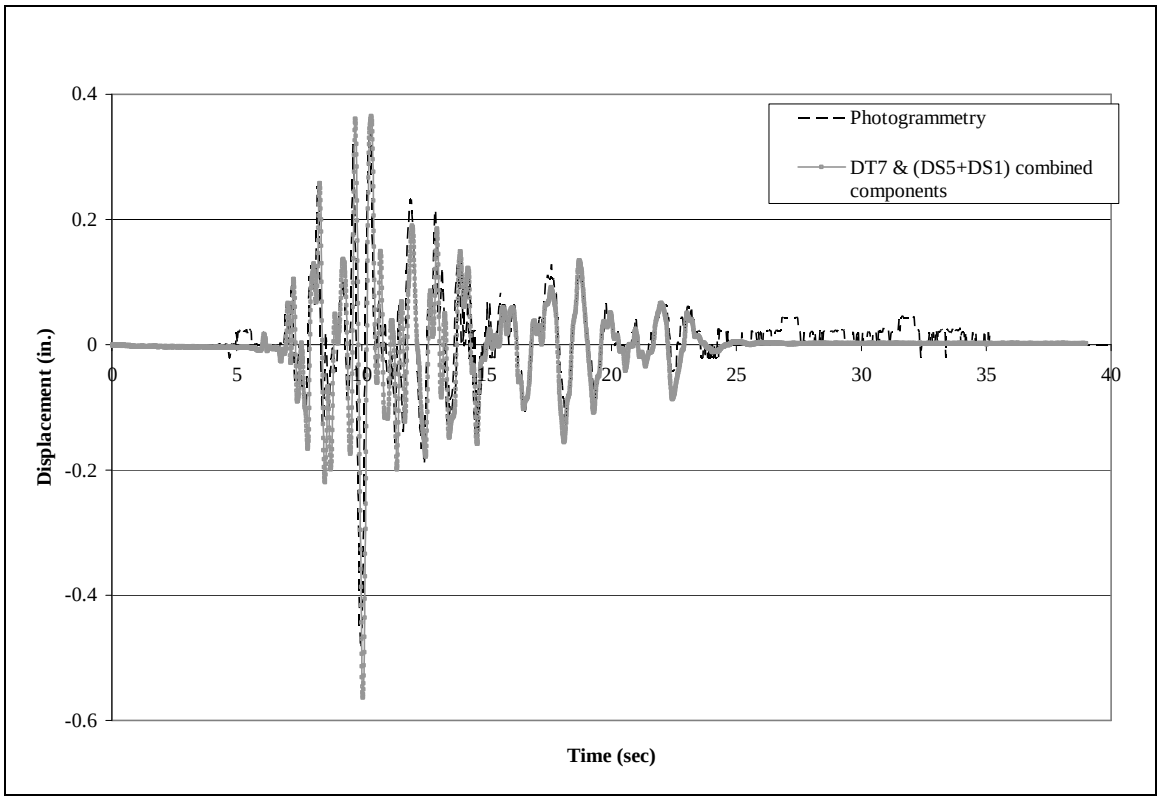

Fig. B-2: Lateral movement of Point 3 for Test 2 (1 in. = 254 mm)

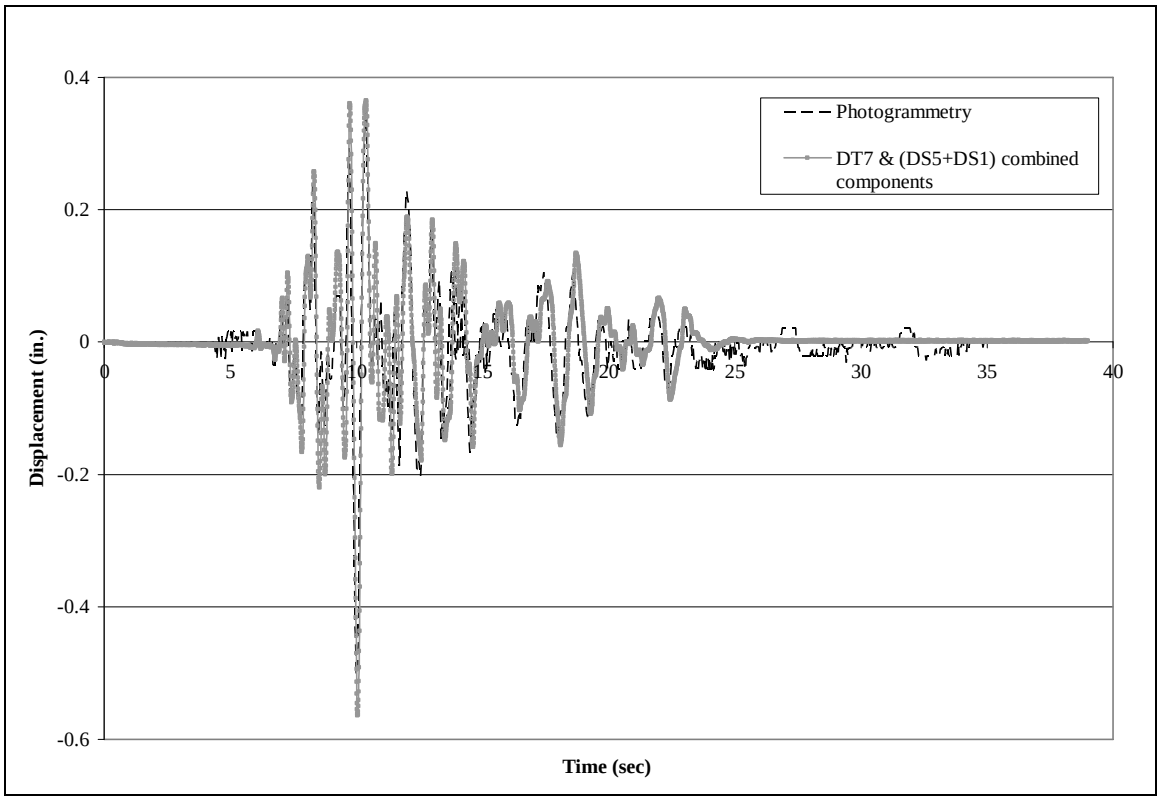

Fig. B-3: Lateral movement of Point 4 for Test 2 (1 in. = 254 mm)

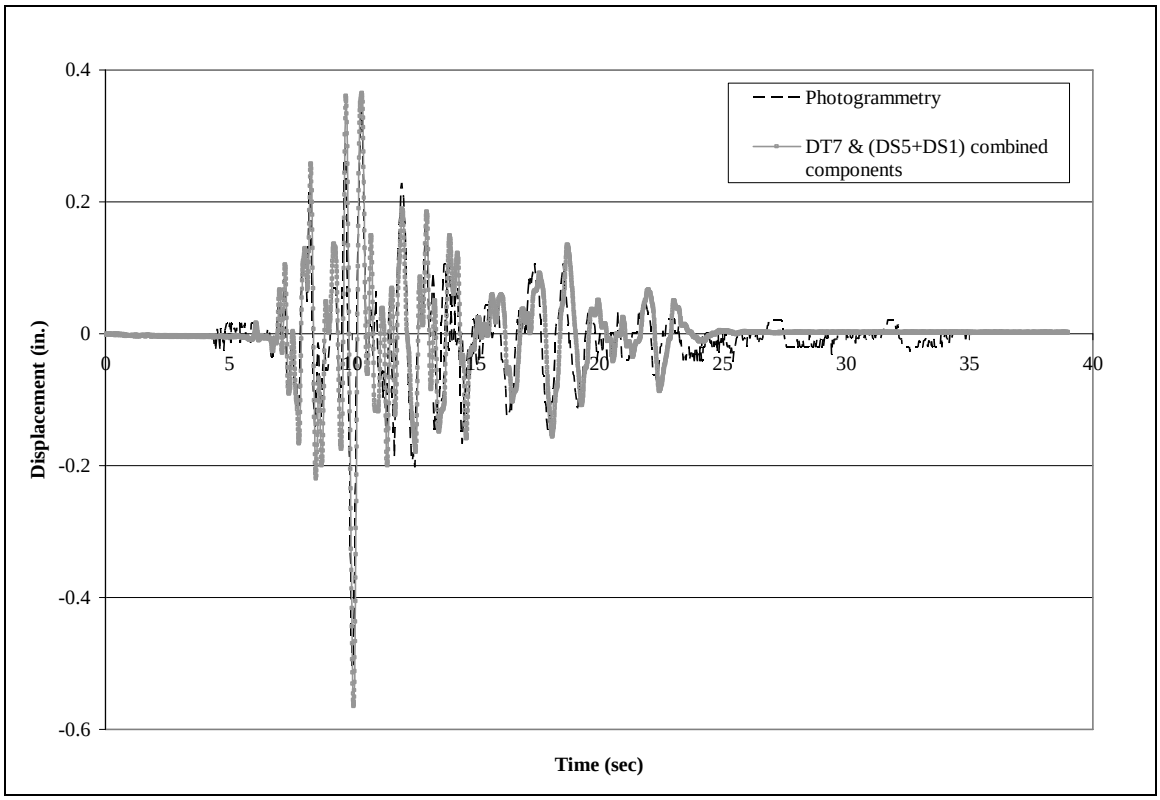

Fig. B-4: Lateral movement of Point 7 for Test 2 (1 in. = 254 mm)

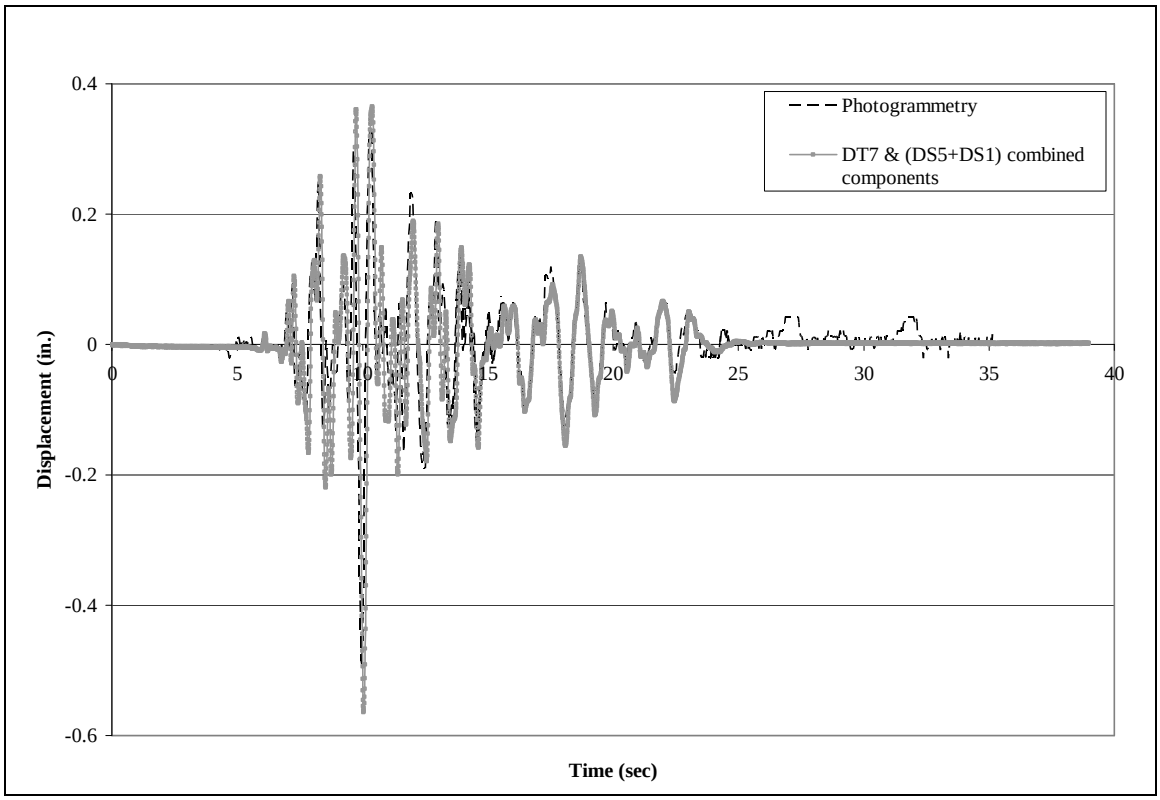

Fig. B-5: Lateral movement of Point 8 for Test 2 (1 in. = 254 mm)

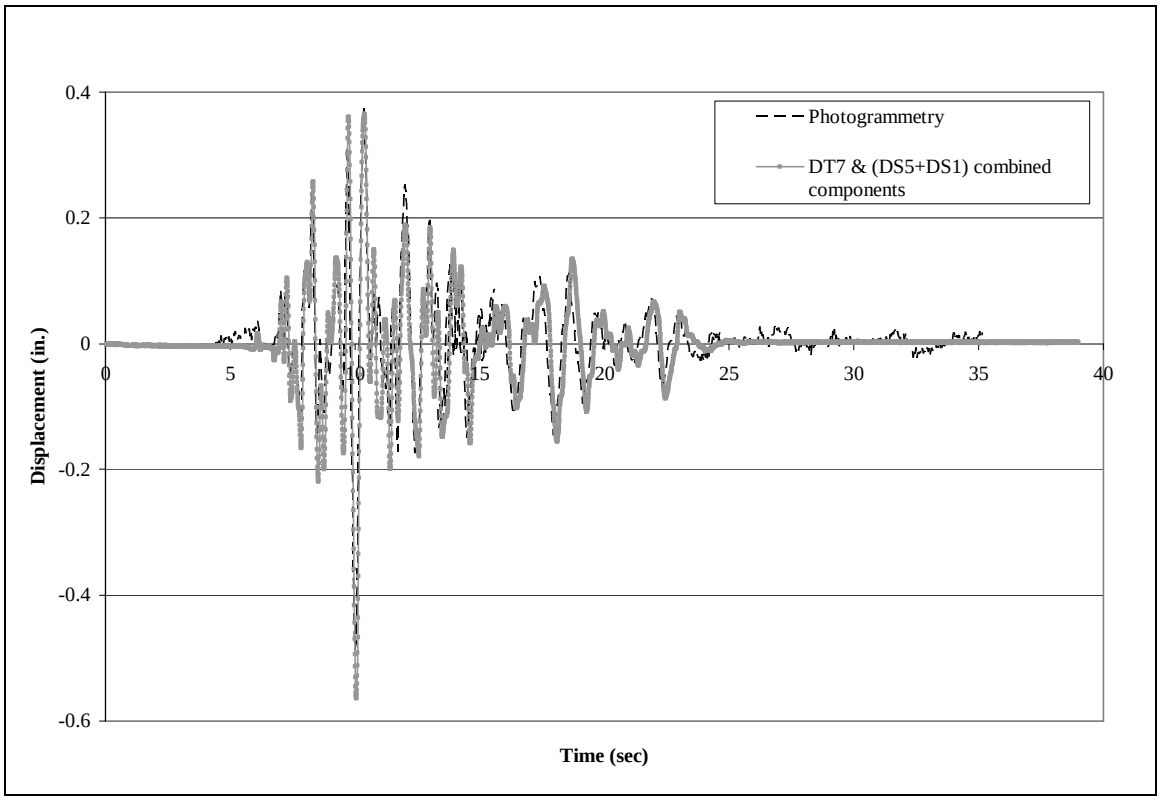

Fig. B-6: Lateral movement of Point 9 for Test 2 (1 in. = 254 mm)

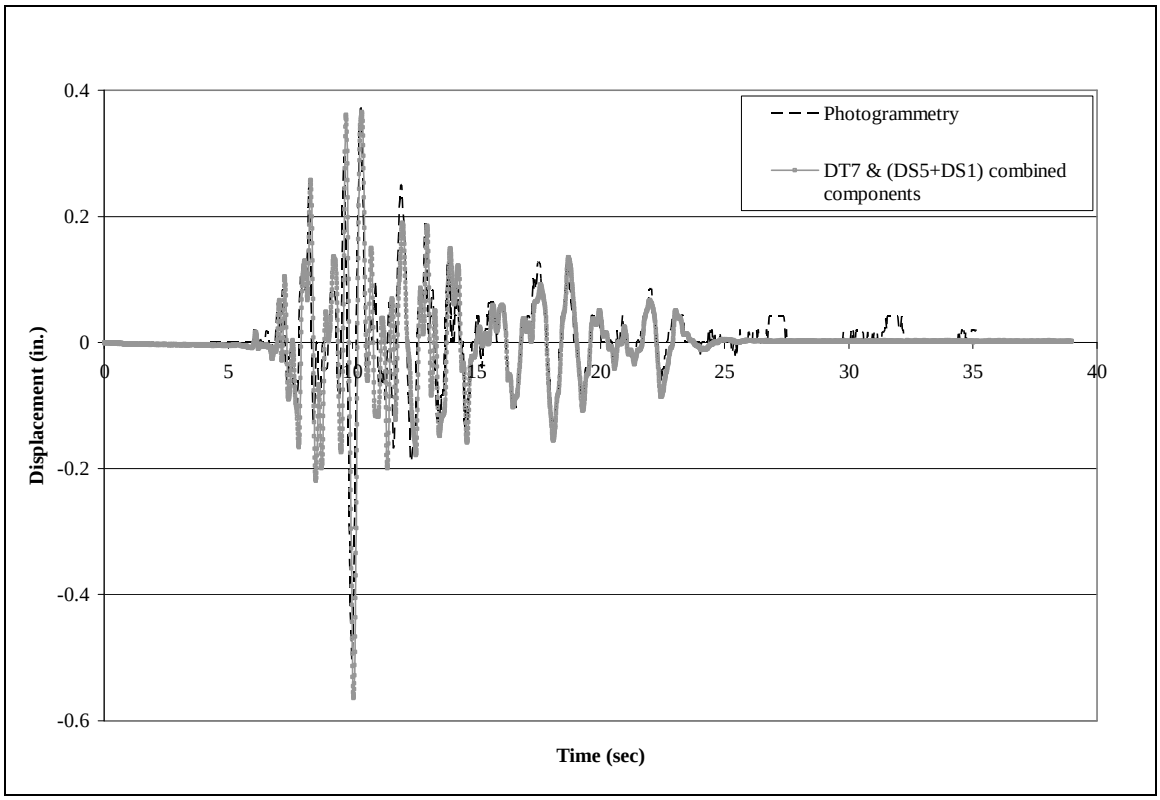

Fig. B-7: Lateral movement of Point 12 for Test 2 (1 in. = 254 mm)

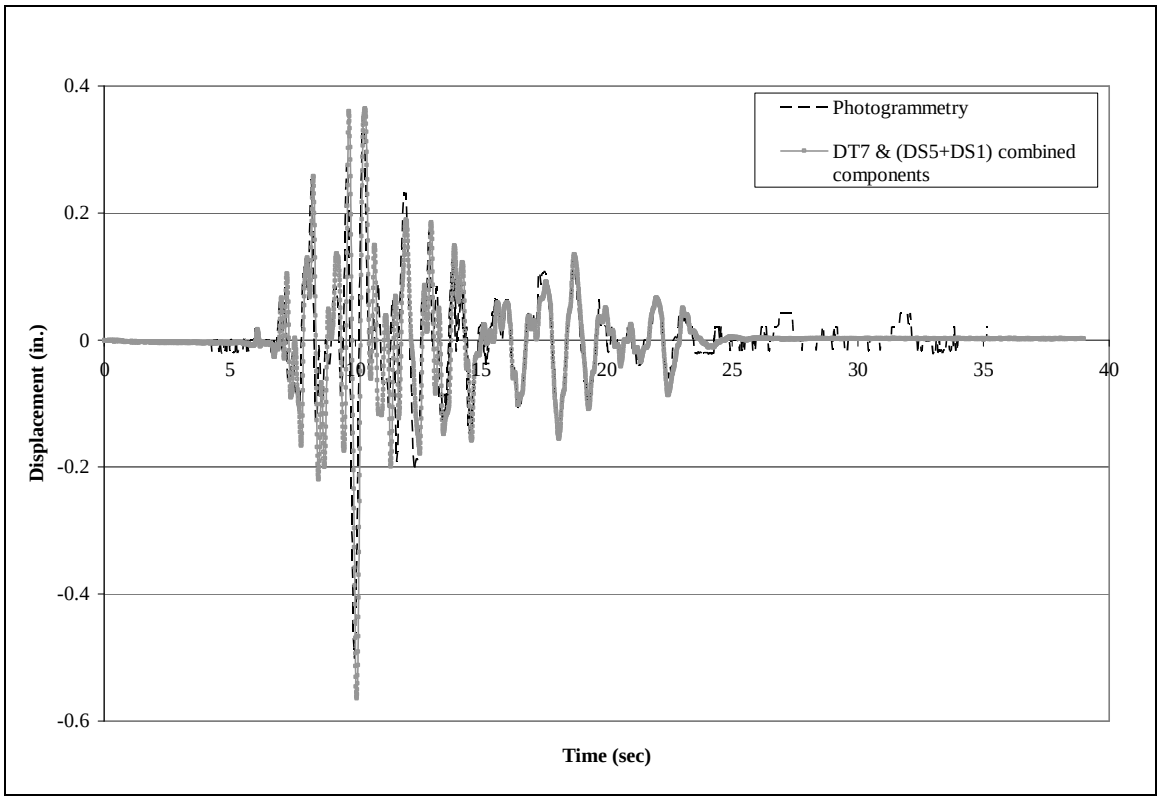

Fig. B-8: Lateral movement of Point 13 for Test 2 (1 in. = 254 mm)

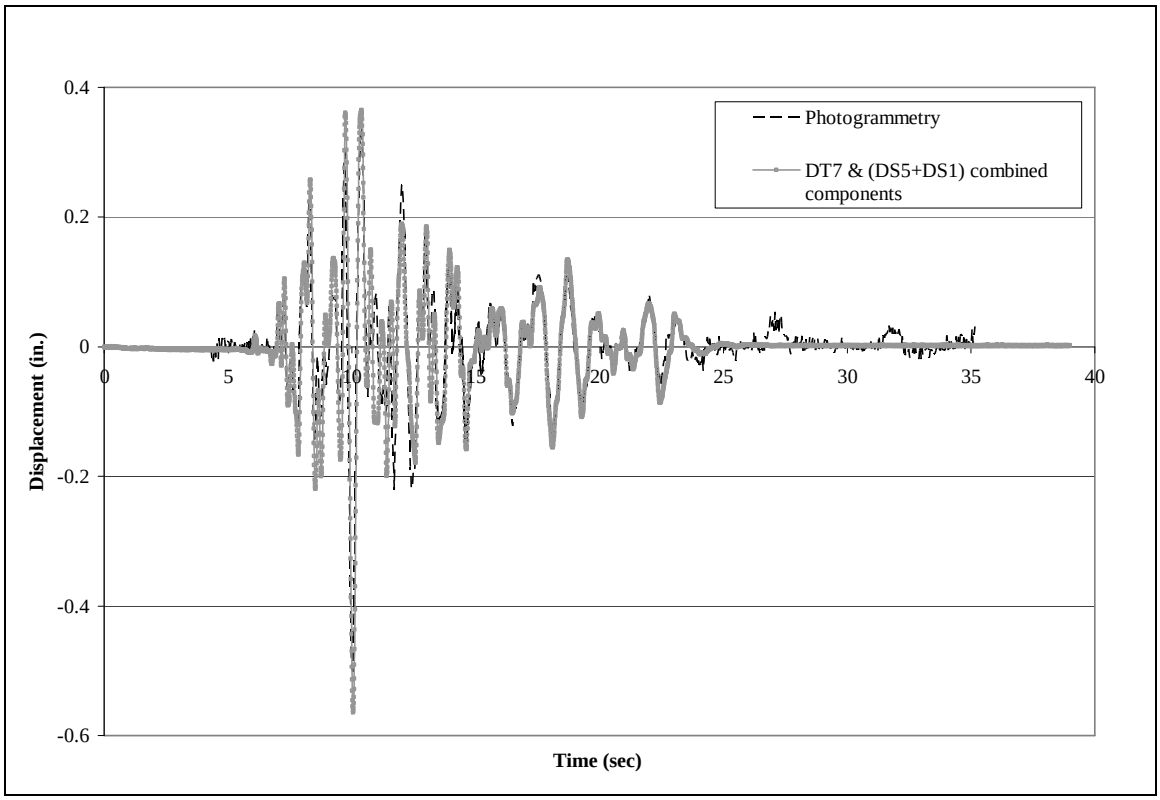

Fig. B-9: Lateral movement of Point 14 for Test 2 (1 in. = 254 mm)

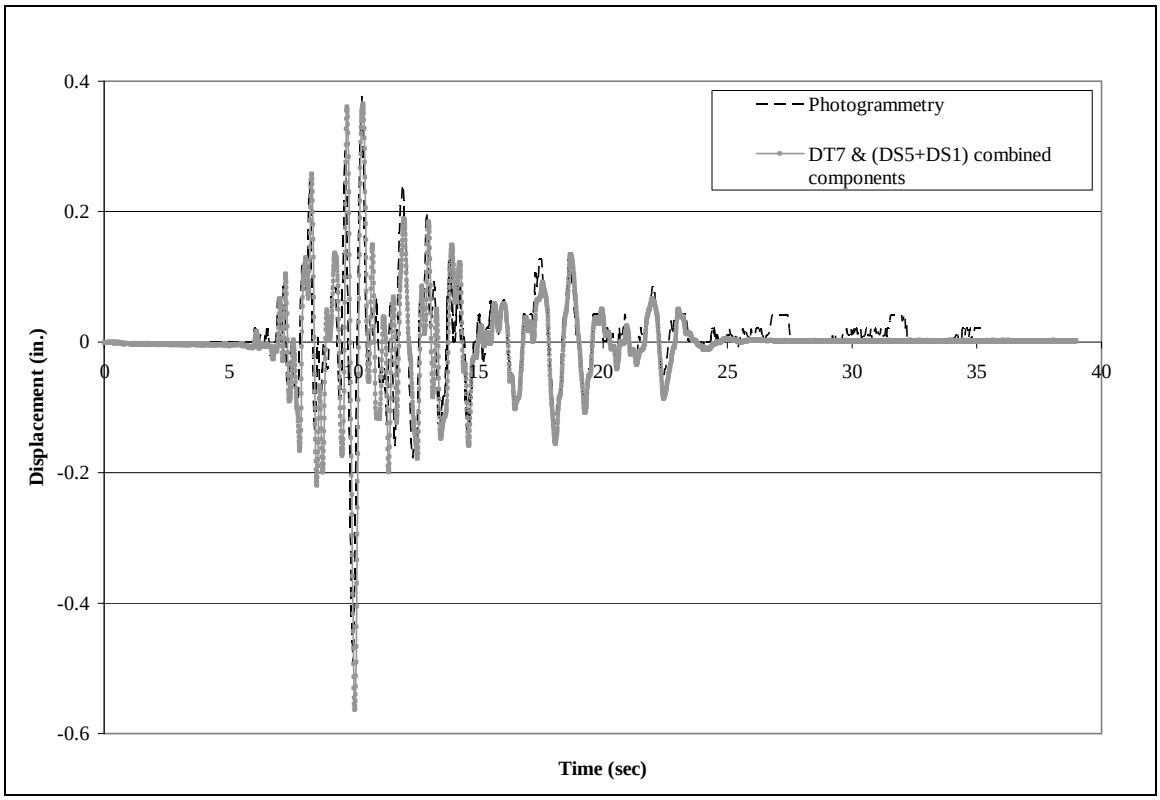

Fig. B-10: Lateral movement of Point 17 for Test 2 (1 in. = 254 mm)

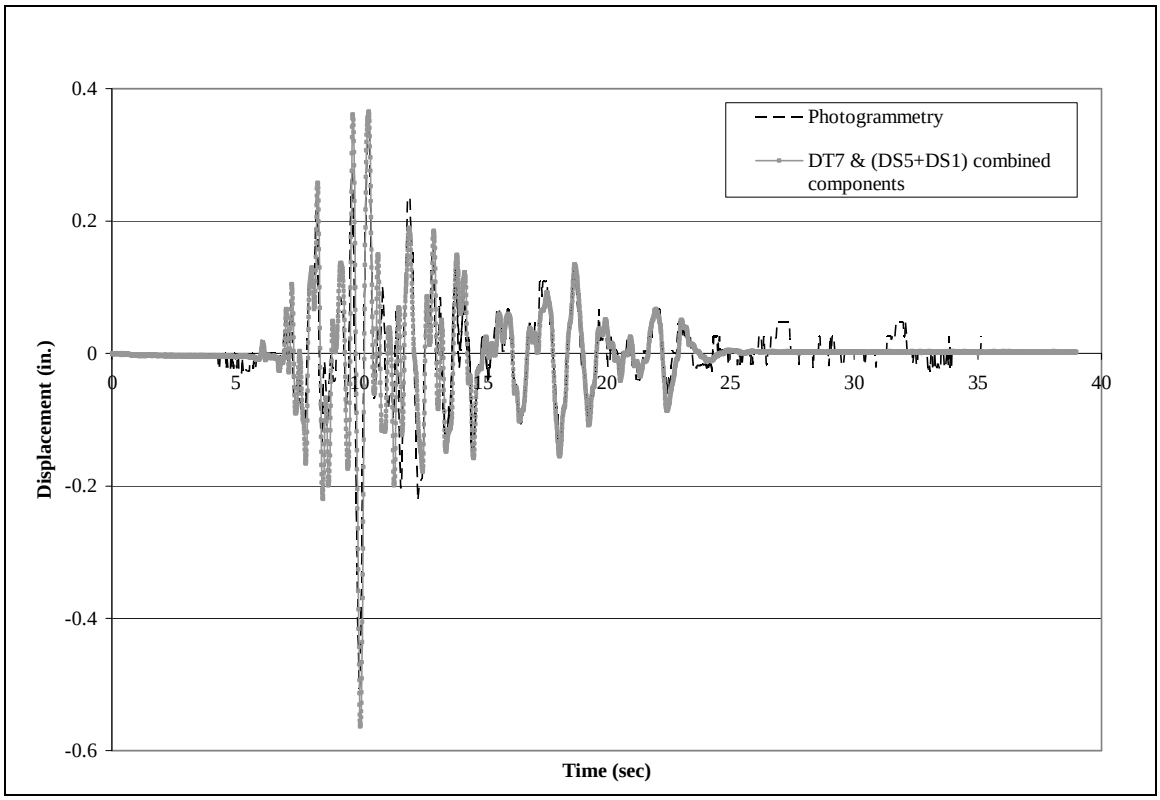

Fig. B-11: Lateral movement of Point 18 for Test 2 (1 in. = 254 mm)

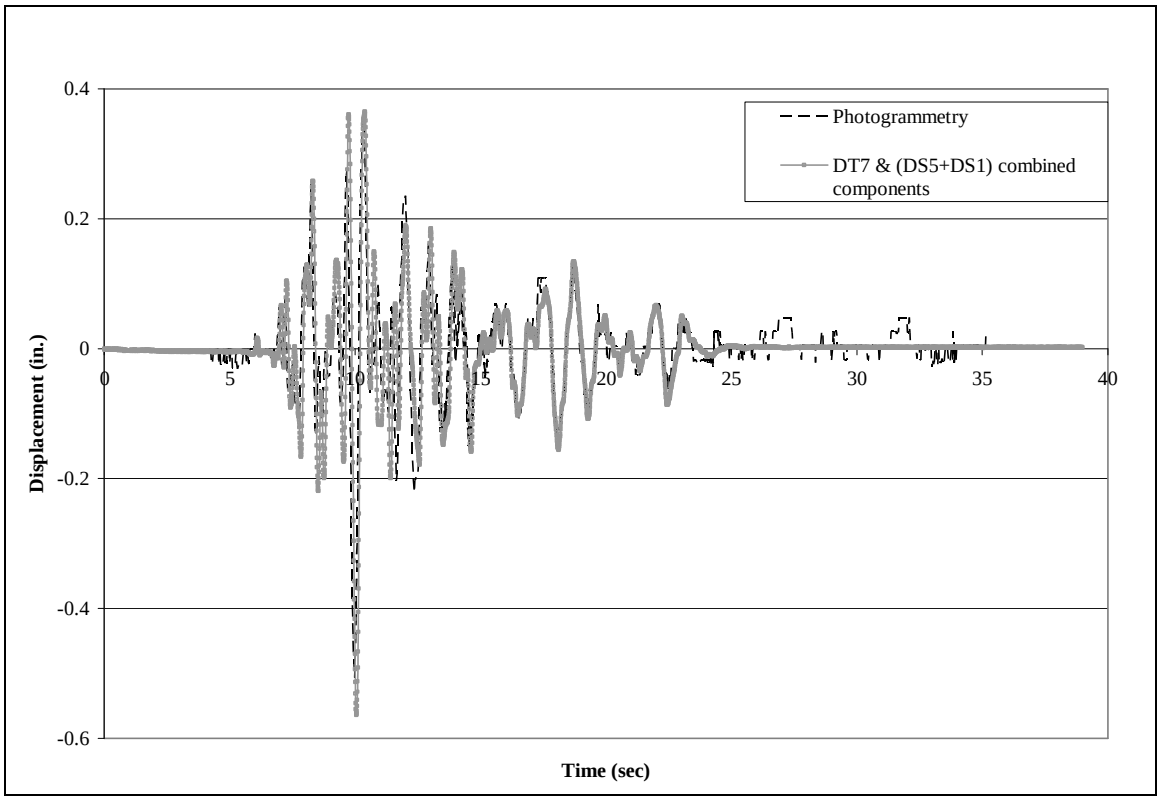

Fig. B-12: Lateral movement of Point 19 for Test 2 (1 in. = 254 mm)

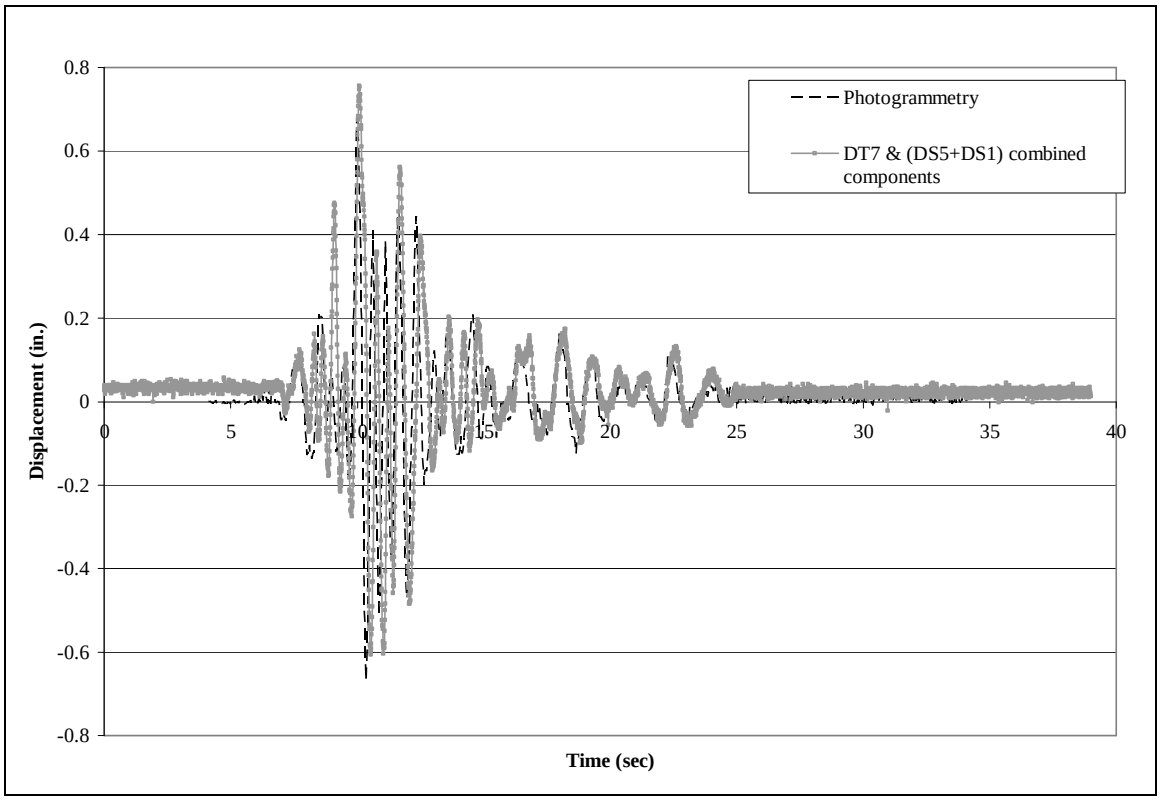

Fig. B-13: Lateral movement of Point 31 for Test 2 (1 in. = 254 mm)

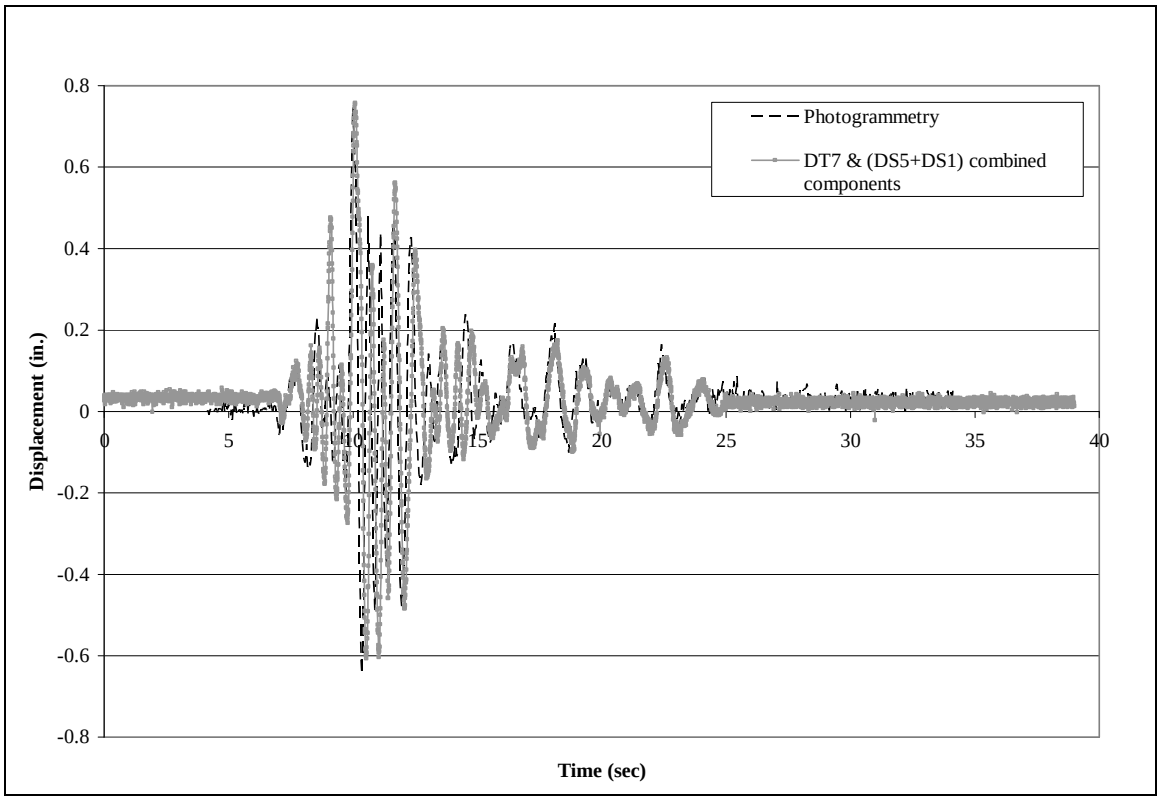

Fig. B-14: Lateral movement of Point 37 for Test 2 (1 in. = 254 mm)

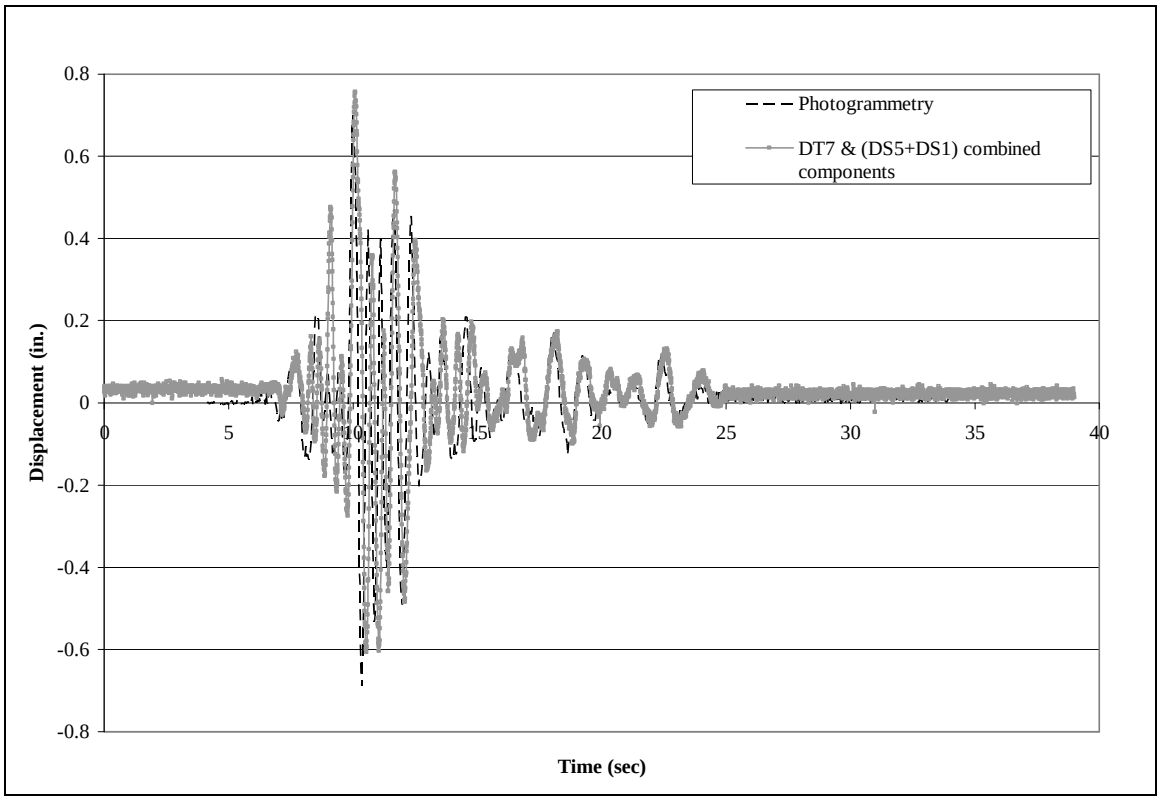

Fig. B-15: Lateral movement of Point 38 for Test 2 (1 in. = 254 mm)

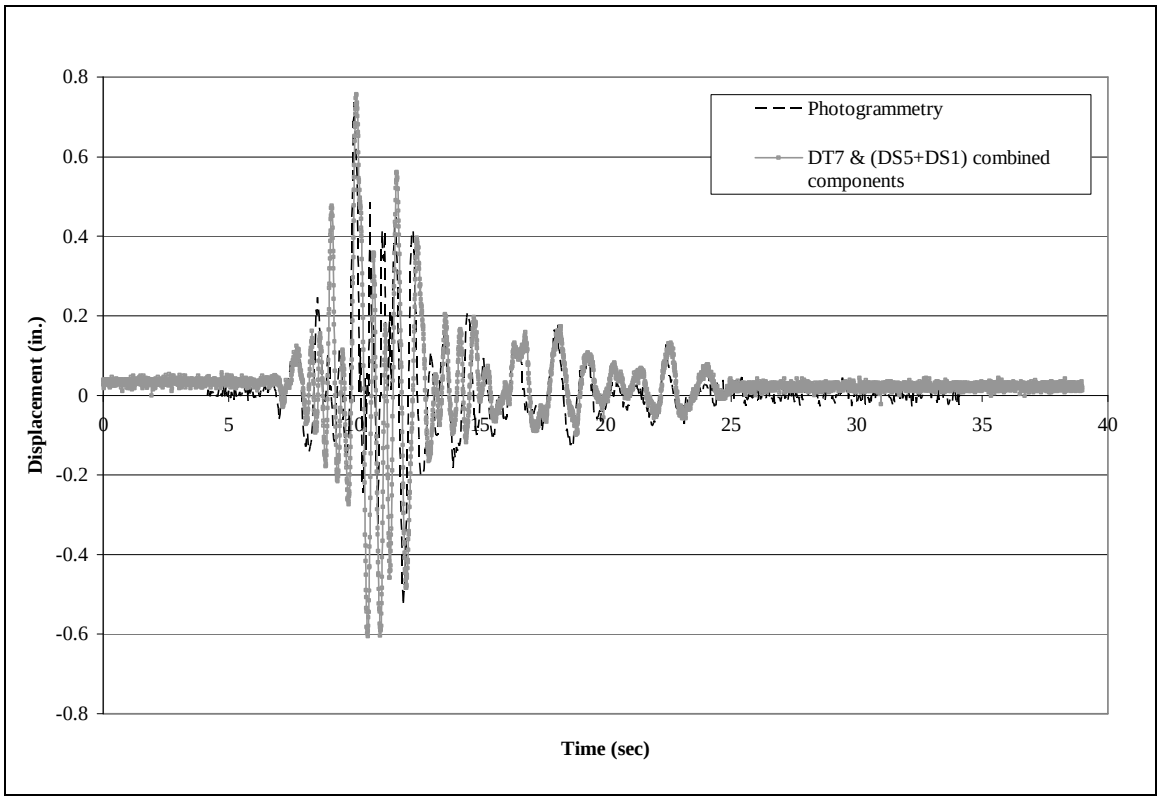

Fig. B-16: Lateral movement of Point 39 for Test 2 (1 in. = 254 mm)

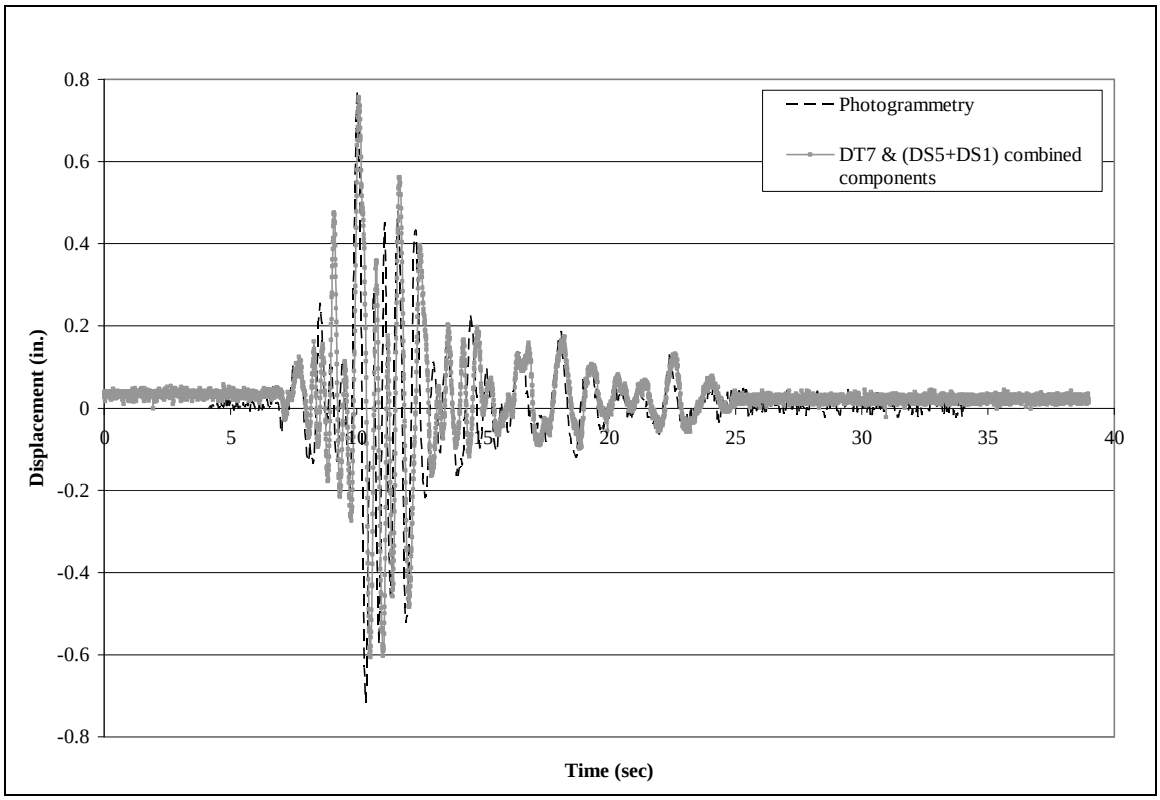

Fig. B-17: Lateral movement of Point 44 for Test 2 (1 in. = 254 mm)

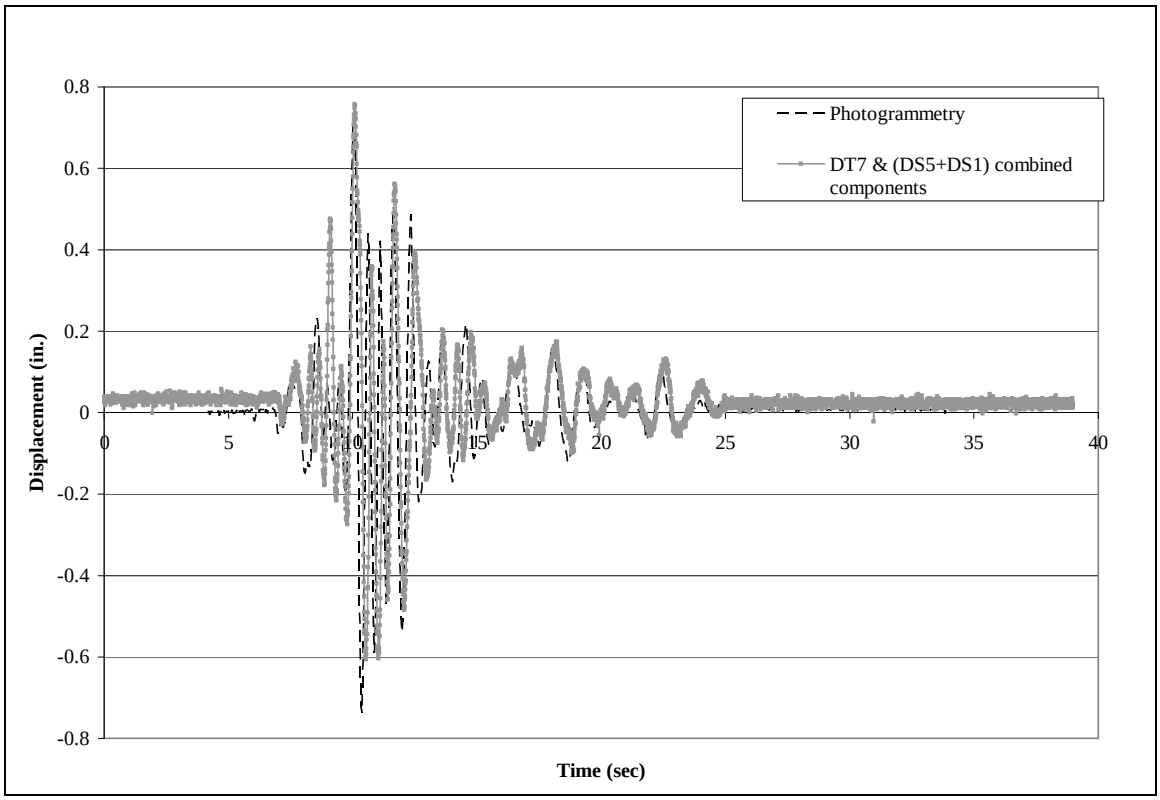

Fig. B-18: Lateral movement of Point 45 for Test 2 (1 in. = 254 mm)

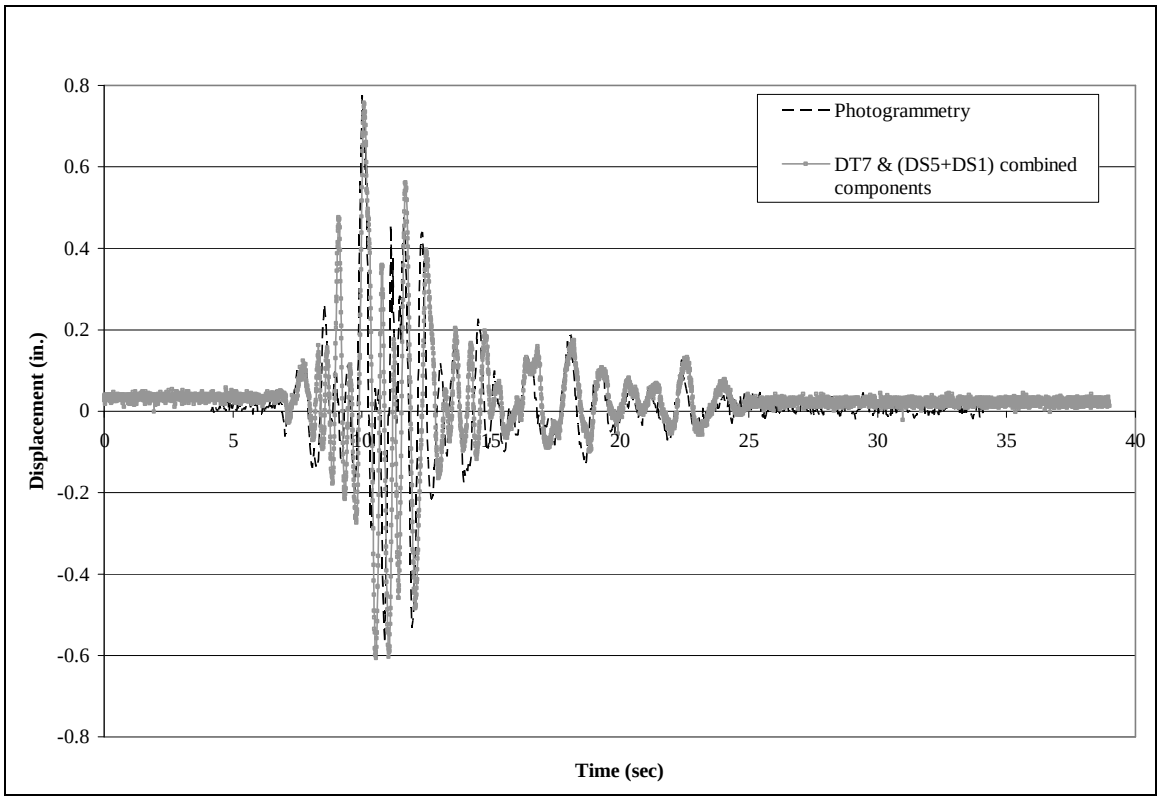

Fig. B-19: Lateral movement of Point 46 for Test 2 (1 in. = 254 mm)

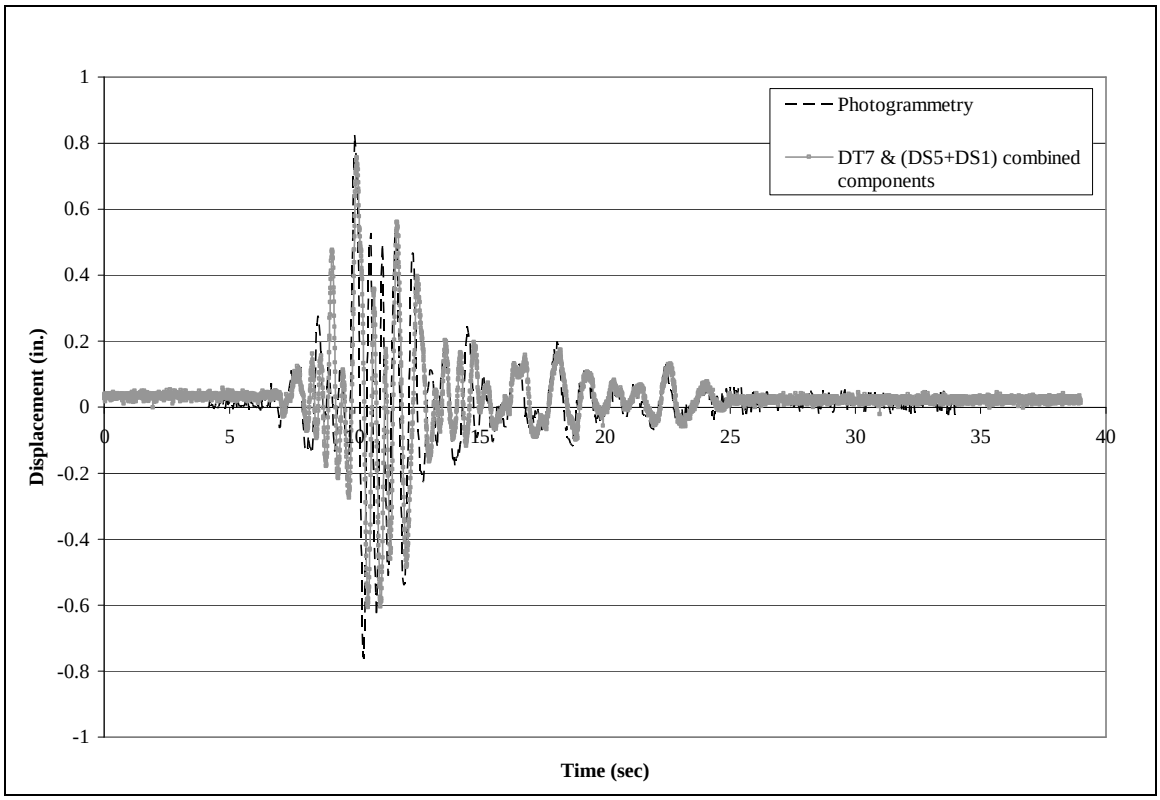

Fig. B-20: Lateral movement of Point 51 for Test 2 (1 in. = 254 mm)

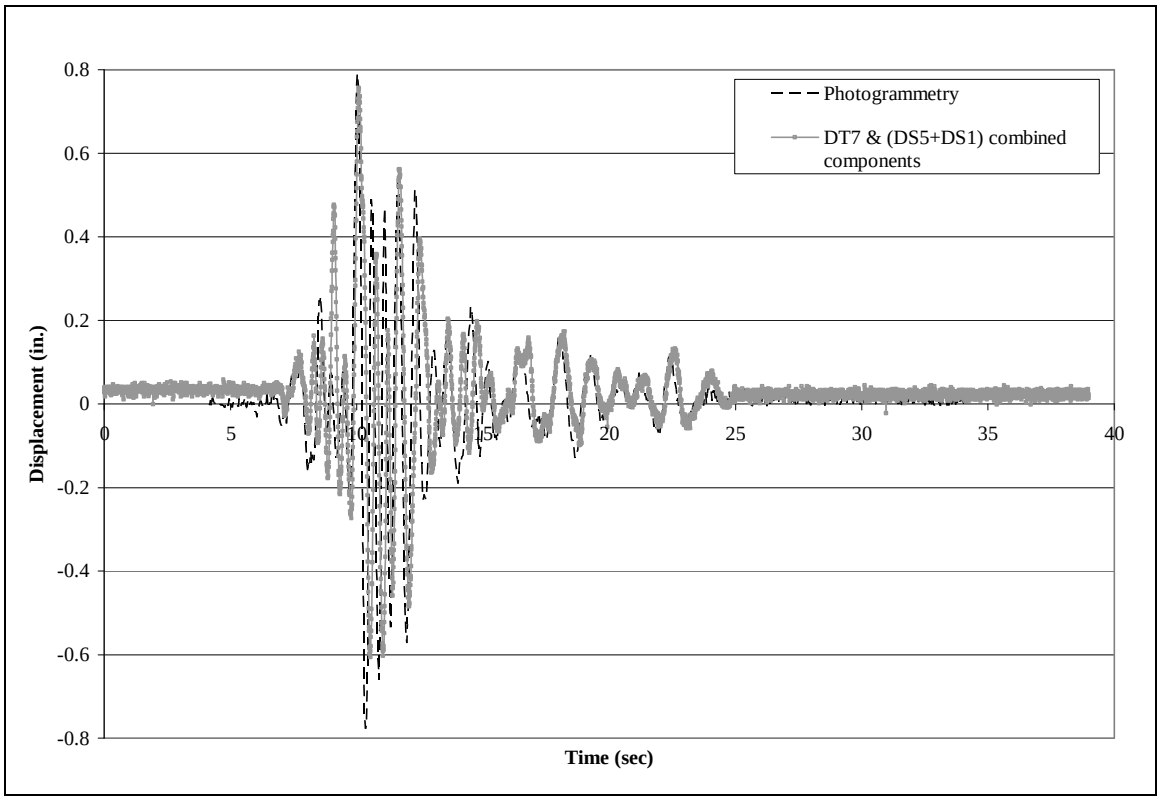

Fig. B-21: Lateral movement of Point 52 for Test 2 (1 in. = 254 mm)

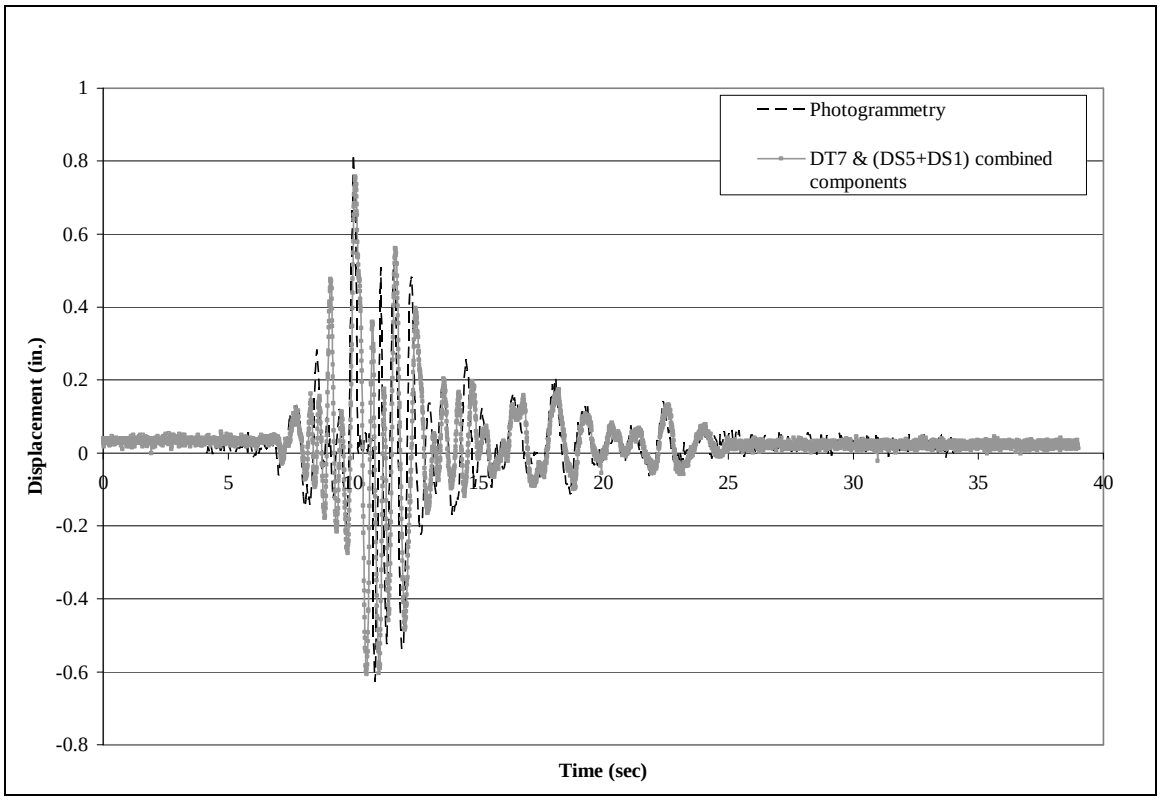

Fig. B-22: Lateral movement of Point 53 for Test 2 (1 in. = 254 mm)

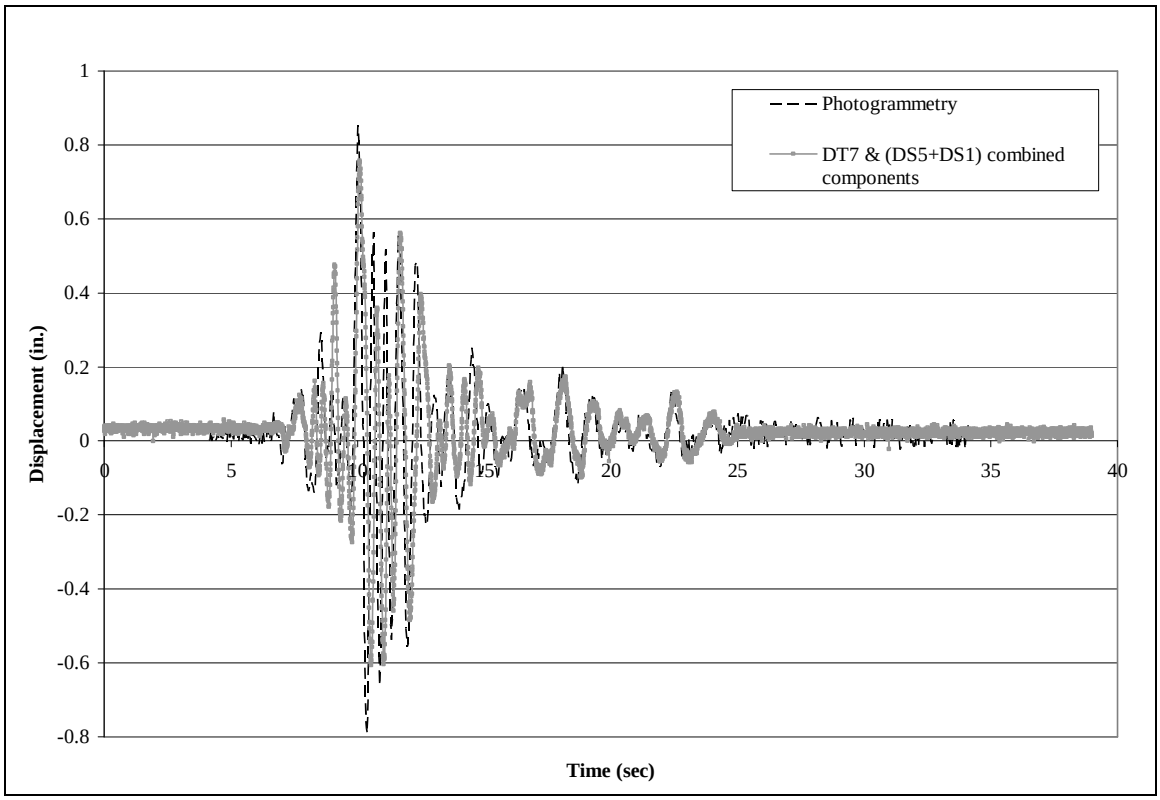

Fig. B-23: Lateral movement of Point 58 for Test 2 (1 in. = 254 mm)

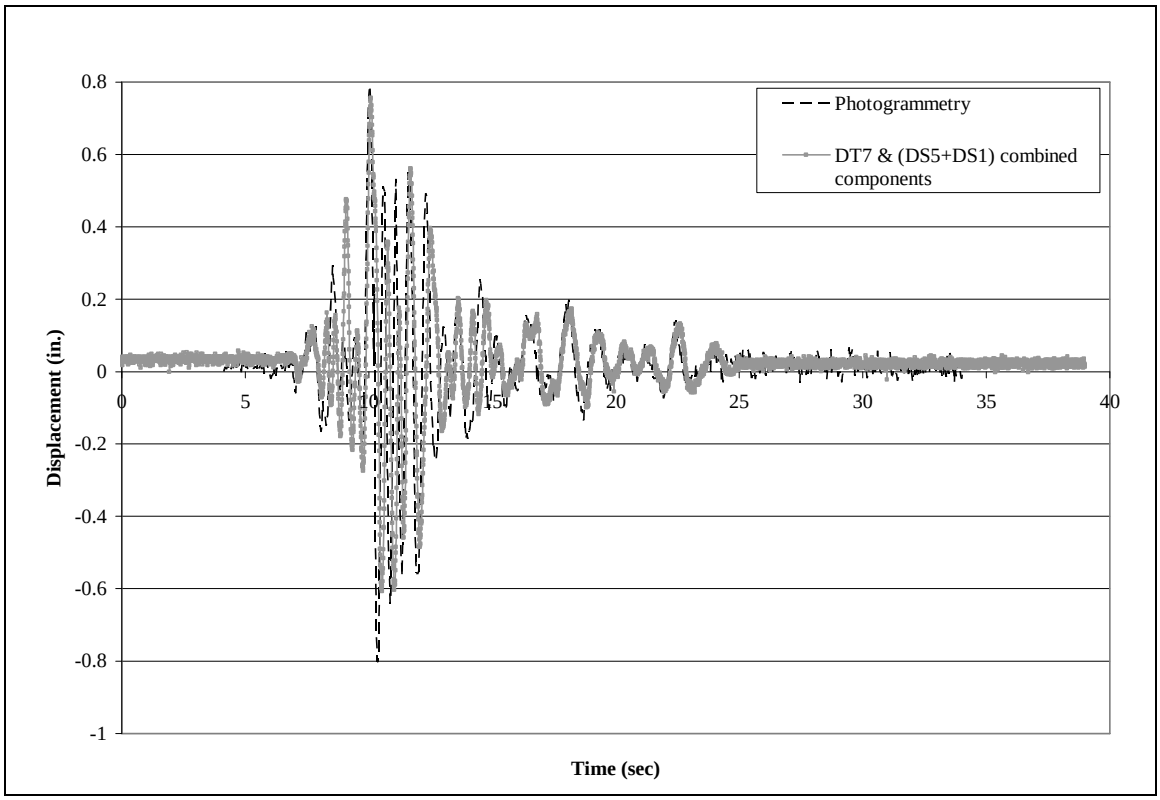

Fig. B-24: Lateral movement of Point 59 for Test 2 (1 in. = 254 mm)

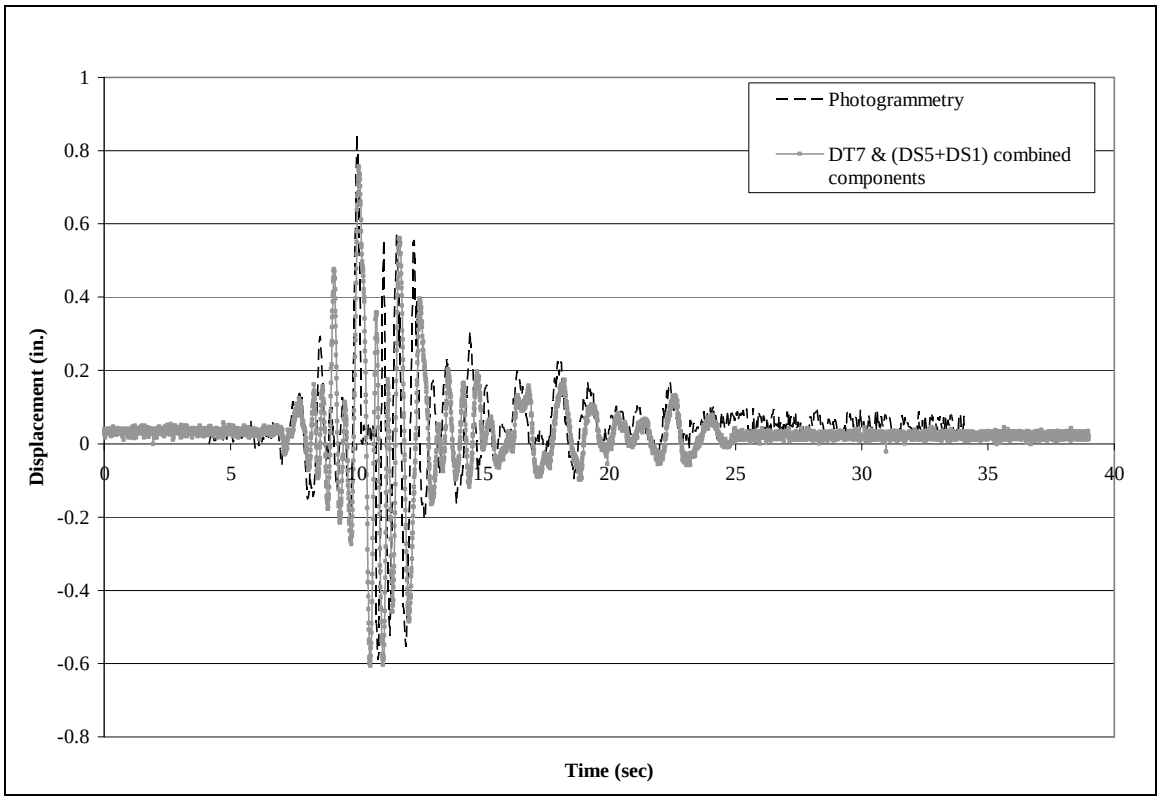

Fig. B-25: Lateral movement of Point 60 for Test 2 (1 in. = 254 mm)

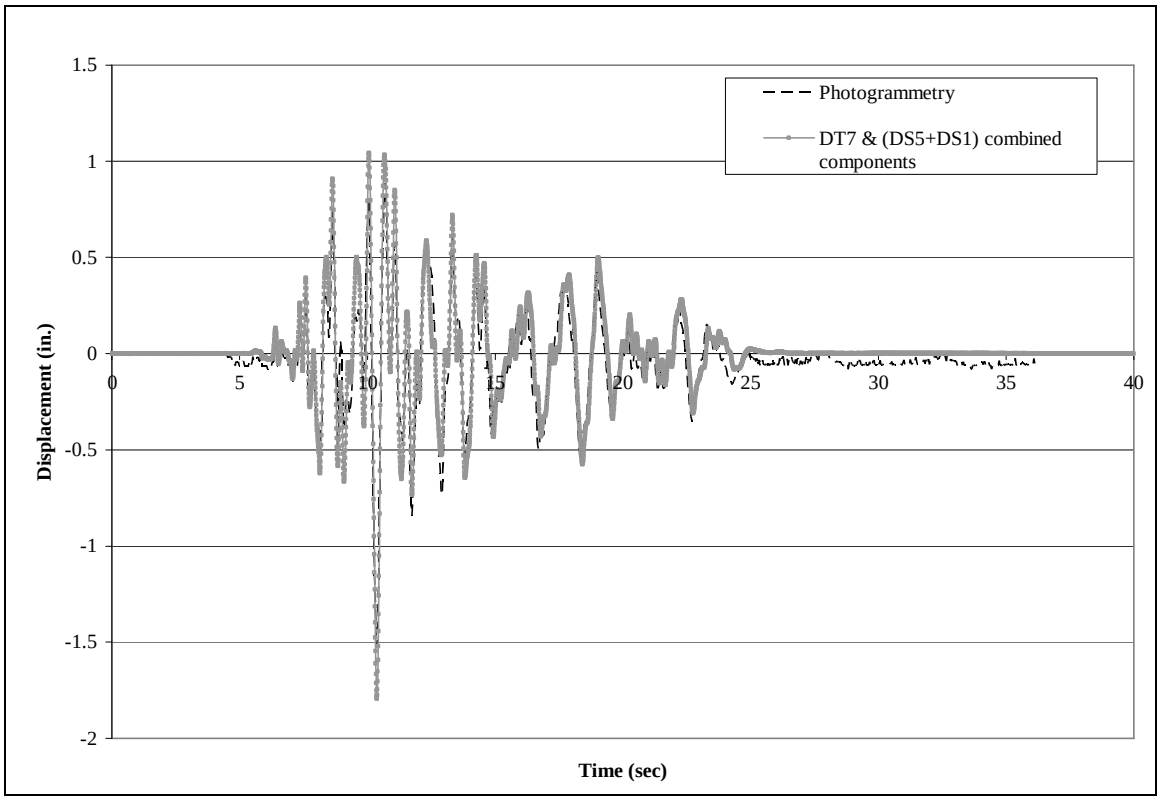

Fig. B-26: Lateral movement of Point 2 for Test 4D (1 in. = 254 mm)

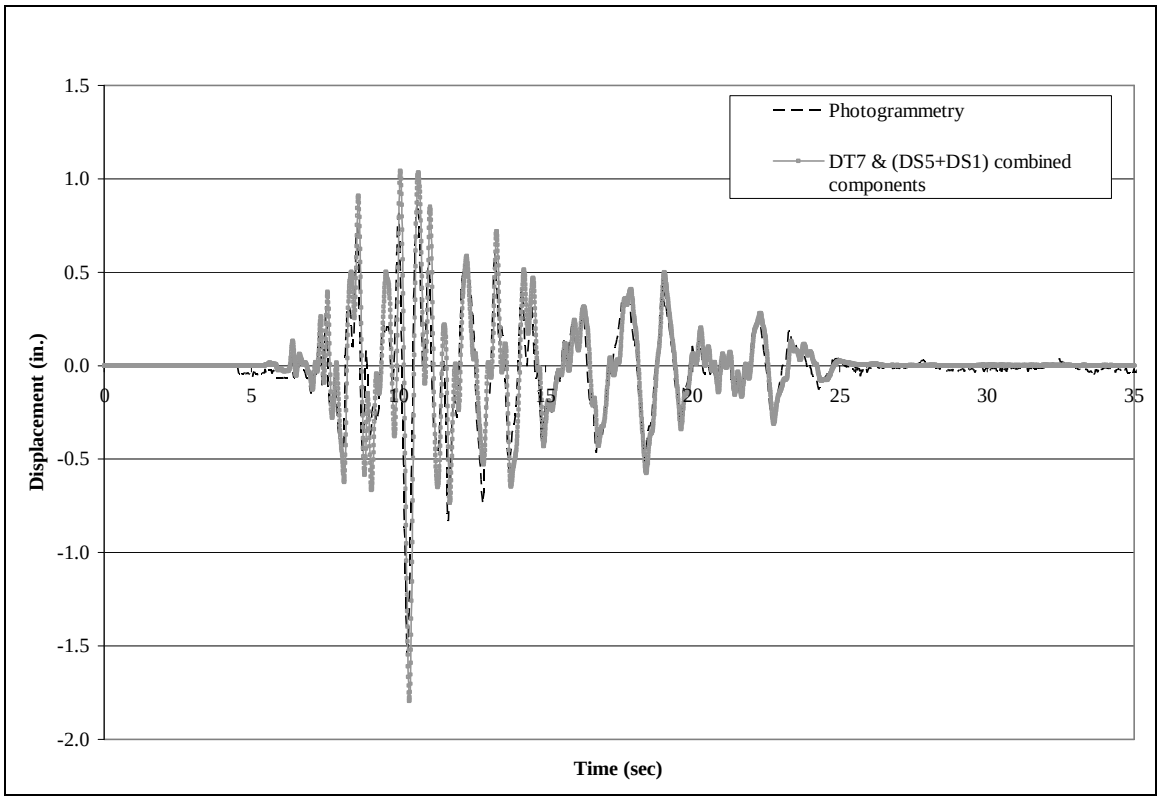

Fig. B-27: Lateral movement of Point 3 for Test 4D (1 in. = 254 mm)

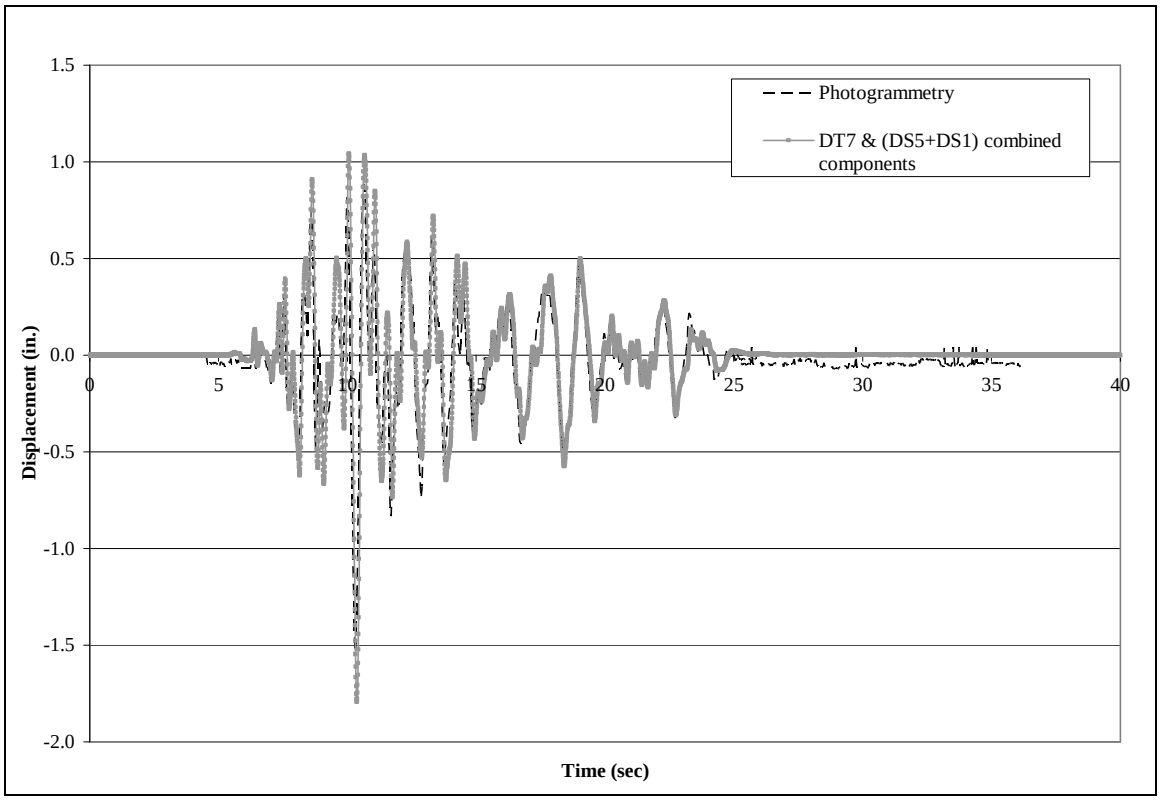

Fig. B-28: Lateral movement of Point 4 for Test 4D (1 in. = 254 mm)

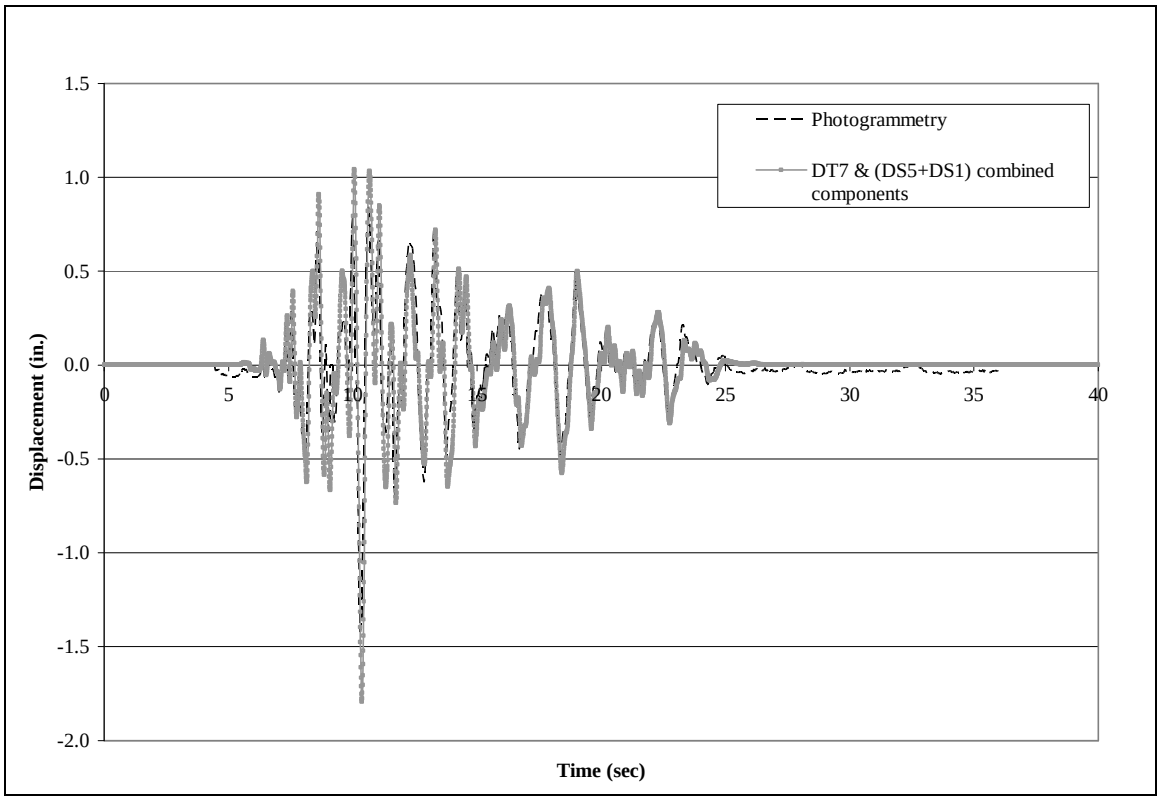

Fig. B-29: Lateral movement of Point 7 for Test 4D (1 in. = 254 mm)

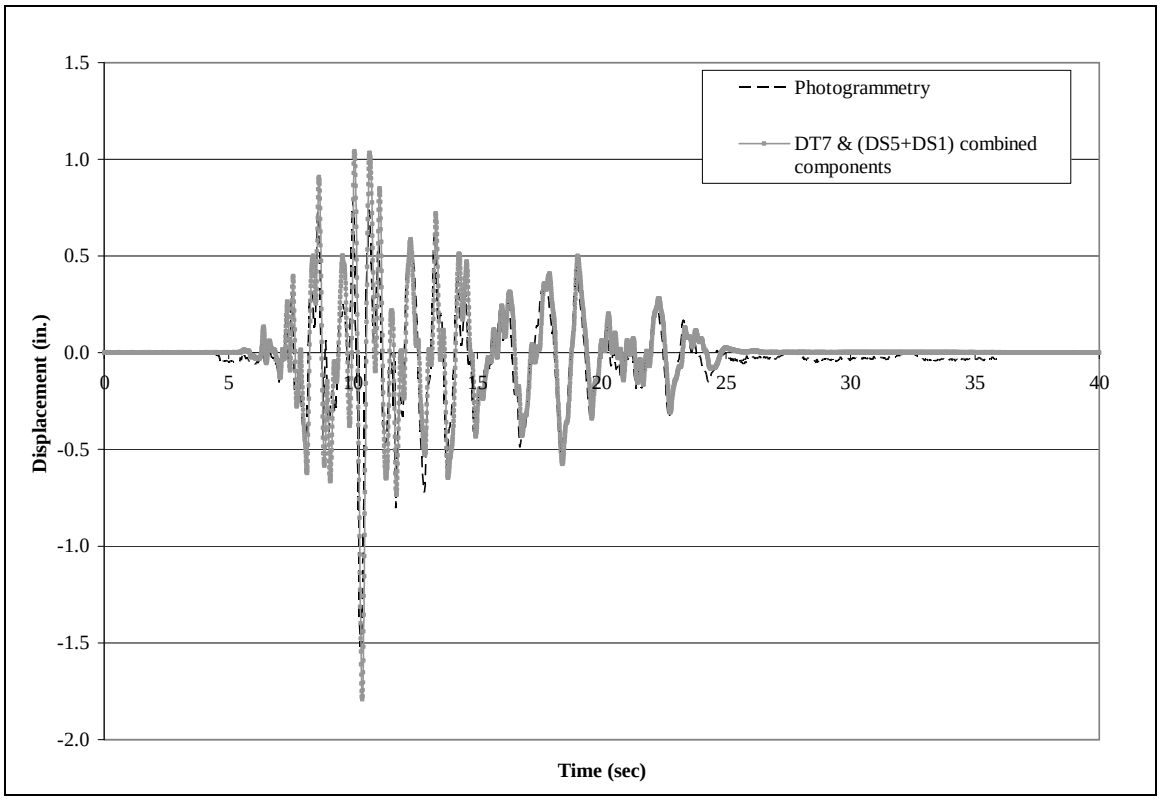

Fig. B-30: Lateral movement of Point 8 for Test 4D (1 in. = 254 mm)

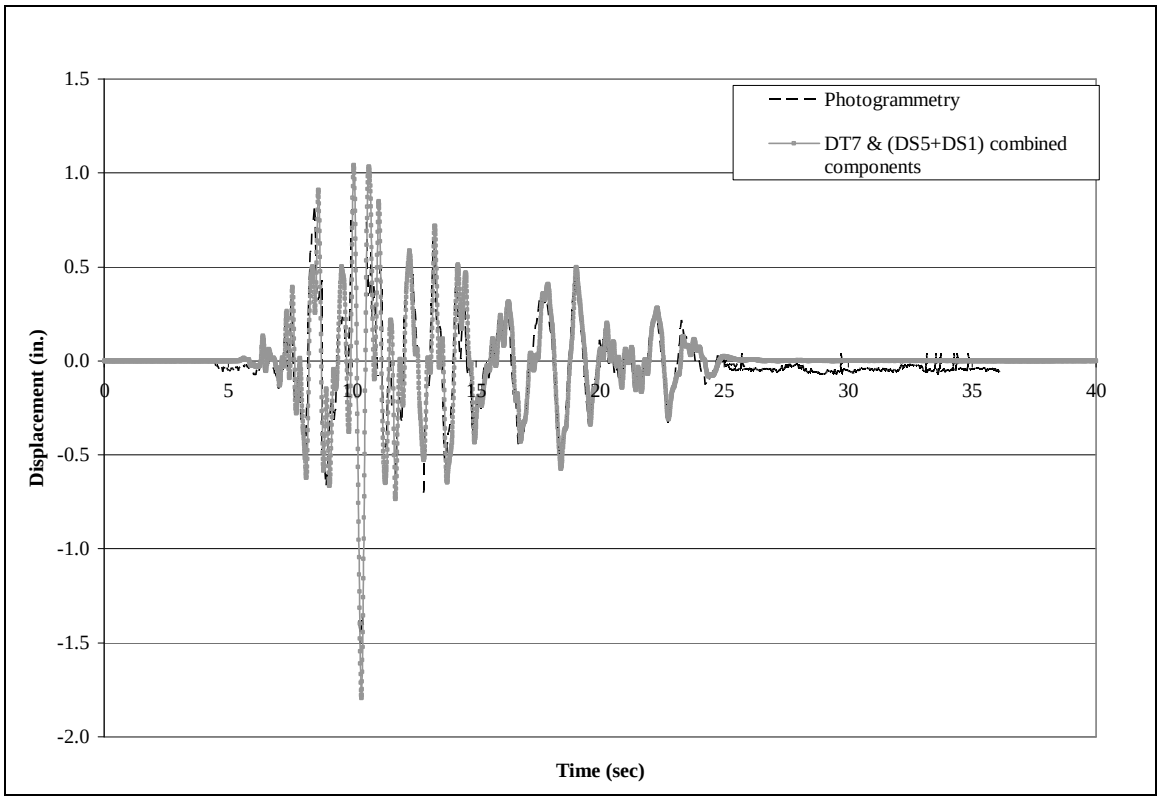

Fig. B-31: Lateral movement of Point 9 for Test 4D (1 in. = 254 mm)

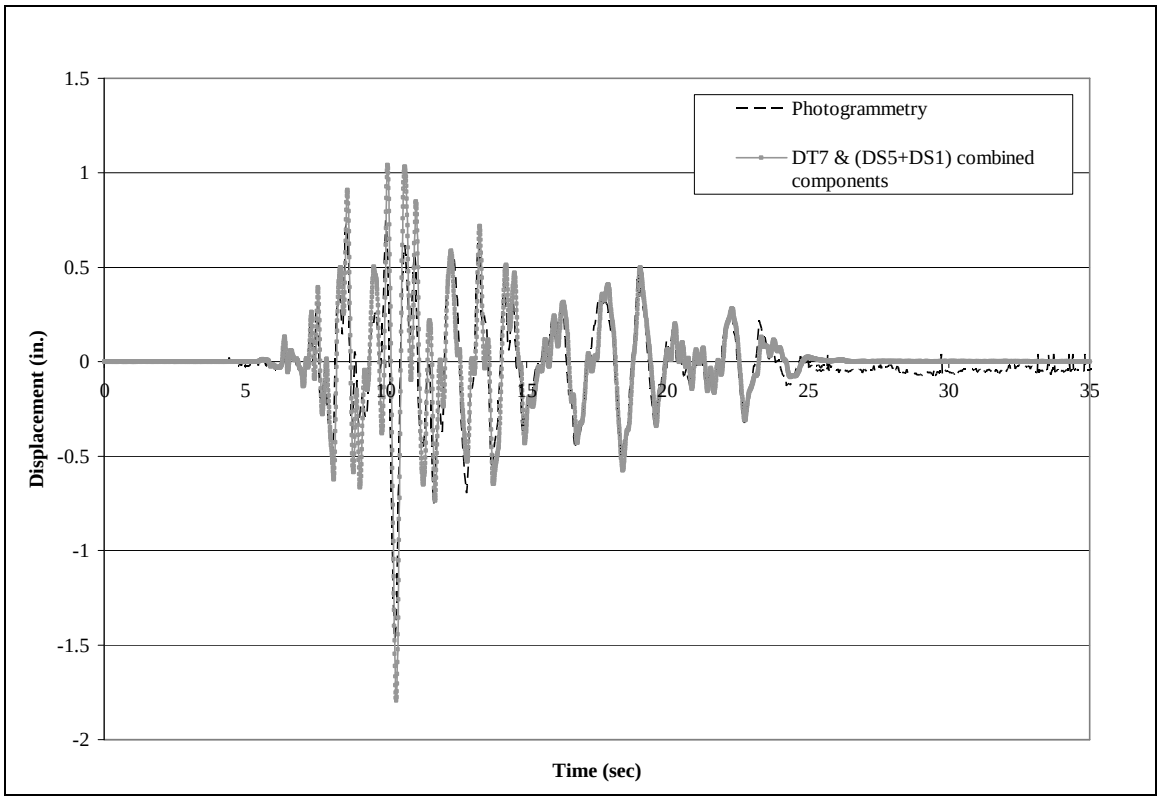

Fig. B-32: Lateral movement of Point 12 for Test 4D (1 in. = 254 mm)

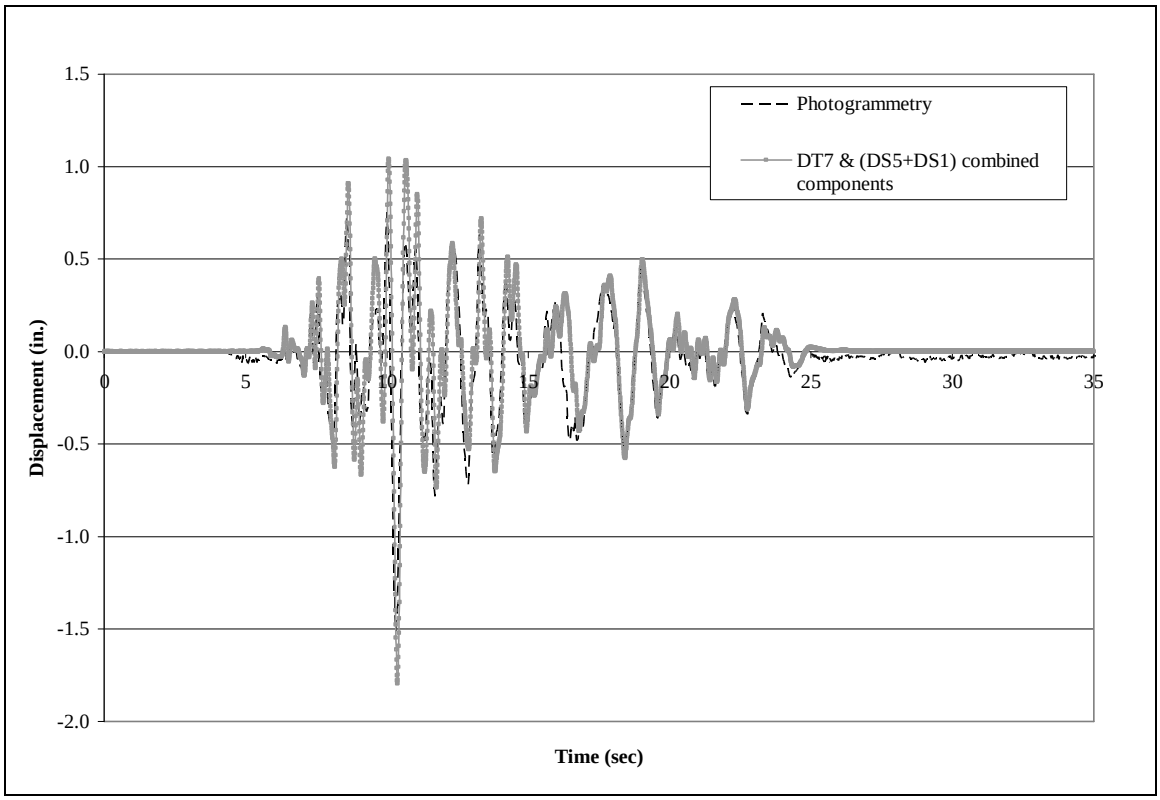

Fig. B-33: Lateral movement of Point 13 for Test 4D (1 in. = 254 mm)

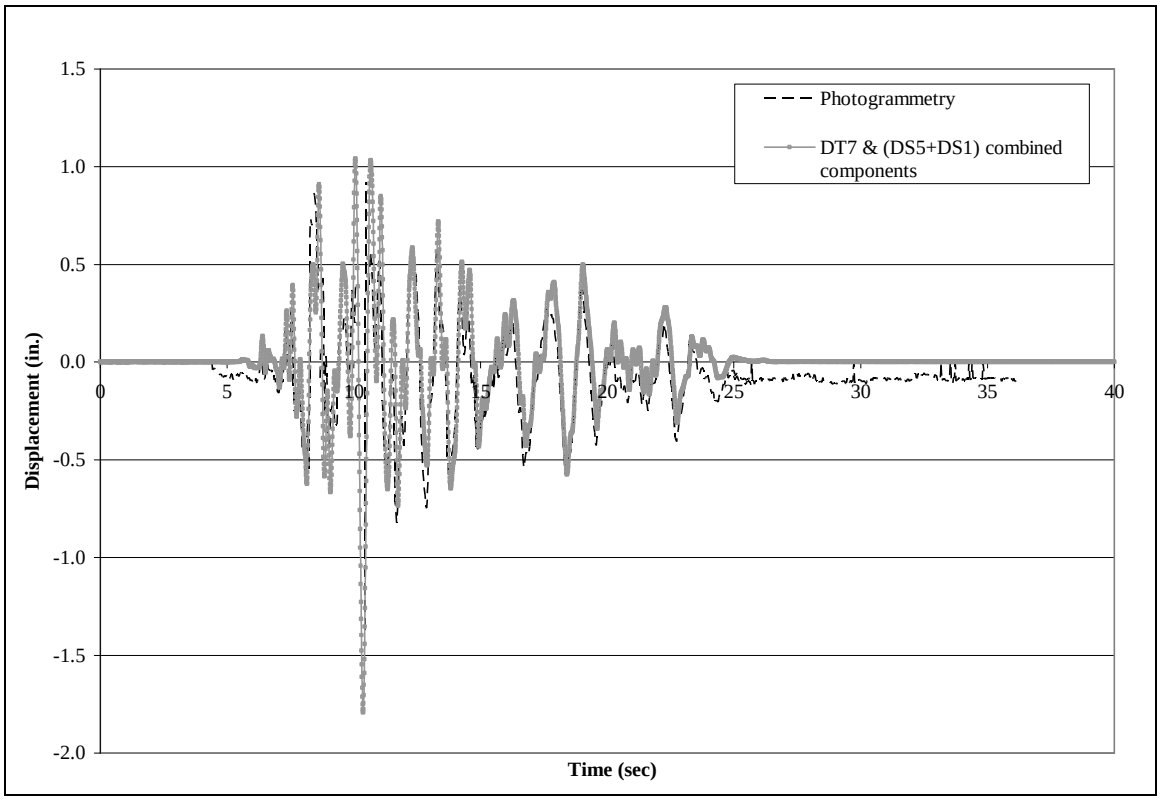

Fig. B-34: Lateral movement of Point 14 for Test 4D (1 in. = 254 mm)

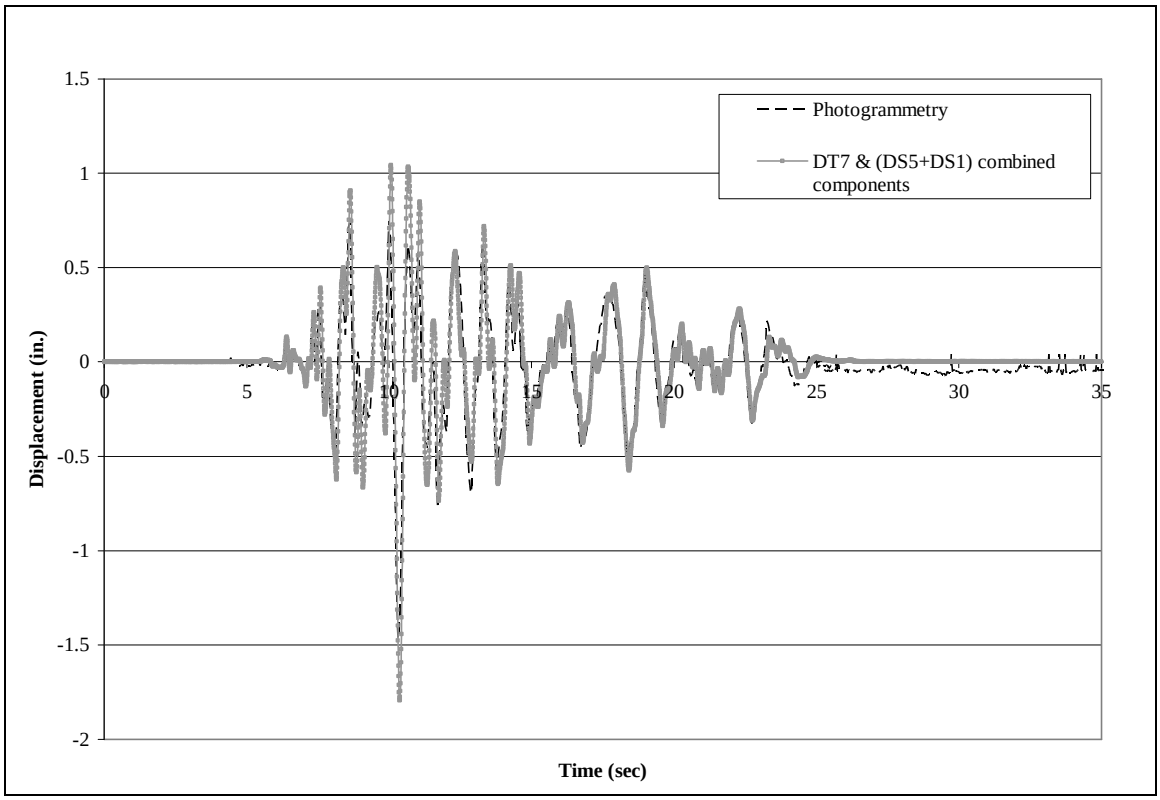

Fig. B-35: Lateral movement of Point 17 for Test 4D (1 in. = 254 mm)

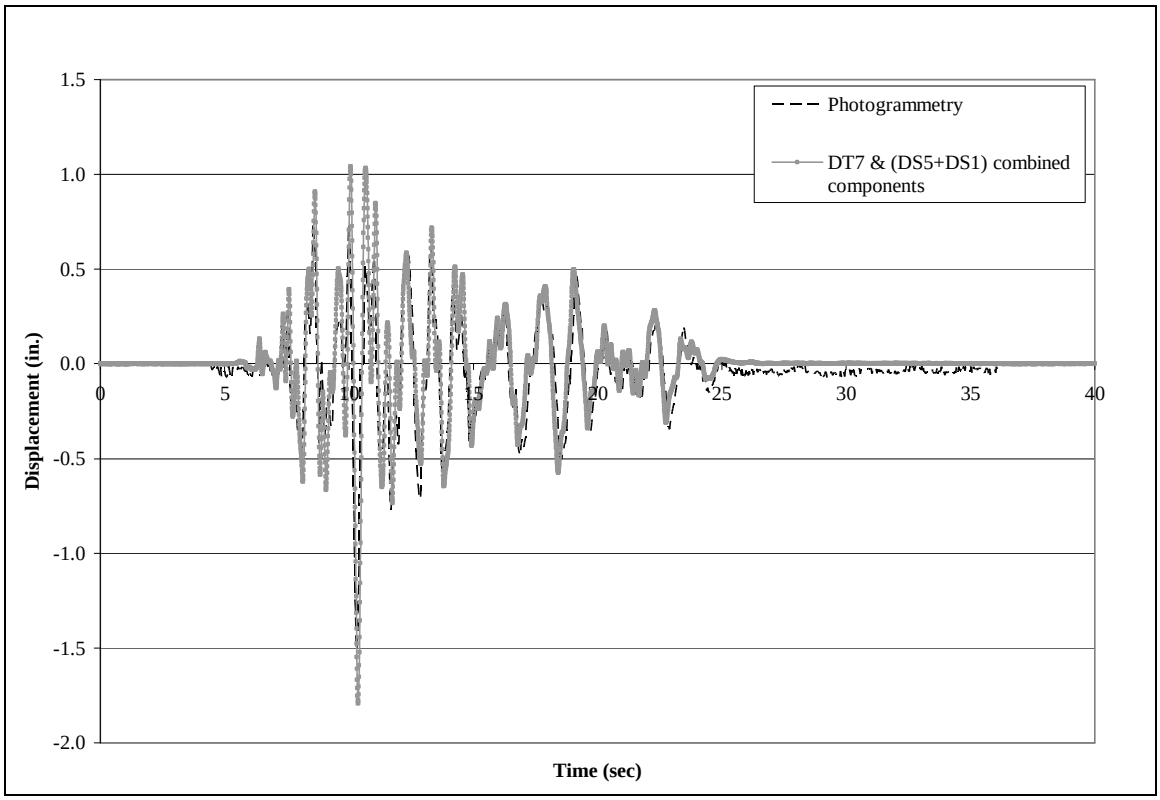

Fig. B-36: Lateral movement of Point 18 for Test 4D (1 in. = 254 mm)

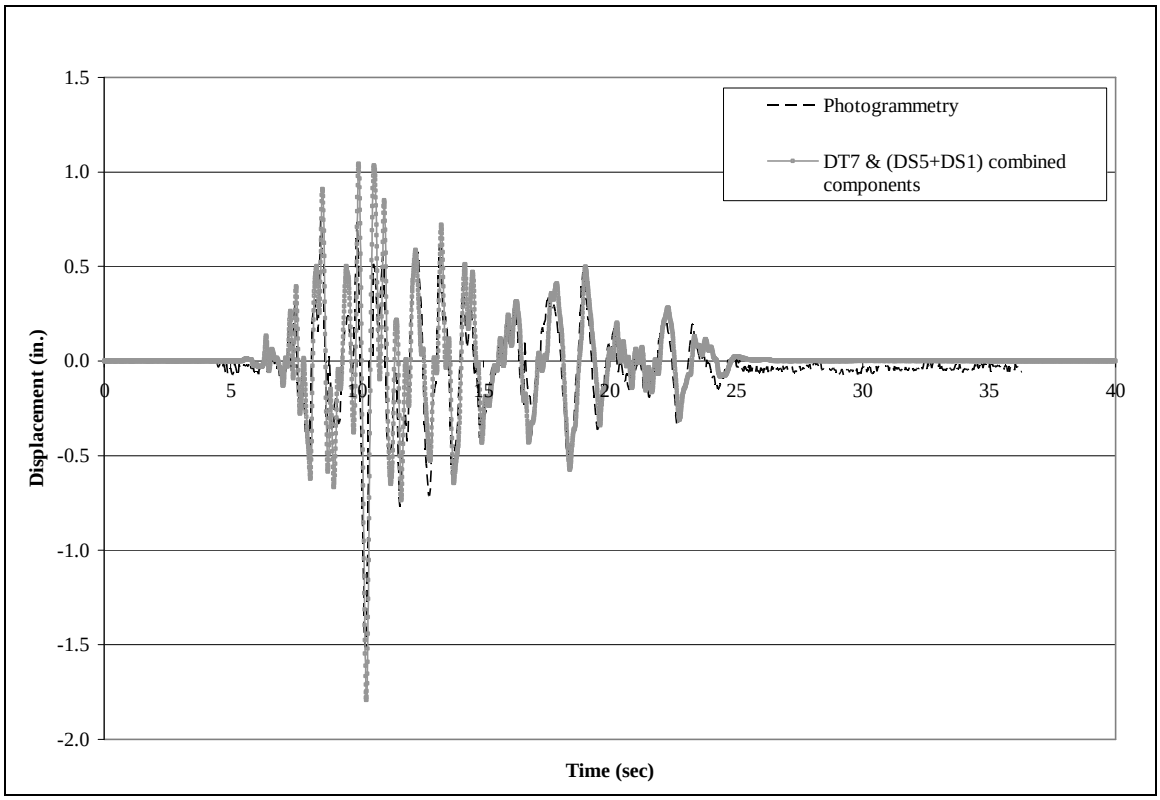

Fig. B-37: Lateral movement of Point 19 for Test 4D (1 in. = 254 mm)

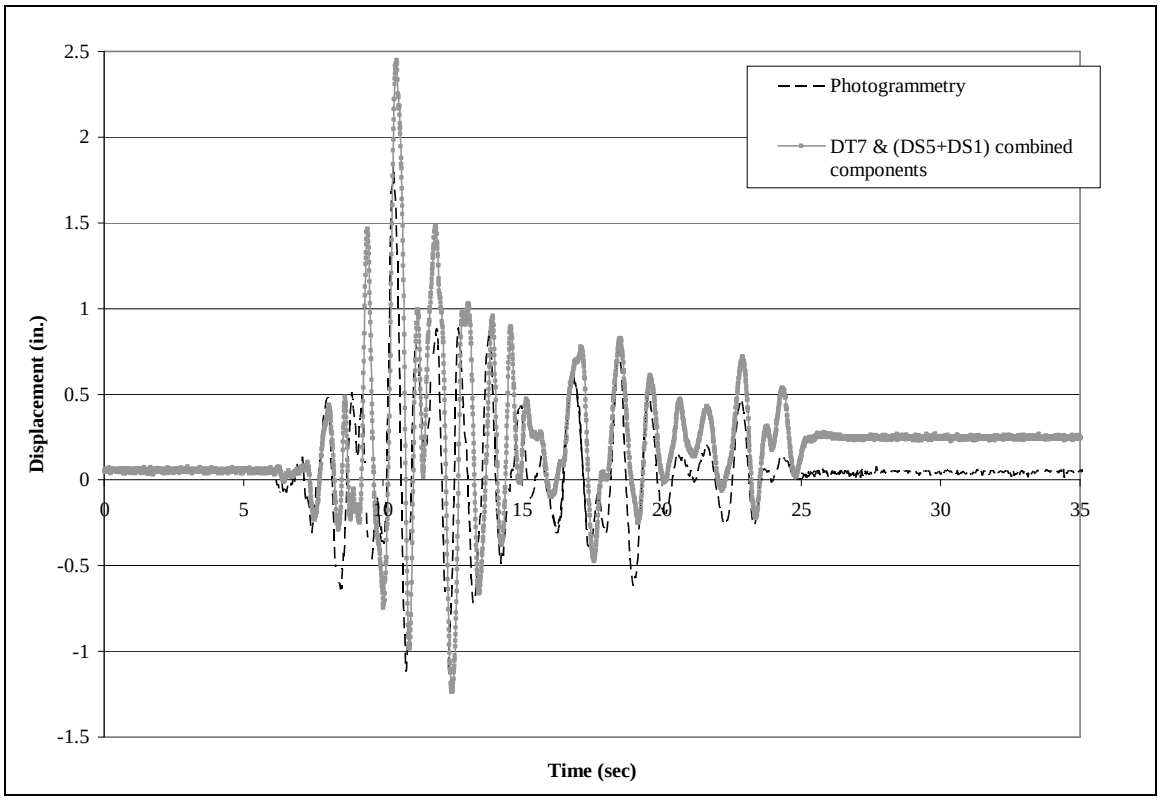

Fig. B-38: Lateral movement of Point 37 for Test 4D (1 in. = 254 mm)

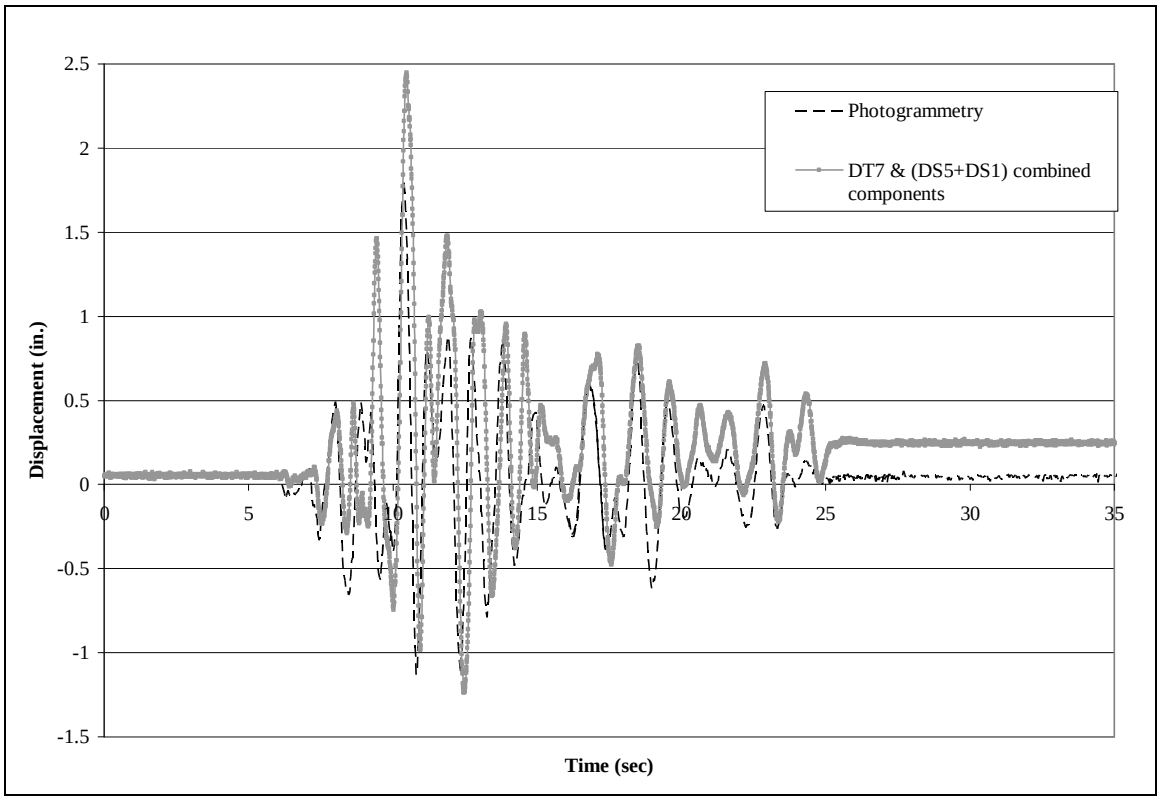

Fig. B-39: Lateral movement of Point 38 for Test 4D (1 in. = 254 mm)

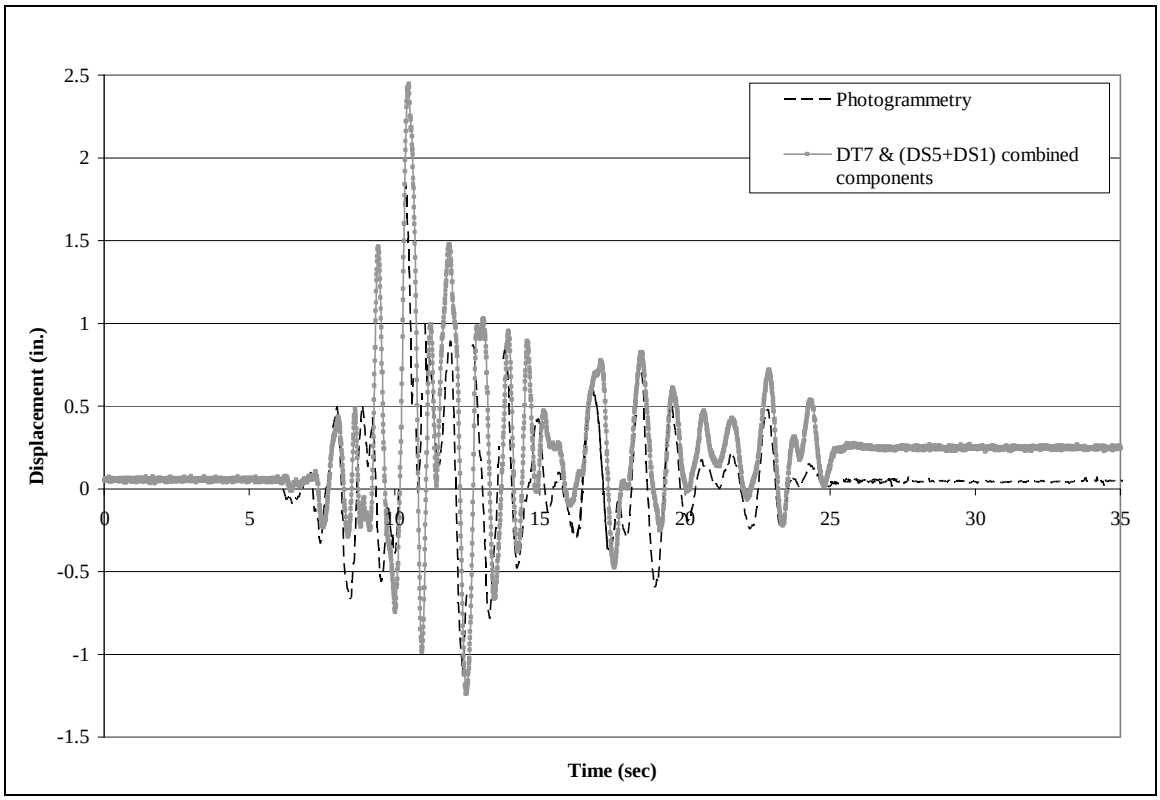

Fig. B-40: Lateral movement of Point 39 for Test 4D (1 in. = 254 mm)

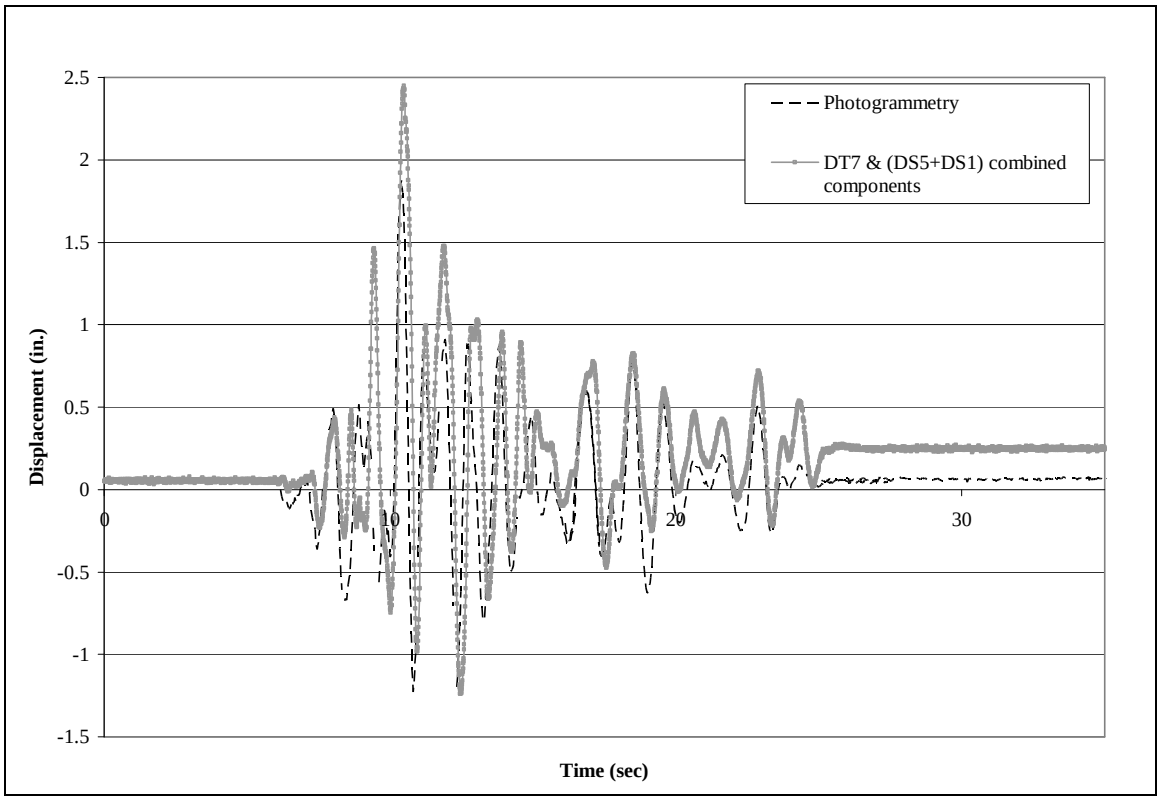

Fig. B-41: Lateral movement of Point 44 for Test 4D (1 in. = 254 mm)

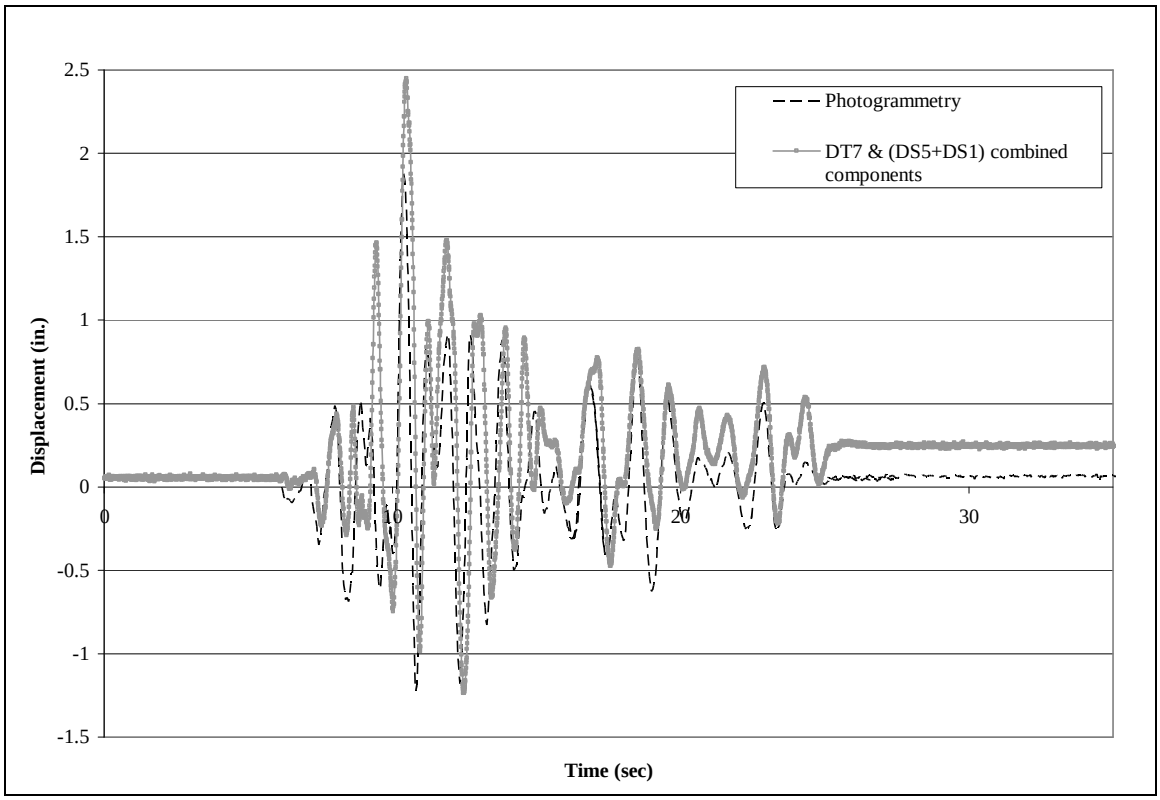

Fig. B-42: Lateral movement of Point 45 for Test 4D (1 in. = 254 mm)

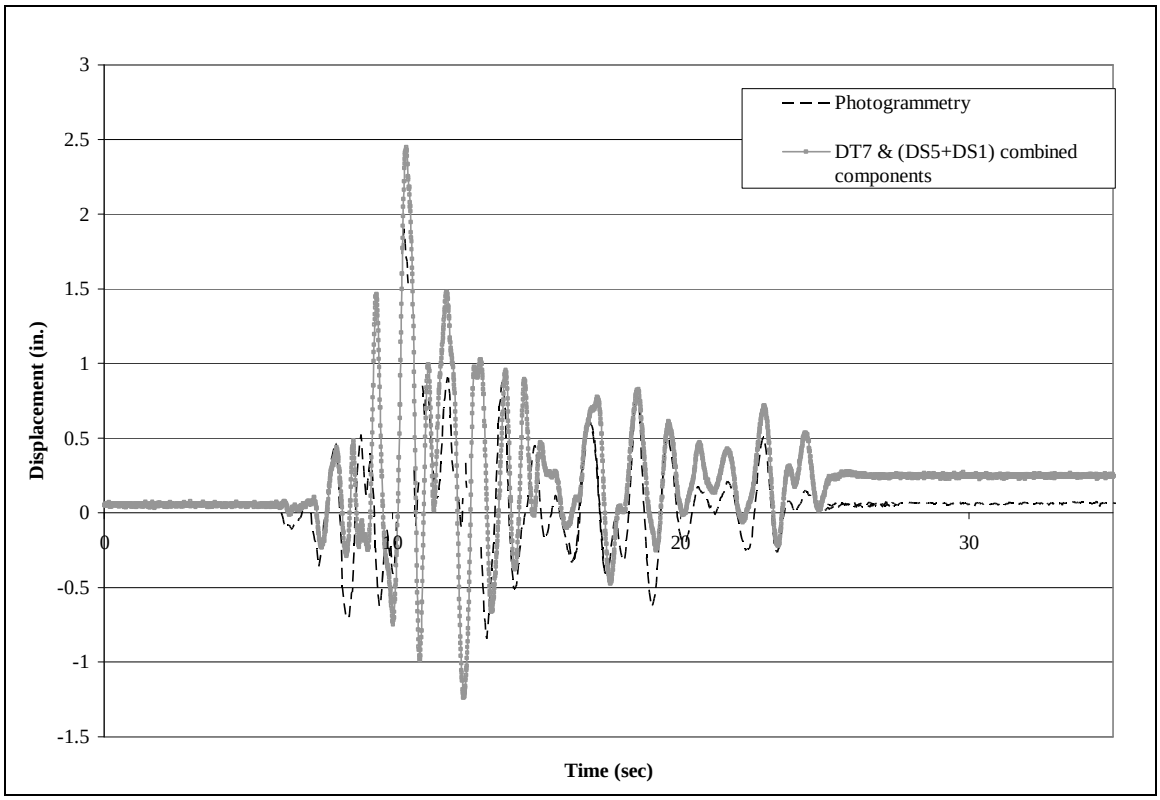

Fig. B-43: Lateral movement of Point 46 for Test 4D (1 in. = 254 mm)

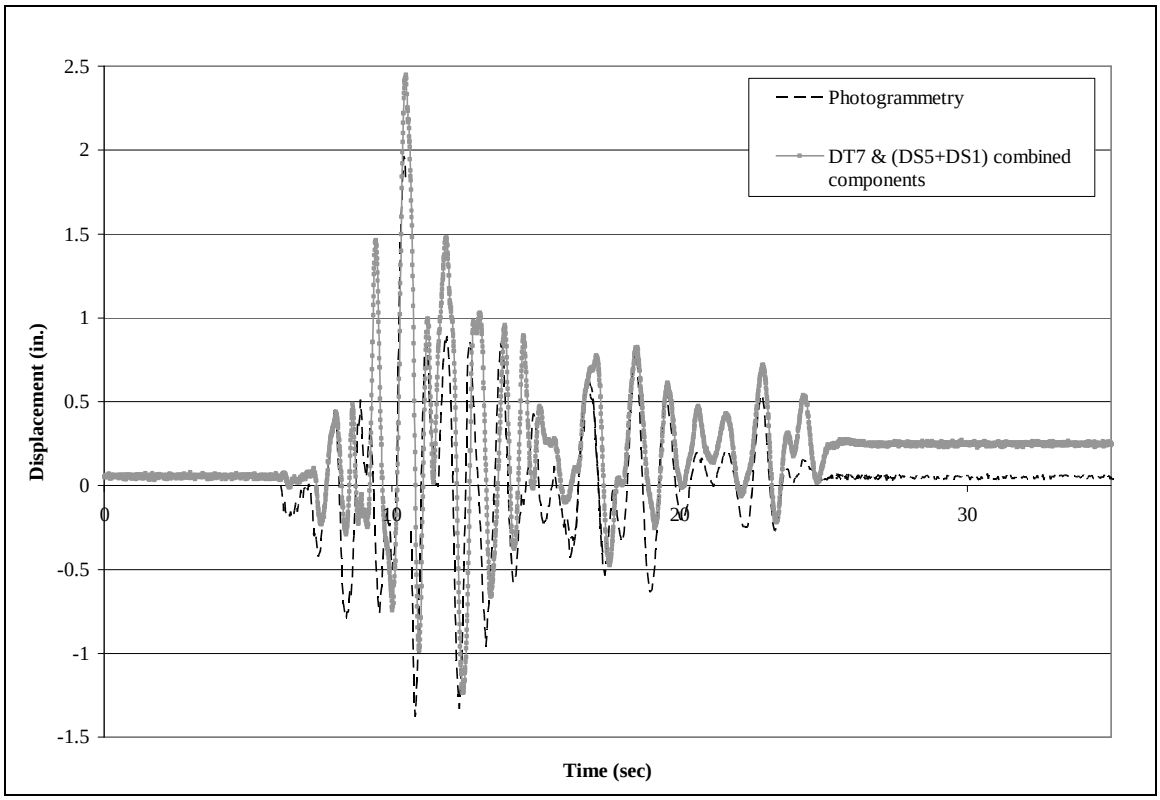

Fig. B-44: Lateral movement of Point 51 for Test 4D (1 in. = 254 mm)

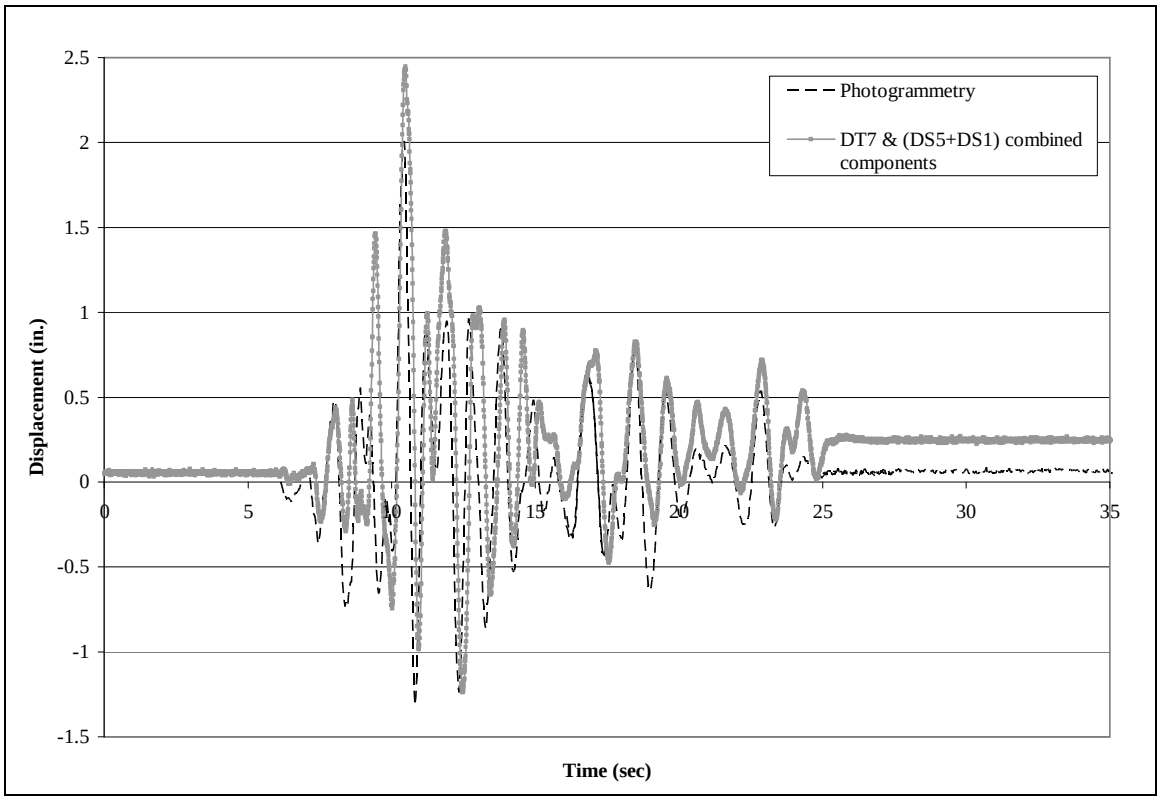

Fig. B-45: Lateral movement of Point 52 for Test 4D (1 in. = 254 mm)

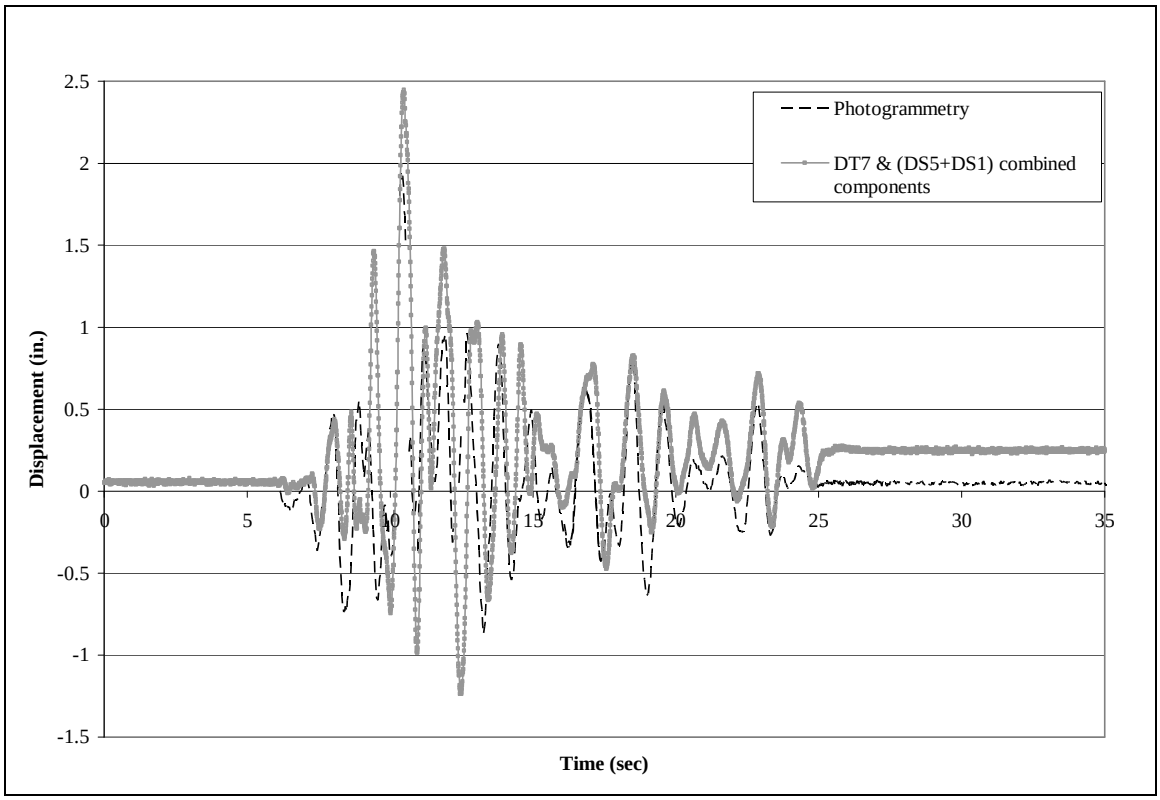

Fig. B-46: Lateral movement of Point 53 for Test 4D (1 in. = 254 mm)

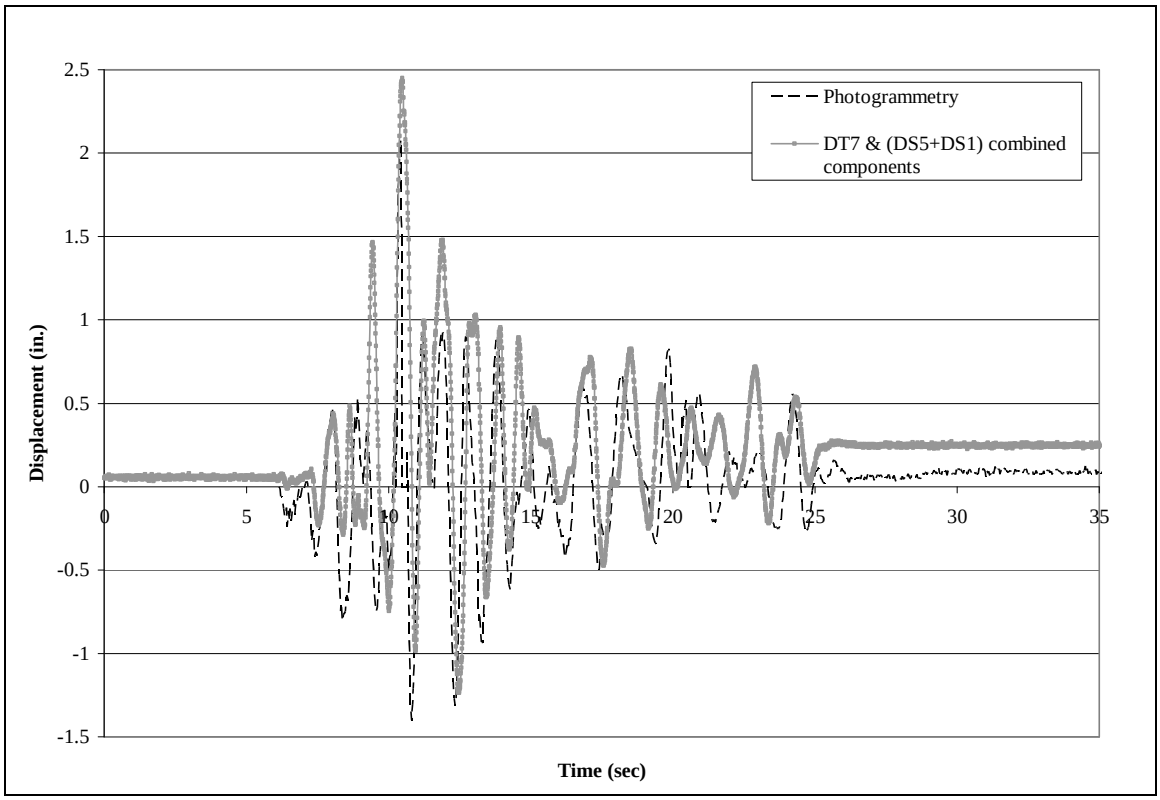

Fig. B-47: Lateral movement of Point 58 for Test 4D (1 in. = 254 mm)

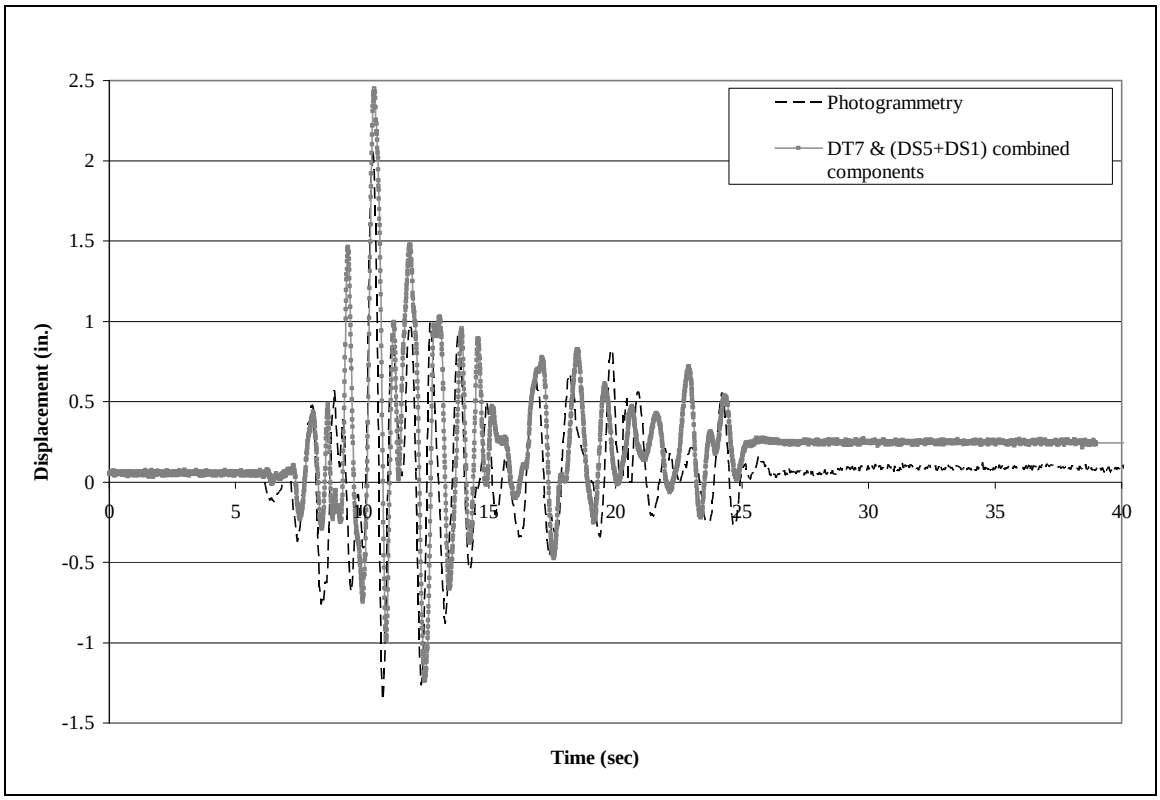

Fig. B-48: Lateral movement of Point 59 for Test 4D (1 in. = 254 mm)

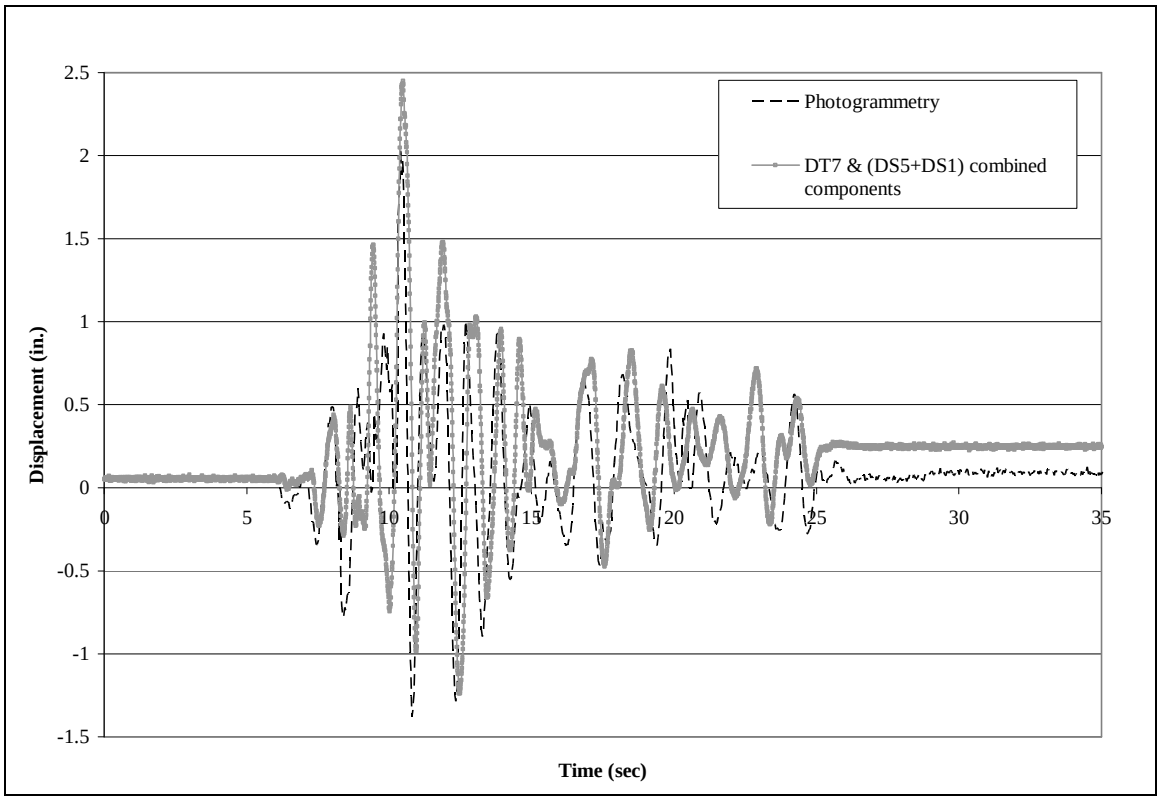

Fig. B-49: Lateral movement of Point 60 for Test 4D (1 in. = 254 mm)

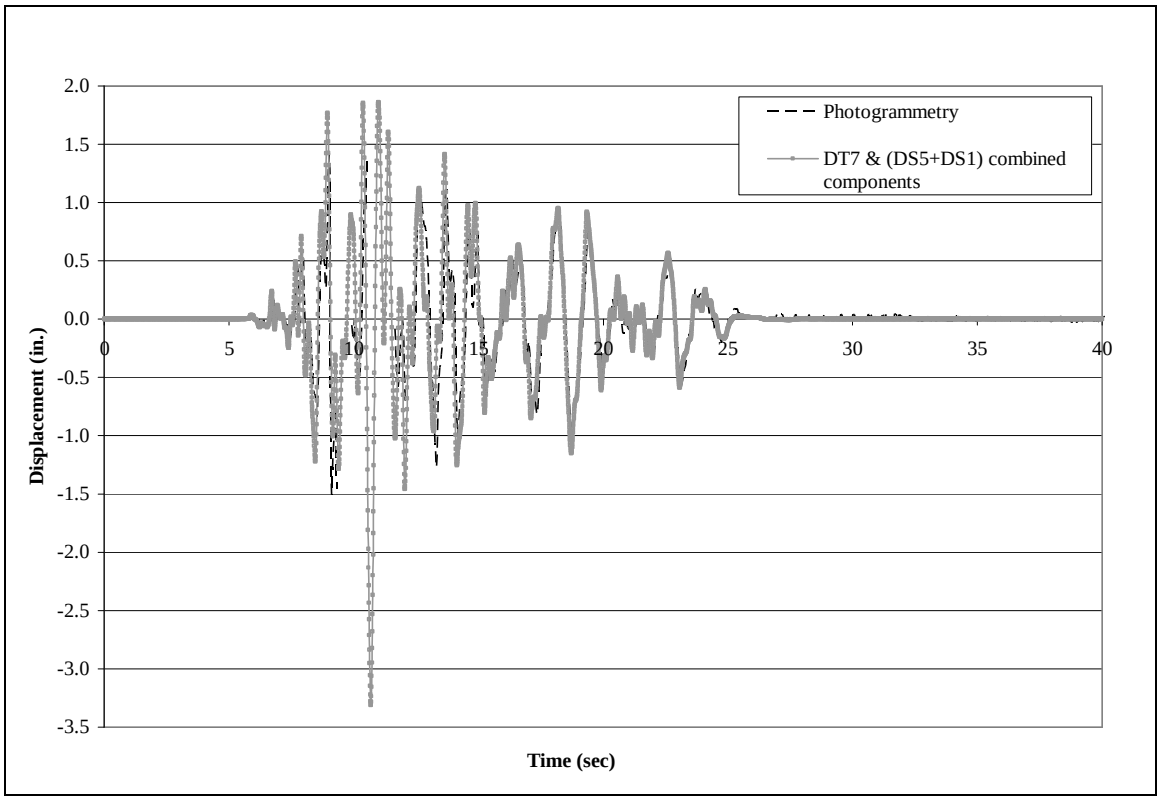

Fig. B-50: Lateral movement of Point 2 for Test 6 (1 in. = 254 mm)

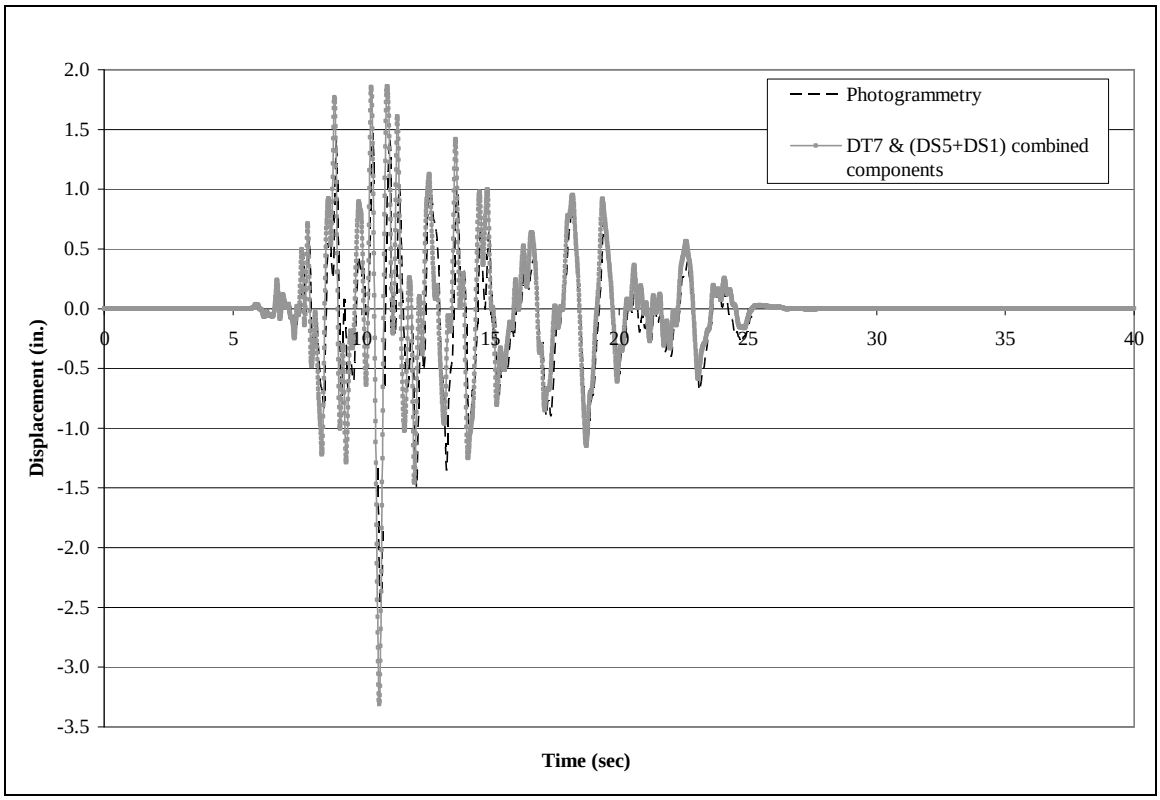

Fig. B-51: Lateral movement of Point 3 for Test 6 (1 in. = 254 mm)

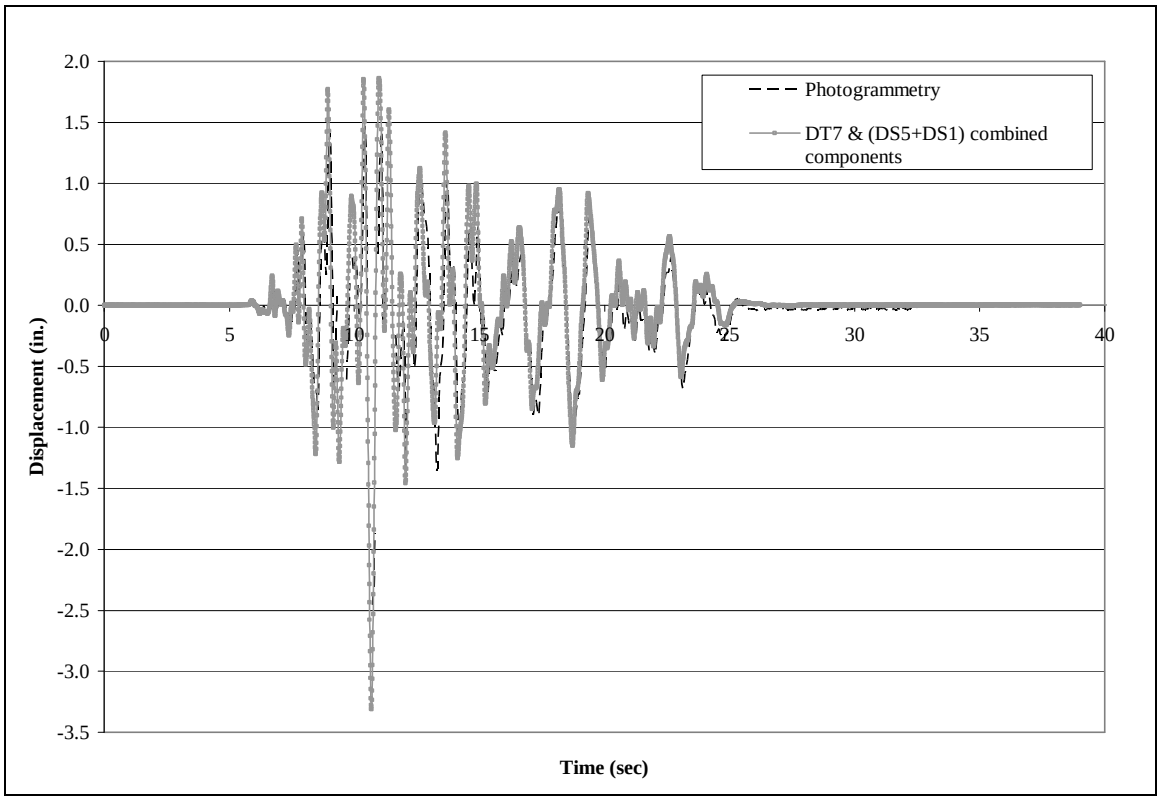

Fig. B-52: Lateral movement of Point 4 for Test 6 (1 in. = 254 mm)

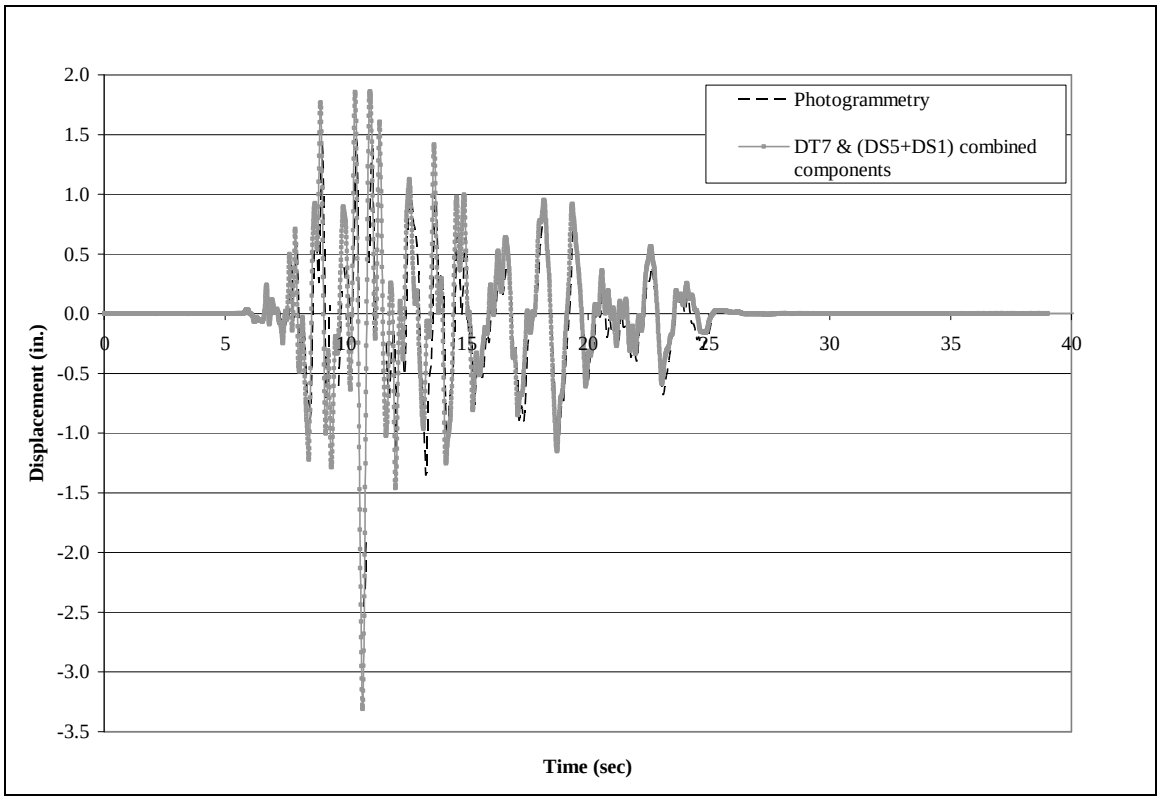

Fig. B-53: Lateral movement of Point 7 for Test 6 (1 in. = 254 mm)

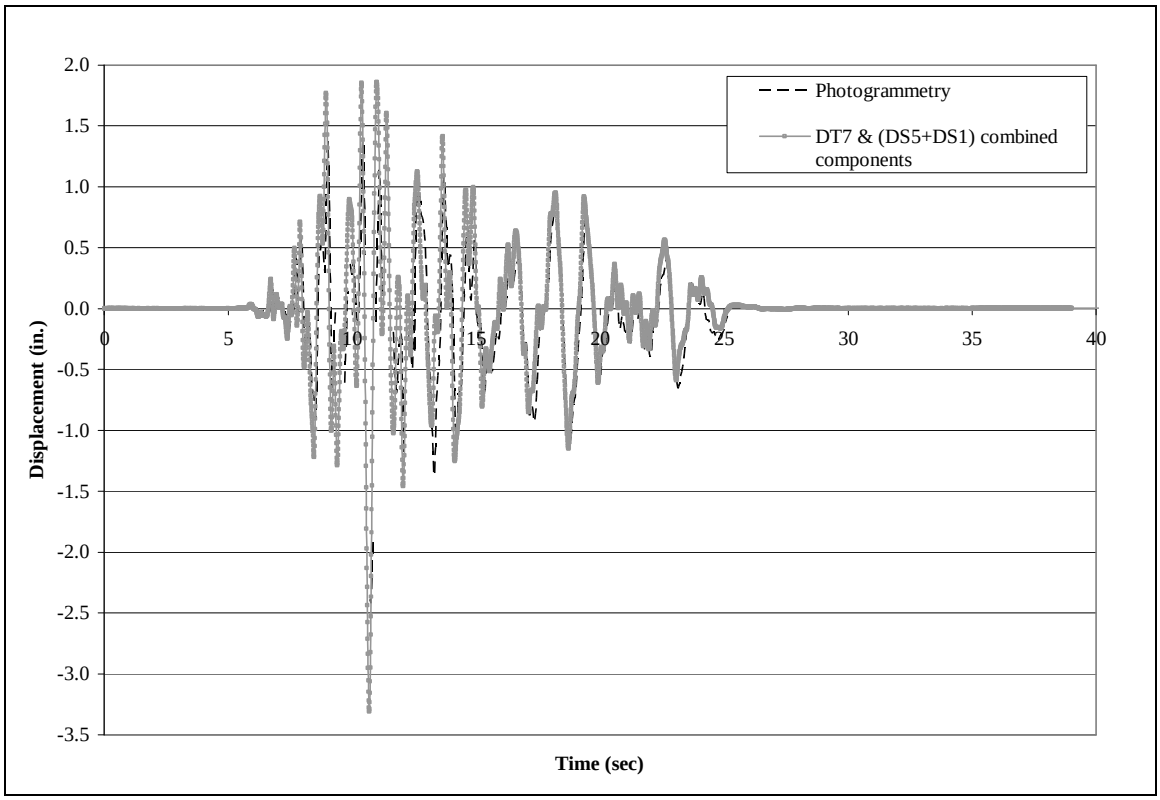

Fig. B-54: Lateral movement of Point 8 for Test 6 (1 in. = 254 mm)

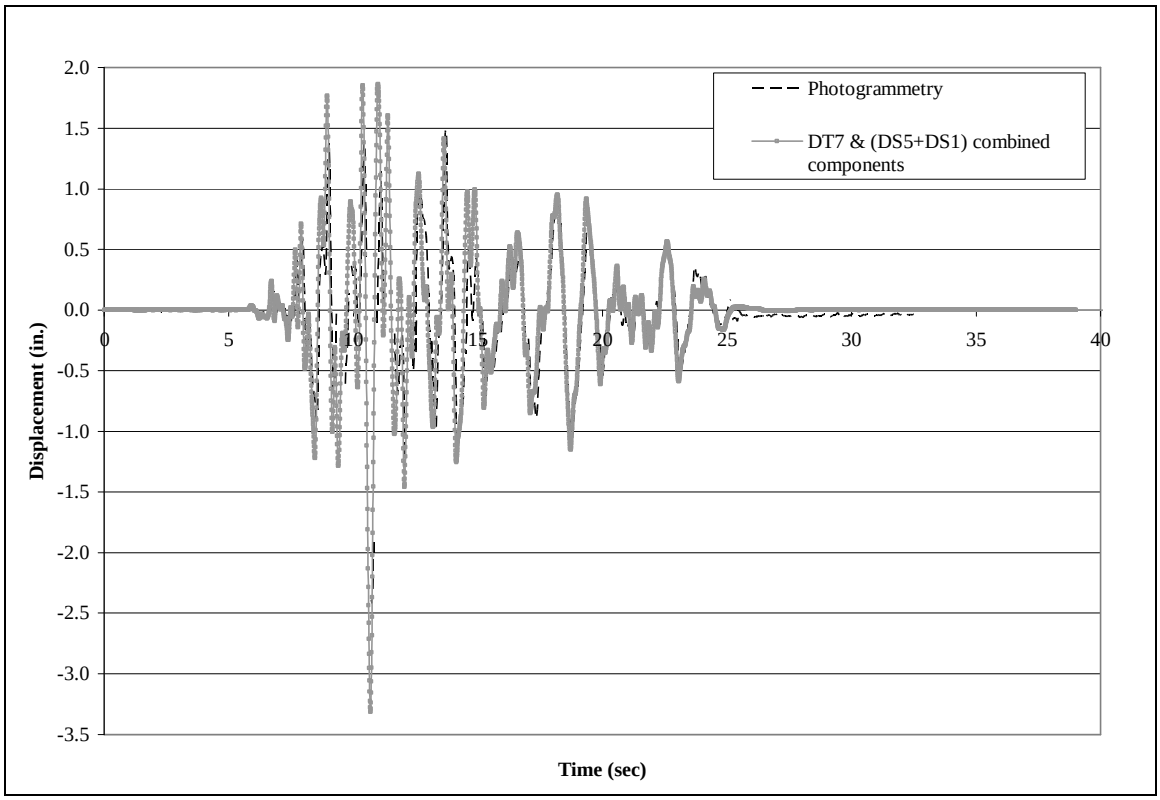

Fig. B-55: Lateral movement of Point 9 for Test 6 (1 in. = 254 mm)

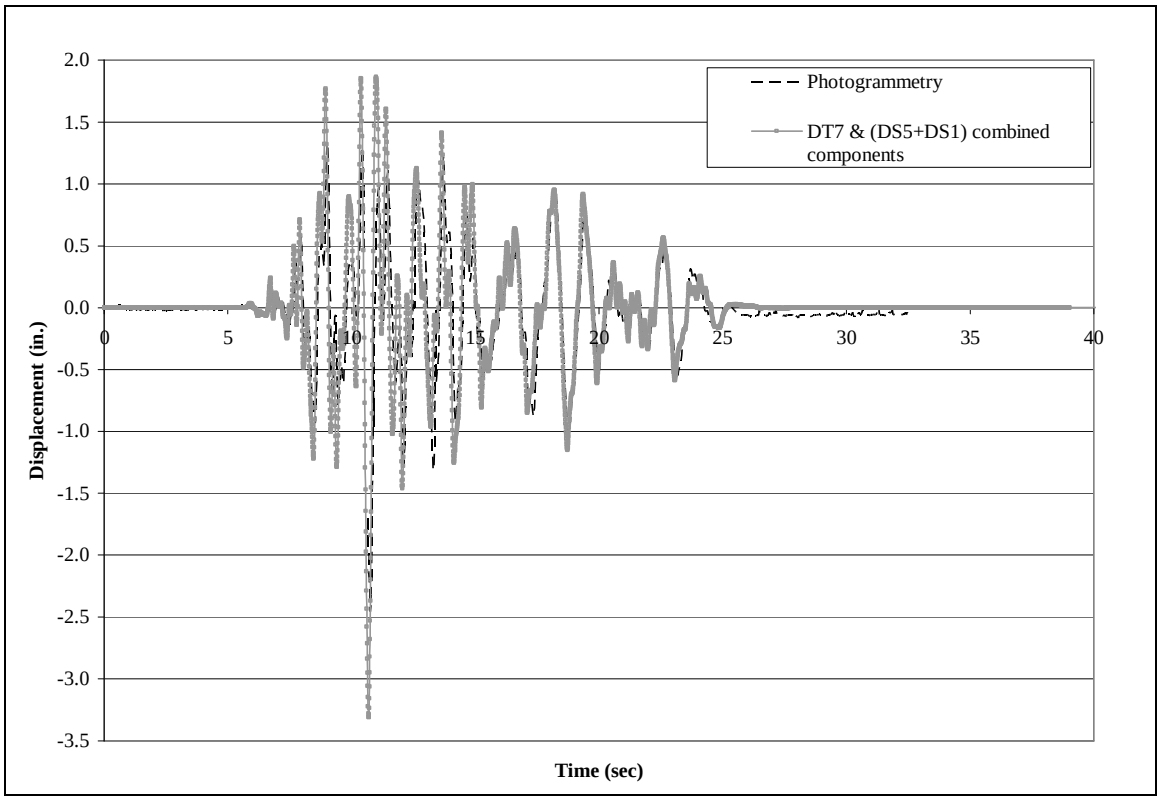

Fig. B-56: Lateral movement of Point 12 for Test 6 (1 in. = 254 mm)

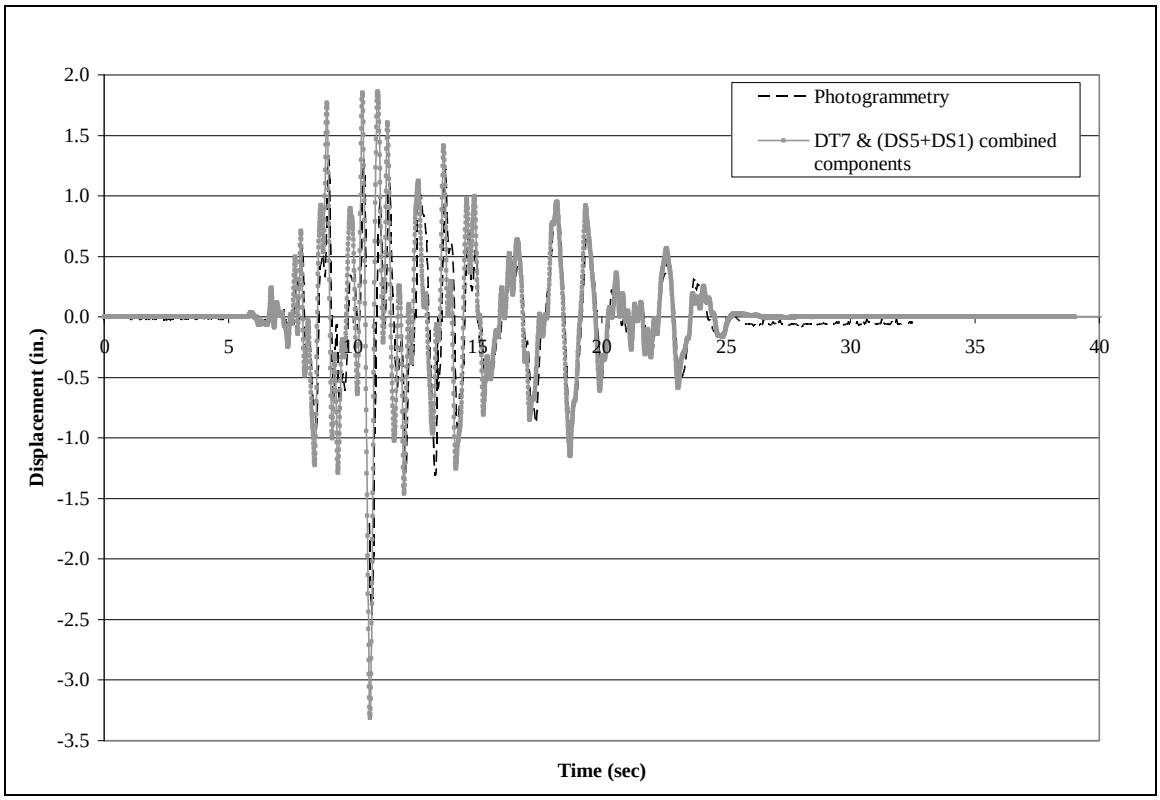

Fig. B-57: Lateral movement of Point 13 for Test 6 (1 in. = 254 mm)

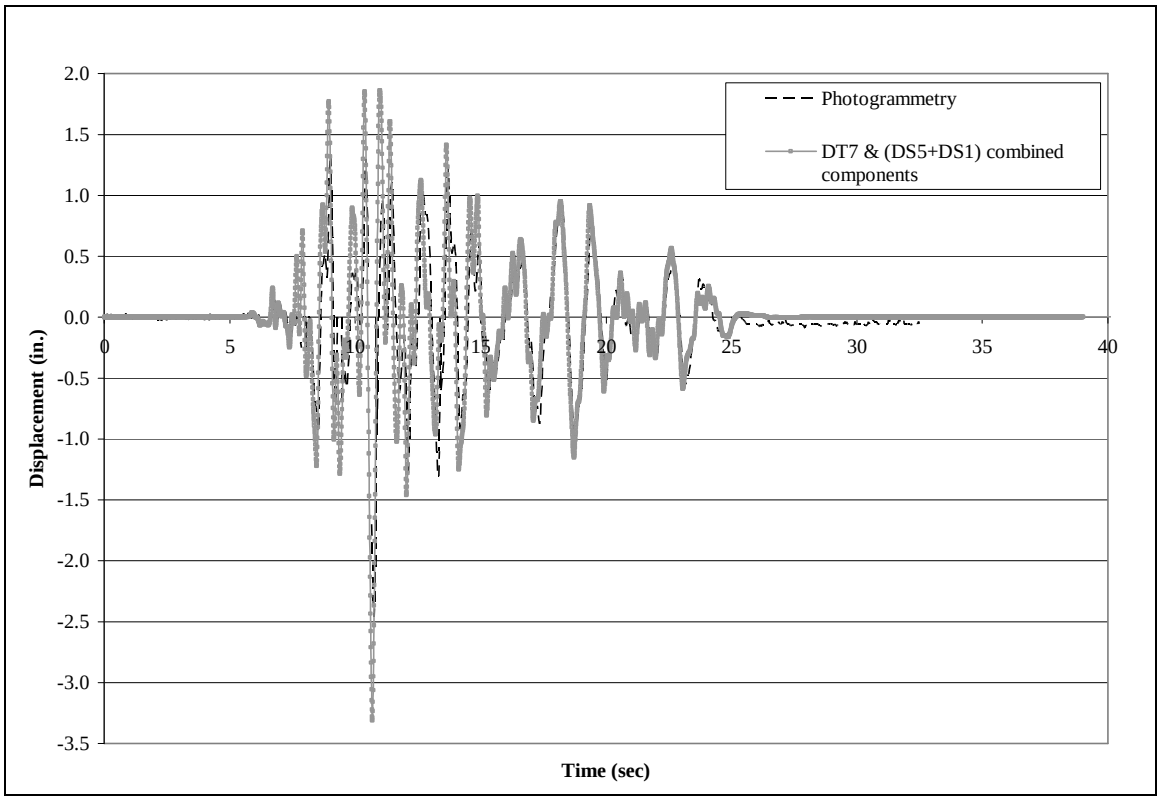

Fig. B-58: Lateral movement of Point 14 for Test 6 (1 in. = 254 mm)

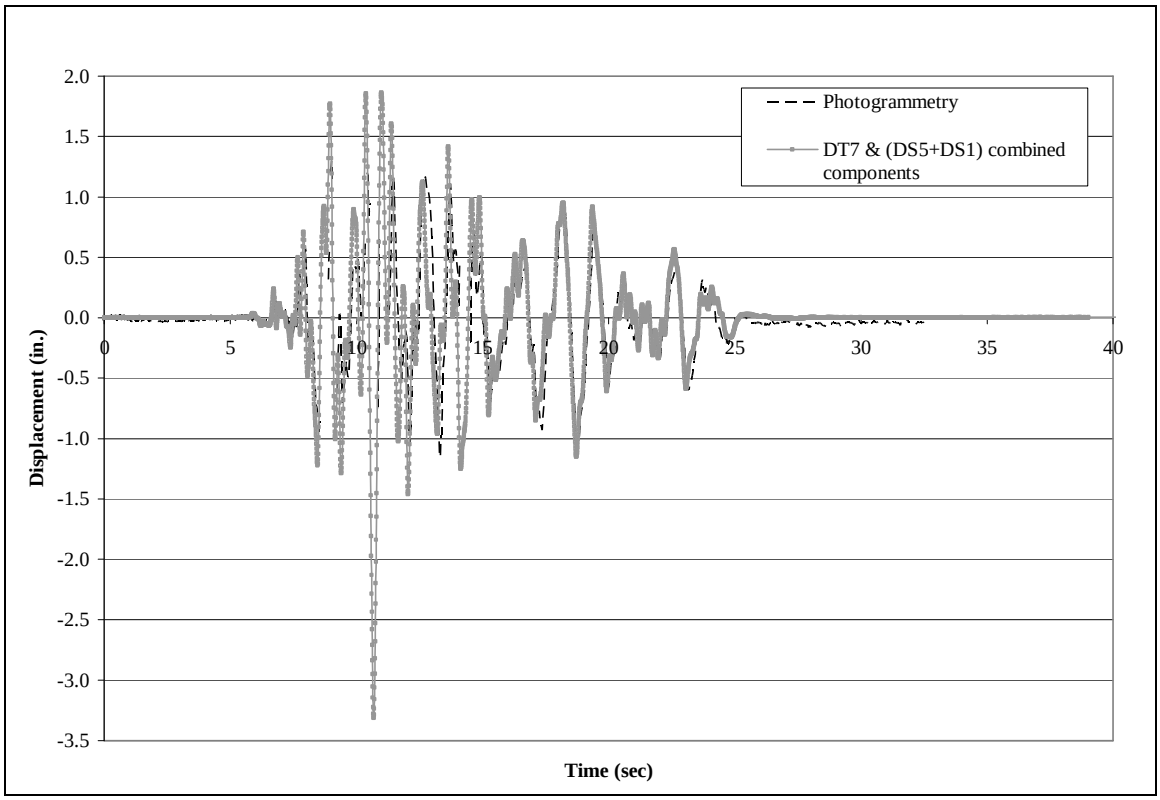

Fig. B-59: Lateral movement of Point 17 for Test 6 (1 in. = 254 mm)

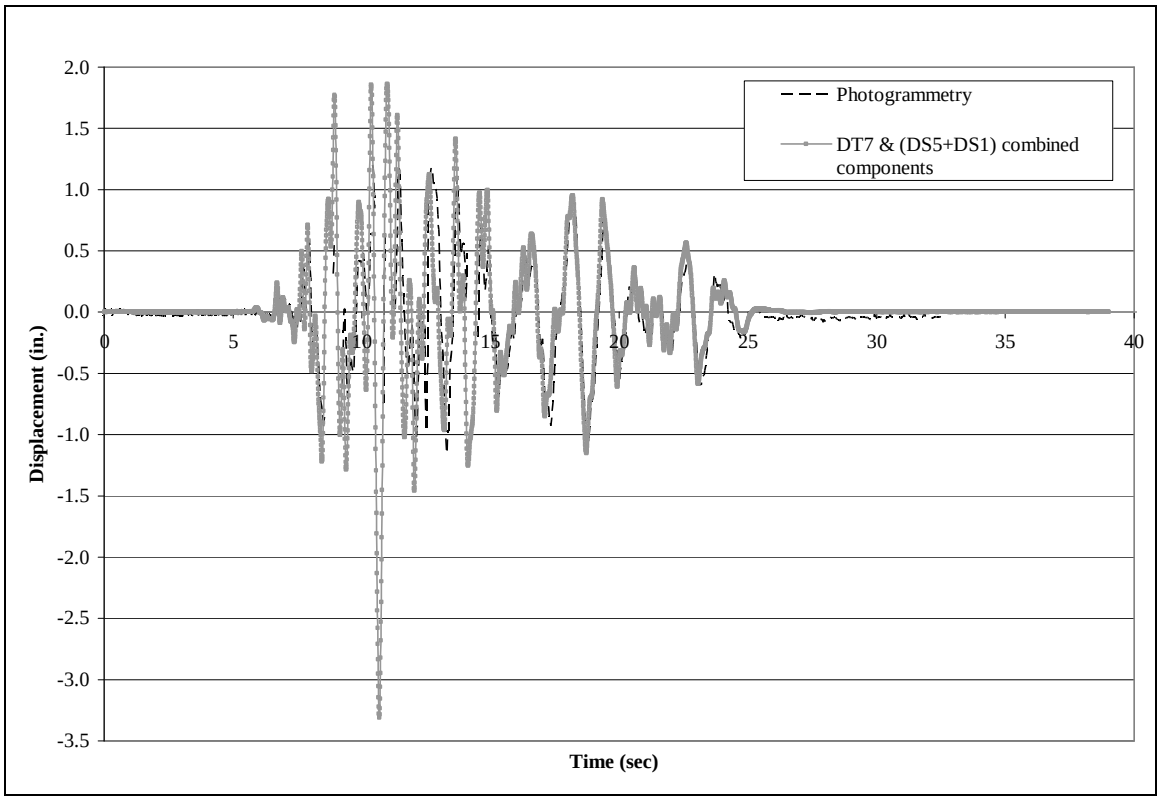

Fig. B-60: Lateral movement of Point 18 for Test 6 (1 in. = 254 mm)

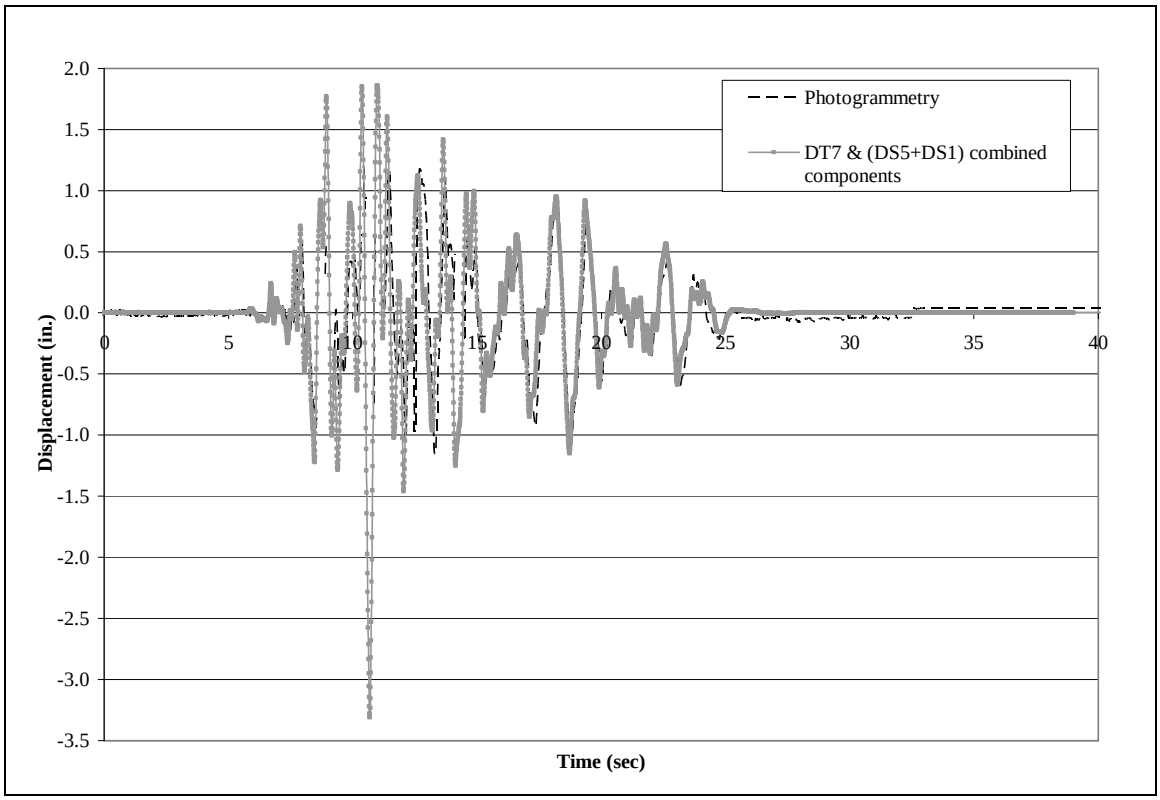

Fig. B-61: Lateral movement of Point 19 for Test 6 (1 in. = 254 mm)

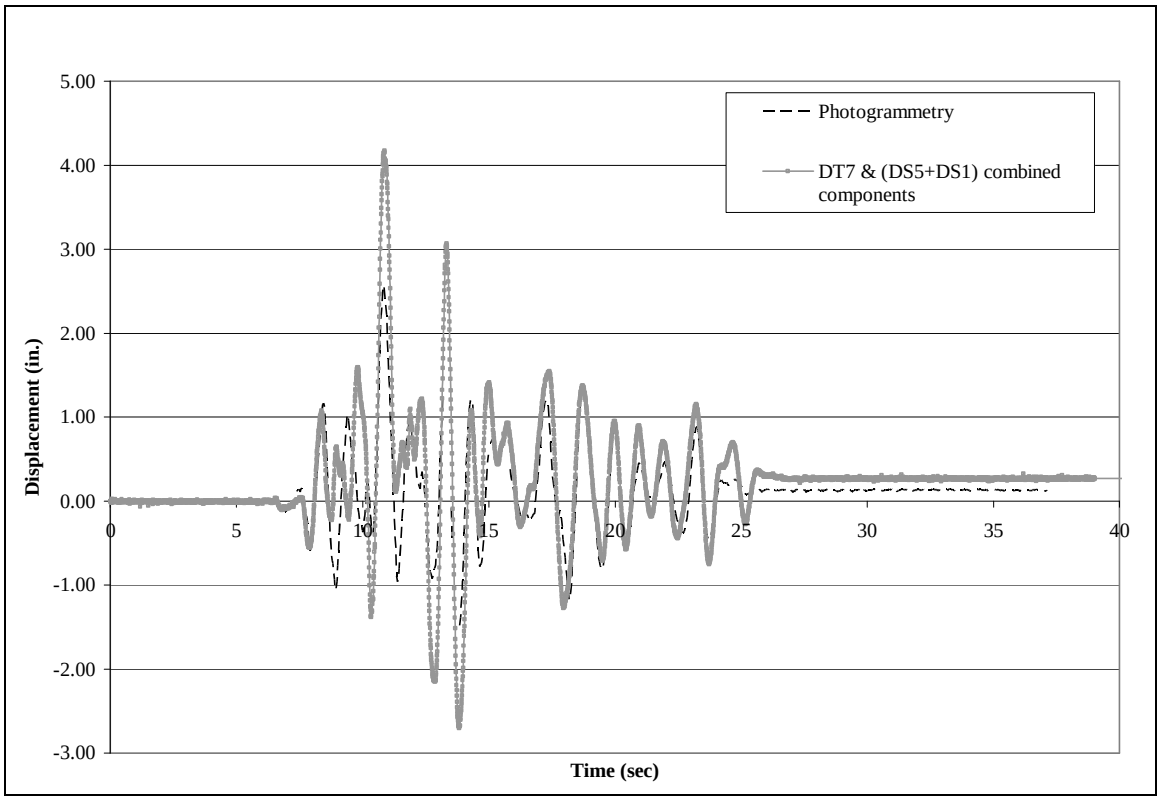

Fig. B-62: Lateral movement of Point 37 for Test 6 (1 in. = 254 mm)

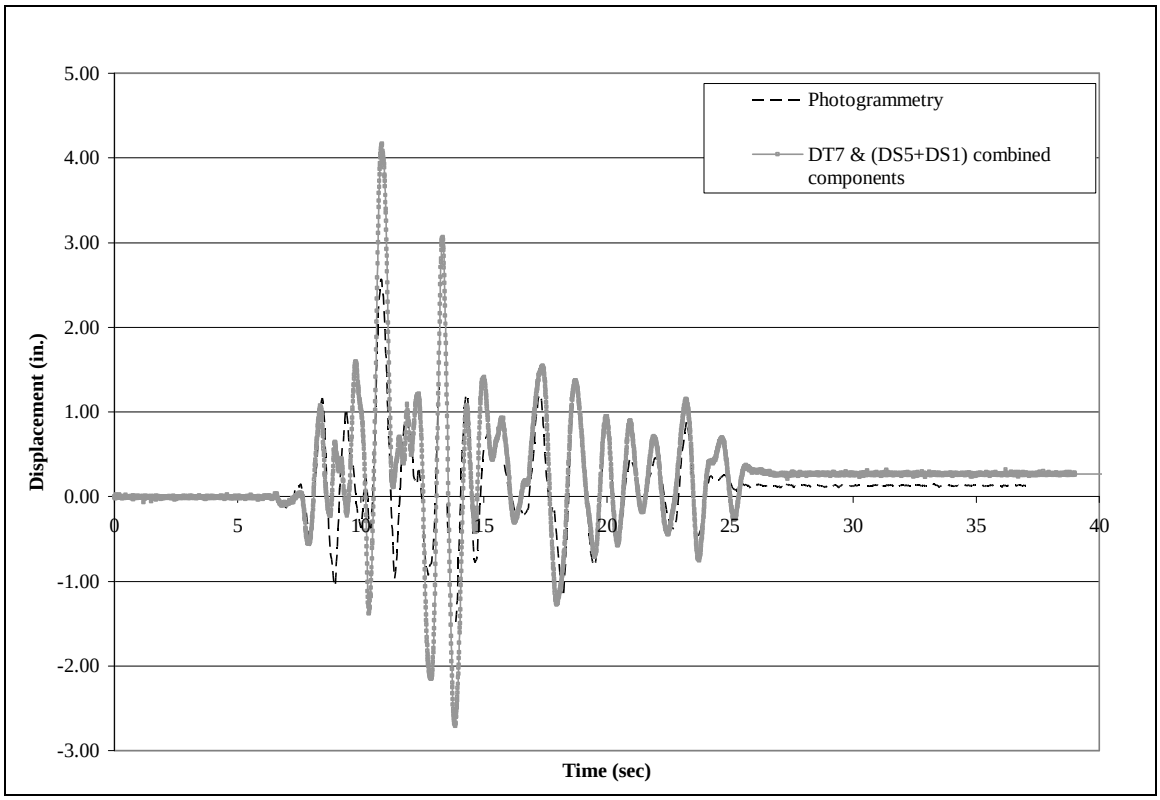

Fig. B-63: Lateral movement of Point 38 for Test 6 (1 in. = 254 mm)

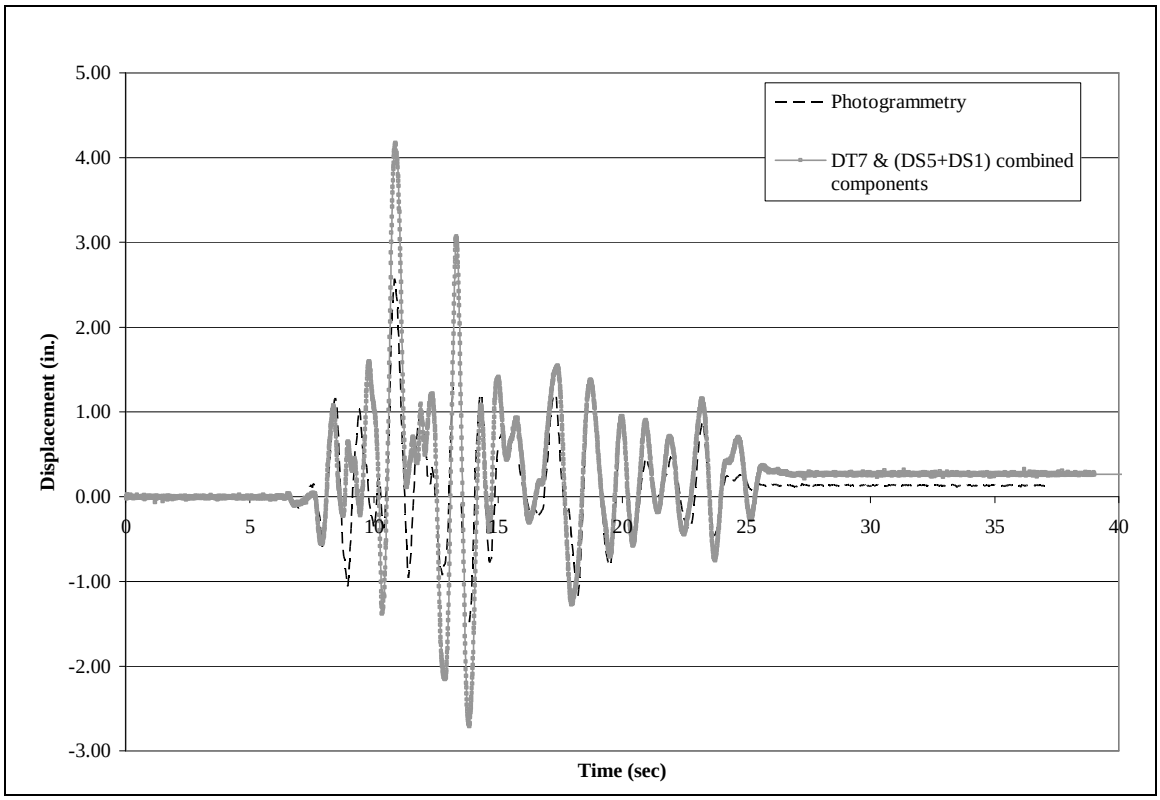

Fig. B-64: Lateral movement of Point 39 for Test 6 (1 in. = 254 mm)

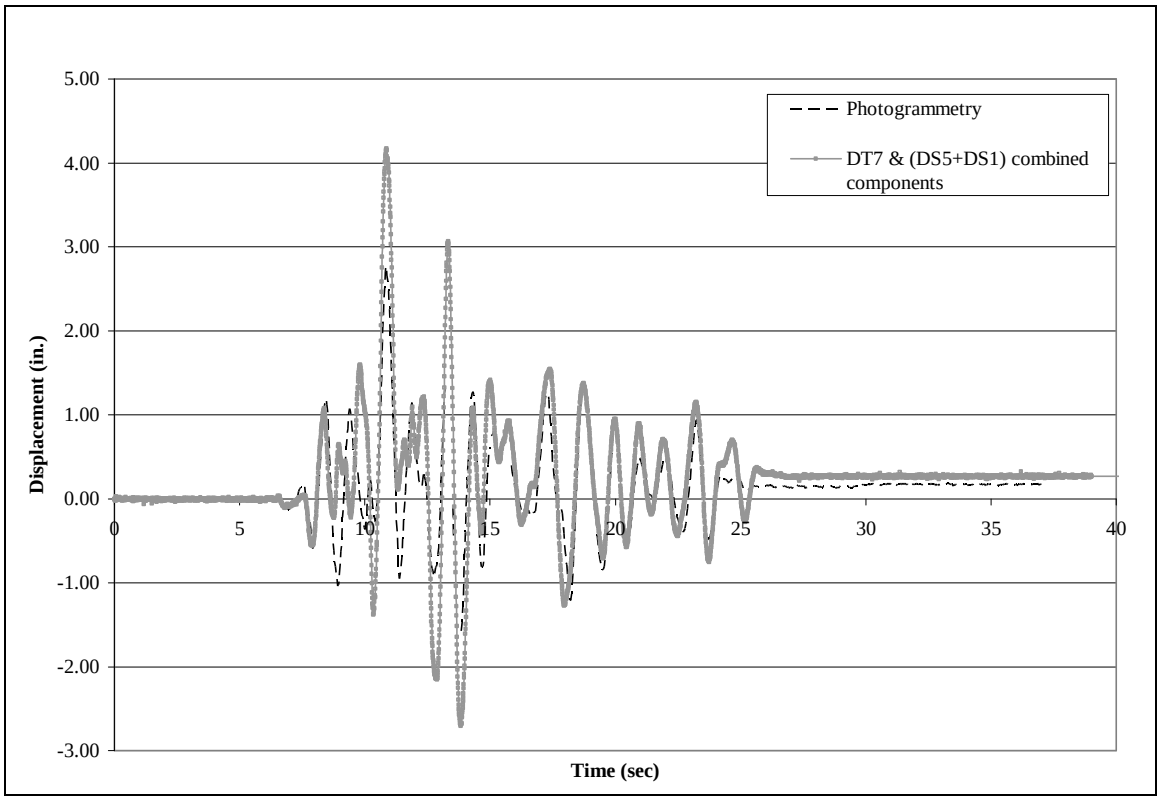

Fig. B-65: Lateral movement of Point 44 for Test 6 (1 in. = 254 mm)

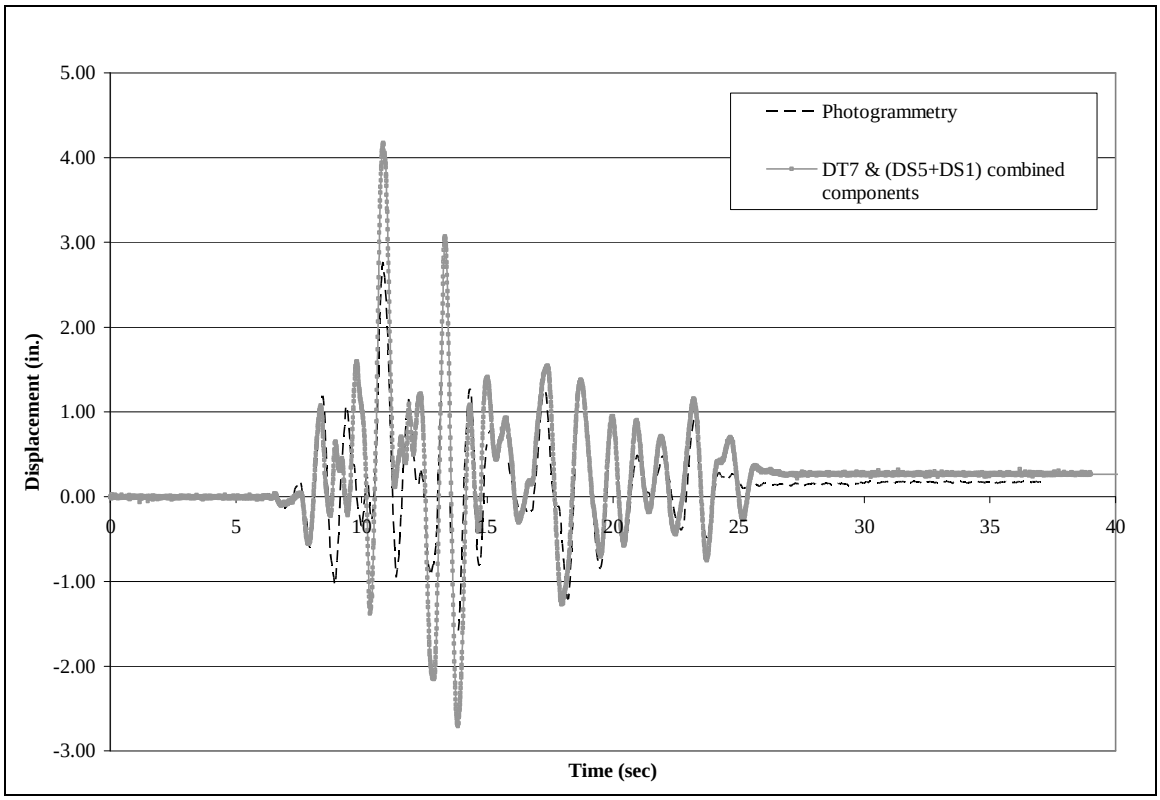

Fig. B-66: Lateral movement of Point 45 for Test 6 (1 in. = 254 mm)

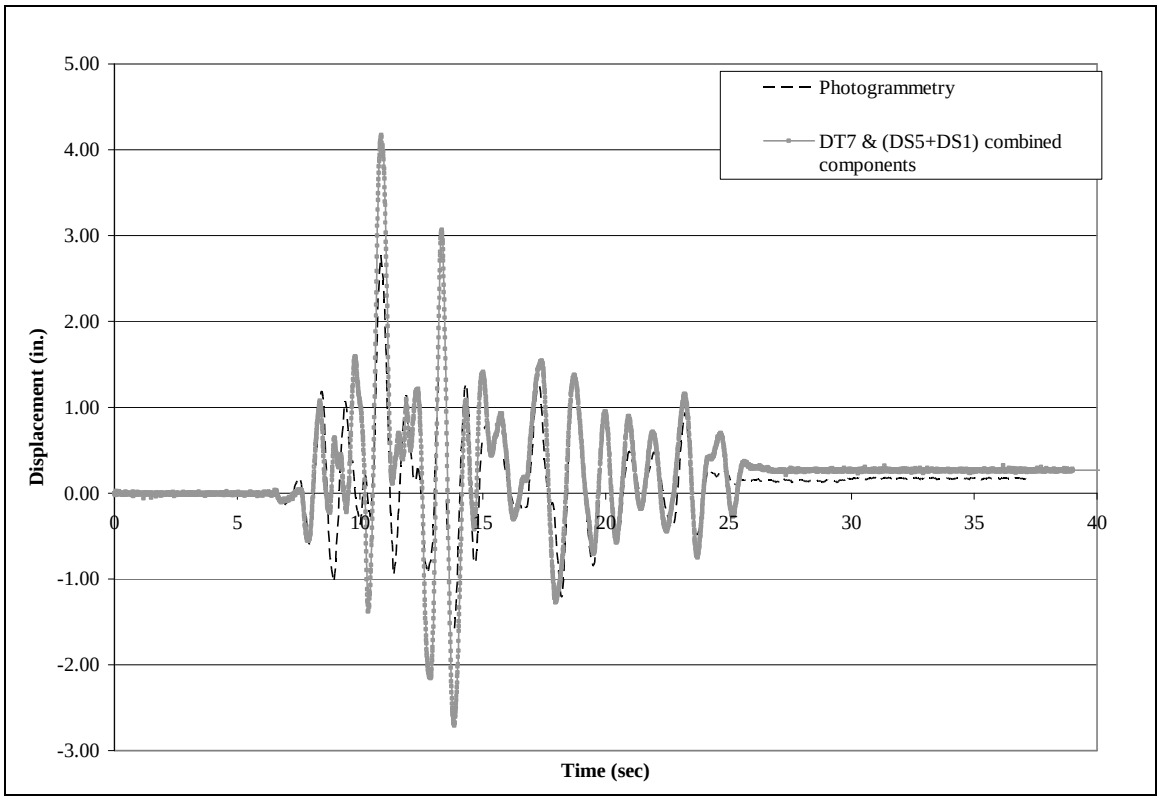

Fig. B-67: Lateral movement of Point 46 for Test 6 (1 in. = 254 mm)

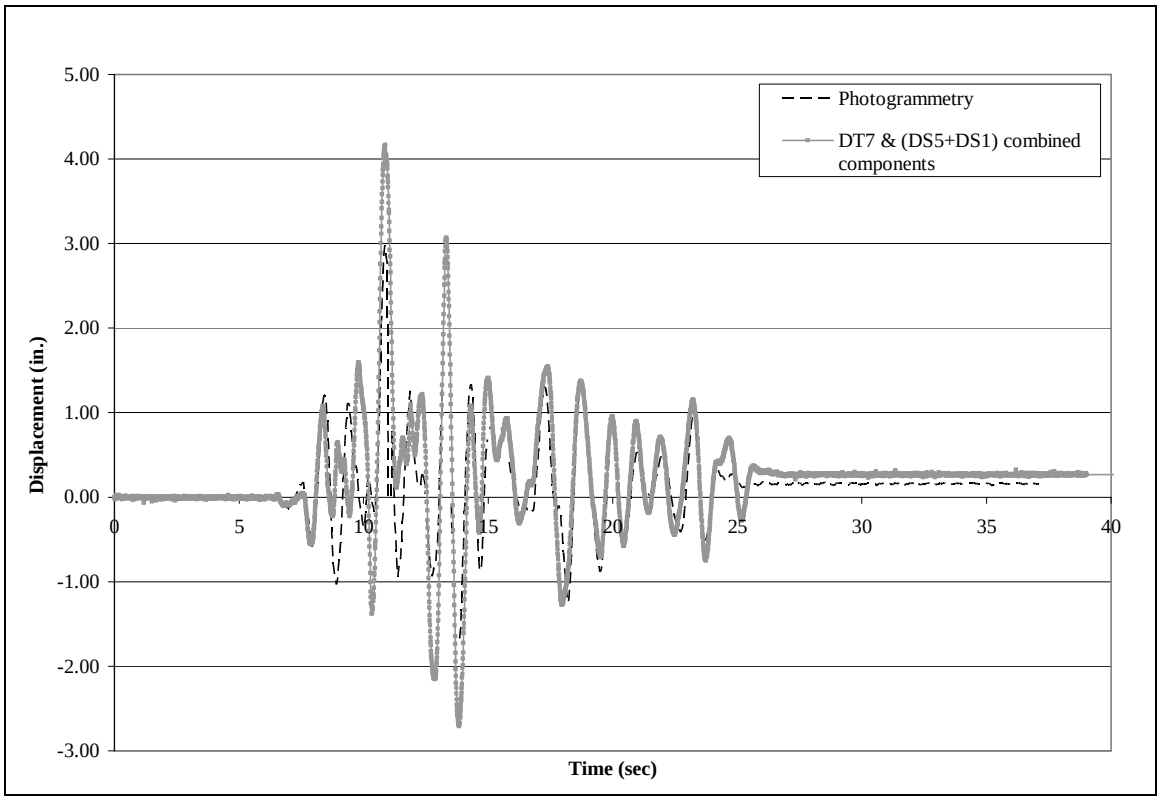

Fig. B-68: Lateral movement of Point 51 for Test 6 (1 in. = 254 mm)

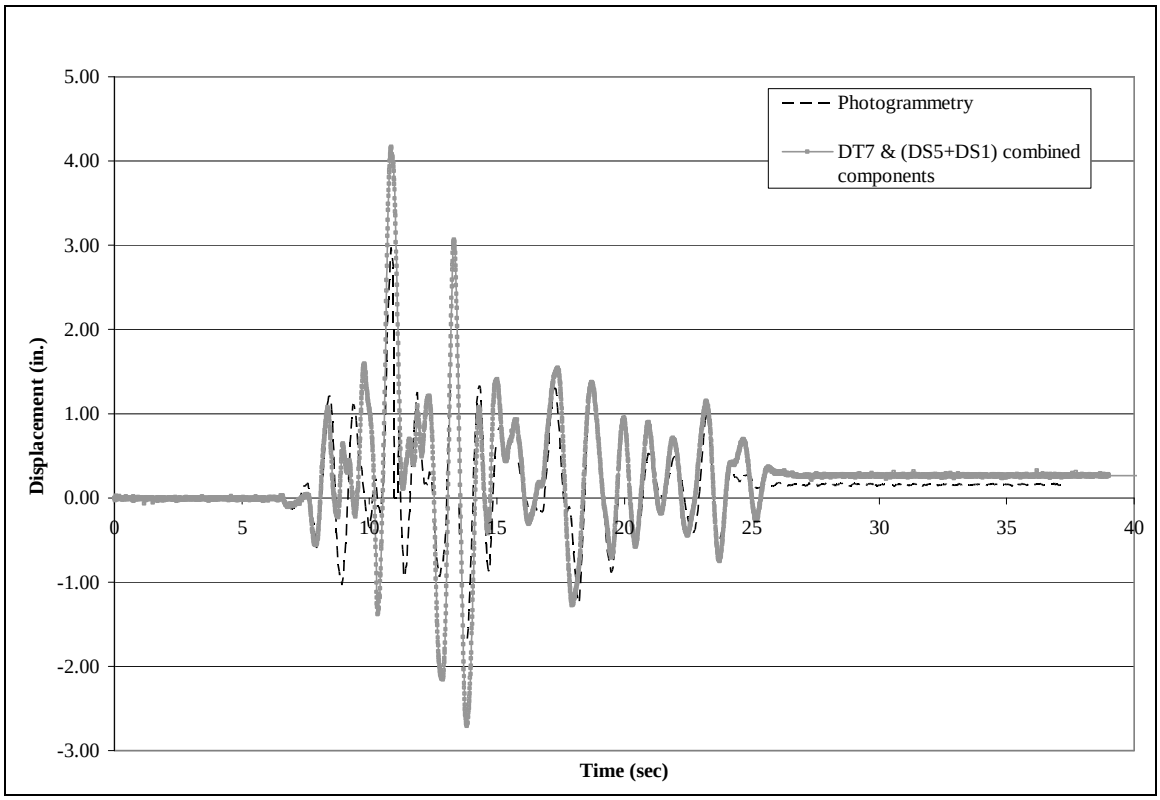

Fig. B-69: Lateral movement of Point 52 for Test 6 (1 in. = 254 mm)

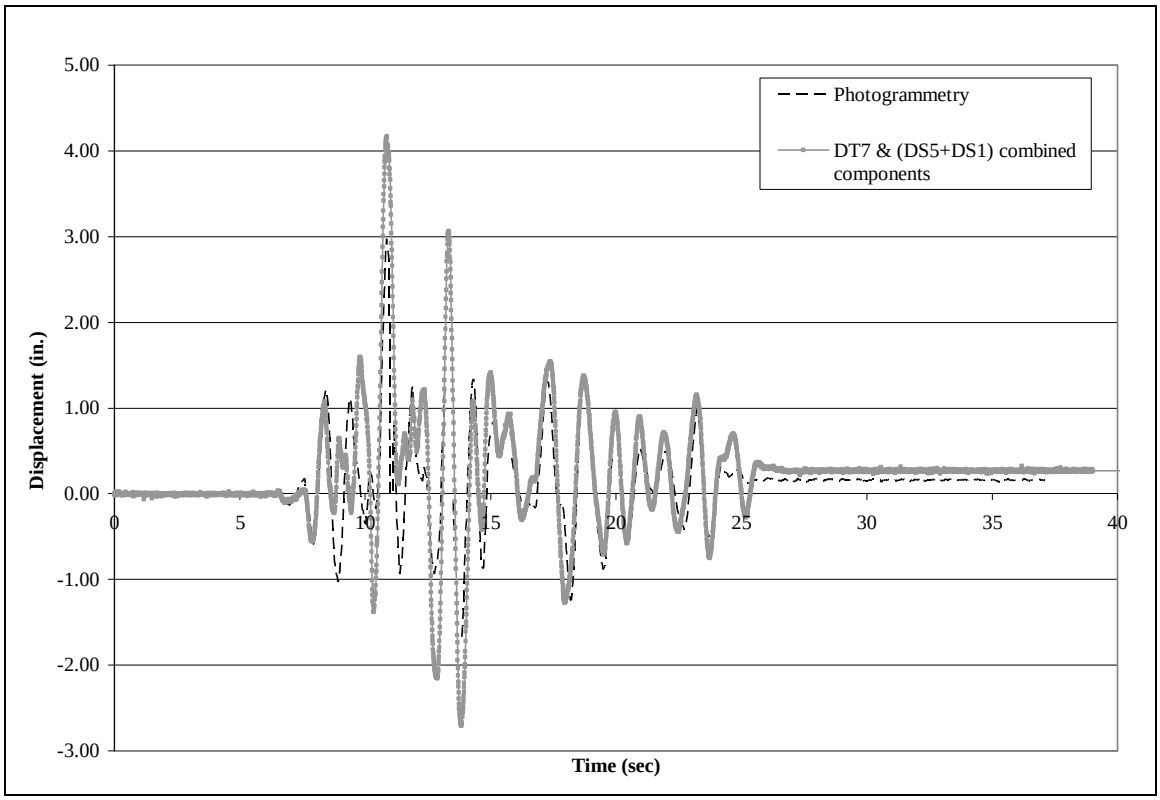

Fig. B-70: Lateral movement of Point 53 for Test 6 (1 in. = 254 mm)

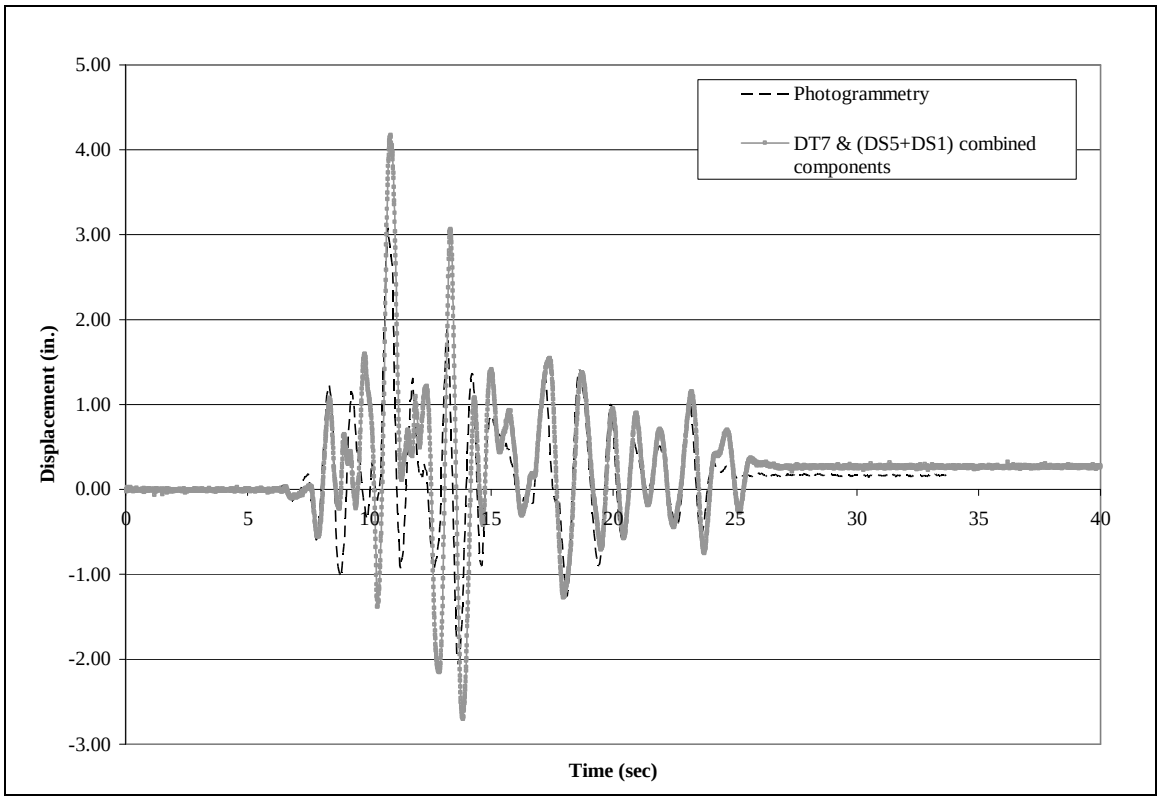

Fig. B-71: Lateral movement of Point 58 for Test 6 (1 in. = 254 mm)

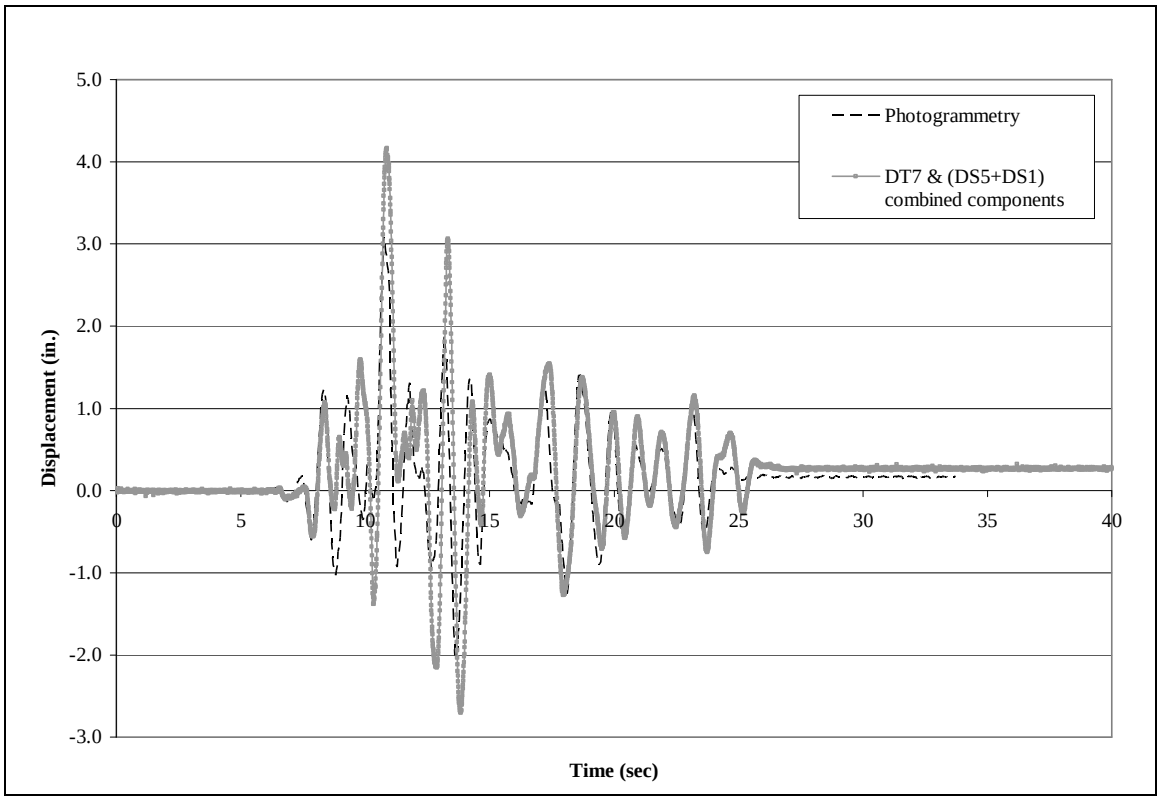

Fig. B-72: Lateral movement of Point 59 for Test 6 (1 in. = 254 mm)

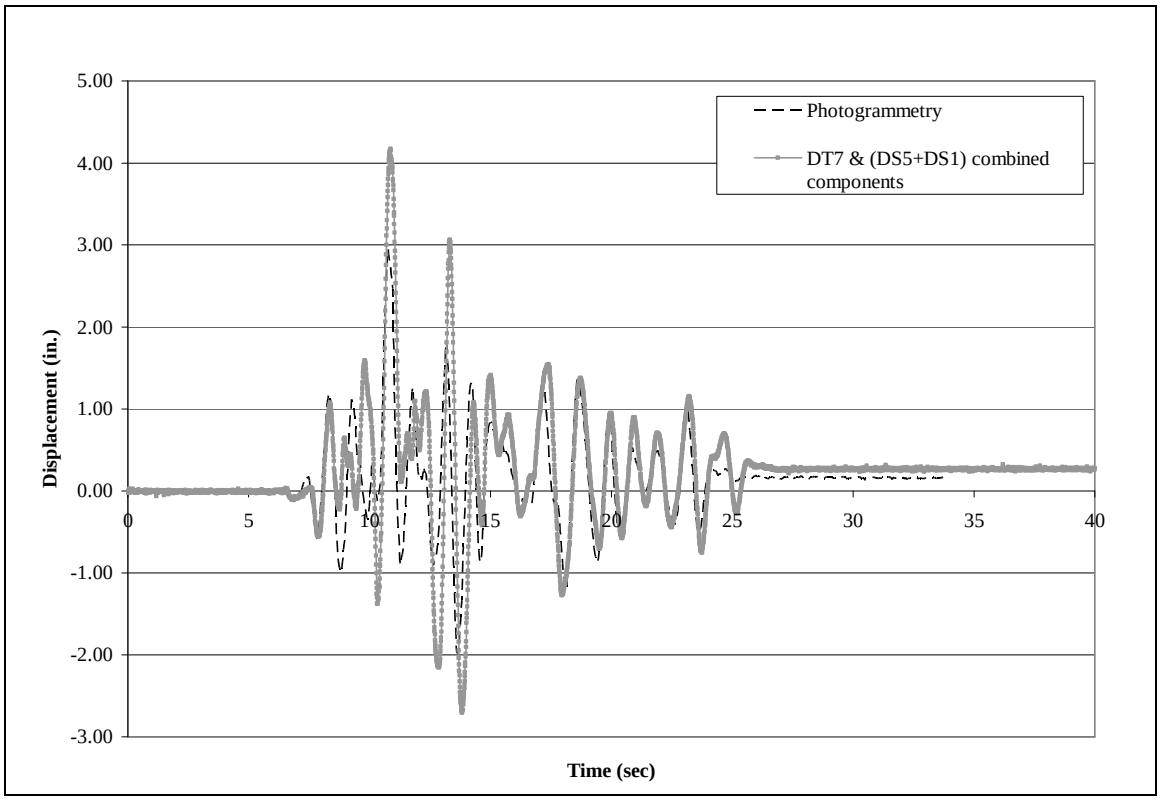

Fig. B-73: Lateral movement of Point 60 for Test 6 (1 in. = 254 mm)